Bitlis Eren Üniversitesi
Fen Bilimleri Dergisi

Bitlis Eren University
Journal of Science

ISSN : 2147-3129
e-ISSN : 2147-3188

Cilt / *Volume*: 11 Sayı / *Number*: 4 Yıl / *Year*: 2022

Yazışma Adresi

Bitlis Eren Üniversitesi
Lisansüstü Eğitim Enstitüsü
13000, Merkez, Bitlis/TÜRKİYE
Tel: 0 (434) 2220071

https://dergipark.org.tr/tr/pub/bitlisfen

BEU FBD

Bitlis Eren Üniversitesi Fen Bilimler Dergisi

Bitlis Eren University Journal of Science

Yıl/*Year:* 2022 - Cilt/*Volume:* 11 - Sayı/*Number:* 4

Editör (Yayın) Kurulu / *Editorial Board*

Danışma Kurulu / *Advisory Board*

Dergi Hakkında / *About Journal*

Bitlis Eren Üniversitesi Fen Bilimleri Dergisi, mühendislik ve temel bilimler alanlarındaki gelişmeleri ve yenilikleri takip etmek, meslek kuruluşlarının, araştırmacıların ve bireylerin ulusal ve uluslararası gelişimlerine katkıda bulunmak ve bu alanlarda elektronik bir kaynak oluşturmak amacıyla yayımlanmaktadır. Derginin yazım dili Türkçe veya İngilizcedir. Fen Bilimleri Dergisi, Bitlis Eren Üniversitesi Lisansüstü Eğitim Enstitüsü yayını olup, 2012 yılından bu yana ücretsiz ve açık erişimli olarak yayın hayatına devam etmektedir. Mühendislik ve temel bilimlerin bilgi tabanına ve teknolojik gelişmelere ışık tutması amacıyla bu alanlarda yapılmış deneysel ve teorik ilerlemeleri konu alan özgün araştırma makalelerine yer verilmektedir. Dergiye gönderilen çalışmaların benzerlik oranı %15'i geçmemelidir. Yazım kurallarına uymayan makaleler, hakemlere gönderilmeden önce düzeltilmek üzere yazara geri gönderilir. Bu nedenle, derginin yazım kuralları dikkate alınmalıdır. Ayrıca, editörlerden yazarlara iletilen düzeltmelere veya taleplere 30 gün içerisinde cevap verilmediği takdirde ilgili makaleler reddedilir. Makaleler şekiller ve tablolar dâhil 20 sayfayı geçmemelidir. Dergiye yayın için gönderilen makaleler en az iki hakem tarafından değerlendirilir. Yazarlardan hakem önerisi talep edilmemektedir. Makalelerin dergide yayımlanabilmesi için hakemler tarafından olumlu görüş bildirilmesi gerekmektedir. Dergi Editör Kurulu, hakem raporlarını (*en aziki hakemin değerlendirmeleri geldikten sonra*) dikkate alarak makalelerin yayımlanmak üzere kabul edilip edilmemesine karar verir. Fen Bilimleri Dergisi, yılda dört defa (*Mart, Haziran, Eylül, Aralık*) yayımlanmaktadır. **Dergimiz Tübitak-Ulakbim Mühendislik ve Temel Bilimler Veri Tabanı Dergi Listesinde taranmaktadır.**

B.E.Ü. Fen Bilimleri Dergisi 11(4), 2022 / *B.E.U. Journal of Science 11(4), 2022*
İÇİNDEKİLER / *CONTENTS*

Bitlis Eren Üniversitesi Fen Bilimleri Dergisi
BİTLİS EREN UNIVERSITY JOURNAL OF SCIENCE
ISSN: 2147-3129/e-ISSN: 2147-3188
VOLUME: 11 NO: 4 PAGE: 943-952 YEAR: 2022
DOI:10.17798/bitlisfen.1107662

AHP Application for Logistics Center Location Selection According to Criteria

Burçin PAÇACI [1 *], Serpil EROL[2], M. Kürşat ÇUBUK[1]

[1]*Gazi Üniversitesi, Mühendislik Fakültesi, İnşaat Mühendisliği Bölümü, ANKARA,*
[2]*Gazi Üniversitesi, Mühendislik Fakültesi, Endüstri Mühendisliği Bölümü, ANKARA,*
(ORCID:0000-0001-6053-0458) (ORCID:0000-0002-6885-3849) (ORCID:0000-0001-8155-7123)

Keywords: Logistic, Economy, Transportation, Multi-criteria selection, AHP.

Abstract
Today, logistics is effective in every field and has an important share in the revival of both domestic and foreign trade. The rapid increase in competition in global trade has increased the importance of the logistics sector and, accordingly, logistics centers. With well-planned and high-performance logistics centers in our country, the contribution of the logistics sector to the economy will increase and it will be ensured that our country is a logistics base in international transport corridors. In this study, criteria were determined by conducting a comprehensive literature review for logistics center location These criteria consist of seven main criteria, namely population, economy, cost, socio-economic status, infrastructure, geographical location and service, and twenty-seven sub-criteria belonging to these main criteria. The criteria were evaluated by benefiting from the opinions of experts in the field of logistics, and the order of importance of the main and sub-criteria determined for the logistics center location determination was found by AHP methods.

1. Introduction

With the systematic and efficient realization of logistics activities, time and cost will be gained in global trade, where competition is rapidly increasing [1]. In order to reduce the cost of logistics facilities and to ensure a better flow of materials, efficient/effective design of distribution centers is required [2]. The development of a logistics center network at the national and international level is a prerequisite for the transport and logistics chain [3].

The main purpose of logistics is to minimize the cost in the supply chain. While the rate of logistics cost is 20% in underdeveloped countries, this rate varies between 3% and 5% in industrialized countries [4]. In addition, a 5% improvement in logistics costs, including shipping, storage, management costs, and inventory costs, is considered equivalent to a 20% improvement in sales. According to a report published by the World Bank, while the ratio of logistics costs to GNP (Gross National Product) is around 10% in developed countries, this ratio is around 30% in developing countries [5]. This difference in rates shows that the cost will be greatly reduced with a well-designed and developed logistics network.

Logistics centers with high performance also have high profits and can provide services both regionally and globally. The profit of logistics centers where both domestic and foreign investors can be used effectively is higher. For this reason, the location of logistics centers should be designed in such a way as to get the most efficiency both in the region and internationally. In order to achieve the desired success in this regard, it is necessary to know the characteristics of the regions such as income sources and employment rates, to evaluate the geographical location in the best way, and to plan the logistics center design for the future correctly. Therefore, factors such as the needed facilities and applicability are important in order to achieve high performance in the logistics center application [6].

In this study, the relevant studies for the logistics center location determination were examined in detail and new criteria were found by taking into account the opinions of experts in the field. The importance levels of these criteria, which were determined for the location of the logistics center,

*Corresponding author: burcinpcc@gmail.com
Received:25.04.2022, Accepted:28.08.2022

relative to each other were found by using the AHP technique by taking the opinions of experts in the field of logistics.

2. Method

In this study, criteria were determined in detail with a comprehensive literature review in line with the opinions of experts in the field of logistics. The knowledge, experience and opinions of nine experts in the field of logistics were take advantage to rank the criteria determined for the location of the logistics center according to each other. These people consist of faculty members in the Industrial Engineering, Civil Engineering, Logistics, City and Regional Planning departments of universities, members of LODER (Logistics Association) and engineers working in the relevant department of TCDD (State Railways of the Republic of Turkey), which carries out the establishment of logistics centers in Turkey. After criterias determined, these criterias were ranked according to weights of importance using the AHP method for the most appropriate logistic center location selection.

2.1. Criteria Selection For The Logistics Center

Many studies have been examined to determine the logistics center location selection criteria. By evaluating these studies, seven main criteria and 27 sub-criteria have been established in line with the opinions of experts in the field. Table 1 shows the studies examined for the criteria determined for the logistics center location selection. These criteria are given below.

1. Population Main Criterion: It expresses the population amount in the province where the logistics center is planned to be established.
2. Economy Main Criterion: It expresses the economic activities of the province where the logistics centers are planned to be established. It consists of five sub-criteria: “Organized Industrial Zone”, “Agricultural Organized Industrial Zone”, “Tourism Activities”, “Export and Import Ratio”, and “Border Gates” covers the criterion. The definitions of these sub-criteria are given below.
   - ✓ Organized Industrial Zone: It refers to the areas (hectares) of the existing organized industrial zones in the province where a logistics center is planned to be established.
   - ✓ Agricultural Organized Industrial Zone: It refers to the areas (decares) of the agricultural organized industrial zones that were put into operation and in the project phase in the province where a logistics center is planned to be established.
   - ✓ Tourism Activities: It expresses the tourism activities in the province where the logistics center is planned to be established.
   - ✓ Export and Import Ratio: It has been determined as the trade volume of the province where the logistics center is planned to be established, and it represents the sum of export and import amounts.
   - ✓ Border Gates: It refers to the presence of active iron, sea, land, and air border gates in the province where a logistics center is planned to be established.
3. Cost Main Criterion: It has been evaluated as a cost parameter for the logistics center planned to be established and consists of the sub-criteria of “Expropriation Cost”, “Installation Cost”, and “Infrastructure Cost”. The explanations of these sub-criteria are explained below.
   - ✓ Expropriation Cost: It refers to the required cost for the expropriation of the location where the logistics center is planned to be established.
   - ✓ Installation Cost: It indicates the required cost for the establishment of the logistics center planned to be established.
   - ✓ Infrastructure Cost: It expresses the infrastructure costs of required transportation connections such as highway and railway for the province of the logistics center is planned to be established.
4. Socio-Economic Status Main Criterion: It expresses the socio-economic status in the province where the logistics center planned to be established. It consists of six sub-criteria as “Employment Rate”, “Labor Force Participation Rate”, “Unemployment Rate”, “Educational Activities”, “Health Activities” and “Cultural Activities”. The explanations of these sub-criteria are explained below.
   - ✓ Employment Rate: It refers to the employment rate of the province where the logistics center is planned to be established.
   - ✓ Labor Force Participation Rate: It refers to the labor force participation rate of the province where the logistics center is planned to be established.
   - ✓ Unemployment Rate: It expresses the unemployment rate of the province where a logistics center is planned to be established.
   - ✓ Educational Activities: It refers to educational activities such as the number of

students at universities in the province where a logistics center is planned to be established.

- ✓ Health Activities: It refers to the health activities of the province where the logistics center is planned to be established.
- ✓ Cultural Activities: It refers to cultural activities such as fairs, symposiums and congresses in the province where a logistics center is planned to be established.

5. Infrastructure Main Criterion: It expresses the existence of transportation infrastructure such as airport, port, railway in the province where a logistics center is planned to be established. It consists of "Capacity", "Equipment" and "Transfer Facilities" sub-criteria. The definitions of these sub-criteria are given below.

- ✓ Capacity: It refers to transportation systems network such as the road, railway, airports and ports which are available to set in the province where a logistics center is planned to be established.
- ✓ Equipment: It expresses as the number of vehicles such as cargo planes, ships, trucks used in the freight transportation in the province and transportation network such as airports, railway and ports of that province where a logistics center is planned to be established.
- ✓ Transfer Facilities: It has been evaluated as the existing railway station, port, airport and road connection used in freight transportation in the province where a logistic center is planned to be established.

6. Geographical Location Main Criterion: It refers to the location of the province where the logistics center is planned to be established. It consists of six sub-criteria as "Land Structure", "Natural Events", "Accessibility", "Distance to Logistics Centers", "Distance to Supplier" and "Distance to Market". This sub-criteria are listed below.

- ✓ Land Structure: It is defined as the percentage expression of the mountainous or flat areas of the province where a logistics center is planned to be established.
- ✓ Natural Events: It refers to natural disasters such as avalanches, landslides and floods of the province where a logistics center is planned to be established.
- ✓ Accessibility: It refers to the calculation of the accessibility levels of road, airway, seaway and railway network of the province where a logistics center is planned to be established with considering all of them together [7].
- ✓ Distance to Logistics Centers: It expresses the distances between the province where the logistics center is planned to be established and the logistics center in other province.
- ✓ Distance to Supplier: It indicates the distance between the province where a logistics center is planned to be established and the capital cities of the importing countries of this province.
- ✓ Distance to Market: It indicates the distance between the province where a logistics center is planned to be established and the capitals of the countries that this province exports to.

7. Service Main Criteria: Four sub-criteria have been determined as "Delivery Time", "Risks", "Environmental Sensitivity" and "Reliability". These sub-criteria are defined as follows.

- ✓ Delivery Time: It refers to the transportation time of the cargo carried between the export and import countries of the province where the logistics center is planned to be established. In this criterion, the type of used transportation and distance between provinces is important.
- ✓ Risks: It is expressed as the climatic conditions of the province where the logistics center is planned to be established.
- ✓ Environmental Sensitivity: It is defined as establishing a connection with the carbon emission values of the used transportation systems in the province where the logistics center is planned to be established.
- ✓ Reliability: It refers to the socio-economic development ranking in Turkey in order to foresee a more effective use of the province where the logistics center is planned to be established in the future.

Table 1. Studies on logistics center location selection

Studies	Criteria						
	Population	Economy	Cost	Infrastructure	Geographical Location	Socia-Economy Status	Service
Xie, et al., [8].	✓		✓	✓			✓
Duyguvar, [9].	✓	✓	✓	✓	✓	✓	✓
Karagülle, [10].	✓			✓	✓	✓	✓
Reis, et al., [11].		✓		✓	✓		✓
Orjuela-Castro, et al., [12].		✓	✓				✓
Zhou, et al., [13].		✓					
Anatol"yevna, et al., [14].		✓		✓	✓		✓
Kıvrak, [15].		✓	✓				✓
Kutsal, [16].		✓		✓	✓		
Kabak, et al., [17].		✓		✓			
Elgün, et al., [18].		✓				✓	
Ors, et al., [19].		✓	✓				
Pérez, et al., [20].		✓		✓	✓		✓
Grine, et al., [21].		✓		✓	✓		✓
Khongkan, et al., [22].		✓		✓	✓	✓	
Alumur, et al., [23].		✓		✓	✓	✓	
Vilko, et al., [24].			✓	✓	✓		✓
Smilowitz, et al., [25].		✓	✓				

2.2. Determination of Criterion Weights with AHP

Many studies have been carried out in the field of logistics with the use of the AHP method. In smart city development, management, economy, livability, people, mobility, and environment criteria were evaluated using the AHP method for the logistics function [26]. In order to evaluate the logistics performance in the postal sector, the importance weights of reliability, delivery time, convenience, flexibility, cost, return on assets, relationship, and innovation criteria are listed using the AHP method [27]. The AHP method was used to determine the importance weights of cost, product, supply, and order criteria for logistics operations in distribution centers [28]. The criteria for supplier selection based on AHP were determined as cost, operational efficiency, service quality, and technology level [29]. The best reverse logistic provider was selected with quality, reverse logistics cost, shipping, and technical capability criteria by using the AHP method [30]. The economic, technical, social, and natural criteria for emergency logistics center location selection are listed by the AHP method [31]. The cities of Doboj, Banja Luka, and Samac were ranked for logistics center location selection using the AHP technique with the criteria of available surface, land price, geographical location, affiliation to the form of transport, macro and micro level, and approach ways accessibility transport [32].

2.2.1. Analytical Hierarchy Process

The criteria of different individuals for the same problem and the importance levels of these criteria differ [33]. While choosing among the alternatives, the decision maker should choose the most suitable one among the criteria and rank the alternatives according to their degrees. In this case, Analytical Hierarchy Process (AHP), one of the multi-criteria decision making methods, helps the decision maker [34]. AHP is developed by Thomas L. Saaty in 1971. AHP allows decision makers to model in a hierarchical structure that shows the relationship between complex problems, the main goal of the problem, criteria, sub-criteria and alternatives [35]. Ease of use in group decisions and the ability to handle inconsistency in judgments are the biggest advantages of AHP when compared to other multi-criteria methods [36]. The most important advantage of AHP is that it is a simple method [37]. The purpose of this study is to inform the reader about the use of AHP for logistics center location selection.
The steps of the AHP method are given below.
Steps of the AHP method [33]:

1. Hierarchical structure: In this step, the decision problem is structured hierarchically. The created hierarchical structure is the most important part of the decision-making process. At the top of this structure is the purpose of the question, the criteria are in the next section, and the alternatives are in the last section.
2. Pairwise comparison matrix: In this step, the comparison matrix of the criteria is created. This comparison matrices with n × n dimensions is a square matrix. Each criterion is compared one-to-one according to its importance values, and the importance scale in Table 2 is used for this comparison.

Table 2. Fundamental scale [38]

Intensity of Importance	*Definition*	*Explanation*
1	Equal Importance	Two activities contribute equally to the objective
2	Weak or slight	
3	Moderate importance	Experience and judgment slightly favor one activity over another
4	Moderate plus	
5	Strong importance	Experience and judgment strongly favor one activity over another
6	Strong plus	
7	Very strong or demonstrated importance	An activity is favored very strongly over another; its dominance demonstrated in practice
8	Very,very strong	
9	Extreme importance	The evidence favoring one activity over another is of the highest possible order of affirmation
1.1–1.9	When activities are very close a decimal is added to 1 to show their difference as appropriate	A better alternative way to assigning the small decimals is to compare two close activities with other widely contrasting ones, favoring the larger one a little over the smaller one when using the 1–9 values.
Reciprocals of above	If activity *i* has one of the above nonzero numbers assigned to it when compared with activity *j*, then *j* has the reciprocal value when compared with *i*	A logical assumption
Measurements from ratio scales		When it is desired to use such numbers in physical applications. Alternatively, often one estimates the ratios of such magnitudes by using judgment

3. Normalization of relationship matrices: In this step, First, the sum of each matrix column divided by the values of the column elements.

$$B_i = \begin{bmatrix} b_{11} \\ b_{21} \\ \cdot \\ \cdot \\ \cdot \\ b_{n1} \end{bmatrix} \qquad b_{ij} = \frac{a_{ij}}{\sum_{i=1}^{n} a_{ij}}$$

Then its importance values (Wi) for a criterion are determined by dividing it in one score levels and matrix size.

$$C = \begin{bmatrix} b_{11} & b_{12} & \cdots & b_{1n} \\ b_{21} & b_{22} & \cdots & b_{2n} \\ \cdot & & & \cdot \\ \cdot & & & \cdot \\ \cdot & & & \cdot \\ b_{n1} & b_{n2} & \cdots & b_{nn} \end{bmatrix} \qquad w_i = \frac{\sum_{j=1}^{n} c_{ij}}{n}$$

After these calculations, the decision matrix is obtained. Finally, the percentage distribution at the decision points is obtained by multiplying the decision matrix by the W column vector. Decision

options can now be prioritized, starting with the highest overall score.

4. Consistency ratio: Since the comparisons are subjective, the consistency rate is calculated. If the calculated rate is below 10%, it is considered sufficient. A low consistency ratio indicates that the decision maker's decisions in pairwise comparisons are consistent, while a high consistency ratio shows that inconsistent.

2.2.2. Determination of Criterion Weights

The main and sub-criteria determined in this study were evaluated in line with the knowledge, experience, and opinions of experts in the field of logistics, and the importance levels of these criteria were listed according to the AHP technique with the help of Super Decision.

The results of the main criteria of "Population", "Economy", "Cost", "Socio-Economic Status", "Infrastructure", "Geographical Location", and "Service" are shown in Table 3 according to the AHP method.

Table 3. The ratios of importance weights of the main criteria

Criteria	Importence weights
Population	0,048124649
Economy	0,242694409
Cost	0,1090094
Socio-Economic Status	0,12460071
Infrastructure	0,186011467
Geographical Location	0,216640538
Service	0,072918826

The main criterion of "Economy" takes the first place in the order of importance weights of the main criteria. The main criteria of "Economy" are followed by "Geographical Location", "Infrastructure", "Socio-Economic Situation", "Cost", "Service", and "Population" main criteria.

The sub-criteria of "Economy", "Cost", "Socio-Economic Status", "Infrastructure", "Geographical Location" and "Service" main criteria were found by applying the AHP technique. The results of the sub-criteria of the "Economy" main criterion according to the AHP method are shown in Table 4.

Table 4. Importance weights of sub-criteria of the "Economy" main criteria

Criteria	Importence weights
Organized Industrial Zone	0,32057
Agricultural Organized Industrial Zone	0,187285
Tourism	0,111853
Export and Import Ratio	0,270581
Border Gates	0,109711

"Organized Industrial Zone" takes first place in the ranking of the importance weights of the sub-criteria of the "Economy" main criterion. "Organized Industrial Zone" is followed by the sub-criteria "Export and Import Ratio", "Agricultural Organized Industrial Zone", "Tourism", "Border Gates", respectively.

The results of the sub-criteria of the "Cost" main criterion according to the AHP method are shown in Table 5.

Table 5. Importance weights of sub-criteria of the "Cost" main criteria

Criteria	Importence weights
Expropriation Cost	0,340139
Installation Cost	0,235791
Infrastructure Cost	0,424069

"Infrastructure Cost" takes the first place in order the importance weights of the sub-criteria of the "Cost" main criterion. This is followed by the "Expropriation Cost" and "Installation Cost" sub-criteria, respectively.

The results of the sub-criteria of the main criterion of "Socio-Economic Status" according to the AHP method are shown in Table 6.

Table 6. Importance weights of sub-criteria of the "Socio-Economic Status" main criterion

Criteria	Importence weights
Employment Rate	0,238598
Labor Force Participation Rate	0,275392
Unemployment Rate	0,178447
Educational Activities	0,141643
Health Activities	0,090562
Cultural Activities	0,075359

In ordering the importance weights of the sub-criteria of the "Socio-Economic Status" main criterion, "Labor Force Participation Rate" has the highest importance weight ratio, and "Employment

Rate", "Unemployment Rate", "Educational Activities", "Health Activities" and "Cultural Activities" follows this order respectively.

The results of the sub-criteria of the "Infrastructure" main criterion according to the AHP method are shown in Table 7.

Table 7. Importance weights of sub-criteria of the "Infrastructure" main criteria

Criteria	Importence weights
Capacity	0,426414
Equipment	0,235696
Transfer Facilities	0,337891

"Capacity" takes the first place in order the importance weights of the sub-criteria of the "Infrastructure" main criterion. The sub-criteria of "Transfer Facilities" and "Equipment" follow this ranking respectively.

The results of the sub-criteria of the "Geographical Location" main criterion according to the AHP method are shown in Table 8.

Table 8. Importance weights of sub-criteria of "Geographical Location" criteria

Criteria	Importence weights
Land Structure	0,108562
Natural Events	0,088571
Accessibility	0,309495
Distance to Logistics Centers	0,109472
Distance to Supplier	0,194161
Distance to Market	0,189738

In the ranking of the importance weights of the sub-criteria of the main criterion of "Geographical Location", the sub-criterion of "Accessibility" takes the first place. This ordering is–followed by sub-criteria of the "Distance to Supplier", "Distance to Market", "Distance to Logistics Centers", "Land Structure", and "Natural Events" respectively.

The results of the sub-criteria of the "Service" main criterion according to the AHP method are shown in Table 9.

Table 9. Importance weights of sub-criteria of "Service" main criteria

Criteria	Importence weights
Delivery time	0,201005
Risks	0,268229
Environmental Sensitivity	0,264372
Reliability	0,266394

The "Risks" sub-criterion ranks first in the ranking of the importance weights of the sub-criteria of the "Service" main criterion. This ranking is followed by the sub-criteria of "Reliability", "Environmental Sensitivity" and "Delivery Time".

3. Conclusion and Suggestions

In this study for logistics center location selection, the order of importance of seven main criteria consisting of "Population", "Economy", "Cost", "Socio-Economic Status", "Infrastructure", "Geographical Location", and "Service" is ranked by taking the opinions of experts in the field using the AHP method. These criteria were evaluated separately according to the AHP technique by taking the opinions of experts in the field of logistics and their importance weights were found according to each other.

In this study conducted for the logistics center location selection, the most important criterion among the seven main criteria, namely "Population", "Economy", "Cost", "Socio-Economic Status", "Infrastructure", "Geographical Location", and "Service", was found to be the "Economy" criterion. In this case, logistics centers should be established in these regions to easily realize the product flow in the regions where economic activities are carried out effectively. Among the main criteria, the population criterion was found to be the criterion with the least importance.

Organized industrial zones were found to have the highest importance in the order of importance of the sub-criteria of the "Economy" main criterion. The production sector has the biggest share of foreign trade in Turkey [39]. For this reason, establishing logistics centers in regions where industrial zones are denser will support the manufacturing sector and provide incentives for production in these regions.

In the sub-criteria of the "Cost" main criterion, the infrastructure cost has been took the first place. This result shows that infrastructure has an important share in terms of the functioning of logistics centers. While the logistics center institution requires more costs for a place with weak transportation infrastructure, the transportation of the products will be more systematic, economical, and easier with the establishing logistics center in a developed transportation network.

The labor force participation rate among the sub-criteria of the "Socio-Economic Status" main criterion has been evaluated as the most important criterion. Establishing logistics centers in places with the highest labor force participation rate will allow for an increase in employment.

When sub-criteria of the "Infrastructure" main criterion is evaluated, it has been concluded that capacity is the most important criteria among the sub-criteria of infrastructure criteria. The developed network structures of railway, sea, air, and road transportation systems and the high transportation potential will ensure that the product flow of logistics centers is easy.

The accessibility sub-criterion has been determined as the most important sub-criterion in the logistics center location selection among the "Geographical Location" main criterion. Using all of the transportation systems in a logistic center will provide the product transportation easier, faster, and more economical. The importance of distance to logistics centers and land structure criteria have been found very close to each other.

The risks sub-criterion is the most important criterion among "Service" main criterion. According to expert opinions, parameters that may constitute a risk such as climate change have been an important place for the logistics center location. Reliability and environmental sensitivity criteria have been found close importance to the risk criteria, and delivery time has been found the least importance.

Our country"s transportation systems should have a more developed network structure and work systematically to be a logistic base in the region. Turkey should devolop coordination between regions and establish connections both within the borders of the country and between the border countries to have a larger share in the logistic field. Also, customs should be facilitated, multimodal transportation should be supported, logistics activities should be rehabilitated, information flow should be accelerated by closely observed technology, modernization in transportation systems should be ensured and infrastructure deficiencies should be eliminated.

References

[1] M. Kaynak, "Uluslararası taşımacılık ve lojistik bağlamında Avrasya ulaştırma koridorlarında bölgesel rekabet ve Türkiye," *4.Türkiye İktisat Kongresi,* vol. 15, pp.3-34, May 2004.

[2] Yücel, M. and Ş. K. Yılmaz, "Türkiye"deki lojistik köyler ve seçimine etki eden unsurlar," *Akademik Yaklaşımlar Dergisi*, vol.10, pp. 72-89, 2019.

[3] F. Zarali, H. R. Yazgan, and Y. A. Delice, "New solution method of ant colony-based logistic center area layout problem," in *Sādhanā*, vol. 43, 2018.

[4] M. Kubon, and A. Krasnodębskı, "Logistic costs in competitive strategies of enterprises," *Agric. Econ.*, vol. 56, pp. 397–402, Czech 2010.

[5] M. Bezirci and A. O. Dündar, "Lojistik köylerin işletmelere sağladığı maliyet avantajları," *Trakya Üniversitesi Sosyal Bilimler Dergisi*, vol. 13, pp. 292-307, 2011.

[6] H. Bütüner, "Kalkınmada lojistik koylerin önemi," [Online]. Available: https://tr.linkedin.com/pulse/kalkinmada-lojistik-koylerin-onemi-hakan-b%C3%BCt%C3%BCner-ph-d- [Accessed: April, 22, 2022].

[7] A. Şimşek, "Erişilebilirliğin bölgesel kalkınmaya etkisi ve iller bazında erişilebilirlik endeksinin geliştirilmesi," in *T.C. Kalkınma Bakanlığı*, 2015.

[8] Y. Xie , W. Lu, W. Wang and L. Quadrifoglio "A multimodal location and routing model for hazardous materials transportation," in *Journal of Hazardous Materials*, vol. 227–228, pp. 135-141, Aug. 15, 2012.

[9] A. S. Duyguvar, "Sürdürülebilir lojistik merkezler için yer seçimi modeli," in *Gazi Üniversitesi Fen Bilimleri Enstitüsü Doktora Tezi*, 2018.

[10] A. Ö. Karagülle, "Taşımacılık sektöründe havayolu ve karayolu işletmelerinin karşılıklı beklentileri ve bir entegre yolcu taşımacılığı modeli önerisi," *İstanbul Üniversitesi Sosyal Bilimler Enstitüsü İşletme Anabilim Dalı Yönetim Organizasyon Bilim Dalı Doktora Tezi,* İstanbul, 2007.

[11] V. Reis, J. F. Meier, G. Pace. and R. Palacin, "Rail and multi-modal transport," in *Research in Transportation Economics,* vol.41, pp.17-30, 2013.

[12] J. A. O. Castro, D. A. Sepulveda-Garcia and I. D. Ospina-Contreras, "Effects of using multimodal transport over the logistics performance of the food chain of uchuva," in *Workshop on Engineering Applications,* pp. 165-177, 2016.

[13] X. Zhou, and J. Du, "Research on optimization of logistics transportation mode based on multimodal transportation," *Advances in Economics, Business and Management Research,* vol. 56, pp. 320-322, 2018.

[14] M. T. Anatol'yevna and E. S. Viktorovich, "Unified multimodal transport center–a tool for the development of the environmental geology of transport," in *Procedia Engineering*, vol. 189, pp. 138-44, 2017.

[15] E. Kıvrak, "Lojistik faaliyetlerde dış kaynak kullanımının analitik ağ süreci ve nötrosofik kümeler ile değerlendirilmesi", *Gazi Üniversitesi Fen Bilimleri Enstitüsü, Doktora Tezi,* 2020.

[16] S. Kutsal, "Türkiye"nin bir lojistik üs olma potansiyelinin kümeleme analizi ile incelenmesi," *Gazi Üniversitesi Fen Bilimleri Enstitüsü Yüksek Lisans Tezi*, 2008.

[17] M. Kabak, and Ö. Uyar, "Lojistik sektöründe ağır ticari araç seçimi problemine çok ölçütlü bir yaklaşım," *Gazi Üniversitesi Mühendislik Mimarlık Fakültesi Dergisi*, vol.28, pp. 115-125, 2013.

[18] M. N. Elgün, "Ulusal ve uluslararası taşıma ve ticarette lojistik köylerin yapılanma esasları ve uygun kuruluş yeri seçimi," *Afyon Kocatepe Üniversitesi İktisadi ve İdari Bilimler Fakültesi Dergisi*, vol. 13, pp.203-26, 2011.

[19] H. Ors and T. Mammadov, "An evaluation on logistic village marketing and the logistic potential of villages in Turkey," in *Global Business Research Congress (GBRC)*, May 26-27, 2016, Istanbul, Turkey.

[20] J. C. Perez, M. H. Carrillo& J. R. Montoya-Torres, "Multi-criteria approaches for urban passenger transport systems: a literature review," in *Annals of Operations Research,* vol. 226, Mar 2015.

[21] F. Z. Grine, O. Kamach, and N. Sefiani, "Developing a multi-criteria decision making model for identifying factors influencing the location of logistic hubs: A case study of Morocco," in *Proceedings of the International Conference on Industrial Engineering and Operations Management Paris, France*, July 26-27, 2018.

[22] T. Khongkan, N. Suthikarnnarunai and W. Rattanawong, "A location analysis of the distribution center and logistic hub in the greater mekong subregion," in *Rev. Integr. Bus. Econ. Res.* Vol. 4, pp.397-409, 2015.

[23] S. Alumur, H. Yaman and B. Y. Kara, "Hierarchical multimodal hub location problem with time-definite deliveries," *Transportation Research Part E: Logistics and Transportation Review*, vol.48, pp.1107-20, 2012.

[24] J. P. P. Vilko and J. M. Hallikas, "Risk assessment in multimodal supply chains,"*International Journal of Production Economics*, vol.140, pp.586-95, 2012.

[25] K. R. Smilowitz and C. F. Daganzo, "Continuum approximation techniques for the design of integrated package distribution systems," *Networks: An International Journal*, vol. 50, pp. 183-96, July 24, 2007.

[26] D. Milošević, A. Stanojević and M. Milošević, "AHP method in the function of logistic in development of smart cities model," in *The Sixth International Conference Transport And Logistics*, 2017.

[27] F. T. Chan, H. Chan, H. C. Lau and R. W. Ip, "An AHP approach in benchmarking logistics performance of the postal industry," in *Benchmarking: An International Journal*, vol. 13, pp. 636-661, 2006.

[28] J. G. V. Vieiraa, M. R. Toso, J. E. A. Ramos da Silvaa and P. C. C. Ribeiro, "An AHP-based framework for logistics operations in distribution centres," in *International Journal of Production Economics*, vol. 187, pp. 246-259, May 2017.

[29] J. Peng, "Selection of logistics outsourcing service suppliers based on AHP," in *Energy Procedia*, vol.17, pp.595 – 601, 2012.

[30] S. R. Divahar. and C. Sudhahar, "Selection of reverse logistics provider using AHP," in *Procedia Engineering*, vol. 38, pp. 2005 – 2008, 2012.

[31] L. Hong and Z. Xiaohua, "Study on location selection of multi-objective emergency logistics center based on AHP," in *Procedia Engineering*, vol. 15, pp. 2128–2132, 2011.

[32] Z. Stević, S. Vesković, M. Vasiljević and G. Tepić, "The selection of the logistics center location using AHP method," in *2nd Logistics International Conference, Belgrade, Serbia*, pp. 86-91, May 21-23, 2015.

[33] O. Adıgüzel, "Personel seçiminin analitik hiyerarşisi prosesi yöntemiyle gerçekleştirilmesi", in *Dumlupınar Üniversitesi Sosyal Bilimler Dergisi*, vol. 24, 2015.

[34] Ö. F. Ünal, "Performans Değerlemede Analitik Hiyerarşi Prosesi (AHP) Uygulamaları", in *Sosyal Bilimler Araştırmaları Dergisi,* vol. 7(1), pp. 37-55, 2012.

[35] A. Kuruüzüm and N. Atsan, "Analitik hiyerarşi yöntemi ve işletmecilik alanındaki uygulamaları", in *Akdeniz İ.İ.B.F. Dergisi,* vol.1, pp. 83-105, 2001.

[36] A. Zkarian and A. Kusiak, "Forming teams: an analytical approach", in *IIE Transactions*, vol. 31(1), pp. 85-97, 1999.

[37] M. J. Liberatore. and R. L. Nydick, (1990), "An analytic hierarchy approach for evaluating product formulations", in *Computer Aided Formulation: A Manual for Implementation, VCH Publishing Company*, New York, 1990.

[38] T. L. Saaty, "Relative measurement and its generalization in decision making why pairwise comparisons are central in mathematics for the measurement of intangible factors the Analytic Hierarchy/Network Process," in *Rev. R. Acad. Cien. Serie A. Mat.* vol. 102, pp. 251–318, 2008.

[39] Ticaret Bakanlığı, "Fasıllara Göre Dış Ticaret", Ticaret Bakanlığı [Online] Available: https://ticaret.gov.tr/data/621cb9a313b8764714eb4739/Ticaret%20Bakanl%C4%B1%C4%9F%C4%B1%202021%20Y%C4%B1l%C4%B1%20Faaliyet%20Raporu_Ek_T%C4%B0CARET%20BAKANLI%C4%9EI%202021%20YILI%20FAAL%C4%B0YET%20RAPORU.pdf.pdf, [Accessed: July, 05, 2021].

Bitlis Eren Üniversitesi Fen Bilimleri Dergisi
BİTLİS EREN UNIVERSITY JOURNAL OF SCIENCE
ISSN: 2147-3129/e-ISSN: 2147-3188
VOLUME: 11 NO: 4 PAGE: 953-959 YEAR: 2022
DOI:10.17798/bitlisfen.1113660

Determination of The Antibacterial Activities of Stinging *Nettle (*Urtica Dioica*)* Ethanol Extract at Different Bacterial Concentrations

Barış GÜLHAN[1], Filiz YANGILAR[2*]

[1]*Erzincan Binali Yıldırım Üniversitesi, Tıp Fakültesi, Mikrobiyoloji Anabilim Dalı, Erzincan*
[2]*Erzincan Binali Yıldırım Üniversitesi, Sağlık Bilimleri Fakültesi, Beslenme ve Diyetetik Bölümü, Erzincan*
(ORCID: 0000-0002-2605-1282) (ORCID: 0000-0001-6447-2419)

Keywords: Extraction, Antimicrobial effect, Nettle (*Urtica dioica* L.), Minimum inhibitory concentration (MIC), Minimum bactericidal concentration (MBC)..

Abstract

The study evaluated the antibacterial effect of stinging nettle extract by the liquid microdilution method to obtain quantitative results. Unlike other studies in the literature, minimum inhibitory concentration (MIC) and minimum bactericidal concentration (MBC) values showing bacteriostatic and bactericidal effects were investigated for four different bacterial concentrations. Six pathogen strains were studied, including *Staphylococcus aureus* ATCC 29213, *Enterococcus faecalis* ATCC 29212, *Streptococcus pneumoniae* ATCC 45615, *Klebsiella pneumoniae* ATCC 70063, *Escherichia coli* ATCC 25922, *Pseudomonas aeruginosa* ATCC 27853 and different levels of antimicrobial effects were determined. While the extract does not affect the *Klebsiella pneumoniae* ATCC 70063 strain at any level, *Pseudomonas aeruginosa* ATCC 27853 in strains with MIC values $1.5x10^5$ and $1.5x10^4$ cfu/mL were found at concentrations, but no effect was observed at the MBC level. While MIC and MBC values were found at the concentrations of *Staphylococcus aureus* ATCC 29213 except for the $1.5x10^7$ concentration, the remaining standard strains had different MIC and MBC values at all concentrations. The standard strain *Streptococcus pneumoniae* ATCC 45615 was the most effective with the extract's lowest MIC and MBC values. This study showed that nettle extract (*Urtica dioica*) would contribute to the research results in the scientific literature on its antimicrobial effect.

1. Introduction

Nettle, a member of the Urticaceae class, whose Latin name is *Urtica dioica*, has many important functions in traditional therapy due to its effects that support medical treatments. Various publications show that this plant is very effective in treating blood pressure, diabetes, and prostatic hyperplasia, rheumatoid arthritis, and allergic rhinitis [1]. Medicinal plants, also called herbs, are traditionally consumed as natural remedies to treat various diseases. The whole plant, parts of the plant, or extracts of these plants can be used. The nettle plant extract is used as a reducing agent for medicinal purposes in the synthesis stages of many nanoparticles [2-3]. Studies have also revealed that although chemical drugs are used successfully in treatments, they may show some side effects. Since natural products such as nettle do not accumulate in the body like other drugs, they have a biological balance and cause fewer side effects [4-5].

Urtica dioica is an endemic plant that grows mainly in tropical regions such as India and Malaysia, with 40 genera and about 500 species with medicinal value [3]. It also grows in Africa and Europe [3]. The leaves and roots of the nettle (*Urtica dioica* L.), also found in our country, are used for medicinal purposes. Among the *Urtica* species, *Urtica dioica* and *Urtica urens* are known in many parts of the world and have been consumed for ages as medicinal plant varieties [6]. Beschia et al. [7] reported that phenolic

*Corresponding author: f_yangilar@hotmail.com
Received: 07.05.2022, Accepted: 23.12.2022

compounds contained in nettle plant extracts provide inhibitory activity against various types of microorganisms and can be effective in food preservation with these properties. When phenolic extract analyzes are examined, it is seen that they contain caffeic, ferulic, sinapic acid, and esculetin [8]. It also contains bioactive compounds such as flavonoids, polysaccharides, carotenoids, lignans, minerals (mostly iron), ascorbic acid, tannins, carvacrol, and thymol. These compounds are also used in the food packaging industry as they have antioxidant and antibacterial properties as an excellent bio preservative [9]. The compound that provides the essential antioxidant effect is quercetin, which accumulates in its leaves [10-11].

Plant extract from *Urtica dioica* L., methicillin-resistant *Staphylococcus*, vancomycin-resistant *Enterococcus*, *Escherichia coli*, *Klebsiella*, *Pseudomonas*, and imipenem-resistant *Acinetobacter* have bacteriostatic effects against some bacteria. They also show antifungal activity that suppresses the proliferation and development of *Aspergillus*, *Mucor* and *Candida albicans* [12].

While numerous studies highlight the beneficial effects of *Urtica dioica*, understanding the molecular mechanisms underlying these effects can uncover new horizons for new therapeutic strategies [13, 14]. Our study aims to evaluate the antibacterial activity of the extract obtained from the leaves of this valuable *U. dioica* against pathogenic microorganisms that mostly affect humans.

In this study, it was also planned to compare the antimicrobial activity of nettle extract obtained from the Erzincan region with the results of other studies.

2. Material and Method

2.1. Materials

Urtica diocia plants were collected from Büyük Çakırman (formerly Vank) village of Erzincan province in the Eastern Anatolia Region of Turkey in May 2021. Identification of the nettle was done by Assoc.Prof.Dr. Mustafa KORKMAZ, "Department of Biology, Faculty of Science and Arts, Erzincan Binali Yıldırım University, Erzincan, Turkey."

2.2. Preparation of Nettle Extract

After the nettle was collected, it was washed, dried in the shade, and turned into powder. The extract was prepared according to the method described by Holopainen et al. [15]. The dried leaves of the plant were extracted using 95% ethanol. The extract was kept at 4°C for two days and filtered through a 45-µm membrane filter. Finally, the extract was separated from the solvent using the evaporator. The extract was placed in dark glass bottles and stored at -20°C.

2.3. Preparation of Test Microorganisms and Detection of MIC and MBC by Broth Microdilution Test

For evaluation of antimicrobial activity, *Staphylococcus aureus* ATCC 29213, *Enterococcus faecalis* ATCC 29212, *Streptococcus pneumoniae* ATCC 45615, *Klebsiella pneumoniae* ATCC 70063, *Escherichia coli* ATCC 25922, and *Pseudomonas aeruginosa* ATCC 27853 standard strains were used. Clinical isolates of microorganisms were obtained from Erzincan Binali Yıldırım University, Faculty of Medicine Microbiology Laboratory. Standard strains were first transferred to a Brain Heart Infusion Broth (bioMerieux, France) medium, and afterward, they were incubated for one night. They were passaged into media with 5% sheep blood (bioMerieux, France) and then inoculated from fresh passages into Brain Heart Infusion Broth (bioMerieux, France) media. Standard strains inoculated into Brain Heart Infusion Broth (bioMerieux, France) media were prepared using a DensiCHEK™ Plus densitometer device (bioMerieux, France) at 0.5 McFarland turbidity standard ($1.5x10^8$ microorganisms in ml). Then, the number of microorganisms in the tubes was diluted to be $1.5x10^7$, $1.5x10^6$, $1.5x10^5$, $1.5x10^4$ cfu/ml with the dilution method. MIC and MBC values were investigated for four different bacterial concentrations. The broth microdilution method was used to investigate the antimicrobial effects of nettle extract. For antimicrobial tests, sterile microdilution plates with 96-well U-bottom wells were used. By making serial dilutions of the nettle extract at a concentration of 3mg/mL, whose antimicrobial activity was investigated, with the brain heart infusion broth (bioMerieux, France), concentrations of 3 mg/mL, 1.5 mg/mL, 0.75 mg/mL, 0.1875 mg/mL, 0.09375 mg/mL, 0.046875 mg/mL, 0.0234375 mg/mL were obtained. Standard strains diluted to 100 microliters in equal volume were added to the wells containing 100 microliters of the extract at different concentrations of $1.5x10^7$, $1.5x10^6$, $1.5x10^5$ and $1.5x10^4$cfu/m. In addition, the last three wells were designed as follows: only the extract was placed in the first well; the broth, which was the positive control with the pathogen added to the second well; and the brain heart infusion broth, which was used as the negative control, was placed in the last well. Then, the plates were incubated at 150 rpm at 35 degrees for 24 hours using a Heidolph brand shaking incubator device (Germany) (Figure 1). After the MIC values

were determined, 10 microliter passages were made on a 5% sheep blood agar medium and incubated for another 24 hours. MBC values were determined by detecting the last well without growth (Figure 2).

Figure 1. Incubation of nettle extracts in the shaking incubator

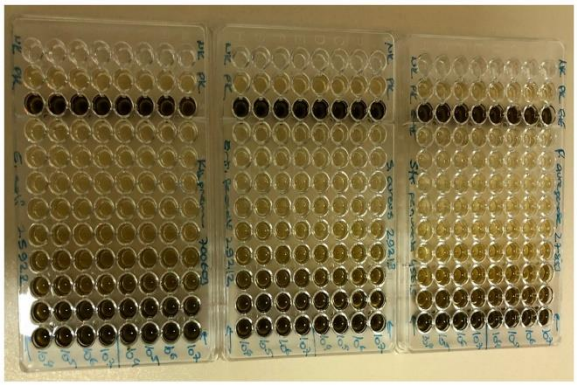

Figure 2. Plates used in MIC and MBC evaluation

3. Results and Discussion

3.1. MIC and MBC values of nettle extract

MIC and MBC breakpoint values obtained against six different standard strains are given in Table 1.

Table 1. MIC and MBC breakpoint values obtained against six different standard strains

Pathogen bacteria	Bacteria concentration (cfu/mL)	MIC value (mg/mL)	MBC value (mg/mL)
Staphylococcusaureus ATCC 29213	$1.5x10^7$	-	-
	$1.5x10^6$	0.375	1.5
	$1.5x10^5$	0.1875	0.75
	$1.5x10^4$	0.1875	0.75
Enterococcus faecalis ATCC 29212	$1.5x10^7$	1.5	3
	$1.5x10^6$	0.75	1.5
	$1.5x10^5$	0.75	1.5
	$1.5x10^4$	0.75	1.5
Streptococcus pneumoniae ATCC 45615	$1.5x10^7$	0.046875	0.375
	$1.5x10^6$	0.0234375	0.375
	$1.5x10^5$	0.0234375	0.1875
	$1.5x10^4$	0.0234375	0.09375
Klebsiella pneumoniae ATCC 70063	$1.5x10^7$	-	-
	$1.5x10^6$	-	-
	$1.5x10^5$	-	-
	$1.5x10^4$	-	-
Escherichia coli ATCC 25922	$1.5x10^7$	0.375	0.75
	$1.5x10^6$	0.375	0.75
	$1.5x10^5$	0.375	0.75
	$1.5x10^4$	0.1875	0.375
Pseudomonas aeruginosa ATCC 278536	$1.5x10^7$	-	-
	$1.5x10^6$	-	-
	$1.5x10^5$	1.5	-
	$1.5x10^4$	1.5	-

In the study, MIC and MBC values were investigated for four different bacterial concentrations. *Klebsiella pneumoniae* MIC and MBC values could not be found for ATCC 70063. No bacteriostatic or bactericidal effect had been observed for *Klebsiella pneumoniae* ATCC 70063 in the extract at the concentrations studied. MIC values were found for *Pseudomonas aeruginosa* ATCC 278536 only at $1.5x10^5$ and $1.5x10^4$ concentrations, and MBC values could not be determined; that is, the bacteriostatic effect could be detected only at $1.5x10^5$ and $1.5x10^4$ concentrations, while no bactericidal effect was observed. MIC and MBC values at various levels were found in the remaining standard strains; bacteriostatic and bactericidal effects were determined at multiple concentrations. The lowest MIC and MBC values at all concentrations were obtained for *Streptococcus pneumoniae* ATCC 45615. The effects of other standard strains, whose MIC and MBC values were determined, were also determined at various concentrations.

When the MIC values showing the bacteriostatic effect were examined, the lowest MIC obtained at the $1.5x10^7$, concentration was found, respectively, in *Streptococcus pneumoniae* ATCC 45615, *Escherichia coli* ATCC 25922, and *Enterococcus faecalis* ATCC 29212 standard strains. The lowest MIC values at the $1.5x10^6$ concentration was detected, respectively, in *Streptococcus pneumoniae* ATCC 45615, *Escherichia coli* ATCC 25922 = *Staphylococcus aureus* ATCC 29213, and *Enterococcus faecalis* ATCC 29212 standard strains. The lowest MIC values at the $1,5x10^5$ concentration were determined, respectively, *in Streptococcus pneumoniae* ATCC45615, *Staphylococcus aureus* ATCC 29213, *Escherichia coli* ATCC 25922, *Enterococcus faecalis* ATCC 29212, and *Pseudomonas aeruginosa* ATCC 278536 standard strains. The lowest MIC values at the $1,5x10^4$ concentration were detected in *Streptococcus pneumoniae* ATCC 45615, *Escherichia coli* ATCC 25922 = *Staphylococcus aureus* ATCC 29213, *Enterococcus faecalis* ATCC 29212, *and Pseudomonas aeruginosa* ATCC 278536 standard strains, respectively.

When the MIC values showing the bacteriostatic effect were examined, the lowest MIC obtained at the $1.5x10^7$, concentration was found, respectively, in *Streptococcus pneumoniae* ATCC 45615, *Escherichia coli* ATCC 25922 and *Enterococcus faecalis* ATCC 29212 standard strains. The lowest MIC values at the $1.5x10^6$ concentration was detected, respectively, in *Streptococcus pneumoniae* ATCC 45615, *Escherichia coli* ATCC 25922 = *Staphylococcus aureus* ATCC 29213, and *Enterococcus faecalis* ATCC 29212 standard strains. At $1.5x10^5$ the lowest MBC values were determined, respectively, in *Streptococcus pneumoniae* ATCC 45615 *Staphylococcus aureu*s ATCC 29213 = *Escherichia coli* ATCC 25922, and *Enterococcus faecalis* ATCC 29212 standard strains. At the $1.5x10^4$ concentration, the lowest MBC values were detected, respectively, in *Streptococcus pneumoniae* ATCC 45615, *Escherichia coli* ATCC 25922, *Staphylococcus aureus* ATCC 29213, and *Enterococcus faecalis* ATCC 29212 standard strains.

When the studies on the antibacterial effects of nettle extract were examined, it was seen that two methods were preferred as disk diffusion method and liquid microdilution method. In this study, the liquid microdilution method was used to obtain quantitative results to examine the nettle extract's antibacterial effect. Unlike other studies, MIC and MBC values were investigated for four different bacterial concentrations.

For comparison, when other studies conducted for the similar purposes as our study were examined in chronological order, Gülçin et al. [16], in their research with the disc diffusion method, have suggested that *Urtica dioica* aqueous extract is effective against *Escherichia coli* ATCC 9837, *Proteus mirabilis* (Clinical isolation), *Citrobacter koseri* (Clinical isolation), *Enterobacter aerogenes* (Clinical isolation), *Staphylococcus aureus* (ATCC 6538, *Streptococcus pneumoniae* (ATCC 49619) *Micrococcus luteus* (Clinical isolation), *Staphylococcus epidermidis* (clinical isolate) and *Candida albicans* (ATCC 10231) because they create a zone diameter. However, they reported

that no zone was formed against *Pseudomonas aeruginosa* (ATCC 9027), and therefore it was ineffective. Although the methods were different, when the results were evaluated, they were compatible with our study.

Dar et al. [17] examined the antibacterial activity of the extracts obtained by using hexane, chloroform, ethyl acetate, and methanol by the disk diffusion method. They found that no zone was formed with the extracts made using methanol and ethyl acetate, which were ineffective. Since they found the hexane extract to be effective, they investigated the MIC values with the tube dilution method and found 10^6 per milliliter concentrations of *E. faecalis, E. coli, K. pneumoniae, P. aeruginosa, S. aureus, S. flexneri,* and *S. typhi* that gave MIC values of 125, 15.62, 31.25, 250, 31.25, 125, and 7.81 μg/mL, respectively. Unlike our study, they found hexane extract to be effective against *K. pneumoniae* and *P. aeruginosa* strains. It is thought that this difference may be due to the different antimicrobial activity of the *Urtica dioica* plant grown in other regions.

In Kukric et al. [18], the antibacterial effects of *Urtica dioica* ethanolic extract were tested against the *Bacillus subtilis* strain isolated from food, *Lactobacillus plantarum*, *Pseudomonas aeruginosa* and *Escherichia coli*, and *Escherichia coli* isolated from urine. They used the macro dilution method against these bacteria in the study and reported that the ethanol extract of *Urtica dioica* leaf, diluted with methanol, showed a weak antibacterial effect on *B. subtilis* and *E. coli* isolated from food, yet no antibacterial activity was observed on *E. coli*, isolated from urine, or on *P. aeruginosa* and *L. plantarum* also isolated from food. Unlike the researchers' study, MIC values were obtained at some concentrations against *P. aeruginosa* in our research. However, it was thought that this might be due to different concentrations, different bacterial concentrations, and different antibacterial effects of extracts obtained from stinging nettles in other regions.

In Modarresi-Chahardehi et al. [19], they examined the antibacterial and antifungal effects of the extracts of *Urtica dioica* prepared with nine different solvents against 28 bacteria, three yeasts, and seven mold fungi; they reported that the extracts had antibacterial activities but did not show antifungal activity. When the bacterial dimension of the study was examined, it was observed that the results were generally similar to our study.

Ghaima et al. [20] investigated the antimicrobial activity of *Urtica dioica* leaf extract against five microorganisms: *Aeromonas hydrophila, Salmonella typhi, Staphylococcus aureus, Bacillus cereus,* and *Escherichia coli*, by the disc diffusion method. They reported that nettle extract was effective on these five bacteria.

Ramtin et al. [5] investigated the effect of alcoholic extract of nettle leaves on *B. cereus*, *S. aureus, K. pneumonia, P. aeruginosa, E. faecalis, E. coli* strains by the disc diffusion and liquid dilution methods. The extract is effective on all strains, and its results are consistent with our study.

Kulcu et al. [21] also investigated the MIC values of extracts made with different solvents of *Urtica dioica* against pathogens, and found the MIC value of the chloroform extract for *S. aureus* as 512 μg/mL, while the MIC value of the hexane extract for *E. faecalis* was >1024 μg/mL. Although the MIC values they obtained were different in our study, it was predicted that this might be due to different bacterial concentrations and the different antibacterial effects of the extracts obtained from nettles in different regions.

In the study conducted by Çolak et al. [22], it was determined that the MIC values for the ethanol extract determined for *Escherichia coli* (clinical isolate), *Enterococcus faecalis* ATCC 29212, *Enterococcus faecium* (clinical isolate), *Staphylococcus aureus* ATCC 29213, and MRSA (Methicillin-Resistant *Staphylococcus aureus*; clinical isolate) were found to be 2, 2, 2, 4, 4 mg/mL, respectively. When compared, the MIC values in our study were lower. It was thought that this result might be due to the different antimicrobial activity of the *Urtica dioica* plant grown in other regions and the difference in bacterial concentrations.

Kačániová et al. [11] determined in their study whether there is an antimicrobial effect in various plant extracts by the disc diffusion method. In addition, they investigated MIC50 and MIC90 values by the liquid microdilution

method for the strains that they detected effects by the disc diffusion method. They found MIC50 and MIC90 values of the *Urtica dioica* extract for *P. aeruginosa, E. faecalis, S. aureus* and *S. pneumoniae* to be 9.56 -10.24, 12.78-13.59, 7.42-8.82, and 8.53-9.54 µg/mL, respectively. In this study, *Urtica dioica* extract was found to be effective in terms of antimicrobials. The results were compatible with our study.

4. Conclusion and Suggestions

In our study, MIC and MBC values were determined for different concentrations of the extract obtained from the leaves of nettles collected from the Erzincan region, starting from 3 mg/mL, were prepared with serial dilutions $1.5x10.^{7}$, $1.5x10^{6}$, $1.5x10^{5}$ and $1.5x10^{4}$ cfu/ml at four different concentrations for pathogen standard bacterial strains. MIC and MBC values could not be determined for *K. pneumoniae*, while MIC values were determined only at two concentrations for *P. aeruginosa*. Since it was stated in the text above that some studies provided an effect against these strains, it is predicted that higher nettle extract concentrations and MIC and MBC values could be detected in our study. In this context, the determination of MIC and MBC values for different bacterial concentrations and nettle extracts at different concentrations will be useful to establish a common standard for comparative studies in which regional differences can be revealed. In addition, evaluating the bioactive compounds, they contain separately or together to understand the molecular mechanisms underlying the antimicrobial activity of *Urtica dioica* may open new horizons in terms of therapeutic strategies.

Contributions of the Authors

The contributions of each author to the article should be indicated.

Conflict of Interest Statement

There is no conflict of interest between the authors.

Statement of Research and Publication Ethics

The study is complied with research and publication ethics.

References

[1] A. F. Fathi, A. R. Garjani, N. Maleki, and D. S. Ranj, "Study of the hypoglycemic activity of the hydroalcoholic extract of *Urtica dioica* in normal and diabetic rats," *Pharmaceutical Sciences*, vol. 2, pp. 65-69, 2005.

[2] G. Vardatsikos, N. R. Pandey, and A. K. Srivastava, "Insulino-mimetic and anti-diabetic effects of zinc", *Journal of Inorganic Biochemistry*, vol. 120, pp. 8-17, 2013

[3] A. Bayrami, S. Haghgooie, S. R. Pouran, F. M. Arvanag, and A. Habibi-Yangjeh, "Synergistic antidiabetic activity of ZnO nanoparticles encompassed by *Urtica dioica* extract," *Advanced Powder Technology*, vol. 31, pp. 2110-2118, 2020.

[4] S. Zaman, "The medicinal plants. 6th ed. Tehran; Naghsh Press"; pp. 9-10, 2005.

[5] M. Ramtin, A. Massiha, K. P. M. R. MAJID, K. Issazadeh, M. Assmar, and S. Zarrabi, "In vitro antimicrobial activity of *Iris pseudacorus* and *Urtica dioica*," *Zahedan Journal of Research in Medical Sciences*, vol. 16, pp. 35-39, 2014.

[6] N. Chaurasia, and M.Wichtl, "Sterols and steryl glycosides from *Urtica dioica*," *Journal of Natural Products*, vol. 50, pp. 881-885, 1987.

[7] M. Beschia, A. Leonte, and I. Oancea, "Phenolic components with biological activity in vegetable extracts," *Bulletin of the University of Galati*, vol. 6, pp. 59-63, 1982.

[8] L. Grauso, B. de Falco, V. Lanzotti, and R. Motti, "Stinging nettle, *Urtica dioica* L.: Botanical, phytochemical and pharmacological overview," *Phytochemistry Reviews*, vol. 19, pp. 1341-1377, 2020.

[9] S. M. T. Gharibzahedi, H. Rostami, and S. Yousefi, "Formulation design and physicochemical stability characterization of nanoemulsions of nettle (*Urtica dioica*) essential oil using a model-based methodology," *Journal of Food Processing and Preservation*, vol. 39, pp. 2947-2958, 2015.

[10] C. Bourgeois, É. A. Leclerc, C. Corbin, J. Doussot, V. Serrano, J. R. Vanier, J. M. Seigneuret, D. Auguin, C. H. Pichon, É. Lainé, C. H. Hano, "Nettle (*Urtica dioica* L.) as a source of antioxidant and anti-aging phytochemicals for cosmetic applications," *Comptes Rendus Chimie*, vol. 19, pp. 1090-1100, 2016.

[11] M. Kačániová, K. Miklášová, S. Kunová, L. Galovičová, P. Borotová, V. Válková and M. Terentjeva, "Antimicrobial and Antioxidant Activity of Black Elder, Stinging Nettle, Marigold and Ribwort Plantain," *Scientific Papers: Animal Science & Biotechnologies/Lucrari Stiintifice: Zootehnie si Biotehnologii*, vol. *54*, 2021.

[12] M. Ghaedi, R. Naghiha, R. Jannesar, N. Dehghanian, B. Mirtamizdoust, V. Pezeshkpour,. "Antibacterial and antifungal activity of flower extracts of *Urtica dioica*, *Chamaemelum nobile* and *Salvia officinalis*: Effects of $Zn[OH]_2$ nanoparticles and Hp-2-minh on their property," *Journal of Industrial and Engineering Chemistry*, vol. 32, pp. 353-359, 2015.

[13] M. H. AlShuwayeb, and A. J. Al-Khatib, "Molecular and chemical therapeutic features of *Urtica* species," *European Scientific Journal*, vol. 9, 2013.

[14] R. Dhouibi, H. Affes, M. B. Salem, S. Hammami, Z. Sahnoun, K. M. Zeghal, and K. Ksouda, "Screening of pharmacological uses of *Urtica dioica* and others benefits," *Progress in Biophysics and Molecular Biology*, vol. 150, pp. 67-77, 2020.

[15] M. Holopainen, L. Jabordar, T. Seppanen-Laukso, I. Laakso, V. Kauppinen, "Antimicrobial Activity of Some Finnish Ericaceous plants," *Acta Pharmaceutica Fennica*, vol. 97, pp. 197-202, 1988.

[16] I. Gülçin, Ö. İ. Küfrevioğlu, M. Oktay, and M. E. Büyükokuroğlu, "Antioxidant, antimicrobial, antiulcer and analgesic activities of nettle (*Urtica dioica* L.)," *Journal of Ethnopharmacology*, vol. 90, pp. 205-215, 2004.

[17] S. A. Dar, F. A. Ganai, A. R. Yousuf, M. U. H. Balkhi, T. M. Bhat, and P. Sharma, "Pharmacological and toxicological evaluation of *Urtica dioica,*" *Pharmaceutical Biology*, vol. 51, pp. 170-180, 2013.

[18] Z. Z. Kukrić, L. N. Topalić-Trivunović, B. M. Kukavica, S. B. Matoš, S. S. Pavičić, M. M. Boroja, and A. V. Savić, "Characterization of antioxidant and antimicrobial activities of nettle leaves (*Urtica dioica* L.)," *Acta Periodica Technologica*, vol.43, pp. 257-272, 2012.

[19] A. Modarresi-Chahardehi, D. Ibrahim, S. Fariza-Sulaiman, and L. Mousavi, "Screening antimicrobial activity of various extracts of *Urtica dioica,*" *Revista de Biologia Tropical*, vol. 60, pp. 1567-1576, 2012.

[20] K. K. Ghaima, N. M. Hashim, and S. A. Ali, "Antibacterial and antioxidant activities of ethyl acetate extract of nettle (*Urtica dioica*) and dandelion (*Taraxacum officinale*)," *Journal of Applied Pharmaceutical Science*, vol. 3, p. 96, 2013.

[21] D. B. Külcü, C. D. Gökışık, and S. Aydın, "An investigation of antibacterial and antioxidant activity of nettle (*Urtica dioica* L.), mint (*Mentha piperita*), thyme (*Thyme serpyllum*) and *Chenopodium album* L. plants from Yaylacık Plateau, Giresun, Turkey," *Turkish Journal of Agriculture-Food Science and Technology*, vol. 7, pp. 73-80, 2019.

[22] S. Çolak, N. Çömlekcioğlu, and A. Aygan, "Investigation of antioxidant and antimicrobial activities of *Urtica dioica* L. plant extracts," *Eurasian Journal of Biological and Chemical Sciences*, vol. 3, pp. 206-212, 2020.

Bitlis Eren Üniversitesi Fen Bilimleri Dergisi
BİTLİS EREN UNIVERSITY JOURNAL OF SCIENCE
ISSN: 2147-3129/e-ISSN: 2147-3188
VOLUME: 11 NO: 4 PAGE: 960-970 YEAR: 2022
DOI:10.17798/bitlisfen.1120885

Thermodynamic Analysis of a Combined Gas Turbine ORC Using Some Organic Fluids

Ahmet ELBİR[1*], Feyza AKARSLAN KODALOĞLU[1], Mehmet Erhan ŞAHİN[2]
İbrahim ÜÇGÜL[1]
[1]*Süleyman Demirel Üniversitesi YEKARUM 32260, Isparta/TURKEY*
[2]*Isparta Aplied Science University, Technical Vocational High School, Isparta/TURKEY*
(ORCID: 0000-0001-8934-7665) (ORCID: 0000-0002-7855-8616)
(ORCID: 0000-0003-1613-7493) (ORCID: 0000-0001-9794-0653)

Keywords: ORC, Cascade Expansion Gas Turbine, Energy Analysis, Exergy Analysis.

Abstract
The increase in energy and environmental problems has led us to use sustainable methods for the optimization of energy systems. In this study, an integrated Organic Rankine Cycle (ORC) has been added to the waste heat of a cascade expansion gas turbine in the name of innovative concepts in industrial competition. In this ORC system, mass flow rates, pressure ratios, net powers and thermodynamic calculations of five different fluids (R123, R245fa, R600, R365mfc and R113) were made by operating them with a certain heat load. Accordingly, the ORC net powers of the refrigerants were found to be 15.54kW for R123, 14.78kW for R245fa, 14.71kW for R600, 14.78kW for R365mfc and 15.45kW for R113. With the net power of 51.4kW from the gas turbine, the net power obtained with the R123 refrigerant used in the ORC system is added to 15.54 kW and it has been calculated that it provides a total net power of 66.94kW. The energy efficiency of the designed integrated system was calculated as 66% and the exergy efficiency as 20%. It is seen that the importance of sustainable energy in the optimization of power systems combined with ORC is inevitable.

1. Introduction

The growing and developing world population has brought industrial competition with it. The maximum use of energy in the concept of industrial competition has given rise to innovative concepts. In particular, the sustainable use of waste heat in industry has not only reduced fossil energy consumption but also reduced the risk of global warming. In this context, the use of combined power systems developed by taking advantage of the waste heat of gas turbines has increased considerably. The principle of operation of these systems gets its name from the combination of combined cycle production technologies of both gas and steam power. A combined-cycle power plant is based on the use of both power and hot waste heat from a gas turbine. In some studies in the literature; Lecompte et. al. [1], the integration of an ORC system into a 100 MW Electric Arc Furnace (EAF) was performed. The effects of evaluations based on average heat profiles, a vapor buffer, and optimized state and ORC architectures have been studied. The results have shown that it is very important to take into account the heat. It has been found that an optimized sub-critical ORC system can produce a net electrical output of 752 kW with a steam buffer operating at 25 bar. If combined heating is considered, the ORC system can be optimized to produce 521 kW of electricity, they also found that it provides 4.52 MW of heat. Javanshir et. al. [2], have studied the analysis and optimization of an ORC used as a dip cycle in Brayton/ORC and steam Rankine/ORC combined cycle configurations. Utility scale steam Rankine cycle orc power output may be obtained by adding a dip in and determine the increase in ambient conditions (heat sink temperature) to determine the effect on the growth of a unified power steam Rankine/ORC cycle analysis pinched. The results

*Corresponding author: ahmetelbir@sdu.edu.tr
Receieved: 24.05.2022, Accepted: 01.11.2022

showed that CO_2 and air are the best working fluids for the top coating of the Brayton Cycle. Depending on the exhaust temperature of the topping cycle (Brayton), Iso-butane, R11 and ethanol, which are the preferred working fluids for the ORC cycle, have achieved the highest efficiency in the combined cycle. Ahmadi et. al. [3], investigated the efficiency of solar-powered gas turbines in various parameters such as pressure ratio, turbine inlet temperature, heat sink geometry and component performance. The results showed that a 10% increase in turbine efficiency could lead to a 6-12% improvement in the efficiency of the closed Brayton cycle. Nassar et. al. [4], designed a gas turbine cycle with a thermal efficiency of 34.5% with a target power output of 9 MW. In order to increase the efficiency of the system, an ORC based system was used as a bottom cycle that draws heat from compressed air (intercooler) and exhaust. The pressure ratios, operating pressures and temperatures of the compressors in the ORC system have been optimized using parametric studies. With the addition of decooperation and recovery to this basic system and the inclusion of the dip cycle, they have increased the efficiency to about 47.94%. Kaşka et. al. [5], aimed to investigate the effects of using an ORC as a decoiler on the overall system efficiency in the Brayton cycle. In addition, they investigated the effects of turbine inlet temperature and pressure ratio on system performance. The exergy destruction and exergy efficiency of all components of the combined cycle at different pressure ratios have been calculated. The net power generated by the ORC has been studied depending on the second law efficiency and exergy destruction of the ORC, the second law of the preheater and the exergy destruction. They noted that there is a correlation between the pressure of the Dec Brayton cycle and the net power output. They observed that as the pressure increased, the temperature of the ORC heat source also increased. In addition, they emphasized that increased pressure increases energy and exergy efficiency. Ren et. al. [6], proposed a combined cycle of a gas turbine and an ORC to further improve the energy efficiency of gas turbines. Simulation results have shown that mixtures allow the combined cycle to achieve higher efficiency than pure fluids. They noted that for gas turbines of different power levels, the toluene benzene mixture is more suitable for the recovery of waste heat from small and medium-sized gas turbines, while cyclopentane is more suitable for microgas turbines. Kaşka et. al. [7], carried out a thermodynamic analysis of an ORC using waste heat from the intercooler and regenerator in the Brayton cycle with decooperation, reheating and regeneration (BCIRR) and decooperation. They have revealed various outputs, such as cycle efficiencies in the Brayton cycle depending on turbine inlet temperature, intercooler pressure ratios and decongestant temperature difference. It is emphasized that for all cycles, the net power generated due to the increased turbine inlet temperature has increased. It has been said that since the heat input to the cycles occurs at high temperatures, the net power generated due to the increased turbine input temperature for all cycles increases. They calculated that the thermal efficiency of the combined cycle is about 11.7% higher than the thermal efficiency of the Brayton cycle alone. Blanco et. al. [8], performed thermodynamic, exergy and environmental impact assessments for a Brayton S-CO_2 (supercritical carbon dioxide) cycle combined with ORC. The results showed that the main turbine and the secondary turbine of the Brayton S-CO_2 cycle offer higher exergetic efficiency, 97% and better thermal and energetic behavior compared to other components of the system. Gürgen and Altın [9], have worked on a comprehensive decision-making strategy for the selection of working fluids in ORC applications. The results obtained for 10 different study fluids were evaluated with a comprehensive decision-making strategy. They have designated R245fa as the final working fluid [9]. Chacartegui et al. [10], investigated, low temperature ORC as a dip cycle in medium and large scaled combined cycle power plants by using 8 different refrigerants (R113, R245, isobutene, toluene, cyclohexane, isopentane, toluene and cyclohexane). Competitive results have been achieved for ORC combined cycles with reasonably high global efficiencies. In Khanet et. al. [11], performance analysis of a combined pre-compression supercritical CO_2 cycle and ORC powered by a solar tower for waste heat recovery is studied. It was found that as the heat exchanger efficiency increased, the waste heat recovery rate also increased. The highest heat exchanger efficiency for R227 was found to be 0.95 and the waste heat recovery rate was 0.5673. Carcasci et. al. [12], investigated the optimization of the organic Rankine cycle for four different working fluids (toluene, benzene, cyclopentane and cyclohexane) by changing the main pressure of the fluid at different temperatures of the oil circuit. In Ighodaro et. al. [13], energy analysis of a Combined Regenerative Gas Turbine Organic Rankine Cycle (CRGTORC) was conducted to use the exhaust heat from an existing power plant in Nigeria in their study. The performance of CRGTORC was compared to the current SGT using cyclopentane as the working fluid used in the ORC section. They found that the CRGTORC model increased the net power output, thermal efficiency, total cycle efficiency and operating rate of the system

by 23.53%, 62.24%, 54.60% and 10.21%, respectively. Flue gas losses, specific fuel consumption and heat rate decreased by 89.21%, 36.26% and 36.26%, respectively. In addition, it has been observed that the increase in compressor inlet air temperature causes an increase in the specific fuel consumption and heat rate and causes a decrease in net power output, thermal efficiency, cycle efficiency, flue gas losses and work rate. Mishra and Kuamar [14], developed a performance equation for three working fluids (R123, R245fa and R134a) to improve the thermodynamic performance of the brayton cycle. They observed that the Brayton cycle working with R123 gave better thermodynamic performances. Jeong et. al. [15], developed a new cycle with three different refrigerants (R123, R134a and R245ca) Rankine and refrigeration cycles and a thermodynamic analysis of the system was made. It was found that the cycle using R123 refrigerant gave the highest cycle efficiency among all cycles. In Lei et. al. [16], performance evaluation of SRC and ORC systems, which are used as bottom systems in a, GT-based combined system, has been conducted for different turbine inlet temperatures and pressures. As a result, R141b was found as the best working refrigerant. They found the maximum net thermal efficiency, exergy efficiency and net power of ORC with R141b as 22.6%, 64.76% and 780.35 kW at 40 bar and 225 °C, respectively. They found the net thermal and exergy efficiency of the overall system (GT-SRC-ORC) with R141b to be 47.65% and 67.35%, respectively. In this case, they determined that waste heat recovery was realized, corresponding to 734.57 kg/h natural gas, which is equivalent to 2203.73 kg-CO_2/h emissions.

In this study, it is aimed to produce electricity again in the ORC cycle by comparing ORC cycle with fluids with different high critical temperatures (R113, R123, R245fa, R365mcf and R600) in the heat remaining after transferring eventual heat energy received from a heat source to a gas turbine-designed system and generating electricity with turbines..

2. Material and Method

2.1. Cascade Expansion Gas Turbine

The cascade expansion gas turbine cycle is shown in figure 1. Accordingly, in state 1, air at atmospheric pressure enters the compressor. The air should be state 2 with increased pressure and temperature being transferred to it should be state 3 with the high heat it receives from the heat source. In case 4, a 1/3 cascade expansion was made in the turbine. In the case of 5, the cascade expanding air is reduced to atmospheric pressure and its output is provided.

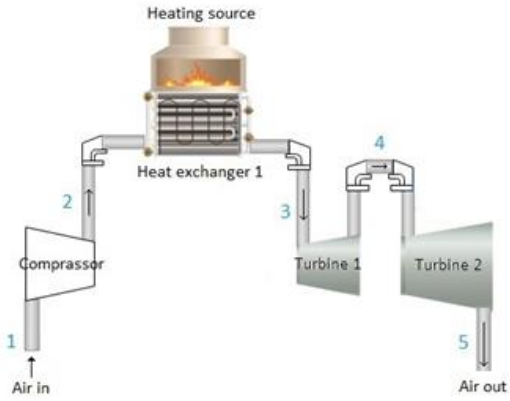

Figure 1. Cascade expansion gas turbine system.

2.2. Model Description

The designed system is shown in Figure 2. The ORC system is integrated into the gas turbine waste heat with step expansion. The step-expansion gas turbine has been described above (Fig. 1). The waste heat received by the ORC system heat exchanger is at 10, and the hot refrigerant expands and generates electricity from the turbine. In 11 cases, heat transfer occurs by condensation thanks to the heat exchanger. In state 7, the fluid, which is saturated liquid, enters the pump and its pressure is increased, and the cycle is completed.

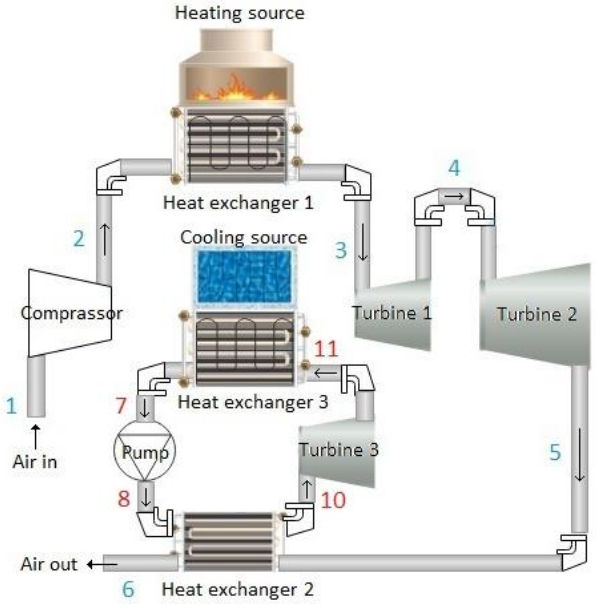

Figure 2. Design of the unified power system.

Assumptions and fixed parameters;

- All components in the system neglect the pressure losses that may occur in the pressure line.

- Their changes in kinetic and potential energy was neglected.
- The heat exchange coefficient was accepted as 1.4. (source of heat = heat entering the system*1,4)
- The instantaneous temperature difference coefficient between the heat sources and the heat exchanger surfaces was accepted as 1.1. (heat source surfaces temperature = heat surfaces temperature entering the system *1.1)
- The source temperatures used in the ORC system were kept constant as 385.5 K for the evaporator (HX2) and 318.8 K for the condenser (HX3).
- The isentropic efficiency of the turbines in the entire system was calculated as 90%, and the isentropic efficiency of the pump and compressor was calculated as 80%.
- The pressure ratio of the turbines that make gradual expansion in the gas turbine cycle was taken as 1/3.
- In the step-expansion gas turbine and ORC system, the flows were assumed to be constant mass flow.
- The dead state was taken at 20 ^{0}C.
- System components are Adiabatic.

2.3. Thermodynamic Analysis

The equations used according to the laws of thermodynamics are as follows:

For the steady state in thermodynamic analysis, the basic equation of mass balance is as follows;

$$\sum \dot{m}_{in} = \sum \dot{m}_{ex} \quad (1)$$

where $\dot{m}$ denotes the mass flow rate, and the in and ex indices denote the input and output states, respectively. The energy balance is:

$$\dot{Q}_{in} + \dot{W}_{in} + \sum_{in} \dot{m}\left(h + \frac{V^2}{2} + gz\right) = \dot{Q}_{ex} + \dot{W}_{ex} + \sum_{ex} \dot{m}\left(h + \frac{V^2}{2} + gz\right) \quad (2)$$

Where $\dot{Q}$ is the heat transfer rate, $\dot{W}$ is the power, h is the specific enthalpy, v is the speed, z is the height, and g is the gravitational acceleration. The entropy equilibrium equation for steady-state conditions is written as:

$$\sum_{in} \dot{m}_{in} s_{in} + \sum_k \frac{\dot{Q}}{T_k} + \dot{S}_{gen} = \sum_{ex} \dot{m}_{ex} s_{ex} \quad (3)$$

where s is the specific entropy and $\dot{S}_{gen}$ is the production rate of entropy. The equation of exergy balance:

$$\sum \dot{m}_{in}\, ex_{in} + \sum \dot{E}\, x_{Q,in} + \sum \dot{E} x_{W,in} = \sum \dot{m}_{ex} ex_{ex} + \sum \dot{E} x_{Q,ex} + \sum \dot{E} x_{W,ex} + \dot{E} x_D \quad (4)$$

Specific flow exergy:

$$ex = x_{ph} + ex_{ch} + ex_{pt} + ex_{kn} \quad (5)$$

The kinetic and potential parts of the exergy have been processed with the assumption that they are negligible. It is also assumed that the chemical exergy is negligible. The physical or flow exergy (ex_{ph}) is defined as:

$$ex_{ph} = (h - h_o) - T_o(s - s_o) \quad (6)$$

where h and s represent the specific enthalpy and entropy, respectively, in the real case. h_o and s_o symbolize the enthalpy and entropy in the reference ambient states, respectively.

The destruction (D) of exergy is equal to the product of mass with specific exergy;

$$\dot{E} x_D = ex * m \quad (7)$$

$\dot{E} x_D$ are the work-related exergy ratios and are given by:

$$\dot{E} x_D = T_0 \dot{S}_{gen} \quad (8)$$

$\dot{E} x_W$ are the work-related exergy ratios and are given by:

$$\dot{E} x_W = \dot{W} \quad (9)$$

$\dot{E} x_Q$, exergy destruction rate related to heat transfer is given as below.

$$\dot{E} x_Q = \left(1 - \frac{T_o}{T}\right) \dot{Q} \quad (10)$$

What is the work that comes out of the system.

$$\dot{W} net_{out} = \dot{Q}_{in} - \dot{Q}_{out} \quad (11)$$

The energy efficiency (η) for the system;

$$\eta th = \frac{\dot{W}net_{out}}{\dot{Q}_{in}} \quad (12)$$

The exergy efficiency (ψ) can be defined as follows;

$$\psi = \frac{\sum useful\ output\ exergy}{\sum input\ exergy} = 1 - \frac{\sum exergy\ loss}{\sum input\ exergy} \quad (13)$$

The instantaneous temperature T(K) value for surfaces was calculated as:

$$T = \frac{h_2 - h_1}{s_2 - s_1} \quad (14)$$

In Table 1, the mass balance, energy balance, entropy balance, exergy balance and exergy yields for each component are presented separately [18], [19]

Table 1. The Gas Turbine and ORC Combined Cycle equilibrium equations

Component	Mass balance	Energy balance	Entropy balance	Exergy balance	Exergy efficiency
Air-Comp. (1-2)	$\dot{m}_1 = \dot{m}_2 = \dot{m}_{air}$	$\dot{W}_{Comp1.} = \dot{m}_{air}(h_2 - h_1)$	$\dot{S}_{gen,Comp1.} = \dot{m}_{air}(s_2 - s_1)$	$\dot{E}x_{D,Comp1} = \dot{m}_{air}(ex_1 - ex_2) + \dot{W}_{Comp1}$	$\psi_{copm1} = \frac{\dot{m}_{air}(ex_2 - ex_1)}{\dot{W}_{Comp1}}$
Air-heat exchanger I (2-3)	$\dot{m}_2 = \dot{m}_3 = \dot{m}_{air}$	$\dot{Q}^{in}_{HXI} = \dot{m}_{air}(h_2 - h_3)$ $\dot{Q}^{out}_{HX1} = \dot{m}_{air}(h_2 - h_3)/1{,}4$	$\dot{S}_{\text{gen.,HX1}} = \dot{m}_{air}(s_2 - s_3) + \left(\frac{\dot{Q}^{out}_{air}}{T_{HX1} * 1{,}1}\right)$	$\dot{E}x_{\text{D,HX1}} = \dot{m}_{air}(ex_2 - ex_3) - \dot{Q}^{out}_{air}\left(1 - \frac{T_0}{T_{HX1} * 1{,}1}\right)$	$\psi_{\text{HX1}} = \frac{\dot{Q}^{out}_{air}\left(1 - \frac{T_0}{T_{HX1} * 1{,}1}\right)}{\dot{m}_{air}(ex_2 - ex_3)}$
Air-Turbine I (3-4)	$\dot{m}_3 = \dot{m}_4 = \dot{m}_{air}$	$\dot{W}_{turb1.} = \dot{m}_{air}(h_3 - h_4)$	$\dot{S}_{gen,turb1.} = \dot{m}_{air}(s_4 - s_3)$	$\dot{E}x_{D,turb1.} = \dot{m}_{air}(ex_3 - ex_4) - \dot{W}_{turb1.}$	$\psi_{turb1.} = \frac{\dot{W}_{turb1.}}{\dot{m}_{air}(ex_3 - ex_4)}$
Air-Turbine II (4-5)	$\dot{m}_4 = \dot{m}_5 = \dot{m}_{air}$	$\dot{W}_{turb2.} = \dot{m}_{air}(h_4 - h_5)$	$\dot{S}_{gen,turb2.} = \dot{m}_{air}(s_5 - s_4)$	$\dot{E}x_{D,turb2.} = \dot{m}_{air}(ex_4 - ex_5) - \dot{W}_{turb2.}$	$\psi_{turb2.} = \frac{\dot{W}_{turb2.}}{\dot{m}_{air}(ex_4 - ex_5)}$
Air-ORC heat exchanger II (5-6) (8-10)	$\dot{m}_5 = \dot{m}_6 = \dot{m}_{air}$; $\dot{m}_8 = \dot{m}_{10} = \dot{m}_{orc}$	$\dot{Q}^{in}_{orc} = \dot{m}_{orc}(h_6 - h_5)/1{,}4$	$\dot{S}_{\text{gen.,HX2}} = \dot{m}_{air}(s_6 - s_5) - \dot{m}_{orc}(s_{10} - s_8)$	$\dot{E}x_{\text{D,HX2}} = \dot{m}_{air}(ex_5 - ex_6) - \dot{m}_{orc}(ex_8 - ex_{10})$	$\psi_{HX2} = \frac{\dot{m}_{orc}(ex_5 - ex_6)}{\dot{m}_{air}(ex_8 - ex_{10})}$
ORC-Turbine III (10-11)	$\dot{m}_{10} = \dot{m}_{11} = \dot{m}_{orc}$	$\dot{W}_{turb3.} = \dot{m}_{orc}(h_{10} - h_{11})$	$\dot{S}_{gen,turb3.} = \dot{m}_{orc}(s_{11} - s_{10})$	$\dot{E}x_{D,turb3.} = \dot{m}_{orc}(ex_{10} - ex_{11}) - \dot{W}_{turb3.}$	$\psi_{turb3.} = \frac{\dot{W}_{turb.}}{\dot{m}_{orc}(ex_{10} - ex_{11})}$
ORC heat exchanger III (7-11)	$\dot{m}_{11} = \dot{m}_7 = \dot{m}_{orc}$	$\dot{Q}^{in}_{HX3} = \dot{m}_{orc}(h_{11} - h_7)$ $\dot{Q}^{out}_{orc} = \dot{m}_{orc}(h_{11} - h_7)/1{,}4$	$\dot{S}_{\text{gen.,HX3}} = \dot{m}_{orc}(s_7 - s_{11}) + \left(\frac{\dot{Q}^{out}_{orc}}{T_{HX3}/1{,}1}\right)$	$\dot{E}x_{\text{D,HX3}} = \dot{m}_{orc}(ex_{11} - ex_7) - \dot{Q}^{out}_{orc}\left(1 - \frac{T_0}{T_{HX3}/1{,}1}\right)$	$\psi_{\text{HX3}} = \frac{\dot{Q}^{out}_{orc}\left(1 - \frac{T_0}{T_{HX3}/1{,}1}\right)}{\dot{m}_{orc}(ex_{11} - ex_7)}$
ORC-pump (7-8)	$\dot{m}_7 = \dot{m}_8 = \dot{m}_{orc}$	$\dot{W}_{pump} = \dot{m}_{orc}(h_8 - h_7)$	$\dot{S}_{gen,pump} = \dot{m}_{orc}(s_8 - s_7)$	$\dot{E}x_{D,pump} = \dot{m}_{orc}(ex_7 - ex_8) + \dot{W}_{pump}$	$\psi_{pump} = \frac{\dot{m}_{orc}(ex_7 - ex_8)}{\dot{W}_{pump}}$

3. Results and Discussion

Figure 3 shows the T-s (temperature enthalpy) diagram for the Brayton cycle.

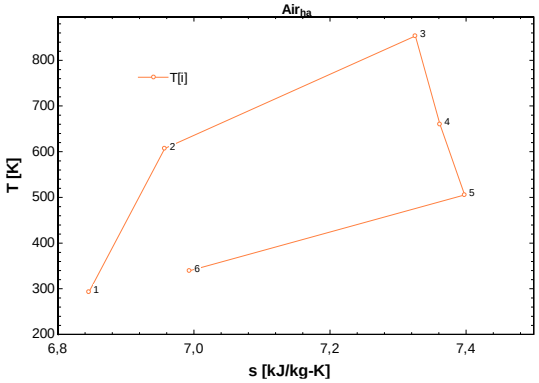

Figure 3. Air cascade expansion gas turbine cycle T-s diagram

In Figure 3, the temperature that changes with the flow direction of the fresh air entering from the 1st point is presented in the temperature-entropy diagram.

The thermodynamic values in Figure 1 for the cascade expansion gas turbine cycle are presented in Table 2. The T_0 point indicates the dead state.

Table 2. Point values in the cascade expansion gas turbine cycle

Cascade-Air	T [K]	s kJ/kg.K	P [bar]	h [kJ/kg]	Ex [kJ/kg]	m [kg/s]
1	293.2	6.846	1	293.4	0	1
2	607.1	6.957	9	614.7	288.6	1
3	853.2	7.325	9	881.4	447.4	1
4	659.3	7.362	3	670.7	226	1
5	505.3	7.398	1	508.8	53.5	1
6	339.6	6.994	1	340.1	3.347	1
T_0	293.2	6.846	1	293.4		

Thermodynamic calculations for the cascade expansion gas turbine cycle are given in Table 3.

Table 3. Thermodynamic consequences of the cascade expansion gas turbine cycle

Cascade-Air	Ex(KW)	Q(KW)in	Q(KW)out	W(KW)	φ
1-2 Compressor	32.72	-	-	321.3	0.90
2-3 Heat exchanger 1	77.23	266.7	373.4	-	0.67
3-4 Turbine1	10.58	-	-	210.8	0.95
4-5 Turbine2	10.62	-	-	161.9	0.94
5-6 Heat exchanger 2	25.07	120.5	168.7	-	0.5

As can be seen in Table 3, the exergy loss for the cascade expansion gas turbine cycle was highest in heat exchanger 1, followed by compressor, heat exchanger 2, turbine 2 and turbine 1. In addition, the heat exchangers are exchanged with a difference of 1.4 heat exchange coefficient from the source, the compressor and turbine power loads and the exergy efficiencies of each component are presented. The total net power was found to be 51.4 kW by subtracting the energy consumed for the compressor from the sum of the powers obtained from Turbine 1 and Turbine 2 (Table 3).

Figure 4-8 shows the T-s diagram for the heat cycle obtained from waste heat combined with an ORC system for refrigerants R600, R113, R 245fa, R 365mfc and R 123.

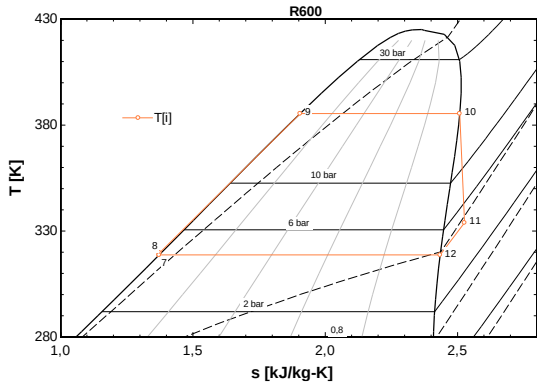

Figure 4. T-s diagram for ORC R600

Thermodynamic values of the ORC for the R 600 are presented in Table 4.

Table 4. Thermodynamic values for ORC-R600

ORC-R600	T [K]	s kJ/kg.K	P [bar]	h [kJ/kg]	Ex [kJ/kg]	m [kg/s]
7	318.7	1.372	4.415	310.7	9.284	0.2869
8	319.8	1.374	19.27	314.1	10.08	0.2869
9	385.5	1.905	19.27	501.5	19.19	0.2869
10	385.5	2.508	19.27	734	35.15	0.2869
11	333.9	2.527	4.415	679.4	17.94	0.2869
12	318.7	2.435	4.415	649.3	17.06	0.2869
T_0		2.532		618.5		

Thermodynamic calculations for the ORC system are given in Table 5.

Table 5. Thermodynamic results for ORC system R600 refrigerant

ORC-R600	Ex(KW)	Q(KW)in	Q(KW)out	W(KW)	φ
7-8 Pump	0.178	-	-	0.970	0.81
8-10 Heat exchanger 2	25.07	120.5	168.7	-	0.50
10-11 Turbine3	1.54	-	-	15.68	0.91
11-12 Heat exchanger 3	21.14	105.7	75.55	-	0.69

As can be seen in Table 5, the exergy loss for the ORC system is highest in heat exchanger 3, followed by heat exchanger 4, turbine 3 and pump. In addition, the heat exchangers are exchanged with a difference of 1.4 heat exchange coefficient from the

source; the compressor and turbine power loads and the exergy efficiencies of each component are presented.

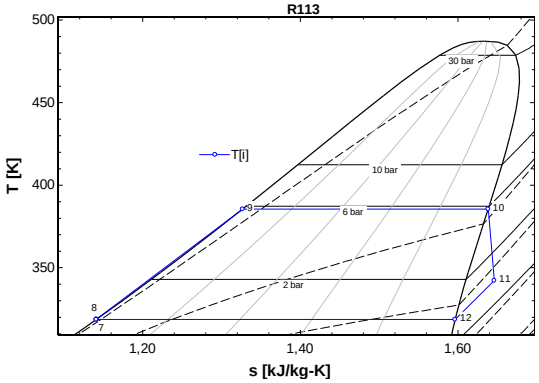

Figure 5. T-s diagram for ORC R113

Thermodynamic values for the ORC cycle are presented in Table 6.

Table 6. Thermodynamic values for ORC-R113

ORC-R113	T [K]	s kJ/kg.K	P [bar]	h [kJ/kg]	Ex [kJ/kg]	m [kg/s]
7	318.7	1.141	0.9463	241.8	0.539	0.6505
8	318.9	1.142	5.781	242.2	0.751	0.6505
9	385.5	1.327	5.781	307.3	7.786	0.6505
10	385.5	1.638	5.781	427.4	26.5	0.6505
11	342.3	1.646	0.9463	403.3	9.289	0.6505
12	318.7	1.596	0.9463	386.8	8.086	0.6505
T_0		1.064		218.3		

Thermodynamic calculations for the ORC system are given in Table 7.

Table 7. Thermodynamic results for ORC system R113 refrigerant

ORC-R113	Ex(KW)	Q(KW)in	Q(KW)out	W(KW)	φ
7-8 Pump	0.047	-	-	0.26	0.81
8-10 Heat exchanger 2	24.4	120.5	168.7	-	0.51
10-11 Turbine3	1.54	-	-	15.71	0.91
11-12 Heat exchanger 3	21.25	105.7	75.55	-	0.70

As seen in Table 7, the exergy loss for the ORC system is highest in heat exchanger 3, followed by heat exchanger 4, turbine 3 and pump. In addition, the heat exchangers are exchanged with a difference of 1.4 heat exchange coefficient from the source, the compressor and turbine power loads and the exergy efficiencies of each component are presented.

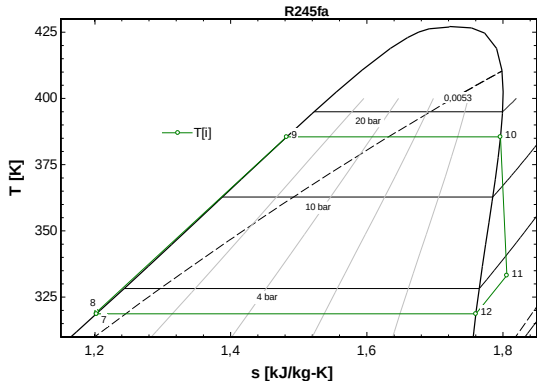

Figure 6. T-s diagram for ORC R245fa

Thermodynamic values for the ORC cycle are presented in Table 8.

Table 8. Thermodynamic values for ORC-R245fa

ORC-R245fa	T [K]	s kJ/kg.K	P [bar]	h [kJ/kg]	Ex [kJ/kg]	m [kg/s]
7	318.7	1.203	2.987	260.2	2.809	0.5493
8	319.5	1.204	16.53	261.5	3.4	0.5493
9	385.5	1.482	16.53	359.7	12.49	0.5493
10	385.5	1.796	16.53	480.8	28.43	0.5493
11	333.2	1.806	2.987	452.6	11.4	0.5493
12	318.7	1.203	2.987	260.2	2.809	0.5493
T_0		1.766		420.1		

Thermodynamic calculations for the ORC system are given in Table 9.

Table 9. Thermodynamic results for ORC system R245fa refrigerant

ORC-R245fa	Ex(KW)	Q(KW)in	Q(KW)out	W(KW)	φ
7-8 Pump	0.13	-	-	0.72	0.81
8-10 Heat exchanger 2	25.13	120.5	168.7	-	0.50
10-11 Turbine3	1.52	-	-	15.5	0.91
11-12 Heat exchanger 3	21.04	105.7	75.55	-	0.69

As seen in Table 9, the exergy loss for the ORC system is highest in heat exchanger 3, followed by heat exchanger 4, turbine 3 and pump. In addition, the heat exchangers are exchanged with a difference of 1.4 heat exchange coefficient from the source, the compressor and turbine power loads and the exergy efficiencies of each component are presented.

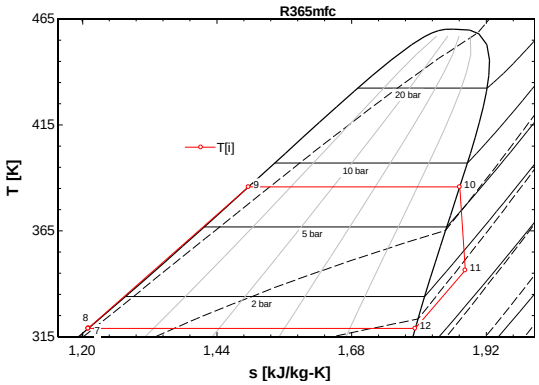

Figure 7. T-s diagram for ORC R365mfc

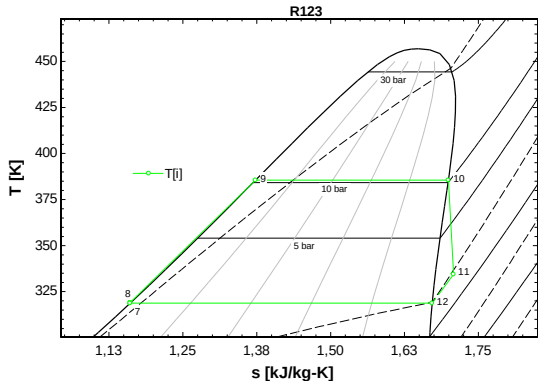

Figure 8. T-s diagram for ORC R123

Thermodynamic values for the ORC cycle are presented in table 10.

Table 10. Thermodynamic values for ORC- R365mfc

ORC-R365mfc	T [K]	s kJ/kg.K	P [bar]	h [kJ/kg]	Ex [kJ/kg]	m [kg/s]
7	318.7	1.211	1.224	262.4	0.674	0.4909
8	318.9	1.211	7.825	263	0.946	0.4909
9	385.5	1.496	7.825	363.4	9.17	0.4909
10	385.5	1.873	7.825	508.5	26.22	0.4909
11	346.2	1.883	1.224	477.7	9.681	0.4909
12	318.7	1.793	1.224	262.4	0.674	0.4909
T_0		1.095		227		

Thermodynamic calculations for the ORC system are given in Table 11.

Table 11. Thermodynamic results for ORC system R365mfc refrigerant

ORC-R365mfc	Ex(KW)	Q(KW)in	Q(KW)out	W(KW)	φ
7-8 Pump	0.06	-	-	0.33	0.81
8-10 Heat exchanger 2	24.88	120.5	168.7	-	0.50
10-11 Turbine3	1.43	-	-	15.11	0.91
11-12 Heat exchanger 3	21.72	105.7	75.55	-	0.70

As can be seen in Table 11, the exergy loss for the ORC system is highest in heat exchanger 3, followed by heat exchanger 4, turbine 3 and pump. In addition, the heat exchangers are exchanged with a difference of 1.4 heat exchange coefficient from the source, the compressor and turbine power loads and the exergy efficiencies of each component are presented.

Thermodynamic values for the ORC cycle are presented in table 12.

Table 12. Thermodynamic results for ORC system R123 refrigerant

ORC-R123	T [K]	s kJ/kg.K	P [bar]	h [kJ/kg]	Ex [kJ/kg]	m [kg/s]
7	318.7	1.161	1.851	247.8	0.752	0.6008
8	319.2	1.161	10.27	248.5	1.119	0.6008
9	385.5	1.373	10.27	323.4	8.82	0.6008
10	385.5	1.699	10.27	449.1	26.89	0.6008
11	334.4	1.708	1.851	422.4	9.336	0.6008
12	318.7	1.672	1.851	410.5	8.573	0.6008
T_0		1.074		221.1		

Thermodynamic calculations for the ORC system are given in Table 13.

Table 13. Thermodynamic results for ORC system R245fa refrigerant

ORC-R123	Ex(KW)	Q(KW)in	Q(KW)out	W(KW)	φ
7-8 Pump	0.08	-	-	0.45	0.81
8-10 Heat exchanger 2	24.38	120.5	168,7	-	0.51
10-11 Turbine3	1.56	-	-	15.99	0.91
11-12 Heat exchanger 3	20.98	105.7	75.55	-	0.69

As can be seen in Table 13, the exergy loss for the ORC system is highest in heat exchanger 3, followed by heat exchanger 4, turbine 3 and pump. In addition, the heat exchangers are exchanged with a difference of 1.4 heat exchange coefficient from the source, the compressor and turbine power loads and the exergy efficiencies of each component are presented.

The energy and exergy efficiencies of ORC and gas turbine cycles are given in Table 14. In addition, the net power, high and low pressure ratios in the ORC system and the amount of fluid used in the system are also presented.

Table 14. Energy and exergy efficiencies, ORC mass and net power in GT and ORC system

Fluid	$\frac{P_{10}}{P_{11}}$	$\dot{W}_{NET,ORC} = \dot{W}_{Turb,ORC} - \dot{W}_{Pump,ORC}$	ORC mass ($\dot{m}$)	Energy efficiencies (GT+ORC)	Exergy efficiencies (GT+ORC)
R 600	4.36	14.71	0.2869	0,66	0,20
R113	6.11	15.45	0.6505	0,66	0,20
R245fa	5.53	14.78	0,5493	0,66	0,20
R365mfc	6.39	14.78	0,4909	0,66	0,20
R123	5.55	15.54	0,6008	0,66	0,20

120.5 kW of the 168.7 kW (120.5*1.4) of heat output from the step-expansion gas turbine was used as useful heat for the ORC system. This was compared by applying it to five different fluids as shown in Table 15. In terms of mass flow rates of the refrigerants used in ORC, at least R600 refrigerant was used and at most R113 refrigerant was used. When looking at the condenser and evaporator pressure ratios in ORC, it was found that at least R600 and at most R365mfc refrigerants. 51.4 kW net power from the cascade gas turbine and 15.54 kW net power from the downcycle R123 refrigerant system of the cascade gas turbine (as shown in table 14). Total energy efficiencies of 66% and exergy 20% of GT and ORC cycles remained constant.

4. Conclusion and Suggestions

In this study, the thermodynamic analysis of the gas turbine (GT) system integrated into a heat source and the Organic Rankine Cycle (ORC) systems integrated into the turbine waste heat of this gas turbine system were made. Thermodynamic calculations were made using the waste heat of 120.5 kW corresponding to the ORC system, five different refrigerants with high critical temperature (R123, R245fa, R600, R365mfc and R113) as the working fluid in the cycle. The heat exchangers are exchanged with a difference of 1.4 heat exchange coefficient from the source, the compressor and turbine power loads and the exergy efficiencies of each component are presented. Engineering Equation Solver (EES) program was used for thermodynamic analysis [20]. According to the results obtained;

- The gas turbine cycle worked with 16% efficiency. The most exergy loss was in heat exchanger 1, which is the main heat source, followed by the air inlet compressor, ORC heat transfer heat exchanger 2, turbine 2 and turbine 1.
- When evaluated in terms of mass flow rates of the refrigerants used in ORC, at least R600 refrigerant was used and at most R113 refrigerant was used.
- When looking at the condenser and evaporator pressure ratios in ORC, it was found that the refrigerants were at least R600 and at most R365mfc.
- Calculated as R123 refrigerant in terms of net power obtained in the ORC system.
- Total energy efficiencies of 66% and exergy 20% of GT and ORC cycles remained constant.

The result of competitive technologies brings competitive approaches. In this context, providing more power generation from waste heat sources will provide added value to both our national economy and our national energy policies. Alternative integrated system designs and applications will offer more possibilities in this contex

Conflict of Interest Statement

There is no conflict of interest between the authors.

Statement of Research and Publication Ethics

The study is complied with research and publication ethics

References

[1] S. Lecompte, O. A. Oyewunmi, C. N. Markides, M. Lazova, A. Kaya, Van den Broek, M., and De Paepe, M., “Case study of an organic rankine cycle (ORC) for waste heat recovery from an electric arc furnace (EAF)”, *Energies*, 10(5), pp. 649, 2017.

[2] A. Javanshir, N. Sarunac and Z. Razzaghpanah, “Thermodynamic analysis of ORC and its application for waste heat recovery”, *Sustainability*, 2017, (11), 1974.

[3] M. H. Ahmadi, M. N. Alhuyi, R. Ghasempour, F. Pourfayaz, M. Rahimzadeh and T. Ming, "A review on solar assisted gas turbines", *Energy Science & Engineering*, vol. 6, pp. 658-674, 2018.
[4] A. Nassar, N. Mehta, O. Rudenko, L. Moroz, and G. Giri, "Design of Waste Heat Recovery System based on ORC for a Locomotive Gas Turbine",2018.
[5] Ö. Kaşka, B. O. R Onur, N. Tokgöz and M.M. Aksoy, "First and second law evaluation of combined Brayton-Organic Rankine power cycle", *Journal of Thermal Engineering*, vol.4, pp.577-591, 2020.
[6] J. Ren, Y. Cao, Y. Long, X. Qiang and Y. Dai, "Thermodynamic comparison of gas turbine and ORC combined cycle with pure and mixture working fluids", *Journal of Energy Engineering*, 145(1), 05018002, 2019.
[7] Ö. Kaşka, B. O. R. Onur, Tokgöz, N., and Aksoy, M. M., "First and second law evaluation of combined Brayton-Organic Rankine power cycle", *Journal of Thermal Engineering*, vol.6(4), pp.577-591, 2020.
[8] E. B. Espinel, G. O. Valencia and J. F. Duarte, "Thermodynamic, exergy and environmental impact assessment of S-CO_2 brayton cycle coupled with ORC as bottoming cycle". *Energies*, vol.13(9), pp. 2259, 2020.
[9] S. Gürgen and İ. Altin, "Novel decision-making strategy for working fluid selection in Organic Rankine Cycle: A case study for waste heat recovery of a marine diesel engine", *Energy*, 124023, 2022.
[10] R. Chacartegui, D. Sánchez, J. M. Muñoz and T. Sánchez, "Alternative ORC bottoming cycles for combined cycle power plants", *Applied Energy*, vol.86(10), pp.2162-2170, 2009.
[11] Y. Khan and R. S. Mishra, "Performance evaluation of solar based combined pre-compression supercritical CO_2 cycle and organic Rankine cycle", *International journal of Green energy*, vol. 18(2), pp. 172-186, 2021.
[12] C. Carcasci, R. Ferraro and E. Miliotti, "Thermodynamic analysis of an organic Rankine cycle for waste heat recovery from gas turbines", *Energy*, vol.65, pp.91-100, 2014.
[13] O. Ighodaro, P. Ochornma and H. Egware, "Energy Analysis of A Retrofitted Regenerative Gas Turbine Organic Cycle in Ihovbor Power Plant", *International Journal of Engineering Technologies IJET*, vol.6(3), pp.45-61, 2020.
[14] R. M. Mishra and M. Kumar, "Thermodynamic analysis of brayton cycle for power generation", 2019
[15] J. Jeong and Y. T. Kang, "Analysis of a refrigeration cycle driven by refrigerant steam turbine", *International journal of refrigeration*, vol.27(1), pp.33-41,2004.
[16] Y. Lei, S. Ye, Y. Xu, C. Kong, C. Xu, Y. Chen and H. Xiao, "Multi-objective optimization and algorithm improvement on thermal coupling of SOFC-GT-ORC integrated system", *Computers & Chemical Engineering*, 164, 107903, 2022.
[18] I. Dincer and M. A. Rosen, "Exergy: energy, environment and sustainable development", Newnes, 2012.
[19] Y. A. Cengel, M. A. Boles and M. Kanoğlu, "Thermodynamics: an engineering approach", *New York: McGraw-hill*, vol. 5, pp. 445, 2011.
[20] S. A. Klein and F. L. Alvarado, Engineering equation solver. F-Chart Software, Madison, WI, 1,2022.

Bitlis Eren Üniversitesi Fen Bilimleri Dergisi
BİTLİS EREN UNIVERSITY JOURNAL OF SCİENCE
ISSN: 2147-3129/e-ISSN: 2147-3188
VOLUME: 11 NO: 4 PAGE: 971-982 YEAR: 2022
DOI:10.17798/bitlisfen.1129632

An Investigation of Optimal Power System Designs for a Net Zero Energy House: A Case Study of Kahramanmaraş

Mustafa EKEN[1], İbrahim ÇELİK[2*]

[1] *Kahramanmaraş İstiklal University, Elbistan Vocational School of Higher Education, Department of Construction, Kahramanmaraş, Turkey*
[2] *Kahramanmaraş İstiklal University, Elbistan Vocational School of Higher Education, Electricity and Energy, Kahramanmaraş, Turkey*
(ORCID: 0000-0002-7559-876X) (ORCID: 0000-0001-5923-554X)

Keywords: Net zero energy, Hybrid, Photovoltaics, Wind power, Homer Pro.

Abstract
This paper aims to optimize the power system design of a vineyard house in Pazarcık, Kahramanmaras. In this process, the electrical energy demand is met by the hybrid Photovoltaic-Wind-Diesel-Battery system because the vineyard house is remote from the electric network. The vineyard house is located in Karagol, southern of Pazarcık. During the summer in Karagol, many people stay in and visit the vineyard houses. However, the vineyard houses are generally unoccupied in winter. Therefore, an economical energy source is required in this process without compromising life quality. Capital costs are high and the running costs are low for stand-alone renewable sources. On the other hand, it is the opposite for stand-alone diesel power generators. This study is designed to take these circumstances into consideration. The optimal design is investigated for a hybrid system of renewable energy sources and a diesel power generator. The Homer software is used during this process. The realized design is evaluated in terms of its technical and environmental aspects. As a result of the study, 6 kW photovoltaic panels, a 1 kW wind turbine, a 1 kW diesel generator, a 2-kW converter, and an optimally sized 8-unit battery system are used to meet the electricity needs of the vineyard house. The renewable energy factor is 99.8% for a vineyard house. This value is an acceptable rate for a net zero energy house. This study shows that the hybrid system meets the house's electric energy demands and has a positive impact on the environment by reducing greenhouse gas emissions.

1. Introduction

The demand for energy in developing countries has been rising due to increased industrial activities and population growth. Therefore, the production of sustainable energy is a necessity for developing countries to meet their energy needs. Despite this, the global consumption of fossil fuels and the production of oil are also increasing day-by-day, leading to excessive greenhouse gas emissions, which has a significant socio-economic impact on the world due to global warming. As a result, it is essential to consider alternative sustainable energy sources in each nation's energy policies. In this context, wind energy and solar energy are among the most effective and efficient renewable energy sources [1]-[4].

The building's massive energy consumption can be attributed to rising living standards and urbanization levels. According to the literature reviewed, the buildings' energy consumption has consisted of a sizeable portion of the energy consumption in the United States, China, and Turkey [5]-[7]. Numerous studies have been conducted on renewable systems such

*Corresponding author: ibrahim.celik@istiklal.edu.tr
Received: 12.06.2022, Accepted: 12.10.2022

as photo voltaic (PV), wind, geothermal, hydro, wave, biomass sources, and hybrid systems made up of a combination of these sources [8]-[16]. Energy systems that combine two or more different energy sources are known as hybrid energy systems. These resources may function in the off-grid or grid-connected modes [17]-[25].

Off-grid diesel generators and solar photovoltaic systems for power generation have different capital and operating costs. Off-grid PV systems have a high initial purchase price and require periodic battery replacements. On the other hand, diesel generators have a lower initial cost but higher fuel and maintenance costs. Off-grid PV systems are widely promoted for use in rural areas to generate cleaner, safer, and more reliable energy [26], [27].

Nowadays, hybrid system installation is completed quickly and easily. If the system is optimized properly, it will be a more effective power source in comparison to others. This situation has led to a great number of hybrid systems being installed around the world. The block diagram of a hybrid wind/PV/diesel system is shown in Figure 1 [28].

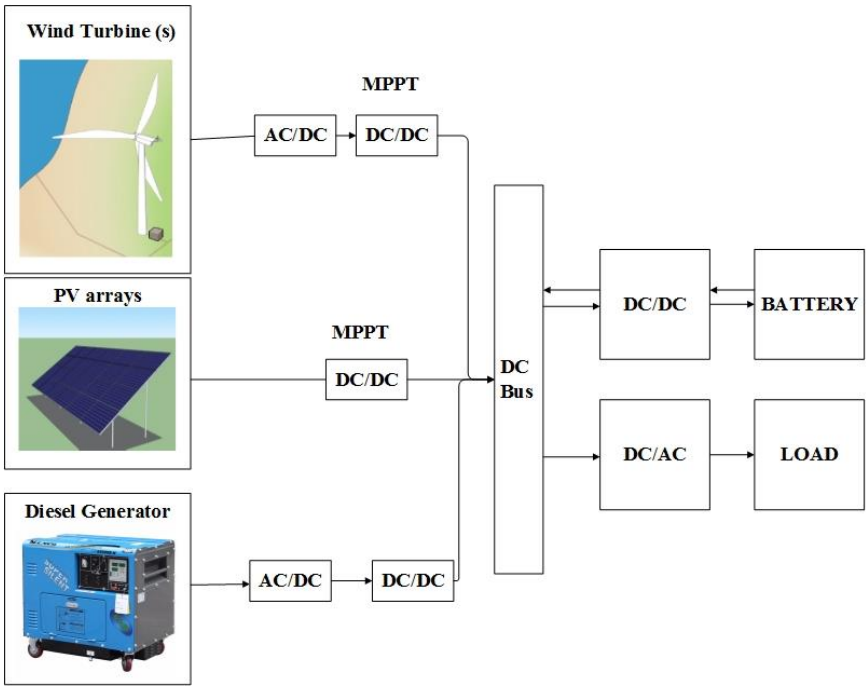

Figure 1. The block diagram of a hybrid wind/PV/diesel system

The aim of the present study is to model a net-zero energy system to meet the demands of a vineyard house. For this purpose, the study was carried out for a vineyard house in Pazarcık (Kahramanmaras). The optimal power system design is realized. The results of the study are evaluated from technical and environmental standpoints, and the energy production of the hybrid system is analyzed to determine whether it is sufficient. Homer optimal sizing software is employed throughout the study.

2. Material and Method

This section is composed of three parts. The first part includes the climate values and site data of Karagol. The second part presents the energy demand of the vineyard house. The third part is composed of the Hybrid Wind-PV-Diesel-battery system simulation with the Homer software.

2.1. Site and Data Collection

The investigation site is located in Karagol, Kahramanmaras, Turkey (Latitude: 37° 29' 06.41" N, Longitude: 36° 46' 57.25 E", Altitude: 1601m). The solar radiation values and average wind speed of Karagol are given in Table 1. In this table, it can be seen that the average wind speed reached maximum values during the summer months. The global radiation map of Kahramanmaras is given in Figure 2. In this figure, the global radiation values vary approximately between 1600 KWh/m^2-year and 1750 KWh/m^2-year depending on the location.

The global radiation value is approximately 1600 KWh/m^2-year in Karagol.

Table 1. The Solar radiation values and average wind speed of Karagol [29]

	Horizontal Global Irradiation kWh/m^2	Horizontal Diffuse Irradiation kWh/m^2	Horizontal Beam Irradiation kWh/m^2	Ambient Temperature ^{o}C	Wind Velocity m/s
January	69.1	30.35	38.7	-1.10	2.2
February	80.6	42.08	38.5	0.49	2.4
March	132.6	59.00	73.6	5.54	2.7
April	165.7	61.72	104.0	9.84	2.7
May	204.1	65.42	138.7	15.37	2.7
June	238.3	62.62	175.7	21.23	3.4
July	247.8	55.82	191.9	25.49	3.6
August	227.9	50.52	177.4	24.85	3.0
September	177.9	41.97	136.0	19.25	2.6
October	129.4	39.13	90.3	13.46	1.9
November	84.9	30.48	54.4	5.58	1.9
December	67.7	27.31	40.3	0.48	2.1
Year	1826.1	566.41	1296.4	11.77	2.6

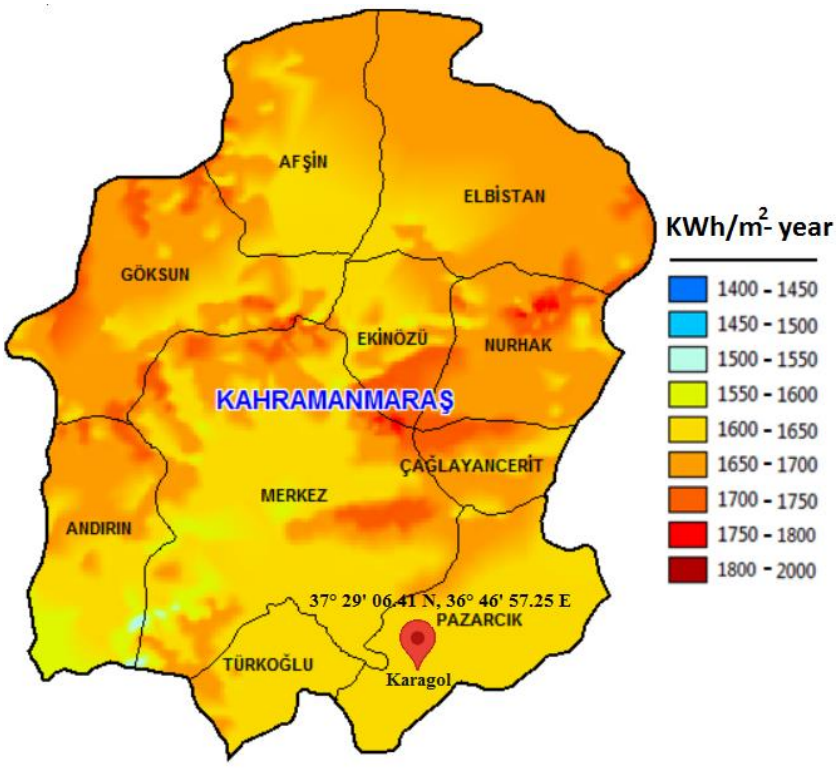

Figure 2. For the map of Karagol, Kahramanmaras (Turkey) [30]

2.2. Energy Demand

There is no national electric grid network connection at this location. Therefore, the house is to be connected to a proposed hybrid system. The hybrid system consists of photovoltaic, wind turbine, and diesel generator. The aim of this system is to economically meet the energy needs compromising the quality of life.

The vineyard houses are completely full during the summer months due to the climate conditions. At this time, energy demand is at a very high level. Table 2 shows the energy demand for a typical vineyard house. By looking at Table 2, it can be seen that the daily, weekly, monthly, and

yearly energy needs of the vineyard house are 10.5 KWh, 73.503 KWh, and 315.013 KWh, respectively. For example, 15 pieces of LED lighting are used for approximately 7 hours a day. The daily, weekly, and monthly energy consumption of LED lighting is 1050 Wh, 7350 Wh, and 315000 Wh, respectively. The daily energy distribution profile is shown in Figure 3. The energy demand peaked between 11:00 and 13:00 hours because of the intensive use of dishwashers and washing machines.

In Figure 3, the peak hour demand time coincided with the most productive hours of solar radiation, which reduces the need for batteries, leading to a reduction in energy costs. The primary sources of energy at this timeare sun throughout the day and the wind in the evening.

Figure 4 shows the monthly energy demand profile of the vineyard house. The annual energy demand of the vineyard house is 3832.5 kWh.

Table 2. Energy demand of vineyard house

	Power (Watt)	Piece (s)	Duration of energy consumption (hour/ day or week)	Energy		
			Daily	Daily	Weekly	Monthly
LED lighting	10	15	7 h/day	1050Wh	7350Wh	31500Wh
TV	80	1	4 h/day	320Wh	2240Wh	9600Wh
Computer	80	2	4 h/day	640Wh	4480Wh	19200Wh
Refrigerator	25	1	24 h/day	600Wh	4200Wh	18000Wh
House Appliances	105	5	5 h/day	2625Wh	18375Wh	78750Wh
Washing Machine	1000	1	5.4 h/week	771Wh	5400Wh	23143Wh
Dishwasher	900	1	2 h/day	1800Wh	12600Wh	54000Wh
Other	2694	1	1 h/day	2694Wh	18858Wh	80820Wh
Total				10500 Wh	73503Wh	315013Wh

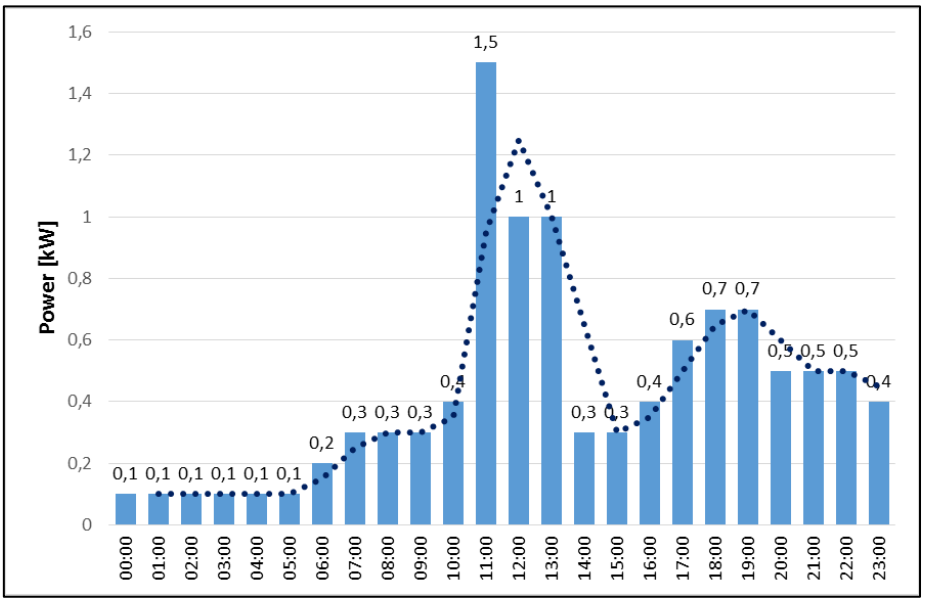

Figure 3. Daily energy demand

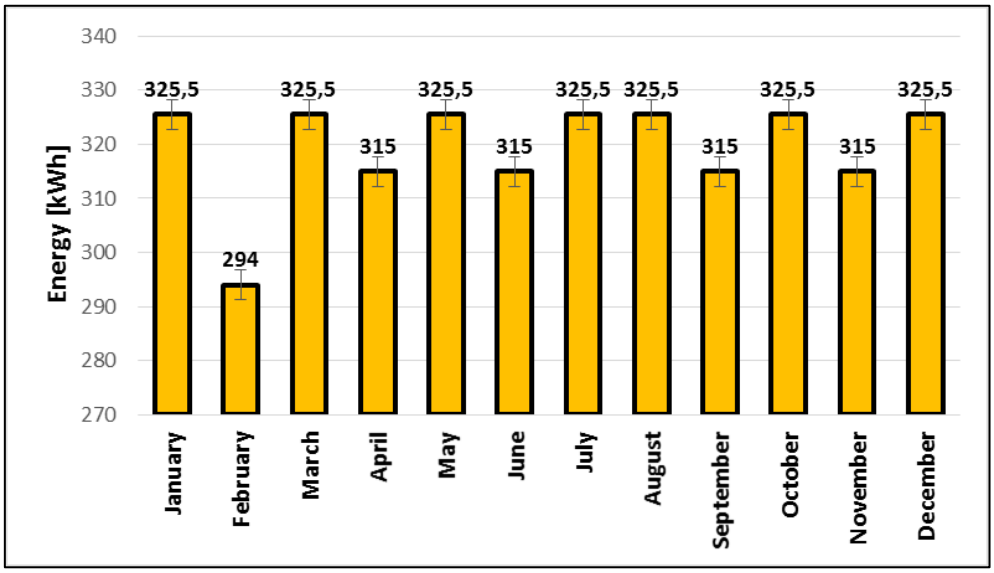

Figure 4. Monthly energy demand

2.3. Optimal Sizing

a global standard in micro grid software. This program is used to design and implement micro grids and distributed power systems. Renewable energy sources, storage, and fossil-based power generation are connected to the power systems in the design process. Simulation and optimization analysis can be performed on the systems designed through the program. The climate and measurement data for the design were sourced from the NASA database.

The energy needs of the vineyard house are met with the hybrid wind-PV-diesel-battery system. The lack of an electricity grid in the vineyard house area explains this. A large amount of the population resides in these houses during the summer season. Thus, there is a need for an economical energy source without sacrificing the quality of life. The capital costs of renewable energy sources alone are very high, while the diesel generator operating costs are even higher. These two systems are used to compose a more economical system design.

Optimal sizing of hybrid wind-PV-diesel-battery systems is considered an economical energy system. The wind-PV-diesel hybrid system for Karagol is realized using Homer optimal sizing software. The wind turbine, PV panels, diesel generator, battery, and converter were modeled and sized using the Homer software program. This model is shown in Figure 5.

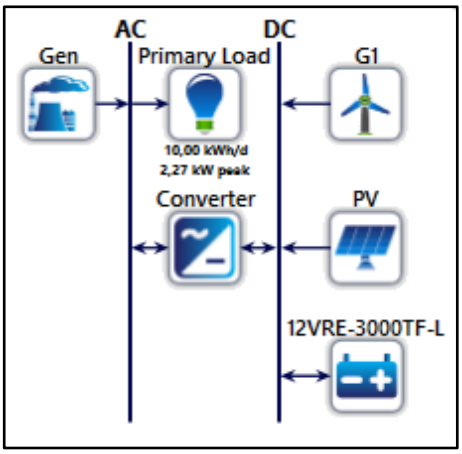

Figure 5. Homer system

The model is designed based on the following assumptions. HOMER's generic diesel generator is used. The diesel price is taken as 1.13 dollars per liter. The generator's lifetime is 15000 hours and the minimum load ratio is 25%. The capacity of the PV panels is 250 W. The current at maximum power point (I_{mpp}) is 8.271 A. Moreover, the voltage at maximum power point (V_{mpp}) is 30.23 V. The converter is 90% efficient and has a 15-year of lifespan. The batteries in this design procedure have a nominal voltage of 12 V with a 245 Ah.

In this optimization, PV panels, wind turbines, power converters, and batteries are used. In this model, various power levels of diesel generators (1,2,3,4,5,6 kW), wind turbines (1, 2, 3, 4 kW), PV panels (0,1,2,3,4,5,6, 7, 8, 9, 10, 11, 12 kW), batteries (0,2,4,6,8,10,12,14,16,18, 20, 22, 24, 26, 28), and converters (1,2,3,4, 5, kW)

were tested separately. These combinations help with cost and performance analysis for optimum sizing and 219000 probabilities. Considering the unit cost of energy and capital costs as a result of optimization, the renewable energy factor is calculated as 99.8%. The wind turbine, PV panels, and diesel generator are used in the design. The wind turbine has a capacity of 1 kWp, while PV panels have a capacity of 6 kWp, the diesel generator has a capacity 1 kWp, and the converter has a capacity of 2 kWp. Eight batteries were used to determine dimensions. The total investment cost is $8,470. And the cost of energy per unit is $0.264. The Homer software outputs are shown in Figure 6.

Architecture											Cost				System
						PV (kW)	G1	Gen (kW)	12VRE-3000TF-L	Converter (kW)	Dispatch	COE ($)	NPC ($)	Operating cost ($)	Initial capital ($)	Ren Frac (%)
						6,00	1	1,00	8	2,00	LF	0,264 $	12.458 $	308,50 $	8.470 $	100
							4	1,00	10	2,00	CC	1,27 $	59.926 $	4.082 $	7.150 $	35
						8,00	4	1,00		2,00	CC	1,84 $	86.745 $	5.848 $	11.150 $	61
							4	2,00		2,00	CC	5,18 $	244.210 $	18.512 $	4.900 $	0,0

Figure 6. Homer software output

The unit cost of the energy in the PV panels, wind turbine, the total cost of investment, and sizing should be appropriate for real values. The appropriate values from the cost map are shown in Figure 7. In this model, environmental effects have been taken into account as well as the cost of the energy. Renewable sizing fraction and the CO_2 emission must be optimum for the designed system. The optimum point in the renewable energy map is shown in Figure 8.

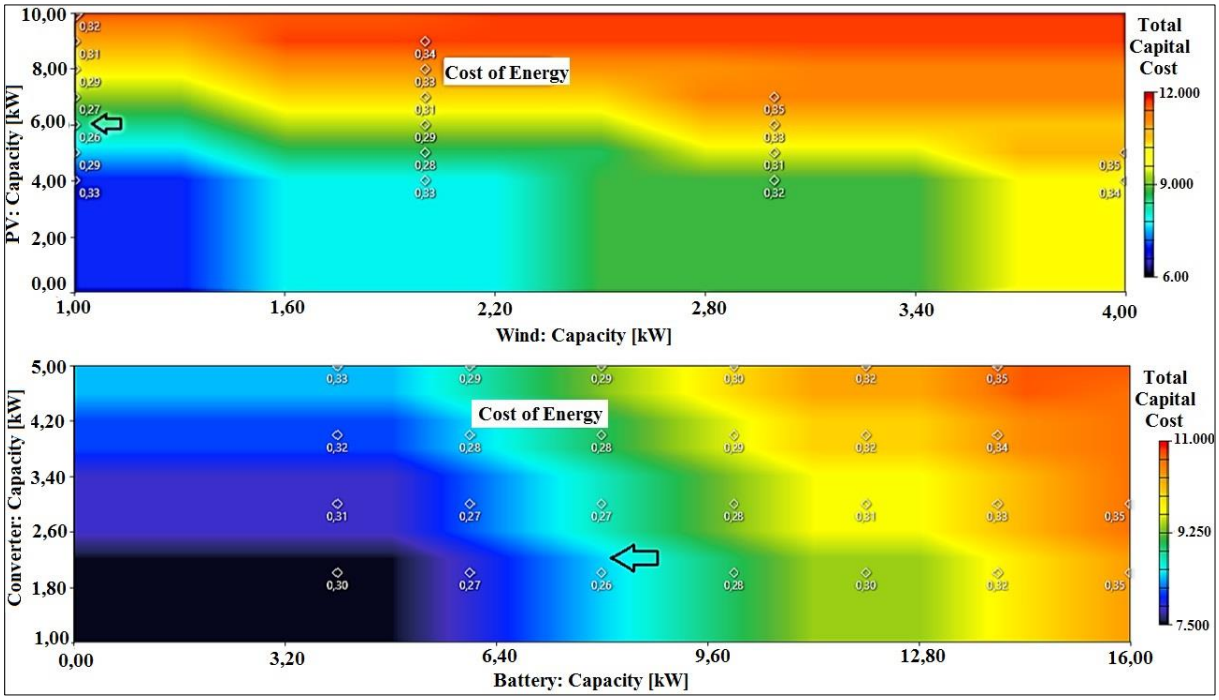

Figure 7. System sizing with the help of cost map

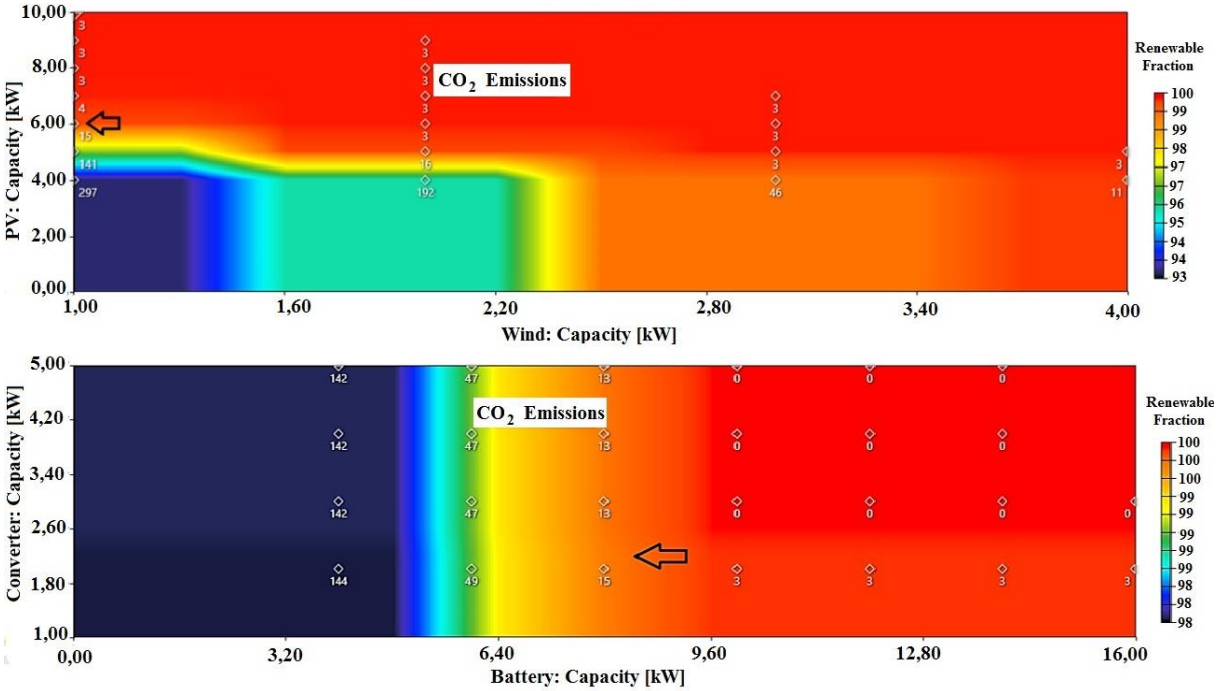

Figure 8. System sizing with the help of renewable energy map

The wind turbine, PV panels, diesel generator, battery, and converter are designed and modeled by Homer software. Figure 9 shows the ideal cost spots. The energy and investment costs are lower at this red circle point. At this point, the total investment cost is 8,470 dollars, and the unit cost of the energy is selected to be $0.264. Figure 10 shows the ideal spots in terms of cost and renewable energy factors.

The 24 solar panels totaling 240 W, 1 kW wind turbine, 1 kW diesel generator, 2 kW converter, and 8-unit 245 Ah batteries make up the optimal hybrid system. PV panels are connected in parallel. Batteries are connected in series in pairs, consisting of four parallel groups. The operating voltage of the battery is 24 volts.

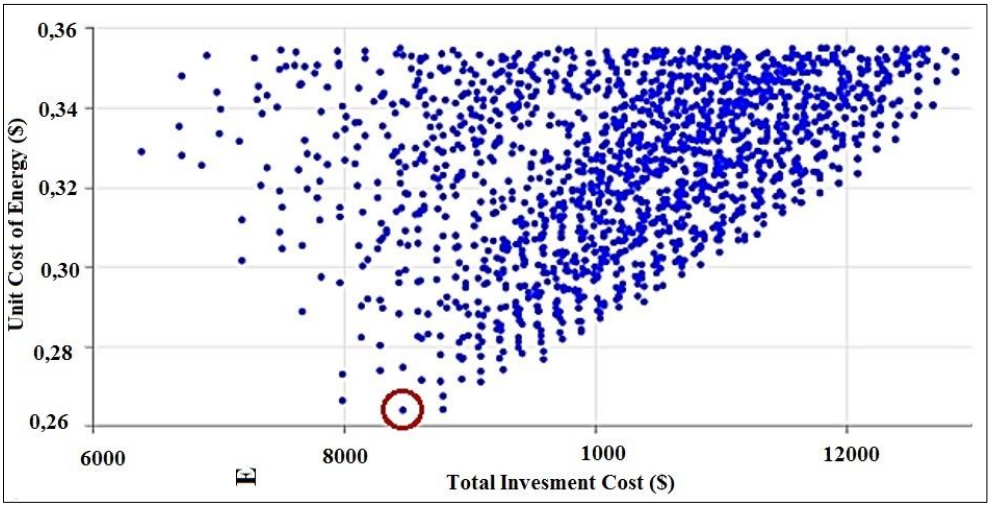

Figure 9. The ideal cost spots

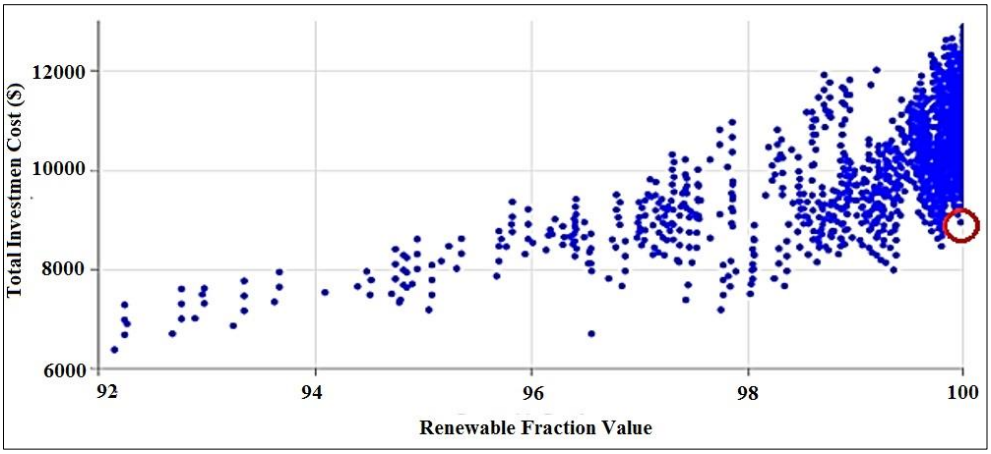

Figure 10. The ideal spots in terms of cost and renewable energy factor

3. Results and Discussion

The investment cost of the wind-PV-diesel-battery hybrid system is $8,470. Nowadays, this cost is considerably high because of the dollar exchange rate. However, the energy demand needs to be met throughout the years. The annual energy demand is 3832.5 kWh, the average daily energy demand is 10.5 kWh, the average hourly energy is 0.44 kW, and the peak energy demand value is 2.38 kW. PV panels have annual energy production of 8817 kWh, a wind turbine has an annual energy production of 589 kWh and a diesel generator has an annual energy production is 8 kWh. The annual energy demand is met by 93.66% from PV panels, 0.8% from the diesel generator, and 6.26% from the wind turbine. Additionally, 1877 kWh of energy is stored in the batteries annually and the 1613 kWh of energy is used from the batteries annually. PV panels have produced 4232 hours and 5.88 kW of electrical energy. The diesel generator used 5.8 liters of diesel for 26 hours of operation per year. The nominal capacity of the battery is 15 kWh and it provided the system with 1613 kWh energy.

An area with strong radiation in the mornings and afternoons and strong winds during the evenings is an excellent candidate for a hybrid wind-PV-diesel-battery system. PV panels will be used to meet energy needs in the morning, and the wind turbine will provide the needed energy during the evening. In cases where the energy requires battery storage, diesel generator will be activated to meet the power need. It is desirable to use more renewable energy sources. The cost-efficient diesel generator will be used very sparingly during the year. Furthermore, the renewable energy factor is calculated at 99.8%. The high amount of unused energy is stored to use during times when adverse weather conditions cause a demand for higher energy. In the summer, the excess energy can be used in areas with irrigation and for other energy needs. Annually, an excess of 5094.8 kWh of energy is produced. This energy is used for irrigation, particularly in rural areas. Another option to reduce excess energy is by selecting smaller PV panels. However, this will not be economical in the long run considering the life span which is 20-25 years. The monthly change of energy sources is shown in Figure 11. Wind speed and change by month according to the amount of radiation are given in Figure 12.

The diagram obtained by modeling of the hybrid system under annual Karagol conditions is given in Figures 13. This figure shows that global solar radiation is rampant in Karagol, especially during the summer. The maximum radiation value is 1.3 kW per meter square. The summer season offers more than 12 hours of radiation each day. Although wind is available throughout the day, it is more abundant in the evening. In the evening, the maximum wind speed is over 17m/s. The hourly maximum output of the PV panels is 5.58 kW.

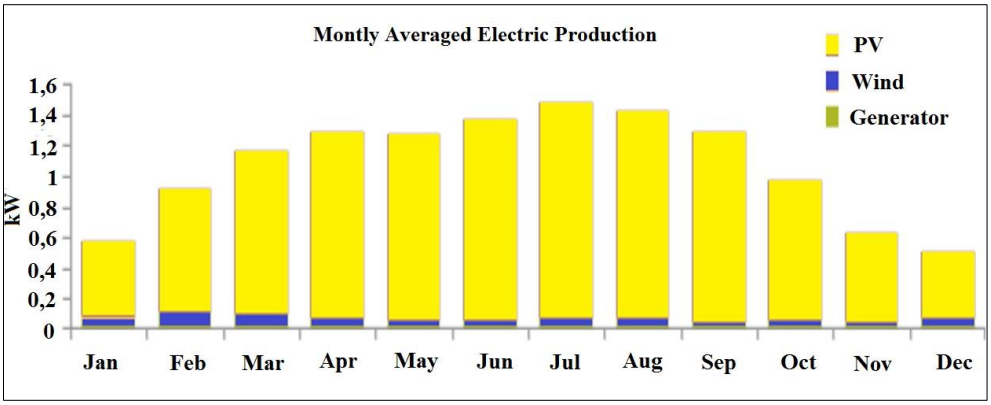

Figure 11. Monthly change of energy sources

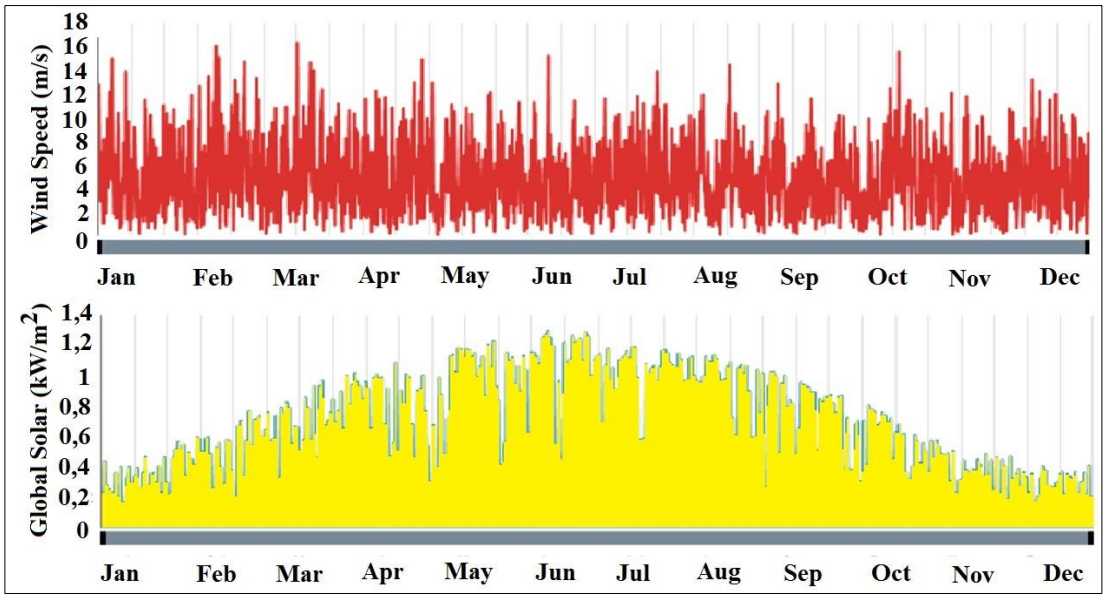

Figure 12. Changing of wind speed and radiation

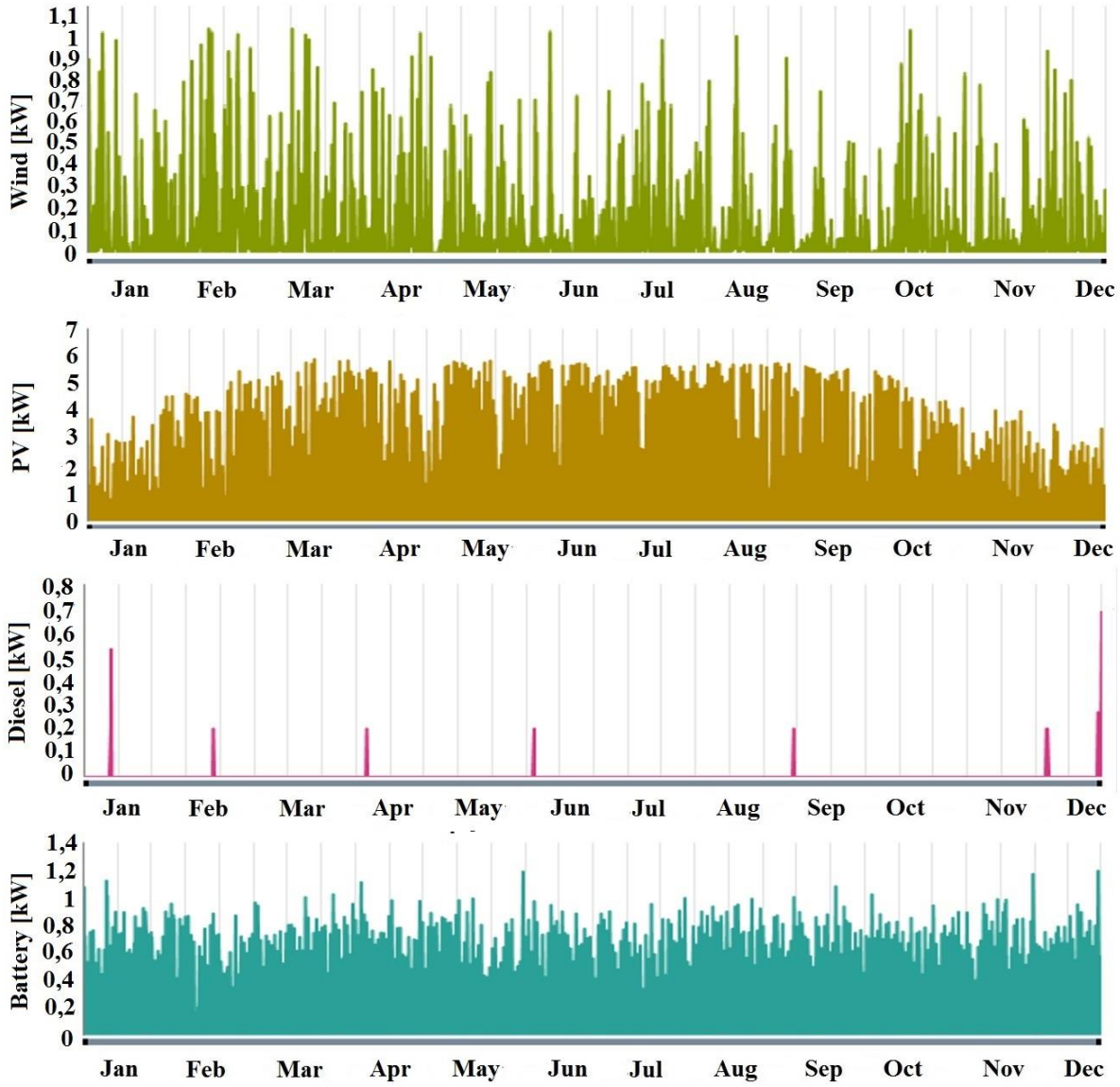

Figure 13. Energy sources for power generation in year

4. Conclusion and Suggestions

In this study, the energy requirement of the vineyard house in Pazarcık, Kahramanmaras (Turkey) is modeled using a wind-PV-diesel-battery hybrid system, as accessing the electricity grid in the remote rural areas of the vineyard houses is not economical. These vineyard houses are generally full during the summer. Therefore, they need a reliable energy source. The use of either a renewable source of energy or a diesel generator alone is not cost-efficient. This study modeled a cost-effective optimal sizing of the hybrid system. The results of the study are listed below:

The optimization result showed that the total investment cost is $8,470 and the unit cost of energy is $0.264.

The hybrid system has 6 kW PV panels and a 1 kW diesel generator, a 1 kW win turbine, a 2 kW converter and 8 units of optimally sized battery system. The vineyard house energy demand will be met throughout the year. Photovoltaic panels produce 8817 kWh, a wind turbine produces 589 kWh, and a diesel generator produces 8kWh energy annually.

The annual energy demand is met by 93.66 % from PV panels, 0.8% from the diesel generator, and 6.26% from the wind turbine. Additionally, the 1877 kWh of energy is stored in the batteries annually. 1613 kWh of energy is taken from the batteries annually. The total

annual energy demand is 3832.5 kWh and unused energy is stored in batteries. Total renewable production is 99.92%, and renewable energy factor is 99.8 %.

According to International Energy Agency (IEA) report in Turkey, the production of 1 kWh of electrical energy causes a 489 g release of carbon dioxide (CO_2) emissions. In this context, this installed system meets energy need of the house and provides a significant contribution to the environment.

Future studies will be able to implement it using the different hybrid systems for houses of different locations without an electricity grid connection. Furthermore, more optimal and environmentalist designs can be proposed.

Contributions of the Authors

All authors contributed equally to the study.

Conflict of Interest Statement

There is no conflict of interest between the authors.

Statement of Research and Publication Ethics

The study is complied with research and publication ethics

References

[1] P. G. Vasconcelos Sampaio, and M. O. Aguirre Gonzales, "Photovoltaic solar energy: Conceptual framework" *Renewable and Sustainable Energy Reviews*, vol. 74, pp. 590-601, 2017.

[2] A. Kumar, A. Adelodun and K. H. Kim, "Solar energy: Potential and future prospects," *Renewable and Sustainable Energy Reviews*, vol. 82, pp. 894-900, 2018.

[3] İ. Çelik, C. Yıldız and M. Şekkeli, *Turkish Journal of Engineering*, vol 5, no.2, pp. 89-94, 2021.

[4] B. Al-Mhairat and A. Al-Quraan, "Assessment of Wind Energy Resources in Jordan Using Different Optimization Techniques," *Processes*, vol. 10, no.1, p. 105, 2022.

[5] C. Xiaodong, D. Xilei, and L. Junjie, "Building energy-consumption status worldwide and the state-of-the-art technologies for zero-energy buildings during the past decade," *Energy and Buildings*, vol. 128, pp. 198-213, 2016.

[6] "Annual energy outlook - U.s. energy Information Administration (EIA)," Eia.gov. [Online]. Available: https://www.eia.gov/outlooks/aeo/. [Accessed: 16-Oct-2022].

[7] Commission européenne. Direction générale de la mobilité et des transports, EU energy, transport and GHG emmissions: Trends to 2030 : Reference scenario 2013. Brussels, Belgium: European Commission, 2014.

[8] J. Liu, X. Chen, H. Yang, and K. Shan, "Hybrid renewable energy applications in zero-energy buildings and communities integrating battery and hydrogen vehicle storage," *Applied Energy*, vol. 290, no. 116733, p. 116733, 2021.

[9] A. Sajid and C. M. Jang, "Optimum design of hybrid renewable energy system for sustainable energy supply to a remote island." *Sustainability*, vol. 12, no. 1280, p. 1280, 2020.

[10] J. Liu, Y. Zhou, H. Yang, and H. Wu, "Net-zero energy management and optimization of commercial building sectors with hybrid renewable energy systems integrated with energy storage of pumped hydro and hydrogen taxis," *Applied Energy*, vol. 321, no. 119312, p. 119312, 2022.

[11] W. Wu and H.M. Skye, "Residential net-zero energy buildings: Review and perspective," *Renewable and Sustainable Energy Reviews*, vol. 142, no. 110859, p. 110859, 2021.

[12] F. Bahramian, A. Akbari, M. Nabavi, S. Esfandi, E. Naeiji, and A. Issakhov, "Design and tri objective optimization of an energy plant integrated with near-zero energy building including energy storage: An application of dynamic simulation," *Sustainable Energy Technologies and Assessments*, vol. 47, no. 101419, p.10419, 2021.

[13] S. Gorjian, H. Ebadi, G. Najafi, S. S. Chandel, and H. Yildizhan, "Recent advances in net-zero energy greenhouses and adapted thermal energy storage systems," *Sustainable Energy Technologies and Assessments*, vol. 43, no. 100940, p. 100940, 2021.

[14] J. Liu, H. Yang, and Y. Zhou, "Peer-to-peer energy trading of net-zero energy communities with renewable energy systems integrating hydrogen vehicle storage," *Applied Energy*, vol. 298, no. 117206, p. 117206, 2021.

[15] N. Sifakis and T. Tsoutsos, "Planning zero-emissions ports through the nearly zero energy port concept," *Journal of Cleaner Production*, vol. 286, no. 125448, p. 125448, 2021.
[16] A. Arabkoohsar, A. Behzadi, and A.S. Alsagri, "Techno-economic analysis and multi-objective optimization of a novel solar-based building energy system; An effort to reach the true meaning of zero-energy buildings," *Energy Conversion and Management*, vol. 232, no. 113858, p. 113858, 2021.
[17] S. Arabi-Nowdeh, S. Nasri, P. B. Saftjani, A. Naderipour, Z. Abdul-Malek, H. Kamyab, and A. Jafar-Nowdeh, "Multi-criteria optimal design of hybrid clean energy system with battery storage considering off-and on-grid application," *Journal of Cleaner Production*, vol. 290, no. 125808, p. 125808, 2021.
[18] K. V. Konneh, H. Masrur, M. L. Othman, N. I. A. Wahab, H. Hizam, H., S. Z. Islam, and T. Senjyu," Optimal design and performance analysis of a hybrid off-grid renewable power system considering different component scheduling, PV modules, and solar tracking systems," IEEE Access, vol. 9, pp. 64393-64413, 2021.
[19] B. Musa, N. Yimen, S. I. Abba, H. H. Adun, and M. Dagbasi, "Multi-state load demand forecasting using hybridized support vector regression integrated with optimal design of off-grid energy Systems—A metaheuristic approach," *Processes*, vol. 9, no. 1166, p. 1166, 2021.
[20] H. M. Farh, A. A. Al-Shamma'a, A. M. Al-Shaalan, A. Alkuhayli, A. M. Noman, and T. Kandil, "Technical and economic evaluation for off-grid hybrid renewable energy system using novel bonobo optimizer," *Sustainability*, vol. 14, no. 1533, p.1533, 2022.
[21] P. Marocco, D. Ferrero, A. Lanzini, and M. Santarelli, "Optimal design of stand-alone solutions based on RES+hydrogen storage feeding off-grid communities. Energy Conversion and Management," vol. 238, no. 114147, p. 114147, 2021.
[22] M. Kharrich, S. Kamel, M. Abdeen, O. H. Mohammed, M. Akherraz, T. Khurshaid, and S. B. Rhee," Developed approach based on equilibrium optimizer for optimal design of hybrid PV/Wind/Diesel/Battery microgrid in Dakhla, Morocco. IEEE Access, vol. 9, pp. 13655-13670, 2021.
[23] F. Wang, J. Xu, L. Liu, G. Yin, J. Wang, and J. Yan, "Optimal design and operation of hybrid renewable energy system for drinking water treatment," *Energy*, vol. 219, no. 119673, p. 119673, 2021.
[24] Z. Ullah, M. R. Elkadeem, K. M. Kotb, I. B. Taha, and S. Wang, "Multi-criteria decision-making model for optimal planning of on/off grid hybrid solar, wind, hydro, biomass clean electricity supply," *Renewable Energy*, vol. 179, pp. 885-910, 2021.
[25] F. Kahwash, A. Maheri, and K. Mahkamov, "Integration and optimisation of high-penetration Hybrid Renewable Energy Systems for fulfilling electrical and thermal demand for off-grid communities," *Energy Conversion and Management*, vol. 236, no. 114035, 2021.
[26] M. El Zein and G. Gebresenbet, "Investigating off-grid systems for a mobile automated milking facility," *Heliyon*, vol. 7, no. 4, p. e06630, 2021.
[27] A. Borodinecs, D. Zajecs, K. Lebedeva, and R. Bogdanovics, "Mobile Off-Grid Energy Generation Unit for Temporary Energy Supply". *Applied Sciences*, vol. 12(2), no. 673, p. 673, 2022.
[28] S. K. A. Shezan, S. Julai, M.A. Kibria, K.R. Ullah, R. Saidur, W.T. Chong, and R.K. Akikur, "Performance analysis of an off-grid wind-PV (photovoltaic)-dieselbattery hybrid energy system feasible for remote areas", *Journal of Cleaner Production*, vol.125, pp. 121-132, 2016.
[29] "Pvsyst", http://www.pvsyst.com/en/. [Accessed: 15-May-2022].
[30] "GEPA", https://gepa.enerji.gov.tr/MyCalculator/pages/46.aspx. [Accessed: 15-May-2022].

Bitlis Eren Üniversitesi Fen Bilimleri Dergisi
BİTLİS EREN UNIVERSITY JOURNAL OF SCIENCE
ISSN: 2147-3129/e-ISSN: 2147-3188
VOLUME: 11 NO: 4 PAGE: 983-992 YEAR: 2022
DOI:10.17798/bitlisfen.1129676

Railway Noise Pollution: An Investigation of Rail Systems in Terms of Noise Pollution Regulations and Land Usage

Raziye PEKER[1*], Kürşat YILDIZ[1]

[1]*Gazi University, Institute of Science and Technology, Department of Civil Engineering, Ankara, Turkey*
(ORCID:0000-0003-1104-61972) (ORCID:0000-0003-2205-9997)

Keywords: Railway, noise pollution, land cover, IDW.

Abstract

Noise pollution caused by transportation has become a problem for societies with increasing traffic volumes and the development of cities day by day. In European countries and Turkey, transportation-related noise pollution has caused health problems and reduced the living standards of the people. It is necessary to carry out detailed studies in order to determine the problems caused by noise pollution, especially in the regions where industry and the labor force are concentrated, and to solve these problems. The city of Izmir is one of the cities where the noise caused by the railway needs to be investigated. As a result of the studies carried out in the research area, the railway noise pollution map was created with the IDW method with the data obtained from 8 different points. Afterwards, the effect of railway systems on the land use types of cities, noise pollution problems, and the period between 2000 and 2018 was examined. The adverse effects of noise pollution caused by the railway in the hinterland of the suburban line in the study area and its effect on the land usage type were investigated with the EU and Turkey Noise Regulation and the land cover data of the European Environment Agency

1. Introduction

In today's conditions, where the amount of mobility is increasing and industrialization is developing day by day, some negative effects of transportation systems on the environment. Noise pollution is one of these effects, and its negative effects on people in terms of physical, physiological, psychological, and performance (such as concentration impairment, and decreased work efficiency) have been revealed in this study. [1, 2, 3, 4, 5, 6, 7, 8]. Although the World Health Organization does not want to exceed the noise limit value of 55 dB (A) during the day and 40 dB (A) at night, according to studies, 20% of the European Union countries have 65 dB (A) and 40% 55 dB (A) noise pollution. [1, 9, 10]. This exposure has caused dissatisfaction among people and an inefficient workforce in densely populated areas [11-13]. For this reason, national and international studies have been carried out about the solution to environmental noise have continued since the 1960s [6, 9, 10]. With the effect of developing technologies and the development of railway systems, it has become highly necessary to investigate the damage of noise pollution and vibration caused by rail systems [14]. Maps of the regional noise have started to be prepared in order to better analyze the environmental noise and in order to make appropriate action plans. Noise pollution maps are generally prepared by using GIS (Geographical Information Systems) based programs. European Union countries, the USA, Japan, China, and Turkey also use CadnaA and Sound plan which are noise simulation software [15, 16]. Noise measurement type, and duration; A noise pollution map was created by using appropriate parameters such as the building information of the region, its height, and distance. Interpolation methods such as inverse distance weighted (IDW), Kriging, and Radial Basis Function

* Corresponding author: raziyepeker@yandex.com
Received: 12.06.2022, Accepted: 22.08.2022

are used to generate noise maps [17]. While the noise pollution maps provide information about the current environmental noise in the region, they may be insufficient to make a comment on the future. Although there are many parameters of noise pollution, knowing the land usage of the region can be used to detect noise sources [18]. Thanks to the land cover data of the European Environment Agency (EEA), it can be observed in which trend the land usage of the regional structure differed until the 1990s. This data allowed us to analyze how housing, schools, and industrial areas around the railway lines changed. In line with this information, the effect of the noise pollution originating from the railway on the İzmir İZBAN line, which was selected as a sample line, was studied in order to determine the regional effect. For the sample region selected for this purpose, the effect of noise pollution and vibration is one of the noise pollution regulations; By using the Environmental Noise Assessment and Management Regulation (ENAMR) in Turkey and the Environmental Noise Directive (END) accepted by the European Union countries. The noise measurement results made by Republic of Türkiye State Railways (TCDD) in the 4750 m area on the IZBAN line were analyzed [19-21]. After the noise pollution analysis, noise pollution maps of the study area were prepared with the IDW method with the ArcGIS 10.7 program. Afterwards, using the CORINE Land Cover CLC (Coordination of Information on the Environment) datasets, the changes in the land cover of the region between 2000 and2018 were compared, and the effect and change of the railway on the region, as well as how the region was affected by noise pollution and vibration, were investigated [22].

2. Material and Method

In this section, each related work is detailed in the subsequent subsections.

2.1. Workspace and Dataset

In addition to being Turkey's third largest city and having a dense population, İzmir was chosen as a study area due to its development in terms of industry, agriculture, logistics, and trade. The population of the city is 4,367,251 according to 2019 (Turkish Statistical Institute -TURKSTAT) data, and the population density of the city is increasing every year [23, 24] (Figure 1)

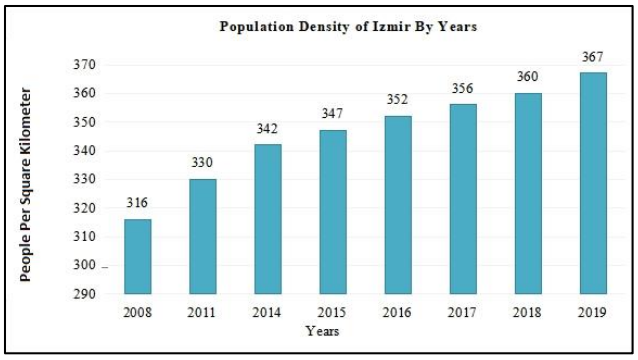

Figure 1. Izmir population density [24]

In the city of Izmir, as a rail system for urban transportation, there are suburban trains operated by IZBAN company on the north-south axis, İzmir metro operated by İzmir Metropolitan Municipality on the east-west axis and TramİzmirTramİzmir operated by İzmir Metro, which was put into service in Konak and Karşıyaka districts in 2017. In addition, main line passenger trains, regional trains and freight trains, which are under the responsibility of TCDD, also operate on the line where IZBAN suburban trains are located. In this study, noise pollution was analyzed within the framework of regulations in line with the measurements obtained in the 4750-meter section of the IZBAN line (Figure 2)

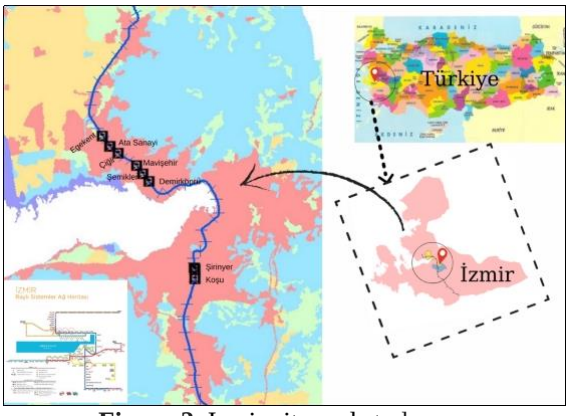

Figure 2. Izmir city and study area

Noise Measurements were made by TCDD in 2017-2018 and are given in able 1 [19] (Table 1). Materials used chart 2 shown with (Figure 2)

Table 1. Long-term noise measurement results* [19]

Location	Date/time	Lday(dBA) 07:00 to 19:00	Levening(dBA) 19.00-23.00	Lnight(dBA) 23.00-07.00
Mavişehir-Demirköprü	2017	69.5	70.7	64.6
Şirinyer-Koşu	2017	62	60.1	54.6
Cigli-Atasanayi	2018	67.5	68.7	61.7
Atasanayi-Egekent	2018	64	61.8	57.1

*Lday: It is the average of the measurements made during the daytime (07.00-17.00) of the year in long-term measurements. Levening: It is the average of the measurements made in the evening (17.00-23.00) of the year in long-term measurements. Lnight: It is the average of the measurements made at night (23.00-07.00) of the year in long-term measurements.

Table 2. Data type and sources used in the study

Data Type	Data	Source of Data
Report	Sound Screen Projects Noise Measurement	TCDD- Republic of Turkey State Railways
Regulation	Evaluation and management of environmental noise	Official Gazette No.27601
EU Directive	2002/49/EC Environmental Noise Directive	Official journal of the european communities
Software	Arcmap 10.7	Software- Esri
Land usage	Maps of the Corine Land usage	EEA (European Environment Agency)

In order to analyze the noise measurements made in this study, the Environmental Noise Directive-Environmental Noise Directive (END) 2002/49/EC, which was accepted by the European Union countries in 2002, was used [21]. In Türkiye, the 'Rail System Environmental Noise Criteria' contained in the Environmental Noise Assessment and Management Regulation (EMR) have been used [20]. CORINE Land Cover datasets prepared by EU (European Union) countries were used to observe the land usage change in the hinterland of the railway line [22].

2.2. Method

The study was prepared by using the point noise measurement results made at 8 different stops, namely Koşu, Şirinyer, Demirköprü, Şemikler, Mavişehir, Çiğli, Atasanayi, Egekent passing through the districts of Buca, Karşıyaka and Çiğli passing through the IZBAN line. Spot measurement results were analyzed using the inverse distance weighted (IDW) method using the ArcGIS 10.7 program. To function in the program of the IDW method, at least three different points should be entered into the system this by the position located Koşu- Şirinyer stops between Şirinyer selected as close as a third point reference point stop is in the made mapping. Since the stops between Demirköprü and Egekent in Karşıyaka-Çiğli region were uninterrupted, the noise measurement results were sufficient for mapping.

The noise pollution maps created afterwards were compared in terms of noise pollution and vibration regulations. The IZBAN line in the region where the noise measurement was made was put into operation in 2010, and the 10 years before the region was put into operation and 8 years after the operation were compared using the CORINE land cover data.

In this study, the noise pollution problem created by the railway line, the effect of the railway line on regional construction, the relationship between railway construction and the change in regional land use were investigated.

3. Results

3.1. The Evaluation of Noise Pollution and Vibration in Terms of Regulations

As a result of the measurement results of 2017 and 2018 obtained on the IZBAN line, it was determined that the noise pollution in the region where the measurements were made is above the threshold value. According to the ENAMR, the limit values must not exceed the limit values Lday 65 dB(A), Levening: 60 dB(A), and Lnight: 55 dB(A). Although similar figures are valid according to END data, these values differ between +5 and -5 depending on the building use of the region (housing, hospital, industrial area). According to the long-term measurement results in Table 3, the exceeded limit values are presented as percentages. As can be seen from the table, it has been revealed that the limit values on the Mavişehir-Demirköprü route are exceeded by almost 17%. The adverse effects of increased noise exposure, especially in the evening and at night, on the surrounding people were determined, and the results of the survey conducted in the literature also showed the negative effects of noise pollution exposure on people

Table 3. % dBA amount exceeded according to long-term measurement results

Location	Limit dBA exceeded in %		
	Ldaytime 07.00-19.00	Levening 19.00-23.00	Lnight 23.00-07.00
Mavişehir-Demirköprü	6.92	17.83	17.45
Şirinyer - Koşu	-	0.17	-
Cigli- Atasanayi	3.85	14.50	12.18
Atasanayi-Egekent	-	3.00	3.82

.2. The Evaluation of Noise Pollution Maps Made by IDW Method

The measurement results were analyzed with the IDW method via ArcGIS. This method was used because the long-term measurement results were point-based. As a result of the analysis, as seen in figure 3, measurements were made between Şirinyer and Koşu in the Buca region. As a result of measurements made in 2017 Lday 62 dBA, where appropriate Lday 60.1 dBA, and Lnight 54.6 dBA were detected and mapped. Since the analysis did not work without at least 3 points, the reference point close to Şirinyer stop was added as an assumption.

According to the analysis, the measurement results between Şirinyer and Koşu do not exceed the limit values specified in the regulation and do not pose a serious problem for the region in its current state

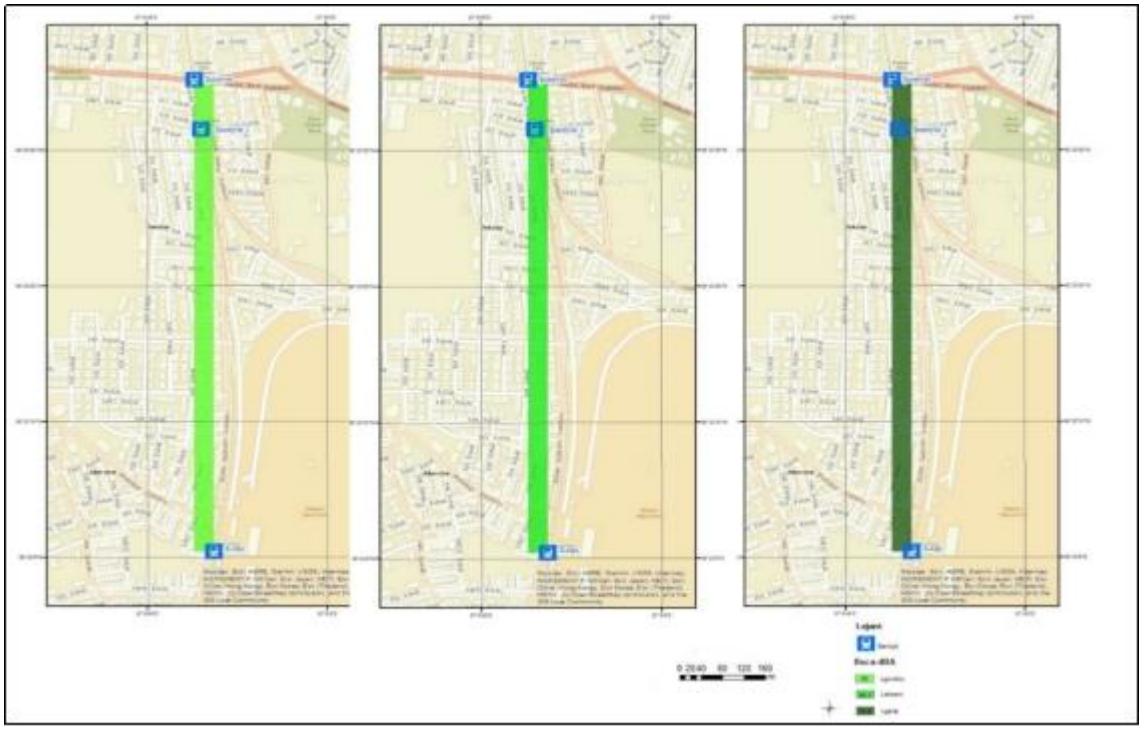

Figure 3. Map of the Buca noise pollution

Demirköprü, Şemikler, Mavişehir, Çiğli, which pass through Karşıyaka and Çiğli districts.

The measurement results at Atasanayi and Egekent stations were analyzed in Figure 4-5-6. As a result of the analysis, it was determined that the daytime limit value of 65 dBA was exceeded in Mavişehir, Şemikler and Demirköprü regions.

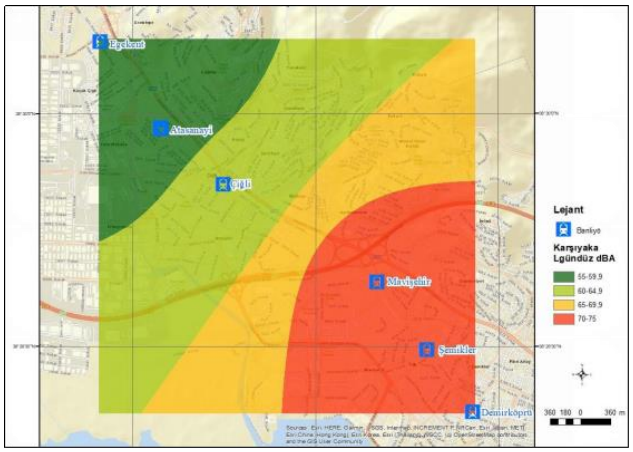

Figure 4. Map of the Karsiyaka daytime noise pollution

Evening noise in the Egekent-Atasanayi region: although the evening noise remained at the limit values, the evening noise regulation limit values were exceeded at Çiğli, Mavişehir, Şemikler, and Demirköprü stops.

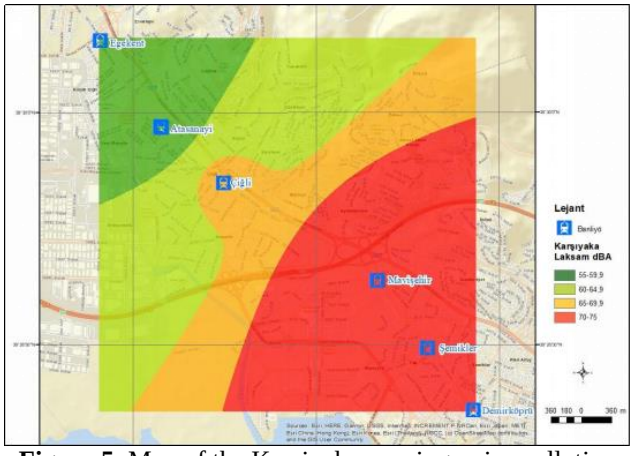

Figure 5. Map of the Karsiyaka evening noise pollution

Railway noise should be at night 55 dB(A) but Demirköprü-Egekent between 55 dB(A) seems to overcome. The limit value of approximately 15 dB (A) has been exceeded between Mavişehir and Demirköprü.

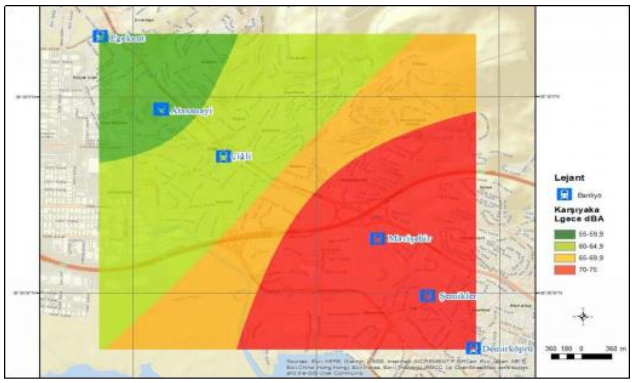

Figure 6. Map of the Karsiyaka night noise pollution

3.3. The Evaluation of Noise Pollution and Vibration in Terms of Land Usage

In the study, the effect of the IZBAN line on the land cover was examined. IZBAN line located in Buca and Karşıyaka districts was put into operation on 30 August 2010. In order to analyze the period before the opening of the IZBAN line, land use maps were selected pre-2010 land use maps, and in order to interpret the change in land use after the railway line was put into operation, the land use maps of 2000-2018 were selected. Considering the area occupied by the IZBAN line; Land usage type and changes from Corine land cover data of CLC2000, CLC2006, CLC2012, and CLC2018 were determined by basic spatial analysis processes made from the ArcMap program (Figure 7, 8,9,10).

The land use types on the maps are numbered as follows;

- 111 Continuous urban fabric
- 112 Discontinuous urban fabric
- 121 Industrial or commercial units
- 122 Road and rail networks and associated land
- 324 Transitional woodland-shrub
- 323 Sclerophyll plants
- 321 Natural grassland
- 313 Mixed forest
- 312 Coniferous forest
- 243 Land principally occupied by agriculture, with significant areas of natural vegetation
- 223 Olive groves
- 211 Non-irrigated arable land
- 133 Construction sites
- 131 Mineral extraction sites
- 333 Sparsely vegetated areas
- 242 Complex cultivation patterns
- 142 Sports and leisure facilities
- 141 Green urban areas

As a result of spatial analysis: it has been determined that the rail systems contribute to the development of the region and increase the housing in the hinterland of the railway line, as they provide convenience in journeys such as home, work, and school. In the 2000s, lands used as agricultural or green areas were converted into housing, industry, and connecting roads to meet demand. This change poses a risk in the long run, especially for the people of the region where housing has increased, in terms of catching diseases related to transportation noise.

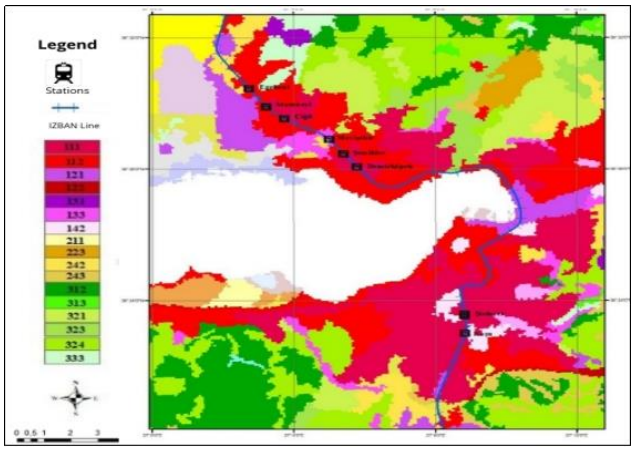

Figure 7. Map of the 2000 land usage

The land cover map of 2000 was prepared with Arcmap at a scale of 1/100,000. As can be seen in Map 5, the land use of the area in the hinterland of the study area is as follows.

There are a continuous urban texture, and sports and recreation areas between Şirinyer and Koşu. When we examine the land in the hinterland of Egekent-Demirköprü stops; continuous-discontinuous urban texture, construction areas, mixed agricultural areas, natural meadows and urban texture with industrial, and commercial units are observed.

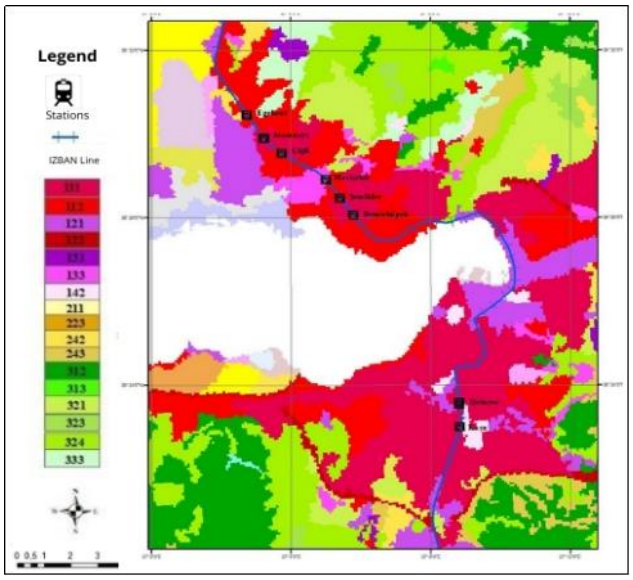

Figure 8. Map of the 2006 land usage

The land cover map of 2006 was prepared by Arcmap at a scale of 1/100,000. As can be seen in Map 6, it was observed that the hinterland of the study area changed from 2000 to 2006 as follows. Some of the sports and recreational areas located between Şirinyer and Koşu have been converted into industrial and commercial units. In the Egekent-Demirköprü hinterland, the mixed agricultural areas in the Mavişehir region have been transformed into construction areas, and the continuous urban texture on the Atasanayi-Çiğli line has increased

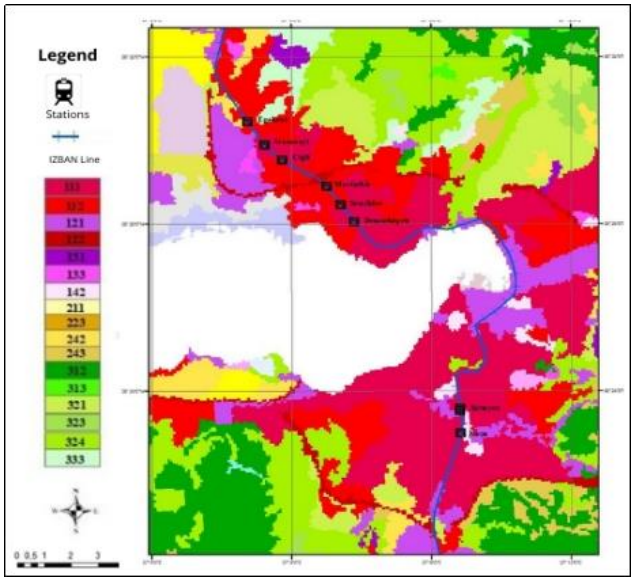

Figure 9. Map of the 2012 land usage

The land cover map of 2012 was prepared by Arcmap on a scale of 1/100,000. As can be seen in Map 7, it was observed that the hinterland of the study area changed from 2006 to 2012 as follows. It is observed that some of the sports and recreational areas in the running hinterland have turned into industrial and commercial units. It is observed that the construction areas in the Mavişehir region turn into a discontinuous urban texture, and the highway line that cuts the suburban line at 90 degrees has been put into operation. This is also one of the points that causes the noise level to be exceeded in the noise pollution maps of the region. It has been observed that some industrial areas in the Atasanayi region have been transformed into reconstructed areas

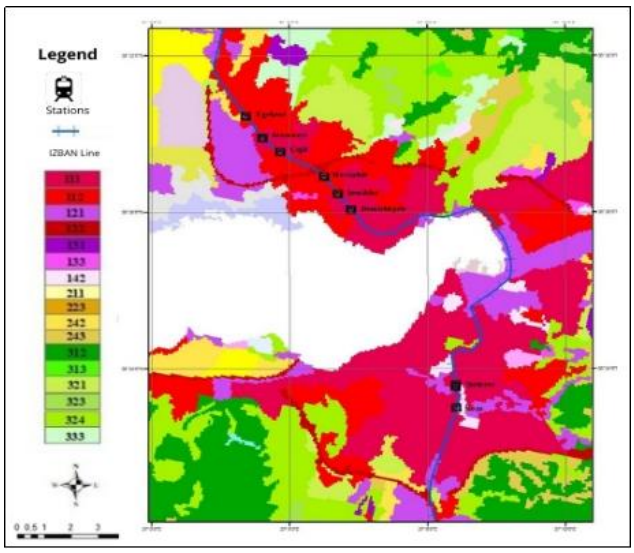

Figure 10. Map of the 2018 land usage

The land cover map of 2018 was prepared with Arcmap on a scale of 1/100,000. As can be seen in Map 8, it has been observed that the hinterland of the study area has changed from 2012 to 2018 as follows. No change was observed in the land use pattern between Şirinyer-Koşu. In the Atasanayi hinterland, the constructions in the industrial and commercial units have been completed and the land texture of the region has not changed much compared to the previous period. Considering that the İZBAN line was put into operation in 2010, we can observe that the land texture of the region does not allow for new changes about 8 years after the line was opened.

4. Discussion

Noise pollution is a serious environmental problem that causes environmental problems throughout the world. Noise pollution caused by railways is also a sub-branch of environmental problems arising from

transportation. Negative effects on humans in terms of physical, psychological, physiological, and labor performance are known, and in order to reduce these negative effects, the railway-induced change in the region's land usage was examined in the period between 2000 and2018, ten years before the opening of the line and eight years after. As a result of the examination, it has been investigated to what extent the noise pollution caused by the rail systems complies with the limit values specified in the EU regulations END and the ENAMR used by Turkey.A noise pollution map of the study area was created with the IDW method. Although it is done in a very limited area, it has been observed that the excess caused by noise pollution is at a level of 17% in places. While this value is above the values prescribed by WHO, it has also been determined that it is not at the appropriate level by the ENAMR and END regulations.

In addition, when the change in land use is examined in the research, the construction areas have increased with the construction of the railway line and the development of the region. When it comes to 2012-2018, changes in land use are now almost never seen. The reason for this is that railway investments do not allow the type of land usage to change after the development of the region reaches a certain saturation point and can servesociety in general. In this context, as can be understood from the findings of the study, the land use type of very limited areas in the region has changed after 2012.

In this study, noise pollution and vibration caused by rail systems were investigated, and the inability to measure vibrations in the region constituted the limitation of my study. It is known that vibration can cause structural damage as well as negative effects on human health. In other studies to be carried out, besides noise pollution and land usage, vibration measurements can be made and the damage to the structures in the region can be clearly determined. In addition, making the measurements at 8 stops enabled us to map with the IDW method. More precise measurements at more points will allow for more precise mapping of noise pollution to be created in ways that no other facility will.
Briefly;

- As a result of the evaluated field measurements, the noise limit value specified in the ENAMR and END regulations has been exceeded at a rate of 1 dB(A) and 10,7 dB(A) in the study area.
- In the type of land use, it was determined that the green areas in general changed from the construction areas to the continuous and discontinuous urban texture between the years 2000 and2012. It is thought that the effect of the Izmir IZBAN suburban line, which was put into operation in 2010, is among the reasons causing these changes.

- It is known that vibration causes structural damage, although vibration measurements could not be reached in this study; its compliance with the legislation should be checked and necessary precautions should be taken.

5. Conclusion

The study is an example for metropolitan cities since it was carried out in the metropolis and the port city of Izmir. In addition, each city can adapt the study to its own region, taking into account its socio-cultural and economic structure. Because noise pollution is environmental pollution that has been found to have negative effects on society in general. Therefore, if the cities are designed by taking into account the effects of noise pollution and vibration before making railway planning and considering the limit values of the regulation, both noise pollution and vibration problems around the rail systems will be prevented; efficient use of the land will be ensured. In addition, the high initial investment cost of the railway and the fact that the project changes are very difficult after the construction phase revealed the necessity of taking into account noise pollution and vibration in every project sensitively.

As a result, noise pollution, which is one of the leading environmental problems in the world, should not be ignored while designing the railway systems' project-construction-operation processes. The use of land usage types in the railway hinterland in accordance with the limit values in the noise pollution regulations is necessary for the sustainability of the cities.

Acknowledgments

We would like to thank the Republic of Turkey State Railways (TCDD) for their support to this study.

References

[1] S. Kurra, *Environmental noise and its management (Volume I).* Istanbul: Bahcesehir University Press,, 55-59, 2009, doi: 2880000043874

[2] E. Murphy, and E. King, *Environmental noise pollution: Noise mapping, public health, and policy.* USA: Newnes Elsevier Publications, 123-138, 2014, doi: 10.1016/C2012-0-13587-0.

[3] K. Kalawapudi, T. Singh, J. Dey, R. Vijay, and R. Kumar, "Noise pollution in Mumbai Metropolitan Region (MMR): *An emerging environmental threat". Environmental Monitoring and Assessment*, 192(2), 1-20, 2020, doi: 10.1007/s10661-020-8121-9.

[4] M. R. Ghotbi, M. R. Monazzam, M. R. Baneshi, M. Asadi, and S. M. B. Fard, "Noise pollution survey of a two-storey intersection station in Tehran metropolitan subway system". *Environmental Monitoring and Assessment, 184(2),* 1097-1106, 2012, doi: 10.1007/s10661-011-2024-8.

[5] S. Kurra, *Environmental noise and its management (Volume II).* Istanbul: Bahcesehir University Press, 295-321, 2009, doi: 2880000043874.

[6] H. Andersson, and M. Ögren, "Noise charges in railway infrastructure: A pricing schedule based on the marginal cost principle." *Transport Policy*, *14*(3), 204-213, 2007, doi: 10.1016/j.tranpol.2007.01.002

[7] M. Brink, B. Schäffer, D. Vienneau, M. Foraster, R. Pieren, IC. Eze, and JM. Wunderli, "A survey on exposure-response relationships for road, rail, and aircraft noise 36 annoyance: Differences between continuous and intermittent noise". *Environment international*, 125, 277-290, 2009, doi: 10.1016/j.envint.2019.01.043

[8] P. Tassi, O. Rohmer, S. Schimchowitsch, A. Eschenlauer, A. Bonnefond, F. Margiocchi, and A. Muzet, Living alongside railway tracks: "Long-term Effects of nocturnal noise on sleep and cardiovascular reactivity as a function of age". *Environment international,* 36(7), 683-689, 2010, doi: 10.1016/j.envint.2010.05.001

[9] T. C. Chan, and K. C. Lam, "The effects of information bias and riding frequency on noise annoyance to a new railway extension in Hong Kong". *Transportation research part D: transport and environment*, *13*(5), 334-339, 2008, doi: 10.1016/j.trd.2008.04.002.

[10] E. Murphy, and EA. "King, Strategic environmental noise mapping. Methodological issues concerning the implementation of the EU Environmental Noise Directive and their policy implications". *Environment international,* 36(3), 290-298, 2010, doi: 10.1016/j.envint.2009.11.006.

[11] C. Tonne, C. Milà, D. Fecht, M. Alvarez, J. Gulliver, J. Smith, and F. Kelly, "Socioeconomic and ethnic inequalities in exposure to air and noise pollution in London". *Environment international,* 115, 170-179, 2008, doi: 10.1016/j.envint.2018.03.023.

[12] B. Schäffer, M. Brink, F. Schlatter, D. Vienneau, and JM. Wunderli, "Residential green is associated with reduced annoyance to road traffic and railway noise but increased annoyance to aircraft noise exposure". *Environment international,* 143, 2020, doi: 10.1016/j.envint.2020.105885.

[13] I. C. Eze, M. Foraster, E. Schaffner, D. Vienneau, R. Pieren, M. Imboden, and N. ProbstHensch, "Incidence of depression in relation to Transportation noise exposure and noise annoyance in the SAPALDIA study". *Environment International,* 144, 2020,doi: 10.1016/j.envint.2020.106014.

[14] G. Paneiro, F.O Durão, M. C. e Silva, and P. F. Neves, "Prediction of ground vibration amplitudes due to urban railway traffic using quantitative and qualitative field data". *Transportation Research Part D: Transport and Environment*, *40*, 1-13, 2015, doi: 10.1016/j.trd.2015.07.006.

[15] F. Farcaş, and A. Sivertunb, "Road traffic noise: GIS tools for noise mapping and a case study for Skane region. *Sweden": Citeseer,* 34-44, 2010, doi: 10.1.1.222.691&rep=rep1&type=pdf.

[16] Stoter, H. De Kluijver, and V. Kurakula, "3D noise mapping in urban areas". *International Journal of Geographical Information Science,* 22(8), 907-924, 2008, doi: 10.1080/13658810701739039.

[17] B. I. Harman, H. Koseoglu, and CO. Yigit, "Performance evaluation of IDW, Kriging and multiquadric interpolation methods in producing noise mapping: A case study at the city of Isparta", Turkey. *Applied Acoustics*, 112, 147-157,2006, doi: 10.1016/j.apacoust.2016.05.024.

[18] L. Zhao, and L. Shen, "The impacts of rail transit on future urban land use development: A case study in Wuhan, China". *Transport Policy*, *81*, 396-405, 2019, doi: 10.1016/j.tranpol.2018.05.004.

[19] TCDD General Directorate-TCDD 3rd Region (İzmir) Railway Maintenance Service Directorate, TCDD Sound Curtain Projects 2017-2018, 2020.

[20] R. Newspaper, Environmental noise assessment and management regulation. Prime Ministry Press, 26809, 20008.
[21] EU Directive, Directive 2002/49/EC of the European parliament and the Council of 25 June 2002 relating to the assessment and management of environmental noise. *Official Journal of the European Communities,* 189(18.07), 2002.
[22] Internet: Land Cover Flows Based On Corine Land Cover Accounting Layers(2000-2018). URL: https://www.eea.europa.eu/data-and-maps/data/land-cover-flows-based-on. Son Erişim Tarihi: 03.01.2020
[23] TurkStat Population Data https://biruni.tuik.gov.tr/medas/?kn=95&locale=tr 10.04.2020,
[24] İzmir in Numbers,http://www.izka.org.tr/tr/dokuman-merkezi, 2020

Bitlis Eren Üniversitesi Fen Bilimleri Dergisi
BİTLİS EREN UNIVERSITY JOURNAL OF SCIENCE
ISSN: 2147-3129/e-ISSN: 2147-3188
VOLUME: 11 NO: 4 PAGE: 993-999 YEAR: 2022
DOI:10.17798/bitlisfen.1141419

An Evaluation of the Effect of Waste Aluminum Sawdust on the Carbonation of Concrete

Tuba DEMİR [1*], Bahar DEMİREL[1], Melek ÖZTÜRK[1]

[1]*Fırat University, Department of Civil Engineering, Türkiye*
(ORCID: 0000-0003-2092-1029) (ORCID: 0000-0001-7483-2668)(ORCID: 0000-0003-4439-7508)

Keywords: Waste aluminium sawdust, Carbonation, Concrete, SEM.

Abstract
The aim of this study is to examine the effect of replacing waste aluminum sawdust (AS) with fine aggregate on the strength and durability properties of concrete. For this, concrete mixtures with a cement dosage of 400 kg/m^3 and water/cement (W/C) ratio of 0.40-0.50-0.60 were prepared. AS obtained from Elazig industrial site was added to the concrete mixtures by replacing 0%, 0.5% and 1% fine aggregate by volume. After curing in the curing pool for 28 days, the produced concrete samples were subjected to accelerated carbonation test in the carbonation tank at three different time periods the 1st, 3rd and 7th days. Compressive strength test and carbonation depth measurement test were performed on the samples before and after carbonation. In addition, the microstructure of AS concrete was investigated using scanning electron microscopic images (SEM). In the microscopic images, larger cracks, openings and interfacial voids were observed in the concrete matrix with the addition of AS. In addition, it has been observed that the carbonation effect contributes to the compressive strength.

1. Introduction

In recent years, there has been a rapid increase in the emergence of waste materials and by-products due to population growth, the development of industry and technology, and the increase in consumption. When these waste materials are not disposed of properly, they cause environmental pollution [1], [2]. Therefore, it is necessary to ensure the disposal of solid wastes by minimizing the damage to the environment.

The expansion of construction has an important role in the increase in environmental problems. Buildings produce harmful emissions and wastes by consuming natural resources and energy during their lifetime. As a result, they create environmental pollution [3], [4]. It is estimated that around 11 billion tons of aggregate are consumed every year around the world. Approximately 8 billion tons of this aggregate amount are used in concrete production [5].

Exposed and unprotected concrete structures cause corrosion damage [6]. In Turkey, it was observed that corrosion damage occurred in all of the structures damaged in the earthquake. There is also a risk of corrosion in our existing structures. The most important factor causing corrosion is carbonation [7]. Carbonation also causes deterioration of the durability of the structures. As a result of carbonation, the pH value of the concrete decreases from 12-13 to 8-9, weakening its basic feature. For this reason, rusting of the reinforcements in the concrete becomes easier. The reinforcement in the carbonation region becomes susceptible to corrosion. As a result of corrosion, the adherence between the concrete and the reinforcement weakens and the strength of the concrete decreases [8].

Many studies have been conducted on the effects of using wastes in concrete, such as wood chips, glass dust, and marble powder [9]. However, there are hardly any studies on the use of aluminum

*Corresponding author: t.demir@firat.edu.tr
Received:06.07.2022, Accepted:01.11.2022

sawdust in concrete production. The aim of this study is to examine the effects of carbonation on the mechanical properties of these sawdust-added concretes by experimentally measuring the mechanical properties of concrete as a result of carbonation at different times. In addition, by ensuring that aluminum sawdust, which is an industrial waste, is used in concrete production, it is aimed to improve the properties of concrete and to bring more environmentally friendly concrete types to the economy by recycling the wastes.

2. Material and Method

In this study, CEM I 42.5 R Portland cement obtained from Elazig Çimentaş cement factory was used [10]. Aluminum sawdust (AS) was used as a waste material. AS was supplied from Elazig industrial zone. In the experiments, the largest grain diameter (D_{max}) obtained from Palu District of Elazig was selected as 8 mm, and stream aggregate was used. Aggregates are used in three classes: 0-2 mm, 2-4 mm and 4-8 mm. The physical properties of the aggregate are given in Table 1, and the granulometry curve of the aggregate is presented in Figure 1. Also, The chemical properties of the materials used in the study are given in Table 2.

Table 1. Physical properties of aggregate

Aggregate Properties	**(0-2) mm**	**(2-4) mm**	**(4-8) mm**
Loose Unit Weight (gr/cm^3)	2.44	2.71	2.81
Water Absorption (%)	3.53	1.71	1.31

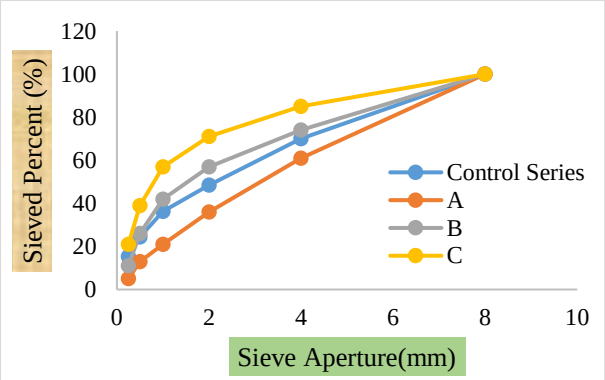

Figure 1. Gradation curve of the aggregate

Table 2. Chemical properties of materials used in the study (%).

Chemical Composition	**Cement (C)**	**Chemical Composition**	**Aluminium Sawdust (AS)**
CaO	63.33	Al	89.96
SiO_2	19.07	Zn	4.97
Fe_2O_3	3.72	Mg	2.11
Al_2O_3	4.82	Cu	0.26
SiO_3	2.83	Mn	0.25
Na_2O	0.39	Fe	0.24
K_2O	0.65	Si	0.15
MgO	1.10	Cr	0.025
Cl	0.009	Ti	0.012
Insoluble residue	0.20	Pb	0.005
Loss of ignition	2.70	Sn	0.003

The waste aluminum sawdust used is aluminum sawdust that became inactive as a result of processing aluminum sheets and profiles and was obtained from the Aykü aluminum workshop operating at the Elazig industrial site. Chip sizes are mixed. The specific gravity of the AS used is 2.7 gr/cm^3. The view of the AS used in the study is shown in Figure 2.

Figure 2. Aluminium sawdust sample used in the study

2.1. Sample Preparation and Mixing Ratios

Before beginning the study, an extensive literature review on mixing ratios was conducted. The trial mixes were then poured. Reference mixtures were determined using the data obtained as a result of these trial mixtures. In this study, 9 different concrete mixtures were prepared in accordance with the mixing principles specified in TS 802. In order to examine the variation range of strength properties of AS reinforced concretes at fixed cement dosage at different ratios, 9 concrete mixtures with cement dosage of 400 kg/m^3, W/C ratio of 0.40-0.50-0.60, respectively, were prepared. In these mixtures, 0.5% and 1.0% AS were used by replacing the fine aggregate by volume. A superplasticizer was not used

since it has a consistency within the workability limits. A total of 9 different concrete series were prepared, 3 for the control series without AS and 6 for the series containing AS. Details of mixing ratios are summarized in Table 3. In the table, naming is done by giving the W/C ratio first and then the AS ratio used in the series names.

Table 3. Proportions of the concrete mixtures (kg/m^3)

Mixture Code	W/C	Cement	Water	AS	Fine aggregate (0-2) mm	Fine aggregate (2-4) mm	Coarse aggregate (4-8) mm
0.40AS0	0.40	400	160	0.00	562	544	659
0.40AS0.5	0.40	400	160	3.11	559	544	659
0.40AS1.0	0.40	400	160	6.21	556	544	659
0.50AS0	0.50	400	200	0.00	528	512	620
0.50AS0.5	0.50	400	200	2.92	526	512	620
0.50AS1.0	0.50	400	200	5.85	523	512	620
0.60AS0	0.60	400	240	0.00	495	480	581
0.60AS0.5	0.60	400	240	2.74	493	480	581
0.60AS1.0	0.60	400	240	5.48	490	480	581

2.2. Production of Samples and Test Schedule

Within the scope of the study, 9 series with and without AS were prepared to investigate the effect of AS on the measurement of compressive strength and carbonation depth before and after carbonation. The samples were kept in standard water cure for 28 days in order to reach the standard compressive strength. Then, the samples were subjected to carbonation test separately for 1 day, 3 days and 7 days in order to determine the carbonation effect. The flow chart of the study is shown in Figure 3.

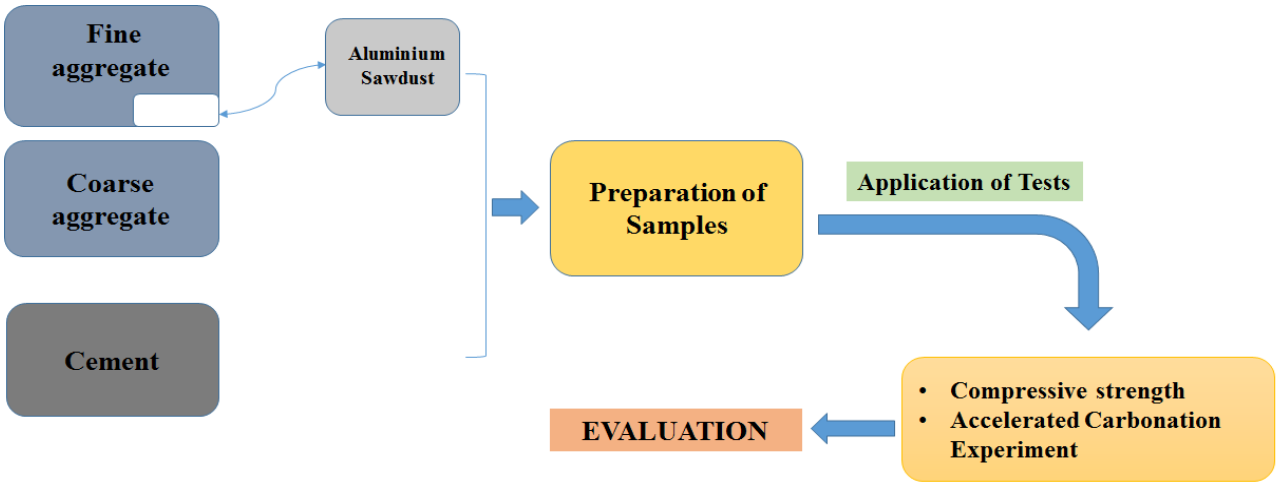

Figure 3. Flow chart of the study

3. Results and Discussion

3.1. Validation and evaluation of experiments

3.1.1. Compressive strength

The compressive strength test of concrete samples was determined according to TS EN 12390-3 standard [11]. The 100x100x100 specimens were placed in the compression testing machine and loaded at 3 kN/sec. The average compressive strength of three cube specimens of each concrete mixture was termed as the compressive strength of that concrete mixture (Figure 4).

Figure 4. Compressive strength test

The compressive strength of the prepared series, with and without AS was determined according to the different curing times before (control series) and after the carbonation test (Figure 5).

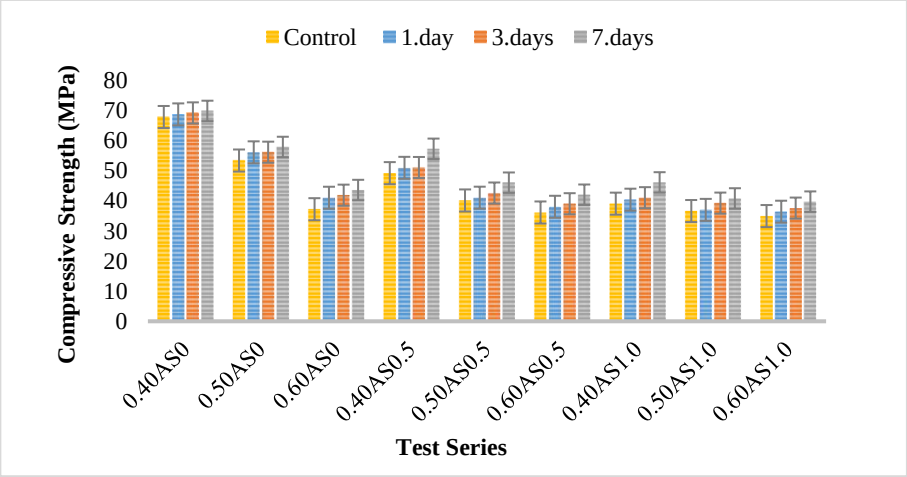

Figure 5. Relationship between compressive strength-carbonation curing age

The compressive strength results of all concrete series before and after carbonation are shown in Figure 4. According to this; the compressive strength values of the concrete samples exposed to carbonation for 1 day increased between 1.29% and 10.26% when compared to the control samples. Among the samples exposed to carbonation for 1 day, the highest compressive strength is seen in the 0.4AS0 series, and the lowest in the 0.60AS1.0 concrete samples. It is seen that the most suitable ratio among the concrete series containing aluminum sawdust exposed to carbonation for 1 day is 0.4AS0.5 concrete series. Likewise, when the 3-day and 7-day concrete series are examined, the highest compressive strength was seen in the 0.4AS0.5 series, similar to the results of the 1-day series. Therefore, these results show that carbonation positively affects the compressive strength of concrete. With the emergence of $CaCO_3$, which is the product of the carbonation reaction in concrete, an increase in density occurred in the carbonated parts, and this increase in density on the surface made itself felt with a slight increase in strength [10], [11]. This situation is also compatible with the literature. Because the water released as a result of the carbonation event, helps the hydration of the cement and causes some increase in strength. This has a positive effect on the compressive strength. [14], [15].

3.1.2. Accelerated carbonation test

Carbonation depth was measured in accordance with the BS EN 13293-2004 standard [16]. For carbonation to take place, sodium dichromate was chosen for 55% humidity at 20 ºC. The saturated solution of sodium dichromate was placed in the water container inside the tank and the temperature of the water was kept at 20 ºC throughout the experiment. The samples were placed in the tank at regular intervals and with no surfaces touching each

other, and the lid of the tank was tightly closed so that there would be no gas leakage. 40% CO_2 was given into the tank from the CO_2 filled tube via a one-way valve (Figure 6).

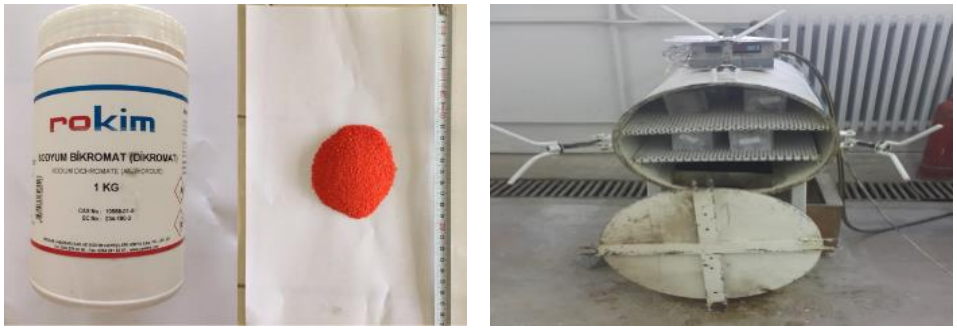

(a) (b)

Figure 6. (a) Sodium bichromate salt (b) Gas-leakproof tank used for carbonation test

For the carbonation test, the concrete samples were exposed to carbonation according to different time periods as 1, 3 and 7 days. For this, after the samples were separated into two and cleaned of dust and particles on the surface, 1% phenolphthalein ($C_2OH_{14}O_4$) - 70% ethyl alcohol solution was sprayed. It reacted with Phenolphtalein and its hydration product, $Ca(OH)_2$, and dyed that area pink, and no color change was observed in the carbonation parts of the samples. The depths of the parts that do not change color on the concrete samples were measured from 8 different places as seen in Figure 7, and the carbonation depth was determined by using Equation 1.

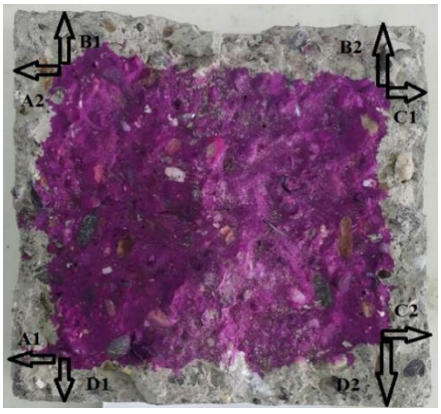

Figure 7. Depth of carbonation measured on the sample surface

$$D = \frac{A_1+A_2+B_1+B_2+C_1+C_2+D_1+D_2}{8} \quad (1)$$

D : Average depth of carbonation (mm)
A,B,C,D : Depth of carbonation of each surface

The data obtained as a result of the carbonation depth measurement are shown graphically in Figure 6. A comparison was made by measuring the carbonation depth of concrete series with and without AS. It is seen that the carbonation depth of the concrete mixtures containing AS is higher than the concrete mixtures without AS, and the carbonation depth increases as the amount of AS increases (Figure 8). AS could not fully settle in the concrete paste due to its grain sizes and formed voids. These voids made it easier for the CO_2 in the tank to enter the concrete. In addition, the carbonation depth increased as the carbonation day time increase

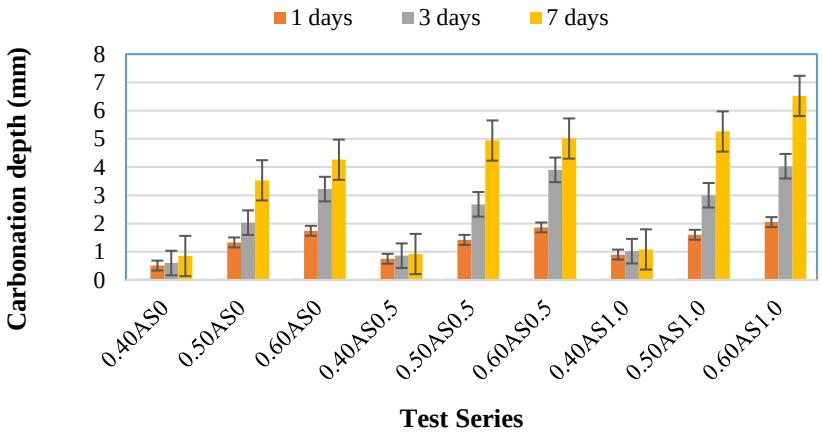

Figure 8. Relationship between carbonation depth-carbonation curing age

3.1.3. Microstructure

The structure of concrete samples obtained by substituting aluminum sawdust with fine aggregate was investigated using scanning electron microscopic images (SEM). SEM images of concrete samples are shown in Figure 9.

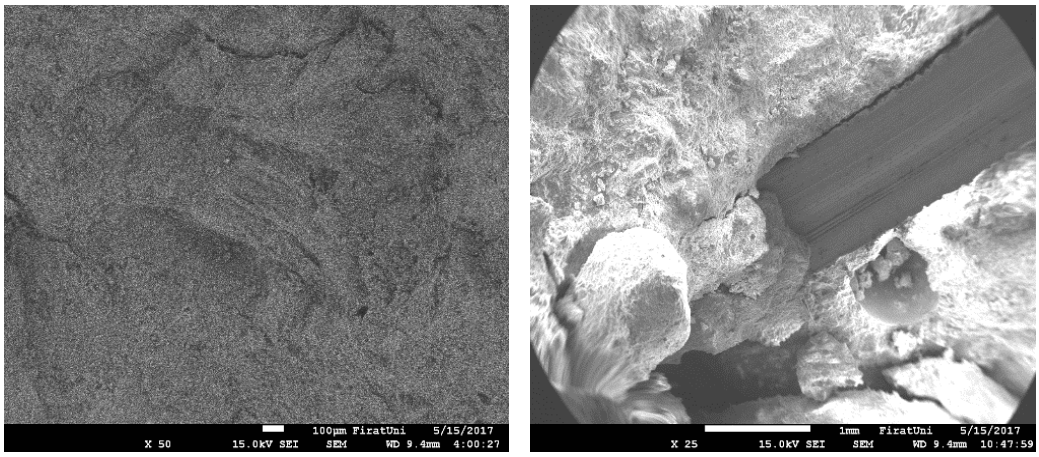

(a) (b)

Figure 9. SEM image of the sample (a) without AS (b) with AS

When Figure 8 (a) is examined, despite the x50 magnification, no obvious cracks were observed in the micro image without AS. When Figure 8 (b) is examined, it is understood from the micro-image of the sample that the adherence due to the use of sawdust is not complete, and from the trace left by the AS peeling off. In addition, microcracks are clearly visible.

4. Conclusions

In this study, the changes in the mechanical properties of the concrete series produced using different AS ratios in 3 different carbonation time periods were investigated. The findings obtained as a result of the study are given below in the articles:

1-Since mixtures with a high W/C ratio were prepared, concrete with an appropriate consistency within the workability limits was obtained. However, although the mixture was poured and placed, the workability decreased as the AS ratio increased. This had a negative impact on the strength of concrete

2-After a certain amount of AS, there was a decrease in the compressive strength, and an increase in the depth of carbonation.

3-The highest increase in the compressive strength value after carbonation is observed in the 0.4AS0.5 series, and this increase value is approximately 16%.

4-In all series, as the number of days exposed to carbonation increased, the compressive strength values increased in parallel with the depth of carbonation.

Since waste aluminum sawdust negatively affects the workability of concrete, it is seen that it is not suitable to be used in concrete. In future studies, it can be aimed to reduce concrete production costs by contributing to recycling by using a different industrial waste.

Contributions of the Authors

In the study, Tuba Demir, Melek Öztürk are related to the subject. literature review, data acquisition, Tuba Demir, Bahar Demirel numerical study titles, evaluation of the results; Bahar Demirel forming the idea, obtaining the data, finding and review of results, spelling and content. They contributed in the titles of checking the article.

Conflict of Interest Statement

There is no conflict of interest between the authors.

Statement of Research and Publication Ethics

The study is complied with research and publication ethics.

References

[1] A. K. Parashar and R. Parashar, "Utility of wastage material as steel fibre in concrete mix M-20," *Int. J. Adv. Res. Technol.*, vol. 3, pp. 2–8, 2012.

[2] I. Martínez-Lage, P. Vázquez-Burgo, and M. Velay-Lizancos, "Sustainability evaluation of concretes with mixed recycled aggregate based on holistic approach: Technical, economic and environmental analysis," *Waste Manag.*, vol. 104, pp. 9–19, 2020.

[3] H. Binici, A. H. Sevinç, and H. Geçkil, "Durability properties of waste iron powder added mortars and concretes," *Çukurova University Faculty of Engineering and Architecture Journal*, vol. 30, no. 1, p. 1–16, 2015.

[4] A. A. Thakare, A. Singh, V. Gupta, S. Siddique, and S. Chaudhary, "Sustainable development of self-compacting cementitious mixes using waste originated fibers: A review," *Resour. Conserv. Recycl.*, p. 105250, 2020.

[5] G. L. Golewski, "Green concrete based on quaternary binders with significant reduced of CO_2 emissions," *Energies*, vol. 14, no. 15, p. 4558, 2021.

[6] Y. Liu, "Modeling the time-to corrosion cracking of the cover concrete in chloride contaminated reinforced concrete structures." Virginia Tech, 1996.

[7] T. Gönen and S. Yazıcıoğlu, "Carbonation and Activity Degrees in Concretes," *Stand. econ. and Single. Journal*, publication, no. 497, pp. 84–88, 2003.

[8] A. Tafraoui, G. Escadeillas, and T. Vidal, "Durability of the Ultra High Performances Concrete containing metakaolin," *Construction and Building Materials*, vol. 112, 2016.

[9] V. M. Sounthararajan and A. Sivakumar, "Effect of the lime content in marble powder for producing high strength concrete," *ARPN J. Eng. Appl. Sci.*, vol. 8, no. 4, pp. 260–264, 2013.

[10] P. and C. C. Cement - Part 1: General Cements, Composition, "TS EN 197-1," Turkey, 2012.

[11] Turkish Standards Institute, Concrete-Hardened Concrete Tests-Part 3: Determination of Compressive Strength of Test Samples, "TS EN 12390-3," Turkey, 2019.

[12] N. Cauberg, O. Remy, and J. Pi√©rard, "Evaluation of durability and cracking tendency of Ultra High Performance Concrete," in Creep, Shrinkage and Durability Mechanics of Concrete and Concrete Structures, Taylor & Francis, 2010, pp. 695–700.

[13] M. Alwaeli and J. Nadziakiewicz, "Recycling of scale and steel chips waste as a partial replacement of sand in concrete," *Constr. Build. Mater.*, vol. 28, no. 1, pp. 157–163, 2012.

[14] T. Erdogan, Concrete. Ankara: METU Press, 2003.

[15] H. Binici, H. Temiz, A. H. Sevinç, E. Mustafa, K. Mehmet, and Z. Şayir, "Investigation of High Temperature Effect of Concretes Containing Aluminum Sawdust, Pumice and Aerated Concrete Powder," *Yapı Teknol. Electron. Journal*, vol. 9, no. 1, p. 1–15, 2013.

[16] M. Safiuddin and N. Hearn, "Comparison of ASTM saturation techniques for measuring the permeable porosity of concrete," *Cem. Concr. Res.*, vol. 35, no. 5, pp. 1008–1013, 2005.

Bitlis Eren Üniversitesi Fen Bilimleri Dergisi
BİTLİS EREN UNIVERSITY JOURNAL OF SCIENCE
ISSN: 2147-3129/e-ISSN: 2147-3188
VOLUME: 11 NO: 4 PAGE: 1000-1013 YEAR: 2022
DOI:10.17798/bitlisfen.1150200

A Multi-Criteria Solution Approach for UAV Engine Selection in Terms of Technical Specification

Ukbe Üsame UÇAR[1*], Aylin ADEM[2], Burak TANYERİ[3]

[1,3] *Department of Aircraft Maintenance and Repair, School of Civil Aviation, Fırat University, Turkey*
[2] *Department of Industrial Engineering, Gazi University, Turkey*
(ORCID: 0000-0002-9872-2890) (ORCID: 0000-0003-4820-6684) (ORCID: 0000-0002-3517-9755)

Keywords: Unmanned Aerial Vehicle, Engine, AHP, Decision Support System, Multi-Criteria Decision Making.

Abstract
Unmanned Aerial Vehicles (UAVs) are electronic systems that are used extensively in every field today and that develop and change very quickly with technology. UAVs are used extensively in many areas, especially in logistics processes, search and rescue activities, military operations, fight to forest fires, photography, monitoring and inspection of agricultural processes. Furthermore, considering their hobby use, it is understood that UAVs have a large commercial market and a high economic value. UAV systems contain many electronic and mechanical systems and many performance criteria can be found for UAV systems. The main ones of these performances are stabilization and engine power. The most important system affecting these performance criteria is the engine. In this study, engine alternatives available in the market for UAVs with take-off weights of 750 to 800 grams were evaluated in terms of mechanical and physical criteria of engine systems, and as a result, the ideal engine model was determined by Analytic Hierarchy Process (AHP) for maximum stabilization and velocity purposes. The article is the first in the literature in terms of the problem obtained and the application of the AHP method to this problem. Thanks to the study, it is aimed to create a Decision Support System for both UAV manufacturers and UAV users so that they can choose the ideal models in engine selection processes.

1. Introduction

Unmanned Aerial Vehicles are electro-mechanical, autonomous or semi-autonomous devices that do not contain humans and can be controlled by means of remote control, etc. UAVs, which have different take-off weights and dimensions, are divided into three different categories in terms of rotors: fixed, rotary wing and hybrid. In addition, it is possible to group UAVs according to their altitude and range. UAV systems, which were used extensively in military operations in previous years, are now being integrated into many fields and are used intensively for civilian and commercial purposes. Mapping, monitoring, seeding and agricultural spraying processes of agricultural regions are made possible by UAV technologies quickly and easily. Taking instant, detailed and high-altitude images and sharing them in television and digital media is very easy thanks to UAVs. UAV technologies are used extensively in tracking and viewing traffic, creating traffic density maps in city centers and solving these problems. UAV systems are used extensively in fire extinguishing operations in summer and avalanche activities in winter, in the transportation of materials such as water, equipment, etc., as well as in taking snapshots from difficult geographical conditions. Thanks to the use of UAV systems in the tasks of monitoring nuclear, biological, radioactive or chemical processes and tracking leaks arising from them, human life is protected and the right decisions are made. Reconnaissance and surveillance missions for military and security purposes are another area where UAV systems and technologies are used. People use

*Corresponding author: uucar@firat.edu.tr
Received: 28.07.2022, Accepted: 17.09.2022

UAV systems for photography and hobby purposes, and the number of civilian users is increasing day by day. In recent years, the use of UAVs has increased considerably in the health sector. In particular, UAV systems are used to quickly deliver first aid materials such as blood and medicine to the beneficiaries or hospitals in traffic jams and difficult geographical and climatic conditions. The effective production and design of these systems, which are used extensively, is of great importance.

Drone systems generally consist of 13 different parts: Chassis, Propellers, Motors, Gimbals, Signal Lights, Screws, Camera, GPS (Global Positioning System), Landing Gear, Batteries, Electronic Speed Control Units, Compass and Cables. Each of these sections has a great importance, and "Engines and Propellers" is one of these systems. Thanks to the motor system, the drones convert the motion information coming through the signal into mechanical motion and can move stably in the desired format and orbit in the air. The effective and efficient design of the engine system is of great importance in terms of drone production. Today, there are many companies that design and manufacture motors and propellers for drones in different categories. Selecting the ideal engine system among many alternative brands under various criteria for the relevant drone is difficult and takes a lot of time if any analytical method is used. There are many studies on the design of drone systems in the literature, and in this article, the related problem is solved by using the Analytical Hierarchy Method, one of the most frequently employed Multi-Criteria Decision Making Methods. There is no study in the literature on the application of the AHP method in UAV engine selection. Furthermore, the studies in the literature regarding the applications of Multi-Criteria Decision Making methods and AHP methodology on Unmanned Aerial Vehicles are given below.

Uçar and İşleyen used the AHP method to select the UAVs that will take part in UAV operations with heterogeneous fleets and to prioritize the targets. [1]. Tamer and Uçakcıoğlu determined the ideal investment project for an enterprise operating in the air defense sector by using the AHP and VIKOR method. [2]. Ulukavak and Miman determined the ideal type of UAV that can be used in emergency transportation using the AHP method [3]. Özaslan et al., evaluated single-engine piston airplanes using AHP and TOPSIS methods and determined the ideal one. [4]. Zhao et al., used AHP and Grey Relational Analysis methodologies for UAV recovery system selection [5]. Tuba et al., used Fuzzy Logic and AHP methods for the meteorological forecasting systems of Unmanned Aerial Vehicles by integrating them [6]. Yan et al., evaluated the UAV equipment maintenance quality by using the AHP method [7]. Yıldızbaşı and Gür, developed a decision support system using AHP and TOPSIS methods for the correct and effective use of UAVs after the earthquake disaster [8]. Wang et al., determined the ideal design strategy to be used in the design of power systems of small UAVs with the Local Gray Relational Analysis-Analytic Hierarchy Process (LGRA-AHP) method [9]. HE et al., utilized the AHP method to determine the PID control parameters of the Unmanned Aerial Vehicle [10]. Lai and Whidborne, benefited from the AHP method in solving the return-to-route automation problem in UAVs [11]. Canetta et al., used the AHP method to evaluate potential partners serving in the UAV industry [12].

In addition to these studies, there are many studies in the literature on the engine and propeller efficiency of UAVs. Gur and Rosen proposed a multidisciplinary solution approach to optimize propeller system designs for ultralight aircraft [13]. Gaggero et al. developed a multidisciplinary design optimization to optimize high-speed craft propeller system [14]. Dundar et al. used the Simulation method to determine the ideal designs of multirotor and propeller systems that will maximize the endurance of fixed-wing UAVs [15]. Bayraktar and Güldaş, investigated the efficiency of the thrust and torque systems of the quadrotors using the simulation method [16]. Foeth used the NSGA-II algorithm to optimize the parameters on the propeller geometry [17]. Lee et al. have benefited from genetic algorithm to increase the hovering time of quadcopters [18]. Bacciaglia et al., have developed a solution approach based on Particle Swarm Optimization to design of the pitch propeller [19]. Zhang et al. developed an optimization approach based on multidisciplinary design for a fixed-wing hybrid UAV [20]. Podsedkowski et al., carried out experimental studies on the propeller pitch systems of UAVs for the purpose of propulsion system [21]. Magnussen et al., have optimized the design of the UAV in terms of propeller, engine, battery and other features thanks to the mathematical modeling solution approach [22]. Sinibaldi and Marino examined the propulsion systems of small drones and investigated the difference between their acoustic signature and conventional propellers [23]. Kuantama and Tarca used the CFD method to optimize the thrust system of the quadcopter which has a ducted-propeller [24]. Ahmet et al., used commercial CFD codes to optimize the drone propeller considering the topological purpose [25]. Kapsalis et al., optimized a fixed-wing tactical UAV design using CFD codes [26]. Dahal et

al., carried out experimental studies to realize the UAV propeller design under the objective of optimal thrust and used the CFD method to verify the experimental results [27]. ElGhazali and Dol enhaced the propeller design of a multi-rotor UAV by conducting experimental studies in the ANSYS Fluent 16. Program [28]. Andria et al., developed a new drone propeller and compared it with different propeller models for the purpose of thrust [29]. Iannace et al., detected the errors in the drone propeller system using the artificial neural network method [30]. Dumıtrache et al., used the Blade Element Momentum Theory (BEMT) for drone propeller design and evaluated the designed propeller systems in terms of performance characteristics [31]. In addition to the information above, studies related to the subject in the literature are given in Table 1.

Table 1. Studies in the literature on UAV

Author(s)	Year	Problem	Methodology	Index
Rakhade et al.	2021	Agricultural drone selection	AHP and TOPSIS	[32]
Sah et al.	2021	Barriers in the logistics applications of drones	Fuzzy FDM and AHP	[33]
Zhang et al.	2021	The use of drones in emergency situations	AHP, ANP, DEMATEL	[34]
Zhou et al.	2021	Use of UAV in fire fighting	Ant Colony Algorithm and AHP	[35]
Zoltan et al.	2013	Meteorological support system	Fuzzy logic–based analog forecasting method and AHP	[36]
Ardil	2021	Military fighter aircraft selection	PARIS	[37]
Adem et al.	2022	UAV use in the logistics industry and logistics 4.0	AHP	[38]
Moaddab et al.	2020	Monitoring of monitoring gas pipeline with UAV	AHP	[39]
Hsiao and Peng	2020	Multirotor drone appearance selection	F-FCE and F-AHP	[40]
Khan et al.	2021	Drone selection	AHP and TOPSIS	[41]
Wang et al.	2013	UAV power system model	LGRA-AHP	[42]
Müezzinoğlu and Karaköse	2021	Drone control with wearable gloves	Machine learning	[43]
Tanyeri et al.	2022	Drone PID control	Statistical analysis	[44]
Petkovics et al.	2017	UAV Selection	AHP	[45]
Radovanović et al.	2021	UAV Selection	Fuzzy AHP-VIKOR	[46]
Hamurcu and Eren	2022	UAV Selection	AHP and TOPSIS	[47]

There are many parameters and constraints that affect the UAV engine selection. It is difficult and takes a lot of time to determine the ideal one among many engine alternatives, taking into account different purposes and parameters simultaneously, without using analytical methods. There is no study in the literature that evaluates engine selection from an analytical point of view. This article differs from the studies in the literature due to the systematic evaluation of engine selection, the absence of any study on UAV engine selection in the literature, and the use of the AHP method, which is one of the MCDM methods, for the first time in solving the problem. In addition, this article differs from other studies in the literature due to the consideration of velocity and stabilization purposes in engine selection. This paper is structured as follows. Section 2 express, the details of the considered problem are expressed and the used methodology is defined in Section 3. Section 4, the application study is carried out. Finally, in Section 5, general evaluations about the study are expressed.

2. Definition of the Problem

Unmanned Aerial Vehicles basically consist of 12 different components (chassis, propeller, electronic speed control unit, Signal lights, Cables, screws, batteries, GPS, landing gear, Camera, Gimbal, Compass and engines one of the most important components of the UAV, are the mechanical systems that enable the UAV to hover in the air and move in the desired formation by transferring the signals coming from the control and the power it receives from the battery to the propeller. In rotary-wing

UAVs, an engine is needed for each propeller and the thrust varies according to the weight of the UAV. Brushless DC motors are generally used in UAV systems. In addition, battery power varies depending on engine power, more powerful batteries are needed to run more powerful engines. The engine structure also affects the propeller design, and in case of using propeller systems with a larger diameter than the engine can handle, the UAV can move unevenly and the flight time is shortened [48]. There are many criteria to consider when determining the ideal engine type for any UAV. In addition, with the developing technology, there are many alternative engine brands in the market and it is difficult to choose the ideal engine type among the relevant engine criteria without using any analytical method. In this study, alternative engine brands are evaluated under the specified engine selection criteria and the best engine brand is determined by using the AHP method. Looking at the studies in the literature on drones, it has been observed that in general, they are concerned with design and mechanical problems. The brand and model selection for the parts to be used in the drone has been ignored. In this study, the ideal engine selection problem for the drone is discussed. In this context, the technical features of the engine in terms of stabilization and speed were determined and the ideal engine was selected according to these features. As far as is known, there is no study in the literature on determining the ideal engine type using the AHP method for speed and stabilization purposes for drone engines. Thanks to the study, it is aimed to create a decision support system for UAV users, whose numbers reach billions. In this article, 7 different criteria and 15 different alternatives are considered. Information on the criteria is given in Table 2. In the next section, information on the details of the AHP method used in solving the problem is given [4].

Table 2. Information regarding engine criteria

Criteria Name	Criteria Unit	Criteria Detail
Motor KV Value	Kv	It is used for brushless motors. It is the expression coefficient of the revolution that can occur in 1 minute with a voltage. As the motor revolution per voltage decreases, the propeller torque increases and the propeller speed decreases. In this case, the aircraft speed decreases, while the stabilization increases.
Operating Voltage	Volt	It states to the potential energy needed for the operation of electric motors. As the operating voltage of the motor increases, the revolutions per voltage decrease. In this case, while the vehicle speed decreases, the stabilization increases.
Operating Current	Ampere	It expresses the electron current needed in electric motors. As the operating current increases, the motor power increases. Stabilization and speed increase as motor power increases.
Motor RPM	Revolutions per Minute	In electric motors, it refers to the number of revolutions per minute of the motor shaft. Engine speed is directly related to the propeller. As engine speed increases, stabilization and aircraft speed increase.
Motor Torque	Newton metre	In electric motors, it refers to the torque used to rotate the motor shaft. Motor torque is the most effective parameter against disturbances. Stabilization increases as engine torque increases.
Motor Power	Watt	It expresses to the potential of an electric motor to convert electrical energy into mechanical energy. Motor power is related to both motor speed and motor torque. As motor power increases, stabilization and aircraft speed increase.
Motor Weight	Gram	It states to the total weight of the components that make up the motor. Engine weight is the parameter that affects the total take-off weight. Stabilization and speed decrease as take-off weight increases.

3. Solution Methodology

In this paper, in order to gain the importance degree or the weights of alternative UAV engines the AHP which was developed by Thomas L. Saaty in 1977 to solve complex multi criteria decision making problems [49] was utilized. The employed version of the AHP technique in this study is the traditional style, which was developed with 1-9 scale. The logic of the AHP is based on linear algebra, and it compares the parts of the decision-making process pairwise [50]. AHP is a hierarchical representation of a decision-making issue [51]. The superiority of this technique can be explained by the fact that it can compute the weights of both tangible and intangible factors in a decision-making issue [52]. The main steps of the AHP technique are given as follows [53]:

1. Define the decision-making problem and the hierarchy of it
2. Construct the pairwise comparison matrices (PCM) and calculate the consistency ratio of them
3. Calculate the priorities / weights

The following explanations about the AHP methodology are based on Saaty [52]. In the first step, the decision problem is defined in detail. The purpose of the decision problem, the alternatives, the criteria that will affect the decision, and the sub-criteria, if exist, are determined. In the second step, PCM(A) are construct (Eq.1). A comparison scale is utilized in the determination of a_{ij} values in these matrices (see Table 3).

$$A = \begin{pmatrix} a_{11} & \cdots & a_{1n} \\ \vdots & \ddots & \vdots \\ a_{m1} & \cdots & a_{mn} \end{pmatrix} \quad (1)$$

Table 3. Importance scale [48].

Importance Degree	Definition
1	Equal
3	Medium importance
5	High importance
7	Very high importance
9	Absolute importance
2,4,6,8	Intermediate values

The values on the diagonal of matrix *A (i.e. i=j)* are equal to 1. Pairwise comparisons are conducted in the upper triangular region. Eq. (2) is utilized to determine the values of the elements in the lower triangle.

$$a_{ji} = 1 / a_{ij} \quad (2)$$

In the third step, the weights of criteria are calculated based on pairwise comparison matrices. This calculation is conducted by determining the column summation of the PCM, dividing each item of the PCM by the corresponding column sum (normalized PCM), and obtaining the priority/weight corresponding to the factor of row averages of the normalized PCM. The mathematical expression of these operations is Eq. (3) and Eq. (4).

$$c_{ij} = \frac{a_{ij}}{\sum_{i=1}^{n} a_{ij}} \quad (3)$$

$$C = \begin{pmatrix} c_{11} & \cdots & c_{1n} \\ \vdots & \ddots & \vdots \\ c_{m1} & \cdots & c_{mn} \end{pmatrix} \quad (4)$$

The *C* matrix represents the normalized PCM. With the row average of this matrix, the *W* vector containing the factor weights is obtained (Eq. (5) and Eq. (6)).

$$w = \begin{pmatrix} w_1 \\ . \\ . \\ . \\ w_n \end{pmatrix} \quad (5)$$

$$w_i = \frac{\sum_{j=1}^{n} c_{ij}}{n} \quad (6)$$

Determining whether the paired comparisons are consistent is an important step for the AHP method. For calculating a consistency ratio for any pairwise comparison matrix the following steps are applied: Multiplying the column values of the PCM with the weight value corresponding to the relevant factor and adding the row values to create a weighted totals vector, dividing the weighted totals vector by the weights corresponding to the elements and calculating the average of the obtained values (λ_{max}), then calculating the consistency index (*CI*), and calculation of the consistency ratio (*CR*). The weighted sum vector is obtained by Eq. (7).

$$D = \begin{pmatrix} w_1 \\ . \\ . \\ . \\ . \\ w_n \end{pmatrix} x \begin{pmatrix} a_{11} & \cdots & a_{1n} \\ a_{21} & & a_{22} \\ \vdots & \ddots & \vdots \\ \vdots & & \vdots \\ a_{m1} & \cdots & a_{mn} \end{pmatrix} = \begin{pmatrix} d_1 \\ . \\ . \\ . \\ . \\ d_n \end{pmatrix} \quad (7)$$

Dividing the weighted sums vector by priorities are expressed by Eq. (8) and Eq. (9).

$$E = \begin{pmatrix} e_1 \\ . \\ . \\ . \\ . \\ e_n \end{pmatrix} \quad (8)$$

$$e_i = \frac{d_i}{w_i} \quad (9)$$

λ_{max} is calculated by utilizing Eq. (10):

$$\lambda_{\max} = \frac{\sum_{i=1}^{n} E_i}{n} \quad (10)$$

Consistency index is computed with the help of Eq. (11):

$$CI = \frac{\lambda - n}{n-1} \quad (11)$$

The consistency ratio is calculated with Eq. (12):

$$CR = \frac{CI}{RI} \quad (12)$$

The RI expression in Eq.12 expresses a standard value, and the values according to the number of factors are shown in Table 4.

Table 4. Random index (*RI*)

Number of element	**1**	**2**	**3**	**4**	**5**	**6**	**7**	**8**	**9**	**10**
RI	0	0	0.58	0.90	1.12	1.24	1.32	1.41	1.45	1.48

If the calculated CR value is less than 0.1, the PCM performed is considered consistent. Otherwise, the PCM should be rearranged [54].

4. Application

In this paper, due to its less complex calculation steps but having powerful solution potential, The AHP technique was utilized in analyzing UAV's engine specifications. The hierarchical decision tree developed for the problem is shown in Figure 1.

In the first step of the application, the weights of criteria were calculated. Table 5 shows the pairwise comparison matrix of the selection criteria. All presented matrices are the compromised matrices by the expert team.

Table 6 shows the calculated weights of criteria by applying Eq. (2)- Eq. (6). The consistency ratio of this PCM was computed as 0.097 with the help of Eq. (7)- Eq. (12), because this value is lower than 0.1, this PCM is consistent.

Table 5. Pairwise comparisons of the criteria

Criteria	**Motor KV Value**	**Operating Voltage**	**Operating Current**	**Motor RPM**	**Motor Torque**	**Motor Power**	**Motor Weight**
Motor KV Value	1	3	5	3	4	5	9
Operating Voltage	-	1	3	1/3	5	3	3
Operating Current	-	-	1	1	3	2	3
Motor RPM	-	-	-	1	4	3	4
Motor Torque	-	-	-	-	1	1/3	1/3
Motor Power	-	-	-	-	-	1	4
Motor Weight	-	-	-	-	-	-	1

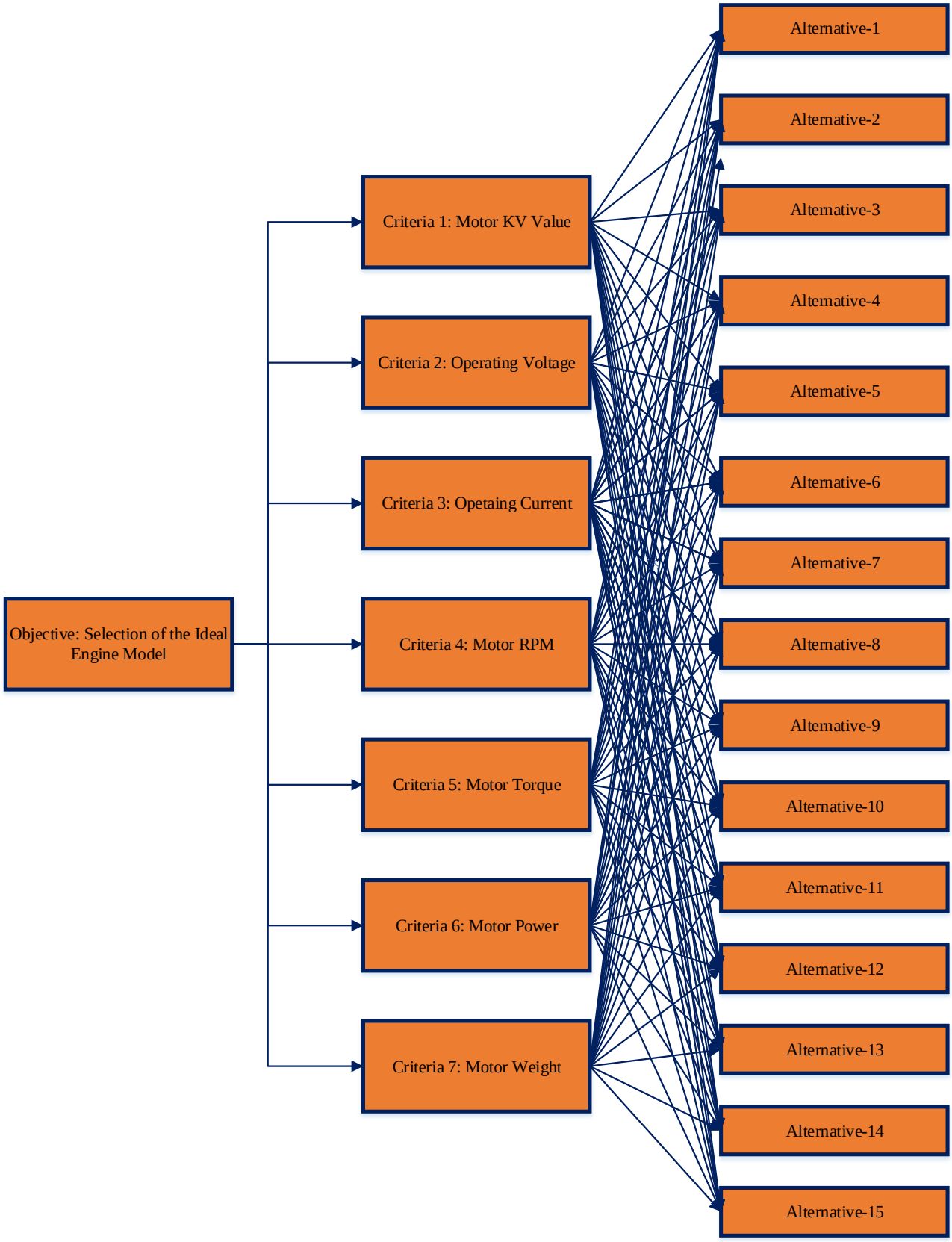

Figure 1. The hierarchical representation developed for the decision problem

Table 6. The weights of the criteria

Criteria	Criteria weights
Motor KV Value	0,371
Operating Voltage	0,161
Operating Current	0,109
Motor RPM	0,186
Motor Torque	0,040
Motor Power	0,084
Motor Weight	0,049

CR=0.097

First of all, on the basis of each criterion, the alternatives were compared in pairs and their weight values were obtained according to both velocity and stabilization. For each aim, 7 comparison matrix (15*15 alternatives) were constructed. The consistency ratios of all evaluation matrices were checked and they were specified as consistent. Table 7 shows the results of the pairwise comparisons of alternatives with respect to each criterion according to the aim of velocity. This table is obtained after a pairwise comparison of 15 alternatives on the basis of each criterion and calculations with AHP.

Table 7. The results of the pairwise comparisons of alternatives with respect to each criterion according to the aim of velocity

Alt.	C1	C2	C3	C4	C5	C6	C7
A1	0.094	0.108	0.036	0.024	0.031	0.041	0.019
A2	0.094	0.063	0.055	0.059	0.041	0.062	0.027
A3	0.094	0.112	0.120	0.024	0.021	0.020	0.102
A4	0.094	0.057	0.019	0.059	0.102	0.100	0.019
A5	0.139	0.057	0.018	0.089	0.067	0.100	0.043
A6	0.029	0.039	0.044	0.038	0.067	0.062	0.043
A7	0.035	0.040	0.040	0.038	0.102	0.072	0.069
A8	0.206	0.057	0.126	0.225	0.011	0.014	0.249
A9	0.063	0.061	0.019	0.038	0.149	0.100	0.013
A10	0.014	0.197	0.267	0.012	0.012	0.011	0.145
A11	0.043	0.022	0.050	0.169	0.206	0.209	0.043
A12	0.014	0.022	0.036	0.125	0.067	0.100	0.043
A13	0.043	0.063	0.035	0.059	0.067	0.059	0.043
A14	0.019	0.068	0.054	0.016	0.030	0.029	0.043
A15	0.019	0.034	0.080	0.024	0.027	0.020	0.100

Table 8 shows the calculated values of alternatives with respect to the aim of velocity. The values in Table 8 are obtained by multiplying the weights of the criteria with the weight of the alternative on the basis of the relevant criteria (see Table 7).

To illustrate, the first row of Table 8 is computed as follows:

$$0.094*0,371 \approx 0.0350$$
$$0.108*0,161 \approx 0.0173$$
$$0.036*0,109 \approx 0.0039$$
$$0.024*0,186 \approx 0.0045$$
$$0.031*0,040 \approx 0.0012$$
$$0.041*0,084 \approx 0.0034$$
$$0.019*0,049 \approx 0.0009$$

The total column shows the summation of these values, thus,

$$0.0350+0.0173+0.0039+0.0045+0.0012+0.0034+0.0009 \approx 0.0663$$

Table 8. The calculated values of alternatives with respect to the aim of velocity.

Alternatives	C1	C2	C3	C4	C5	C6	C7	Total
A1	0.0350	0.0173	0.0039	0.0045	0.0012	0.0034	0.0009	0.0663
A2	0.0350	0.0102	0.0061	0.0110	0.0016	0.0052	0.0013	0.0705
A3	0.0350	0.0180	0.0131	0.0045	0.0008	0.0017	0.0051	0.0782
A4	0.0350	0.0091	0.0021	0.0110	0.0041	0.0084	0.0009	0.0706
A5	0.0515	0.0092	0.0020	0.0165	0.0026	0.0084	0.0021	0.0922
A6	0.0107	0.0063	0.0049	0.0070	0.0026	0.0052	0.0021	0.0388
A7	0.0129	0.0064	0.0044	0.0070	0.0041	0.0060	0.0034	0.0443
A8	0.0766	0.0092	0.0137	0.0418	0.0005	0.0012	0.0123	0.1553
A9	0.0235	0.0098	0.0021	0.0070	0.0059	0.0084	0.0006	0.0573
A10	0.0050	0.0317	0.0292	0.0022	0.0005	0.0009	0.0072	0.0768
A11	0.0159	0.0035	0.0054	0.0314	0.0082	0.0175	0.0021	0.0841
A12	0.0050	0.0036	0.0040	0.0231	0.0026	0.0084	0.0021	0.0488
A13	0.0159	0.0102	0.0038	0.0110	0.0026	0.0050	0.0021	0.0506
A14	0.0070	0.0110	0.0059	0.0030	0.0012	0.0024	0.0021	0.0326
A15	0.0072	0.0055	0.0088	0.0045	0.0011	0.0017	0.0050	0.0336

Figure 2 shows the priority values of alternatives for velocity aim. As a result, it was determined that the most suitable engine models for "velocity aim" are A8 and A11, respectively. In addition, it has been determined that the engines with the lowest importance were A14-A15 and A6, respectively

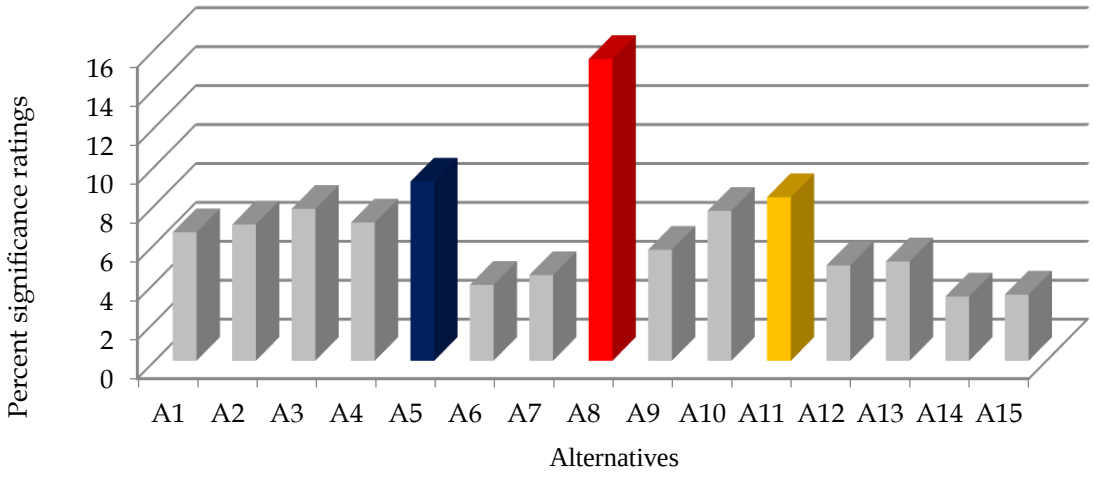

Figure 2. Priority values of alternatives for velocity aim

For stabilization aim, 7 comparison matrix (15*15) were constructed. The consistency ratios of all evaluation matrices were checked and they were specified as consistent. Tale 9 is obtained after a pairwise comparison of 15 alternatives on the basis of each criterion and calculations with AHP.

Table 9. The results of the pairwise comparisons of alternatives with respect to each criterion according to the aim of stabilization.

Alt	C1	C2	C3	C4	C5	C6	C7
A1	0.095	0.131	0.042	0.024	0.030	0.041	0.019
A2	0.095	0.055	0.063	0.059	0.041	0.063	0.027
A3	0.095	0.131	0.132	0.024	0.020	0.020	0.102
A4	0.095	0.055	0.020	0.059	0.102	0.101	0.019
A5	0.139	0.055	0.020	0.089	0.067	0.101	0.043
A6	0.029	0.034	0.042	0.038	0.067	0.063	0.043
A7	0.029	0.034	0.040	0.038	0.102	0.063	0.069
A8	0.207	0.055	0.125	0.225	0.012	0.015	0.249
A9	0.064	0.055	0.020	0.038	0.149	0.101	0.013
A10	0.014	0.237	0.221	0.012	0.012	0.011	0.145
A11	0.043	0.012	0.061	0.169	0.206	0.210	0.043
A12	0.014	0.012	0.035	0.125	0.067	0.101	0.043
A13	0.043	0.055	0.037	0.059	0.067	0.063	0.043
A14	0.020	0.055	0.057	0.016	0.030	0.029	0.043
A15	0.020	0.023	0.085	0.024	0.030	0.020	0.100

Table 9 show the results of the pairwise comparisons of alternatives with respect to each criterion according to the aim of stabilization. Same calculation steps to velocity purpose were repeated for the aim of the stabilization and the results were summarized Table 10.

Table 10 presents the calculated values of alternatives with respect to the aim of stabilization. Table 9 are obtained by multiplying the weights of the criteria (see Table 6) with the weight of the alternative on the basis of the relevant criteria (see Table 9).

As seen in Figure 3, it can be concluded that A8, A5 and A11 engine types are respectively the best engine for stabilization purpose as well as for speed. In addition, it is expressed in the results that the A14, A15 and A16 alternatives are the least important engine models.

Based on the results of two analyses, it has been determined that the ideal engine type for the Unmanned Aerial Vehicle between 750 and 800 grams is A8 and a decision support system has been created for decision makers.

Table 10. The calculated values of alternatives with respect to the aim of stabilization

Alternatives	C1	C2	C3	C4	C5	C6	C7	Total
A1	0.035	0.021	0.005	0.004	0.001	0.003	0.001	0.071
A2	0.035	0.009	0.007	0.011	0.002	0.005	0.001	0.070
A3	0.035	0.021	0.014	0.004	0.001	0.002	0.005	0.083
A4	0.035	0.009	0.002	0.011	0.004	0.008	0.001	0.071
A5	0.052	0.009	0.002	0.016	0.003	0.008	0.002	0.092
A6	0.011	0.005	0.005	0.007	0.003	0.005	0.002	0.038
A7	0.011	0.005	0.004	0.007	0.004	0.005	0.003	0.040
A8	0.077	0.009	0.014	0.042	0.000	0.001	0.012	0.155
A9	0.024	0.009	0.002	0.007	0.006	0.008	0.001	0.057
A10	0.005	0.038	0.024	0.002	0.000	0.001	0.007	0.078
A11	0.016	0.002	0.007	0.031	0.008	0.018	0.002	0.084
A12	0.005	0.002	0.004	0.023	0.003	0.008	0.002	0.047
A13	0.016	0.009	0.004	0.011	0.003	0.005	0.002	0.050
A14	0.007	0.009	0.006	0.003	0.001	0.002	0.002	0.031
A15	0.007	0.004	0.009	0.004	0.001	0.002	0.005	0.033

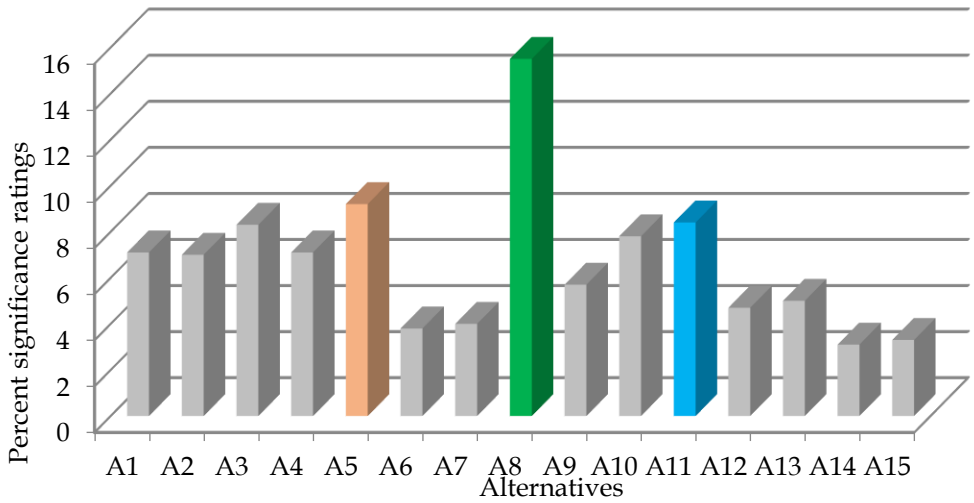

Figure 3. Priority values of alternatives for stabilization purpose.

5. Conclusion

Thanks to the developing technology, the production and user of UAVs for civil and military purposes are increasing rapidly and these technologies are used intensively in many areas, especially in traffic, health, logistics, security, transportation, agriculture, photography and hobby. UAV technologies consist of many different systems and it is of great importance that these components are produced effectively, efficiently and safely. In addition, there are many UAV manufacturers that produce components with different quality and features for any UAV type, and choosing the ideal brand and model for the UAV is of great importance in terms of UAV performance. In this study, the ideal engine type engine was determined by considering 7 different criteria among 15 different alternative engine types for drones with take-off weights of 750 to 800 grams. "Motor KV Value", "Operating Voltage", "Operating Current", "Motor Speed", "Motor Torque", "Motor Power" and "Motor Weight" criteria have been taken into account in the selection of the engine, thus allowing the drone to achieve maximum stabilization and power. The ideal engine brand has been determined. The study is the first in the literature due to the problem addressed and the use of the AHP method in this problem. As a result of the analysis study, it has been determined that the most important criterion in engine selection is the "Motor KV" value, and the ideal engine brand is "A8".

The study is a decision support system for UAV manufacturers and users. With the proposed mechanism, UAV users will be able to evaluate the suitable brand among themselves among performance and different criteria and make the right choices. Furthermore, UAV manufacturers will be able to identify the ideal supplier among their own suppliers using the determined solution approach. Considering that there are millions of UAV users in the world, the benefit of the proposed approach can be better understood.

In future studies, it is predicted that researchers can increase the number of criteria and alternatives and obtain more effective and comprehensive solutions by using different solution methodologies. Besides, it is anticipated that highly efficient and flexible decision support systems can be developed by supporting a large database, a user-interactive interface and artificial intelligence technologies of the proposed approach.

Contributions of the Authors

Each author contributed equally to the article.

Conflict of Interest Statement

There is no conflict of interest between the authors.

Statement of Research and Publication Ethics

The study is complied with research and publication ethics

References

[1] U. Ü. Uçar and S. K. İşleyen "A new solution approach for UAV routing problem with moving target – heterogeneous fleet", *Journal of Polytechnıc*, 22(4): 999-1016, 2019.

[2] B. Uçakcıoğlu and T. Eren, "Investment Selection Project in Air Defense Industry with Analytic Hierarchy Process and VIKOR Methods". *Harran University Journal of Engineering*, 2(2), pp. 35-53, 2017.

[3] M. Ulukavak and M. Miman, "Selection of The Most Proper Unmanned Aerial Vehicle for Transportation in Emergency Operations by Using Analytic Hierarchy Process". *International Journal of Environment and Geoinformatics*, 8(1), pp. 78-91, 2019.

[4] İ. H. Özaslan, B. Kocaoğlu and Ş. Odabaşoğlu "Türkiye'de Pistonlu Tek Motorlu Uçak Seçiminde Çok Kriterli Karar Verme Ahp ve Topsis Yöntemlerinin Kullanılması", *Journal of Aviation Research*, 3 (2) , pp. 243-263, 2021. DOI: 10.51785/jar.955683

[5] Y. Zhao, W. Lou, J. Wang, W. Liu and Z. Su, "Evaluation of the unmanned aerial vehicle (UAV) recovery system based on the analytic hierarchy process and grey relational analysis". In 2019 IEEE International Conference on Unmanned Systems (ICUS) (pp. 285-290). IEEE. 2019, October.

[6] Z. Tuba, Z. Vidnyánszky, Z. Bottyán, F. Wantuch and K. Hadobács, Application of Analytic Hierarchy Process in fuzzy logic–based meteorological support system of unmanned aerial vehicles1. AARMS, AARMS, 12(2), pp. 221–228, 2013.

[7] Y. Yan, W. Pei, W. Su and J. Ye "Research on Maintenance Quality Evaluation Method for Unmanned Aerial Vehicle", In 2019 IEEE 3rd Advanced Information Management, Communicates, Electronic and Automation Control Conference (IMCEC) pp. 237-240, IEEE, 2019, October

[8] A. Yıldızbaşı and L. Gür, "A decision support model for unmanned aerial vehicles assisted disaster response using AHP-TOPSIS method" *European Journal of Science and Technology*, (20), pp. 56-66, 2020.

[9] J. R. Wang, Y. L. Tsai, L. N. Wu, and Y. C. Lin, "The power system design of small unmanned aerial vehicle". In Proceedings of the 2013 IEEE/SICE International Symposium on System Integration (pp. 838-843). IEEE, 2013, December.

[10] M. L. HE, H. Jilin and A. Xiaole. "Genetic Algorithm Based on Analytic Hierarchy Process PID Parameter Tuning of UAV Control System". 2nd International Conference on Advances in Mechanical Engineering and Industrial Informatics, AMEII 2016

[11] C. K. Lai and J. F. Whidborne. "Automated return-to-route maneuvers for unmanned aircraft systems". In 2012 IEEE/AIAA 31st Digital Avionics Systems Conference (DASC) (pp. 8C4-1). IEEE, (2012, October)

[12] L. Canetta, G. Mattei and A. Guanziroli, "Multi criteria analysis applied on value chain definition in unmanned aerial vehicle (UAV) sector." In 2017 International Conference on Engineering, Technology and Innovation (ICE/ITMC) (pp. 1096-1103). IEEE, (2017, June)

[13] O. Gur and A. Rosen, "Optimization of propeller based propulsion system" *Journal of Aircraft*, 46(1), pp. 95-106, 2009.

[14] S. Gaggero, G. Tani, D. Villa, M. Viviani, P. Ausonio, P. Travi and F. Serra, "Efficient and multi-objective cavitating propeller optimization: an application to a high-speed craft", *Applied Ocean Research*, 64, pp. 31-57, 2017.

[15] Ö. Dundar, M. Bilici and T. Ünler, "Design and performance analyses of a fixed wing battery VTOL UAV", *Engineering Science and Technology, an International Journal*, 23, pp. 1182–1193, 2020.

[16] Ö. Bayraktar and A. Güldaş, "Optimization of Quadrotor's Thrust and Torque Coefficients and Simulation with Matlab/Simulink", *Journal of Polytechnic*, 23(4), pp. 1197-1204, 2020.

[17] E. J., Foeth and F. Lafeber, "Systematic propeller optimization using an unsteady Boundary Element Method". *In Fourth International Symposium on Marine Propulsors (SMP15)*; Austin, TX, USA, 2015.

[18] Y. Lee, E-T. Park, J. Jeong, H. Shi, J. Kim, B-S. Kang and W. Song, "Weight optimization of hydrogen storage vessels for quadcopter UAV using genetic algorithm", *International Journal of Hydrogen Energy*, 45, pp. 33939-33947, 2020.

[19] A. Bacciaglia, A. Ceruti and A. Liverani, "Controllable pitch propeller optimization through meta-heuristic algorithm". *Engineering with Computers*, pp 1-15, 2020.

[20] H. Zhang, B. Song, F. Li and J. Xuan, "Multidisciplinary design optimization of an electric propulsion system of a hybrid UAV considering wind disturbance rejection capability in the quadrotor mode". *Aerospace Science and Technology*, 110, p. 106372, 2021.

[21] M. Podsędkowski, R. Konopiński, D. Obidowski and K. Koter, "Variable Pitch Propeller for UAV-Experimental Tests". *Energies*, 13(20), p.5264, 2020

[22] A. F. ElGhazali and S. S. Dol, "Aerodynamic Optimization of Unmanned Aerial Vehicle through Propeller Improvements". *Journal of Applied Fluid Mechanics*, 13(3), pp. 793-803, 2020.

[23] G. Sinibaldi and L. Marino, "Experimental analysis on the noise of propellers for small UAV". *Applied Acoustics*, 74(1), pp.79-88, 2013.

[24] E. Kuantama and R. Tarca, "Quadcopter thrust optimization with ducted-propeller". In MATEC Web of Conferences (Vol. 126, p. 01002). EDP Sciences, 2017.

[25] F. Larocca, D. D'ambrosıo, L. Raıola, A. Tutor and E. F. Zamboni, "Topological optimization of a drone propeller using commercial CFD code". Master's Thesis in Aerospace Engineering Thesis. Polıtecnıco Dı Torıno, 2019.

[26] S. Kapsalis, P. Panagiotou and K. Yakinthos, "CFD-aided optimization of a tactical Blended-Wing-Body UAV platform using the Taguchi method" *Aerospace Science and Technology*, 108, p.106395, 2021.

[27] C. Dahal, H. B. Dura and L. Poudel, "Design and Analysis of Propeller for High Altitude Search and Rescue Unmanned Aerial Vehicle". *International Journal of Aerospace Engineering*, pp. 1-13, 2021.

[28] A. F. ElGhazali and S. S. Dol, "Aerodynamic Optimization of Unmanned Aerial Vehicle through Propeller Improvements". *Journal of Applied Fluid Mechanics*, 13(3), pp. 793-803, 2020.

[29] G. Andria, A. Di Nisio, A. M. L. Lanzolla, M. Spadevecchia, G. Pascazio, F. Antonacci and G. M. Sorrentino, "Design and performance evaluation of drone propellers". In 2018 5th IEEE International Workshop on Metrology for AeroSpace (MetroAeroSpace) (pp. 407-412). IEEE, (2018, June).

[30] G. Iannace, G. Ciaburro and A. Trematerra, "Fault diagnosis for UAV blades using artificial neural network". *Robotics*, 8(3), p.59, 2019.

[31] A. Dumıtrache, M. V. Prıcop, M. L. Nıculescu, M. G. Cojocaru and T. Ionescu, "Desıgn And Analysıs Methods For Uav Rotor Blades". *Scientific Research & Education İn The Air Force-Afases*, 1, 2017

[32] R. D. Rakhade, N. V. Patil, M. R. Pardeshi and C. S. Mhasde, "Optimal Choice of Agricultural Drone using MADM Methods". *International Journal of Technological Innovation in Modern Engineering and Science (IJTIMES)*, e-ISSN, pp. 2455-2585, 2017.

[33] B. Sah, R. Gupta & D. Bani-Hani, "Analysis of Barriers to Implement Drone Logistics". *International Journal of Logistics Research and Applications*, 24(6), pp. 531-550, 2021.

[34] J. Z. Zhang, P. R. Srivastava & P. Eachempati, "Evaluating The Effectiveness of Drones in Emergency Situations: A Hybrid Multi-Criteria Approach". *Industrial Management & Data Systems*, 2021.

[35] C. Zhou, J. Yin, A. Rong, D. Guo and J. Li, "Research on UAV Fire Fight based on Analytic Hierarchy Process". In Proceedings of the 2021 International Conference on Control and Intelligent Robotics (p. 16-22, (2021, June).

[36] T. Zoltan, Z. Vidnyánszky, Z. Bottyán, F. Wantuch and K. Hadobács, "Application of analytic hierarchy process in fuzzy logic-based meteorological support system of unmanned aerial vehicles", 2013.

[37] C. Ardil, "A Comparative Analysis of Multiple Criteria Decision Making Analysis Methods for Strategic, Tactical, and Operational Decisions in Military Fighter Aircraft Selection". *International Journal of Aerospace and Mechanical Engineering*, 14(7), pp. 275-288, 2021.

[38] A. Adem, K. B. Yilmaz and M. Dağdeviren, "Technology Analysis for Logistics 4.0 Applications: Criteria Affecting UAV Performances". *In Intelligent and Fuzzy Techniques in Aviation 4.0* pp. 497-520. Springer, Cham, 2022.

[39] H. Moaddab, M. Ebrahimi and M. N. Ahangar, "Civil Unmanned Aerial Vehicle Assessment for Short Range Monitoring Gas Pipeline Using AHP Methodology", 18th Int. Conference of Iranian Aerospace Society Amirkabir University of Technology, (February - 2020)

[40] S. Hsiao and P. Peng, "Using FCE and FAHP to Explore the multirotor drone appearance preference, in Boess", S., Cheung, M. and Cain, R. (eds.), Synergy - DRS International Conference, pp. 11-14 2020 August,

[41] M. S. Khan, S. I. A. Shah, A. Javed, N. M. Qadri and N. Hussain, "Drone selection using multi-criteria decision-making methods". In 2021 *International Bhurban Conference on Applied Sciences and Technologies (IBCAST)* (pp. 256-270). IEEE, (2021, January)

[42] J. R. Wang, Y. L. Tsai, L. N. Wu and Y. C. Lin, "The power system design of small unmanned aerial vehicle". *In Proceedings of the 2013 IEEE/SICE International Symposium on System Integration* (pp. 838-843). IEEE, 2013, December.

[43] T. Müezzinoğlu and M. Karaköse, "An intelligent human–unmanned aerial vehicle interaction approach in real time based on machine learning using wearable gloves". *Sensors*, 21(5), 1766, 2021.

[44] B. Tanyeri, Z. U. Bayrak and U. U. Uçar, "The Experimental Study of Attitude Stabilization Control for Programmable Nano Quadcopter". *Journal of Aviation*, 6(1), pp. 1-11, 2022.

[45] I. Petkovics, J. Simon, A. Petkovics and Z. Čović, "Selection of unmanned aerial vehicle for precision agriculture with multi-criteria decision making algorithm". I*n 2017 IEEE 15th international symposium on intelligent systems and informatics* (SISY) (pp. 000151-000156). IEEE, 2017, September

[46] M. Radovanović, A. Petrovski, V. Žindrašič and A. Ranđelović, "Application of the Fuzzy AHP-VIKOR hybrid model in the selection of an unmanned aircraft for the needs of tactical units of the armed forces". *Scientific Technical Review*, 71(2), pp. 26-35, 2021.

[47] M. Hamurcu and T. Eren, "Selection of unmanned aerial vehicles by using multicriteria decision-making for defence". *Journal of Mathematics*, 2020.

[48] https://bilgeis.net/docs/40_B2_1.pdf Accesed: 21.09.2021

[49] T. L. Saaty, "How to make a decision: the analytic hierarchy process", *Euro. J. Oper. Res*., 48: pp. 9-26, 2019.

[50] M. Şenol, A. Adem, M. Dağdeviren. "A Fuzzy MCDM Approach to Determine the Most Influential Logistic Factors", *Journal of Polytechnic*, 22(3), pp. 793–800, 2019.

[51] M. Dağdeviren, S. Yavuz, N. Kılınç, "Weapon selection using the AHP and TOPSIS methods under fuzzy environment". *Expert Systems with Applications*, 36, pp. 8143-8151, 2009.

[52] T. L. Saaty, The Analytic Hierarchy Process, Mcgraw-Hill, New York (1980).

[53] M. Dağdeviren, "Decision making in equipment selection: an integrated approach with AHP and PROMETHEE", *J. Intel. Manuf*., 19:pp. 397-406, 2008

[54] M. Dağdeviren and T. Eren, "Analytic hierarchy process and use of 0-1 goal programming methods in selecting supplier firm", *J. Fac. Eng. Archit.*, Gazi Univ. Cilt 16, pp 41-52, 2020

Bitlis Eren Üniversitesi Fen Bilimleri Dergisi
BİTLİS EREN UNIVERSITY JOURNAL OF SCIENCE
ISSN: 2147-3129/e-ISSN: 2147-3188
VOLUME: 11 NO: 4 PAGE: 1014-1017 YEAR: 2022
DOI:10.17798/bitlisfen.1150947

On Closed Subspaces of Grand Lebesgue Spaces

Yasin KAYA[1*]

[1]*Dicle University, Department of Mathematics*
(ORCID:0000-0002-7779-6903)

Keywords: Grand Lebesgue spaces, Embeddings, Hilbert spaces.

Abstract
We prove a generalized version of a theorem of Grothendieck over finite measure space. We prove a closed subspace of grand Lebesgue space that consist of functions of L^{∞} must be finite dimensional. By using embeddings of Banach spaces $L^{p}(\Omega), L^{p)}(\Omega)$ and $L^{2}(\Omega)$ we work inside space $L^{2}(\Omega)$. Then we take advantage of many useful properties of Hilbert space.

1. Introduction

In [1] Iwaniec and Sbordone aimed to tackle problem of integrability of the Jacobian under minimal assumptions, introduced grand Lebesgue spaces $L^{p)}(\Omega)$. Grand Lebesgue spaces $L^{p)}(\Omega)$ are a generalization of classical Lebesgue spaces $L^{p}(\Omega)$. Among many applications of $L^{p)}(\Omega)$ one is this: $L^{p)}(\Omega)$ spaces gave rise to be the convenient spaces in which several nonlinear equations in the theory of partial differential equations have to be considered [2,3]. For a detailed discussions of properties and some generalization of grand Lebesgue spaces we refer the readers to book [4]. We recall here briefly some basic definitions and general facts about grand Lebesgue spaces. Let $\Omega \subset \mathbb{R}^{n}$ be a Lebesgue measurable set with $|\Omega| < \infty$ and $1 < p < \infty$. Grand Lebesgue space $L^{p)}(\Omega)$ is defined as the spaces of the measurable functions f on Ω such that

$$\|f\|_{p)} = \sup_{0<\varepsilon<p-1}\left(\frac{\varepsilon}{|\Omega|}\int_{\Omega}|f|^{p-\varepsilon}\,dx\right)^{\frac{1}{p-\varepsilon}} < \infty. \tag{1}$$

Grand Lebesgue spaces $L^{p)}(\Omega)$ are Banach spaces. Let X and Y be two normed linear spaces such that $X \subset Y$. If the operator $I : X \to Y$ defined by $I(x) = x$ is continuous we say the embedding $X \subset Y$ continuous. Getting back to the spaces $L^{p)}(\Omega)$, the following continuous embeddings holds:

$$L^{p}(\Omega) \subset L^{p)}(\Omega) \subset L^{p-\varepsilon}(\Omega) \quad \text{for} \quad 0 < \varepsilon < p-1. \tag{2}$$

Furthermore, since $g(x) = x^{-\frac{1}{p}} \in L^{p)}(0,1)$ and $g(x) = x^{-\frac{1}{p}} \notin L^{p}(0,1)$ hold. $L^{p)}(\Omega)$ space is strictly larger than Lebesgue space $L^{p}(\Omega)$. The subspace $C_0^{\infty}(\Omega)$ is not dense in $L^{p)}(\Omega)$. Its closure $\left[L^{p}\right]_{p)}$ consists of all those functions $f \in L^{p)}(\Omega)$ which satisfy

$$\lim_{\varepsilon\to 0}\varepsilon\int_{\Omega}|f|^{p-\varepsilon}\,dx = 0. \tag{3}$$

2. Material and Method

There are many advantages of Hilbert spaces comparing with unspecific Banach spaces. One of them Hilbert spaces have bases with fine adequate properties and notion of orthogonality of vectors. One of the most useful examples of a Hilbert space is the

*Corresponding author: ykaya@dicle.edu.tr
Received: 29.07.2022, Accepted: 31.10.2022

space $L^2(\Omega)$. The space $L^2(\Omega)$ equipped with the following inner product space

$$\langle f, g \rangle = \int_\Omega f(x)\overline{g(x)}d\mu(x) . \quad (4)$$

Proof of the following lemma is to be found in any book on functional analysis**.**

Lemma 2.1. (Generalized Pythagorean Theorem**)** Let $(D, \langle . \rangle, \|.\|)$ be an inner product space over field F. If the vectors $g_1, g_2, ..., g_n \in D$ are orthogonal, then

$$\|g_1 + g_2 + ... + g_n\|^2 = \|g_1\|^2 + \|g_2\|^2 + ... + \|g_n\|^2 \quad (5)$$

3. Results and Discussion

Our result is the following theorem. Our proof is an adaptation of the proof given in [5]. But actually the clasical result of this theorem due to Grothendieck [6]. In [7] this theorem was proved for variable exponent Lebesgue space $L^{p(x)}(\Omega)$, which is an another generalization of classical Lebesgue space $L^p(\Omega)$. For a discussion of $L^{p(x)}(\Omega)$ spaces see [8] and references therein.

Theorem 3.1. Let $\Omega \subset \mathbb{R}^n$ have finite Lebesgue measure. Let D be a closed subspace of grand Lebesgue space $L^{p)}(\Omega)$ such that $D \subset L^\infty(\Omega)$. Then the space D is finite dimensional.

Before proceeding with the proof the theorem we need the following lemma whose proof can be found in [5, lemma 4.3 page 175] . (Actually we state a part of the lemma).

Lemma 3.2. With the same set of hypoteses of theorem 3.1 there exists $\beta > 0$ such that

$$\|f\|_{L^p} \le \beta \|f\|_{L^2} \text{ for all } f \in D. \quad (6)$$

Proof of the theorem 3.1. Since D is a closed subspace of the Banach space $L^{p)}(\Omega)$ then D is itself a Banach space. Let define an identity mapping by

$$I : D \to L^\infty(\Omega) \text{ and } I(f) = f .$$

The identity mapping is obviously linear, now we show it also has a closed graph. Let $f_n \in D$ and $g \in L^\infty(\Omega)$ such that $f_n \to f$ in D and $I(f_n) = f_n \to g$ in $L^\infty(\Omega)$. Since

$$\|f_n - g\|_{p)} = \sup_{0<\varepsilon<p-1} \left(\frac{\varepsilon}{|\Omega|} \int_\Omega |f_n - g|^{p-\varepsilon} dx \right)^{\frac{1}{p-\varepsilon}} \le \|f_n - g\|_{L^\infty} \sup_{0<\varepsilon<p-1} \left(\frac{\varepsilon}{|\Omega|} \int_\Omega dx \right)^{\frac{1}{p-\varepsilon}} \quad (7)$$

holds we have $f = g$ almost everywhere, so by the closed graph theorem I is continuous, and so there is a constant $c > 0$ such that

$$\|f\|_{L^\infty} \le c \|f\|_{L^{p)}} \text{ for all } f \in D. \quad (8)$$

From (8), $L^p(\Omega) \subset L^{p)}(\Omega)$ embedding and Lemma 3. there exists $K > 0$ such that

$$\|f\|_{L^\infty} \le K \|f\|_{L^2} \text{ for all } f \in D. \quad (9)$$

Now we are aware that we placed D inside $L^2(\Omega)$. We know $L^2(\Omega)$ is a Hilbert space. There are many advantages to be gained from working with $L^2(\Omega)$ space. Let $\{g_1, g_2, ..., g_n\}$ be an orthonormal set in $L^2(\Omega)$ of functions in D. Define

$$B = \left\{ c = (c_1, c_2, ..., c_n) \in \mathbb{C}^n : \sum_{j=1}^n |c_j|^2 \le 1 \right\}. \quad (10)$$

For each $c = (c_1, c_2, ..., c_n) \in B$ let us define a function

$$g_c = \sum_{j=1}^n c_j g_j(x) \quad (11)$$

Moreover $g_c(x) \in D$ and by the generalized Pythagorean theorem (Lemma 2.1.)

$$\|g_c(x)\|_{L^2} = \left\| \sum_{j=1}^n c_j g_j(x) \right\|_{L^2} = \left(\sum_{j=1}^n \|c_j g_j(x)\|_{L^2}^2 \right)^{\frac{1}{2}} = \left(\sum_{j=1}^n |c_j|^2 \right)^{\frac{1}{2}} \le 1. \quad (12)$$

Consequently from (9) we have

$$\|g_c\|_{L^\infty} \le K \tag{13}$$

Hence for each c there exists a Lebesgue measurable set Ω_c of full measure in Ω i.e., $|\Omega_c| = |\Omega|$, such that

$$|g_c(x)| \le K \text{ for all } x \in \Omega_c \tag{14}$$

By first using a countable dense subset of points in B, then applying the continuity of the mapping $c \to g_c(x)$, we notice that (14) gives

$$|g_c(x)| \le K \text{ for all } x \in \Omega' \text{ and all } c \in B \tag{15}$$

Where Ω' is a set of full measure in Ω. Furthermore, we claim that for every $x \in \Omega'$ we have

$$\sum_{j=1}^{n} |g_j(x)|^2 \le K^2 \tag{16}$$

It is sufficies to prove this inequality under the assumption that the left- hand side not zero. Let us define

$$\theta = \left(\sum_{j=1}^{n} |g_j(x)|^2 \right)^{\frac{1}{2}} \tag{17}$$

and set $c_j = \overline{g_j(x)}/\theta$ then by (15) we obtain for each $x \in \Omega'$

$$\frac{1}{\theta} \sum_{j=1}^{n} |g_j(x)|^2 \le K, \tag{18}$$

that means $\theta \le K$, as we claimed.

Finally, integrating (16) and being aware that $\int_\Omega |g_j(x)|^2 \, dx = 1$ we have $n \le K^2 |\Omega|$. Since $K^2 |\Omega|$ is a constant number the dimension of D must be finite.

4. Conclusion and Suggestions

We proved the theorem for Lebesgue measure, also the same proof methods can be applied to case when (M, Σ, μ) is a given measure space provided that $\mu(M) < \infty$. It will be interesting to search whether theorem 3.1 remains valid under weaker hypotheses.

Acknowledgment

If necessary, the people, institutions and organizations that helped in the study should be thanked for their help and support.

Contributions of the authors

The contributions of each author to the article should be indicated.

Conflict of Interest Statement

There is no conflict of interest between the authors.

Statement of Research and Publication Ethics

The study is complied with research and publication ethics

References

[1] T. Iwaniec and C. Sbordone, "On the integrability of Jacobian under minimal hypotheses," *Archive for Rational Mechanics and Analysis*, vol. 119, no. 2, pp.129-143,1992.

[2] L. Greco, T. Iwaniec, and C. Sbordone, "Inverting the $p-$harmonic operator,"*manuscripta mathematica*, vol.92, pp. 249-258,1997.

[3] A. Fiorenza and C. Sbordone, "Existence and uniqueness results for solutions of nonlinear equations with right hand side in L^1, " *Studia Mathematica*, vol. 3, no.127, pp. 223-231,1998.

[4] R. Castillo and H. Rafeiro, *An introductory course in Lebesgue Spaces*. Cham, Switzerland: Springer international publishing, 2018.

[5] E.M. Stein and R. Shakarchi, *Functional analysis: Introduction to further topics in analysis*. Princeton, NJ: Princeton University Press, 2011.

[6] A. Grothendieck, "Sur certains sous-espaces vectoriels de L^p , " *Canadian Journal of Mathematics*, vol. 6, pp.158-160,1954.

[7] Y. Kaya, "On a closed subspace of $L^{p(.)}(\Omega)$," *Bitlis Eren Üniversitesi Fen Bilimleri Dergisi,* vol. 9, no. 2, pp. 682-688, 2020.

[8] D.V. Cruz-Uribe and A. Fiorenza, *Variable Lebesgue spaces: Foundations and Harmonic Analysis.* Springer Science & Business Media, 2013.

Bitlis Eren Üniversitesi Fen Bilimleri Dergisi
BİTLİS EREN UNIVERSITY JOURNAL OF SCIENCE
ISSN: 2147-3129/e-ISSN: 2147-3188
VOLUME: 11 NO: 4 PAGE: 1018-1025 YEAR: 2022
DOI:10.17798/bitlisfen.1167047

Antioxidant and Antimicrobial Capacity of Quinic Acid

Leyla ERCAN[1*], Mehmet DOĞRU[2]

[1]*Mardın Artuklu Unıversıty Central Research Laboratory, Mardin, 47000, Turkey*
[2]*Dicle University, Faculty of Ziya Gökalp Education, Department of Chemistry, Diyarbakır, Turkey*
(ORCID: 0000-0002-6570-8128) (ORCID: 0000-0002-2287-2913)

Keywords: Quinic acid, DPPH, ABTS, Antimicrobial activity

Abstract

Recently, agents with natural antioxidant and antimicrobial properties have been popularly studied. For this purpose, phenolic compounds, terpenes, and organic acids are examined for their antioxidant and antimicrobial properties. Of these, organic acids are increasingly being used in pharmacology, medicine, food, and industry. Quinic acid is a natural organic compound found in many edible fruits and plants. In this study, the antioxidant effect of quinic acid, which has the structure of cyclohexane carboxylic acid, was determined *in vitro* using seven different methods (DPPH, ABTS, CUPRAC, DMPD, FRAP, Fe^{3+} reduction, and Total antioxidant method). In addition, its antimicrobial effect on fungi (C. albicans), gram-positive bacteria (*S. aureus, S. pyogenes*), and gram-negative bacteria (*E. coli, K. pneumoniae, and P. aeruginosa*) were determined by the disk diffusion method. As a result, it was found that quinic acid has broad-spectrum antimicrobial properties, but its antioxidant properties are too low to be highlighted. While its antimicrobial activity was quite good, especially on *K. pneumoniae E. coli, S. aureus, S. Pyogenes*, and *P. aeruginosa*, it did not show any effect on *C. albicans*. Although the antioxidant property of quinic acid is low, it showed more antioxidant properties in the DMPD method, which is one of these methods, because it dissolves very well in water.

1. Introduction

Quinic acid (1, 3, 4, 5-tetrahydroxy cyclohexane carboxylic acid) is a cyclohexanecarboxylic acid found in coffee beans, cinchona bark, potatoes, apples, and peaches [1]–[4]. It has been reported that quinic acid has radioprotective, anti-diabetic, and anti-neuroinflammatory activities and is also an antimutagenic and anti-inflammatory agent [2], [5]–[8]. Quinic acid improves DNA repair and leads to NF-κB inhibition [9]–[11]. In addition, experiments on mice have shown that quinic acid has neuroprotective effects on dementia [12].

Antioxidants are compounds that can scavenge free radicals in the human body [13]. Antioxidants are compounds that can prevent oxidation processes that occur under reactive oxygen species. Because of these properties, they are used to stabilize pharmaceuticals, foodstuffs, petrochemicals, and cosmetics [14]. In addition to antioxidant compounds, research is carried out on what antimicrobial agents are. With these aspects, it finds study area in organic acids found in plants [15].

In this area, revealing the antioxidant and antimicrobial effects of natural products is very important in terms of being economical and yielding efficient results [16]. Therefore, in this study, the antioxidant and antimicrobial effects of quinic acid were investigated.

2. Material and Method

D-Quinic acid, DPPH (2,2 Diphenyl-1-picrylhydrazyl), $FeCl_36H_2O$, NH_4SCN, $FeCl_24H_2O$, $CH_3COONa3H_2O$, Na_2HPO_4, CH_3COONH_4, $CuCl_2$, ABTS (2,2'-azino-bis(3-ethylbenzothiazoline-6-sulfonic acid) diammonium salt), DMPD (N,N-Dimethyl-p-phenylenediamine dihydrochloride) are purchased from Sigma Aldrich.

*Corresponding author: leylaercan@artuklu.edu.tr
Received: 25.08.2022, Accepted: 25.10.2022

Tested Microorganisms; *Klebsiella pneumoniae* ATCC 13883, *Pseudomonas aeruginosa* ATCC 9027, *Escherichia coli* ATCC 11229, *Candida albicans* ATCC 10231, *Staphylococcus aure*us ATCC 25923, strains are purchased from Microbiologics. *Streptococcus pyogenes* (ATCC 19615) was obtained from Ankara Refik Saydam Public Health.

250 µM DPPH solution has used the determination of the DPPH radical scavenging activity of quinic acid [17]. DPPH inhibition activities of quinic acid, BHT, BHA, and Trolox were determined at a wavelength of 517 nm in a spectrophotometer. To measure ABTS scavenging activity of quinic acid; 2 ml 2mM ABTS was added to Quinic acid, Trolox, BHT, and BHA solutions from ABTS radical formed by stirring 2 mM ABTS and 2.45 mM $K_2O_8S_2$ and incubated for half an hour. Then the % reduction against the control solution at 734 nm was determined [18], [19]. The cupric ion (Cu^{2+}) reducing capacities of quinic acid and standards were determined by the CUPRAC method. For this, 0.25 ml $CuCl_2$ of 0.01 M, 0.25 ml of $7.5x10^{-3}$M methanolic neocuprine solutions, and 1 M ammonium acetate buffer (pH: 6.5) were transferred to test tubes. After mixing the solution, different concentrations of quinic acid and standards were added. The absorbances were recorded at 450 nm [20]. Quinic acid and standards were taken into test tubes with $NaCH_3COO$ buffer solution with a pH of 3.6 for antioxidant analysis according to the FRAP method. Then, 20 mM $FeCl_3$ solution and FRAP reagent were added. The test tubes were mixed by vortex and their absorbances were recorded at 593 nm [21]. The DMPD radical scavenging activity of quinic acid was performed using the method of Fogliano et al [22]. For this, 0.001 M DMPD· solution was prepared by adding 0.1M DMPD, acetate buffer (pH: 5.3), and 0.05 M $FeCl_3$ solution. Absorbance measurements were made at 505 nm [22]. Fe^{3+}- Fe^{2+} reducing capacity was determined according to the Oyaizu method [23]. Quinic acid and standard solutions prepared at different concentrations were added to test tubes. The mixture formed by adding 0.2 M phosphate tampon (pH: 6.6) and 1 ml 1% $K_3[Fe(CN)_6]$ was incubated at 50°C. After these procedures, 10% (TCA) and 0.1% $FeCl_3$ were added to the reaction mixture, and absorbances were recorded at 700 nm [23]. Total antioxidant activity determination was carried out according to the Ferric Thiocyanate Method [24]. In this method, lipid peroxides formed in linoleic acid emulsion are left to auto-oxidation in the dark at 37°C; It is based on measuring the color change resulting from the reaction with $FeCl_2$ and NH_4SCN solutions at regular intervals at 500 nm [24].

To determine antimicrobial activity, bacteria grown in a liquid medium were first inoculated into a solid medium on sterile discs. Then, the antimicrobial activity of quinic acid was investigated according to the Disk Diffusion method using erythromycin as a positive control [25]. Inhibition zone diameters were measured for *E. coli, S. aureus, P. aeruginosa,* and *S. pyogenes* bacteria after 24 hours of incubation at 37°C and after 48 hours of incubation at 30°C for *C. albicans*. The same procedure was repeated for the positive (erythromycin 15µg) and negative control (water). Each test was performed in 3 replicates at different times [26].

3. Results and Discussion

According to the results given in Figure 1, it was found that the inhibition capacity of DPPH• of quinic acid is very low.

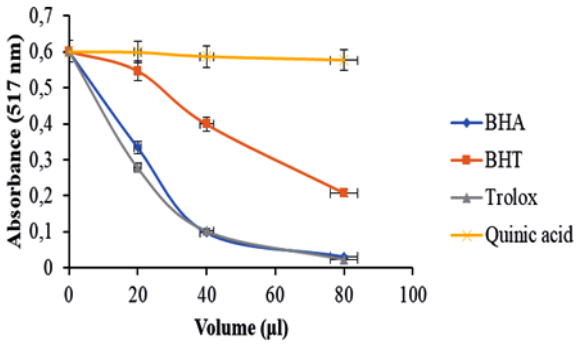

Figure 1. DPPH• radical scavenging activity of quinic acid (30 mg/ml) and standards (at 1mg/ml concentration)

It has been determined that quinic acid does not inhibit ABTS radical as a result of experiments with solutions of quinic acid prepared at concentrations of 1 mg/ml, 30 mg/ml, and 100 mg/ml. $ABTS^{\bullet+}$ scavenging of quinic acid (30mg/ml) and standard antioxidants (at 1 mg/ml concentration) is given in Figure 2.

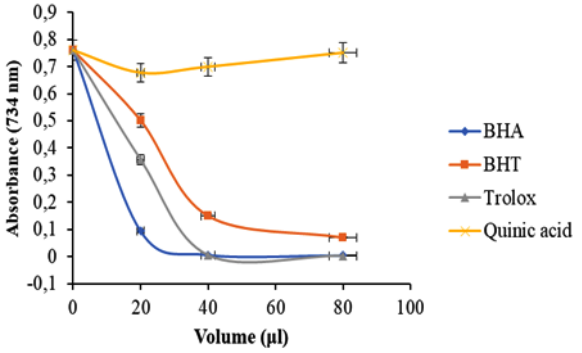

Figure 2. $ABTS^{+}$ radical scavenging activity of quinic acid and standards

$DMPD^{\cdot+}$ inhibition was determined with the solutions of quinic acid prepared at 30 mg/ml concentration, and a decrease was observed in the results, which increased regularly with the increase in concentration (Figure 3). On the other hand, since 30 mg/ml and 100 mg/ml were quite high concentrations, it was observed that quinic acid had a scavenging activity of $DMPD^{\cdot+}$ radical, but this was low.

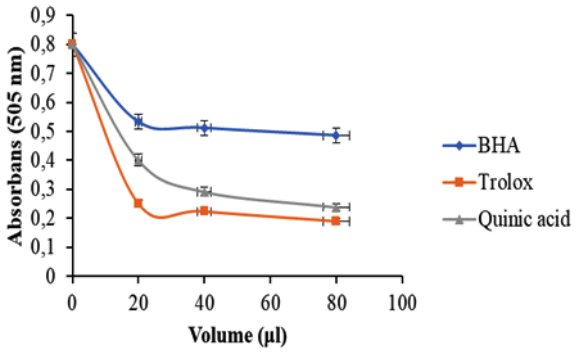

Figure 3. $DMPD^{\cdot+}$ radical scavenging activity of quinic acid and standards

The antioxidant capacities of quinic acid (30 mg/ml), BHT, BHA, and Trolox (at 1 mg/ml concentration) were determined by the CUPRAC method and given in the graph in Figure 4. According to the test results, quinic acid did not show antioxidant properties in the CUPRAC method.

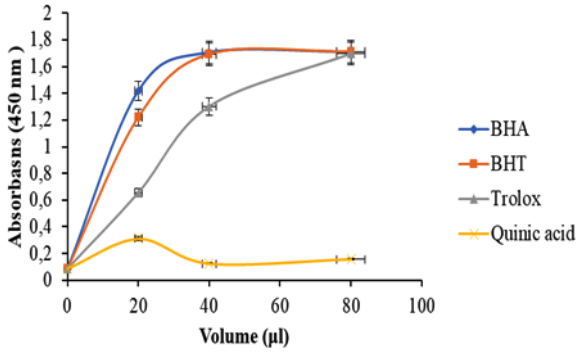

Figure 4. Reducing capacity results of quinic acid and standard antioxidants by the CUPRAC method

In addition, the ferric ion-reducing capacities of 30 mg/ml quinic acid and standard antioxidants (BHA, BHT, and Trolox (at 1 mg/ml concentration)) were compared and shown in Figure 5. As a result of the experiments, the ability of quinic acid to reduce CUPRAC, FRAP, and ferric ions was not observed.

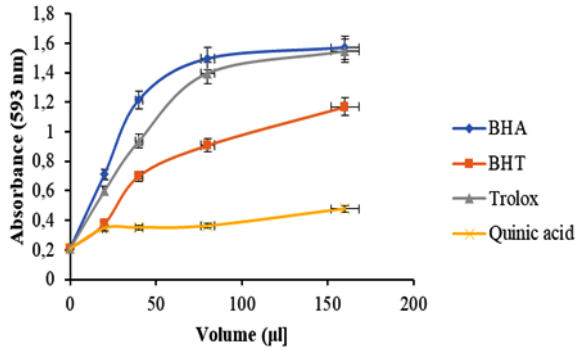

Figure 5. Reducing the capacity of quinic acid and standard antioxidants by the FRAP method

Fe^{3+}- Fe^{2+} reducing activity assay was also performed for quinic acid (30 mg/ml), Trolox, BHA, and BHT (1 mg/ml) the results are given in the graph in figure 6. According to these results, quinic acid did not show antioxidant properties according to the Fe^{3+}-Fe^{2+} reduction method.

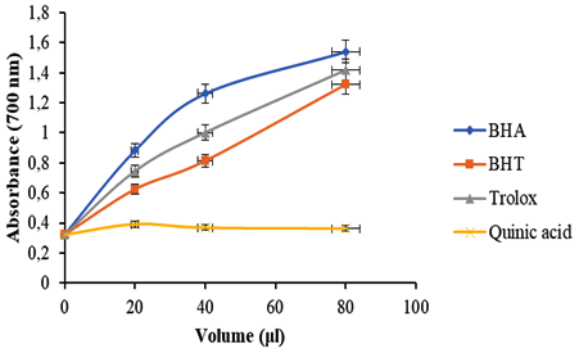

Figure 6. Fe^{3+} Fe^{2+} reduces the capacity of quinic acid and standard antioxidants

Total antioxidant activity determination according to Ferric Thiocyanate Method was also performed in 30 mg/ml concentration quinic acid solution and standards (1mg/ml), and the results are given in the graph in figure 7. The percentages of lipid peroxidation in 80 µl of quinic acid prepared at a concentration of 30 mg/ml at 72 hours and Ferric Thiocyanate lipid peroxidation reduction percentages of the standards, respectively; BHT (99.90%) > BHA (93.93%) > Trolox (80.92%) > quinic acid (44.75%) (Figure 7).

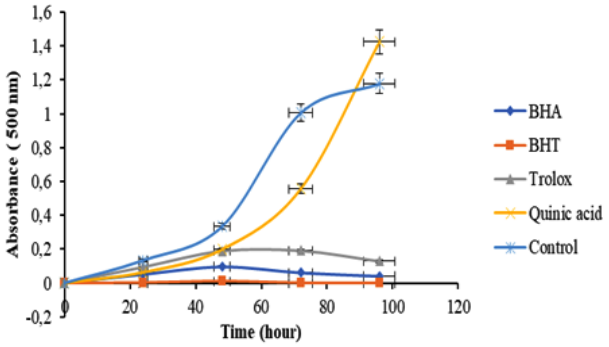

Figure 7. Total antioxidant activity of quinic acid and standard antioxidants

Table 1. Antioxidant activity test results

	IC_{50} (µg/ml)			$A_{0.5}$ (µg/ml)			% Reduction (at 72.hour)
Standards and sample	**DPPH**	**ABTS**	**DMPD**	**CUPRAC**	**FRAP**	**Fe^{3+} reduction**	**Total antioxidant**
BHA	23.07	13.70	83.68	6.35	12.17	5.78	92.82
BHT	63.78	26.79	-	9.60	33.29	12.83	98.10
Trolox	18.79	18.10	18.14	15.33	17.20	8.85	80.62
Quinic acid	-	-	2965	-	-	-	44.75

IC_{50}: Concentration that inhibits 50 percent of the radical, $A_{0.5}$: Concentration at 0.5 nm

The antimicrobial activity of quinic acid was investigated and the results are given in Table 2. Quinic acid was highly effective on gram-negative and gram-positive bacteria, but not on *Candida albicans* (Figure 8). In addition, the % inhibition values of quinic acid according to the erythromycin antibiotic are given in Table 3.

Table 2. Results of antimicrobial activity of quinic acid (mm)

	K. pneumoniae	***E. coli***	***S. aureus***	***S. Pyogenes***	***P. aeruginosa***	***C. albicans***
Quinic acid (100 mg/ml)	16.53±1.48	15.10±0.18	17.57±0.9	16.41±0.7	13.20±1.2	-
Eritromisin (E-15)	16.43±0.02	14.31±1.4	18.97±0.47	20.70±0.0	12.63±0.02	15.19±1.13

Table 3. % Inhibition values of quinic acid compared to erythromycin antibiotic

	% Inhibition					
	K. pneumoniae	***E. coli***	***S. aureus***	***S. Pyogenes***	***P. aeruginosa***	***C. albicans***
Quinic acid (100 mg/ml)	100.6	105.52	92.62	79.27	104.51	-

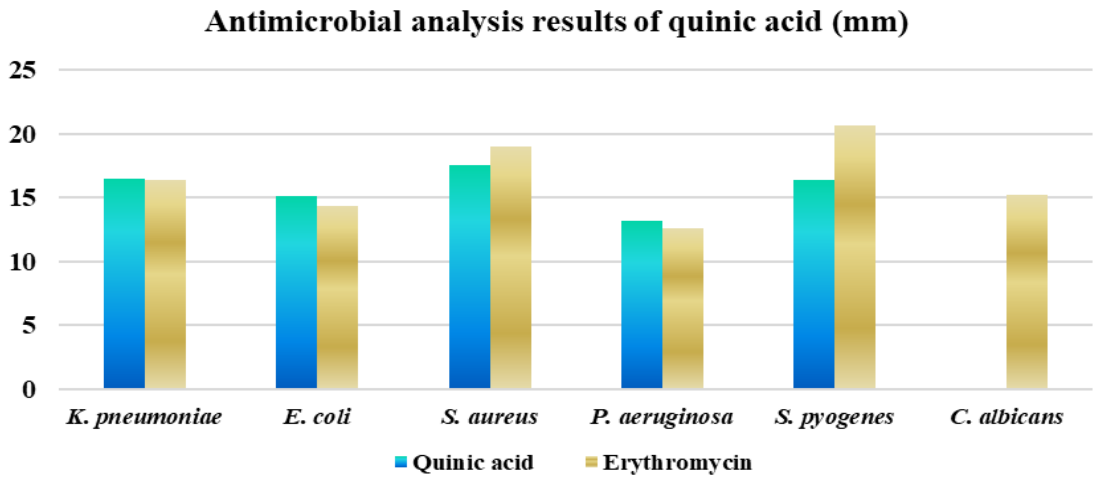

Figure 8. Results of antimicrobial analysis of quinic acid

As a result of the experiments (Table 1), it was found that the inhibition capacity of $DPPH^{\bullet}$ radical is almost non-existent. It also does not inhibit $ABTS^{+\bullet}$ radical which was determined as a result of experiments performed with quinic acid solutions prepared at concentrations of 1 mg/ml, 30 mg/ml, and 100 mg/ml. The $DMPD^{\bullet+}$ radical scavenging activity of quinic acid was determined with quinic acid solutions prepared at 30 mg/ml and 100 mg/ml concentrations, and it gave a reduction result that increased regularly with concentration. The IC_{50} value for the DMPD of quinic acid was found to be 2965 µg/ml. Accordingly, the antioxidant capacity of quinic acid is very low. The reason for the inhibition of the $DMPD^{\bullet+}$ radical of quinic acid in repeated experiments can be shown as its extremely good solubility in water. It was determined that quinic acid did not show antioxidant activity in experiments performed at different concentrations according to the CUPRAC method. It was also observed that quinic acid did not have FRAP-reducing activity at 30 mg/ml and 100 mg/ml concentrations. Fe^{3+}- Fe^{2+} reduction activity test was carried out in quinic acid solutions prepared at different concentrations and standard antioxidants, but according to the results, quinic acid did not show antioxidant properties according to the Fe^{3+} reduction method. In the determination of total antioxidant activity according to the ferric thiocyanate method, the percentage of lipid peroxidation of ferric thiocyanate in 72 hours was determined as 44.75% at a 30 mg/ml concentration of quinic acid. According to the results, it was observed that quinic acid inhibited lipid peroxidation, albeit in a small amount. In the experiments, it was determined that quinic acid, which was mentioned as an antioxidant before, could not be highlighted in terms of antioxidant properties [12], [27]. It has been reported that quinic acid supports the synthesis of tryptophan and nicotinamide, thus increasing serum thiols and showing antioxidant properties [28]. On the other hand, it was previously reported that quinic acid did not show antioxidant properties compared to DPPH, TEAC, and FRAP methods [29]. In this study, the contradiction about whether quinic acid has antioxidant properties has been eliminated and it has been determined that quinic acid cannot be shown as an antioxidant. In addition, studies are showing that phenolic compound derivatives of quinic acid have strong antioxidant properties [30], [31]. However, while these quinic acid derivatives have a phenolic ring, quinic acid is in the cyclohexane structure, which is a more stable chemical structure. Although there are OH groups in the antioxidant compounds in the chemical structure of quinic acid, the absence of the aromatic ring negatively affected its antioxidant properties.

The antimicrobial activity of quinic acid; was examined on gram-positive and gram-negative bacteria and fungi and the results are given in Tables 2 and 3. The antimicrobial activity of quinic acid solution prepared at 100 mg/ml concentration was investigated on *E. coli*, *K. pneumoniae*, *S. aureus*, *P. aeruginosa*, *S. pyogenes*, and *C. albicans.* According to these results, it was observed that quinic acid is highly effective, especially on gram-positive bacteria (*S. aureus*, *S. pyogenes*) and gram-negative bacteria (*P. aeruginosa*, *E. coli*, *K. pneumoniae*). It even inhibited *K. pneumoniae*, *E. coli*, and *P. aeruginosa* bacteria more than the antibiotic erythromycin. On the other hand, no effect of quinic acid on C. albicans was found in triple experiments. In other words, the antifungal effect of quinic acid was not observed. It

has been previously reported that quinic acid has an effect, especially on foodborne pathogens, and inhibits *S. aureus* by reducing the membrane fluidity, damaging and inhibiting the cell membrane, and also has an antimicrobial effect on *E.coli, Salmonella enterica, Bacillus cereus, Clostridium perfringens* bacteria [32]. Quinic acid damages L-lysine and peptidoglycan synthesis to inhibit cell wall synthesis [33]. In addition, it has been reported that quinic acid prevents bacterial biofilm formation against *P. aeruginosa* and can be used against *P. aeruginosa*-related infections [34]. This study found results supporting this conclusion. In addition, it was determined that quinic acid inhibited *K. pneumoniae, S. pyogenes* bacteria, but did not have an antifungal effect. Because of these properties, quinic acid can be used as a preservative in foods, as well as in the treatment of various infections.

4. Conclusion and Suggestions

In the antioxidant experiments performed with 7 different methods, it was observed that the antioxidant property of quinic acid was not found in DPPH, ABTS, CUPRAC, FRAP, Fe^{3+} reduction methods, but it was very low in DMPD and total antioxidant methods. In addition, antimicrobial activity studies have shown that quinic acid can be used as a good antimicrobial agent. It has been shown that quinic acid can be used efficiently in biotechnological products with antimicrobial properties.

Acknowledgment

This work was supported by the Dicle University Scientific Research Projects Coordination Unit [With project no ZGEF.20.001]. We would like to thank Dicle University Scientific Research Projects Coordination Unit for their project support.

Contributions of the authors

Author 1: Writing-original draft preparation, data collection, data curation, visualization, analysis, data interpretation. Author 2: Conceptualization, methodology, validation, writing review, editing, supervision, provision of analysis tools. All authors have accepted responsibility for the entire content of this manuscript and approved its submission.

Conflict of Interest Statement

There is no conflict of interest between the authors.

Statement of Research and Publication Ethics

The study is complied with research and publication ethics.

References

[1] G. W. Chapman and R. J. Horvat, "Determination of Nonvolatile Acids and Sugars from Fruits and Sweet Potato Extracts by Capillary GLC and GLC/MS," *J Agric Food Chem*, vol. 37, no. 4, pp. 947–950, Jul. 1989, doi: 10.1021/JF00088A026/ASSET/JF00088A026.FP.PNG_V03.

[2] N. Cinkilic *et al.*, "Radioprotection by two phenolic compounds: chlorogenic and quinic acid, on X-ray induced DNA damage in human blood lymphocytes in vitro," *Food Chem Toxicol*, vol. 53, pp. 359–363, Mar. 2013, doi: 10.1016/J.FCT.2012.12.008.

[3] S. S. Dhondge, P. H. Shende, L. J. Paliwal, and D. W. Deshmukh, "Volumetric and acoustic study of aqueous binary mixtures of quinine hydrochloride, guanidine hydrochloride and quinic acid at different temperatures," *J Chem Thermodyn*, vol. 81, pp. 34–43, Feb. 2015, doi: 10.1016/J.JCT.2014.09.011.

[4] S. A. Jang *et al.*, "Quinic acid inhibits vascular inflammation in TNF-α-stimulated vascular smooth muscle cells," *Biomed Pharmacother*, vol. 96, pp. 563–571, Dec. 2017, doi: 10.1016/J.BIOPHA.2017.10.021.

[5] A. Arya *et al.*, "Synergistic effect of quercetin and quinic acid by alleviating structural degeneration in the liver, kidney and pancreas tissues of STZ-induced diabetic rats: a mechanistic study," *Food Chem Toxicol*, vol. 71, pp. 183–196, 2014, doi: 10.1016/J.FCT.2014.06.010.

[6] J. S. Bonita, M. Mandarano, D. Shuta, and J. Vinson, "Coffee and cardiovascular disease: in vitro, cellular, animal, and human studies," *Pharmacol Res*, vol. 55, no. 3, pp. 187–198, Mar. 2007, doi: 10.1016/J.PHRS.2007.01.006.

[7] J. Boyer and R. H. Liu, "Apple phytochemicals and their health benefits," *Nutr J*, vol. 3, no. 1, pp. 1–15, Dec. 2004, doi: 10.1186/1475-2891-3-5/FIGURES/4.

[8] S. Y. Lee, E. Moon, S. Y. Kim, and K. R. Lee, "Quinic acid derivatives from Pimpinella brachycarpa exert anti-neuroinflammatory activity in lipopolysaccharide-induced microglia," *Bioorg Med Chem Lett*, vol. 23, no. 7, pp. 2140–2144, Apr. 2013, doi: 10.1016/J.BMCL.2013.01.115.

[9] O. Mortelé, J. Jorissen, I. Spacova, S. Lebeer, A. L. N. van Nuijs, and N. Hermans, "Demonstrating the involvement of an active efflux mechanism in the intestinal absorption of chlorogenic acid and quinic acid using a Caco-2 bidirectional permeability assay," *Food Funct*, vol. 12, no. 1, pp. 417–425, Jan. 2021, doi: 10.1039/D0FO02629H.

[10] R. W. Pero, H. Lund, and T. Leanderson, "Antioxidant metabolism induced by quinic acid. Increased urinary excretion of tryptophan and nicotinamide," *Phytother Res*, vol. 23, no. 3, pp. 335–346, Mar. 2009, doi: 10.1002/PTR.2628.

[11] R. W. Pero and H. Lund, "Dietary quinic acid supplied as the nutritional supplement AIO + AC-11® leads to induction of micromolar levels of nicotinamide and tryptophan in the urine," *Phytother Res*, vol. 25, no. 6, pp. 851–857, Jun. 2011, doi: 10.1002/PTR.3348.

[12] L. Liu, Y. Liu, J. Zhao, X. Xing, C. Zhang, and H. Meng, "Neuroprotective Effects of D-(-)-Quinic Acid on Aluminum Chloride-Induced Dementia in Rats," *Evid Based Complement Alternat Med*, vol. 2020, 2020, doi: 10.1155/2020/5602597.

[13] V. M. Victor, M. Rocha, and M. de La Fuente, "Immune cells: free radicals and antioxidants in sepsis," *Int Immunopharmacol*, vol. 4, no. 3, pp. 327–347, Mar. 2004, doi: 10.1016/J.INTIMP.2004.01.020.

[14] A. M. Pisoschi and G. P. Negulescu, "Methods for Total Antioxidant Activity Determination: A Review," *Biochemistry & Analytical Biochemistry*, vol. 01, no. 01, 2012, doi: 10.4172/2161-1009.1000106.

[15] L. Kovanda *et al.*, "In Vitro Antimicrobial Activities of Organic Acids and Their Derivatives on Several Species of Gram-Negative and Gram-Positive Bacteria," *Molecules 2019, Vol. 24, Page 3770*, vol. 24, no. 20, p. 3770, Oct. 2019, doi: 10.3390/MOLECULES24203770.

[16] A. Das and K. Satyaprakash, "Antimicrobial properties of natural products: A review Annada Das and Kaushik Satyaprakash," *~ 532 ~ The Pharma Innovation Journal*, vol. 7, no. 6, pp. 532–537, 2018, Accessed: Aug. 15, 2022. [Online]. Available: www.thepharmajournal.com

[17] M. S. Blois, "Antioxidant Determinations by the Use of a Stable Free Radical," *Nature*, vol. 181, no. 4617, pp. 1199–1200, 1958, Accessed: Aug. 15, 2022. [Online]. Available: https://www.academia.edu/3348938/Antioxidant_Determinations_by_the_Use_of_a_Stable_Free_Radical

[18] E. Bursal, E. Köksal, I. Gülçin, G. Bilsel, and A. C. Gören, "Antioxidant activity and polyphenol content of cherry stem (Cerasus avium L.) determined by LC-MS/MS," *Food Research International*, vol. 51, no. 1, pp. 66–74, Apr. 2013, doi: 10.1016/J.FOODRES.2012.11.022.

[19] R. Re, N. Pellegrini, A. Proteggente, A. Pannala, M. Yang, and C. Rice-Evans, "Antioxidant activity applying an improved ABTS radical cation decolorization assay," *Free Radic Biol Med*, vol. 26, no. 9–10, pp. 1231–1237, May 1999, doi: 10.1016/S0891-5849(98)00315-3.

[20] R. Apak *et al.*, "Comparative evaluation of various total antioxidant capacity assays applied to phenolic compounds with the CUPRAC assay," *Molecules*, vol. 12, no. 7, pp. 1496–1547, Jul. 2007, doi: 10.3390/12071496.

[21] I. Gülçin, "Antioxidant activity of food constituents: an overview," *Arch Toxicol*, vol. 86, no. 3, pp. 345–391, Mar. 2012, doi: 10.1007/S00204-011-0774-2.

[22] V. Fogliano, V. Verde, G. Randazzo, and A. Ritieni, "Method for Measuring Antioxidant Activity and Its Application to Monitoring the Antioxidant Capacity of Wines," *J Agric Food Chem*, vol. 47, no. 3, pp. 1035–1040, Mar. 1999, doi: 10.1021/JF980496S.

[23] M. Oyaizu, "Studies on products of browning reaction. Antioxidative activities of products of browning reaction prepared from glucosamine.," *The Japanese Journal of Nutrition and Dietetics*, vol. 44, no. 6, pp. 307–315, 1986, doi: 10.5264/EIYOGAKUZASHI.44.307.

[24] G. C. Yen and H. Y. Chen, "Antioxidant Activity of Various Tea Extracts in Relation to Their Antimutagenicity," *J Agric Food Chem*, vol. 43, no. 1, pp. 27–32, Jan. 1995, doi: 10.1021/JF00049A007/ASSET/JF00049A007.FP.PNG_V03.

[25] National Committee for Clinical Laboratory Standards., *NCCLS Performance Standards for Antimicrobial Disk Susceptibility Tests: Approved Standard Enclose -A 7*, April 1997 ed. Wayne PA USA: NCCLS, 1997.

[26] L. Ercan and M. Doğru, "Su Teresi (Nasturtium Officinale) Bitkisinin Antioksidan Kapasitesinin Belirlenmesi," Institute of Science, Diyarbakır, 2021.

[27] B. Devi, S. Bais, and N. S. Gill, "A Review on quinic acid and its therapeutic potential," *Inventi Rapid: Molecular Pharmacology*, vol. 3, pp. 1–6, 2017, Accessed: Aug. 15, 2022. [Online]. Available: https://inventi.in/journal/article/140/22705/Inventi%20Rapid:%20Molecular%20Pharm/Pharmaceutical

[28] R. W. Pero, H. Lund, and T. Leanderson, "Antioxidant metabolism induced by quinic acid. Increased urinary excretion of tryptophan and nicotinamide," *Phytother Res*, vol. 23, no. 3, pp. 335–346, Mar. 2009, doi: 10.1002/PTR.2628.

[29] J. G. Uranga, N. S. Podio, D. A. Wunderlin, and A. N. Santiago, "Theoretical and Experimental Study of the Antioxidant Behaviors of 5-O-Caffeoylquinic, Quinic and Caffeic Acids Based on Electronic and Structural Properties," *ChemistrySelect*, vol. 1, no. 13, pp. 4113–4120, Aug. 2016, doi: 10.1002/SLCT.201600582.

[30] R. Roesler, R. R. Catharino, L. G. Malta, M. N. Eberlin, and G. Pastore, "Antioxidant activity of Annona crassiflora: Characterization of major components by electrospray ionization mass spectrometry," *Food Chem*, vol. 104, no. 3, pp. 1048–1054, Jan. 2007, doi: 10.1016/J.FOODCHEM.2007.01.017.

[31] Y. J. Yang *et al.*, "Radical scavenging activity and cytotoxicity of active quinic acid derivatives from Scorzonera divaricata roots," *Food Chem*, vol. 138, no. 2–3, pp. 2057–2063, Jun. 2013, doi: 10.1016/J.FOODCHEM.2012.10.122.

[32] J. Bai *et al.*, "In vitro and in vivo characterization of the antibacterial activity and membrane damage mechanism of quinic acid against Staphylococcus aureus," *J Food Saf*, vol. 38, no. 1, p. e12416, Feb. 2018, doi: 10.1111/JFS.12416.

[33] J. Bai, Y. Wu, Q. Bu, K. Zhong, and H. Gao, "Comparative study on antibacterial mechanism of shikimic acid and quinic acid against Staphylococcus aureus through transcriptomic and metabolomic approaches," *LWT*, vol. 153, p. 112441, Jan. 2022, doi: 10.1016/J.LWT.2021.112441.

[34] L. Lu *et al.*, "Quinic acid: a potential antibiofilm agent against clinical resistant Pseudomonas aeruginosa," *Chinese Medicine (United Kingdom)*, vol. 16, no. 1, pp. 1–17, Dec. 2021, doi: 10.1186/S13020-021-00481-8/FIGURES/5.

Bitlis Eren Üniversitesi Fen Bilimleri Dergisi
BİTLİS EREN UNIVERSITY JOURNAL OF SCIENCE
ISSN: 2147-3129/e-ISSN: 2147-3188
VOLUME: 11 NO: 4 PAGE:1026-1041 YEAR: 2022
DOI: 10.17798/bitlisfen.1168077

The Determination of the Most Appropriate Probability Distribution Models for the Meteorological Variables

Musa EŞİT[*1]

[1]A *Civil Engineering Department, Adiyaman University, Adiyaman, Turkey*
(ORCID: 0000-0003-4509-7283)

Keywords: Meteorological Variables, Distribution, Goodness of Fit, Ankara

Abstract
Every component of the hydrological cycle is essential for controlling water supplies and assessing potentially catastrophic events like floods and droughts. The variables of the hydrological system are unexpected and unique to each place. In this paper, the most crucial variables, including precipitation, temperature, relative humidity, and evaporation, are examined for Ankara province. For meteorological parameters, the Lognormal, Log-logistic, Gamma, Weibull, Normal, and Gumbel models are used to find the best suitable distributions. Kolmogorov-Smirnov, Cramers-von Mises, Akaike's Information Criterion, Bayesian Information Criterion, Anderson-Darling, and Maximum Loglikelihood methods are utilized to test these models. The results show that there is a distinct distribution model for each parameter. In particular, it has been determined that the Gumbel distribution is a better model for annual total precipitation, whereas the Normal distribution is a better model for annual minimum temperature. At stations 17130 and 17664, the gamma distribution is observed to be the best fit distribution at annual total precipitation, but station 17128 is found to be the most appropriate for both Log-logistic and normal distribution. Stations 17128, 17130, and 17664 for annual maximum temperature series are fitted with the Normal, Log-logistic, and Lognormal, respectively. Gamma is found to be the best fit when analyzing annual mean temperature for stations 17128 and 17130, whereas Lognormal is selected for station 17664. It is expected that these results will contribute to the planning of water resources projects in the region.

1. Introduction

The hydrological cycle plays a substantial role in the social, economic, and cultural development of any country. The amount and pattern of meteorological variables at a given location are essential factors in a variety of natural and socioeconomic systems, including flood control, water resource management, agriculture, forestry, and tourism [1]. Therefore, it is essential to consider the regime and dynamics of a certain hydrologic phenomenon, particularly the time-based aspects [2]. In addition, the importance of time series analysis is highlighted by the lack of complete understanding of the physical processes involved and the resulting uncertainties in the magnitudes and frequencies of future events [3], [4]. Time series analysis is necessary for developing mathematical models that generate synthetic hydrologic records, detect intrinsic stochastic properties, and forecast hydrologic events of hydrologic variables [5], [6].

In hydrology, it provides the alternative of an acceptable probability distribution function to study rainfall, runoff, and temperature series in various locations [7]. Extreme flooding and rain, however, will cause many people's lives to be disrupted and cost millions of dollars. Hence, the possibility of such an event is necessary for flood control programs, reservoirs, bridges, and other survey management and design staff. The effects of contaminants, unusually low flows, and loads on water must all be taken into consideration in the study of hydrology. As a result,

*Corresponding author: mesit@adiyaman.edu.tr
Received:29.08.2022 Accepted:17.10.2022

they affect the quality and sources of water [8], [9]. Engineering design, planning, and management of water systems and hydraulic structures, including the identification of drought risks, urban planning, and growth forecasting, all largely advantage from understanding the frequency of occurrence of probable values of a random variable through probability distribution. [10], [11].

According to statistical theory, for extremes, the frequency of such occurrences is significantly more influenced by changes in variability (or, more usually, the scale parameter) than by changes in the mean climate (more usually, the location parameter) [12]. The meteorological parameters differ from one country to another as well as from one weather station to another. For example, Khudri [7] discovered that for 50% of the survey stations, generalized gamma four parameter distributions and the generalized extreme value provided the best fit, while no other distribution was consistently detected to be appropriate for the remaining stations in Bangladesh. Unal et al. [13] evaluated the flood flow rates of 2, 5, 10, 25, 50, and 100 years by using the 22-year flow data of 11 AGI stations located in the Gediz Basin. The K-S test was performed to define the most appropriate distribution among Log Normal, Normal, Log Pearson Type III, Gamma, and Gumbel. They determined that the most compatible probability distribution for the flow observation data was Log Pearson Type III. Anli and Anli [14] used the K-S test to find the probability distribution that best fits the 39-year maximum flow data in the Giresun Aksu Basin. As a result of the test, he observed that the distribution most suitable for the annual maximum flow data was the Weibull distribution. Yavuz and Ergül [15] modeled the annual mean flow value of the Eskişehir Porsuk Dam using the Normal, Log Normal, Logistic, Gamma, and Weibull probability distributions. In terms of selecting the best probability distribution for 33 years of data, they discovered that the Weibull probability distribution was more appropriate as a result of the K-S test. Sandalcı [16] employed Normal, Log Normal, and Gumbel probability distributions to determine the flood flow rates for the Akçay Stream, one of the most significant tributaries of the Sakarya River, for recurrence intervals of 5, 10, 25, 50, 100, and 250 years. He utilized the K-S test to identify the probability distribution that was the most consistent and found that the Log Normal distribution was the most entirely compatible. According to Salami [17], it is possible to forecast the amount of rainfall extremely precisely for various durations using a certain probability distribution, even if precipitation varies with time and has unpredictable features. Due to the time and space constraints on rainfall data, accurate estimations are not always possible. Knowledge about extreme rainfall is crucial for many hydrological applications [18]–[20]. Meteorological variables are typically calculated in hydrological research using normal distribution, Pearson type 3, the lognormal distribution, generalized distribution of extreme value (GEV), exponential function, Gumbel distribution, Weibull and Pareto distributions [21], [22]. Haddad [23] investigates various goodness-of-fit (GOF) standards used in various scientific disciplines and examines the benefits and limitations of each GOF in order to compare potential probability density functions (pdfs) to annual maximum temperature data. The annual maximum temperature series is generally best fitted by generalized extreme values and normal distributions. Vivekanandan [24] discovered that the Log-Pearson III distribution was more appropriate for temperature and rainfall data in Hissar, India. On the basis of Australian daily maximum temperatures, Trewin [25] employed a variety of probability distributions; his findings demonstrated that Gaussian distributions represented by various parameters were effective in capturing extremes in the data.

In this study, the most appropriate distribution among the Lognormal, Log-logistic, Gamma, Weibull, Normal, and Gumbel are determined for annual maximum temperature, annual mean temperature, annual minimum temperature, annual total precipitation, annual total evapotranspiration, and annual mean relative humidity for Ankara province. The most suitable distribution is found to perform Cramers-von Mises (CvM), Kolmogorov-Smirnov (KS), Akaike's Information Criterion (AIC), Bayesian Information Criterion (BIC), Anderson-Darling (AD) and Maximum Loglikelihood methods

2. Study Area and Data

Throughout the province's wide territory, there are climatic variations from location to location. The Central Anatolian climate's characteristic steppe climate may be seen in the south, and the temperate and rainy conditions of the Black Sea climate can be observed in the north. In this area, which has a continental climate, winters are cold and summers are hot. The hottest months are July and August, while January is the coldest. The northern and southern parts of the region experience different amounts of precipitation. Ankara displays the climate characteristic of the Central Anatolia Region in the south and the precipitation regime of the Black Sea Region in the north. Fog is a common occurrence and has a negative impact on life because of the region's geography, particularly in the winter. The province

has an average annual temperature of 11.7 °C and 389.1 millimeters of precipitation. The highest recorded temperature was 40.8 °C, while the lowest recorded temperature was -24.9 °C. The highest snow thickness was determined as 30 cm. According to data measured over a long period of time, Ankara's average pressure value is 913.1 mb, the greatest pressure value was 935.0 mb, and the lowest pressure value was 891.0 mb [26], [27]. Time series of meteorological parameters are obtained from the General Directorate of Meteorology Turkey (MGM) for 3 stations located in Ankara (Figure 1). Observations of meteorological station periods and geographic locations are given in Table 1.

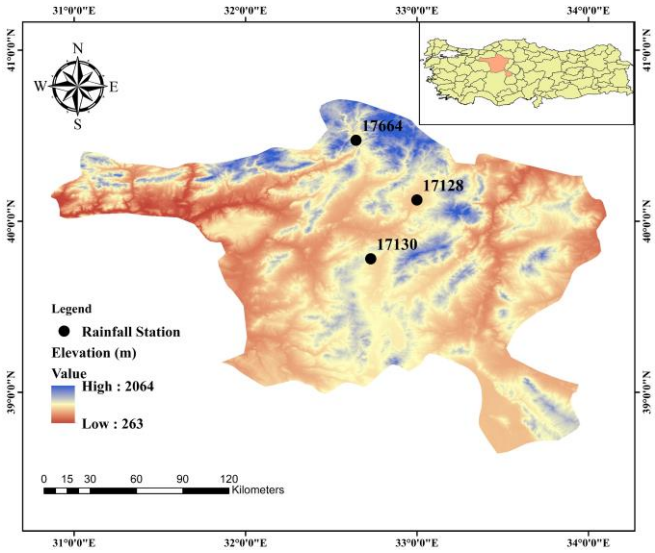

Figure 1. Selected meteorological stations on study area

Table 1. Observation of meteorological stations periods and geographic locations.

Station No	Station Name	Parameters	Longitude	Latitude	Record Years
17128	Ankara Airport	Annual total precipitation (mm) Annual max, min and mean temperature (°C) Annual mean relative humidity (%) Annual total evapotranspiration (mm)	32.999	40.124	1956-2021
17664	Ankara Center	Annual total precipitation (mm) Annual max, min and mean temperature (°C) Annual mean relative humidity (%) Annual total evapotranspiration (mm)	32.644	40.472	1959-2021
17130	Ankara-Kızılcahamam	Annual total precipitation (mm) Annual max, min and mean temperature (°C) Annual mean relative humidity (%) Annual total evapotranspiration (mm)	32.863	39.972	1926-2021

3. Metodology

The decision of probability distribution models is significant for choosing the best-fit probability distribution for a specific area. The chosen distribution models that are frequently employed in assessments of meteorological parameters are given in this section. The approach for parameter estimation is defined, along with numerical and graphical goodness-of-fit assessments for model selection.

3.1. Marginal Probability Distribution

3.1.1 Normal (Gaussian) Distribution

The normal distribution is widely used in the social sciences and plays a significant role in statistics. It illustrates real-valued random variables in the natural sciences when their distribution is not clear [28]. In analyses of annual rainfall and streamflow series, the Gaussian or N distribution is frequently used [29]. The parameters of the normal distribution are mean μ and variance σ^2. For a normal random variable x, the probability density function (pdf), f(x), and cumulative distribution function (cdf), F(x), are given as;

$$f(x) = \frac{1}{\sigma\sqrt{2\pi}} \exp\left[-\frac{1}{2\sigma^2}(x-\mu)^2\right] \quad (1)$$

$$F(x) = \frac{1}{\sigma\sqrt{2\pi}} \int_{-\infty}^{\infty} \left(\exp\left[-\frac{1}{2\sigma^2}(x-\mu)^2\right]\right) dx \quad (2)$$

Here, μ represents mean and σ denotes standard deviation. The case where $\mu \to 0$ and $\sigma \to 1$ is referred to the standard normal distribution.

3.1.2.Weibull Distribution

One of the most often used in various fields is the Weibull distribution, which was developed by Swedish physicist Waloddi Weibull. It outlines the quantified failure of a number of different groups of phenomena and components [30]. Pdf (f(x)) and cdf (F(x)) of Weibull distribution are presented as;

$$f(x) = \frac{\gamma}{\alpha}\left(\frac{x-\mu}{a}\right)^{\gamma-1} exp\left(-\left(\frac{x-\mu}{a}\right)^{\gamma}\right) \quad x \geq \mu; \gamma, a > 0 \qquad (3)$$

$$F(x) = 1 - e^{-\left(\frac{x^{\gamma}}{a}\right)} \quad x \geq 0; \gamma > 0 \qquad (4)$$

where α, μ and γ denote scale, location, and shape parameter. If $a = 1$ and $\mu = 0$, it is noted as the standard Weibull distribution, and if $\mu = 0$, it is called the two-parametric Weibull distribution

3.1.3. Gamma Distribution

Due to the gamma distribution's dependence on the normal and exponential distributions, statistics makes extensive use of it. It is described as a two-parametric distribution with continuous probability, just as the logistic distribution. Special cases of the gamma distribution include the exponential, chi-squared, and Erlang distributions [31]. The gamma distribution's fundamental formula for the pdf is written as;

$$f_{(x)} = \frac{\left(\frac{x-\mu}{\beta}\right)^{\gamma-1} exp\left(-\frac{x-\mu}{\beta}\right)}{\beta\Gamma(\gamma)} \qquad x \geq \mu; \gamma, \beta > 0 \quad (5)$$

where shape, location, and scale parameter are represented as $\gamma, \beta,$ and μ, respectively. The gamma function Γ, represented as;

$$\Gamma(a) = \int_0^{\infty} t^{a-1} e^{-t} dt \qquad (6)$$

The cdf of gamma distribution is;

$$F(x) = \frac{\Gamma_x(\gamma)}{\Gamma(\gamma)} \quad x \geq 0; \gamma > 0 \qquad (7)$$

3.1.4. The Logistic Distribution

The logistic distribution, which has two parameters, is a continuous probability distribution function in statistics. It is typically used in a variety of fields, including logistic regression, logit models, neural networks, finance, sport modeling, physical science, and most recently hydro-climatologic area [32]. Mathematical notation is defined as $X \sim Logistic\ (\mu, s), s > 0$, here μ ($0 \leq \mu \leq \infty$) and s ($s > 0$) represent location parameter and scale parameter respectively. The probability density function (pdf) of logistic distribution is presented by

$$f_X(x) = \frac{e^{-\frac{x-\mu}{s}}}{s\left(1+e^{-\frac{x-\mu}{s}}\right)^2}, \qquad -\infty < x < \infty \qquad (8)$$

The cumulative distribution function (cdf) is given as

$$F_X(x) = \int_{-\infty}^{x} x f_X(x) dx = \frac{1}{1+e^{-\frac{x-\mu}{s}}}, \quad -\infty < x < \infty \qquad (9)$$

3.1.5. Lognormal Distribution

For probabilistic design, the lognormal statistical distribution is essential since negative values might occasionally complicate engineering processes. The description of failure rates, fatigue failure, and other circumstances with a wide range of data is generated using lognormal distribution in practice [33]. The lognormal distribution of random variable X, considering expected value μ_x, standard deviation σ_x , given as LN (μ_x, μ_x), is obtained as

$$f_X(x) = \frac{1}{\sqrt{2\pi}\sigma_Y} e^{-\frac{1}{2}\left(\frac{\ln(x)-\mu_Y}{\sigma_Y}\right)^2}, \qquad 0 < x < \infty \qquad (10)$$

where, $f_X(x)$ is the pdf of the variable X, and

$$\sigma_y = \sqrt{ln\left(\left(\frac{\sigma_x}{\mu_x}\right)^2 + 1\right)} \qquad (11)$$

and

$$\mu_Y = \ln(\mu_X) - \frac{1}{2}{\sigma_y}^2 \qquad (12)$$

If Y variable indicates a normal distribution, then $X = exp(Y)$. In a same way, if X variable shows a normal distribution, $Y = \ln(X)$.

3.1.6. Gumbel Distribution

The Gumbel model, also known as the extreme value type I distribution, is the most used probabilistic model for addressing extreme events [34] the Gumbel model is presented as

$$F(x) = exp\big(-exp(-(x-u)/\alpha)\big) \qquad (12)$$

where x is the value of the random variable X, u and an are the location and scale parameters, respectively, and F(x) represents for the cumulative distribution function. The pdf of Gumbel distribution is expressed as

$$f(x) = e^{-(x+e^{-x})} \qquad (13)$$

3.2. Goodness-of-Fit Tests

The goodness of fit test (GoF) is used to determine if a variable fits a particular population's distribution. These tests determine whether the distribution is appropriate for random data, to put it another way. The goodness of fit test can be assessed using a variety of techniques. The most often used techniques in this study include Akaike's Information Criterion (AIC) [35], Bayesian Information Criterion (BIC) [36], Cramer-von Mises (CvM), Kolmogorov-Smirnov (K-S) [37], Anderson-Darling (AD) [38], and Maximum Likelihood (ML) methods.

3.2.1. Anderson-Darling Test

Any distribution can be tested using the Anderson-Darlin test [38], which can also be used to determine whether a random variable originated from a population with a particular distribution. It is a modification of the Kolmogorov-Smirnov (K-S) test that gives the tails more weight. The A^2 test statistic for the normal, lognormal, Weibull, and Gumbel distributions can be calculated as

$$A^2 = -n - \left(\frac{1}{n}\right)\sum_{i=1}^{n}(2i-1)[ln(w_i) + ln(1 - w_{n-i+1})] \qquad (14)$$

where n is the sample size and w is the standard normal cdf ($\Phi\left[\frac{(x-\mu)}{\sigma}\right]$)

For Weibull and Gumbel distribution

$$w_i = F(x) = 1 - \exp\left(-\left(\frac{x_i}{n}\right)^{\beta}\right) \qquad (15)$$

where n, β are the model scale and shapes parameters

3.2.2 Kolmogorov-Smirnov (K-S) Test

Kolmogorov-Smirnov test, proposed by Smirnov [39], is weak against variations in distribution tails. Calculations are performed for the directional hypothesis as

$$D^+ = max\{F_{(x)} - G_{(x)}\}$$
$$D^- = min\{F_{(x)} - G_{(x)}\} \qquad (16)$$

where, $F_{(x)}\ and\ G_{(x)}$ indicate the empirical distribution function for the data compared and the combined statistic is given by

$$D = max(|D^+|, |D^-|) \qquad (17)$$

Calculating the asymptotic limiting distribution can indicate the p-value for this theoretical statistic.

$$\lim_{m,n\to\infty} Pr\left\{\sqrt{\frac{mn}{(m+n)}}D_{m,n} \le z\right\} = 1 - 2\sum_{i=1}^{\infty}(-1)^{i-1}exp(-2i^2z^2)$$

3.2.3. Cramer-von Mises (CvM) Test

The Cramer-von Mises test enables the modeling of a sample vector's $X = (X^1, \dots, X^{nx})$ probability distribution. It examines at whether a random data set and a previously selected candidate probability distribution are compatible [40]. The Cramer-von Mises distance is presented as

$$D = \int_{-\infty}^{\infty}\big(F(x) - F_0(x)\big)^2 dF_0(x) \qquad (19)$$

This test measures the distance between the candidate distribution F and the cumulative distribution function F_0. For testing the hypothesis, $H_o \to F = F_0$. The test statistic mathematically is presented by

$$\widehat{D_N} = \frac{1}{12N} + \sum_{i=1}^{N}\left[\frac{2i-1}{2} - F(x_i)\right]^2 \qquad (20)$$

where the sample size is N and $\widehat{D_N}$ is the asymptotically known probability distribution distance

3.2.4. Information Criterion (AIC) Test

The Akaike's Information Criterion (AIC) [35] is another method for choosing the best model from a group of models. The chosen model displays the smallest difference between the truth and the model. Based on information theory, the results of this test are calculated as

$$AIC = -2\big(ln(likelihood)\big) + 2K \quad (21)$$

Where K stands for the number of free parameters in the model and likelihood is the probability of a variable given a model. AICc is the second-order information criterion taking sample size into account. It is calculated as

$$AICc = -2\big(ln(likelihood)\big) + 2K \times \left(\frac{n}{n-K-1}\right) \quad (22)$$

where n is the sample size.

3.2.5. Bayesian Information Criterion (BIC) Test

The Bayesian Information Criterion (BIC) [36] is another method for choosing appropriate models from a limited number of options. BIC differs from AIC in general, particularly in the second term, which is related to sample size and calculated as

$$BIC = -2logp(L) + plog(n) \quad (23)$$

Where p is the number of predicted parameter and n is the number of the observations. Here, the minimum AIC and BIC are determined as the best distribution.

3.2.6. Maximum likelihood (ML) Method

The maximum likelihood (ML) method identifies an appropriate strategy for parameter prediction problems [41]. The key benefit of utilizing ML is that it extracts all of the valuable data from the input.

Consider a sample $y = [y_1 \ \dots y_i \ \dots \ y_n]$ from the population. Pdf (or the probability density function) of a random variable y_i conditioned on parameters θ is written by $f(y_i, \theta)$. The joint density of n identically and individually disturbed observation is showed as

$$f(y, \theta) = \prod_{i=1}^{N} f(y_i, \theta) = L(\theta|y) \quad (24)$$

And first term $f(y_i, \theta)$ can be given as

$$f(y_i, \theta) = f(y_i, \mu|\sigma^2 = 1) = \frac{1}{\sqrt{2\pi\sigma^2}}\, e^{\frac{-(y_i-\mu)^2}{2\sigma^2}} \quad (25)$$

It is general practice to study with the Log-Likelihood function.

$$L(\theta|y) = \sum_{i=1}^{N} ln\left(\frac{1}{\sqrt{2\pi\sigma^2}}\, e^{\frac{-(y_i-\mu)^2}{2\sigma^2}}\right)$$

4. Results and Discussion

4.1. Initial Evaluation and Visualization

To help with data visualization and model selection, Figure 2 displays an initial skewness-kurtosis graph of the unbiased distribution of the meteorological parameters. Due to the limited article page, the data of station 17130 are shown as an example. In this paper, uniform, exponential distributions displayed in the Cullen and Frey graph, developed by Cullen et al. [42] are not selected for best fitting distribution. While the probable beta regions are displayed by larger areas, the probable Lognormal, Gamma, and Weibull regions are depicted by lines. The Cullen and Frey graph shows the kurtosis and squared skewness of the precipitation, temperature, relative humidity, and evapotranspiration series as a blue point representing "observation." According to Figure 2, Given their frequent right-skewed nature and positive skewness, the common right-skewed distributions lognormal, normal, gamma, and Weibull are suggested as potential model distribution options. But, because of the substantial variances in skewness and kurtosis across all distributions, this visualization can only be regarded as suggestive.

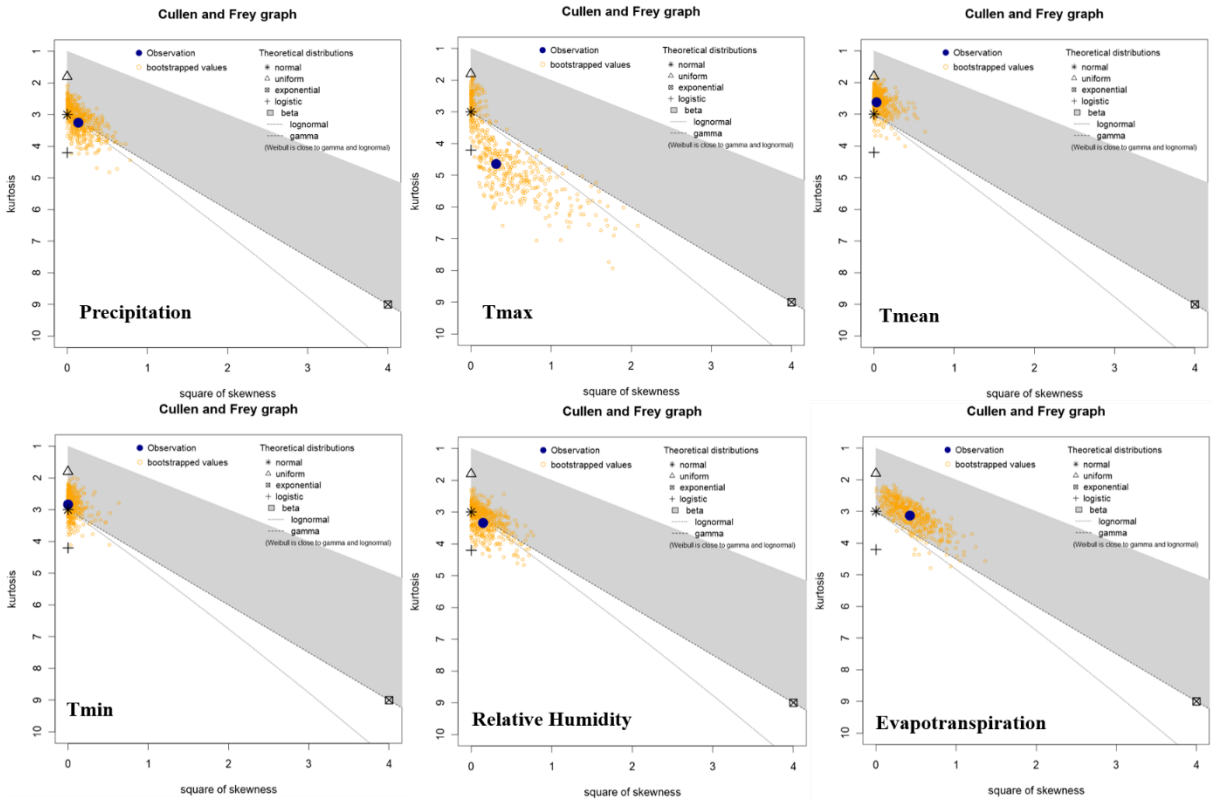

Figure 2. An explanation of precipitation, Tmax, Tmean, Tmin, relative humidity and evapotranspiration series for station 17130 from a normal distribution with estimated bootstrap skewness and kurtosis

Using Assessment-Based Graphs for the GOF

With the help of several graphical functions, the goodness-of-fit of models can be investigated. Figure 3 indicates the theoretical densities of six selected marginal distribution models of precipitation, Tmax, Tmean, Tmin, relative humidity, and evapotranspiration for station 17030. Data analytics requires knowledge of a data's normality or non-normality because it has a significant impact on the algorithms that may be used and how the dataset should be handled. According to Figure 3, log-logistic and Gamma distribution are found the most appropriate models among the selected six distributions for the annual total precipitation series. log-logistic, Gamma and Normal distributions seem to fit the annual maximum, mean, and minimum temperature, respectively. In addition, Log-logistic distribution for annual mean relative humidity and annual total evapotranspiration are observed as more appropriate distribution.

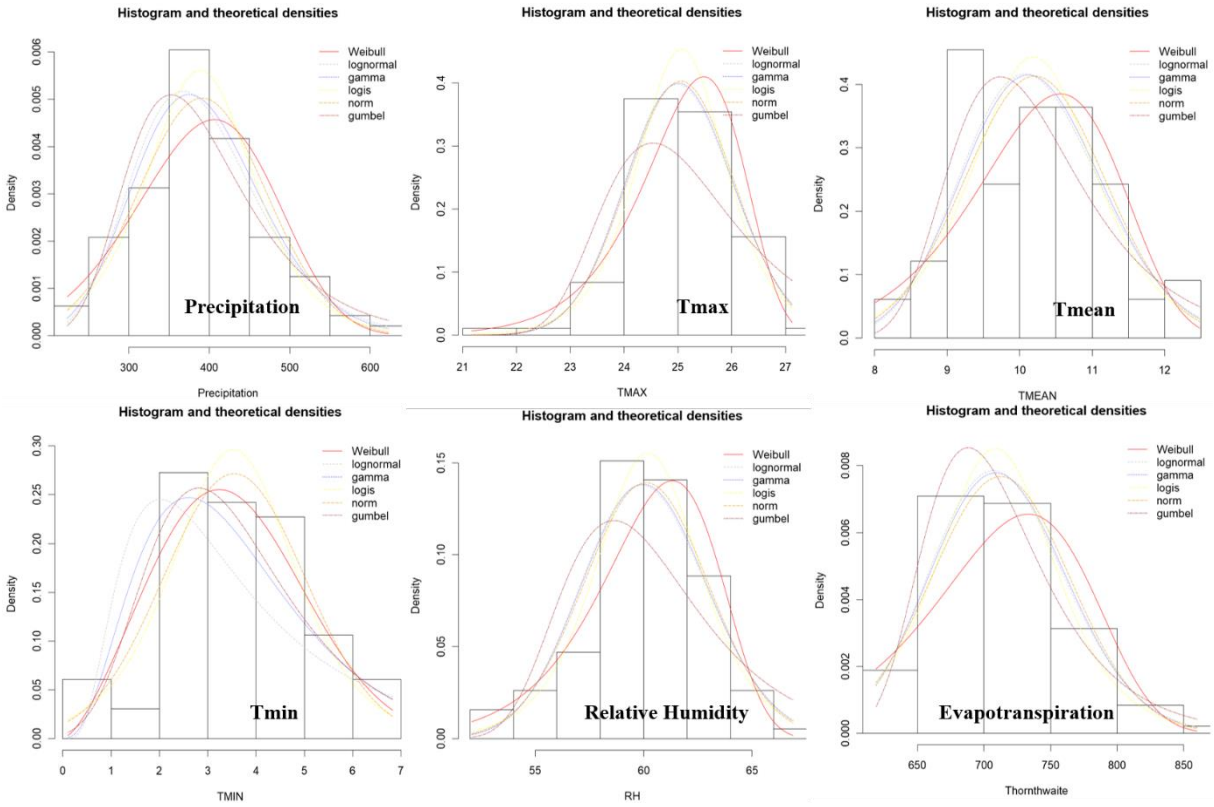

Figure 3. Fitted theoretical densities of six selected marginal distribution models of precipitation, Tmax, Tmean, Tmin, relative humidity and evapotranspiration for station 17030

A probability-probability (P-P) plot is a straightforward graphical technique used to evaluate the accuracy of a forecast prediction and its level of uncertainty. To examine if the dataset series were derived from the six chosen theoretical distributions, quantile-quantile (Q-Q) plots are created for the graphical assessment and visualization of the quality of fit of the selected model distributions. P-P and Q-Q plots are presented for station 17030 in Figures 4 and 5, respectively. The P-P plot compares a uniform distribution to the probability values of the observed meteorological series within the meteorological ensemble, which range from 0 to 1.0. if one of the meteorological series is entirely normally distributed, The P-P plot will be 1:1. The same is also true for the Q-Q plot of the meteorological series. According to Figure 4, P-P plot for all data series is clustered around 1:1 line which means normally distributed. However, the Q-Q plot demonstrates small gaps between empirical quantiles and theoretical quantiles for all marginal selected distributions. Hence, the best fit distribution model is selected considering six different methods and their parameters are predicted by Maximum likelihood method.

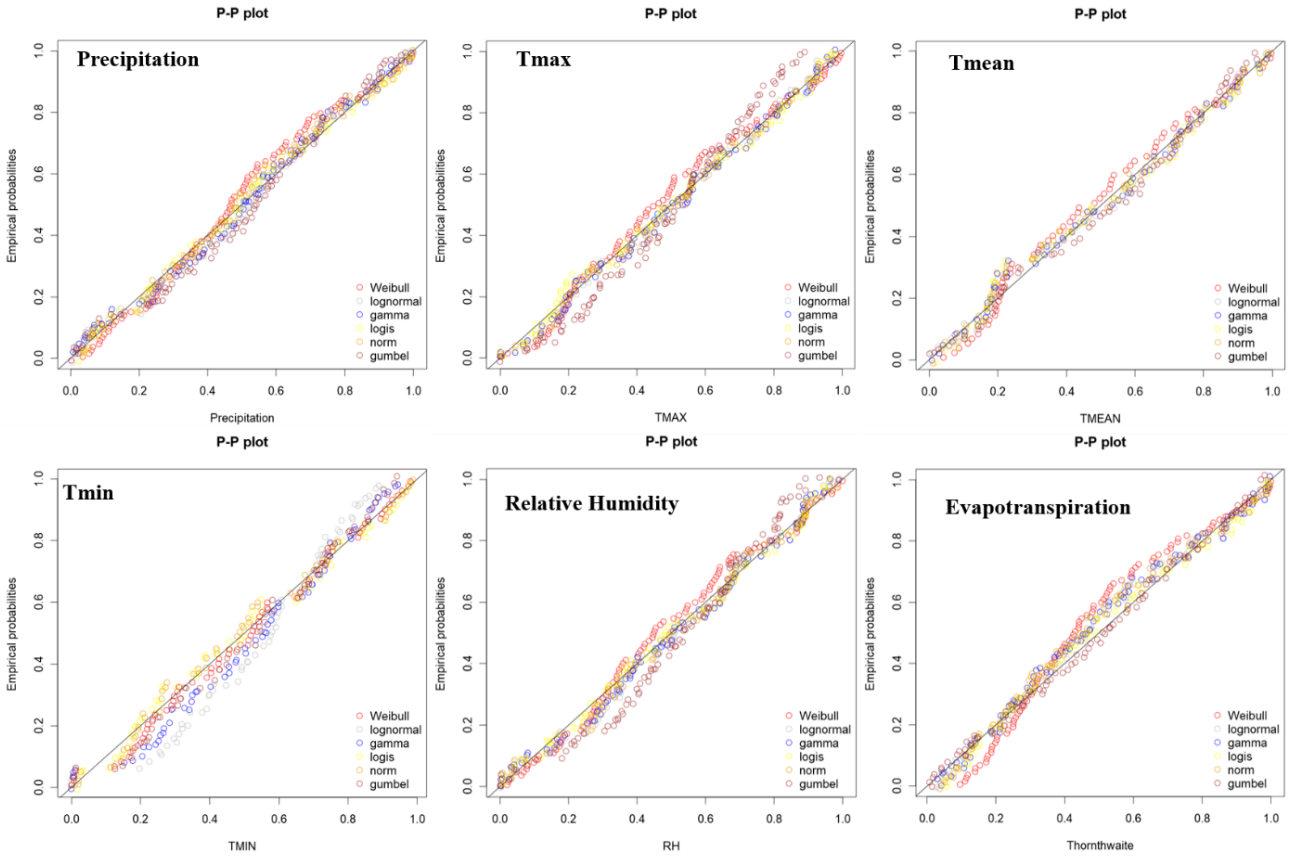

Figure 4. Probability-Probability (P-P) plot for precipitation, Tmax, Tmean, Tmin, relative humidity and evapotranspiration series at station 17030

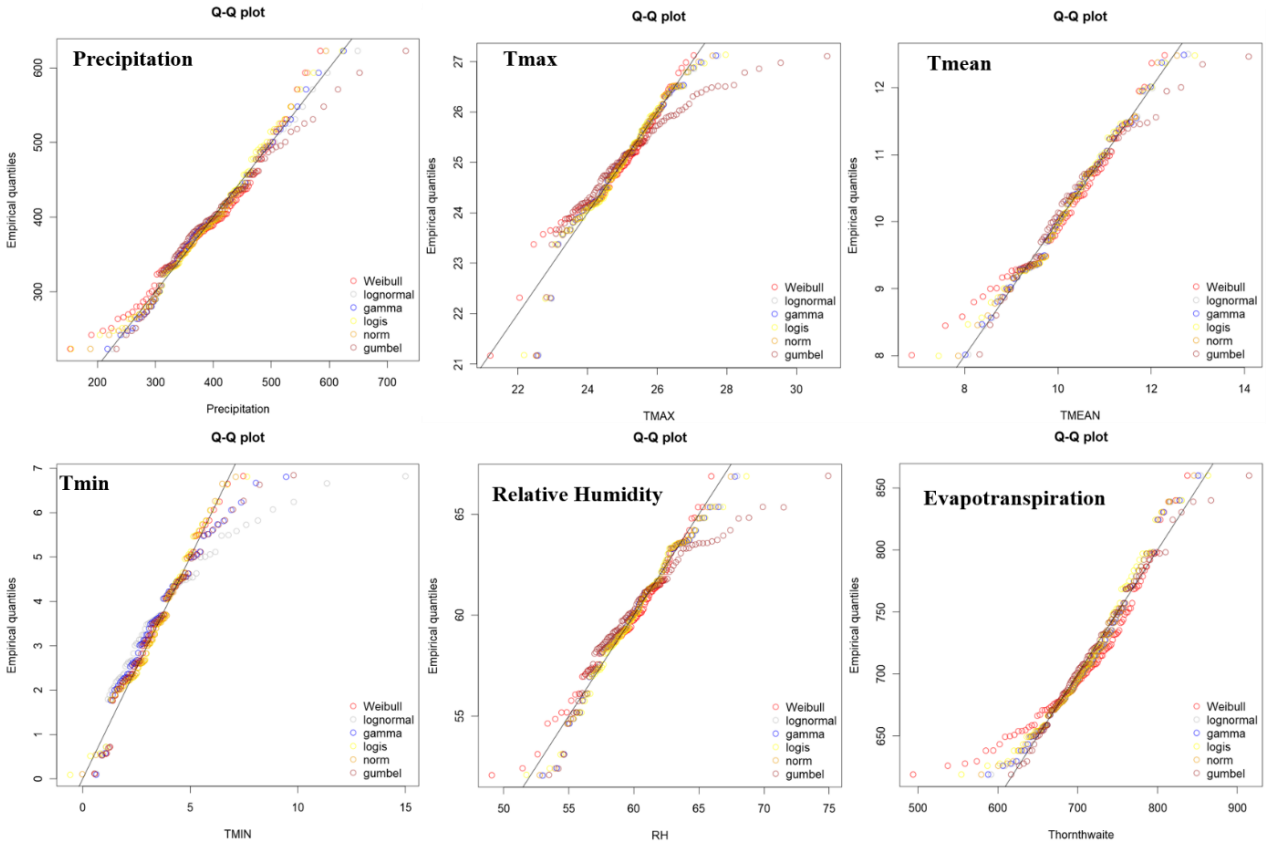

Figure 5. Quantile-Quantile (Q-Q) plot for precipitation, Tmax, Tmean, Tmin, relative humidity and evapotranspiration series at station 17030

Selecting the Best Fitting Distribution Model for Meteorological Parameters

Tables 2, 3, and 4 show the best fitting distribution considering Kolmogorov-Smirnov, Cramer-von Mises, Anderson-Darling, Akaike's Information Criterion, Bayesian Information Criterion, and Maximum Loglikelihood tests. According to station 17128, the annual total precipitation series fit the logistic and normal distribution. In addition, annual maximum, mean, and minimum temperature series are found to have the best fit distribution as the Normal, Gamma, and Normal models, respectively. While Weibull and Normal distributions are selected as the best fits for annual mean relative humidity, Gumbel distribution is observed as the best fit for annual total evapotranspiration data.

According to the results of station 17130 shown in Table 3, Gamma distribution is selected for annual total precipitation and annual mean temperature. In contrast,the logistic distribution is observed as the best-fit model for maximum yearly temperature, annual mean relative humidity, and annual total evapotranspiration. Furthermore, Normal distribution is fitted to the yearly minimum temperature. At station 17664, the Gamma distribution for annual total precipitation, the Lognormal distribution for maximum yearly and mean temperature, the Normal distribution for annual minimum temperature and annual mean relative humidity, and the Gumbel distribution for annual total evapotranspiration series are selected as the best fit models. Figure 6 shows the best fit model of annual total precipitation for station 17130. It can be inferred from Figure 6 that the Gamma distribution is the most appropriate model for annual total precipitation. Because the Gamma distribution is evenly distributed on the P-P and Q-Q plots, as well as empirical versus theoretical CDFs and theoretical densities.

Table 2. The best fit distribution selection based on GOF tests result for station 17128

Parameters	GOF Tests	Distribution Models					
		Lognormal	logistic	Gamma	Weibull	Normal	Gumbel
Annual total precipitation	K-S	0.1202559	**0.067988**	0.105785	0.095323	0.076522	0.131255
	CvM	0.1285157	**0.035468**	0.090285	0.081791	0.052198	0.214214
	AD	0.788356	**0.235019**	0.551954	0.518097	0.334663	1.34532
	AIC	781.0656	775.7574	778.1951	777.1193	**775.7013**	786.9399
	BIS	785.4449	780.1367	782.5744	781.4986	**780.0807**	791.3192
	ML	-388.5328	-385.879	-387.098	-386.56	**-385.851**	-391.47
Annual max temperature (°C)	K-S	**0.0678967**	0.078759	0.065335	0.085254	0.068022	0.113044
	CvM	0.0595307	0.068418	0.057687	0.069746	**0.054693**	0.128325
	AD	0.3610128	0.447236	0.352026	0.532555	**0.338798**	0.83663
	AIC	181.7881	185.8037	181.6889	185.2186	**181.5621**	189.0137
	BIS	186.1674	190.183	**186.0682**	189.5979	185.9414	193.393
	ML	-88.89405	-90.9019	-88.8445	-90.6093	**-88.7811**	-92.5068
Annual mean temperature (°C)	K-S	0.0857837	0.095759	0.088061	0.077975	0.091818	**0.073505**
	CvM	0.0414913	0.058039	**0.040968**	0.097416	0.044406	0.073541
	AD	**0.2516943**	0.384278	0.254316	0.725902	0.290303	0.503931
	AIC	186.1898	189.4969	**186.1832**	193.4018	186.6707	191.1205
	BIS	190.5691	193.8762	**190.5625**	197.7811	191.05	195.4998
	ML	-91.0949	-92.7484	**-91.0916**	-94.7009	-91.3354	-93.5602
Annual min temperature (°C)	K-S	0.1648745	**0.06674**	0.11403	0.076445	0.067414	0.082981
	CvM	0.5346656	0.044796	0.205697	0.048539	**0.039353**	0.098305
	AD	3.495754	0.313408	1.538355	0.527281	**0.290093**	0.890256
	AIC	283.4662	243.7153	258.4139	246.1259	**242.0193**	250.8365
	BIS	287.8455	248.0946	262.7932	250.5052	**246.3986**	255.2158
	ML	-139.7331	-119.858	-127.207	-121.063	**-119.01**	-123.418
Annual mean relative humidity (%)	K-S	0.1282492	0.097581	0.124824	**0.091136**	0.117984	0.179648
	CvM	0.237001	0.131574	0.22307	**0.129056**	0.197262	0.485943
	AD	1.2798149	0.90904	1.209926	**0.841278**	1.08174	2.584301
	AIC	351.4985	350.723	351.022	352.1487	**350.2268**	364.5233
	BIS	355.8778	355.1024	355.4013	356.528	**354.6061**	368.9026
	ML	-173.7493	-173.362	-173.511	-174.074	**-173.113**	-180.262
Annual total evapotranspiration (mm)	K-S	**0.0824141**	0.096885	0.087604	0.145495	0.097873	0.088929
	CvM	0.1079248	0.111347	0.119375	0.269006	0.144793	**0.040659**
	AD	0.6299967	0.814455	0.690994	1.56304	0.828604	**0.303065**
	AIC	707.9854	713.433	708.5523	720.2482	709.9679	**706.2462**
	BIS	712.3647	717.8123	712.9316	724.6275	714.3472	**710.6255**
	ML	-351.9927	-354.717	-352.276	-358.124	-352.984	**-351.123**

Table 3. The best fit distribution selection based on GOF tests result for station 17130

Parameters	GOF Tests	Distribution Models					
		Lognormal	logistic	Gamma	Weibull	Normal	Gumbel
Annual total precipitation	K-S	0.0573773	0.046804	**0.044613**	0.090082	0.06815	0.079426
	CvM	0.0684747	**0.025833**	0.049171	0.161488	0.063115	0.154016
	AD	0.4135475	**0.23078**	0.297224	0.972485	0.383833	0.910215
	AIC	1115.012	1116.333	**1114.12**	1122.952	1116.305	1119.97
	BIS	1120.14	1121.462	**1119.249**	1128.081	1121.434	1125.098
	ML	-555.5058	-556.167	**-555.06**	-559.476	-556.153	-557.985
Annual max temperature (°C)	K-S	0.0479969	0.056489	0.046959	0.085357	**0.045029**	0.133601
	CvM	0.0346659	0.034154	0.031711	0.138342	**0.027902**	0.480255
	AD	0.3903718	**0.301876**	0.362578	0.912396	0.321002	3.56543
	AIC	277.0407	**272.2233**	276.1155	275.1528	274.4949	314.5435
	BIS	282.1694	**277.352**	281.2442	280.2815	279.6236	319.6722
	ML	-136.5203	**-134.112**	-136.058	-135.576	-135.247	-155.272
	K-S	0.0857837	0.095759	0.088061	0.077975	0.091818	**0.073505**

Annual mean temperature (°C)	CvM	0.0414913	0.058039	**0.040968**	0.097416	0.044406	0.073541
	AD	**0.2516943**	0.384278	0.254316	0.725902	0.290303	0.503931
	AIC	186.1898	189.4969	**186.1832**	193.4018	186.6707	191.1205
	BIS	190.5691	193.8762	**190.5625**	197.7811	191.05	195.4998
	ML	-91.0949	-92.7484	**-91.0916**	-94.7009	-91.3354	-93.5602
Annual min temperature (°C)	K-S	0.1648745	0.06674	0.11403	0.076445	**0.067414**	0.082981
	CvM	0.5346656	0.044796	0.205697	0.048539	**0.039353**	0.098305
	AD	3.495754	0.313408	1.538355	0.527281	**0.290093**	0.890256
	AIC	283.4662	243.7153	258.4139	246.1259	**242.0193**	250.8365
	BIS	287.8455	248.0946	262.7932	250.5052	**246.3986**	255.2158
	ML	-139.7331	-119.858	-127.207	-121.063	**-119.01**	-123.418
Annual mean relative humidity (%)	K-S	0.0757018	**0.050717**	0.073137	0.079285	0.068393	0.133978
	CvM	0.0732437	**0.031862**	0.065636	0.117333	0.053929	0.404769
	AD	0.5548106	**0.282883**	0.500136	0.663733	0.410646	2.686226
	AIC	480.61	**478.3472**	479.8269	480.2198	478.4959	505.1448
	BIS	485.7387	**483.4759**	484.9556	485.3485	483.6246	510.2735
	ML	-238.305	**-237.174**	-237.913	-238.11	-237.248	-250.572
Annual total evapotranspiration (mm)	K-S	0.0442227	0.045106	**0.042755**	0.091797	0.043138	0.109601
	CvM	0.0314271	**0.028243**	0.03046	0.176214	0.029738	0.377656
	AD	0.2833243	**0.246648**	0.272055	1.018951	0.256942	2.710638
	AIC	1029.194	**1027.25**	1028.669	1030.115	1027.74	1061.124
	BIS	1034.323	**1032.379**	1033.798	1035.244	1032.868	1066.253
	ML	-513.5756	-515.89	-514.146	-526.363	-515.503	**-511.536**

Table 4. The best fit distribution selection based on GOF tests result for station 17664

Parameters	**GOF Tests**	**Distribution Models**					
		Lognormal	logistic	Gamma	Weibull	Normal	Gumbel
Annual total precipitation	K-S	0.0888718	0.109425	0.097235	0.104947	0.111849	**0.08782**
	CvM	0.0686	0.10174	0.070188	0.104645	0.087928	**0.068184**
	AD	**0.3503738**	0.582867	0.358499	0.694099	0.487882	0.414419
	AIC	776.3796	780.6651	**776.262**	781.9715	778.0524	778.6765
	BIS	780.6659	784.9514	**780.5483**	786.2577	782.3386	782.9628
	ML	-386.1898	-388.333	**-386.131**	-388.986	-387.026	-387.338
Annual max temperature (°C)	K-S	0.0926571	0.071249	0.095576	0.156059	0.10175	**0.083661**
	CvM	0.0711191	**0.052849**	0.077104	0.30413	0.092019	0.101617
	AD	0.448108	**0.449418**	0.48386	1.776835	0.571741	0.598906
	AIC	**247.0407**	249.3076	247.3349	260.7433	248.1131	250.1337
	BIS	**251.5941**	253.8609	251.8883	265.2966	252.6664	254.687
	ML	**-121.5204**	-122.654	-121.668	-128.372	-122.057	-123.067
Annual mean temperature (°C)	K-S	0.1080861	0.115509	0.112297	0.12538	0.120214	**0.072696**
	CvM	0.0886428	0.111676	0.095552	0.219952	0.112631	**0.083039**
	AD	**0.4885319**	0.637827	0.525097	1.354886	0.624441	0.618401
	AIC	**159.2294**	161.7821	159.4363	169.1497	160.2626	163.4278
	BIS	**163.5156**	166.0684	163.7226	173.436	164.5489	167.714
	ML	**-77.61469**	-78.891	-77.7182	-82.5749	-78.1313	-79.7139
Annual min temperature (°C)	K-S	0.1715909	0.055575	0.127459	0.072962	**0.051689**	0.09267
	CvM	0.5278401	0.024178	0.247025	0.065153	**0.020259**	0.11883
	AD	3.2952866	0.224151	1.654357	0.662941	**0.194787**	0.917298
	AIC	252.1272	222.2973	232.9113	222.4683	**219.6381**	228.4958
	BIS	256.4134	226.5835	237.1976	226.7545	**223.9244**	232.7821
	ML	-124.0636	-109.149	-114.456	-109.234	**-107.819**	-112.248
Annual mean relative humidity (%)	K-S	0.0668988	**0.047915**	0.064259	0.075603	0.059161	0.119563
	CvM	0.0352033	0.033941	0.032352	0.109548	**0.028284**	0.170716
	AD	0.2267838	0.237346	0.21153	0.844457	**0.190637**	1.067333
	AIC	367.808	368.7252	367.7452	378.9523	**367.7756**	377.8099
	BIS	372.3613	373.2785	**372.2985**	383.5057	372.3289	382.3632

	ML	-181.904	-182.363	**-181.873**	-187.476	-181.888	-186.905
Annual total evapotranspiration (mm)	K-S	0.1153349	0.10198	0.120032	0.168421	0.129182	**0.066654**
	CvM	0.1306428	0.124834	0.142467	0.311237	0.167772	**0.048188**
	AD	0.7032216	0.853407	0.763978	1.76613	0.897946	**0.325685**
	AIC	656.7236	660.9225	657.2795	670.3473	658.6173	**655.0107**
	BIS	661.0099	665.2087	661.5658	674.6336	662.9036	**659.297**
	ML	-326.3618	-328.461	-326.64	-333.174	-327.309	**-325.505**

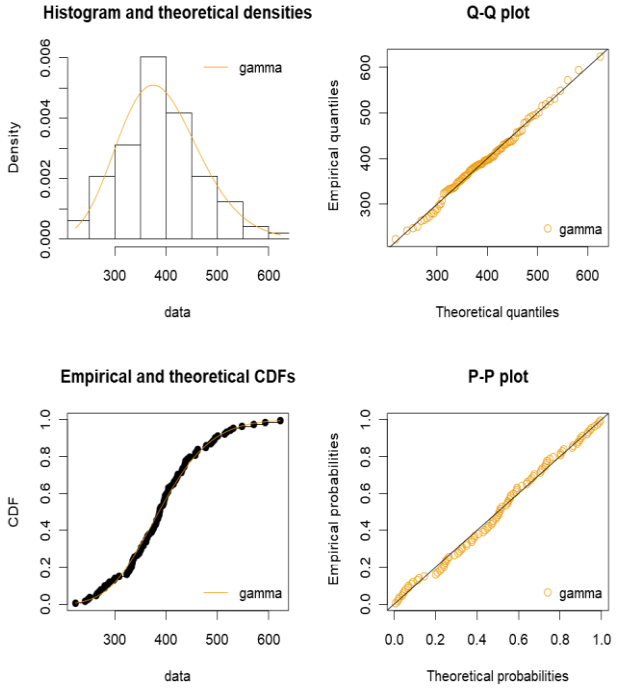

Figure 6. The best fit model for annual total precipitation at station 17130

5. Conclusion

Every component of the hydrological cycle is crucial for managing water supplies and predicting extreme events like floods and droughts. A hydrological system's inputs are unpredictable, thus they are specific to every region. In this study, the most important parameters such as precipitation, temperature, relative humidity, and evaporation are investigated for Ankara province. The most appropriate distributions are determined for meteorological parameters using the Lognormal, Log-logistic, Gamma, Weibull, Normal and Gumbel models. These models are tested by Kolmogorov-Smirnov (KS), Akaike's Information Criterion (AIC), Cramers-von Mises (CvM), Bayesian Information Criterion (BIC), Anderson-Darling (AD), and Maximum Loglikelihood methods.

According to the results, Gamma distribution is found as the best fit distribution for annual total precipitation at stations 17130 and 17664, while Log-logistic and Normal are observed the most appropriate for station 17128. At maximum yearly temperature, all station shows different models. Normal, Log-logistic, and Lognormal are fitted to stations 17128, 17130, and 17664, respectively. When we consider annual mean temperature, for stations 17128 and 17130, Gamma is determined to be the best fit, whereas Lognormal is chosen for station 17664. In addition, Normal distributions are reported as the best fit for all stations at annual minimum temperature series. At the annual mean relative humidity series, Normal is observed to be the best fit for stations 17128 and 17664, while Log-logistic is found as the best fit at station 17130. According to the annual total evapotranspiration series, Gumbel distribution is more appropriate for stations 17128 and 17664, and Log-logistic is fitted better at station 17130. Results indicate that every parameter has a unique distribution model. To be specific, the Gumbel distribution is found more appropriate among other distributions for annual total precipitation, while the Normal distribution is observed more appropriate model at the annual minimum temperature for Ankara province. These findings will serve as a guide for decision-makers on the construction of hydraulic structures for water management in the Ankara province.

Acknowledgments

Acknowledgments are due to state water Works (DSI), general directorate of meteorology (MGM) for providing meteorological data

Contributions of the Authors

Musa Esit: data gathering, hydrometeorological data trend analysis, interpretation of the findings, manuscript writing, and submission

Conflict of Interest Statement

There is no conflict of interest between the authors.

References

[1] U. J. M. A. Alam, K. Emura, C. Farnham, and J. Yuan, "Best-Fit Probability Distributions and Return Periods for Maximum Monthly Rainfall in Bangladesh," *Climate*, vol. 6, no. 1, Art. no. 1, Mar. 2018, doi: 10.3390/cli6010009.

[2] M. J. Mamman, O. Y. Martins, J. Ibrahim, and M. I. Shaba, "Evaluation of Best-Fit Probability Distribution Models for the Prediction of Inflows of Kainji Reservoir, Niger State, Nigeria," *Air, Soil and Water Research*, vol. 10, p. 1178622117691034, Jan. 2017, doi: 10.1177/1178622117691034.

[3] I. E. Ahaneku and M. Y. Otache, "Stochastic Characteristics and Modelling of Monthly Rainfall Time Series of Ilorin, Nigeria.," *NONE*, 2014, Accessed: Aug. 27, 2022. [Online]. Available: http://repository.futminna.edu.ng:8080/jspui/handle/123456789/8342

[4] M. Esit, S. Kumar, A. Pandey, D. M. Lawrence, I. Rangwala, and S. Yeager, "Seasonal to multi-year soil moisture drought forecasting," *npj Climate and Atmospheric Science*, vol. 4, no. 1, Art. no. 1, Mar. 2021, doi: 10.1038/s41612-021-00172-z.

[5] E. A. Njoku and D. E. Tenenbaum, "Quantitative assessment of the relationship between land use/land cover (LULC), topographic elevation and land surface temperature (LST) in Ilorin, Nigeria," *Remote Sensing Applications: Society and Environment*, vol. 27, p. 100780, Aug. 2022, doi: 10.1016/j.rsase.2022.100780.

[6] P. Sharma, S. Singh, and S. D. Sharma, "Artificial Neural Network Approach for Hydrologic River Flow Time Series Forecasting," *Agric Res*, Jun. 2021, doi: 10.1007/s40003-021-00585-5.

[7] M. M. Khudri, "Determination of the Best Fit Probability Distribution for Annual Extreme Precipitation in Bangladesh," *European Journal of Scientific Research*, Jan. 2013, Accessed: Aug. 27, 2022. [Online]. Available: https://www.academia.edu/38182722/Determination_of_the_Best_Fit_Probability_Distribution_for_Annual_Extreme_Precipitation_in_Bangladesh

[8] J. Yuan, K. Emura, C. Farnham, and M. A. Alam, "Frequency analysis of annual maximum hourly precipitation and determination of best fit probability distribution for regions in Japan," *Urban Climate*, vol. 24, pp. 276–286, Jun. 2018, doi: 10.1016/j.uclim.2017.07.008.

[9] E. Eris *et al.*, "Frequency analysis of low flows in intermittent and non-intermittent rivers from hydrological basins in Turkey," *Water Supply*, vol. 19, no. 1, pp. 30–39, Feb. 2019, doi: 10.2166/ws.2018.051.

[10] J. Liu, C. D. Doan, S.-Y. Liong, R. Sanders, A. T. Dao, and T. Fewtrell, "Regional frequency analysis of extreme rainfall events in Jakarta," *Nat Hazards*, vol. 75, no. 2, pp. 1075–1104, Jan. 2015, doi: 10.1007/s11069-014-1363-5.

[11] M. I. Yuce and M. Esit, "Drought monitoring in Ceyhan Basin, Turkey," *Journal of Applied Water Engineering and Research*, vol. 0, no. 0, pp. 1–22, Jun. 2021, doi: 10.1080/23249676.2021.1932616.

[12] R. W. Katz and B. G. Brown, "Extreme events in a changing climate: Variability is more important than averages," *Climatic Change*, vol. 21, no. 3, pp. 289–302, Jul. 1992, doi: 10.1007/BF00139728.

[13] H. B. Unal, S. Asik, M. Avci, S. Yasar, and E. Akkuzu, "Performance of water delivery system at tertiary canal level: a case study of the Menemen Left Bank Irrigation System, Gediz Basin, Turkey," *Agricultural Water Management*, vol. 65, no. 3, pp. 155–171, Mar. 2004, doi: 10.1016/j.agwat.2003.10.002.

[14] A. S. Anli and A. S. Anli, "Giresun Aksu Havzası Maksimum Akımlarının Frekans Analizi," *Akdeniz Üniversitesi Ziraat Fakültesi Dergisi*, vol. 19, no. 1, Art. no. 1, Mar. 2006.

[15] H. Yavuz and S. Erdoğan, "Spatial Analysis of Monthly and Annual Precipitation Trends in Turkey," *Water Resour Manage*, vol. 26, no. 3, pp. 609–621, Feb. 2012, doi: 10.1007/s11269-011-9935-6.

[16] M. Sandalci, "Flood Frequency Analysis of Akçay Stream," *Sakarya Üniversitesi Fen Bilimleri Enstitüsü Dergisi*, vol. 22, no. 5, Art. no. 5, 2018, doi: 10.16984/saufenbilder.402190.

[17] A. W. Salami, "Best-fit Probability Distribution model for peak daily rainfall of selected Cities in Nigeria," *New York Science Journal*, Jan. 2009, Accessed: Aug. 27, 2022. [Online]. Available: https://www.academia.edu/1593242/Best_fit_Probability_Distribution_model_for_peak_daily_rainfall_of_selected_Cities_in_Nigeria

[18] M. T. Amin, M. Rizwan, and A. A. Alazba, "A best-fit probability distribution for the estimation of rainfall in northern regions of Pakistan," *Open Life Sciences*, vol. 11, no. 1, pp. 432–440, Jan. 2016, doi: 10.1515/biol-2016-0057.
[19] H. Sun, G. Wang, X. Li, J. Chen, B. Su, and T. Jiang, "Regional frequency analysis of observed sub-daily rainfall maxima over eastern China," *Adv. Atmos. Sci.*, vol. 34, no. 2, pp. 209–225, Feb. 2017, doi: 10.1007/s00376-016-6086-y.
[20] G. Chen, J. Norris, J. D. Neelin, J. Lu, L. R. Leung, and K. Sakaguchi, "Thermodynamic and Dynamic Mechanisms for Hydrological Cycle Intensification over the Full Probability Distribution of Precipitation Events," *Journal of the Atmospheric Sciences*, vol. 76, no. 2, pp. 497–516, Feb. 2019, doi: 10.1175/JAS-D-18-0067.1.
[21] N. Boudrissa, H. Cheraitia, and L. Halimi, "Modelling maximum daily yearly rainfall in northern Algeria using generalized extreme value distributions from 1936 to 2009," *Meteorological Applications*, vol. 24, no. 1, pp. 114–119, 2017, doi: 10.1002/met.1610.
[22] M. Douka, T. S. Karacostas, E. Katragkou, and C. Anagnostolpoulou, "Annual and Seasonal Extreme Precipitation Probability Distributions at Thessaloniki Based Upon Hourly Values," in *Perspectives on Atmospheric Sciences*, Cham, 2017, pp. 521–527. doi: 10.1007/978-3-319-35095-0_75.

[23] K. Haddad, "Selection of the best fit probability distributions for temperature data and the use of L-moment ratio diagram method: a case study for NSW in Australia," *Theor Appl Climatol*, vol. 143, no. 3, pp. 1261–1284, Feb. 2021, doi: 10.1007/s00704-020-03455-2.
[24] N. Vivekanandan, "Comparison of probability distributions in extreme value analysis of rainfall and temperature data," *Environ Earth Sci*, vol. 77, no. 5, p. 201, Mar. 2018, doi: 10.1007/s12665-018-7356-z.
[25] B. C. Trewin, "Extreme temperature events in Australia," 2001. Accessed: Aug. 27, 2022. [Online]. Available: https://scholar.google.com/scholar_lookup?title=Extreme+temperature+events+in+Australia&author=Trewin%2C+Blair+C.&publication_year=2001
[26] S. Sensoy and M. Demircan, "Climate of Turkey," Mar. 2016.
[27] A. Danandeh Mehr, A. U. Sorman, E. Kahya, and M. Hesami Afshar, "Climate change impacts on meteorological drought using SPI and SPEI: case study of Ankara, Turkey," *Hydrological Sciences Journal*, vol. 65, no. 2, pp. 254–268, Jan. 2020, doi: 10.1080/02626667.2019.1691218.
[28] A. Lyon, "Why are Normal Distributions Normal?," *Br J Philos Sci*, vol. 65, no. 3, pp. 621–649, Sep. 2014, doi: 10.1093/bjps/axs046.
[29] R. D. Markovic, "Probability functions of best fit to distributions of annual precipitation and runoff," 1965. Accessed: Aug. 27, 2022. [Online]. Available: https://scholar.google.com/scholar_lookup?title=Probability+functions+of+best+fit+to+distributions+of+annual+precipitation+and+runoff&author=Markovic%2C+Radmilo+D.&publication_year=1965
[30] C.-D. Lai, D. N. Murthy, and M. Xie, "Weibull Distributions and Their Applications," in *Springer Handbook of Engineering Statistics*, H. Pham, Ed. London: Springer, 2006, pp. 63–78. doi: 10.1007/978-1-84628-288-1_3.
[31] K. J, O. Ngesa, and G. Orwa, "On Generalized Gamma Distribution and Its Application to Survival Data," *International Journal of Statistics and Probability*, vol. 8, no. 5, pp. 85–102, 2019.
[32] R. Kissell and J. Poserina, *Optimal Sports Math, Statistics, and Fantasy*. Academic Press, 2017.
[33] K.-H. Chang, "Chapter 3 – Solid Modeling," 2015. doi: 10.1016/B978-0-12-382038-9.00003-X.
[34] E. Castillo, *Extreme Value Theory in Engineering*. Elsevier, 2012.
[35] H. Akaike, "'An information criterion (AIC).,'" *Math Sci*, vol. 14 (153), pp. 5–7, 1976.
[36] M. Stone, "Comments on Model Selection Criteria of Akaike and Schwarz," *Journal of the Royal Statistical Society. Series B (Methodological)*, vol. 41, no. 2, pp. 276–278, 1979.
[37] N. Smirnov, "Table for Estimating the Goodness of Fit of Empirical Distributions," *The Annals of Mathematical Statistics*, vol. 19, no. 2, pp. 279–281, 1948.

[38] M. A. Stephens, "EDF Statistics for Goodness of Fit and Some Comparisons," *null*, vol. 69, no. 347, pp. 730–737, Sep. 1974, doi: 10.1080/01621459.1974.10480196.
[39] N. Smirnov, "Estimate of deviation between empirical distribution functions in two independent samples," *Bulletin Moscow University*, vol. 2 (2), no. 3–16, 1939.
[40] F. Laio, "Cramer–von Mises and Anderson-Darling goodness of fit tests for extreme value distributions with unknown parameters," *Water Resources Research*, vol. 40, no. 9, 2004, doi: 10.1029/2004WR003204.
[41] C. Schwarz, "Sampling, Regression, Experimental Design and Analysis for Environmental Scientists, Biologists, and Resource Managers," Mar. 2011.
[42] A. C. Cullen, H. C. Frey, and C. H. Frey, *Probabilistic Techniques in Exposure Assessment: A Handbook for Dealing with Variability and Uncertainty in Models and Inputs*. Springer Science & Business, 1999.

Bitlis Eren Üniversitesi Fen Bilimleri Dergisi
BİTLİS EREN UNIVERSITY JOURNAL OF SCIENCE
ISSN: 2147-3129/e-ISSN: 2147-3188
VOLUME: 11 NO: 4 PAGE: 1042-1049 YEAR: 2022
DOI:10.17798/bitlisfen.1169380

Investigation of ZrO_2-Y_2O_3 Added Al Matrix Composites Produced by T/M Method

Serkan ÖZEL[1*], Tural HAMİDLİ[1]

[1]*Bitlis Eren Üniversitesi, Mühendislik Mimarlık Fakültesi, Makine Müh. Böl., 13000, Bitlis (ORCID: 0000-0003-0700-1295) (ORCID: 0000-0003-4200-0933)*

Keywords: Powder Metallurgy, ZrO_2-Y_2O_3, Al, Composite, Microstructure, Microhardness.

Abstract

In this study, 5% by weight copper powder was added to the aluminum powder and this powder mixture was used as the matrix component. As a reinforcement element, 5%, 10%, and 15% ZrO_2-Y_2O_3 powder was mixed into the Al+ 5% Cu matrix component. The mixed powders were pressed unidirectional with 300MPa pressure to obtain powder metal samples. Pressed specimens were sintered at 500 ºC. Optical microstructure and SEM images of sintered samples were taken. EDS, XRD, and microhardness analyzes were performed. According to the results obtained, the highest microhardness value was measured in the sample with 15% ZrO_2-Y_2O_3 powder sintered at 500 ºC. In the XRD examination, it was determined that ZrO_2, AlCu, Cu_3Al, Al_3Y and Al_2O_3 compounds were also formed together with the Al main phase.

1. Introduction

Powder metallurgy is a technology that prepares high-performance materials by forming high metals, alloys, and composites with high yield and tensile strength, fine-grained, uniform structure, good thermal processing treatment, and isotropy [1]. With powder metallurgy technology, scrap losses can be reduced, material tolerances can be followed closely, complex-shaped products can be designed, and reproducibility can be allowed. [2]. Powder metallurgy includes processes such as mixing, pressing, and sintering of pre-alloyed or pre-mixed powders. In addition, it is a method that can be applied to many materials and is still under development [3].

The powder metallurgy method has many advantages over metal matrix composite methods. In this method, the matrix material (continuous phase) and reinforcement materials (discrete phases) are mixed and compressed under sufficient pressure and the green compact is formed. The green compacts are heated at a high temperature below the melting point of the matrix material for a sufficient time for diffusion bonding to occur. This process is also known as the sintering process. The powder metallurgy process is most affected by the compaction pressure, holding temperature, and time parameters [4], [5], [6].

Many researchers have been working on aluminum matrix composites in recent years. These advanced composites are used in engineering applications, automotive, and aerospace industries. In addition to some reinforcements, intermetallics have also been found as reinforcement material for aluminum. Their coefficient of thermal expansion (CTE) is close to aluminum and less brittle than ceramic [7].

The packaging, automobile, defense, and aerospace industries highly demand Aluminum Matrix Composites (AMCs) or Aluminum-based Metal Matrix Composites (MMCs) due to their high strength, lightweight, and excellent tribological properties. These parameters play an important role in determining the properties of a powder metallurgy product. In addition, reinforcement materials are also effective in defining the properties of the composite material. The nature of the reinforcement materials and their bonding with the matrix material also affect the properties of composite materials. [4]. While aluminum matrix composite materials are produced by powder metallurgy, their strength can be

*Corresponding author: sozel@beu.edu.tr
Received: 31.08.2022, Accepted: 02.12.2022

increased with reinforcement particles such as SiC, Al_2O_3, ZrO_2, MgO, B_4C, TiB_2 [8]-[13].

Zirconium dioxide (ZrO_2) can be widely used in high-tech engineering applications because it has remarkable properties such as the ability to work at high temperatures, resistance to corrosion and abrasion, high strength and fracture toughness, semiconductivity, thermal and diffusion barrier behavior, and biocompatibility [10]. Cubic zirconia (YSZ) stabilized with Ytria (Y_2O_3) is used in many fields such as aerospace, aviation, automobile, health, high-temperature turbine blades, and most importantly solid electrolyte [14]. YSZ has properties such as high melting point (~2700 °C), low thermal conductivity (~2.6W/m K), relatively low density (6.4 g cm^{-3}), high hardness (14GPa), high resistance to atmospheric and high-temperature corrosion [15].

In this study, 5% by weight of copper powder was mixed with aluminum powder. As a reinforcement element, 5%, 10%, and 15% ZrO_2-Y_2O_3 powder was added to this matrix mixture powder. The effect of the reinforcement particle ratio on the samples after sintering at 500 °C was investigated.

2. Material and Method

In this study, Al powders were used as matrix material. The aluminium was used as a matrix with purity level were 99% manufactured by (Praxair Al-104, -90 µm/+45 particle size) and remaining are impurities. ZrO_2-8%Y_2O_3 (Yttria stabilized zirconia) powder was manufactured by Oerlikon Metco's (with 99.5% purity and –125 +11 µm particle size). 5% Cu powder (Alfa Aesar, -45 µm , 99%) was added to the Al powder. Prepared mixtures are shown in Table 1.

Table 1. Prepared powder mixes

Specimens	Matrix Powder (Al+%5Cu)	Supplement powder (ZrO_2-Y_2O_3)
1	%100	0
2	%95	%5
3	%90	%10
4	%85	%15

5%, 10%, and 15% ZrO_2-Y_2O_3 powders were added to the Al+5% Cu powder mixture as reinforcement material. For the homogeneous distribution of the powders, the mixing process was carried out at a speed of 45 rpm in 45 minutes. Mixing of powders was carried out dry.

After mixing, each powder mixture was cold pressed unidirectionally at a pressure of 300 MPa with a size of 12 mm diameter. The sintering process was applied to the pressed samples in the Protherm brand furnace in the Advanced Research Laboratory of Bitlis Eren University (see Figure 1). Samples of each powder mixture were sintered at 500 ºC for 60 minutes. The sintering temperature was chosen by examining the Al-Cu equilibrium diagram. The amount of Cu and temperature at which precipitation hardening can be achieved were selected.

Figure 1. Sintering furnace.

In order to be able to examine metallographically, the samples were sanded with 320, 600, 800, and 1200 mesh sandpapers, respectively. After the sanding process, the samples were polished with the help of diamond paste on the polishing felt. Then, the etching process was carried out in order to see the grain boundaries of the samples more clearly. The composition of the cauterizer used in the etching process consists of 1 ml of HF, 2.5 ml of HNO_3, and 95 ml of H_2O. Etching of the samples was done for 10-15 seconds and washed with alcohol and dried. After etching, the microstructure pictures of the samples were examined and illustrated with a Nikon brand optical microscope in the Yahya Eren Advanced Research Laboratory of Bitlis Eren University. In addition, SEM images and EDS analyzes were made with a

Zeiss scanning electron microscope in Van Yüzüncü Yıl University Science Research and Application Center laboratory. The hardness measurements of the samples were made in the Qness Q10M microhardness device in Vickers (HV0.5) type (Figure 2). XRD analyzes were performed for compound phase detection. XRD analyzes of the samples were made on the Rigaku brand RadB model XRD device in the Scientific and Technological Research Laboratory of İnönü University.

Figure 2. Microhardness tester.

3. Results and Discussion

3.1. Microstructure Characterization of Specimens

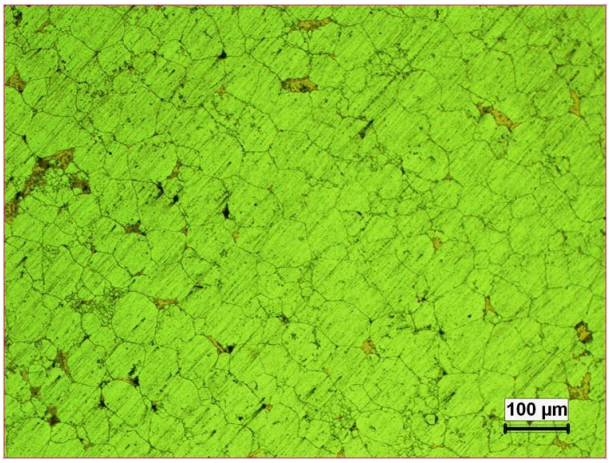

(a)

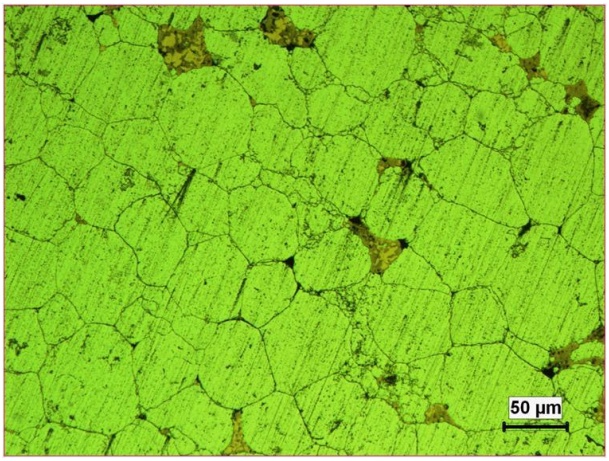

(b)

Figure 3. Optical microstructure pictures taken from Al+5%Cu based sample sintered at 500 °C.

In Figure 3, optical microstructure pictures of the Al+5% Cu sample are shown. Grain boundaries are clearly visible in the microstructure. In the structure consisting of equiaxed grains, it is seen that the element Cu (in red color) is located at the grain boundaries. Porosity is inevitable in samples produced with powder metallurgy. The black-colored pores can be seen in Figure 3.

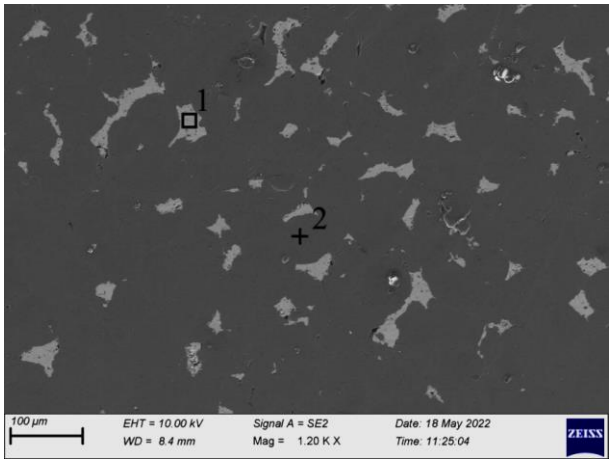

(a)

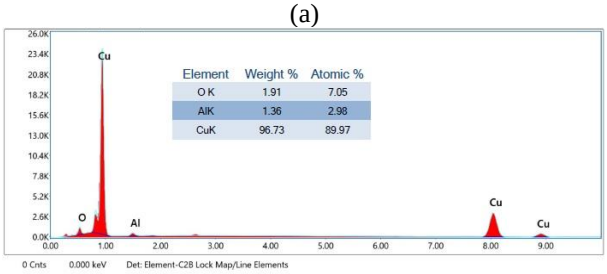

(b)

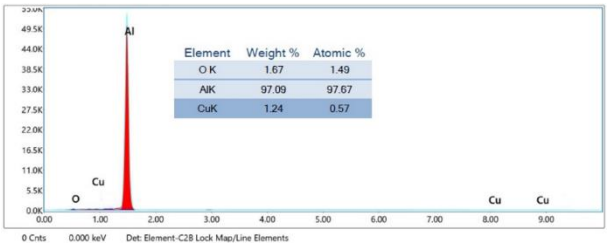

(c)

Figure 4. a) SEM photograph taken from Al+5%Cu based sample sintered at 500 ºC, b) EDS analysis no. 1 and c) EDS analysis no. 2.

The SEM photograph and EDS analysis results taken from the Al+5%Cu-based sample are shown in Figure 4. It is seen that the structure, which is seen in different colors at the grain boundaries and mentioned in the optical microstructure pictures (Figure 3), consists of a high-weight Cu element by EDS field analysis no 1. In addition, it was determined that 1.36% Al and 1.91% O elements were also present in the analysis. As a result of this EDS, it is thought that Cu_xAl_y type intermetallic compounds and oxide compounds of Cu and Al elements are formed in area 1. In the EDS analysis at point 2 given in Figure 4-c, the presence of Al matrix structure is seen. In addition, Cu element dissolved in the matrix and a small amount of O element belonging to possible oxide compounds are present at point 2.

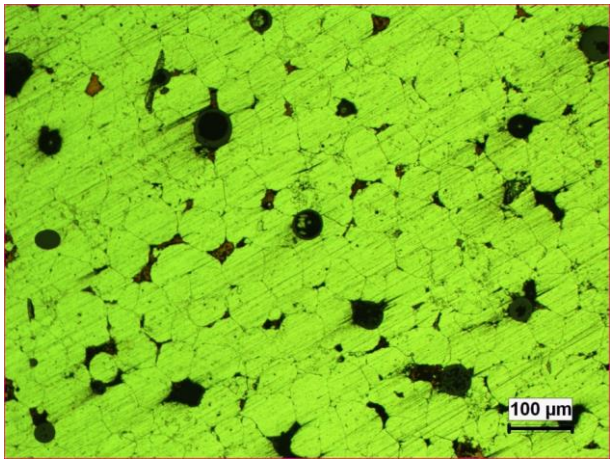

(a)

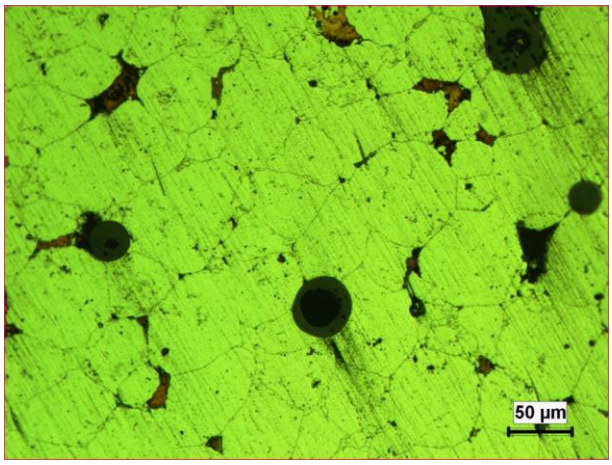

(b)

Figure 5. Optical microstructure pictures taken from Al+5%Cu+5% ZrO_2-Y_2O_3 based sample sintered at 500 ºC.

Optical microstructure pictures of Al+5%Cu + 5% ZrO_2-Y_2O_3 sample are shown in Figure 5. Grain boundaries can be seen in the microstructure of this sample. In the structure of equiaxed grains, the element Cu (in red color) is located at the grain boundaries. The black colored pores can be seen in Figure 5. The porosity increased more compared to the Al+5%Cu sample with 5% added ZrO_2-Y_2O_3 oxide compound.

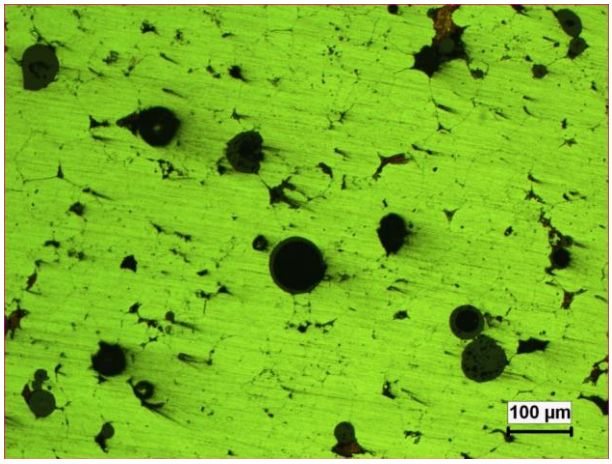

(a)

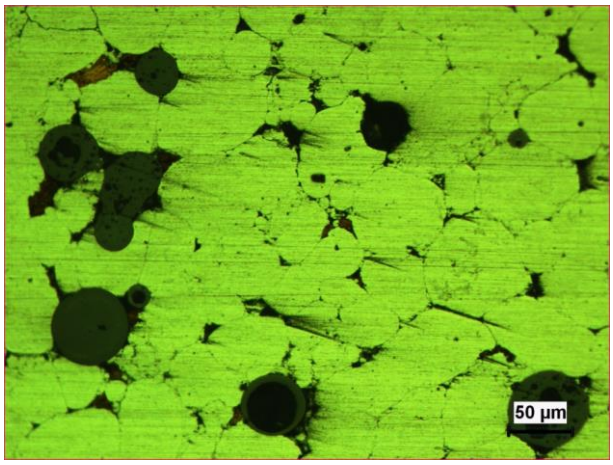

(b)

Figure 6. Optical microstructure pictures taken from Al+5% Cu+10% ZrO_2-Y_2O_3 based sample sintered at 500 ºC.

Figure 6 shows the optical microstructure pictures of the Al + 5% Cu + 10% ZrO_2-Y_2O_3 sample. Grain boundaries can be seen in the microstructure of this sample. In the structure consisting of equiaxed grains, the element Cu (in red color) is located at the grain boundaries. It is seen in Figure 6-b that the ZrO_2-Y_2O_3 oxide also settles at the grain boundaries during sintering and is found in black colored pores. It can be seen in Figure 6 that the porosity increased even more compared with the samples with Al+5% Cu and Al+5% Cu +5% ZrO_2-Y_2O_3.

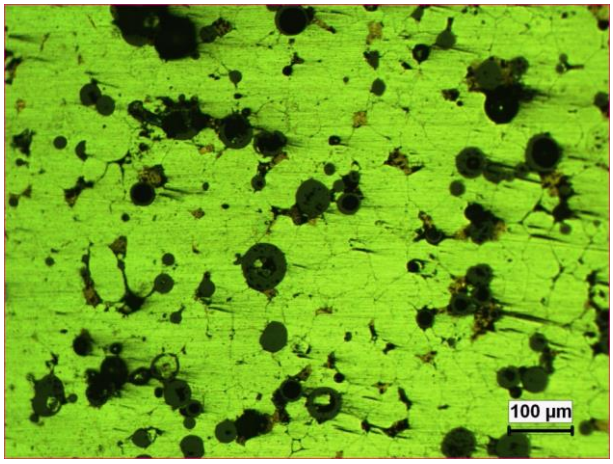

(a)

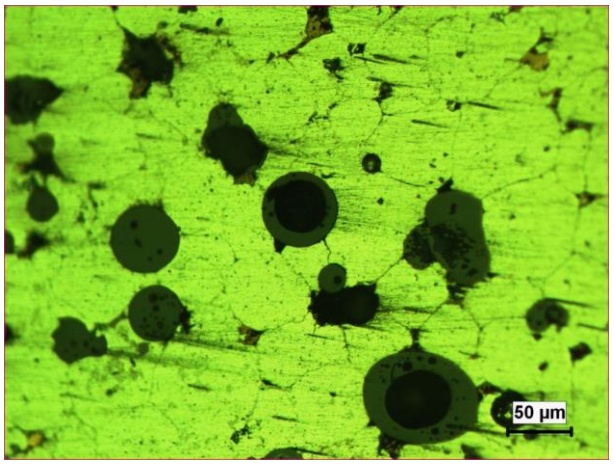

(b)

Figure 7. Optical microstructure pictures taken from Al+5% Cu+15% ZrO_2-Y_2O_3 based sample sintered at 500 ºC.

Optical microstructure pictures of the Al + 5% Cu + 15% ZrO_2-Y_2O_3 sample are shown in Figure 7. It is seen in Figure 7-b that the ZrO_2-Y_2O_3 oxide also locates at the grain boundaries during sintering. It is seen in Figure 7 that the porosity increased with the addition of 15% ZrO_2-Y_2O_3 oxide compound compared to the other samples. It was also observed that pieces of ZrO_2-Y_2O_3 dust particles were broken off and voids were formed in the dust particles during sanding.

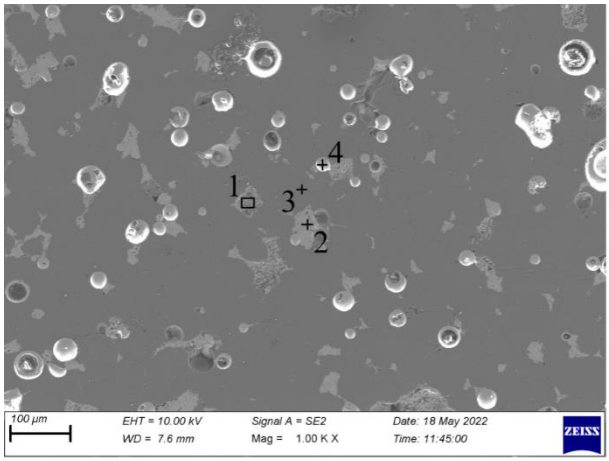

(a)

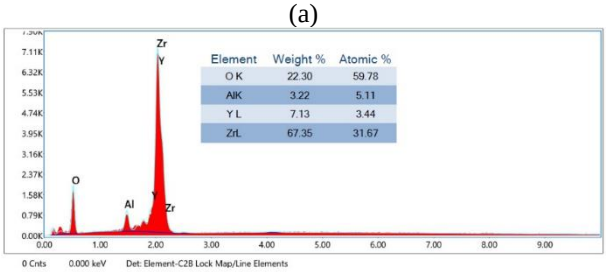

(b)

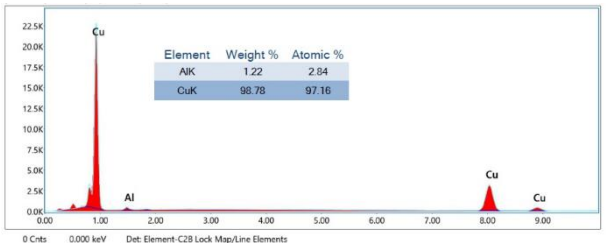

(c)

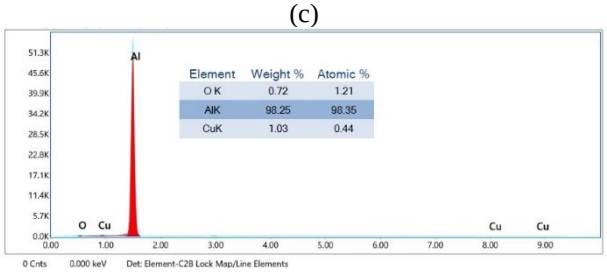

(d)

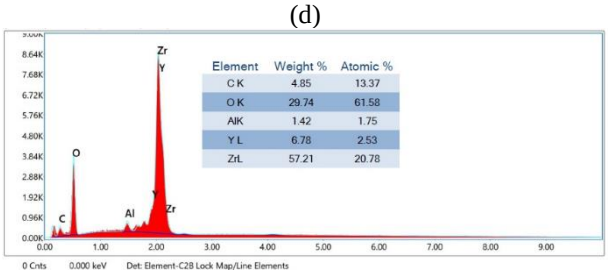

(e)

Figure 8. Al+5%Cu+15% ZrO_2-Y_2O_3 based sample sintered at 500 ºC taken from a) SEM photograph, b) EDS analysis no. 1 and c) EDS analysis no. 2 d) EDS analysis no. 3 e) EDS analysis no. 4.

SEM photograph and EDS analysis results taken from Al + 5% Cu + 15% ZrO_2-Y_2O_3 sample sintered at 500 ºC are shown in Figure 8. EDS analyzes were taken from matrix structure, grain boundaries, and dust particles. The presence of Zr, Y, Al, and O elements is seen in the EDS analysis given in Figure 8-b, taken from the light gray area no 1 in Figure 8-a. It is thought that area no. 1 consists of the added ZrO_2-Y_2O_3 powder and the oxide compound of the Al element. The same situation is seen in the EDS analysis taken from point 4 (Figure 8-e). At this point, the presence of Zr, Y, Al, and O elements indicates that ZrO_2-Y_2O_3 and Al_2O_3 type compounds can be formed. In the EDS analysis given in Figure 8-c, Cu can be seen at the point 2. The presence of 98.78% Cu and 1.22% Al elements indicates that Cu_xAl_y type intermetallic compounds can be formed. In the EDS analysis given in Figure 8-d, the point 3 is composed of the matrix dust Al element, a small amount of Cu and O elements. At point 3, it is thought that Cu, Al and O elements possible brought about Cu_xAl_y, Al_xO_y and Cu_xO_y type compounds.

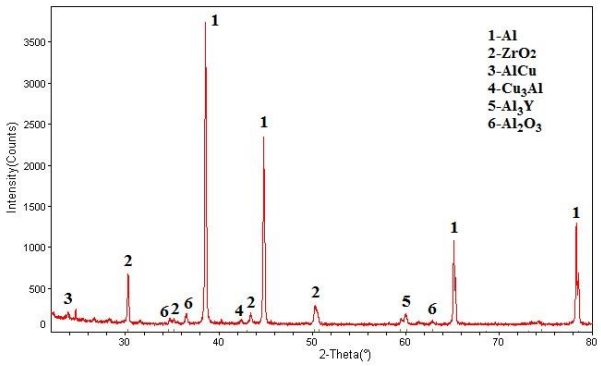

Figure 9. XRD analysis of Al+5%Cu+15% ZrO_2-Y_2O_3 based sample sintered at 500 ºC.

The XRD analysis of the sample obtained from Al+5%Cu+15% ZrO_2-Y_2O_3 powder mixture is shown in Figure 9. As a result of XRD analysis, it was determined that different types of compounds were formed. The main phase was determined as the Al element, which is the matrix powder. In addition, AlCu, Cu_3Al, Al_3Y, and Al_2O_3 compounds were formed together with the ZrO_2 compound.

It was observed that the possible compounds related to the detected elements in the EDS analyses (Figure 8) taken from the Al + 5% Cu + 15% ZrO_2-Y_2O_3 sample sintered at 500 ºC are compatible with the XRD analysis taken from the same sample.

3.2. Microhardness Test Results

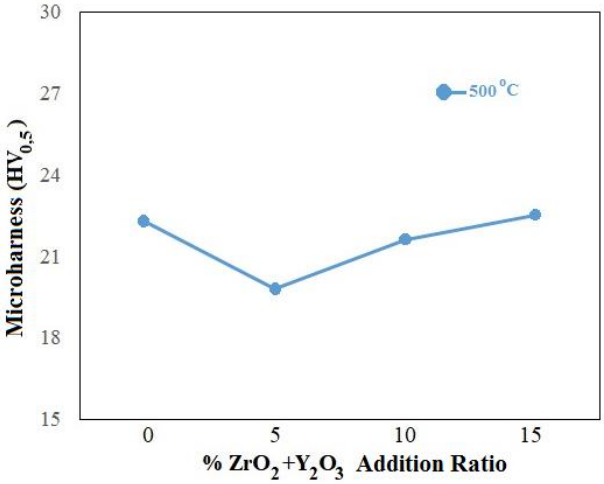

Figure 10. Microhardness value of specimens.

The microhardness values of the samples are given in Figure 10. The microhardness value was measured as 22.3 HV from the sample obtained by adding 5% Cu powder to Al. Microhardness values of 18.4 HV in the sample obtained by adding 5% ZrO_2-Y_2O_3 powder into Al+5% Cu powder, 21.5 HV in the sample obtained by adding 10% ZrO_2-Y_2O_3 powder

into Al+5% Cu powder, and 22.5 HV in the sample obtained by adding 15% ZrO_2-Y_2O_3 powder into Al+5% Cu powder were measured. With the addition of ZrO_2-Y_2O_3 powder, the number of pores in the microstructure increased in comparison to the sample without ZrO_2-Y_2O_3 powder, as can be seen in the microstructure photographs in Figures 3, 5, 6, 7. While the microhardness value was expected to increase with the addition of the ZrO_2-Y_2O_3 oxide compound, the microhardness value decreased generally due to the increase in the pore amount. However, a small increase in the microhardness value was observed as the amount of added ZrO_2-Y_2O_3 powder increased to 15% (see Fig. 10).

4. Conclusion and Suggestions

1. With the addition of ZrO_2-Y_2O_3 powder, the pores became more prominent at the grain boundaries.
2. In the samples sintered at 500 ºC, the microhardness value decreased depending on the number of pores increased with the addition of ZrO_2-Y_2O_3 powder.
3. Among the samples, the highest microhardness value was found as a value of 22.5 HV in the sample having 15% ZrO_2-Y_2O_3 in Al+5%Cu. The hardness value increased with the increase of the ZrO_2-Y_2O_3 ratio.

Acknowledgment

We would like to thank the Bitlis Eren University Scientific Research Project Coordinator for their support for the Postgraduate Thesis project with the project numbered BEBAP 2022.01.

Contributions of the authors

This study is a part of Tural HAMİDLİ's master thesis.

Conflict of Interest Statement

There is no conflict of interest between the authors.

Statement of Research and Publication Ethics

The study is complied with research and publication ethics.

References

[1] H. Su, X. Yan, X. Liu, Y. Ai, K. Ma, R. Li, Z. Zhang, Y. Sun, and S. Liu, "Research on high-temperature mechanical properties and microstructure of powder metallurgical rhenium," *Int. J. of Refractory Metals and Hard Mat.*, Vol. 106, 2022, Art. no. 105861.

[2] B. Deepanraj, N. Senthilkumar, T. Tamizharasan, "Sintering parameters consequence on microstructure and hardness of copper alloy prepared by powder metallurgy," *Mat. Today: Proc.*, 2021, https://doi.org/10.1016/j.matpr.2021.06.389.

[3] K. Köprülü, N. Mutlu, A. Kurt, B. Gülenç, and Y. Özçatalbaş, "Al+%4,5 Cu Ön karışımlı tozların alaşımlanmasına isıl işlemlerin etkisi," *Gazi University J. of Sci. Part C: Des. and Tech.,* Vol 6, no. 2, 283-293. DOI: 10.29109/http-gujsc-gazi-edu-tr.341722

[4] N. Kumar, A. Bharti, K. K. Saxena, "A re-investigation: Effect of powder metallurgy parameters on the physical and mechanical properties of aluminium matrix composites," *Mater. Today: Proc.*, Vol. 44, Part 1, 2021, Pages 2188-2193, https://doi.org/10.1016/j.matpr.2020.12.351.

[5] Y. Sayan, V. Venkatesan, E. Guk, H. Wu, and J. S. Kim, "Single-step fabrication of an anode supported planar single-chamber solid oxide fuel cell," *Int. J. Appl. Ceram. Technol*., vol. 15, no. 6, pp. 1375–1387, 2018, doi: 10.1111/ijac.13012.

[6] Y. Sayan, J. Kim, and H. Wu, "Residual stress measurement of a single-step sintered planar anode supported SC-SOFC using fluorescence spectroscopy," *Bitlis Eren Üniversitesi Fen Bilim. Derg*., vol. 11, no. 3, pp. 902–910, 2022, doi: 10.17798/bitlisfen.1139679.

[7] I. Bahaj, M. Kaddami, A. Dahrouch, N. Labjar, M. Essahli, "The effect of particle content and sintering time on the properties of Al-Al_9Co_2-$Al1_3Co_4$ composites, made by powder metallurgy," *Mater. Today: Proc*., 2022, https://doi.org/10.1016/j.matpr.2022.07.220.

[8] M. Pul,. "Alüminyum 7075 matrisli kompozitlerde SiC, B_4C Ve TiB_2 takviye elemanlarının mekanik özelliklere etkilerinin karşılaştırılması," *Düzce Üniversitesi Bilim ve Teknoloji Dergisi* , 7 (1) , pp. 180-193, 2019 . DOI: 10.29130/dubited.431573.

[9] S. Deniz, "Al_2O_3 takviyeli alüminyum matrisli kompozit üretimi, mekanik ve fiziksel özellikleri ile mikroyapı Karakterizasyonu," Yıldız Teknik Üniversitesi, Fen Bilimleri Enstitüsü, Doktora Tezi, 2000, İstanbul. 105 sayfa.

[10] İ. B. Nilüfer, H. Gökçe, H. Çimenoğlu, L.Öveçoğlu, "Seryum dioksit ilavesinin zirkonyum dioksit özelliklerine etkisinin incelenmesi," *Mühendis ve Makina*, cilt 55, sayı 652, s. 30-33, 2014.

[11] H. Karabulut, "Toz metalurjisi yöntemiyle Al_2O_3, SiC Ve B_4C takviyeli al matrisli kompozit üretiminde mekanik alaşımlama süresinin kompozit özelliklerine etkisi," Gazi Üniversitesi Fen Bilimleri Enstitüsü, Doktora Tezi, 2011, Ankara. 119 sayfa.

[12] M. Aslan, E. Ergul, A. Kaya, H. İ. Kurt, N. F. Yılmaz, "Toz metalurjisi yöntemiyle üretilen Al-MgO kompozitlerin özelliklerine sinterleme sıcaklığının etkisi," *El-Cezerî Fen ve Mühendislik Dergisi* Cilt: 7, No: 3, pp.1131-1139, 2020.

[13] M. C. Şenel, "Toz metalürjisi yöntemiyle üretilen Saf Al ve Al-B_4C, Al-Al_2O_3 kompozitlerin mekanik ve mikroyapı özelliklerinin karşılaştırılması," *Gümüşhane Üniversitesi Fen Bilimleri Enstitüsü Dergisi*, 10 (3), pp.783-795, 2020.

[14] B. Aktaş, S. Tekeli, G. Küpeli, Y. Bozkurt, Ö. Gülsoy, S. Salman, "Nio / Ysz (Yitriya İle Kararlı Hale Getirilmiş Zirkonya) Seramiklerin Kırılma Tokluğuna Mikro Yapının Etkisi," *Afyon Kocatepe Üniversitesi Fen Bilimleri Dergisi*, Özel Sayı, pp.61-67, 2009.

[15] I. Gulyaev, V. Kuzmin, E. Kornienko, A. Vyalova, P. Tyryshkin, D. Sergachev, S. Vashchenko, "Plasma spraying of thermal barrier coatings using YSZ powders," Mater. Today: Proc., Vol. 19, Part 5, pp. 2134-2138, 2019. https://doi.org/10.1016/j.matpr.2019.07.226.

Bitlis Eren Üniversitesi Fen Bilimleri Dergisi
BİTLİS EREN UNIVERSITY JOURNAL OF SCIENCE
ISSN: 2147-3129/e-ISSN: 2147-3188
VOLUME: 11 NO: 4 PAGE: 1050-1058 YEAR: 2022
DOI:10.17798/bitlisfen.1170707

The Optimization of the Zinc Electroplating Bath Using Machine Learning and Genetic Algorithms (NSGA-II)

Ramazan KATIRCI[1*], Bilal TEKİN[2]

[1]*Sivas University of Science and Technology, Faculty of Engineering and Natural Sciences, Department of Metallurgy and Materials Engineering, Türkiye*
[2]*Sivas University of Science and Technology, Faculty of Engineering and Natural Sciences, Department of Computer Engineering, Türkiye*
(ORCID: 0000-0003-2448-011X) (ORCID: 0000-0002-6690-3152)

Keywords: Machine learning, Zinc electroplating, Genetic algorithm, Optimization, Image processing, Surface detection.

Abstract
In this study, our aim is to predict the compositions of zinc electroplating bath using machine learning method and optimize the organic additives with NSGA-II (Non-dominated Sorting Genetic Algorithm) optimization algorithm. Mask RCNN was utilized to classify the coated plates according to their appearance. The names of classes were defined as “Full Bright”, “Full Fail”, “HCD Fail” and “LCD Fail”. The intersection over union (IoU) values of the Mask RCNN model were determined in the range of 93–97%. Machine learning algorithms, MLP, SVR, XGB, GP, RF, were trained using the classification of the coated panels whose classes were detected by the Mask RCNN. In the machine learning training, the additives in the electrodeposition bath were specified as input and the classes of the coated panels as output. From the trained models, RF gave the highest F1 scores for all the classes. The F1 scores of RF model for “Full Bright”, “Full Fail”, “HCD Fail” and “LCD Fail” are 0.95, 0.91, 1 and 0.80 respectively. Genetic algorithm (NSGA-II) was used to optimize the compositions of the bath. The trained RF models for all the classes were utilized as the objective function. The ranges of organic additives, which should be used for all the classes in the electrodeposition bath, were determined.

1. Introduction

Electrodeposition is extensively utilized in the world because it is cheap and can be applied to the wide surfaces easily [1]. Many metallic coatings such as nickel, chrome, zinc, bronze, brass, copper and etc. can be performed using this method [2]–[6]. Zinc coating among the metallic coatings is the most vastly used method to protect the steels from the corrosion [7]. Two types of zinc coating baths are present. One is acidic and the other is alkaline zinc electroplating bath [7], [8]. Many parameters are present to perform the coating in the electrodeposition bath [8]. Except for parameters such as temperature and current, the other parameters are constantly changing during operation. Hence, they should be kept under control to ensure the stability of the electroplating bath. Organic additives are very important factor to enhance the physical properties (brightness, throwing/covering power and etc.) of the coating [9]. In the industry, the lack of organic additives [10] and the other needs in the electroplating bath is estimated by the engineer using the Hull-cell panels or examining the coated parts. The defects formed on the surface of the panels during the coating are closely related to the deficiencies in the electroplating bath. Thanks to this relationship, the experienced engineer can solve the problem of the electroplating bath by examining the surface of the coated panels.

Machine learning principles have widely been used to detect objects and faces in many areas [11]. Especially, material scientists have utilized these methods to identify surface properties of the materials. For instance, in order to estimate the

*Corresponding author:ramazankatirci@sivas.edu.tr
Received: 06.09.2022, Accepted: 23.12.2022

adhesion force of the materials to the sublayer by utilizing a scratch test technique (DIN EN ISO 20502:2016–11) [12]. Wang and et al. also used CNN technique to estimate the factors influencing particles in plasma spray [13]. The method is a promising method which can be used to estimate the content of electroplating bath in the field of the electroplating process. Katırcı et al. utilized Mask RCNN method to extract the related part from the whole image and machine learning method was used to predict the quality of the Hull-cell panel [1]. Also, the same group used machine learning algorithms such as MLP (Multilayer perceptron), SVR (Support vector machine regression) and XGB (eXtreme gradient boosting) to estimate ZnNi thickness and Ni% ZnNi alloy coating [14].

The aim of this study is to adapt the artificial intelligence methods to the electroplating process to keep the variable parameters under control during operation. In this study, the Mask RCNN technique was implemented to define the deposited panels according to the appearance of the coating. To measure the additives in the electrocoating bath affecting the view of the coating, machine learning algorithms were used. Genetic algorithm (NSGA-II) was implemented to optimize the amount of organic additives in the working electroplating bath.

2. Material and Method

Zn electrodeposition was carried out utilizing a Thurlby 30V 1A-model DC model direct-current generator. The composition of the basic Zn electroplating bath is presented in Table 1 and named basic-Zn. The pH of the bath was maintained at 4.5. All electroplating was performed in the room temperature. KOH was added to dissolve ZnO and to rise the conductivity of the Zn electroplating bath. The additives were included to the bath to enhance the surface properties, such as brightness, color and etc., of the coating. Potassium silicate (PS), imidazole-epichlorohydrin (IME) and mirapol (MP) were used as carrier. Carriers ensure that the coating thickness is homogeneous [15]. The orthochloro benzaldehyde chloride (OCB) and benzyl pyridinium 3-carboxylate (BPC) chemicals were used as a brightener. The brighteners reduce the crystal size to increase in the brightness of the coating [16]. Hull-cell was used to deposit the panels; whose surface area is 1 dm^2 (Figure 1).

Table 1. The basic Zn electroplating bath

Chemicals	Quantity (g/L)
ZnO	12.5
KOH	170
K_2CO_3	50

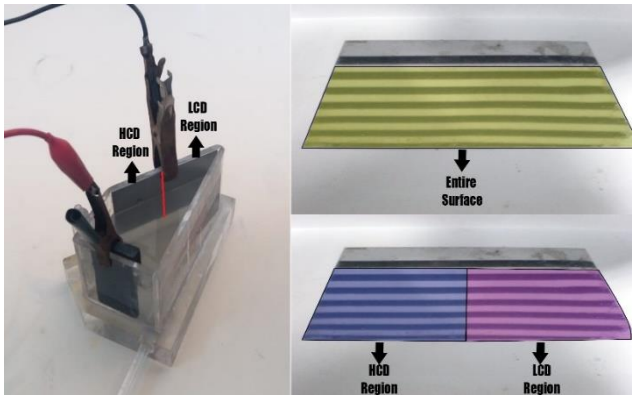

Figure 1: Hull-cell (left) and panels (right).

The images of the plates were taken to generate the dataset for training and test. The code implementations were performed on Anaconda platform and Truba HPC system. Python language was used to write the codes. Sklearn libraries were utilized for machine learning (ML). Mask RCNN codes were fitted to this study. Tensorflow 1.14 and keras 2.2.4 libraries were utilized in the Mask RCNN. The images of the Zn deposited plates were acquired and resized to 128*128 pixel. The via-2.0.10 software and polygon frame were utilized for labeling. The parts within the electrodeposition bath were labeled and classified according to the appearance of the panels. Four classes were used for classification. These are “Full Bright”, “Full Fail”, “LCD Fail” and “HCD Fail”. “Full Bright” indicates that the entire surface of the coating is bright, “Full Fail” indicates that the entire surface is either mat or has defects. “HCD Fail” and “LCD Fail” depict defects in HCD (High Current Density) and LCD (Low Current Density) regions respectively. The experimental studies were performed in 38 different electroplating baths to acquire the images from the deposited panels. The images were augmented with the image processing techniques such as blur, brightness, contrast, gaussian blur, median, salt and pepper noise, saturation and sharpen. For the test dataset, 114 “Full Bright”, 76 “Full Fail”, 114 “LCD Fail” and 114 “HCD Fail” images were generated. The Zn electrodeposition bath having the different content was trained versus the class of the coated panels using MLP (Multi-layer perceptron), SVC (Support vector

classifier), XGB (eXtreme gradient boosting), GP (Gaussian process) and RF (Random forest) machine learning algorithms. The achievement of the models was measured with F1 score. The leave-one-out (loo) method was utilized for cross-validation because it is favored for small dataset [17]. In this technique, one data is extracted from the dataset and the rest of data is utilized for training. Afterwards, the extracted data is predicted by the model trained. This event is reiterated for each data. The hyperparameters providing the best model were investigated using the grid search technique. The flowchart of the whole study is summarized in Figure 2.

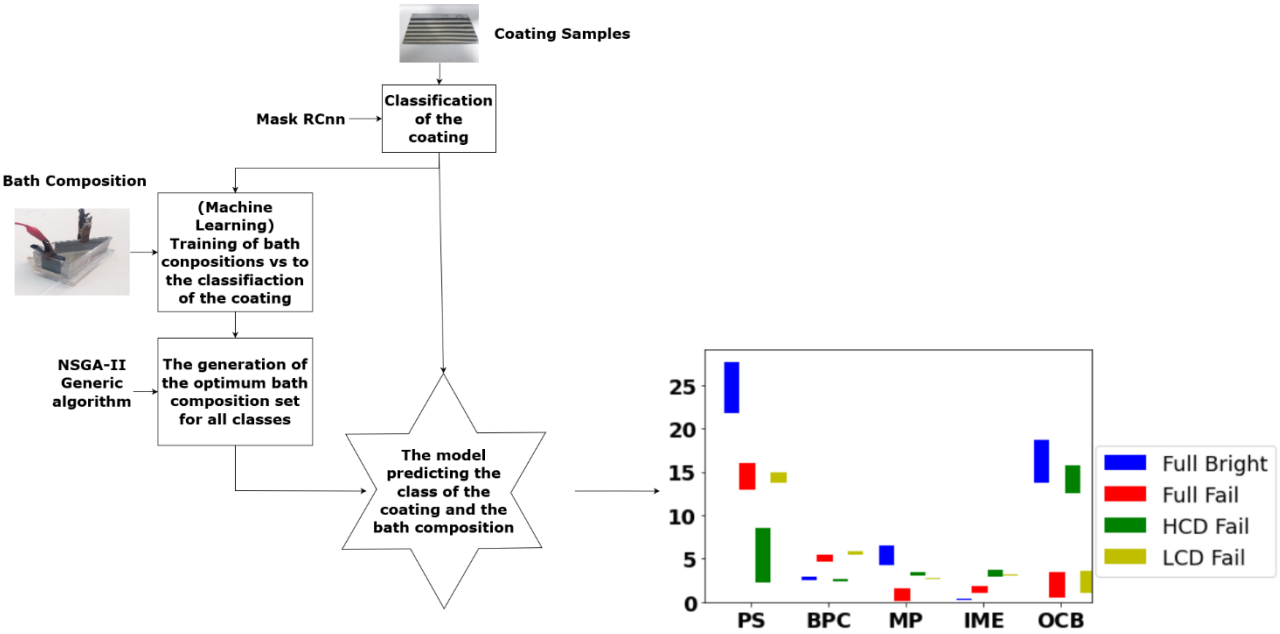

Figure 2. The flowchart of the whole study.

3. Results and Discussion

3.1. MASK RCNN

Figure 3 shows the samples coated Zn metals. The black lines on the plates are not actual but the reflection of the background. Thanks to the reflection, it is possible to define the level of the brightness of the coating. For example, in Figure 3a, the black lines on the plate are clearly seen, which means that the surface is fully bright. In Figure 3b, there are some defects and mat regions. As seen in Figure 3c, the black lines are not seen because the surface is fully mat. With this technique, it is possible to analyze the surface of the coating easily in terms of defects and brightness sequentially.

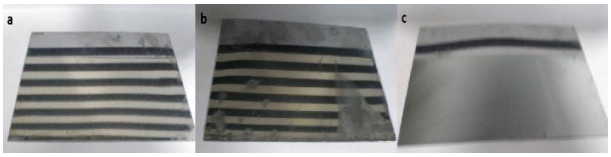

Figure 3. Zn coated panels obtained in the electroplating baths with varied compositions.

The electroplating baths are dynamic. The concentration of additives varies constantly in the operation. Therefore, it is crucial to keep them under control. The surface view of the coating provides the knowledge about the deficiencies in the electroplating bath. For example, the dullness at higher current density (HCD) region of the coated panel indicates the lack of brightener in the zinc electroplating bath. The cloudy deposit points out the metal contamination in the bath. The surface appearance of the coating was divided into 4 categories. These are “Full Bright”, “Full Fail”, “LCD Fail” and “HCD Fail”. The Mask RCNN algorithm was used to define which category the surface views belonged to. This step is crucial because these outputs were used in the machine learning algorithms to identify the related organic additives affecting the surface on the plate. The Mask RCNN algorithm detected all categories without error in the test dataset. This result is very promising to identify the additives in the electroplating bath. Figure 4 indicates the loss values of the training and validation dataset. The lower loss is expected for thriving model. Region proposal network (RPN) refers to a deep CNN technique for suggesting regions

in object recognition. 'rpn_class_loss' is the loss value computed during the classification, and 'rpn_bbox_loss' is the loss value computed during the bounding box detection. The three outputs emerge in the Mask RCNN structure: box delimiter, classification and masking. 'mrcnn_bbox_loss', 'mrcnn_class_loss', 'mrcnn_mask_loss' values show the errors of these outcomes. Figure 5 illustrates some examples for the ground truth and predicted mask from the test images. The results depict that the underfitting or overfitting was not observed because the trained model predicted all classes 100% correctly in the test dataset. The intersection over union (IoU) values of the object detection in the test dataset are in the range of 93–97%.

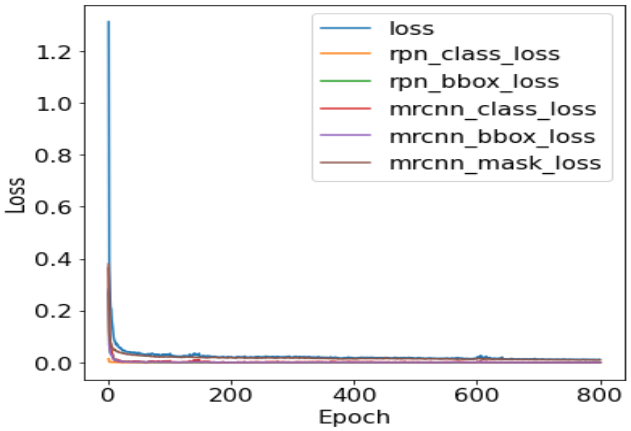

Figure 4. The loss vs. epoch number.

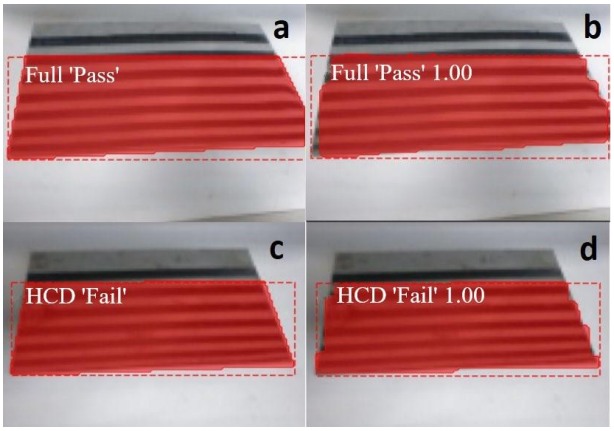

Figure 5. a) Ground truth and b) predicted mask for "Full Bright" class c) ground truth and d) predicted mask for "HCD Fail" class.

3.2 Machine Learning

Organic additives are the most important parameters in the electroplating bath because they influence the appearance of the coating directly. The concentration of organic additives is constantly changing in the running bath, so they should be kept within a certain range. To achieve this, the machine learning algorithms are a promising technique to estimate the organic additives in the electroplating bath. Some organic additives with different concentration were added to the Hull-cell and coatings were performed in these electroplating baths. The coatings were labelled as "Full Bright", "Full Fail", "HCD Fail" and "LCD Fail" according to the quality of the coating. The design of experimental studies is presented in the excel file named as contents of the solution in the supplementary material. The SVC [18], [19], MLP [20], [21], XGB [22], [23], GP [24], [25] and RF [26], [27] algorithms were used to train the dataset generated from the experimental studies. The hyperparameters of all models were optimized at two levels. For example, the hyperparameter of 'n_estimators' in RF model were tested in 10 and 50 values. The other hyperparameters in all models were tested in the same way. The highest F1 score was used to select the best hyperparameters in all models. The hyperparameters giving the highest F1 score were printed in the txt files. The accuracy, F1 score, Precision and Recall of all the models are presented in Table 2. The model having the highest F1 score was selected as the best model. As seen in Table 2, the best model is RF model. It predicted all classes in the test dataset with high accuracy. RF model was selected for further optimization. The equations to calculate the accuracy, F1 score, Precision and Recall metrics are indicated in Eq.1. The meanings of the terms of TP, TN, FP and FN are depicted in Table 3.

Table 2. The accuracy, F1 score, Precision and Recall of all models.

	ML Methods	Accuracy	F1 score	Precision	Recall
Full Bright	**MLP**	0.76	0.77	0.71	0.83
	SVC	0.66	0.68	0.61	0.78
	GP	0.58	0.58	0.55	0.61
	XGBoost	0.84	0.82	0.88	0.78
	RF	0.95	0.95	0.90	1.00
Full Fail	**MLP**	0.60	0.48	0.00	0.62
	SVC	0.61	0.48	0.54	0.44
	GP	0.39	0.38	0.33	0.44
	XGBoost	0.58	0.60	0.50	0.75
	RF	0.92	0.91	0.88	0.94

HCD Fail	**MLP**	0.95	0.50	0.50	0.50
	SVC	0.95	0.00	0.00	0.00
	GP	0.95	0.00	0.00	0.00
	XGBoost	0.95	0.00	0.00	0.00
	RF	1.00	1.00	1.00	1.00
LCD Fail	**MLP**	0.95	0.00	0.00	0.00
	SVC	0.95	0.00	0.00	0.00
	GP	0.95	0.00	0.00	0.00
	XGBoost	0.95	0.00	0.00	0.00
	RF	0.97	0.80	0.67	1.00

$$Accuracy = \frac{(TP + TN)}{(TP + FP + TN + FN)}$$

$$F1\ score = \frac{2 * Precision * Recall}{(Precision + Recall)}$$

$$Precision = \frac{TP}{(TP + FP)} \quad (1)$$

$$Recall\ = \frac{TP}{(TP + FN)}$$

Table 3. The meanings of the terms of TN, TP, FP and FN.

Confusion Matrix		**Y-predicted**	
		0	**1**
Y-true	**0**	True Negative (TN)	False Positive (FP)
	1	False Negative (FN)	True Positive (TP)

Recall indicates that how much of the proportion of true positives (TP) is described correctly. Precision shows how much of the ratio of predicted positives are actually 1. F1 score is the weighted average of precision and recall values [28], [29]. The confusion matrix of all models is presented in CM excel file in the supplemental materials. In the next step, the main and interaction effects of hyperparameters of RF model were investigated. Figure 6 shows the main effects of hyperparameters for "Full Bright" class in RF. As seen in figure 6, 'n_estimators', criterion and 'warm_start' is the most efficient hyperparameters affecting the F1 score. While 'n_estimators' and 'warm_start' hyperparameters indicates the enhancing effect, 'criterion' hyperparameter depicts the decreasing effect. It is significant to examine the interaction effects of these hyperparameters to each other. Figure 7 indicates the interactions of hyperparameters. It is seen from the figure that the small interaction among 'n_estimators', 'warm_start' and 'criterion' hyperparameters are present. An important point which can be seen in this figure is that 'warm_start' hyperparameter indicates robust effect. When it is kept in True, the influence of 'n_estimators' and 'criterion' disappear and the maximum F1 score is acquired. The similar results were observed in other classes. In all the classes, 'warm_start' emerged as the most important hyperparameter. The task of 'warm_start' hyperparameter in the algorithm is that when 'warm_start' hyperparameter set to True, the previous solution is used to fit the trees. Otherwise, it fits a whole fresh forest. The warm start hyperparameter is an effective way to add more trees until the training reaches a satisfying accuracy [30]. The optimum hyperparameters for all classes in the RF model to acquire the highest F1 score are presented in Table 4.

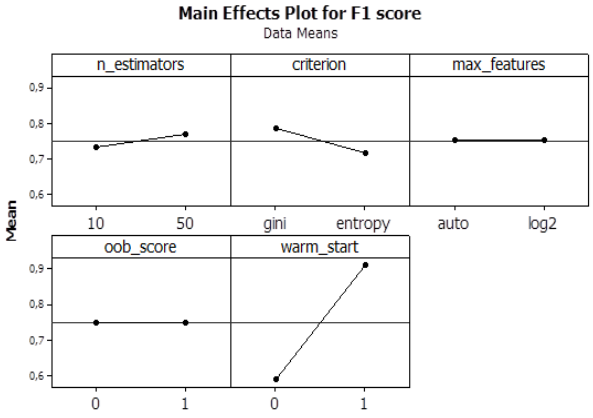

Figure 6: The main effects of hyperparameter for "Full Bright" class.

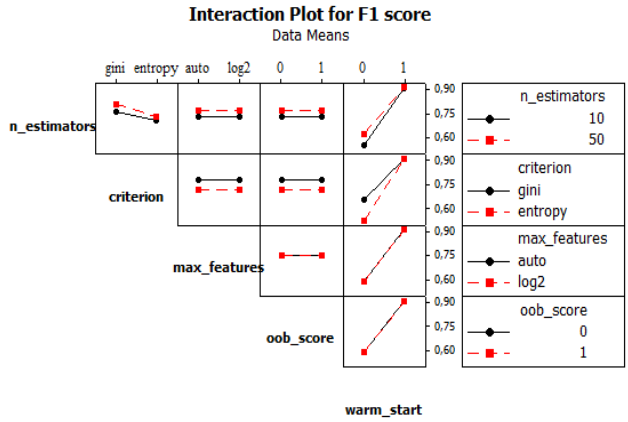

Figure 7: The interaction of hyper parameters for "Full Bright" class.

Table 4: The optimum hyper parameters for all classes in RF model.

Classes	Hyperparameters
Full Bright	n_estimators: 10, criterion: gini, max_depth: None, min_samples_split: 2, min_samples_leaf: 1, min_weight_fraction_leaf: 0.0, max_features: sqrt, max_leaf_nodes: 17, min_impurity_decrease: 0.0, bootstrap: False, oob_score: False , warm_start: True, class_weight: None, ccp_alpha: 0.0, max_samples: None
Full Fail	n_estimators: 10, criterion: gini, max_depth: None, min_samples_split: 2, min_samples_leaf: 1, min_weight_fraction_leaf: 0.0, max_features: sqrt, max_leaf_nodes: None, min_impurity_decrease: 0.0, bootstrap: True, oob_score: False , warm_start: True, class_weight: None, ccp_alpha: 0.0, max_samples: None
HCD Fail	n_estimators: 10, criterion: entropy, max_depth: None, min_samples_split: 2, min_samples_leaf: 1, min_weight_fraction_leaf: 0.0, max_features: sqrt, max_leaf_nodes: None, min_impurity_decrease: 0.0, bootstrap: False, oob_score: False , warm_start: True, class_weight: None, ccp_alpha: 0.0, max_samples: None
LCD Fail	n_estimators: 10, criterion: gini, max_depth: None, min_samples_split: 2, min_samples_leaf: 1, min_weight_fraction_leaf: 0.0, max_features: sqrt, max_leaf_nodes: None, min_impurity_decrease: 0.0, bootstrap: True, oob_score: False , warm_start: True, class_weight: None, ccp_alpha: 0.0, max_samples: None

3.3 Optimization

NSGA-II (Non-dominated Sorting Genetic Algorithm) algorithm were utilized to optimize the electroplating bath composition. The NSGA-II algorithm is a multi-objective optimization algorithm based on non-dominated sorting and crowding proposed by Deb et al [31], [32]. It was designed based on genetic algorithm. The algorithm was created to eliminate the shortcomings of the NSGA algorithm developed by Srinivas and Deb [33]. In addition to the steps of the genetic algorithm, non-dominated sorting and crowding distance calculations are performed. Since NSGA-II is an algorithm with low computational complexity and fast, it has many applications in the literature [34]–[36]. After the bath composition of electroplating bath was trained versus the appearance of the surface, the best models, having the highest F1 score, were used as the objective function in the optimization algorithm. The optimization problem is generally defined as follows.

$$min\ f_m(x) \qquad m = 1,..,M$$
$$g_j(x) \le 0 \qquad j = 1,...,J \qquad \textit{Inequality constraints}$$
$$h_k(x) = 0 \qquad k = 1,..,K \qquad \textit{Equality constraints}$$
$$x^L = [x_1, x_2, ..., x_i]$$
$$x^U = [x_1, x_2, ..., x_i]$$
$$x \in \Omega$$

where x_i shows the i-th variable to be optimized, x_i^L and x_i^U depict the upper and lower bounds. $f_m(x)$, $g_j(x)$ and $h_k(x)$ illustrate the m-th objective function, j-th inequality constraint and k-th equality constraint respectively [37]. The models generated separately for "Full Bright", "Full Fail",

"HCD Fail" and "LCD Fail" classes were used as the objective function computing the output. In the "Full Bright" objective function, the maximum was defined as the best. No constraint was determined. The problem definition was made as follows,

$max\ f_m(x)$	*models generated in machine learning*
$g_j(x)$	*no constraint*
$h_k(x)$	*no constraint*
$x_l = [1, 0, 0, 0, 0, 0]$	*lower bound*
$x_u = [2, 30, 6, 10, 5, 20]$	*upper bound*

The bath composition ranges for all classes were determined and their results are illustrated in Figure 8. As shown in the figure, to acquire the "Full Bright" surface, PS, BPC, MP, IME and OCB materials should be kept in the ranges of 21.8-27.7, 2.5-2.9, 4.3-6.5, 0.2-0.4 and 13.8-18.7 respectively. OCB and BPC chemical amounts are overlapped in "HCD Fail" class, so the amount of PS chemicals should not fall below 20 and IME chemical should not exceed 0.5. The composition of the bath can be estimated from this figure showing the ranges of the bath compositions versus the class of the coating, which is determined by Mask RCNN algorithm.

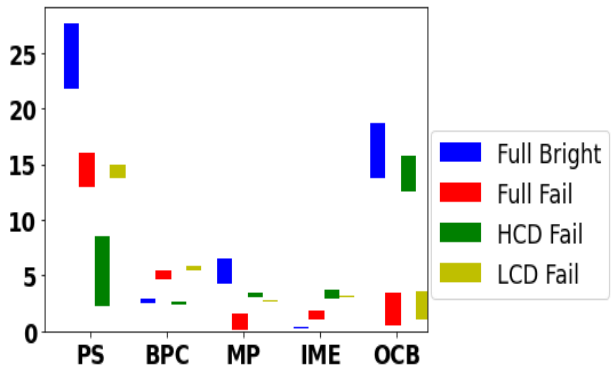

Figure 8: Optimized electroplating bath composition for all classes.

4. Conclusion and Suggestions

In this study, the optimum electroplating bath composition for "Full Bright" surface was investigated. In the first step, Mask RCNN were utilized to classify the coating, which was evaluated for the four classes, "Full Bright", "Full Fail", "HCD Fail" and "LCD Fail". These classes were generated in accordance with the appearance of the coating, which were affected by the organic additives in the electrodeposition bath. In the second step, the electroplating bath compositions were trained versus the classes of the coating. The scope of this step is to generate the model predicting the class of the coating from the bath composition. RF algorithm was detected as the best model for all the classes. The hyperparameters of RF model were further optimized to increase the F1 score. The optimum RF models for each class was generated. These models were used as the objective function in the NSGA-II optimization process. In the last step, the bath composition ranges for all classes were found by using NSGA-II algorithm. The flow chart summarizing the whole study is presented in Figure 2.

Consequently, thanks to this study, it has been possible to predict the content of the electrodeposition bath from the appearance of the coating. The suggested method indicates that it is possible to keep the organic additives in the electroplating process under control using artificial intelligent methods. If this study is implemented in the industry, it is expected that time and operating cost decrease abruptly. Also, the process will be automated. By extending the number of class and samples in the dataset, the achievement in estimating the content of the electroplating bath, ie organic additives, can be increased.

Acknowledgment

The experiments reported in this paper were partially performed at TUBITAK ULAKBIM, High Performance and Grid Computing Center (TRUBA resources) and some computing resources were provided by the National Center for High Performance Computing of Turkiye (UHeM).

Contributions of the Authors

Ramazan Katırcı: Conceptualization, Software, Validation, Formal analysis, Investigation, Data curation, Writing - original draft, Visualization, Resources.
Bilal Tekin: Software, Investigation, Validation, Data curation, Visualization.

Conflict of Interest Statement

There is no conflict of interest between the authors.

Statement of Research and Publication Ethics

The study is complied with research and publication ethics.

References

[1] R. Katirci, E. K. Yilmaz, O. Kaynar, and M. Zontul, "Automated evaluation of Cr-III coated parts using Mask RCNN and ML methods," *Surf. Coat. Technol.*, vol. 422, no. 127571, p. 127571, Sep. 2021.

[2] E. Sezer, B. Ustamehmetoğlu, and R. Katirci, "Effects of a N,N-dimethyl-N-2-propenyl-2-propene-1-ammonium chloride-2-propenamide copolymer on bright nickel plating," *Surf. Coat. Technol.*, vol. 213, pp. 253–263, Dec. 2012.

[3] R. Katirci and U. Yilmaz, "Statistical studies of Zn–Ni alloy coatings using non-cyanide alkaline baths containing polyethyleneimine complexing agents," *Transactions of the IMF*, vol. 92, no. 5, pp. 245–252, Sep. 2014.

[4] R. Katirci, "A chrome coating from a trivalent chromium bath containing extremely low concentration of Cr3+ ions," *Int. J. Surf. Sci. Eng.*, vol. 10, no. 1, pp. 73–85, Jan. 2016.

[5] L. N. Bengoa, W. R. Tuckart, N. Zabala, G. Prieto, and W. A. Egli, "Bronze electrodeposition from an acidic non-cyanide high efficiency electrolyte: Tribological behavior," *Surf. Coat. Technol.*, vol. 253, pp. 241–248, Aug. 2014.

[6] Z. Lai et al., "Computational analysis and experimental evidence of two typical levelers for acid copper electroplating," *Electrochim. Acta*, vol. 273, pp. 318–326, May 2018.

[7] M. Kul, S. U. of Science, and 58050 Sivas Turkey Technology Department of Aeronautical Engineering, "Effect of process parameters on the electrodeposition of zinc on 1010 steel: Central composite design optimization," *Int. J. Electrochem. Sci.*, vol. 15, pp. 9779–9795, Oct. 2020.

[8] M. Chotirach et al., "Systematic investigation of brightener' s effects on alkaline non-cyanide zinc electroplating using HPLC and molecular modeling," *Mater. Chem. Phys.*, vol. 277, no. 125567, p. 125567, Feb. 2022.

[9] N. Sorour, W. Zhang, E. Ghali, and G. Houlachi, "A review of organic additives in zinc electrodeposition process (performance and evaluation)," *Hydrometallurgy*, vol. 171, pp. 320–332, Aug. 2017.

[10] R. Katirci, E. Sezer, and B. Ustamehmetoğlu, "Statistical optimisation of organic additives for maximum brightness and brightener analysis in a nickel electroplating bath," *Transactions of the IMF*, vol. 93, no. 2, pp. 89–96, Mar. 2015.

[11] K. Hameed, D. Chai, and A. Rassau, "Score-based mask edge improvement of Mask-RCNN for segmentation of fruit and vegetables," *Expert Syst. Appl.*, vol. 190, p. 116205, Mar. 2022.

[12] B. Lenz, H. Hasselbruch, A. G. Holger, and Mehner, "Application of CNN networks for an automatic determination of critical loads in scratch tests on a-C:H:W coatings," *Surf. Coat. Technol.*, vol. 393, p. 125764, Jul. 2020.

[13] J. Zhu, X. Wang, L. Kou, L. Zheng, and H. Zhang, "Prediction of control parameters corresponding to in-flight particles in atmospheric plasma spray employing convolutional neural networks," *Surf. Coat. Technol.*, vol. 394, p. 125862, Jul. 2020.

[14] R. Katirci, H. Aktas, and M. Zontul, "The prediction of the ZnNi thickness and Ni % of ZnNi alloy electroplating using a machine learning method," *Transactions of the IMF*, vol. 99, no. 3, pp. 162–168, May 2021.

[15] M. P. M. Schlesinger, Modern Electroplating. Elsevier, 2011.

[16] Y. Nakamura, N. Kaneko, M. Watanabe, and H. Nezu, "Effects of saccharin and aliphatic alcohols on the electrocrystallization of nickel," *J. Appl. Electrochem.*, vol. 24, no. 3, Mar. 1994.

[17] A. Kirtis, M. Aasim, and R. Katirci, "Application of artificial neural network and machine learning algorithms for modeling the in vitro regeneration of chickpea (Cicer arietinum L.)," *Plant Cell Tissue Organ Cult.*, Mar. 2022.

[18] T. V. Dinh, H. Nguyen, X.-L. Tran, and N.-D. Hoang, "Predicting rainfall-induced soil erosion based on a hybridization of adaptive differential evolution and support vector machine classification," *Math. Probl. Eng.*, vol. 2021, Feb. 2021.

[19] A. Rizwan, N. Iqbal, R. Ahmad, and D.-H. Kim, "WR-SVM model based on the margin radius approach for solving the minimum enclosing ball problem in support vector machine classification".

[20] Y. Wei, J. Jang-Jaccard, F. Sabrina, A. Singh, W. Xu, and S. Camtepe, "AE-MLP: A hybrid deep learning approach for DDoS Detection and Classification," *IEEE Access*, vol. 9, pp. 146810–146821, 2021.

[21] M. Ramkumar, C. G. Babu, K. V. Kumar, D. Hepsiba, A. Manjunathan, and R. S. Kumar, "ECG Cardiac arrhythmias Classification using DWT, ICA and MLP neural networks," J. *Phys. Conf. Ser*., vol. 1831, no. 1, p. 12015, Mar. 2021.
[22] M. Ma et al., "XGBoost-based method for flash flood risk assessment," *J. Hydrol.*, vol. 598, p. 126382, Jul. 2021.
[23] D. Zhang et al., "iBLP: An XGBoost-based predictor for identifying bioluminescent proteins," *Comput. Math. Methods Med*., vol. 2021, p. 6664362, Jan. 2021.
[24] C. Villacampa-Calvo, B. Zaldivar, E. C. Garrido-Merchán, and D. Hernández-Lobato, "Multi-class Gaussian process classification with noisy inputs," *J. Mach. Learn. Res*., vol. 22, no. 36, pp. 1–52, 2021.
[25] B. Gips, "Texture-based seafloor characterization using gaussian process classification," IEEE *J. Oceanic Eng*., pp. 1–11, 2022.
[26] Y. Chen, W. Zheng, W. Li, and Y. Huang, "Large group activity security risk assessment and risk early warning based on random forest algorithm," *Pattern Recognit. Lett*., vol. 144, pp. 1–5, Apr. 2021.
[27] K. Liu, X. Hu, H. Zhou, L. Tong, W. D. Widanage, and J. Marco, "Feature analyses and modeling of lithium-ion battery manufacturing based on random forest classification," *IEEE/ASME Trans. Mechatron*., vol. 26, no. 6, pp. 2944–2955, Dec. 2021.
[28] B.-C. Yan, H.-W. Wang, S.-W. F. Jiang, F.-A. Chao, and B. Chen, "Maximum f1-score training for end-to-end mispronunciation detection and diagnosis of l2 english speech".
[29] B. Ćwiklinski, A. Giełczyk, and M. Choraś, "Who Will Score? A machine learning approach to supporting football team building and transfers," *Entropy*, vol. 23, no. 1, Jan. 2021.
[30] F. Pedregosa et al., "Scikit-learn: Machine learning in python," *Journal of Machine Learning Research*, vol. 12, pp. 2825–2830, 2011.
[31] K. Deb, A. Pratap, S. Agarwal, and T. Meyarivan, "A fast and elitist multiobjective genetic algorithm: NSGA-II," *IEEE Trans. Evol. Comput*., vol. 6, no. 2, pp. 182–197, Apr. 2002.
[32] E. D. Durmaz and R. Sahin, "NSGA-II and goal programming approach for the multi-objective single row facility layout problem," *Journal of the Faculty of Engineering and Architecture of Gazi University*, vol. 32, no. 3, pp. 941–955, 2017, doi: 10.17341/gazimmfd.337647.
[33] N. Srinivas and K. Deb, "Muiltiobjective optimization using nondominated sorting in genetic algorithms," *Evolutionary Computation*, vol. 2, no. 3, pp. 221–248, Sep. 1994, doi: 10.1162/evco.1994.2.3.221.
[34] A. Ala, F. E. Alsaadi, M. Ahmadi, and S. Mirjalili, "Optimization of an appointment scheduling problem for healthcare systems based on the quality of fairness service using whale optimization algorithm and NSGA-II," *Sci. Rep.*, vol. 11, no. 1, p. 19816, Oct. 2021.
[35] S. Verma, M. Pant, and V. Snasel, "A Comprehensive review on NSGA-II for multi-objective combinatorial optimization problems," *IEEE Access*, vol. 9, pp. 57757–57791, 2021.
[36] P. Wang, J. Huang, Z. Cui, L. Xie, and J. Chen, "A Gaussian error correction multi-objective positioning model with NSGA-II," *Concurr. Comput*., vol. 32, no. 5, Mar. 2020.
[37] J. Blank and K. Deb, "Pymoo: Multi-objective optimization in python," IEEE Access, vol. 8, pp. 89497–89509, 2020.

Bitlis Eren Üniversitesi Fen Bilimleri Dergisi
BİTLİS EREN UNIVERSITY JOURNAL OF SCIENCE
ISSN: 2147-3129/e-ISSN: 2147-3188
VOLUME: 11 NO: 4 PAGE: 1059-1072 YEAR: 2022
DOI: 10.17798/bitlisfen.1170909

A Comparison of Risks Assessment for the Project Phase of Solar Power Plant Installation with FMEA Pareto and AHP Methods

Hülya KESKİN ÇITIROĞLU[1], Deniz ARCA[2], Eray CAN[3*]

[1]*Directorate of Investment Monitoring and Coordination, YIKOB, 09020, Aydın, Türkiye*
[2]*Dokuz Eylul University, Department of Architecture and Urban Planning, Izmir Vocational School, 35390, İzmir, Türkiye*
[3]*Yalova University, Engineering Faculty, Transportation Engineering Department, 77200, Yalova, Türkiye*
(ORCID: 0000-0002-2999-9570) (ORCID: 0000-0002-0439-4938) (ORCID: 0000-0002-8192-1703)

Keywords: Solar power plant (SPP), Solar energy, Risk Assessment, Failure Mode and Effects Analysis (FMEA), Pareto Analysis, Analytic Hierarchy Process (AHP).

Abstract

As a result of the rapid depletion of fuels, high costs and environmental concerns which is in today's conditions in energy production by traditional methods cause rapid orientation to renewable energy sources. In this context, the number of alternative researches and studies on the phenomenon of energy, which has become an indicator of the development of countries, has increased steadily. Taking measures by analysing possible failures and risks in the establishment and operation of renewable energy plants is of great importance in terms of cost control, efficiency, sustainability of production and ensuring the safety of life and property. For this reason, in this study, failures and risks occurring in the projecting stage, which is the first and important stage of the installation of solar power plants (SPP), which are among the sustainable and renewable energy sources that have become an important part of our lives are analysed using Failure Mode Effect Analysis (FMEA). In the FMEA analysis, the precautions that can be taken against the mistakes and risks that may be encountered regarding the researched subject were investigated. In addition, the opinions of experts on this subject expressed in the literature and researches were also taken into consideration. Then, with the Pareto analysis and Analytical Hierarchy Process (AHP) method systematic, the order of importance of the risks was determined and the similarities between them were tried to be determined.

1. Introduction

In recent years, the need for electrical energy in developed and developing countries has been increasing in every field. The increase in demand for electrical energy due to the rapid development of industrialization and technology has become more noticeable with the increase in the quality of life in cities. The increase in the need for electrical energy causes a rapid decrease in fossil underground resources that cannot be renewed and consequently to be depleted in the future. For this reason, it is also important to use alternative and renewable energy sources instead of traditional and depletable fossil fuels in the production of sustainable and environmentally friendly electricity [1]. Thanks to renewable energy sources, electricity needs are met and at the same time, nature and living creatures are protected and furthermore, an undeniable assistance is provided to prevent global climate change. Solar energy is one of the renewable energy sources because it is environmentally friendly and has been preferred in recent years due to its ease of use and high potential. The carbon level is increasing due to the use of various technologies. Therefore, solar energy, which does not cause carbon emissions and protects nature, has become an energy type that countries have invested in [2]. In their study, [3], regarding the integration of the system used in concentrated solar power plants to the thermal power

*Corresponding author: can.eray@hotmail.com
Received:04.09.2022, Accepted:22.10.2022

plant using coal, demonstrated that this hybrid system can be economical. Regarding the preference of solar energy power plants (SPP) that generate electricity using solar energy, the following aspects are the main reasons that should be considered:

- Solar energy is one of the non-depletable sources of energy.
- The usage areas of solar energy are diverse in the fields of electricity generation, heating, cooling, drying, lighting, calculators, clocks and energy supply of traffic sign lamps, producing hot water, distilling water, charging mobile phones batteries, portable power supplies, and cooking etc. [4],
- Since solar energy applications are completely natural, there is no harm to the environment,
- Since it is easy to generate electricity from solar energy, any person can produce his own electricity with solar energy without requiring professionalism,
- The installation of SPP facilities is easy and it is possible to establish these facilities in approximately 1-9 months depending on the plant capacity,
- Maintenance of SPP facilities is easy; in addition, operation and maintenance costs are low,
- Due to the construction with durable materials, photovoltaic solar panels can resist harsh weather conditions [5].

Compliance of the installation site with the power plant project is of great importance in all stages of the plan-project, installation, activation and operation of the power plants that produce electricity from solar energy. Therefore, in the SPP plan-project, installation, activation, operation and maintenance stages of the power plant; Conditions such as the location of the power plant and the topographic conditions of the land, weather conditions, basic engineering, geological and geotechnical features of the installation site, material supply and material properties, technical calculations of the power plant, placement of panels and inverters, annual maintenance and monitoring should be taken into consideration. Sustainability is of great importance in electrical energy generation. Unless sustainability of a non-depletable and endless energy source like the sun is ensured, sustainability will not be achieved in electrical energy generation [6]. For this reason, as in all renewable energy sources, the risks, failures and problems that may be encountered in the production of electricity with solar energy, should be clearly revealed, analyzed and solution suggestions should be determined in order to avoid these risks and failures before they occur. Successful completion of the plan-project phase, which is the first step in the SPP installation, determining the installation area and ensuring its compatibility with the facility, determining the possible risks that may be encountered and taking measures against these risks; has positive effects in terms of the safety, efficiency, life cycle of the planned power plant, keeping the project cost at the level determined and ensuring sustainability in electricity generation. For this reason, in this study, failures and risks that may be encountered in the SPP plan-project phase were investigated by means of failure mode and effects analysis (FMEA), Pareto and analytical hierarchy process (AHP) systematic and the results obtained were compared.

In literature studies, it is seen that many risk analysis studies such as Fault Tree Analysis (FTA), Weighted Sum Method (WSM), Strengths, weaknesses, opportunities and threats analysis (SWOT), AHP, FMEA, Pareto methods for identifying the risks that may occur in projects targeting electrical energy production using renewable energy resources, have been conducted in order to increase efficiency [7]. [8] conducted a risk analysis study using fuzzy FMEA technique in the use of renewable energy resources. In their studies, they calculated the risk priority numbers (RPN) with FMEA techniques by classifying the risks related to solar, wind and geothermal energy in terms of environmental, financial, technological aspects and construction and operation features. In wind power plant (WPP) projects, one of the renewable energy types, [1] examined failures and risks arising in aerial photography and mapping activities. [9] showed in their study that FMEA techniques provide a more realistic risk analysis to revise the maintenance plan of photovoltaic plants and optimize their efficiency. [10] has studied failure probabilities for SPP photovoltaic systems using FMEA method and revealed that the FMEA approach is a protective method in photovoltaic applications. [11] has determined that there will be an increase in the amount of energy produced by using a thermoelectric cooler in the photovoltaic panel. [12] as a result of his research on FMEA analysis of solar modules, proposed the FMEA method in order to increase the efficiency of solar modules. [13] investigated the suitability for solar farms of Ulleung Island in Korea using Geographical Information Systems (GIS), Fuzzy Sets and AHP. [14] evaluated to economic, environmental and social factors in their study using

AHP and Fuzzy-VIKOR methods in some solar projects in Türkiye.

In this study, the possible risks that may arise in the plan-project stages of SPP projects and the measures that can be taken to prevent these possible risks have been investigated. For this, the opinions of the experts in these subjects in the literature and researches were also taken into consideration. In addition, graphical reviews of these investigated risks were made by ranking their importance within the Pareto analysis. In addition, these risks were re-examined with the AHP method and comparisons of the results specific to the methods were performed. Consequently a new contribution was tried to be made to the literature.

2. Material and Method

2.1. Risk Parameters Used in Analysis

In Solar Power Plant (SPP) construction projects; there are stages such as plan-project, installation, commissioning, operation and maintenance of the power plant. In this study, it is aimed to pre-define the negativities that may arise from the risks that may occur while the SPP plan-project and design phase is carried out. In this study, it is aimed to predefine the risks that may occur during the planning phase of SPP projects. For this reason, the opinions of those who have expertise in SPP projects, (such as map / geodesy and photogrammetry / geomatics, geology, construction, geophysics, machinery, industrial engineers) expressed in the literature and researches, are also considered. As a result, it has been observed that possible failures and risks listed below have been encountered.

- Process No: A1- Failures and risks in solar radiation measurement and determination of weather conditions according to the location of the region,
- Process No: A2- Failures and risks arising from the lack of maps of the land to be installed or the lack and inaccuracies in the maps, (topographic, settlement, vegetation, geology, etc.)
- Process No: A3- Failures and risks made in the slope and aspect calculation of the land where the SPP will be built,
- Process No: A4- Failures and risks made in explaining the geological structure of the land where the SPP will be installed,
- Process No: A5- Lack, failures and risks in the geotechnical and static analysis of the land where the SPP will be installed,
- Process No: A6- Failures and risks in the detection and measurement of the existing and potential landslides of the land where the SPP will be installed,
- Process No: A7- Failures and risks made in the drainage system of the land where a SPP will be installed,
- Process No: A8- Failures and risks in cadastral and ownership / expropriation measurements of the land where SPP will be installed,
- Process No: A9- Failures and risks in calculating the distance of the system to be installed to the distribution lines and center,
- Process No: A10- Failures and risks arising from delays in obtaining permits.

2.2. Failure Mode and Effects Analysis (FMEA), Pareto Analysis, Analytic Hierarchy Process (AHP)

Although there is no standard method for the analysis of risks by hand in SPP facility projects, it is of great importance to create sensitive data, to determine standard comparison criteria, to apply risk analysis methods that are accepted in the literature and have also been successful as a result of the application. Many unexpected risk factors can be encountered in the installation of a solar power plant. For this reason, the risk analysis to be applied in these projects is of great importance in terms of completing the SPP installation on time, keeping the project cost at a specified level, working in a healthy environment and ensuring the continuity of production. FMEA is a systematic method used to identify risks before they harm the project and to implement the necessary measures as soon as possible. Moreover, this method is also widely used in the literature [15-18]. FMEA is a method that adopts systematic solutions to identify potential problems in projects focuses on factor problems and solves problems according to the importance of the factor [19]. FMEA method ensures the quality of the projects in which it is applied, the priority order of the work items, the prevention of mistakes, and the determination of the risks and their effects. For these purposes, 3 basic elements are taken into consideration: probability of occurrence of failure (Table 1), severity of failure (Table 2) and detectability of failure (Table 3) in order to determine the priorities of risks and failures in projects [16, 17, 20, 21].

Table 1. Occurrence probability of risk (O) [16, 20,21]

Occurrence level of failure	Failure occurrence level	Frequency rating
Very high-inevitable	½ or more than	ten
	1/3	nine
High-recurring failure	1/8	eight
	1/20	seven
Medium-rarely failure	1/80	six
	1/400	five
Low-relatively low failure	1/2000	four
	1/15000	three
Very low-less likely failure	1/150000	two
	1/150000 or less	one

Table 2. Risk Severity classification (S) [16]

Effect	Effect of weight-severity	Severity rating
High level hazard coming without notice	It is the type of sudden failure that has a catastrophic effect	ten
Hazard coming without notice	It is a type of failure that comes on suddenly with a high damaging effect.	nine
Very high	It is the type of failure with a devastating impact that causes a project to suffer too much and to a high degree.	eight
High	It is the type of failure that causes too much damage to the equipment.	seven
Medium	It is the type of failure that affects the operation of the system and the applicability of the project.	six
Low	It is the type of failure that causes minor negativities in the project.	five
Very low	It is the type of failure that causes slight damage to the system.	four
Small	It is the type of failure that slows down the implementation of the system.	three
Very small	It is the type of failure that will cause confusion in the realization of the project.	two
No effect	It is the type of failure that has no effect in the application	one

In the planned project, it is necessary to determine the Risk Priority Number (RPN) coefficient for each of the risks that are determined to occur (Table 4). This coefficient is calculated as shown in Eq. (1) with the failure and risk occurrence probability, severity and detectability parameters [15, 16, 17, 20, 21].

RPN= Occurrence (O) x Severity (S) x Detectability (D) (1)

Table 3. Detectability (discoverability) stages (D) [16]

Detectability	Probability of detectability	Rating
Imperceptible	It is not possible to determine the cause of the risk and the failure that follows the risk.	ten
Very far	It is not possible to determine the cause of the risk and it is too far away.	nine
Far	The determination of the cause of the risk is far away.	eight
Very low	Detection of the cause of risk is very low.	seven
Low	Detection of the cause of risk is low.	six
Medium	Determination of the potential cause of failure is medium	five
Above medium	Determination of the potential cause of failure is above medium	four
High	Determination of the potential cause of failure is high	three
Very high	Determination of the potential cause of failure is very high	two
Nearly sure	Determination of the potential cause of failure is nearly sure	one

Table 4. Risk priority number (RPN) and precautions [16]

Risk priority number (RPN)	Precaution and prevention
RPN<40	Low risk- There is no need for prevention
40≤ RPN≤100	Medium risk- prevention may be taken
RPN>100	High risk- prevention must be taken

RPN is a helpful factor in determining which of the failures and risks that may be encountered in projects should be resolved first. However, it is an important guide in taking precautions for failures and risks in projects. Pareto, another of the applied analysis methods, shows the priority status and importance of failures and risks, depending on the threshold values of the failures and risks detected. In this analysis, the general rate is 20% risk number and 80% limit value = 100%. However, these values can be 30% risk number and 70% limit value = 100%, 40% risk number and 60% limit value = 100% depending on the nature of the risks in the project and the type of the project [22]. The meaning of these values is that 20% of the number of risks constitutes 80% of the total risks in the project or 40% of the number of risks constitutes 60% of the total risks in the project. The important point here is that the sum of these two ratios gives the ratio of 100. For example, if the 80% limit value of 10 risks occurs in the first 2 risks, this ratio is expressed as 20% risk number and 80% limit value = 100% ratio. In the study, it was first decided which of these ratios would be appropriate depending on the type of project and risks, and then the analysis made at these ratios was considered as the first alternative (20%-80%=100%, 30%-70%=100%, 40%-60%=100%). The main purpose of Pareto analysis is to represent the vast majority of problems with a small number of risk factors. With this method, it is aimed to take measures at low cost for a few risks that are important in the projects and also make up a large percentage of the problems in the whole project. In addition, it is aimed that the progress of the project is not damaged. AHP, on the other hand, ensures the practitioners to consider all possibilities together with all factors and perform pairwise comparison of probabilities under relative priorities [23]. AHP is an easy to use and straightforward method and it is a highly preferred method by decision makers because takes into account the user subjective criteria in multi-criteria decision analysis (MCDA) [24-26]. The most common problem encountered in MCDA applications is to be able to determine the superiority, importance or weight in order to be able to select the factor by considering more than one option among different options. In the solution of this problem, AHP, which can be used effectively, is preferred because it is a mathematical method in decision making that handles all variables together by considering the priorities of both the individual and the group. AHP starts with determining the comparative decision making and preference matrix. In order to make a pairwise comparison, a pairwise comparison matrix is created using the AHP evaluation scale (Table 5) as suggested

by [27] and [28]. When creating a pairwise comparison matrix, it should be answered which one of the criteria pairs takes precedence over the other and what should be the importance of this priority criterion than the other.

Table 5. AHP evaluation scale [27, 28]

Importance degree	Description
1	Equally important
3	1st criterion slightly more important than 2nd
5	1st criterion moderately more important than 2nd
7	1st criterion much more important than 2nd
9	1st criterion is absolutely more important than 2nd
2,4,6,8	Intermediate values are used in cases that require agreement

The next step after the creation of comparison matrix is to calculate the weights of the criteria, spite that AHP has a consistent systematic in itself, the results will be based on the consistency that emerges as a result of comparing the existing criteria with each other by the practitioners, hence, after the weight calculation of the criteria, the Consistency ratio (CR), which means likelihood in a randomly generated matrix gradation, needs to be calculated [29]. [30] suggests the rate of 10% as a maximum consistency rate. If a value found is above this value the pairwise comparison matrix should be reconstructed [31]. The consistency rate is calculated by the formula of Eq. (2) depending on the random index value (RI) and consistency index value (CI) (Eq. (3)).

$$\mathrm{CR}=\frac{\mathrm{CI}}{\mathrm{RI}} \quad (2)$$

$$\mathrm{CI}=\frac{(\lambda-n)}{(n-1)} \quad (3)$$

Here λ is consistency vector mean and n is number of criteria.

3. Results and Discussion

Depending on the location of the area where the SPP installation is planned, parameters such as solar radiation, weather conditions, annual insolation, temperature, rainfall, snow and fog are among the most important criteria, because these parameters directly affect the amount and sustainability of the energy to be obtained from the power plant to be established. In this context, up-to-date, detailed and precise maps, plans and sections of the land where the project will be located should be prepared in the SPP installation. In addition, it is necessary to prepare 3 dimensional digital elevation models. For these reasons, it is also important to prepare simulations according to the slope and the aspect direction of the land where the SPP installation is planned. In the first phase of this work, in order to pre-define the negative situations that may arise from the risks that may occur while the plan-project phase is carried out for the purpose of SPP installation. In the first stage of this study, the risks that may occur in SPP installation projects were defined. For this purpose, the opinions of experts (mapping / geodesy and photogrammetry / geomatics, geology, construction, geophysics, machinery, industrial engineers, etc.) expressed in the literature and researches were also taken into consideration and the failures and risks encountered at this stage were investigated. Ten risks (Process No: A1-A10) detected as a result of the research were examined in FMEA systematic. In the second stage, as in the determination of failures and risks, likewise, taking into account the suggestions and ideas of experts on SPP installation, the probability of occurrence of these failures and risks (Table 1), their severity (Table 2) and their detectability (discoverability) (Table 3) were discussed together and RPN has been determined. Later, using Table 4, the risk group belonging to the risk was determined. RPN numbers were re-evaluated, taking into account the measures to be implemented in order to prevent the occurrence of failures and risks whose probability of occurrence was determined. With the implementation of the precautions, it was observed that these failures and risks were included in the low risk group (Table 6).

Table 6. Determination of failures and risks encountered during the project of SPPs with FMEA form

DETERMINATION OF FAILURES AND RISKS ENCOUNTERED DURING THE PROJECTING OF SOLAR POWER PLANTS
---FMEA FORM---

RPL=OCCURRANCExSEVERITYxDETECTIBILITY

OCCURRANCE	SEVERITY	DETECTIBILITY	RPN VALUE (Risk Priority Number)
1-2 Very Low	1-2 No effect or slightly	1. Sure 2.Very High	RPL<40 No need to take precaution LOW RISK
3-4 Low	3-4 Slightly	3. High 4. Above Average	40≤ RPL ≤100 Caution can be taken MEDIUM RISK
5-6 medium	5-6 Medium	5. Medium 6.Low Level	RPL >100 Caution must be taken. HIGH RISK
7-8 High	7-8 Serious	7. Very Low 8. Little	
9-10 Very High	9-10 Very serious	9.Very Little 10. Undetectible	

Process No	POTENTIAL CAUSES OF FAILURE		RISK EVALUATION					PRECAUTION ACTIVITY	RESPONSIBILITY	RISK EVALUATION				
	Failure	Reference	Occurrance	Severity	Detectibility	R.P.N	Importance			Occurrance	Severity	Detectibility	R.P.N	Importance
A.1	Failures and risks in solar radiation measurement and determination of weather conditions according to the location of the region	Regulations for wind and solar measurements for wind and solar energy license applications Regulations on meteorological data assessment.	5	7	5	175	HIGH RISK	The solar radiation coming to the land where the solar power plant will be installed should be calculated very well, taking into account the long years and atmospheric conditions. In addition, daily, weekly, monthly and annual periodic controls should be made and the effects of atmospheric effects such as temperature, precipitation and humidity on the power plant should be examined.	Meteorology Engineers	2	3	1	6	LOW RISK
A.2	Failures and risks arising from the lack of maps of the land to be installed or the lack and inaccuracies in the maps (topographic, settlement, vegetation, geology, etc.)	Large Scale Map and Map Information Production Regulation	7	9	5	315	HIGH RISK	In the field where the solar power plant will be established, the errors and deficiencies that will occur in the topographic maps should be corrected and completed by using terrestrial, aerial photography (photogrammetry) or remote sensing systems. These measurements should be adapted to Geographical Information systems and the map data including many data should be evaluated as a whole by using merging analysis. If the topographic measurements are outside the error limits, these measurements should be checked in the field and repeated.	Surveying / Geodesy and Photogrammetry / Geomatics Engineers	2	3	2	12	LOW RISK
A.3	Failures and risks made in the slope and aspect calculation of the land where the solar power plant will be built	Large Scale Map and Map Information Production Regulation	6	6	5	180	HIGH RISK	Topographic measurements should be checked on the field where solar power plant will be built and renewed if necessary. In addition, 3D digital elevation models of the field should be created and slope calculations should be made again on these models. If necessary, these analyzes and controls should be provided with geographic information systems.	Surveying / Geodesy and Photogrammetry / Geomatics Engineers and Geology Engineers	2	3	3	18	LOW RISK
A.4	Failures and risks made in explaining the geological structure of the land where the solar power plant will be installed	Regulations regarding geological maps, geology and geophysical studies.	6	9	5	270	HIGH RISK	The stratigraphic, lithological, geological features and discontinuity environment of the area where the solar power plant will be installed and its surroundings should be explained. However, map and section drawings should be made, well or drilling studies should be applied using geophysical methods, as well as ground and underground conditions should be explained.	Geology and Geophysics Engineers	2	3	2	12	LOW RISK
A.5	Lack, failures and risks in the geotechnical and static analysis of the land where the solar power plant will be installed	Regulations regarding geological maps, geology and geophysical studies.	6	9	7	378	HIGH RISK	According to the laboratory test results, the soil and soil structure properties, the chemical structure of the soil and the groundwater level should be determined. In addition, the solar panel construction and inverter weight that is planned to be used in the power plant area should be determined. Again, calculations should be made to prevent the solar panels from falling against the wind and the weight of snow. However, the chemical properties of concrete must be determined for the foundation.	Geology, Geophysics and Mechanical Engineers	4	3	3	36	LOW RISK
A.6	Failures and risks in the detection and measurement of the existing and potential landslides of the land where the solar power plant will be installed	Large Scale Map and Map Information Production Regulation	6	9	6	324	HIGH RISK	Periodic GPS and leveling studies should be carried out in the field where the solar power plant will be established. In addition, deformation and displacement (unit displacement, elongation, shortening, curvature, etc.) movements in horizontal and vertical directions should be determined. Topographic measurements in the field should be made with millimeter precision. In addition, deformation vectors in the field should be determined. Again, maps that reflect the topographical features of the region should be produced. In addition, the geological and topographical sections of the region should be examined and detailed field studies should be done. As a result, if there is no possibility of landslides in the field, planning studies of the solar power plant project should be done.	Geology, Geophysics Engineers, Surveying / Geodesy and Photogrammetry / Geomatics Engineers	3	3	3	27	LOW RISK
A.7	Failures and risks made in the drainage system of the land where a solar power plant will be installed	Regulations on meteorological data assessment. Large Scale Map and Map Information Production Regulation	5	6	4	120	HIGH RISK	The adequacy of environmental drainage should be checked, and the risk of flooding due to precipitation should be calculated. In addition, if the land does not have a risk in terms of flood / overflow potential, solar power plant project planning studies should be carried out.	Geology, Geophysics and Mechanical Engineers	3	3	2	18	LOW RISK
A.8	Failures and risks in cadastral and ownership / expropriation measurements of the land where solar power plant will be installed	Large Scale Map and Map Information Production Regulation Laws and regulations regarding expropriation	5	7	4	140	HIGH RISK	If there are deficiencies in terms of cadastral work in the area where the solar power plant will be established, the necessary topographic measurement and observation studies should be carried out.The studies can be carried out by geodetic, photogrammetric and remote sensing systems, as well as by digitizing the existing and reliable sheets.	Surveying / Geodesy and Photogrammetry / Geomatics Engineers	2	3	2	12	LOW RISK
A.9	Failures and risks in calculating the distance of the system to be installed to the distribution lines and centre	Large Scale Map and Map Information Production Regulation Technical and administrative specifications of the project and related regulations	4	7	4	112	HIGH RISK	Analysis techniques and planning such as geographic information systems based network analysis, proximity analysis and location analysis should be used in the areas where a solar power plant is planned to be built. Analysis accuracy should be further increased by using accurate, up-to-date and sensitive database information in accordance with these analyzes.	Surveying / Geodesy and Photogrammetry / Geomatics Engineers	2	3	4	24	LOW RISK
A.10	Failures and risks arising from delays in obtaining permits	Regulation on Solar Energy Based Electricity Generation Plants, Regulation on Technical Evaluation of Applications, Regulations of the relevant Public Institutions	5	7	3	105	HIGH RISK	Regarding the solar power plant project, establishment permits must be obtained from the relevant public institutions and organizations.In addition, the project for this power plant should be prepared and approved. However, after the establishment, it must be accepted by official institutions.	Project Management Engineers	2	2	2	8	LOW RISK

In the third stage of the study, Pareto Analysis systematic was applied in order to determine the order of importance and priority of the identified failures and risks. Two alternatives are considered in the study and the first alternative is 40% Risk Number and 60% Threshold Value=100% Ratio. The second alternative is at which risk the 80% Threshold Value is obtained in the Project. In the applied Pareto analysis, the first alternative, 40% Risk Number and 60% Threshold Value=100% ratio was chosen. This ratio was chosen from the rates of 20%-80%=100%, 30%-70%=100%, 40%-60%=100% (It is important that the total is 100%.). In addition, while choosing this ratio, the

number of RPNs and cumulative risk values in the project was also taken into account. According to the Pareto Analysis applied, when the ratios (40%-60%=100%) are considered first, it is seen that the risks of A5, A6, A2, A4 come to the fore during the design phase of SSP projects. With this alternative, it can be commented that 40% of the risks determined during the design phase of SSP projects constitute 60% of all problems in the project. (Table 7, Fig. 1). When these risks are analyzed in a second Pareto analysis according to this threshold ratio, it is seen that A5, A6 risks come to the fore. (Table 8, Fig. 2). In the second alternative in the study, according to the rule of 20%-80%=100%, the issue of which risk threshold value of 80% corresponds to the number of risks in the projecting and design stage of project was investigated. In the ratios of 20% Risk Number and 80% threshold value = 100%, 80% threshold value ratio is taken into consideration. Accordingly, in the second alternative research, it was seen that the 80% limit value in the project coincided with the first 6 risk numbers. Accordingly, A5, A6, A2, A4, A3, A1 risks are on the forefront of the SPP project during the design phase for this threshold value (Table 7, Fig. 1). With this alternative, it can be interpreted that 60% of the risks identified during the SPP installation phase constitute 80% of all the problems in the project. When these risks are analyzed in a second Pareto analysis according to this threshold ratio, it is seen that A5, A6, A2, A4 risks come to the fore (Table 9, Fig. 3).

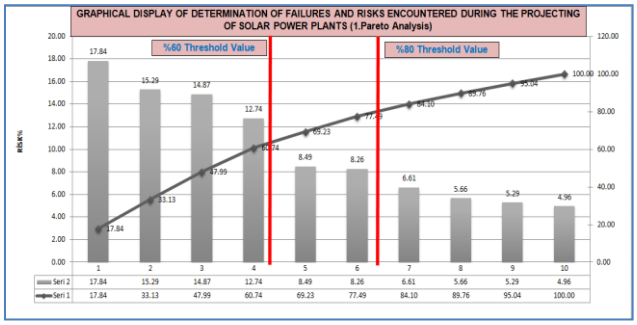

Figure 1. Graphic display of possible risks in the project of SPPs in Pareto system ((first alternative 40% Risk number and 60% limit value=100% ratio) and (second alternative 80% limit value obtained risk number))

Table 7. Examining the possible risks to occur in the SPP project in the 1st stage Pareto systematic ((first alternative 40% risk number and 60% limit value=100% ratio) and (second alternative risk number where 80% limit value is obtained) together)

DETERMINATION OF FAILURES AND RISKS ENCOUNTERED DURING THE PROJECTING OF SOLAR POWER PLANTS (1.PARETO ANALYSIS)						
SEQUENCE NO	FAILURE MODE	PROCESS NO	RPN VALUE	RISK(%)	CUMULATIVE RISK %	RISK STATE
1	Lack, Failures and risks in the geotechnical and static analysis of the land where the solar power plant will be installed	A5	378	17.84	17.84	HIGH RISK
2	Failures and risks in the detection and measurement of the existing and potential landslides of the land where the solar power plant will be installed	A6	324	15.29	33.13	HIGH RISK
3	Failures and risks arising from the lack of maps of the land to be installed or the lack and inaccuracies in the maps (topographic, settlement, vegetation, geology, etc.)	A2	315	14.87	47.99	HIGH RISK
4	Failures and risks made in explaining the geological structure of the land where the solar power plant will be installed	A4	270	12.74	60.74	HIGH RISK
5	Failures and risks made in the slope and aspect calculation of the land where the solar power plant will be built	A3	180	8.49	69.23	HIGH RISK
6	Failures and risks in solar radiation measurement and determination of weather conditions according to the location of the region	A1	175	8.26	77.49	HIGH RISK
7	Failures and risks in cadastral and ownership / expropriation measurements of the land where solar power plant will be installed	A8	140	6.61	84.10	HIGH RISK
8	Failures and risks made in the drainage system of the land where a solar power plant will be installed	A7	120	5.66	89.76	HIGH RISK
9	Failures and risks in calculating the distance of the system to be installed to the distribution lines and centre	A9	112	5.29	95.04	HIGH RISK
10	Failures and risks arising from delays in obtaining permits	A10	105	4.96	100.00	HIGH RISK

%60 Threshold Value

%80 Threshold Value

Table 8. Determination of failures and risks encountered during the project of SPPs with 2.Pareto analysis with 60% threshold Value

DETERMINATION OF FAILURES AND RISKS ENCOUNTERED DURING THE PROJECTING OF SOLAR POWER PLANTS (2.PARETO ANALYSIS) (60% THRESHOLD VALUE)						
SEQUENCE NO	FAILURE MODE	PROCESS NO	RPN VALUE	RISK(%)	CUMULATIVE RISK %	RISK STATE
1	Lack, Failures and risks in the geotechnical and static analysis of the land where the solar power plant will be installed	A5	378	29.37	29.37	HIGH RISK
2	Failures and risks in the detection and measurement of the existing and potential landslides of the land where the solar power plant will be installed	A6	324	25.17	54.55	HIGH RISK
3	Failures and risks arising from the lack of maps of the land to be installed or the lack and inaccuracies in the maps (topographic, settlement, vegetation, geology, etc.)	A2	315	24.48	79.02	HIGH RISK
4	Failures and risks made in explaining the geological structure of the land where the solar power plant will be installed	A4	270	20.98	100.00	HIGH RISK

%60 Threshold Value

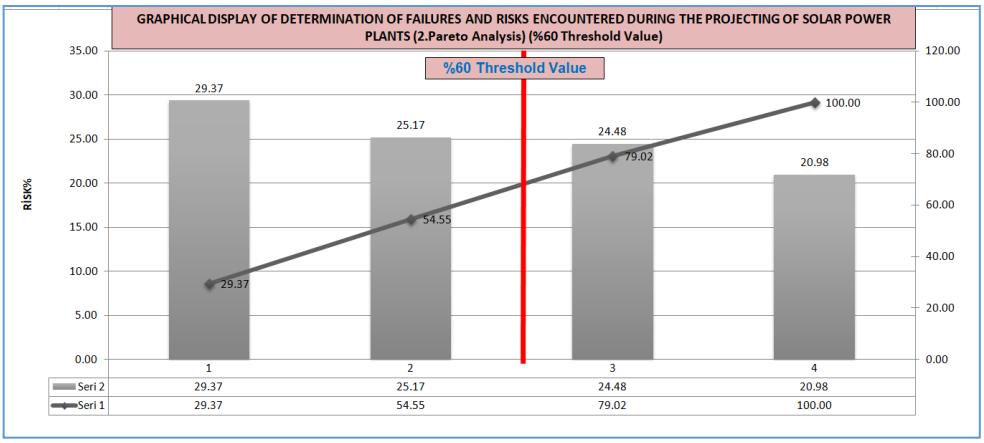

Figure 2. Graphical display of determination of failures and risks encountered during the project of SPPs with 2.Pareto analysis with 60% threshold value.

Table 9. Determination of failures and risks encountered during the project of SPPs with 2.Pareto analysis with 80% threshold value

DETERMINATION OF FAILURES AND RISKS ENCOUNTERED DURING THE PROJECTING OF SOLAR POWER PLANTS (2.PARETO ANALYSIS) (80% THRESHOLD VALUE)						
SEQUENCE NO	FAILURE MODE	PROCESS NO	RPN VALUE	RISK(%)	CUMULATIVE RISK %	RISK STATE
1	Lack, Failures and risks in the geotechnical and static analysis of the land where the solar power plant will be installed	A5	378	23.02	23.02	HIGH RISK
2	Failures and risks in the detection and measurement of the existing and potential landslides of the land where the solar power plant will be installed	A6	324	19.73	42.75	HIGH RISK
3	Failures and risks arising from the lack of maps of the land to be installed or the lack and inaccuracies in the maps (topographic, settlement, vegetation, geology, etc.)	A2	315	19.18	61.94	HIGH RISK
4	Failures and risks made in explaining the geological structure of the land where the solar power plant will be installed	A4	270	16.44	78.38	HIGH RISK
5	Failures and risks made in the slope and aspect calculation of the land where the solar power plant will be built	A3	180	10.96	89.34	HIGH RISK
6	Failures and risks in solar radiation measurement and determination of weather conditions according to the location of the region	A1	175	10.66	100.00	HIGH RISK

%80 Threshold Value

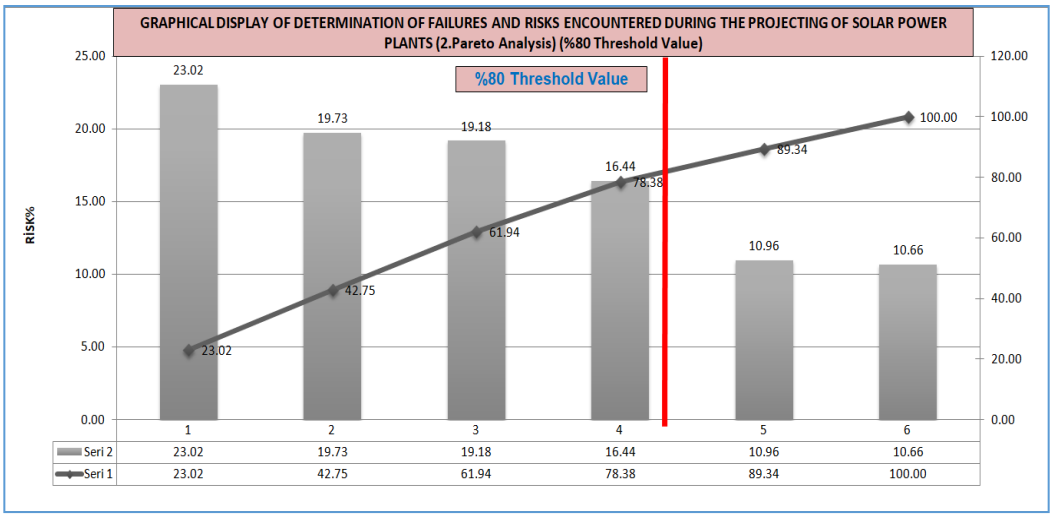

Figure 3. Graphical display of determination of failures and risks encountered during the project of SPPs with 2.Pareto analysis with 80% threshold value.

In the fourth stage of the study, the weight of each risk criterion was calculated with the comparison matrix created using AHP for the risks that occur in the plan-project phase of SPP installation. The pairwise comparison matrix is shown in Table 10, and the resulting weight matrix is shown in Table 11. The factors with the highest weight obtained from the comparison matrix were determined as A5, A6, A2, A4, A1, A3, A8, A7, A9, A10, respectively.

Table 10. Pairwise comparison matrix

Parameters	A1	A2	A3	A4	A5	A6	A7	A8	A9	A10
A1	1	1/5	3	1/2	1/9	1/7	3	3	2	2
A2		1	3	2	1/2	1	7	5	7	7
A3			1	1/3	1/5	1/5	3	2	3	3
A4				1	1/3	1/3	5	3	5	5
A5					1	3	7	5	7	7
A6						1	5	3	5	5
A7							1	1/2	2	2
A8								1	2	2
A9									1	1
A10										1

Table 11. Weight matrix

Parameters	A1	A2	A3	A4	A5	A6	A7	A8	A9	A10	Weight
A1	0.04	0.03	0.14	0.04	0.03	0.02	0.09	0.13	0.06	0.06	0.06
A2	0.19	0.18	0.14	0.19	0.16	0.15	0.21	0.21	0.20	0.20	0.18
A3	0.01	0.06	0.05	0.03	0.06	0.03	0.09	0.09	0.08	0.08	0.06
A4	0.08	0.09	0.14	0.09	0.11	0.05	0.15	0.13	0.14	0.14	0.11
A5	0.35	0.35	0.23	0.28	0.32	0.46	0.21	0.21	0.20	0.20	0.28
A6	0.27	0.18	0.23	0.28	0.11	0.15	0.15	0.13	0.14	0.14	0.18
A7	0.01	0.02	0.01	0.02	0.05	0.03	0.03	0.02	0.06	0.06	0.03
A8	0.01	0.03	0.02	0.03	0.06	0.05	0.06	0.04	0.06	0.06	0.04
A9	0.02	0.03	0.02	0.02	0.05	0.03	0.01	0.02	0.03	0.03	0.03
A10	0.02	0.03	0.02	0.02	0.05	0.03	0.01	0.02	0.03	0.03	0.03
Sum of Weights	1	1	1	1	1	1	1	1	1	1	1

The "Consistency ratio" (CR) has been calculated as 0.06 which was determined in order to detect the values in the comparison matrix created and the obtained weights are consistent or not. Since the ratio obtained is below 0.10 suggested by [30], it has been concluded that the values found as a result of the pairwise comparison matrix are consistent with each other.

4. Conclusion and Suggestions

In the planning and projecting phase of SPP projects, it is an important issue to determine the location, geometry and geological and geophysical conditions of the land where the SPP facility to be installed. In these projects, in the process of creating maps, sections and geological sections, field observations and studies, drilling activities, engineering measurements and evaluating all these studies together with previous studies are very important. In this study, failures and risks that may occur during the implementation of the plan-project stage, which is the first stage of SPP installation, have been investigated in FMEA Pareto and AHP systematic. In addition, the measures to be taken against these failures and risks have been determined by taking into account the opinions of experts in the literature and researches. As a result of the review of the FMEA systematic analysis, failures and risks in the high risk group and the precautions of the said were determined and afterwards, Pareto analysis was performed. In the first alternative Pareto analysis, it was determined that 4 failures and risks with process numbers A5, A6, A2 and A4 are important, depending on the 60% threshold value (40% Risk Number and 60% Threshold Value=100% ratio). This ratio was chosen from the rates of 20%-80%=100%, 30%-70%=100%, 40%-60%=100%. (It is important that the total is 100%). When the second Pareto analysis made in this first alternative group, it was observed that the risks A5 and A6 came to the fore according to 60% threshold value. In the second alternative in the study, according to the rule of 20%-80%=100%, the issue of which risk threshold value of 80% corresponds to the number of risks in the project was investigated. In the ratios of 20% Risk Number and 80% Threshold Value = 100%, 80% threshold value ratio is taken into consideration. When the examination is made depending on the 80% threshold value in the Pareto analysis, it has been revealed that 6 failures and risks with process numbers A5, A6, A2, A4, A3 and A1 need to be taken into consideration more while working on the plan-project phase of SPP installation. After that, in the second Pareto analysis made in this second alternative group, it was observed that the risks with numbers A5, A6, A2, A4 and A3 came to the fore according to 80% threshold value. For SPP projects, Pareto analysis was applied twice in both alternatives. In the project phase, it is aimed to find as few risks as possible, which constitute the majority of the problem. In addition, in the progress of SPP projects, a small number of risks have been identified, making it possible to solve most of the problems in the project.

As a result of the analysis made with AHP, it was revealed that there are 4 failures and risks with process numbers A5, A6, A2 and A4, and more attention should be paid to the plan-project phase of the SPP installation. The failures and risks that may occur during the planning-project phase of the SPP installation have been analyzed using FMEA, Pareto and AHP methods, taking into account the opinions of the relevant experts in the literature and researches. When the results are compared, the requirement to consider failures and risks with process numbers A5, A6, A2 and A4 in all 3 methods is highly recommended. Among these risks, it has been determined that the risks A5 and A6 are more important. This situation reveals that the results of the analysis applications are quite compatible with each other. The methods applied in the study are very important in terms of producing results that are compatible with each other and showing the reliability of the opinions of experts in the literature and researches. With this work carried out, contribution was made to the creation of risk criteria with minimum level that should be included in the SPP standard risk analysis review lists, moreover, it is emphasized that FMEA, Pareto analysis and AHP methods are very powerful methods in performing risk analysis of SPP installation.

Contributions of the Authors

All authors contributed equally to the study.

Conflict of Interest Statement

There is no conflict of interest between the authors.

Statement of Research and Publication Ethics

The study is complied with research and publication ethics.

References

[1] E. Can, "Analysis of risks that are based on the aerial photography used in photogrammetric monitoring maps for environmental wind power energy plant projects", *Environ Monit Assess.,* vol. 191, number. 746, 2019, DOI: 10.1007/s10661-019-7944-8

[2] U. U. Dündar, and M. A. Ertem, *Risk assessment guide for the installation of solar power plants,* TMMOB Chamber of Mechanical Engineers, pp.27, Ankara, 2016.

[3] B. Çetin, and H. Avcı, "Technical and economic analysis of the conversion on an existing coal-fired thermal power plant to solar-aided hybrid power plant", *Journal of the Faculty of Engineering and Architecture of Gazi University,* vol. 35, no. 2, pp. 1027-1045, 2020, DOI: 10.17341/gazimmfd.418417

[4] Alternatürk, "Usage areas of solar energy". 2020. https://www.alternaturk.org/gunes-enerjisi-kullanim-alanlari.php [Accessed: June 16, 2020].

[5] Energy Five Clean Energy Portal, "What are the advantages and disadvantages of solar energy?". 2021. https://www.enerjibes.com/gunes-enerjisinin-avantajlari-dezavantajlari-nelerdir/ [Accessed: January 03, 2021].

[6] Y. Şimşek, "Risk management approach and risk analysis in solar thermal energy projects", M.Sc Thesis, ITU Energy Institute Department of Energy Science and Technology, Istanbul, Türkiye pp. 106, 2014.

[7] S. Pervee, H. Ashfaq, and M. Asjad, "Reliability assessment of solar photovoltaic systems based on fuzzy fault tree analysis", *Life Cycle Reliab Saf Eng,* vol. 8, pp. 129–139, 2019, DOI: 10.1007/s41872-018-0068-2

[8] H. Yörükoğlu, C. Özkale, B. Özkan, and C. Çelik, "The analysis of the risks of renewable energy resources by using fuzzy FMEA technique", *Dumlupınar University Journal of Social Sciences Special Issue of XIV. International Symposium on Econometrics, Operations Research and Statistics*, pp. 227-242, October 2014.

[9] M. Villarini, V. Cesarotti, L. Alfonsi, and V. Introna, "Optimization of photovoltaic maintenance plan by means of a FMEA approach based on real data", *Energy Convers Manag*, vol. 152, pp. 1–12, 2017, DOI: 10.1016/j.enconman.2017.08.090

[10] A. Colli, "Failure mode and effect analysis for photovoltaic systems", Renew Sust Energ Rev, vol 50, pp. 804–809, 2015, DOI: 10.1016/j.rser.2015.05.056

[11] A. Yılancı, "Performance analysis of a photovoltaic panel cooled by thermoelectric effect", *Journal of the Faculty of Engineering and Architecture of Gazi University*, vol. 35, no. 2, pp. 619-634, 2020, DOI: 10.17341/gazimmfd.494485

[12] M. Molhanec, *Model based FMEA method for solar modules*, Proceedings of 36th Int. Spring Seminar on ElectronicsTechnology, pp. 183-188, 08-12 May 2013, DOI: 10.1109/ISSE.2013.6648239

[13] J. Suh, and J. R. S. Brownson, "Solar farm suitability using geographic information system fuzzy sets and analytic hierarchy processes: Case study of Ulleung Island, Korea", *Energies*, vol. 9, issue. 8, no. 648, 2016, DOI: 10.3390/en9080648

[14] M. K. Anser, M. Mohsin, Q. Abbas, and I. S. Chaudhry, "Assessing the integration of solar power projects: SWOT-based AHP–F-TOPSIS case study of Turkey", *Environmental Science and Pollution Research*, vol. 27, pp. 31737–31749, 2020, DOI: 10.1007/s11356-020-09092-6

[15] H. C. Liu, L. Liu, and N. Liu, "Risk evaluation approaches in failure mode and effects analysis: A literature review", *Expert Syst Appl*, vol. 40, no. 2, pp. 828-838, 2013, DOI: 10.1016/j.eswa.2012.08.010

[16] B. Akın, *Failure Mode and Effect Analysis (FMEA) in ISO 9000 Applications, Businesses*. Bilim Teknik Yayınevi, Istanbul, pp. 182, (in Turkish), 1998.

[17] Y. M. Wang, K. S. Chin, G. K. K. Poon, and J. B. Yang, "Risk evaluation in failure mode and effects analysis using fuzzy weighted geometric mean", *Expert Syst Appl*, vol. 36, issue. 2, pp. 1195-1207, 2009, DOI: 10.1016/j.eswa.2007.11.028

[18] K. S. Chin, Y. M. Wang, G. K. K. Poon, and J. B. Yang, "Failure mode and effects analysis using a group-based evidential reasoning approach", *Computers & Operations Research*, vol. 36, issue. 6, pp. 1768–1779, 2009, DOI: 10.1016/j.cor.2008.05.002

[19] S. B. Tsai, J. Yu, L. Ma, F. Luo, J. Zhou, Q. Chen, and L. Xu, "A study on solving the production process problems of the photovoltaic cell industry", *Renew Sustain Energy Rev*, vol. 82, pp. 3546–3553, 2018, DOI: 10.1016/j.rser.2017.10.105

[20] X. Su, Y. Deng, S. Mahadevan, and Q. Bao, "An improved method for risk evaluation in failure modes and effects analysis of aircraft engine rotor blades", *Eng Fail Anal*, vol. 26, pp. 164-174, 2012, DOI: 10.1016/j.engfailanal.2012.07.009

[21] N. Xiao, H. Z. Huang, Y. Li, L. He, and T. Jin, "Multiple failure modes analysis and weighted risk priority number evaluation in FMEA", *Eng Fail Anal*, vol. 18, pp. 1162-1170, 2011, DOI: 10.1016/j.engfailanal.2011.02.004

[22] S. Özcan, "Pareto analysis, one of statistical process control technics, and an application in the cement industry", *Sivas Cumhuriyet University Journal of Economics and Administrative Sciences*, vol. 2, no. 2, pp. 151-174, 2001.

[23] A. Saral, and N. Musaoğlu, Flood risk analysis with the Multi Criteria Decision Analysis and information diffusion methods. 13. Türkiye Surveying Scientific and Technical Conference, Ankara, 18-22. April 2011.

[24] A. Kuruüzüm, and N. Atsan, "The analytic hierarchy process approach and its applications in business", *Akdeniz IIBF Journal*. Vol. 1, no. 1, pp. 83-105, 2001.

[25] N. Ömürbek, S. Üstündağ, and Ö. C. Helvacıoğlu, "Use of analytic hierarchy process (AHP) in location decision: A study in Isparta Region", *Journal of Management Sciences*, vol. 11, no. 21, pp. 101-116, 2013.

[26] M. Soba, and T. Bildik, "Determining the selection of faculty place in towns by using analytic hierarchy process", *Kafkas University Journal of Economics and Administrative Sciences Facult*, vol. 4, no. 5, pp. 51-63, 2013.

[27] T. L. Saaty, "A scaling method for priorities in hierarchical structures", *Journal of Mathematical Psychology*, vol. 15, pp. 234-281, 1977, DOI: 10.1016/0022-2496(77)90033-5

[28] T. L. Saaty, "The analytic hierarchy and analytic network measurement processes: Applications to decisions under risk", *European Journal of Pure and Applied Mathematics*, vol. 1, no. 1, pp. 122-196, 2008, DOI: 10.29020/nybg.ejpam.v1i1.6

[29] M. Mutlu, and M. Sarı, "Multi-criteria decision making methods and use of in mining industry", *Scientific Mining Journal*, vol. 56, no. 4, pp. 181-196, 2017.

[30] T. L. Saaty, *Fundamentals of Decision Making and Priority Theory*. 2. Edition, RWS Publications, pp. 478, Pittsburgh, 2000.

[31] S. Drobne, and A. Lisec, "Multi-attribute decision analysis in GIS: weighted linear combination and ordered weighted averaging", *Informatica an International Journal of Computing and Informatics*, vol. 33, no. 4, pp. 459-474, 2009.

Bitlis Eren Üniversitesi Fen Bilimleri Dergisi
BİTLİS EREN UNIVERSITY JOURNAL OF SCIENCE
ISSN: 2147-3129/e-ISSN: 2147-3188
VOLUME: 11 NO: 4 PAGE: 1073-1083 YEAR: 2022
DOI: 10.17798/bitlisfen.1171266

Design of Wearable Patient Lying Position Tracking and Warning System to Prevent Pressure Injury

Ali Erdem KOŞUN[1], Mehmet Yakup ATÇI[1], Ahmet Burak TATAR[2*], Alper Kadir TANYILDIZI[1], Beyda TAŞAR[1]

[1]*Faculty of Engineering, Department of Mechatronics Engineering, Fırat University, Elazığ, 23200, Turkey*
[2]*Faculty of Engineering, Department of Mechanical Engineering, Adıyaman University, Adıyaman, 02040, Turkey*
(ORCID: 0000-0002-5221-2879) (ORCID: 0000-0003-0676-8224) (ORCID: 0000-0001-5848-443X) (ORCID: 0000-0003-3324-5445) (ORCID: 0000-0002-4689-8579

Keywords: Pressure injuries, lying position tracking and classification, inertial measurement unit.

Abstract
Within the scope of this study, a wearable lying position tracking system equipped with inertial measurement unit sensors has been developed to prevent the formation of pressure injuries in bedridden patients. Three inertial measurement unit sensors were placed on the patient's chest, one on the right upper leg and the other on the left upper leg, and the angular orientation expressions of the limbs were calculated. Datasets were created for three different lying positions, and machine learning models were used to classify the patient's lying position. The success of the classifiers was compared by calculating the accuracy, sensitivity, specificity, precision and F1 score values. The average accuracy values in the lying position classification were obtained as 99.506%, 99.977%, 99.972%, 99.838%, and 99.967% respectively, using linear discriminant analysis, k-nearest neighbor, decision tree, support vector machine and random forest classification methods. The highest accuracy rate was obtained as a result of the k-nearest neighbor method with high variation. The time that the person remained fixed in the determined lying position was also calculated, and if it remained longer than the specified time, an audible warning signal was generated to change the position. Thus, it has been tried to prevent the person to apply pressure by lying on a single muscle group and tissue for a long time and to prevent the formation of pressure injuries over time.

1. Introduction

Prolongation of people's life expectancy, unhealthy diet, diabetes, etc. Pressure injuries from prolonged sitting and laying have become more common as a result of diseases and sedentary lifestyles, particularly in the elderly and the disabled [1]. Pressure injuries, also known as bedsores and pressure sores, are more common in people who use wheelchairs and those who are paralyzed and must lie down for long periods of time as Figure 1

*Corresponding author: ahmetburakttr23@gmail.com
Received:05.09.2022, Accepted: 27.10.2022

Figure 1. Bed- and wheelchair-bound patient with high risk of pressure injuries

The main factors contributing to pressure injuries;

- the skin without changing the position frequently bed, chair, etc. is placed on it.
- skin contact of the patient with urine or feces,
- diabetes,
- injuries,
- unhealthy diet
- several medical conditions that affect circulation system of the blood

Localized lesions known as pressure sores are caused by a reduction in blood supply to immobile bodily parts that are subjected to persistent pressure [2]. Over the bony prominence, these lesions typically develop in the skin and subcutaneous tissues [3].

In the European Pressure Injuries Advisory Panel (EPUAP), pressure injuries are divided into four main stages according to tissue type and wound width and depth [4]. From Stage 1 to Stage 4, there is an increase in the depth of tissue injury and the degree of damage at the wound site [5]. These stage of pressure injuries are shown in Figure 2.

Figure 2. Stages of pressure injury [5]

Stage 1 involves undamaged skin in the pressure injury area and red skin on the surface. The skin is still red even when the pressure is released, primarily because this is muscular tissue. Because of its aerobic metabolism, muscle tissue has a greater need for oxygen than the skin surface. Deep muscle levels experience lesions due to inadequate blood flow. Stage 1 pressure injuries may cause the area they are applied to to become uncomfortable, warm, or softer than the nearby tissues. Stage 2 involves damage and opening to the top layer of skin in the pressure sore location. Skin tissue damage and pink or red coloration appear where the skin layer is lacking. Where the pressure injury occurred, stage 3 damage extends to the adipose tissue and may include dead tissue. The deepest ulcer from a pressure injury occurs in stage 4, and the damage may even affect the bones and/or muscular tissue. Pressure injuries in stage 4 may contain dead tissue. The quality of life is impacted by pressure injuries since they are so painful.

Despite the fact that most inpatients get pressure injuries, if they are detected early enough, they can be averted [6]. Integrative medicine and a multidisciplinary team approach are necessary for the prevention and treatment of pressure ulcers [7]. Depending on the nature and extent of the pressure damage, a different course of treatment may be necessary. To prevent infection when the wound is still healing, it needs to be gently cleaned and properly dressed. If poor circulation and other risk factors such malnutrition, diabetes, vascular disease and inactivity are constantly present together with a pressure injury that is in Stage 3 or Stage 4, healing could take many months.

Between 10% and 18% of pressure injuries occur in intensive care units, and 0%-29% in home care units. Even with all the safeguards adopted as part of preventive care, pressure injuries still happen [8]. Pressure sores are an important health problem worldwide due to high care costs and also one of the most important indicators of the quality of care in

hospitals [9-12]. Therefore, it is extremely important to prevent pressure injuries before they occur. This can only be possible with the follow-up of inpatients and intermittent position changes. However, considering the patient density in hospitals, it is not possible for each patient to be followed up continuously by nurses or caregivers. For this reason, there is a need for wearable technologies that will warn the patient or their relatives and remind them that the patient needs to change position.

In the field of identification of movements by means of inertial measurement unit (IMU) sensors, researchers focused on basic daily movements such as going up and down stairs, getting up and walking, and sitting [13-18]. The degrees of freedom (DoF), number of sensors and information, signal processing and motion detection techniques and sensor configuration used in studies in this field differ from study to study [13,19,20]. There is no generally accepted protocol on this subject [15]. Barshan conducted a laboratory study on the classification of 19 daily body and sports activities by means of MIMU sensors produced by X-sens company, and the results they presented are the most detailed study in this field [21-24]. Altun and Barshan tried to classify the movements of walking, running, climbing stairs, sitting on a chair and getting up. Volunteers wore a 9 degree of freedom IMU sensor (gyroscope, accelerometer and magnetometer) on their right or left ankles and motion data were collected. These data were evaluated in the motion detection algorithm they developed and the motion type of the person was determined. Xia et al. [25] proposed a deep learning method for accurate and robust motion type classification with only a single inertial measurement unit (IMU) sensor and achieved a maximum success of 87.16% and a minimum of 73.80%. The most specific movement recognition studies are carried out in the field of sports. For example, table tennis [26], baseball [27], basketball [28], volleyball [29], and swimming [30] have studies on the recognition of sports movements. Vleugels [31]; developed a CNN algorithm to classify six movements in ice hockey and classified them with an average success rate of 76%.

Within the scope of this study, aimed to develop a wearable technology that will prevent the formation of pressure sores in the bed care processes of the elderly, special care patients, and short-term patients. Machine learning algorithms have been developed to determine the lying positions of people. If the person stays in the same lying position for a long time, an audible warning will be given and an incentive to change position will be made. The organization of the study, on the other hand, contains details of the methods used for the collection, feature extraction, and classification of lying position data in Section 2: Material Method. In addition, this section contains information about the metrics used to test the success of classification methods. In Section 3, under the heading Experimental Results and Discussion, the performance comparison table and confusion matrices of the five classification methods used in the study are included.

2. Material and Method

The methodological approach of this study is given in Figure 3. Within the scope of the study, first of all, IMU sensor data were collected. One of the three IMU sensors was placed on the patient's chest, one on the right upper leg and the other on the left upper leg.

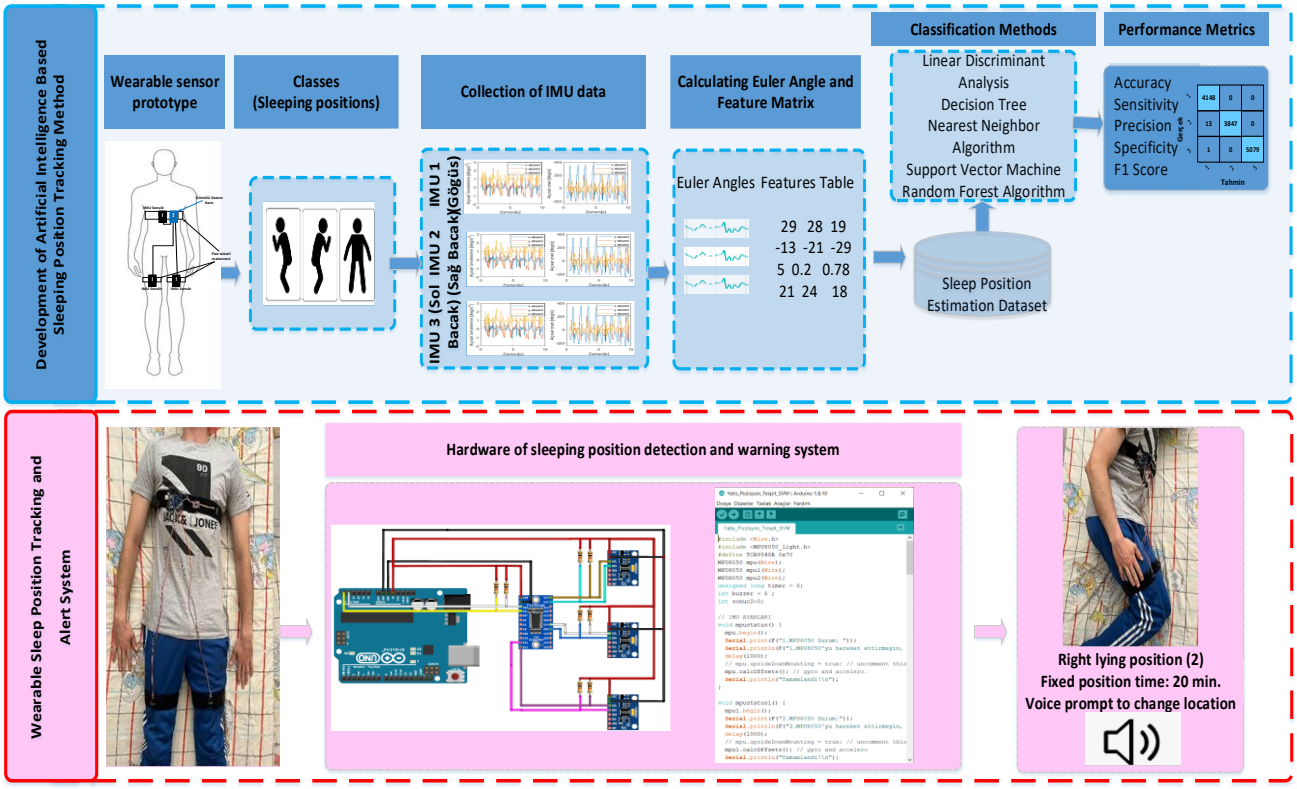

Figure 3. Methodical approach

Angular acceleration and gyroscope data were combined and the angular orientation (Euler) angles of the limb were calculated. Then, machine learning algorithms were developed for the classification of the patient's lying position by using the collected data set for three different lying positions. The time the person remained fixed in the determined position was calculated and if the person remained fixed in the determined position for a long time, an audible warning signal was generated to change the position. Thus, it has been tried to prevent the person to apply pressure by lying on a single muscle group and tissue for a long time and to prevent the formation of pressure sores over time.

2.1. Design of Wearable Sensor Structure and Collection of Lying Position Dataset

The MPU6050 IMU sensors placed on the chest and legs are mounted on a soft-bottomed flex tape textile material that will not deform the skin. The total weight of the entire system is around 200 g. The Arduino Uno embedded system board is positioned between the chest/waist as seen in Figure 4. Angular acceleration and gyroscope information from all sensors are collected on a single embedded system board with the serial communication protocol. The TCA9548A I2C multiplexer module is used to transmit data from three IMU modules to a single embedded system board.

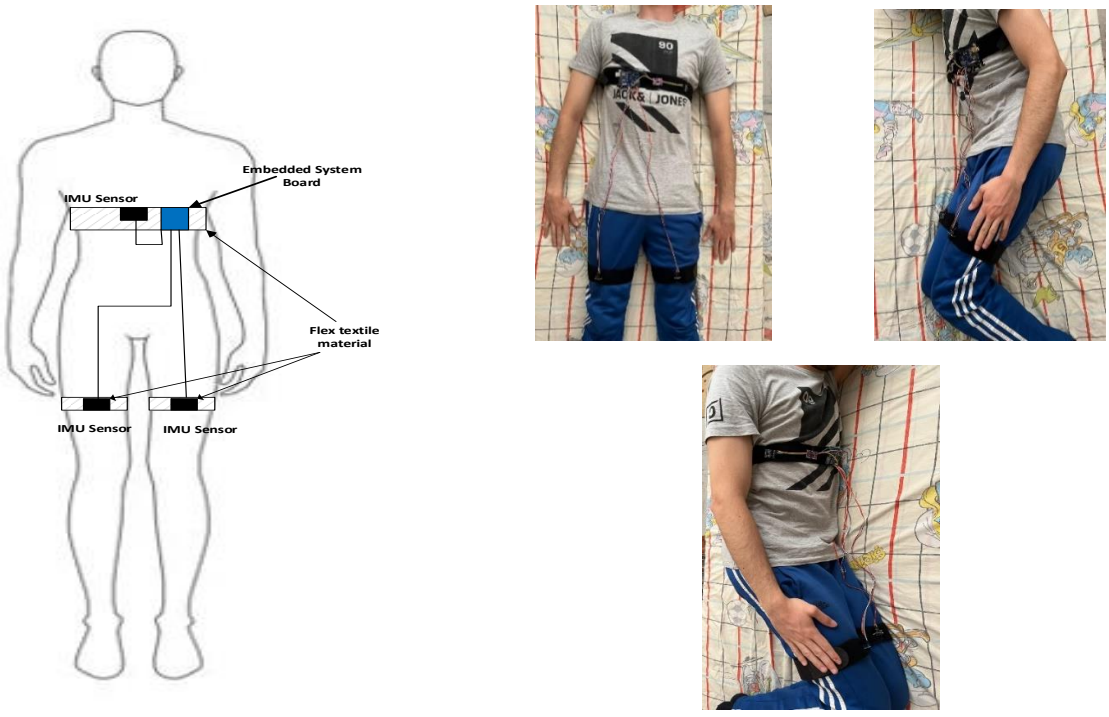

Figure 4. a) preliminary wearable sensor suit design and b) prototype images

Permission was obtained from the non-interventional ethics committee of Fırat University to collect data from volunteers. In this study, three participants are joining the study, two of them are male and one female in the 18-40 age range. They are healthy individuals. They have no any neurological, orthopedic, or systemic diseases and have active hearing and speaking abilities. Since it is important for the volunteers to have both legs and both arms to perform the movement correctly, it was sought as a criterion in the selection of volunteers.

During the data collection phase, people were asked to lie still for 5 minutes in each of the lying positions shown in Figure 4. In the meantime, motion data were collected from the designed wearable IMU sensors. The person was verbally instructed to move from one position to another. Total data recording time for each person is 15 minutes. The serial bound rate of the embedded system board is 115200 bits per second. The sample rate is 0.01 s.

2.2. Calculating Euler Angles and Features Extraction

IMU is an electronic unit that collects the angular velocity and linear acceleration data sent to the main processor in a single module. The components of the system are an accelerometer, a gyroscope and sometimes a magnetic field meter (magnetometer). accelerometer; Measures angular acceleration in three axes. Due to the propulsion system and physical limits, the most important thing in these sensors that measure acceleration is that they are affected by gravity. The sensor is constantly under the influence of gravity. The gyroscope can also be referred to as a turn meter. Gyroscopes and accelerometers alone cannot provide secure and stable data. For this reason, information from gyroscopes and accelerometers is usually synthesized and used in the most appropriate way. Synthesis algorithms conceptually consist of two separate blocks;

- Orientation value calculated from gyroscopes
- Orientation value calculated from accelerometers

This combines the results of the two independent predictions and the orientation angles (Euler angles) are calculated. Euler angles are used to describe the rotational motion of objects in 3D space and are the common name given to the three angles (pitch, yaw, and roll).

In this study, three IMU sensors are placed on the patient's chest and right and left upper legs. Accelerometer and gyroscope data measured from the sensor for three axes were collected on the embedded system board and Euler angles were calculated. The maximum value of the rolling angle was used as the feature set to detect the lying position. Figure 5 shows

the variation of the rolling angles calculated based on the information collected from the three sensors

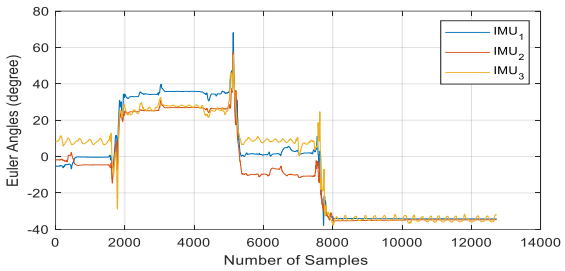

Figure 5. Rolling angle variation graph calculated for three different lying positions

2.3. Development of Motion Classification Algorithms and Lying Position Detection

Five basic machine learning algorithms were used to determine the lying position and the results were compared. Detailed information about the used algorithms is briefly summarized.

Support vector machines are learning machines that use the inductive principle of Structural Risk Minimization to achieve a high level of generalization over a small number of learning models. SVM is an effective learning method for identifying patterns in complex datasets that are difficult to evaluate. The Support Vector Machine algorithm looks for a hyperplane in N-dimensional space (N — number of features) that clearly classifies the data points. There are many possible hyperplanes that can be used to separate classes of data points. The aim is to find the planes with the largest margin, which is the largest distance between data points in each class [32].

A supervised machine learning technique called a decision tree continuously separates data based on a particular parameter. Two entities can be used to describe the tree: decision nodes and leaves. Decision trees are one of the most widely used methods in classification models. Since it is a simpler technique to configure and grasp, it gives transparency to the model and has a visual presentation [33].

The k-nearest neighbor method is a non-parametric classification algorithm. The KNN model is easy as it is based on basic mathematical expressions and is widely used in many industries. The basic principle is based on the assumption that the class of an unknown variable will be the same as that of its nearest neighbors. The average of the current states of the k nearest elements in the training dataset is used to calculate the prediction result. The number of neighbors is indicated by the letter "k" in the method name. The k number is very important when it comes to determining the optimum classification or estimation. It can use trial and error or cross-validation approaches to choose the correct k number [33]. The data class is determined by averaging the k data points calculated as the closest distance to the training set. The threshold value is calculated before the found value is interpreted.

The random forest model is a method of creating a decision ensemble (forest) consisting of multiple decision trees. The RF model is a combination of hundreds of decision trees, and the decision results from all trees are evaluated by majority voting method to produce the final result of the decision tree to get a comprehensive result.

The purpose of the linear discriminant analysis technique is to project the original data matrix into a lower-dimensional space. To achieve this goal, three steps need to be accomplished. The first step is to calculate the separability (i.e. the distance between the means of different classes) between different classes, called the between-class variance or the between-class matrix. The second step is to calculate the distance between the mean and samples of each class, called the within-class variance or the within-class matrix. The third step is to create a sub-dimensional space that maximizes the variance between classes and minimizes the variance within the class [34].

The hyper parameters used in the design of the classification methods developed for the detect of the lying position type within the scope of this study are presented in Table 1.

Table 1. Hyper parameters of used classification algorithm

Decision Tree	K-Nearest Neighbor	Support Vector Machine
Present: Fine	Present: Fine	Present: Linear SVM
Split Criterion: Gini index	Distance metric: Euclidean	Kernel scale: Automatic
Maximum number of splits: 100	Distance weight: Equal	Kernel function: Linear
	Number of Neighbors: 3	Box constant level : 3
	Standardize data: True	Multi-class method: One vs one
		Standardize data: True
Linear Discriminant Analysis	**Random Forest**	
Present: Linear Dicriminat	Present: Bagged trees	
Covariance Structure: Full	Maximum number of splits: 12727	
	Number of learners: 30	

2.4. Performance Evaluation Method (PEM)

We used five standard evaluation methodologies to compare the performance of machine learning classification algorithms for detect lying position. These are accuracy, sensitivity, specificity, precision, f1 score The performance evaluation criteria used are given in Table 2 [32]. An estimate is made for performance measures for true positive (TP), true negative (TN), false positive (FP), and false negative (FN).

Table 2. Performance evaluation metrics used in the study

Performance Metric	Abbreviation	Equation
Positive Predictive Value	PPV, Precision	$\frac{TP}{TP+FP}$
Negative Predictive Value	NPV	$\frac{TN}{TN+FN}$
True Positive Ratio	TPR, Sensitivitiy	$\frac{TP}{TP+FN}$
True Negative Rate	TNR , Specificity	$\frac{TN}{TN+FP}$
Multi-Class Accuracy	ACC	$\frac{TP+TN}{TP+TN+FP+FN}$
F1-Score	F1	$\frac{TP+TN}{TP+TN+FP+FN}$

3. Experimental Results and Discussion

In this study, a computer with 3.60 GHz Intel i7-7700 CPU, Windows 10 and 16 GB RAM was used. The Matlab 2020 program was used to implement the proposed methodological approach. The cross-validation rate was selected k=10 for this data set, and each classification algorithm was run 100 times to calculate the best, minimum, mean and standard deviation values for accuracy, sensitivity, specificity and precision and are presented in Table 3.

In the lying position detection problem, an average accuracy of 99.506%, 99.972%, 99.838%, and 99.967% was achieved with linear discriminant analysis, k-nearest neighbor, decision tree, support vector machine, and random forest classification methods, respectively. sensitivity, specificity, precision, F1 values obtained for all methods are 99% and above. The highest success was obtained with the random forest method.

Table 3. Performance of classification methods

Classifier	Metric	Accuracy	Sensitivity	Specificity	Precision	F1
Linear Discriminant Analysis	**Maximum**	99.520	99.516	99.451	99.449	99.484
	Minimum	99.505	99.501	99.435	99.433	99.468
	Average	99.506	99.515	99.450	99.448	99.483
	Standard deviation	0.0032	0.0037	0.0038	0.0038	0.0037
K-Nearest Neighbor	**Maximum**	100	100	100	100	100
	Minimum	99.960	99.985	99.985	99.985	99.985
	Average	99.977	99.998	99.998	99.998	99.998
	Standard deviation	0.0065	0.0041	0.0041	0.0041	0.0041
Decision Tree	**Maximum**	99.992	99.991	99.990	99.990	99.991
	Minimum	99.929	99.953	99.956	99.956	99.954
	Average	99.972	99.990	99.988	99.988	99.989
	Standard deviation	0.0114	0.0062	0.0053	0.0053	0.0057
Support Vector Machine	**Maximum**	99.866	99.857	99.849	99.849	99.853
	Minimum	99.803	99.831	99.822	99.822	99.827
	Average	99.838	99.856	99.849	99.849	99.853
	Standard deviation	0.0144	0.0035	0.0038	0.0038	0.0037
Random Forest	**Maximum**	99.984	99.982	99.982	99.982	99.982
	Minimum	99.937	99.966	99.966	99.966	99.966
	Average	99.967	99.981	99.981	99.981	99.981
	Standard deviation	0.0109	0.0029	0.0027	0.0027	0.0028

In addition, confusion matrices were obtained for each classifier showing the number of correct and incorrect predictions of our classification model and are given in Figure 6.

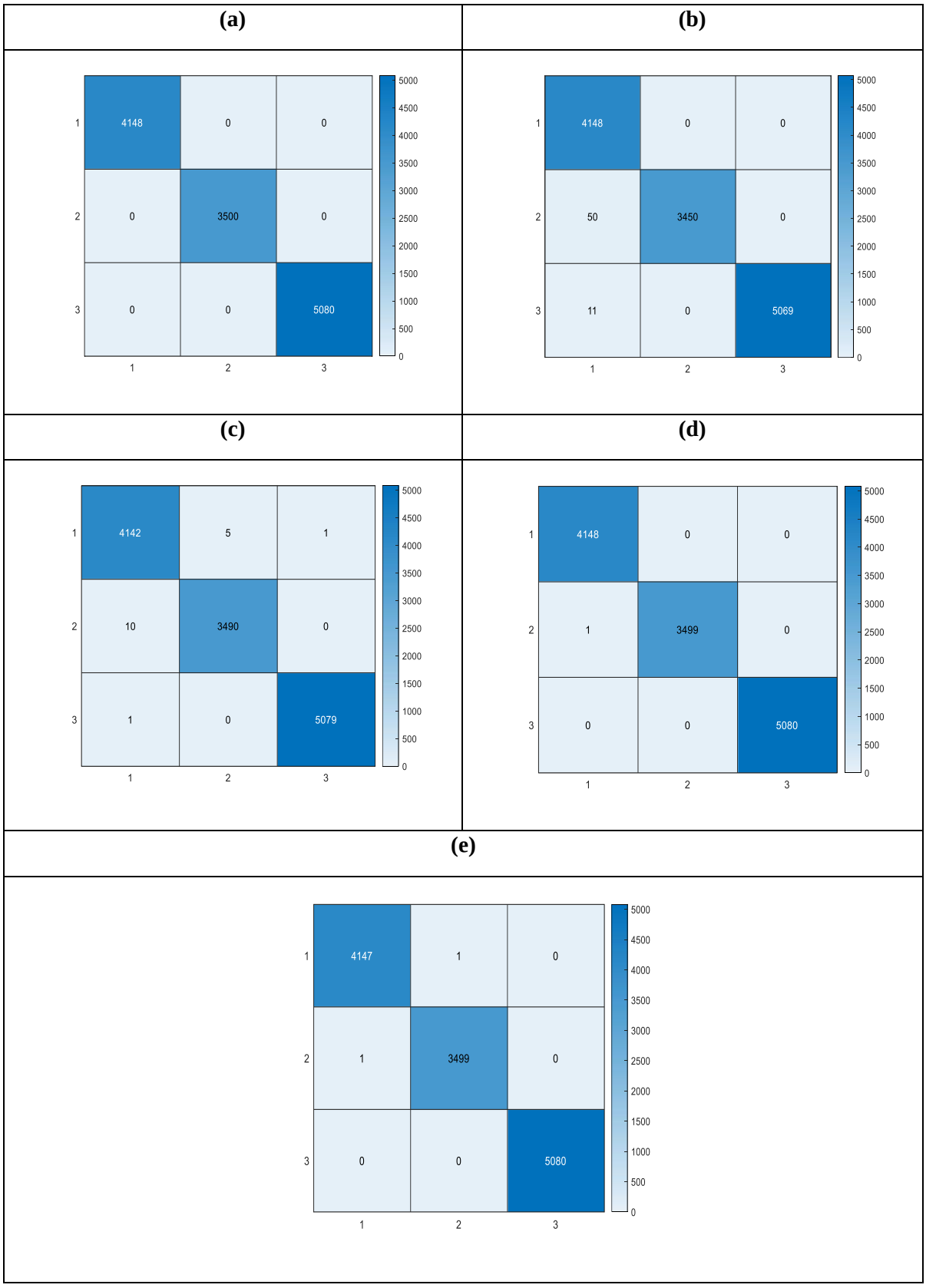

Figure 6. Confusion matrix of (a) K-nearest neighbor, (b) Linear discriminant analysis, (c) Support vector machine, (d) Decision tree, (e) Random forest.

4. Conclusion

Although pressure sores can be seen in most inpatients, it is known to be preventable if diagnosed early. With this proposed wearable sensor technology, the application success of the patient position tracking system on the real-time embedded system board is 99% on average. This success shows that the system is reliable enough to be used for monitoring the lying position of the patients under expert control. This application has the potential to create a solution to an important problem in the field of health.

In future studies, it is aimed to increase the lying position dataset collected from volunteers, especially in the clinical setting, to carry out method validation studies in which patients are included under the supervision of specialist physicians.

.

Acknowledgment

This study was supported by Fırat University within the scope of MF 21.14 Graduate Scıentıfic Research Project.

The data set collected and used in this study can be obtained by contacting the responsible author of the article to be used for academic purposes.

Contributions of the Authors

The contributions of each author to the article should be indicated.

Conflict of Interest Statement

There is no conflict of interest between the authors.

References

[1] D. C. Klonoff, "The increasing incidence of diabetes in the 21st century". *Journal of Diabetes Science and Technology*, vol. 3(1), pp. 1-2, 2009.

[2] B. Pieper, "Pressure ulcers: impact, etiology, and classification". *Wound Management*, vol. 110, pp. 124-139, 2015.

[3] S. D. Horn, S. A. Bender, M. L. Ferguson, J. S. Randall, N. Bergstrom, G. Taler, A. S. Cook, S. S. Sharkey, A.C. Voss, "The National Pressure Ulcer Long-Term Care Study: pressure ulcer development in long-term care residents". *Journal of the American Geriatrics Society*, vol. 52(3), pp. 359-367, 2004.

[4] L. E. Edsberg, J. M. Black, M. Goldberg, L. McNichol, L. Moore, M. Sieggreen, "Revised National Pressure Ulcer Advisory Panel pressure injury staging system: revised pressure injury staging system." *Journal of Wound, Ostomy and Continence Nursing*, vol. 43, pp. 585-597, 2016.

[5] B. Ay, B. Taşar, Z. Utlu, K. Ay, G. Aydın, "Deep transfer learning-based visual classification of pressure injuries stages". *Neural Computing and Applications*, vol. 34, pp. 16157-16168, 2022.

[6] Q. Jiang, X. Li, X. Qu, Y. Liu, L. Zhang, C. Su, X. Guo, Y. Chen, Y. Zhu, J. Jia, S. Bo, L. Liu, R. Zhang, L. Xu, L. Wu, H. Wang, J. Wang, "The incidence, risk factors and characteristics of pressure ulcers in hospitalized patients in China". *International Journal of Clinical and Experimental Pathology*, vol. 7(5), pp. 2587-2594, 2014.

[7] G. Brown, "Long-term outcomes of full-thickness pressure ulcers: healing and mortality." *Ostomy Wound Manage*, vol. 49(10), pp. 42-50, 2003.

[8] D. Berlowitz, L. C. Vandeusen, V. Parker, et. al., "Preventing pressure ulcers in hospitals". *Agency for healthcare research & Quality*, 2018.

[9] J. J. S Agreda, J. E. T. I. Bou, J. Posnett, J. V. Soriano, L. S. Miguel, M. M. Santos, "The Burden of Pressure Ulcers in Spain". *Wounds a Compend Clin Res Pract*, vol. 19(7), pp. 201-206, 2007.

[10] A. Tubaishat, P. Papanikolaou, D. Anthony, L. Habiballah, "Pressure Ulcers Prevalence in the Acute Care Setting: A Systematic Review", 2000-2015. *Clinical Nursing Research*, vol. 27(6), pp. 643-659, 2018.

[11] S. Zahia, Z. M. B. Garcia, X. Sevillano, A. Gonzalez, P. J. Kim, A. Elmaghraby, "Pressure injury image analysis with machine learning techniques: A systematic review on previous and possible future methods". *Artificial Intelligence in Medicine*, vol. 102, 101742, 2020.

[12] B. Taşar, A. B. Tatar, Ö. Nazlı, O. Kalkan, "Remote Control of Unmanned Ground Vehicle via Myo-Electrical Signals". *Düzce University Journal of Science & Technology,* vol. 8(1), pp. 233-245, 2020.

[13] M. J. Mathie, A. C. F. Coster, N. H. Lovell, B. G. Celler, "Accelerometry: providing an integrated, practical method for long-term, ambulatory monitoring of human movement". *Physiological Measurement*, vol. 25(2), pp. 1-20, 2004.

[14] M. J. Mathie, B. G. Celler, N. H. Lovell, A. C. F. Coster, "Classification of basic daily movements using a triaxial accelerometer". *Medical & Biological Engineering & Computing*, vol. 42(5), pp. 679-687, 2004.

[15] L. Bao, S. S. Intille, "Activity recognition from user-annotated acceleration data. *in Ferscha A", Mattern F (Eds.). Pervasive Computing, New York, USA. Springer-Verlag Berlin Heidelberg Press*, pp. 1-17, 2004.

[16] P. H. Veltink, H. B. J. Bussmann, W. De Wries, W. L. J. Martens, R. C. Van Lummel, "Detection of static and dynamic activities using uniaxial accelerometers". *IEEE Transactions on Rehabilitation Engineering*, vol. 4(4), pp. 375-385, 1996.

[17] K. Kiani, C. J. Snijders, E. S. Gelsema, "Computerized analysis of daily life motor activity for ambulatory monitoring". *Technology and Health Care*, vol. 5(4), pp. 307-318, 1997.

[18] F. Foerster, M. Smeja, J. Fahrenberg, "Detection of posture and motion by accelerometry: a validation study in ambulatory monitoring". *Computers in Human Behavior*, vol. 15(5), pp. 571-583, 1999.

[19] D. M. Karatonis, M. R. Narayanan, M. Mathie, N. H. Lovell, B. G. Celler, "Implementation of a real-time human movement classifier using a triaxial accelerometer for ambulatory monitoring". *IEEE Transactions on Information Technology*, vol. B10(1), pp. 156-157, 2006.

[20] F. R. Allen, E. Ambikairajah, N. H. Lovell, B. G. Celler, "Classification of a known sequence of motions and postures from accelerometry data using adapted Gaussian mixture models". *Physiological Measurement*, vol. 27(10), pp. 935-951, 2006.

[21] B. Barshan, W. H. F. Durrant, "Inertial navigation systems for mobile robots". *IEEE Trans. Robotics Automation*, vol. 11(3), pp. 328-342, 1995.

[22] B. Barshan, W. H. F. Durrant, "Evaluation of a solid-state gyroscope for robotics applications". *IEEE Transaction Instrumentation Measurement*, vol. 44(1), pp. 61-67, 1995.

[23] B. Barshan, A. Yurtman, "Classifying daily and sports activities invariantly to the positioning of wearable motion sensor units". *IEEE Internet Things J.*, vol. 7, pp. 4801-4815, 2020.

[24] B. Barshan, M. C. Yüksek, "Recognizing daily and sports activities in two open source machine learning environments using body-worn sensor units". *The Computer Journal*, vol. 57(11), pp. 649-667, 2014.

[25] S. Xia, L. Pei, Z. Zhang, W. Yu, R. C. Qui, "Learning Disentangled Representation for Mixed- Reality Human Activity Recognition with a Single IMU Sensor". *IEEE Transactions On Instrumentation and Measurement*, vol. 70, 2514314, 2021.

[26] P. Blank, J. Hoßbach, D. Schuldhaus, B. M. Eskofier, "Sensor-based stroke detection and stroke type classification in table tennis." *In Proceedings of the 2015 ACM International Symposium on Wearable Computers, Osaka, Japan, 7–11 September 2015*, pp. 93-100, 2015.

[27] N. G. Punchihewa, G. Yamako, Y. Fukao, E. Chosa, "Identification of key events in baseball hitting using inertial measurement units." *J. Biomech.*, 87, pp. 157-160, 2019.

[28] R. Ma, D. Yan, H. Peng, T. Yang, X. Sha, Y. Zhao, L. Liu, "Basketball movements recognition using a wrist wearable inertial measurement unit". *In Proceedings of the 2018 IEEE 1st International Conference on Micro/Nano Sensors for AI, Healthcare, and Robotics (NSENS), Shenzhen, China, 5–7 December 2018*, pp. 73-76, 2018.

[29] T. Kautz, B. H. Groh, J. Hannink, U. Jensen, H. Strubberg, B. M. Eskofier, "Activity recognition in beach volleyball using a Deep Convolutional Neural Network". *Data Min. Knowl. Discov.*, 31, pp. 1678-1705, 2017.

[30] Z. Zhang, D. Xu, Z. Zhou, J. Mai, Z. He, Q. Wang, "IMU-based underwater sensing system for swimming stroke classification and motion analysis." *In Proceedings of the 2017 IEEE International Conference on Cyborg and Bionic Systems (CBS), Beijing, China, 17–19 October 2017*, pp. 268-272, 2017.

[31] R. Vleugels, B. V. Herbruggen, J. Fontaine, E. Poorter, Ultra-Wideband "Indoor Positioning and IMU-Based Activity Recognition for Ice Hockey Analytics". *Sensors*, 21, 4650, 2021.

[32] M. Pal, G. M. Foody, "Feature selection for classification of hyperspectral data by SVM". *IEEE Transactions on Geoscience Remote Sensing*, 48, pp. 2297-2307, 2010.

[33] O. Yaman, T. Tuncer, B. Tasar, DES-Pat: "A novel DES pattern-based propeller recognition method using underwater acoustical sounds". *Appl. Acoust.*, 175, 107859, 2021.

[34] A. Tharwat, T. Gaber, A. İbrahim, A. E. Hassanien, "Linear discriminant analysis: A detailed tutorial". *AI Communications*, pp. 1-22, 2017.

Bitlis Eren Üniversitesi Fen Bilimleri Dergisi
BİTLİS EREN UNIVERSITY JOURNAL OF SCIENCE
ISSN: 2147-3129/e-ISSN: 2147-3188
VOLUME: 11 NO: 4 PAGE: 1084-1092 YEAR: 2022
DOI: 10.17798/bitlisfen.1174512

The Separation of glaucoma and non-glaucoma fundus images using EfficientNet-B0

Buket TOPTAŞ[1*], Davut HANBAY[2]

[1]*Computer Eng Dept., Engineering and Natural Science Faculty, Bandırma University Onyedi Eylül University Balıkesit, Turkey*
[2]*Computer Eng Dept., Engineering Faculty, Inonu University, 44280 Malatya, Turkye*
(ORCID: 0000-0003-2556-8199) (ORCID: 0000-0003-2271-7865)

EfficientNet, Glaucoma, Fundus Image

Abstract

Glaucoma is an eye disease that causes vision loss. This disease progresses silently without symptoms. Therefore, it is a difficult disease to detect. If glaucoma is detected before it progresses to advanced stages, vision loss can be prevented. Computer-aided diagnosis systems are preferred to understand whether the fundus image contains glaucoma. These systems provide accurate classification of healthy and glaucoma images. In this article, a system to separate images of a fundus dataset as glaucoma or healthy is proposed. The EfficientNet B0 model, which is a deep learning model, is used in the proposed system. The input of this deep network model is designed as six layers. The experimental results of the designed model were obtained on the publicly available ACRIMA dataset images. In the end, the average accuracy rate was determined to be 0.9775.

1. Introduction

Fundus images are frequently used in the examination of eye diseases. Ophthalmologists make a diagnosis by examining these images. However, reasons such as fatigue of the ophthalmologist, observation errors, and poor image may cause misleading results. Computer-aided diagnosis systems (CADs) are needed to reduce these misleading results. These systems are designed to assist ophthalmologists and support diagnostic accuracy. The most distinctive features of these systems are that they produce reliable, fast, and robust results.

There are many CADs proposed in the literature on glaucoma. Muramatsu et al. proposed a method that analyzes the optic disc (OD) and automatically measures the CDR ratio [1]. The method uses stereo images. These images are obtained of patients with glaucoma symptoms and healthy patients. In the proposed method, an edge detector and active contour method are used. Thus, the OD is segmented. A depth map is created to remove the unevenness of the stereo images. Noises on the depth map are reduced using mean and median filters. Next, edges are searched in radial directions on the depth maps. Thus, the optic cup (OC) contours are determined. After determining the OD and OC contours, the CDR ratio is calculated. Issac et al. presented a method of diagnosing glaucoma disease using CDR, the Neuroretinal rim (NRR), and the blood vessels in the OD region [2]. The method is based on image processing. This method is designed to be invariant to the quality of the images and resistant to noise. The OC region is segmented using the R channel of the fundus image in RGB space, and the OD region is segmented using the G channel. Then, CDR, ISNT, and NRR ratios are extracted as features. Extracted features are given to various classifiers and classification is provided. Divya et al. presented a feature-based method for the diagnosis of glaucoma [3]. Firstly, the gray-scale image of the color fundus image is obtained, and the color fundus image is divided into color channels. Then, a 2-D empirical wavelet transform is used to generate the sub-band images. Co-entropy is subtracted from the

* Corresponding author: btoptas@bandirma.edu.tr
Received:13.09.2022, Accepted: 02.11.2022

disaggregated components. Some of the obtained features are selected using student-t and principal component analysis methods. A least-squares support vector machine is used to classify features as glaucoma or non-glaucoma. Al-Bander et al. proposed a deep learning-based method to segment OD and OC regions [4]. In this method, the DenseNet network architecture is used. Fundus images are given as input to the network and trained without preprocessing. Then, preprocessed fundus images are given to the network, which it has never seen before, and segmentation of the relevant regions is performed. The CDR ratio is calculated by segmenting the OD and OC regions. The CDR ratio has been used in the diagnosis of glaucoma. Gómez-Valverde et al. conducted a study evaluating the application of different CNN architectures for glaucoma detection [5]. In the study, the success of many network architectures on fundus images with the transfer learning method was examined. All fundus images were preprocessed to train the meshes homogeneously. Optical disc were centered and the same size standard patches were used for all datasets. Also, the mean in each channel is subtracted to ensure that all data inputs have a concentric distribution. Finally, all CNN network architectures are compared and their performances are evaluated. Yu et al. performed optic disc segmentation with a customized U-net architecture for glaucoma detection [6]. The customized U-net architecture is obtained by combining the encoding layers of the trained ResNet-34 model with the classical U-net decoding layers. Pre-processed fundus images are reproduced by data augmentation methods. Then, the OD and OC regions of the images given to the model training are determined. Claro et al. proposed a method that extracts features from fundus image pixels. This method allows for the classification of retinal fundus images as glaucoma or non-glaucoma [7]. Methods such as local binary texture, gray level co-occurrence matrix, histogram of directed gradients, Tamura and gray level running length matrix, morphology, and CNN architecture are used as feature extraction methods. Extracted features were selected according to the earnings ratio. The selected features were classified by giving them to the classifiers. Through the generative adversarial network (GAN) algorithm [8], Bisneto et al. developed a method for diagnosing glaucoma disease. In the method, the training of the GAN is carried out for the segmentation of the OD region. Then, the images are subjected to the post-processing process. At this stage, the holes in the segmented OD region are filled and contrast enhancement is performed. Then, using the taxonomic diversity index, the tissue features of the OD region are extracted. The WEKA program was used as the classifier, and the results were verified here. Pruthi et al. presented the firefly swarm optimization algorithm [9]. This algorithm is designed to facilitate automatic detection of the OD region in fundus images. OC pixels are the brightest pixels in the OD region. Therefore, all the light worms have moved to the OC region, which is the brightest region. This method has been tested in various optimization algorithms. Nayak et al. used an evolutionary convolutional network to automatically detect glaucoma [10]. This network is designed for feature extraction. A real coded genetic algorithm is used to improve the weights in the layers of the network. The network architecture is trained using a criterion that maximizes the distance between classes and minimizes within-class variance. The final features were classified with many different classifiers and the success of the system was proven. Mrad et al. proposed a system that can detect glaucoma disease [11]. Fundus images captured from a smartphone are used as retinal images. The ROI region is selected from fundus images, and images are preprocessed with the CLAHE method. Blood vessels are extracted from the preprocessed ROI images. At this stage, morphological operations are used. Then, the localization of the OD region is determined. Thus, there extracted the feature from the OD region. In feature extraction, the NNR and ISNT rule (inferior (I) > superior (S) > nasal (N) > temporal (T)) are used. These features are classified by support vector machines.

As technological developments progress, CADs about glaucoma are also advancing and developing. Although many methods have been proposed and many systems have been designed in this field, it is still a field open to research. In this paper, the EfficientNet model, which has emerged in recent years and is a deep learning network model, is used. With this model, fundus images are classified as healthy and glaucoma. The performance of the proposed method has been tested on the publicly available ACRIMA dataset. Test results are presented with various performance measurement metrics.

The rest of the paper is organized as follows. Firstly, the material and method are explained. In this section, the datasets used in the proposed method, related work, and the proposed method are presented. Then, the experimental results and discussion of the proposed approach are given. In this section, the main stages of the study are explained. In addition, in this section comparisons and discussions of the experimental results with other literature studies are made. Later, the conclusions section is given. In this section, the proposed method is evaluated.

2. Material and Method

In this section, each related work is detailed in the subsequent subsections.

2.1. Dataset Used

The ACRIMA dataset is a publicly available fundus image dataset [12]. This dataset consists of glaucoma and healthy fundus images. It has 705 fundus images in total. 396 of these images are fundus images of glaucoma, and 309 of them are healthy. Image classification was done by an experienced glaucoma expert. These dataset images contain only the OD region. All images were acquired with the Topcon TRC retina camera and have a FOV of 35º. A few of the images from this data set are given in Figure 1.

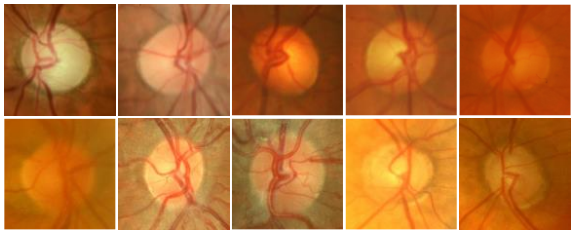

Figure 1. The first row is healthy images, the second row is images with glaucoma

2.2. Contrast Limit Adaptive Histogram Equalization

It is a method developed by Pizer et al. [13] for image enhancement. This method first splits the original image into the M×N size regions. It then calculates the gray-level histogram for each of these regions. Firstly, the average gray level pixel values are calculated for each region. The histogram of each region is then cropped according to the clipping boundary. This boundary is determined by the user. Then, the cumulative distribution function of the contrast bound histogram values is determined. Finally, each pixel value is mapped using the bi-linear interpolation method. This method has been applied to fundus images in previous studies and has produced successful results [14-17].

2.3. EfficientNet

EfficientNet is a deep learning network architecture developed in 2019 [18]. This architecture gives the relationship between three terms that significantly affect the performance of deep network architectures. These terms are depth, width, and resolution. This architecture is based on the decompound scaling method. In the first step of this method, a grid search algorithm is used. This algorithm allows the network to establish the relationship between different scaling dimensions. The target deep learning network is started with the specified scaling dimensions [19]. Mathematical expressions for the composite scaling method are given in Equations (1)-(3).

$$\alpha^{\phi}, w=\beta^{\phi}, r=\gamma^{\phi} \quad (1)$$

$$\alpha.\beta^2.\gamma^2 \approx 2 \quad (2)$$

$$\alpha \geq 1, \beta \geq 1, \gamma > 1 \quad (3)$$

where, the ϕ parameter represents a user-defined coefficient. The α, β, γ parameters are used for depth, width and resolution, respectively.

Depth is related to the number of layers of a deep learning network architecture. A deep network can get complex features by going into more detail. However, increasing the depth of the network is not always desirable because the depth will cause a cost increase and loss of time. Also, increased accuracy gain may not always be predicted. Width is related to the size of the layers of deep network architecture. The increase of neurons in the layers causes the expansion of the network. Resolution is related to the aspect ratio of the input data of a deep learning network architecture. The high resolution of the input image contains fine details in the image. Tan et al. [18] developed the EfficientNet-B0 architecture, known as the starter model. The parameter values of this architecture are given in Table 1

Table 1. EfficientNet-B0 architecture

Stage	Operator	Resolution	Channels	Layer
1	Conv 3×3	224×224	32	1
2	MBCon1, k3×3	112×112	16	1
3	MBCon6, k3×3	112×112	24	2
4	MBCon6, k5×5	56×56	40	2
5	MBCon6, k3×3	28×28	80	3
6	MBCon6, k5×5	14×14	112	3
7	MBCon6, k5×5	14×14	192	4
8	MBCon6, k3×3	7×7	320	1
9	Conv 1×1 & Pooling & FC	7×7	1280	1

2.4. Proposed Methodology

In this paper, the EfficientNet-B0 model is used to separate color fundus images of glaucoma from non-glaucoma. The flow diagram of this method is shown in Figure 2. Firstly, in this method, the input images are prepared. Then, a data augmentation technique is applied to these images. Thus, image diversity is provided and the number of images is increased. Secondly, the prepared input images are given to the EfficientNet-B0 model. As a result of the deep learning model, glaucoma and non-glaucoma fundus images are separated. The final results obtained are tested on various performance measures.

Firstly, in the proposed method, the input data of the EfficientNet-B0 model is prepared. This input data has six channels. The first channel is the first channel of the new color space proposed by [20]. This color space is created to reveal the OD region in fundus images. The OD region provides information about glaucoma disease. Therefore, this new color space is preferred in the proposed method. You can find the details of obtaining the new color space in the original article. The second channel is the R channel of the CLAHE method applied to the original fundus image. The third channel is the G channel of the CLAHE method applied to the original fundus image. These two-color channels have been used frequently in previous studies on fundus images [21],[2]. The R channel is effective in the OD region due to the intensity of the red hue. The G channel reveals the retinal vessels. The effect of this color channel is important, as there are retinal main vessels in the OD region. The last three channels are a three-channel image with a Gaussian filter applied to the new color space. Here, the core of the Gaussian filter is chosen with a size of 15×15 pixels. The Gaussian filter blurs the image by removing noise. The process of obtaining the six-channel input image is given in Figure 3.

The first block in Figure 3 is the preferred color channel. The second block is the six-channel input image obtained.

The next stage of the proposed method is the data augmentation stage. As it is known, deep learning is more successful in big data. However, datasets are limited. In this case, data augmentation is required. These operations diversify and increase the number of data. Some of these data augmentation methods are operations such as rotating, scaling, flipping, cropping, and color space transformation. In this proposed method, the rotate operation is used for the ACRIMA dataset. In this process, each fundus image is rotated at 0-9-degree angle. This data augmentation technique is the technique with the best experimental success. It has also been used in other fundus studies and has proven successful [22]. The data numbers of the ACRIMA data set after data augmentation are given in Table 2.

Table 2. The number of fundus images after data augmentation

Fundus Image	Original	Data augmentation
Glaucoma	396	3960
Non-Glaucoma	309	3090
Total	705	7050

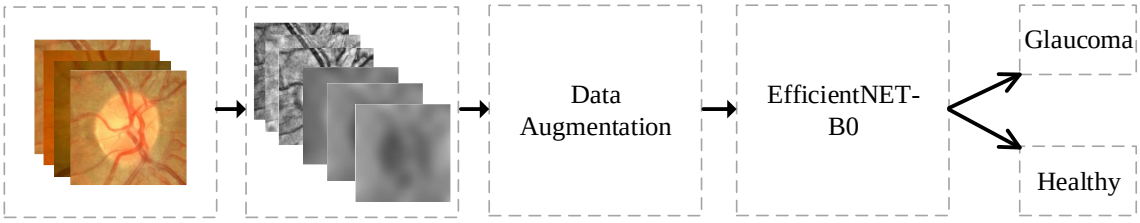

Figure 2. Flow Diagram

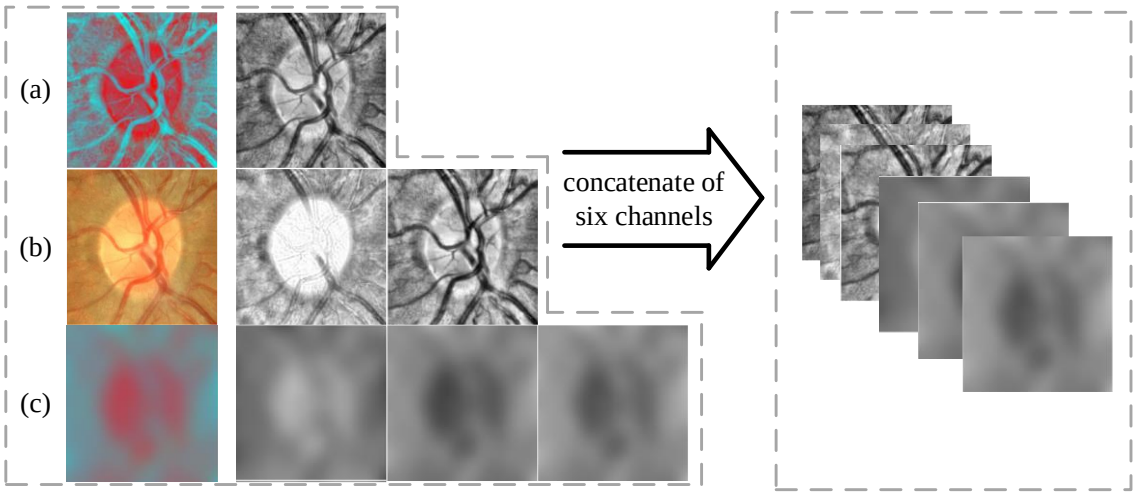

Figure 3. Six-channel input display. (a) New color space and the first channel of this color space, (b) original fundus image and R, G channel this image, (c) gaussian image result applied on (a) and color channels of this image

3. Experimental Result and Discussion

3.1. Performance Metrics

Performance metrics are used to demonstrate the experimental success of the proposed method. The most frequently used performance metrics are used to make the method comparable. The metrics used are accuracy, sensitivity, specificity, precision, and F-measure, respectively. The mathematical expressions of these metrics are given in Equations (4) -(8).

$$\text{Accuracy (Acc)}=(TP+TN)/(TP+TN+FP+FN) \quad (4)$$

$$\text{Sensitivity (Sn)/Recall}=TP/(TP+FN) \quad (5)$$

$$\text{Specificity (Sp)}=TN/(TN+FP) \quad (6)$$

$$\text{Precision (Pr)}=TP/(TP+FP) \quad (7)$$

$$\text{F-measure}=(2*\text{Precision}*\text{Recall})/(\text{Precision}+\text{Recall}) \quad (8)$$

3.2. EfficientNet-B0 Architecture

The structure of this architecture is given in Table 3. The images obtained after data augmentation are divided into three groups. The reason for this is to use different data in training, validation, and testing processes. The number of data used in training, validation, and testing processes is given in Table 3. The deep network architecture has trained and tested the ACRIMA dataset based on these data numbers.

Table 3. The number of training, validation, and test data

Fundus Image	Train	Validation	Test
Glaucoma	2440	610	910
Non-Glaucoma	1600	400	1090
Total	4040	1010	2000

There are parameters that affect the performance of the proposed method. These parameters are called hyper-parameters. The selection of hyper-parameters is very important for the model to give the best performance. Here, optimization of learning parameters is performed with stochastic gradient descent with momentum (SGDM). In this network architecture, the initial learning rate is used in two ways. Firstly, its value is set to 0.0001. This rate is kept constant throughout the network training. The training is completed with a learning rate of 0.0001 in different epoch numbers. Secondly, the initial learning rate is started from 0.001. This rate is multiplied by 0.9 in each epoch. Thus, the initial learning rate is reduced at each epoch and given to the network. The deep network architecture is shuffled in each epoch to prevent overfitting. The mini-batch parameter is for processing multiple inputs piece by piece, not altogether. In this method, the mini-batch size value is set to 32. Thus, the training of the model is done in this batch size in each iteration.

The experimental results of the proposed method are obtained by studying the learning rates mentioned above in different epochs. The learning rate is kept constant and runs for 10, 25, and 50 epochs, respectively. The accuracy metric of the results

obtained in this experimental study is 0.9235, 0.9650, and 0.9465, respectively. When the learning rate is reduced in each epoch, the accuracy of the results for 10, 25, and 50 epochs, respectively, is 0.9655, 0.9775, and 0.9750. Here, the highest accuracy rate was obtained in 25 epochs at a non-constant learning rate. Table 4 shows the results of other performance metrics at three epochs and two learning rates.

Table 4. Constant learning rate (0.0001)

Performance metrics	Maximum epoch		
	10	25	50
Accuracy	0.9235	0.9650	0.9465
Sensitivity	0.8890	0.9375	0.9118
Specificity	0.9562	0.9904	0.9795
Precision	0.9505	0.9890	0.9769
F-measure	0.9187	0.9626	0.9432
Training Time (s)	1551	3949	8054

Table 5. Reduced learning rate (each epoch)

Performance metrics	Maximum epoch		
	10	25	50
Accuracy	0.9655	**0.9775**	0.9750
Sensitivity	0.9394	**0.9577**	0.9498
Specificity	0.9895	0.9953	**0.9981**
Precision	0.9879	0.9945	**0.9978**
F-measure	0.9630	**0.9757**	0.9732
Training Time (s)	1562	3829	**7613**

In Table 5, the highest performance metric values are given in bold. Considering the performance metric results obtained in Table 4 and Table 5, the highest result was obtained with the decreasing learning rate in each epoch. It can be said that the ideal epoch number is between 25 and50. As a result of the accuracy being taken at 50 epochs, there was a decrease of 0.0025. However, Sp and Pr parameters increased. The confusion matrix of the EfficientNet-B0 architecture trained according to these hyper parameters is given in Figure 4. In this matrix, the intersection of 'true healthy' and 'predicted healthy' is represented by the parameter TN. The intersection of 'true healthy' and 'predicted glaucoma' is represented by the FN parameter. The intersection of 'true glaucoma' and 'predicted healthy' is represented by the FP parameter. The intersection of 'true glaucoma' and 'predicted glaucoma' is represented by the TP parameter.

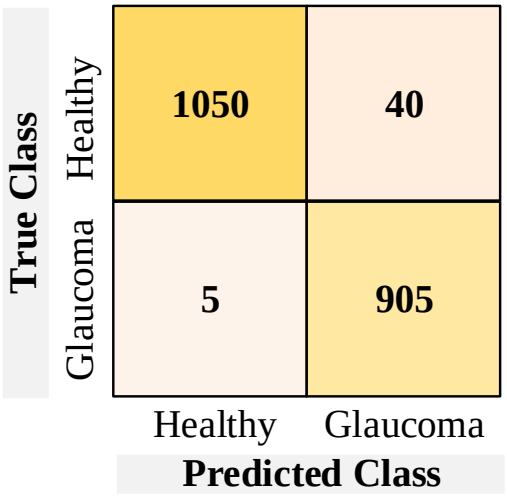

Figure 4. Confusion Matrix

The proposed method was compared with the state-of-the-art technological methods according to the performance metric parameters. This comparison process is given in Table 6.

According to this table, the proposed method showed a competitive performance. The results obtained are quantitative proof that the proposed method is the correct method. Ultimately, it has been shown that the EfficientNet-B0 model can differentiate fundus photographs from glaucoma and healthy in clinical settings.

4. The Conclusions

The proposed method aims to classify a fundus image as glaucoma or healthy without human intervention. The performance metrics of the proposed method showed better performance compared to the state-of-the-art methods. These performance metrics reflect the effectiveness of the EfficientNet-B0 model for glaucoma disease.

The performance results of the proposed method are obtained from the publicly available ACRIMA dataset. The hyper-parameters of the EfficientNet-B0 model are set as mentioned in Section 3.2. Here, the learning rate of the model is initialized at 0.001 and decreased at each epoch. The epoch number was determined as 25. Firstly, the original dataset images are given to this tuned model. Here, the performance metrics of the obtained results were calculated as 0.9610 for the Acc metric, 0.9315 for the Sp metric, 0.9884 for the Sn metric, 0.9868 for the Pr metric, and 0.9584 for the F-measure metric. In this experiment, it was observed that the details of the image were lost in the hierarchy of the network. Therefore, to reliably distinguish images with glaucoma, the input images are set to have six layers. Then, data augmentation was applied so that the input images are diverse and prevent overfitting. Thus, the performance metrics of the results obtained were calculated as 0. 9775 for the Acc metric, 0.9577 for the Sp metric, 0.9953 for the Sn metric, 0.9945 for the Pr metric, and 0.9757 for the F-measure metric. Considering these metrics parameters, the positive effects of the proposed six-layer input image are clearly evident. The scope of the proposed method is to present a useful CAD system that can distinguish between glaucoma and healthy images on retinal fundus images. In this method, glaucoma disease was used in the new color space for the first time. The aim in the future is to use the EfficienNet-B0 model and other EfficientNet models in different datasets on glaucoma disease.

Table 6. Other state-of-the-art methods that separate glaucoma and healthy fundus images using the ACRIMA dataset

Author	Method(s)	Data augmentation	Performance measures
[22]	CNN	Applied (G:3960 Non-G:3090)	Acc:0.9664 Sn:0.9607 Sp:0.9739 Pr:0.977
[23]	ResNet-152	Applied (G:2976 Non-G: 2400)	Auc:0.77 Acc:0.48 Sp: 0.83
[24]	UCSD and UTokyo	Not Applied	Auc:0.86
[25]	CDR and using traditional method	Not Applied	Acc:0.9461 Sp:0.9500 Se:0.9457
Proposed Method	EfficientNet-B0	Applied (G:3960 Non-G:3090)	Acc:0.9775 Se: 0.9577 Pr:0.9945 Sp:0.9953

F1-measure: 0.9757

Contributions of the Authors

In the scope of this study, Author 1 put forward the formation of idea, performed the design and the spelling, and checked the article; Author 2 is examined the results for the article in terms of content were contributed.

Conflict of Interest Statement

There is no conflict of interest between the authors.

Statement of Research and Publication Ethics

There is no need to obtain permission from the ethics committee for the article prepared. There is no conflict of interest with any person / institution in the article prepared.

References

[1] Muramatsu C, Nakagawa T, Sawada A, Hatanaka Y, Yamamoto T, Fujita H. "*Automated determination of cup-to-disc ratio for classification of glaucomatous and normal eyes on stereo retinal fundus images*". J Biomed Opt., 16(9), 2011.

[2] Issac A, Partha SM, Dutta MK. "*An adaptive threshold-based image processing technique for improved glaucoma detection and classification*". Computer Methods and Programs in Biomedicine, 122(2):229–244, 2015

[3] Divya L, Jacob J. "*Performance analysis of glaucoma detection approaches from fundus images*". Procedia Computer Science, 143:544–551. 8th International Conference on Advances in Computing and Communications (ICACC-2018)

[4] Al-Bander B, Williams BM, Al-Nuaimy W, Al-Taee MA, Pratt H, Zheng Y. "*Dense fully convolutional segmentation of the optic disc and cup in colour fundus for glaucoma diagnosis*". Symmetry, 10(4),2018.

[5] Gómez-Valverde JJ, Antón A, Fatti G, Liefers B, Herranz A, Santos A, ... Ledesma-CMJ. "*Automatic glaucoma classification using color fundus images based on convolutional neural networks and transfer learning*". Biomedical optics express, 10(2), 892-913,2019.

[6] Yu S, Xiao D, Frost S, Kanagasingam Y. "*Robust optic disc and cup segmentation with deep learning for glaucoma detection*". Computerized Medical Imaging and Graphics, 74:61–71,2019

[7] Claro M, Veras R, Santana A, Araujo F, Silva R, Almeida, J, Leite D. "*An hybrid feature space from texture information and transfer learning for glaucoma classification*". Journal of Visual Communication and Image Representation, 64:102597,2019.

[8] Bisneto TRV, de Carvalho FAO, Magalhaes DMV. "*Generative Adversarial network and texture features applied to automatic glaucoma detection*". Appl. Soft Comput., 90:106165,2020

[9] Pruthi J, Khanna K, Arora S. "*Optic cup segmentation from retinal fundus images using glowworm swarm optimization for glaucoma detection*". Biomedical Signal Processing and Control, 60:102004, 2020.

[10] Nayak DR, Das D, Majhi B, Bhandary SV, Acharya UR. "*Ecnet: An evolutionary convolutional network for automated glaucoma detection using fundus images*". Biomedical Signal Processing and Control, 67:102559, 2021.

[11] Mrad Y, Elloumi Y, Akil M, Bedoui M. "*A fast and accurate method for glaucoma screening from smartphone-captured fundus images*". IRBM,2021.

[12] Diaz-Pinto A, Morales S, Naranjo V, Kohler T, Mossi JM, Navea A. (2019). "*Cnns for automatic glaucoma assessment using fundus images: an extensive validation*". BioMed Eng OnLine,18(29), 2019.

[13] Pizer SM, Amburn EP, Austin JD, Cromartie R, Geselowitz A, Greer T, ter Haar RB, Zimmerman JB, Zuiderveld K. "*Adaptive histogram equalization and its variations*". Computer Vision, Graphics, and Image Processing, 39(3):355–368, 1987.

[14] dos Santos JCM, Carrijo GA, de Fátima dos SCC., Ferreira JC, Sousa PM, Patrocínio AC. "*Fundus image quality enhancement for blood vessel detection via a neural network using CLAHE and Wiener filter*". Research on Biomedical Engineering, 36(2), 107-119, 2020.

[15] Sonali SS, Singh AK, Ghrera S, Elhoseny M. "*An approach for de-noising and contrast enhancement of retinal fundus image using clahe*". Optics and Laser Technology, 110:87–98, 2019.
[16] Toptaş B, Hanbay D. "*Retinal blood vessel segmentation using pixel-based feature vector*". Biomedical Signal Processing and Control, 70:103053, 2021.
[17] Uysal E, Güraksin G. "*Computer-aided retinal vessel segmentation in retinal images: convolutional neural networks*". Multimed Tools Appl, 80, 2021.
[18] Tan M, Le Q. "*Efficientnet: Rethinking model scaling for convolutional neural networks*". In International conference on machine learning (pp. 6105-6114). PMLR.,2019.
[19] Gupta N, Garg H, Agarwal R. "*A robust framework for glaucoma detection using CLAHE and EfficientNet*". The Visual Computer, 1-14,2021.
[20] Toptaş B, Toptaş M, Hanbay D. "*Detection of Optic Disc Localization from Retinal Fundus Image Using Optimized Color Space*". Journal of Digital Imaging, 1-18,2022.
[21] Azzopardi G, Strisciuglio N, Vento M, Petkov N. "*Trainable COSFIRE filters for vessel delineation with application to retinal images*". Medical image analysis, 19(1), 46-57,2015.
[22] Elangovan P, Nath MK. "*Glaucoma assessment from color fundus images using convolutional neural network*" International Journal of Imaging Systems and Technology, 31(2), 955-971,2021.
[23] Serte S., Serener A. "*A generalized deep learning model for glaucoma detection*". In 2019 3rd International symposium on multidisciplinary studies and innovative technologies (ISMSIT) (pp. 1-5). IEEE,2019.
[24] Christopher M., Nakahara K., Bowd C., Proudfoot J. A., Belghith A., Goldbaum M. H., ... Zangwill L. M. "*Effects of study population, labeling and training on glaucoma detection using deep learning algorithms*". Translational vision science & technology, 9(2), 27-27,2020.
[25] Almeida-Galárraga D, Benavides-MK., Insuasti-Cruz E, Lovato-Villacís N, Suárez-Jaramillo V, Tene-Hurtado D, Tirado-Espín A, Villalba-Meneses GF. "*Glaucoma detection through digital processing from fundus images using MATLAB*". In 2021 Second International Conference on Information Systems and Software Technologies (ICI2ST) (pp. 39-45). IEEE, 2021.

Bitlis Eren Üniversitesi Fen Bilimleri Dergisi
BİTLİS EREN UNIVERSITY JOURNAL OF SCIENCE
ISSN: 2147-3129/e-ISSN: 2147-3188
VOLUME: 11 NO: 4 PAGE: 1093-1101 YEAR: 2022
DOI:10.17798/bitlisfen.1176937

Finite Element Analyses of Stresses Developed in Oil Separator Composite Tank Used in Screw Type Compressor Systems

Volkan GEZGİNCİ [1], Cem BOĞA [2*], Mirsadegh SEYEDZAVVAR[2]

[1]*Sarmak Compressors and Engineering, Adana, 01350, Adana, Turkey*
[2]*Department of Mechanical Engineering, Faculty of Engineering, Adana Alparslan Türkeş Science and Technology University, Adana, Turkey*
(ORCID: 0000-0003-4031-6969) (ORCID: 0000-0002-9467-1141) (ORCID: 0000-0002-3324-7689)

Keywords: Separator tank, Carbon fiber/epoxy, Glass fiber/epoxy, Kevlar fiber/epoxy, Stress, Total deformation.

Abstract

Pressure vessels are geometrically cylindrical, spherical or conical work equipment used for the storage and transportation of pressurized fluid. In the case of design and/or manufacturing deficiency, or for the case of improper applications of such vessels due to working conditions, the damages that may occur can cause serious harm to the environment and employees. The aim of this study is to estimate the performance of a typical oil separator pressure vessel used in screw compressor systems, exposed to high pressure and temperature, using finite element method. Here, the aim is to estimate performance of this tank after modifications in design and to compare the results with that of pressure vessel designed using conventional materials. The inner liner of the separator tank is metal material and the other layers are wrapped with three different composite materials, including carbon fiber/epoxy, glass fiber/epoxy and kevlar fiber/epoxy, at different angles, and then were exposed to high pressures in the environment of finite element simulation software. As a result of the study, stress and deformation values were examined and the most suitable material and orientation angle for the composite pressure vessel were decided. According to the results, it was observed that the lowest first-ply equivalent stress value was obtained in glass fiber/epoxy coated separator tanks at 11.25 bar pressure and 45 degree winding angle. In addition, it was observed that the lowest total deformation value was obtained in kevlar fiber/epoxy coated separator tanks at 11.25 bar pressure and 45 degree winding angle.

1. Introduction

Pressure vessels inherit potential hazards that may affect human health and safety. For this reason, a careful and detailed analysis should be made in the pressure vessel design, all loads that may affect the system should be accurately determined and included in the calculations. Pressure vessels are generally produced using metal alloys. However, the need for more durable and lighter containers is increasing day by day. Manufacturers have started to produce cylindrical composite pressure vessels with fiber winding of thanks as a developing technology in production of high-pressure vessels. It has been demonstrated experimentally that the production of composite pressure vessels is not efficient for large pressure vessels.

Therefore, evaluation of the performance of such vessels using numerical methods such as finite element analyses are of high importance before initiating the production process in terms of both time and cost of production. There are some studies on this subject in the literature as summarized below.

Bozkurt [1] used the finite element approach to analyze maximum strains and stresses with filament and centrifugal winding methods. When designing the composite pressure vessel, glass fiber/epoxy, carbon fiber/epoxy and kevlar

*Corresponding author: cboga@atu.edu.tr
Received:18.09.2022, Accepted: 27.12.2022

fiber/epoxy materials with winding angles of [30°/-30°], [45/-45°], [60°/-60°] and [75 °/-75°] were used. After examining Von-Mises stresses and total deformations, the author reported that the optimum values of maximum stresses and strains occur in pressure vessels designed with glass fiber/epoxy composite material with an orientation angle of 60°/-60°. Yaylagan [2] investigated the optimal layer angle orientation at different temperatures and maximum burst pressure for the first layer damage of antisymmetrical layered, thin-walled, internally plastic-lined composite pressure tubes by using the finite element method and experimentally. The author found that the most suitable winding angle was about 55º for helical angle coiled composite pipes under internal pressure. Pehlivan [3] worked on the modeling composite pressure vessels produced with fiber winding techniques at different loads. After validation of analytical model using experimental results, the author evaluated the optimum winding angles at which the maximum compressive strength of pressure vessels were obtainable. Sinha and Pandit [4] conducted a study on the cylindrical part of a four-layer carbon fiber reinforced polymer (CFRP) composite pressure vessel. The pressure vessel was designed and modeled using the finite element software ANSYS. They estimated burst pressures for various fiber orientations using Tsai-Wu criteria. The results showed that the optimum fiber orientation angle for the composite pressure vessel subjected to high internal pressures was ±45°. Zhang et al. [5] obtained an analytical solution based on the theory of thermo-elasticity to determine the stress distribution of a multilayer composite pressure vessel subjected to internal fluid pressure and thermal loading. The results showed that the proposed process can be used in the initial stages of multi-layer composite pressure vessel design involving fluid pressure and thermal load. In addition, there are other studies in the literature that were focused on the design and analysis of conventional pressure vessels. Sancaklı [6] has introduced the basic design rules of pressure vessels according to ASME Chapter 8 Part 1, ASME Chapter 8 Part 2, EN 13445 and AD 2000 codes. Accordingly, certain design conditions and geometries resulted in the minimum wall thickness for the vessels of different configurations of the head, including elliptical, torispheric and hemispherical. Thus, these codes benefited the engineers and designers with developing the pressure vessels of desired features, while the cost of production is minimized. Mestan [7] applied hydrostatic pressure tests to pressure vessels under the influence of internal pressure. The author employed the theoretical approach of a cylindrical pressure vessel subjected to axially symmetrical loading, calculated the Von Mises stresses from the SOLIDWORKS program and compared the displacements and stresses obtained as a result of stress analysis. Usta [8] investigated the resistance of welded joints in thick-walled pressure vessels under the hydrostatic pressures determined according to the TS 377 standard. The author examined the welded areas of the heating boiler, steam boiler and air tank according to the TS 17020 standard. The thick-walled pressure vessels under the examination were tested for their suitability for dynamic working conditions, sweating, and leakage or crack formation in the vessel. Tjelta [9] studied the advantages and disadvantages of different methods used in the design of pressure vessels. The author disclosed the details of tools used in pressure vessel analysis and the calculation for the relevant standard. Raparla and Seshaiah [10] examined the advantages of multilayer high pressure vessels over single layer high pressure vessels according to ASME VIII-1 standard. The theoretically calculated results of the stresses in the pressure vessels were compared with the results obtained from the ANSYS program. It has been determined that the cost of the multi-layer container is about 26% less than the single layer vessel, plus the variation of strain along the thickness is less, and it is more durable under high temperatures and pressures. Ahmet et al. [11] calculated Von-Mises stresses, tangential stresses and deformations in pressure vessels with different geometries subjected to thermal and static loads using the finite element method (ANSYS) for optimization. The results revealed that the tangential stresses increase with a decrease in the pressure vessel thickness. Wadkar et al. [12] designed various pressure vessels with different head types according to ASME VIII-1 and calculated equivalent stresses both analytically and numerically. The author reported that the smallest equivalent stresses were observed in the cylindrical container with a hemispherical head. Kolekar and Jewargi [13] analyzed 8 bar pressure and 24-liter pressure vessels designed according to ASME VIII-1 in five different head types (hemispherical, flanged, elliptical, flat and conical) based on finite element analyses using ANSYS program. The results showed that the least stresses were developed in the vessels with hemispherical head. Khan [14] investigated the variations in the loadings applied to the pressure vessel support legs through changing the geometric parameters. It was aimed to introduce the most appropriate values for the ratio of the support distance to the pressure vessel length and the ratio of the pressure vessel length to the vessel radius. The author

reported that the minimum stresses developed at the ratios of 0.25 for the former and the less than 16 for the latter.

In this study, the oil separator tank used in a typical commercial screw compressor system, produced by the SARMAK Co. according to ISO 1217 standard, have been analyzed based on finite element method for three different operating pressures. These thanks were composed of a metallic vessel that have been warped with different composite materials, including carbon fiber/epoxy, glass fiber/epoxy and kevlar fiber/epoxy, at different angles. The aim was to introduce the most appropriate composite material and winding angle of fibers around the metallic vessel that would result in the least stress and deformation of the composite pressure vessel under internal pressure.

2. Material and Method

In this study, the following cases were handled separately, and first-ply equivalent stress values and total deformation values were investigated for three different internal pressures 11.25, 15 and 19.5 bar and a maximum temperature of 110 °C using the finite element method.

Case 1: 0.5 mm structure steel covered with 3.5 mm E-glass.

Case 2: 0.5 mm structure steel covered with 3.5 mm E-kevlar.

Case 3: 0.5 mm structure steel covered with 3.5 mm E-carbon.

As in 3 cases, carbon, glass and kevlar fibers/epoxies composites were used as reinforcement material. According to the literature, the most accepted methods of fabrication of such composite pressure vessels are filament winding and centrifugal winding technique [2]. Therefore, to be able to obtain reliable results from finite element analyses of these vessels, the accurate properties of density, Young's modulus, Poisson's ratio, tensile and shear modulus of composite structures should be assigned to the model developed in FEM software. The mechanical and thermal properties of carbon, glass and kevlar fibers/epoxies and structural steel are given in Tables 1 and 2, respectively.

Table 1. Mechanical properties of Carbon Fiber/Epoxy [15]

Properties	Carbon Fiber/Epoxy	Glass Fiber/Epoxy	Kevlar Fiber/Epoxy
Density (kg/m^3)	1490	2000	1402
Young's Modulus (MPa) (x, y, z)	121000; 8600; 8600	45000; 10000; 10000	95710; 1.045E+5; 1.045E+5
Poisson's Ratio (xy, yz, xz)	0.27; 0.4; 0.27	0.3; 0.4; 0.3	0.34; 0.37; 0.34
Tensile (MPa) (x, y, z)	2231; 29; 29	1100; 35; 35	2231; 29; 29
Shear Modulus (MPa) (xy, yz, xz)	4700; 3100; 4100	80; 46.154; 80	25080; 25080; 25080

Table 2. Mechanical properties of Structural Steel.

Properties	Structural Steel
Density (kg/m^3)	7850
Young's Modulus (MPa)	1.98E+5
Poisson's Ratio	0.35
Tensile Yield Strength (MPa)	265
Shear Modulus (MPa)	73333

2.1. Geometry

The solid model of the separator tank used in the study was designed in the Autodesk Invertor package program according to 29/EU/2014 standards (Figure 1). Accordingly, the total height of the separator pressure vessel from the top flange to the leg support is 698 mm. The thickness of the dish ends and the cylindrical shell is 4 mm. The thickness of the flange is 24 mm. The inside radius of the separator pressure vessel is 342 mm. The reason for choosing the upper flange thickness to be larger than the thickness of the cylindrical shell is that the stresses on sharp surfaces are higher. Thus, a surface thickness that is more resistant to stresses is preferred in the upper flange with sharp corners.

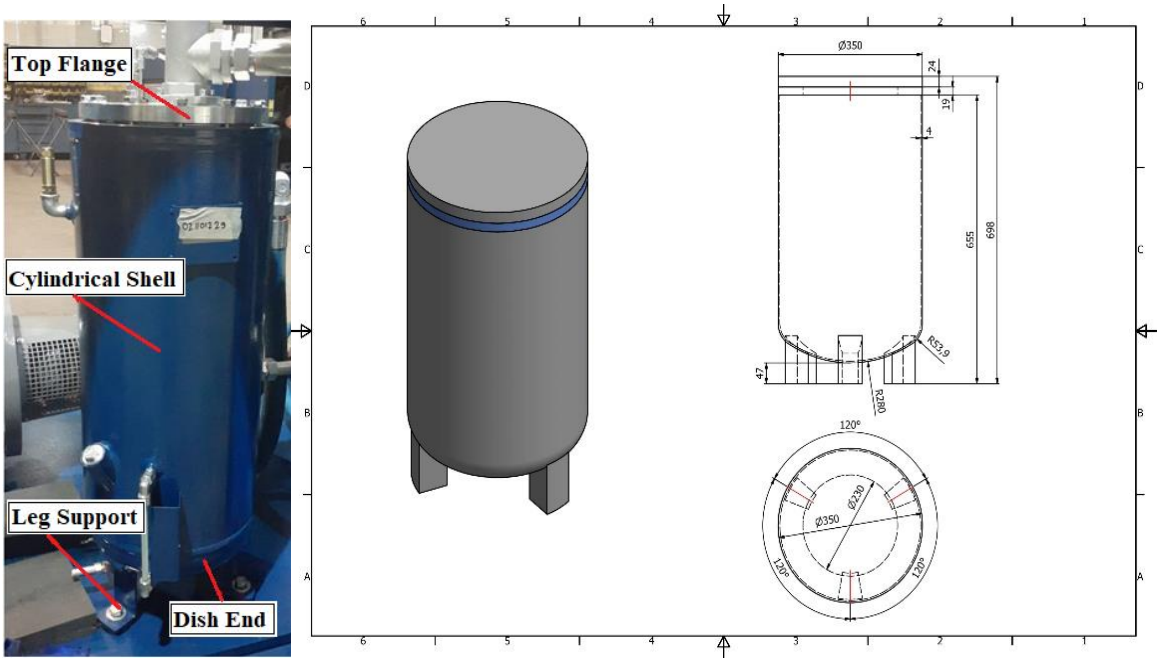

Figure 1. Figure of in-house developed oil separator pressure vessel components and technical details

2.2. Finite Element Analysis

The safety tests of pressure vessels are generally carried out at hydrostatic test pressures of about 1.5 times the operating pressure. The separator tank discussed in the study operates at three different operating pressures 7.5, 10 and 13 bar. Therefore, the boundary condition for 7.5, 10 and 13 bar internal pressures were applied as 11.25, 15 and 19.5 bar, respectively. Furthermore, the FEM analyses were carried out considering that the separator tank operates at a maximum temperature of 110 °C.

ANSYS finite element package was used to model the development of stresses and deformations in the high-pressure composite vessels under the aforementioned hydrostatic pressures. ACP (Pre) module was used to cover the design with composite, Static Structural module was used to determine the boundary conditions and ACP (Result) module was used to read the results. The layer thickness, material properties, total thickness and orientation angle of the pressure vessel were selected from the Stackups section (Figure 2).

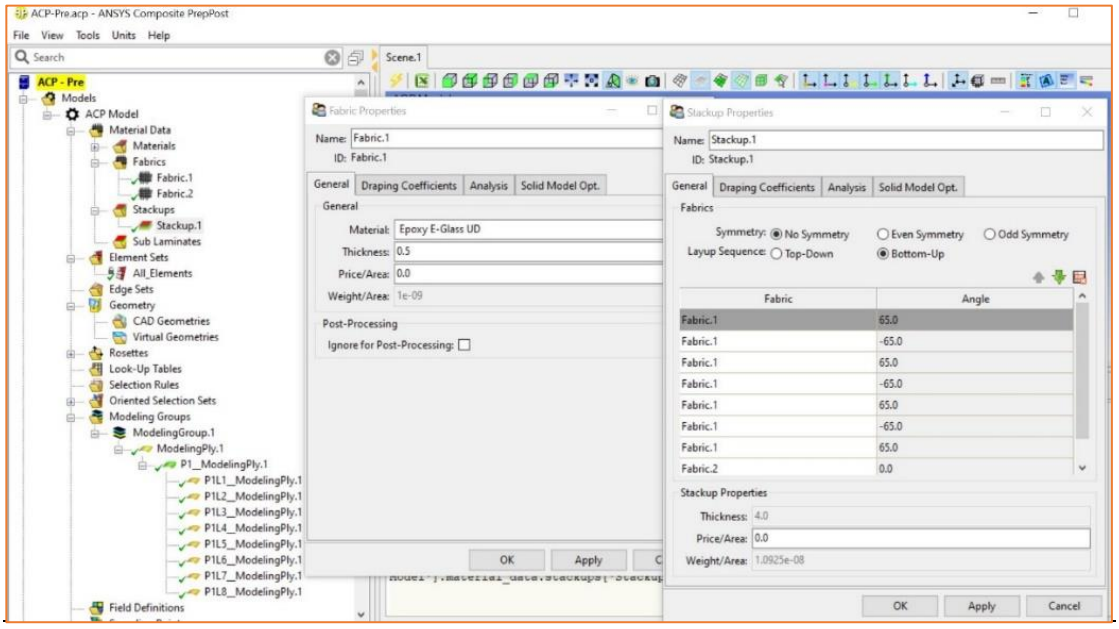

Figure 2. Display of material property, layer thickness, and orientation angles for epoxy E-glass

As shown in Figure 3, after defining the geometry conditions and element properties, the model was precisely meshed. To this end, the pressure vessel model is divided into very small areas called hexahedron elements of 0.5 mm thickness structural steel covered with 3.5 mm thickness composite material. For 0.5 mm structural steel, 262123 number of nodes and 77323 number of elements were assigned.

Figure 3. Meshed CAD Model

After the pressure and temperature values the boundary conditions were defined, the results of FEM in the form of equivalent stresses and total deformations of the model were obtained. A typical result of equivalent stresses distributed in the model of pressure vessel with the carbon fiber/epoxy as composite material and under the hydrostatic pressure of 19.5 bar is represented in Figure 4.

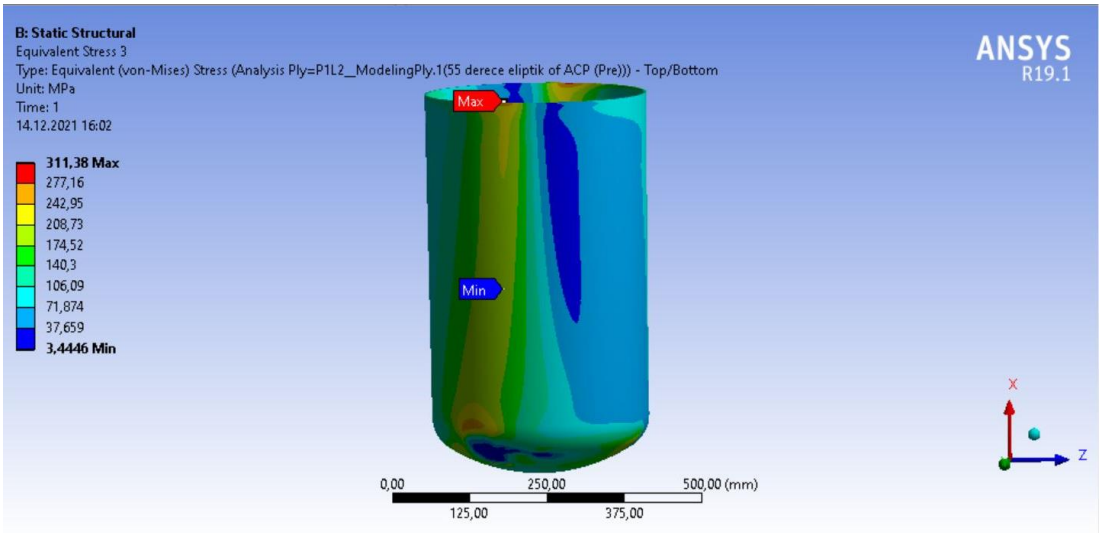

Figure 4. Typical result of equivalent stress distribution in the pressure vessel carbon fiber/epoxy composite material under the hydrostatic pressure of 19.5 bar

3. Results and Discussion

As explained in previous sections, in this study, a FEM was developed in the ANSYS environment in order to analyze the stress and total deformations developed in the composite pressure vessels. The model was composed of a metal body of separator tank that was covered with 7 layers of different composite materials, including glass fiber/epoxy, carbon fiber/epoxy and kevlar fiber/epoxy, each layer with a thickness of 0.5 mm. The material properties, wall thickness, number of layers, orientation angles and boundary conditions of the pressure vessel model were introduced to the model in the ANSYS environment. Analyses were performed at a constant internal temperature of 110 °C, using different winding angles (35°/-35°, 45°/-45°, 55°/-55° and 65°/-65°) and different internal pressure levels. The stresses and total deformations obtained as a result of the analysis were examined and the most suitable composite material and winding angle were decided for different pressures. The results of FEM analyses are represented and discussed as follows.

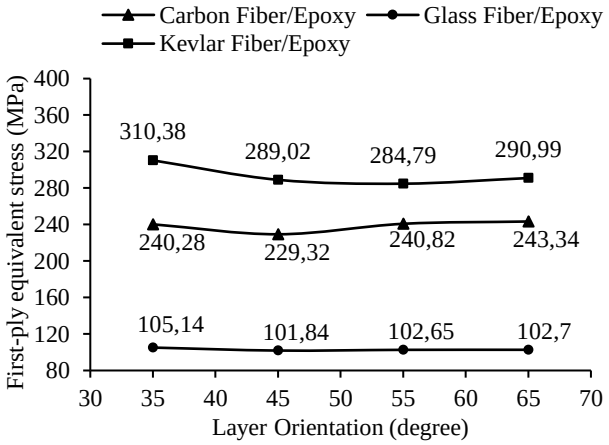

Figure 5. The graph of first-ply equivalent stress on the pressure vessel at hydrostatic pressure of 11.25 bar

Figures 5 to 7 represent the First-ply equivalent stresses (FPES) developed in different composite vessels versus the winding angle of the fibers of composites at hydrostatic pressures of 11.25, 15 and 19.5 bar, respectively. As shown in Fig. 5, the lowest FPES value is 101.84 MPa developed in the pressure vessel covered with glass fiber/epoxy with the orientation angle of 45°. In contrast, the highest FPES value under the 11.25 bar internal pressure was observed in the separator tank with kevlar fiber/epoxy composite material and a 35° layer orientation.

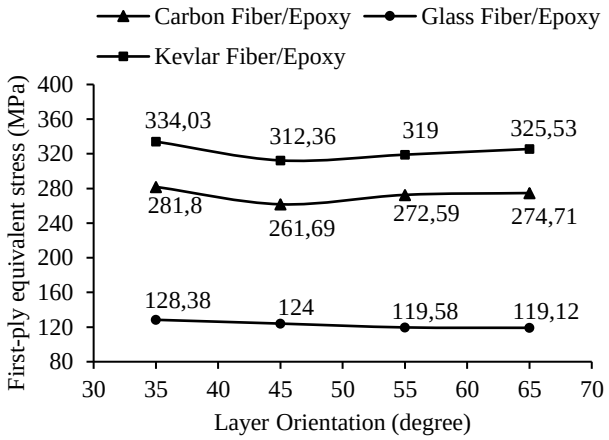

Figure 6. The graph of first-ply equivalent stress on the pressure vessel at hydrostatic pressure of 15 bar

According to Fig. 6, the lowest level of FPES of 119.12 MPa under the internal pressure of 15 bar has been seen in the pressure vessel covered with glass fiber/epoxy at the orientation angle of 65°. In contrast, the highest FPES was observed on the separator tank with kevlar fiber/epoxy composite material and at 35° layer orientation. An important observation from the results of analyses was that the stresses decreased while the layer orientation for the glass fiber/epoxy composite material increased from 35° to 65°.

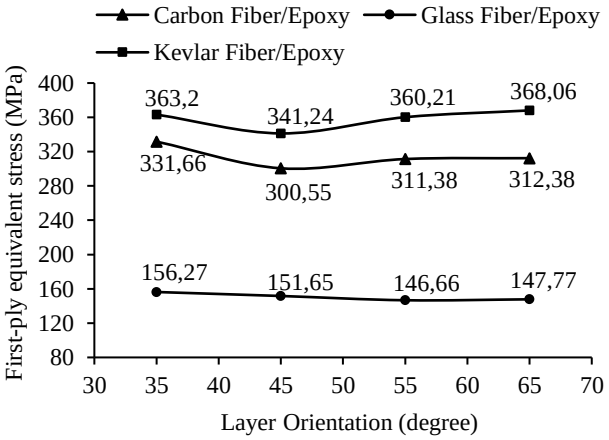

Figure 7. The graph of first-ply equivalent stress on the pressure vessel at hydrostatic pressure of 19.5 bar

Additionally, as shown in Fig. 7, the lowest FPES of about 146.66 MPa under the internal pressure of 19.5 was developed in the pressure vessel covered with glass fiber/epoxy at the orientation angle of 55°. In contrast, the highest FPES value was observed in the separator tank with kevlar fiber/epoxy composite material winded at orientation angle of 65°.

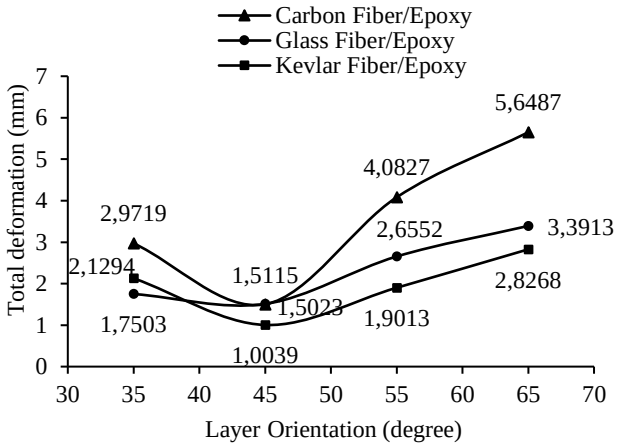

Figure 8. The graph of total deformations on pressure vessel at hydrostatic pressure of 11.25 bar

Furthermore, Figs. 8 to 10 represent the total deformation of different composite vessels versus the winding angle of the fibers of composites at hydrostatic pressures of 11.25, 15 and 19.5 bar, respectively. As shown in Fig. 8, under the internal pressure of 11.25 bar, the lowest total deformation value of about 1.0039 mm was obtained in the pressure vessel covered with kevlar fiber/epoxy with the orientation angle of 45°. In contrast, the highest total deformation value was observed on the separator tank covered with carbon fiber/epoxy composite at a winding angle of 65°. In general, under the internal pressure of 11.25 bar, the lowest levels of total deformation for all the composite vessels were observes at the composite later orientation of 45°.

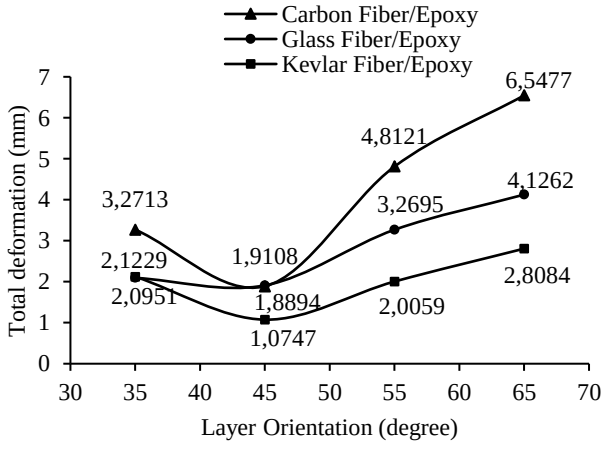

Figure 9. The graph of total deformations on pressure vessel at hydrostatic pressure of 15 bar

Under the internal pressure of 15 bar, as shown in Fig. 9, the lowest level of total deformation of 1.0747 mm was obtained for the pressure vessel covered with kevlar fiber/epoxy winded at orientation angle of 45°. In contrast, the highest total deformation occurred in the separator tank with carbon fiber/epoxy composite at orientation angle of 65°. Similar to the behavior of composite pressure vessels under the internal pressure of 11.25 bar, the lowest level of total deformation under the internal pressure of 15 bar, regardless of the type of composite material, was observed at layer orientation of 45°.

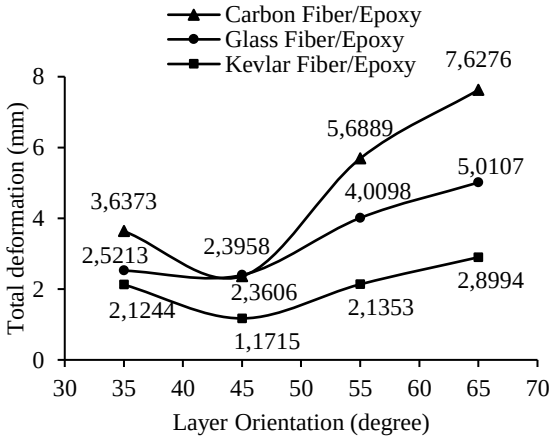

Figure 10. The graph of total deformations on pressure vessel at hydrostatic pressure of 19.5 bar.

Additionally, as shown in Fig. 10, the lowest level of total deformation of about 1.1715 mm under the internal pressure of 19.5 bar was has been obtained for the pressure vessel covered with kevlar fiber/epoxy composite at an orientation angle of 45°. Similar to previous cases, the highest total deformation value under the internal pressure of 19.5 bar was observed in the separator tank with carbon fiber/epoxy composite material winded at layer orientation of 65°.

4. Conclusion

In this study, the analyses of high pressure composites separator tanks, the base layer of which is 0.5 mm structural steel and the other layers are covered with three different types of composite materials, were conducted using finite element method under three different levels of internal pressure. It has been observed that the results of first-ply equivalent stress (FPES) and total deformation vary according to the types of composite material and orientation angle of the layers. Analyses were made using three different types of composite materials, namely carbon, glass, and kevlar fiber/epoxy, at four different winding

angles of 35°/-35°, 45°/-45°, 55°/-55°, and 65°/-65°, and three different internal pressures of 11.25, 15 and 19.5 bar. In summary, it was seen that the lowest FPES values of about 101.84, 119.12, and 146.66 MPa under the internal pressure of 11.25, 15 and 19.5 bar were obtained in the separator tanks coated with glass fiber/epoxy with a winding angle of 45°/-45°, 65°/-65° and 55°/-55°, respectively. Furthermore, the lowest total deformation levels of about 1.0039, 1.0747 and 1.1715 under the internal pressure of 11.25, 15 and 19.5 bar, respectively, were observed in the separator tank coated with kevlar fiber/epoxy at a winding angle of 45°/-45°. According to the results, the lowest stress value was observed in glass fiber/epoxy coated separator tanks at 11.25 bar pressure and 45 degree winding angle. In addition, the lowest total deformation value was obtained in the kevlar fiber/epoxy coated separator tanks at the same pressure and winding angle. In addition, it is the type of material that is suitable for composite pressure vessels that will operate at 15 and 19.5 bar pressures, due to the low stresses obtained in glass fiber / epoxy material. However, the winding angles should be 65°/-65° for 15 bar and 55°/-55° for 19.5 bar.

Contributions of the Authors

VG: methodology, software, validation, formal analysis, investigation, writing—original draft, writing - review & editing, visualization CB: conceptualization, methodology, validation formal analysis, writing—original draft, writing—review and editing, visualization, supervision, project administration. MS: conceptualization, software, validation, writing-review and editing.

Conflict of Interest Statement

There is no conflict of interest between the authors.

Statement of Research and Publication Ethics

The study is complied with research and publication ethics

References

[1] S. Bozkurt, "2014/29/AB standartlarına uygun içten basınca maruz kompozit basınçlı kap tasarımı ve analizi," Yüksek Lisans Tezi, Bingöl Üniversitesi, Fen Bilimleri Enstitüsü, Bingöl, 2018.

[2] E. Yaylağan, "Determination of Composite Pressure Vessels Under Various Loadings," Dokuz Eylül University Graduate School of Natural and Applied Sciences, İzmir, 2010.

[3] A. Pehlivan, "Elyaf Sarma ile Üretilen Kompozit Yapıdaki Basınçlı Kapların Değişik Yüklemelerde Modellenmesi," Yüksek Lisans Tezi, İstanbul Teknik Üniversitesi Bilişim Enstitüsü Hesaplamalı Bilim ve Mühendislik Anabilim Dalı, İstanbul, 2017.

[4] M. Sinha and D. Pandit, "Design and Burst Pressures Analysis of CFRP Composite Pressure Vessel for Various Fiber Orientations Angles," *International Journal of Advances in Engineering Science and Technology*, vol. 1(1), pp. 35-40, 2012.

[5] Q. Zhang, Z.W. Wang, C.Y. Tang, D.P. Hu, P.Q. Liu, and L.Z. Xia, "Analytical solution of the thermo-mechanical stresses in a multilayered composite pressure vessel considering the influence of the closed ends," *International Journal of Pressure Vessels and Piping*, vol. 98, pp. 102-110, 2012, doi: 10.1016/j.ijpvp.2012.07.009

[6] İ. Sancaklı, "Basınçlı kap konstrüksiyonlarına etki eden parametrelerin incelenmesi ve tasarımı," Yüksek Lisans Tezi, Yıldız Teknik Üniversitesi, Fen Bilimleri Enstitüsü, İstanbul, 2017.
[7] F. Mestan, "Basınçlı kapların deneysel ve teorik olarak incelenmesi," Yüksek Lisans Tezi, Hava Harp Okulu, Havacılık ve Uzay Teknolojileri Enstitüsü, İstanbul, 2010.
[8] M. Usta, "Birbirinden farklı kalın cidarlı basınçlı kaplarda kaynaklı bölgelerin TS 17020 uygunluğunun araştırılması," Yüksek Lisans Tezi, Namık Kemal Üniversitesi, Fen Bilimleri Enstitüsü, Tekirdağ, 2011.
[9] F. Tjelta, "A comparison study of pressure vessel design using different standards," Master Thesis, University of Stavanger, Faculty of Science and Technology, Stavanger, 2012.
[10] S.K. Raparla and T. Seshaiah, "Design and analysis of multilayer high pressure vessels, International *Journal of Engineering Research and Applications*," vol. 2(1), pp. 355-361, 2012.
[11] M. Ahmed, R.U. Khan, S. Badshah, and S. Jan, "Finite element investigation of geometry effect on pressure vessel under combined structural and thermal loads," *International Journal of Engineering and Advanced Technology*, vol. 4(2), pp. 118-124, 2014.
[12] V.V. Wadkar, S.S. Malgave, D.D. Patil, H.S. Bhore, and P.P. Gavade, "Design and analysis of pressure vessel using ANSYS," *Journal of Mechanical Engineering and Technology*, vol. 3(2), pp. 01-13, 2015.
[13] D. Kolekar and S.S. Jewargi, "Stress analysis of pressure vessel with different type of end connections by FEA," *International Journal of Innovative Research in Science*, vol. 04 (5), pp. 2769-2775, 2015.
[14] S.M.A. Khan, "Stress distributions in a horizontal pressure vessel and the saddle supports," International *Journal of Pressure Vessels and Piping*, vol. 87 (5), pp. 239-244, 2010, doi:10.1016/j.ijpvp.2010.03.005
[15] V. Gezginci, "Design and analysis of oil seperator tank used in screw type compressor systems," Master's Thesis, Adana Alparslan Türkeş Science and Technology University, Institute of Graduate School, Adana, 2022.

Bitlis Eren Üniversitesi Fen Bilimleri Dergisi
BİTLİS EREN UNIVERSITY JOURNAL OF SCIENCE
ISSN: 2147-3129/e-ISSN: 2147-3188
VOLUME: 11 NO: 9 PAGE: 1102-1111 YEAR: 2022
DOI: 10.17798/bitlisfen.1179758

Histological Evaluation of Spleen and Thymus of Acomys cilicicus

Hatice MUTLU EYİSON[1*], Seda KIRALP[2], Nesrin ÖZSOY ERDAŞ[1], Suna CEBESOY[1]

[1]*Ankara University/Faculty of Science*
[2]*Girne American University/Faculty of Health Sciences*
(ORCID: 0000-0002-4637-5268) (ORCID: 0000-0002-9431-9180) (ORCID: 0000-0002-0470-3745) (ORCID: 0000-0001-7484-2882)

Keywords: *Acomys cilicicus*, Thymus, Spleen, Histology

Abstract

Acomys cilicicus (Turkish Spiny Mouse), a species of the genus *Acomys*, which is the first mammal to have regeneration ability and attracts attention with its spiny-like structure, is only found in a small area near Silifke in Turkey. In recent years, species in the genus *Acomys* have been examined histologically due to their regeneration abilities. Although there are studies on the taxonomy of that species, there are not enough studies on the histology of its tissues. The overall goal of this study is to evaluate the available histomorphological data and document the normal microscopic features of the spleen and thymus tissues in *A. cilicicus*. In this study, adult spiny mice (n=3, 2 males and one female) were examined. All tissues obtained from those samples were fixed in 10% formalin and embedded in paraffin. Periodic Acid Schiff (PAS), Masson's trichrome, Gomori's silver impregnation, and Hematoxylin and Eosin (H&E) were used for staining the sections. Histological examination was carried out using light microscopy. Histological data of the spleen and thymus tissues of *A.cilicicus* were reported in detail.

1. Introduction

The genus *Acomys* is distributed in Africa, the Middle East, and southwest Asia. The number of species belonging to the genus *Acomys* has changed due to taxonomic studies. The genus has 21 species according to the IUCN Red List of Threatened Species (2022-1 version) which provides a comprehensive description of the habitat and geographic range of the genus *Acomys*, *(A. airensis, A. cahirinus, A. cilicicus, A. cineraceus, A. dimidiatus, A. ignitus, A. johannis, A. kempi, A. minous, A. mullah, A. nesiotes, A. percivali, A. russatus, A. seurati, A. spinosissimus, A. wilsoni, A. louisae, A. subspinosus, A. ngurui, A. selousi, A.muzei)* [1]. However, taxonomic research regarding the genus is still problematic [2]-[6].

The genus *Acomys*, which has the ability of regeneration within the mammalian class, has been utilized to analyze a number of topics such as physiology (especially adaptations to desert habitats), behavior, ecology, evolution, and metabolism [7]. These studies have led to the use of this genus as a model organism for the treatment of some human diseases. Recent studies have mostly focused on the study of diabetes, menstrual cycle, prenatal development, and regeneration [8]-[12].

The cells that are able to develop into a variety of cells are stem cells, and these cells form the immune system. In order for these cells to become immunologically active, they must first differentiate and develop in the primary lymphoid organs. After completing their development, B and T lymphocytes are directed to specific locations in the secondary lymphoid organs. As effector cells, these cells interact with the antigen and produce humoral and cellular immune responses [13].

The thymus, the primary lymphoid organ, develops in rodents from the endoderm of the third and fourth pharyngeal pouches and is surrounded by

*Corresponding author: hmutlu@science.ankara.edu.tr
Received: 24.09.2022, Accepted: 08.11.2022

the mesenchyme [14]. Immediately after birth, it grows significantly as a response to postnatal antigen stimulation and the requirement for large numbers of mature T cells. Both the rate and age of onset of thymus dependent immunological function are affected by genetic factors. Also, the same factors influence the size of the thymus. In rats and mice, the thymus reaches its largest magnitude by sexual maturity and then involutes gradually [15]. Thymus has an important role in the immune response against infections [16]. Efficient functioning of the thymus is critical for establishing and maintaining effective adaptive immunity [17].

The spleen is a secondary peripheral lymphoid organ that is located in the left-upper part of the abdominal cavity between the diaphragm and the fundus of the stomach. It is also located below the 9^{th} and11^{th} costae under the left side of the diaphragm and is characterized by its dark red-blue-black color [18]. The spleen is one of the major organs responsible for vital functions in the systemic circulation, especially in the breakdown of erythrocytes and the recirculation of lymphocytes. Therefore, it is a lack of afferent lymphatic vessels. Functionally and morphologically, it consists of two parts, red pulp and white pulp. Both damaged erythrocytes and foreign materials are filtered from blood by the red pulp. Besides, platelets, erythrocytes, and iron are stored in the red pulp. The spleen is not only an area of hematopoiesis in rodents, especially in the fetal and neonatal period but also it includes about one-fourth of the body's lymphocytes and starts immune responses to blood-borne antigens. The white pulp contains T and B cells. It is located around the central arterioles [19]-[22].

Even though research on the immune system of spiny mice was limited [23], studies on this subject increased after the discovery of their regeneration ability. Besides, how the immune response to injury contributes to tissue regeneration is not well understood [24]-[26]. The aim of this study is to evaluate the available histomorphological data and document the normal microscopic features of the spleen and thymus tissues in *A. cilicicus*. Also, the thymus and spleen of the species were analyzed histologically in detail for the first time.

2. Material and Method

The spiny mouse specimens were obtained from the project that was titled "Taxonomy, Biology and Distribution of Spiny Mouse" (Project number: 2003 07 05 074 and funded by the Scientific Research Project Coordination Unit of Ankara University). In total, three adult lab grown specimens (2 male and one female) were used. Animals were fed a diet of assorted seeds, supplemented with fresh apples, corn, or carrots weekly. These specimens were kept on a 13/11 h light/dark cycle and under standard laboratory conditions.

Histological analysis: Samples were processed using routine histological protocols. Spleen and thymus tissue samples were dissected from specimens and then fixed in neutralized buffered formaldehyde solution (10%), dehydrated in alcohol, and embedded in paraffin wax, and transverse sections (5 μm thick) were prepared and mounted on slides. The slides were stained with Gomori's silver impregnation, Masson's Trichrome, Periodic Acid Schiff (PAS) and Hematoxylin and Eosin (H&E). The stained slides were examined using a light microscope (Leica DM LS2) and photographed (Leica DFC320).

3. Results and Discussion

According to the histological analysis of the thymus with H&E staining, the thymus is surrounded by a fibro-adipose tissue containing fibroblasts and adipocytes, and its two lobes are attached to each other by this fibro-adipose tissue. Each lobule contains a thin capsule and septa that reach the inner space between lobules inside the capsule. Each lobule is formed by the cortex, which is seen as a dark-colored area, and the medulla, which is seen as a light-colored area at the inner side (Figure 1A). There are plenty of tightly bound lymphocytes and a few epithelial cells dispersed in the cortex. However, it is found that there are more epithelial cells in the medulla than in the cortex. There are vascular structures of various diameters, enclosed with endothelial, and containing blood tissue in their lumen (Figure 1B).

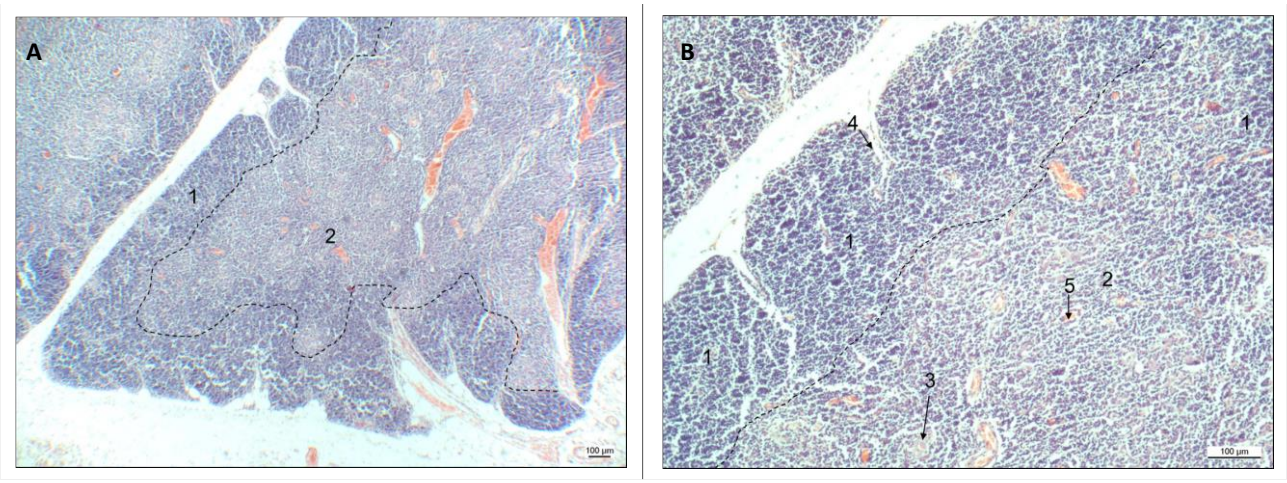

Figure 1 (**A)**. Photomicrograph of H&E-stained thymus section to show the general structure of organ, 1- cortex, 2-medulla (**B).** 1- cortex 2-medulla 3- Hassall's corpuscles, 4-septum, 5- venule

In the medulla, although the number of lymphocytes is low compared to the cortex, their size and appearance are similar to those in the cortex. Epithelial reticular cells are high in number compared to the cortex, but their histological characteristics are similar. The medulla contains Hassall's corpuscles of various shapes and numbers, and their colors are varied from light to dark purple (Figure 2).

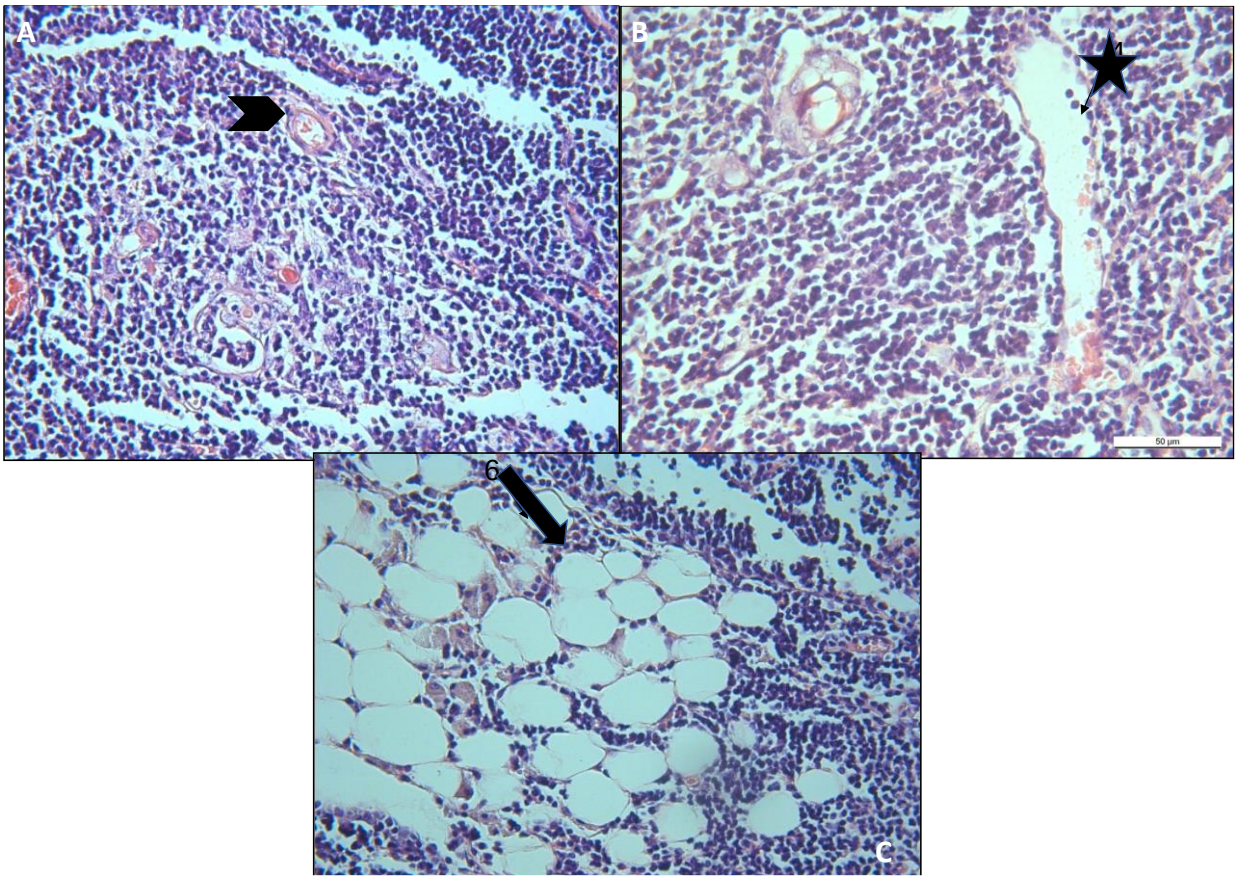

Figure 2. Thymus stained with H&E, Hassall's corpuscles (A), septum (B), adipocytes (C) (Bar indicates 50 µm)

The difference between the cortex and the medulla is observed by using Masson's Trichrome staining. Both of them are pink, but the modular area is lighter colored. It is also observed that fibrous connective tissue, septa, and vein walls are light blue (Figure 3)

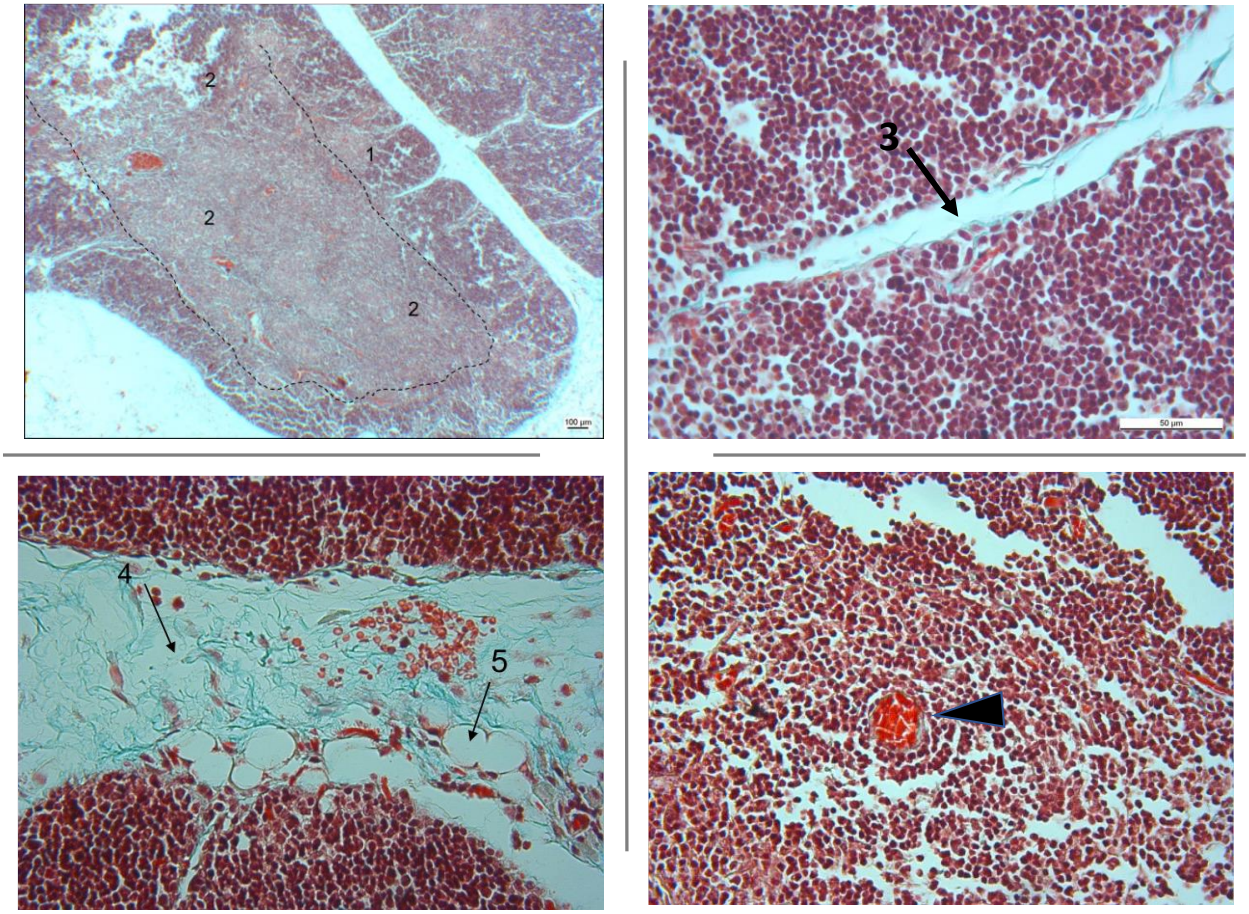

Figure 3. Thymus stained with Masson's Trichrome 1-Cortex, 2-Medulla, 3-septum, 4- fibrous connective tissue, 5-adipocyte, arrow- blood vessel

Cortex and medulla are differentiated from each other using PAS, where cortex is dark blue colored and medulla is light blue colored. Dark pink-colored PAS (+) plasmacytoid cells are seen loosely in the medulla and cortex (Figure 4)

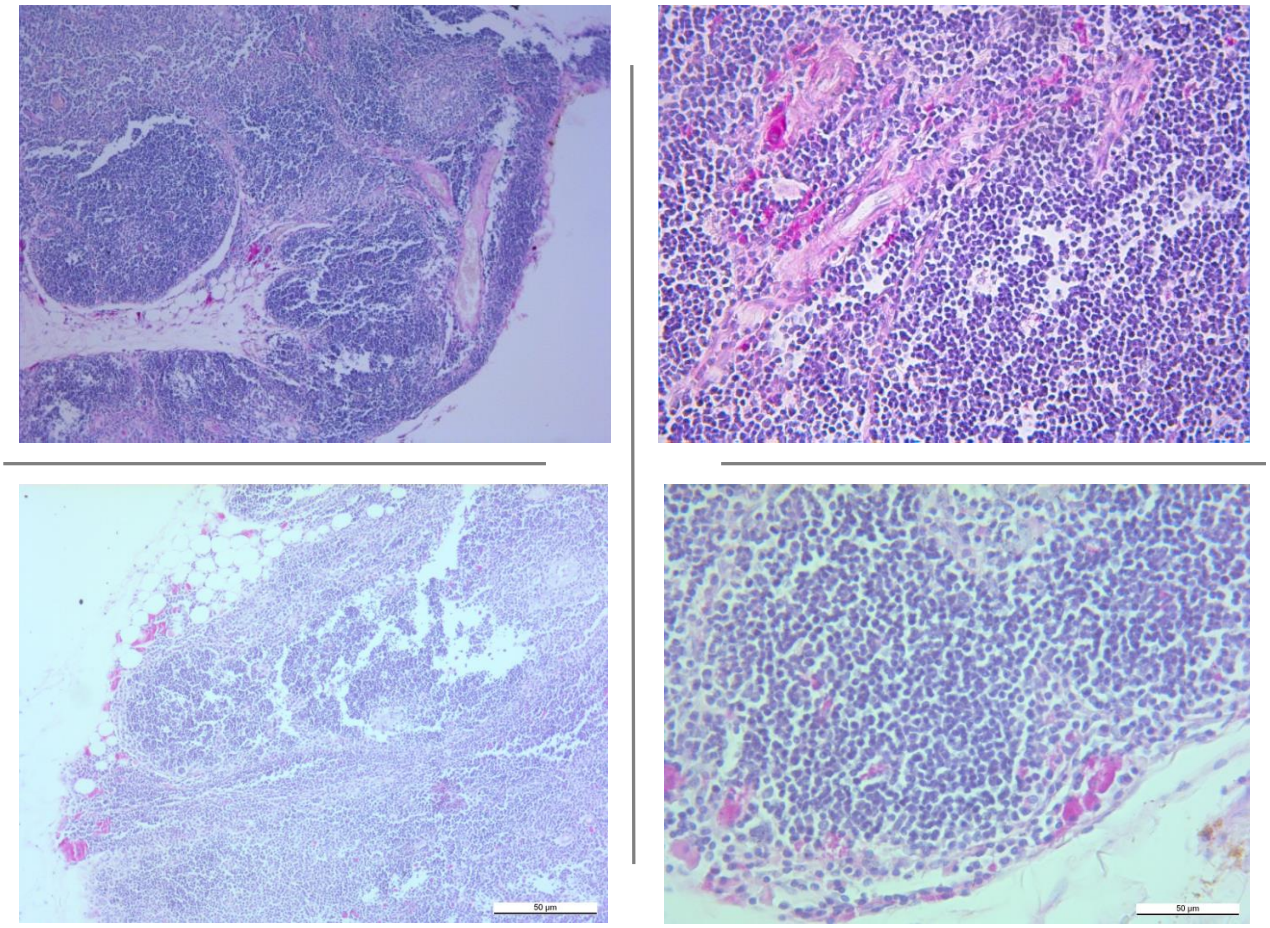

Figure 4. Photomicrograph of PAS-stained thymus section to show the general structure of organ

Gomori's silver impregnation staining gives a result like dark brown cortex and a light brown medulla. Epithelial reticular cells are observed as grey cells with indistinguishable cytoplasmic borders. Extensions of reticular cells are long thin black fibrils which are more in the medulla than in the cortex. Fibrous connective tissue capsule enclosing the organ and septa is observed as dark brown fibrils (Figure 5).

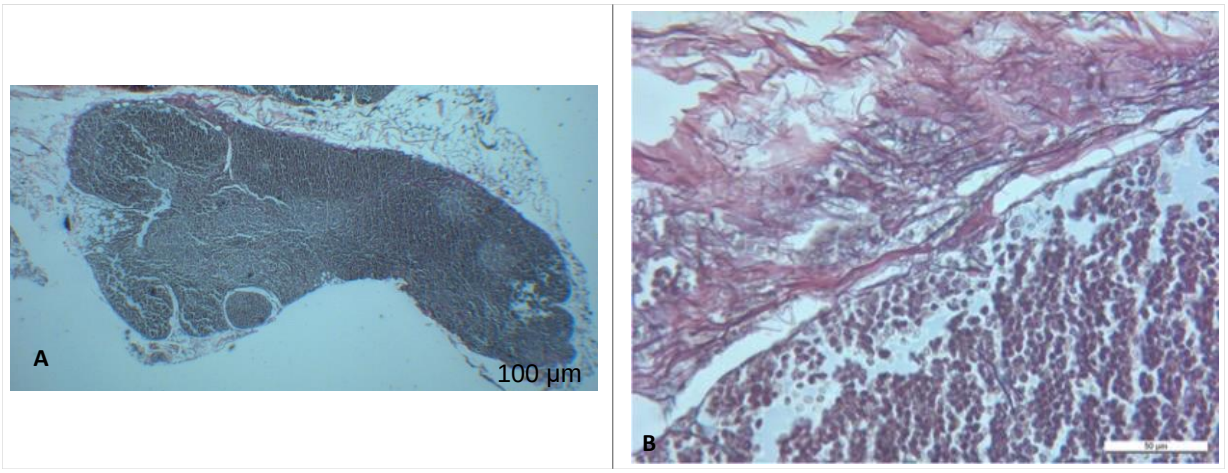

Figure 5. (A) Photomicrograph of Gomori's silver impregnation stained thymus section to show the general structure of organ, (B) reticular fibrils

The spleen's H&E staining revealed that it was surrounded by a capsule composed of connective tissue and the trabeculae gradually thinned into the spleen (Figure 6). White pulp is surrounded by the red pulp in the spleen tissue, and sinuses and trabeculae can be seen between the cells. White and red pulps are separated from each other by the marginal zone (Figure 7). The micrographs, stained with PAS, Masson's Trichrome, and Gomori's silver impregnation, revealed the general structure of the organ (Figure 8). Trabeculae are located between cells in the red pulp. PAS staining of the trabecular arteries of the cell wallsresulted in PAS (+) reaction. The connective tissue of the trabeculae was stained blue with Masson's Trichrome (Figure 9). Reticular fibers are stained with PAS (+) and silver due to their glycoprotein content. In this study, it was found that reticular fibers were quite common in tissues stained with Gomori's silver impregnation (Figure 10).

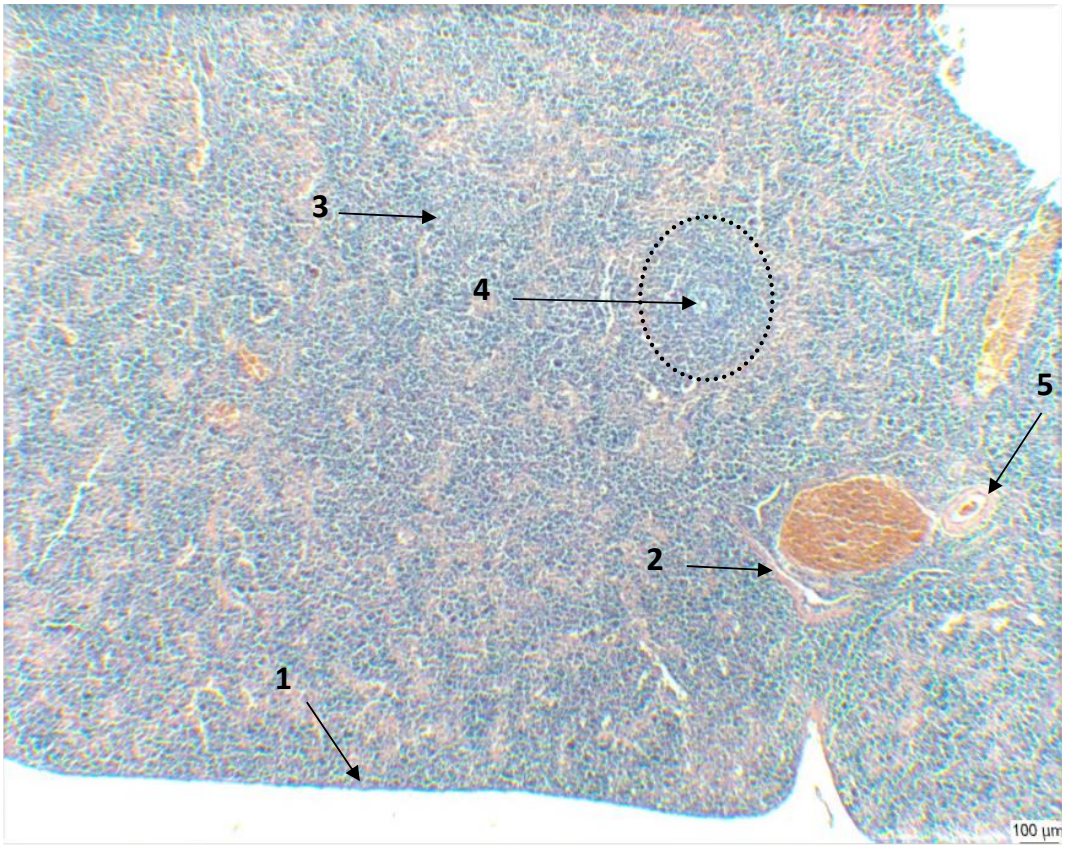

Figure 6. Photomicrograph of H&E-stained spleen section to show the general structure of the organ. 1-capsule, 2-trabeculae (connective tissue), 3-red pulp, 4-lymphoid follicle (white pulp), 5- central arteriole

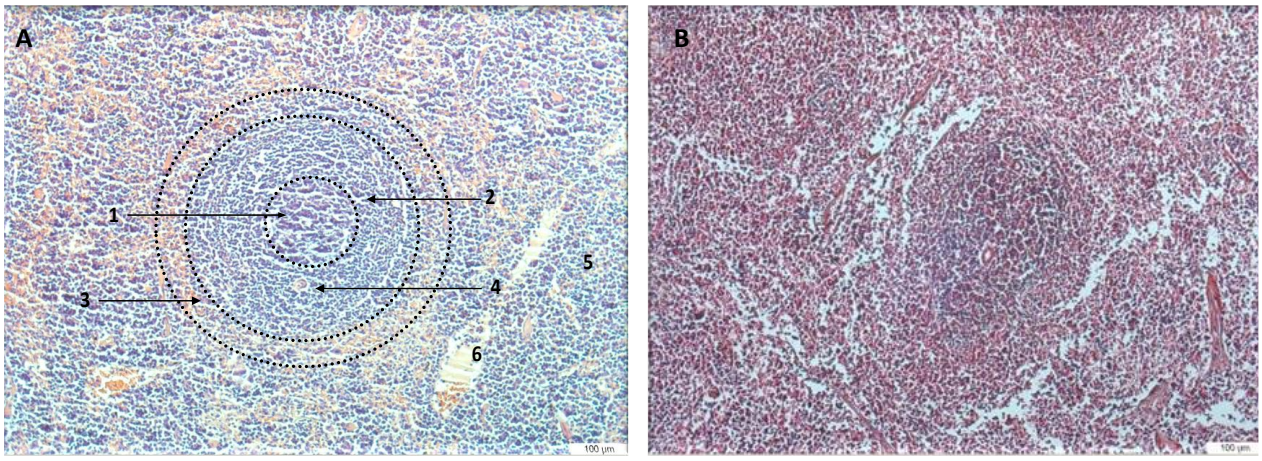

Figure 7. Photomicrograph of the spleen, showing a white pulp surrounded by a red pulp. (A) H&E stained. Bar=100µm. 1-germinal center of the follicle, 2-mantle zone of the follicle, 3-marginal zone of the follicle, 4-central arteriole, 5-red pulp, 6-trabeculae; (B) Masson's Trichrome stained

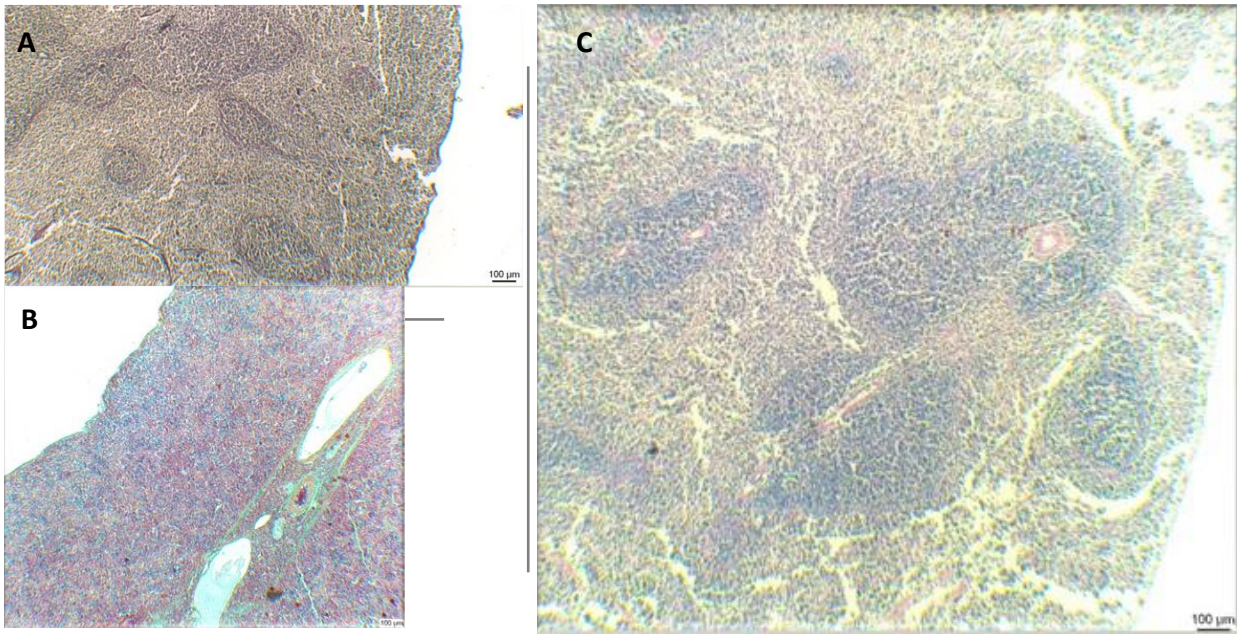

Figure 8. General structure of the white and red pulp in the spleen with different staining. (A) Gomori's silver impregnation, (B) Masson's Trichrome and (C) Periodic Acid Schiff (PAS)

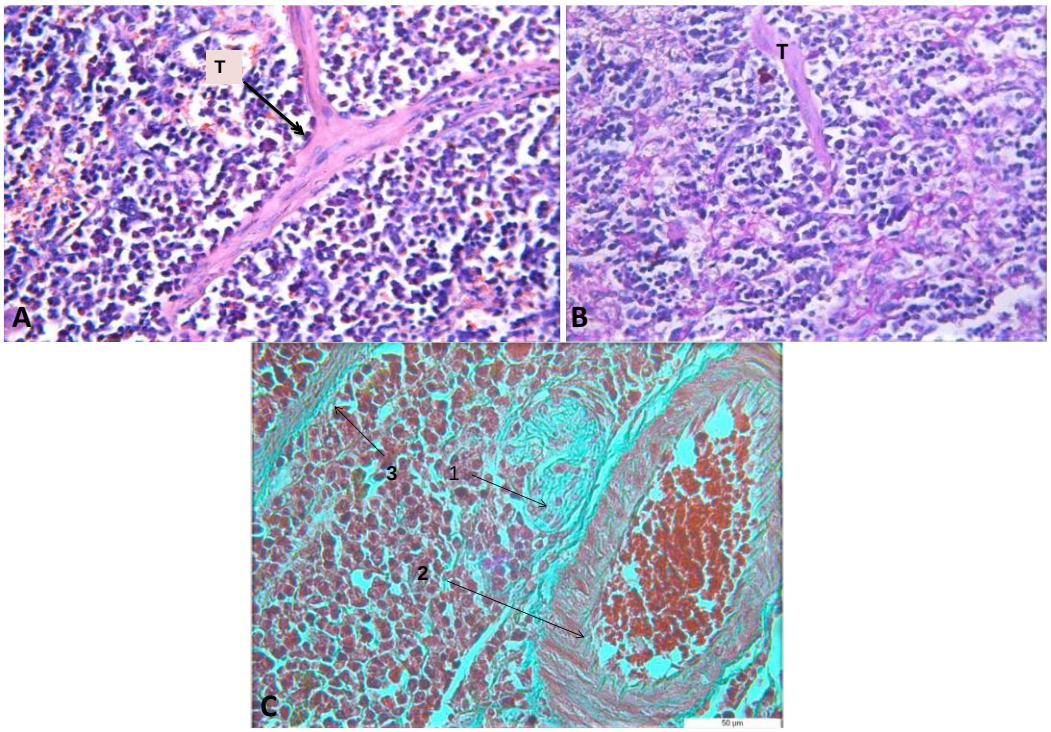

Figure 9. Photomicrograph of splenic trabeculae of spleen with different stains, A: H&E-(x400); B: PAS; C: Masson's Trichrome and 1- central arteriole, 2- vein, 3- trabecula. Bar indicates 50 µm

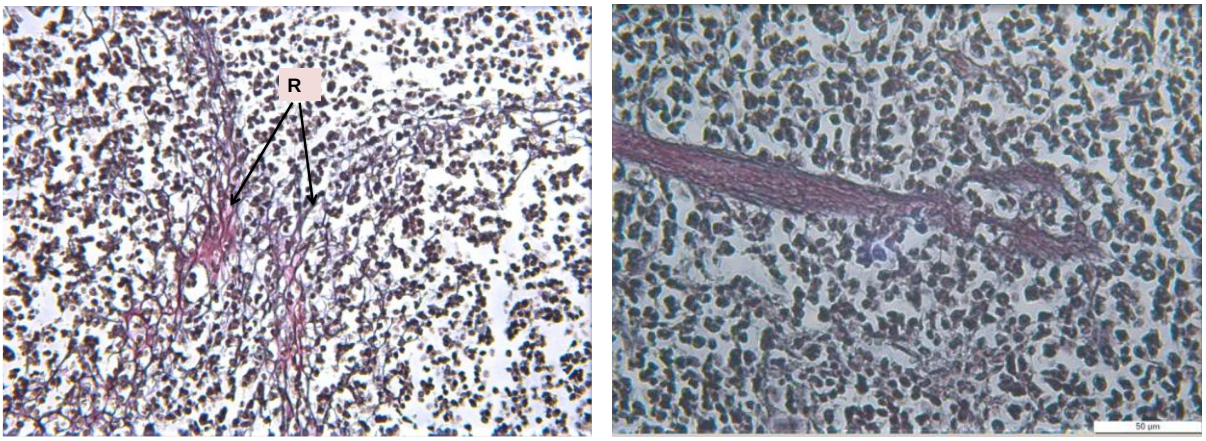

Figure 10. Photomicrograph of the network of splenic reticular fibers (R-reticular fibers x400). Gomori's silver impregnation-stained section

3.4. The Conclusion and Suggestions

Despite not being a laboratory animal, *Acomys* species have been used in numerous studies on physiology, ecology, evolution, behavior, and metabolism. They have also recently gained attention for their remarkable abilities in organ and tissue regeneration. These studies have led to the use of *Acomys* species as a model organism in the treatment of various human diseases. In order to understand the mechanisms that regulate regeneration, there are studies on the thymus and spleen cells of *Acomys* [23]- [26]. However, there are no histological studies on these organs of *Acomys*. *Acomys cilicicus* distributes only in a small area, which is formed with sparse limestone rock blocks, near Silifke in Turkey.

Although *Acomys cilicicus* is in the DD category in the "IUCN Red List" evaluation, this species is now considered to be endangered due to the destruction of its habitat, [27],[28].

In this study, the histomorphological structures of the thymus and spleen tissues, which play an important role in the immune system of the species, were examined using different histological stains. This study is important in terms of revealing the first histological data of the species.

Acknowledgment

We thank to Prof. Dr. Erkut Kıvanç for supplying the *Acomys cilicicus* samples for this study.

Contributions of the Authors

Conceptualization and supervision: HME, SK, NÖE, and SC. Methodology: NÖE. Investigation: HME, SK, NÖE, and SC. Writing—original draft: HME and SK. Writing—review & editing: HME and SC. Visualization: HME. All authors contributed to the article and approved the submitted version.

Conflict of Interest Statement

There is no conflict of interest between the authors. This Article was presented in part as a poster at the 34th FEBS Congress Life's Molecular Interactions, "Histological Analysis of Spleen of *Acomys cilicicus*" and "Histological Analysis of Thymus of *Acomys cilicicus*" Prague, Czech Republic, 4-9 July 2009.

Statement of Research and Publication Ethics

The study is complied with research and publication ethics. The samples of this article obtained from the project that was titled as "Taxonomy, Biology and Distribution of Spiny Mouse" (Project number: 2003 07 05 074) and funded by Scientific Research Project Coordination Unit of Ankara University. No additional animals were killed for this study

References

[1] The IUCN Red List Threatened Species, (September 2022 online: https://www.iucnredlist.org/search?query=acomys&searchType=species)

[2] P. O., Barome, V., Volobouev, M., Monnerot, J. K., Mfune, W., Chitaukali, J. C., Gautun and C Denys, "Phylogeny of *Acomys spinosissimus* (Rodentia, Muridae) from north Malawi and Tanzania: evidence from morphological and molecular analysis."*Biological Journal of the Linnean Society*, vol. 73 (3), pp. 321-340, 2001.

[3] S. J., Steppan, R. M., Adkins, P. Q., Spinks and C., Hale, "Multigene phylogeny of the Old World mice, Murinae, reveals distinct geographic lineages and the declining utility of mitochondrial genes compared to nuclear genes."*Molecular phylogenetics and evolution*, vol. 37(2), pp. 370-388, 2005.

[4] D., Frynta, K., Palupčíková, E., Bellinvia, P., Benda, H., Skarlantova, L., Schwarzova and D., Modrý, "Phylogenetic relationships within the cahirinus-dimidiatus group of the genus *Acomys* (Rodentia: Muridae): new mitochondrial lineages from Sahara, Iran and the Arabian Peninsula."*Zootaxa*, vol. 2660 (1), pp. 46-56, 2010.

[5] P. H., Fabre, L., Hautier, D., Dimitrov and E. J., Douzery, "A glimpse on the pattern of rodent diversification: a phylogenetic approach."*BMC evolutionary biology*, vol.12 (1), pp. 1-19, 2012.

[6] S., Renaud, E. A., Hardouin, P., Chevret, K., Papayiannis, P., Lymberakis, F., Matur,... and G. P., Mitsainas, "Morphometrics and genetics highlight the complex history of Eastern Mediterranean spiny mice."*Biological Journal of the Linnean Society*, vol.130 (3), pp. 599-614, 2020.

[7] G., Pinheiro, D. F., Prata, I. M., Araújo and G., Tiscornia, "The African spiny mouse (*Acomys* spp.) as an emerging model for development and regeneration."*Laboratory animals*,vol. 52(6), pp. 565-576, 2018.

[8] A. E., Gonet, W., Stauffacher, R., Pictet and A. E., Renold, "Obesity and diabetes mellitus with striking congenital hyperplasia of the islets of Langerhans in spiny mice (*Acomys cahirinus*)."*Diabetologia*, vol. 1(3), pp.162-171, 1966.

[9] E., Shafrir, Z., Ehud and K. Rony "Nutritionally induced diabetes in desert rodents as models of type 2 diabetes: *Acomys cahirinus* (spiny mice) and Psammomys obesus (desert gerbil), "*ILAR journal*, vol. 47(3), pp. 212-224, 2006.

[10] B. A., O'Connell, K. M., Moritz, D. W., Walker and H., Dickinson, "Sexually dimorphic placental development throughout gestation in the spiny mouse (*Acomys cahirinus*)."*Placenta*, vol. 34(2), pp. 119-126, 2013.
[11] N., Bellofiore, S. J., Ellery, J., Mamrot, D. W., Walker, P., Temple-Smith and H., Dickinson, "First evidence of a menstruating rodent: the spiny mouse (*Acomys cahirinus*)."*American journal of obstetrics and gynecology*, vol. 216(1), pp. 40-51, 2017.
[12] M., Maden, and J. A. Varholick. "Model systems for regeneration: the spiny mouse, *Acomys cahirinus*." Development vol. 147(4), dev167718, 2020.
[13] H.-Ü., Lüleyap. *Moleküler genetiğin esasları*. Nobel Kitabevi, 2008.
[14] C.-D., Dijkstra, and T., Sminia. "Normal anatomy, histology, immunohistology, ultrastructure, rat." Hemopoietic System. Springer, Berlin, Heidelberg, pp.249-256, 1990.
[15] G., Pearse. "Normal structure, function and histology of the thymus."*Toxicologic pathology*, vol. 34(5), pp. 504-514, 2006.
[16] P., Thapa, and D. L., Farber. "The role of the thymus in the immune response."*Thoracic surgery clinics*, vol. 29(2), pp. 123-131, 2019.
[17] J.-F., Miller. "The function of the thymus and its impact on modern medicine."*Science* , vol. 369 (6503), eaba2429, 2020.
[18] P., Losco. "Normal development, growth and aging of the spleen."Pathobiology of the aging rat, pp. 75-93, 1992.
[19] C. F., Kuper, C., Ruehl-Fehlert, S. A., Elmore and G. A., Parker, "Immune system." Haschek and Rousseaux's handbook of toxicologic pathology. Academic Press, pp.1795-1862, 2013.
[20] P., Balogh, G., Horváth, and A. K., Szakal. "Immunoarchitecture of distinct reticular fibroblastic domains in the white pulp of mouse spleen." *Journal of histochemistry & cytochemistry*, vol. 52(10), pp. 1287-1298, 2004.
[21] M. A., Nolte, R., Arens, M., Kraus, M. H., van Oers, G., Kraal, R. A., van Lier and E. R., Mebius, "B cells are crucial for both development and maintenance of the splenic marginal zone."*The Journal of Immunology*, vol.172(6), pp. 3620-3627, 2004.
[22] M.-F., Cesta. "Normal structure, function, and histology of the spleen."*Toxicologic pathology*, vol. 34(5), pp. 455-465, 2006.
[23] A., Pennello, J., Taylor, R., Matlack, J., Karp and J., Riggs, "Spiny mice (*Acomys cahirinus*) do not respond to thymus-independent type 2 antigens." *Developmental & Comparative Immunology*, vol. 30(12), pp. 1181-1190, 2006.
[24] J., Simkin, T. R., Gawriluk, J. C., Gensel and A. W., Seifert,"Macrophages are necessary for epimorphic regeneration in African spiny mice."*Elife*, vol. 6, e24623, 2017.
[25] J. O., Brant, J. H., Yoon, T., Polvadore, W. B., Barbazuk and M., Maden, "Cellular events during scar-free skin regeneration in the spiny mouse, *Acomys*." *Wound repair and regeneration*, vol. 24(1), pp. 75-88, 2016.
[26] T. R., Gawriluk, J., Simkin, C. K., Hacker, J. M., Kimani, S. G., Kiama, V. O., Ezenwa and A. W., Seifert, "Complex tissue regeneration in mammals is associated with reduced inflammatory cytokines and an influx of T cells." *Frontiers in immunology*, vol.11, pp. 1695, 2020.
[27] E., Kivanc, H. M., Eyison and S., Kiralp. "The distribution, habitat and conservation status of the Turkish spiny mouse, *Acomys cilicicus* Spitzenberger, 1978." *Journal of Entomology and Zoology Studies*, vol. 5(2), pp. 1443-1447, 2017.
[28] B. K., Özdemirel, O., Çetintaş, M., Sözen, M., Çoğal and F., Matur, "Modelling Distribution of Asia Minor Spiny Mouse (*Acomys Cilicicus*) Using Maximum Entropy." *International Journal of Environment and Geoinformatics*, vol.9(3), pp. 118-125, 2022.

Bitlis Eren Üniversitesi Fen Bilimleri Dergisi
BİTLİS EREN UNIVERSITY JOURNAL OF SCIENCE
ISSN: 2147-3129/e-ISSN: 2147-3188
VOLUME: 11 NO: 4 PAGE: 1112-1116 YEAR: 2022
DOI: 10.17798/bitlisfen.1180367

On Error Analysis of Systems of Linear Equations with Hadamard Coefficients

Emine Tuğba AKYÜZ[1*]

[1]*Selçuk University, Kadınhanı Faik İçil Vocational School (ORCID: 0000-0002-7189-0974)*

Keywords: Hadamard matrices, Error analysis, Relative error, Absolute error.

Abstract
In this study, error analysis for linear equation systems whose coefficients matrix is Hadamard matrix is discussed. In the Hx=f problem, the effect of the change in the elements in the f vector at the same rate and the change in the elements in the f vector at different rates were examined, and the relative error and absolute error equations for this system were given.

1. Introduction

A special type of matrix, Hadamard matrices, was first described by James Sylvester in 1867, but after Jacques Hadamard changed the definition of the size of these matrices in 1893, this matrix type was named after him. Looking at the literature, it can be said that the studies on Hadamard matrices have progressed in two directions. The first is the studies on the development of the theory of Hadamard matrices and generally includes the methods of obtaining these matrices, and the second is the studies on the use of Hadamard matrices in different fields. Numerous studies show that Hadamard matrices are used in many areas such as error detection, coding of audio and video signals, code correction and statistics. To get an idea the use of Hadamard matrices in areas such as error correction coding, signal processing and statistics, the book Hadamard Matrix Analysis and Synthesis can be reviewed [1]. Similarly, the book Hadamard Matrices and Their Applications contains sections on the applications of Hadamard matrices in signal processing, coding and cryptography [2].

In this study, in the event that the coefficient matrix of a linear equation system is Hadamard matrix, relative error and absolute error analysis were performed.

2. Introduction of Hadamard Matrices

Let H is the square matrix with all elements ±1, and I_n is the identity matrix of size nxn

$$H.H^T = n.I_n \quad (1)$$

the H matrix that provides the equality is called the n-dimensional Hadamard matrix and is denoted by H_n [1], [2], [3], [4]. Below are 1,2 and 4 dimensional Hadamard matrices

$$[1],\ \begin{bmatrix} 1 & -1 \\ -1 & -1 \end{bmatrix},\ \begin{bmatrix} 1 & 1 & -1 & -1 \\ 1 & 1 & 1 & 1 \\ 1 & -1 & 1 & -1 \\ 1 & -1 & -1 & 1 \end{bmatrix} \quad (2)$$

In order for an n-dimensional Hadamard matrix to exist, it must be n=1, n=2, or n=4k (k∈N) [4]. That is, the size of Hadamard matrices is n=1,2,4,8,12,16,20,24,….

2.1. Norm and condition number for the Hx = f problem

Table 1. Condition number of Hadamard matrices in different norms

α	$\|H\|_\alpha$	$\|H^{-1}\|_\alpha$	$K_\alpha(H) = \|H\|_\alpha \|H^{-1}\|_\alpha$
1-norm	n	1	n
2-norm	$\sqrt{n}$	$1/\sqrt{n}$	1
Frobenius-norm	n	1	n
İnfinity-norm	n	1	n

*Corresponding author: tugbaakyuz@selcuk.edu.tr
Received: 26.09.2022, Accepted: 20.10.2022

According to this table, as the size of the system increases (as the *H* matrix gets larger), the condition number for 1-norm, frobenius-norm andinfinity-norm will also increase. The fact that the condition number is large does not mean that our system is unsolvable or badly conditional. Systems of linear equations with Hadamard coefficients (SLEHC) are solvable systems and have only one solution. This is shown by the condition number according to the 2-norm ($K_2(H) = 1$). The 2-norm best characterizes the condition number for SLEHC.

If *Q* is an orthogonal matrix, since $K_2(H) = 1$ for the 2-norm, orthogonal matrices are called "perfectly conditioned" [5]. In this case, it can be said that SLEHC is "perfectly defined" since $K_2(H) = 1$.

If *H* is an n-dimensional Hadamard matrix, the following equations are obtained when 2-norm is used in the *Hx=f* problem:

$$\|Hx\|_2 = \|H\|_2\|x\|_2 \quad (3)$$

$$\|x\|_2 = \frac{\|f\|_2}{\sqrt{n}} \quad (4)$$

3. Error Analysis for the Hx = f Problem

In error analysis in numerical calculations, there are two ways to measure the size of the error: Absolute error and Relative error [6].
For a vector $x \in R^n$, where $\|.\|$ is any vector norm, the relative and absolute error are as follows [5]

$$\varepsilon_{absolute} = \|x - \hat{x}\| \quad (5)$$

$$\varepsilon_{relative} = \frac{\varepsilon_{absolute}}{\|x\|} = \frac{\|x-\hat{x}\|}{\|x\|}\ ,\ x \neq 0 \quad (6)$$

3.1. Error evaluation 1

Since *H* is a fixed matrix in the $Hx = f$ system, errors in the solution of this problem would result from changes in the f vector. Consider the problem $H_4x = f$, whose real solution is given below for the 4-dimensional Hadamard

$$\begin{bmatrix} 1 & 1 & 1 & 1 \\ 1 & -1 & 1 & -1 \\ 1 & 1 & -1 & -1 \\ 1 & -1 & -1 & 1 \end{bmatrix} \begin{bmatrix} x_1 \\ x_2 \\ x_3 \\ x_4 \end{bmatrix} = \begin{bmatrix} 1{,}1345 \\ 2{,}4567 \\ 3{,}5678 \\ 4{,}6789 \end{bmatrix}$$

$$x = \begin{bmatrix} 2{,}959475 \\ -0{,}052775 \\ -1{,}163875 \\ -0{,}608325 \end{bmatrix}$$

Now let's see how the errors in the *f* vector will be reflected in the result.
Let there be an error of 0.0001 in one element of *f* (on the first element).

$$\hat{f} = \begin{bmatrix} 1{,}1346 \\ 2{,}4567 \\ 3{,}5678 \\ 4{,}6789 \end{bmatrix} \quad \hat{x} = \begin{bmatrix} 2{,}9595 \\ -0{,}05275 \\ -1{,}16385 \\ -0{,}6083 \end{bmatrix}$$

$$\hat{x} - x = \begin{bmatrix} 0{,}000025 \\ 0{,}000025 \\ 0{,}000025 \\ 0{,}000025 \end{bmatrix}$$

A difference of 10^{-4} in one element of *f* is reflected in each element of the result vector as a difference of $\mp 25.10^{-6}$. Absolute error here:
$\|\hat{x} - x\| = 50.10^{-6}$
The result is a change of 0.0001 in two elements of *f* (selected 2nd and 3rd):

$$\hat{f} = \begin{bmatrix} 1{,}1345 \\ 2{,}4568 \\ 3{,}5679 \\ 4{,}6789 \end{bmatrix} \quad \hat{x} = \begin{bmatrix} 2{,}959525 \\ -0{,}052825 \\ -1{,}163875 \\ -0{,}608325 \end{bmatrix}$$

$$\hat{x} - x = \begin{bmatrix} 0{,}00005 \\ -0{,}00005 \\ 0{,}00000 \\ 0{,}00000 \end{bmatrix} \quad \|\hat{x} - x\| = \sqrt{2}.50.10^{-6}$$

A difference of 10^{-4} in the two elements of *f* is reflected as a difference of $\mp 50.10^{-6}$ in the two elements of the result vector.
With a change of 0.0001 in the three elements of *f* (selected 1,2 and 4), the result is:

$$\hat{f} = \begin{bmatrix} 1{,}1346 \\ 2{,}4568 \\ 3{,}5678 \\ 4{,}679 \end{bmatrix} \quad \hat{x} = \begin{bmatrix} 2{,}95955 \\ -0{,}05275 \\ -1{,}16385 \\ -0{,}608385 \end{bmatrix}$$

$$\hat{x} - x = \begin{bmatrix} 0{,}000075 \\ 0{,}000025 \\ 0{,}000025 \\ -0{,}000025 \end{bmatrix} \quad \|\hat{x} - x\| = \sqrt{3}.50.10^{-6}$$

With a change of 0.0001 in the four elements of *f*, the result is:

$$\hat{f} = \begin{bmatrix} 1{,}1346 \\ 2{,}4568 \\ 3{,}5679 \\ 4{,}679 \end{bmatrix} \quad \hat{x} = \begin{bmatrix} 2{,}959575 \\ -0{,}052775 \\ -1{,}163875 \\ -0{,}608325 \end{bmatrix}$$

$$\hat{x} - x = \begin{bmatrix} 0{,}0001 \\ 0{,}0000 \\ 0{,}0000 \\ 0{,}0000 \end{bmatrix} \|\hat{x} - x\| = 0{,}000 = 2.50.10^{-6}$$

Now, Can we write the above results as follows?

$$\|\hat{x} - x\| = \sqrt{number\ of\ changing\ elements}.\frac{1}{\sqrt{n}}. \quad (7)$$

To answer this question, it was applied for H_8, similar to the work done for H_4 above and it was seen that the above formula is provided for the absolute error that will ocur when there are differences of $\varepsilon = 10^{-4}$, $\varepsilon = 10^{-3}$, $\varepsilon = 10^{-2}$, $\varepsilon = 10^{-1}$, in one or more elements of the *f* vector [7].

Here, the reason why ε is chosen as $\varepsilon = 10^{-k}$ instead of any number is to give an idea about rounding errors. In the rounding of numbers, while the section after the decimal part to be rounded is discarded, the previous digit will either stay the same or increase by 1. Equality (7) is valid when the elements of vector f are changed at the same rate. If different changes are made in the elements of f, what can be said about how the system behaves and how these differences are reflected in the result? The answer to this question is covered in 3.2.

3.2. Error evaluation 2

Let $\hat{x}$ be the approximate solution of the linear equation system $Ax = f$. The cause of the error may be rounding errors in the operation process or incorrect input of the matrix *A* and the vector *f*.

e, solution error ($e = x - \hat{x}$) provides the following system

$$Ae = r \quad (8)$$

Here r is as follows and is called the remaining vector or residual vector [8]

$$r = f - A\hat{x} \quad (9)$$

There is the following inequality with $r = f - A\hat{x}$ and $e = x - \hat{x}$ [8]:

$$\frac{1}{K(A)}\frac{\|r\|}{\|f\|} \le \frac{\|e\|}{\|x\|} \le K(A)\frac{\|r\|}{\|f\|} \quad (10)$$

According to this theorem, the lower limit of the relative error in the solution of the Ax = f system is $\frac{1}{K(A)}\frac{\|r\|}{\|f\|}$ and the upper limit is $K(A)\frac{\|r\|}{\|f\|}$. Now let's apply this theorem to the Hadamard matrix:

Since $K_2(A)$=1 for SLEHC, inequality (10)

$$\frac{\|r\|_2}{\|f\|_2} \le \frac{\|e\|_2}{\|x\|_2} \le \frac{\|r\|_2}{\|f\|_2} \quad (11)$$

takes the form. Hence,

$$\|\mathrm{r}\|_2\|\mathrm{x}\|_2 = \|\mathrm{e}\|_2\|\mathrm{f}\|_2 \quad (12)$$

equality is achieved.

Since $r = f - \hat{f}$ and $e = x - \hat{x}$ as a result, according to the 2-norm for the relative error of the $Hx = f$ problem;

$$\frac{\|x-\hat{x}\|_2}{\|x\|_2} = \frac{\|f-\hat{f}\|_2}{\|f\|_2} \quad (13)$$

is obtained.

3.3. Error evaluation 3

There are two cases for errors in the f vector:

- ε the amount of error is the same or different in each element
- The error exists in every element or some elements

The case where all elements of *f* change at the same rate

$$Hx = f = \begin{bmatrix} \mathrm{f}_1 \\ \mathrm{f}_2 \\ \vdots \\ \mathrm{f}_n \end{bmatrix},\ H\hat{x} = \hat{f} = \begin{bmatrix} \mathrm{f}_1 + \varepsilon \\ \mathrm{f}_2 + \varepsilon \\ \vdots \\ \mathrm{f}_n + \varepsilon \end{bmatrix}, \hat{f} - f = \begin{bmatrix} \varepsilon \\ \varepsilon \\ \vdots \\ \varepsilon \end{bmatrix}$$

$$\|x - \hat{x}\|_2 = \frac{\left\|f - \hat{f}\right\|_2}{\sqrt{n}} = \frac{1}{\sqrt{n}}\sqrt{\varepsilon^2 + \varepsilon^2 + \cdots + \varepsilon^2}$$
$$= \frac{1}{\sqrt{n}}\sqrt{n\varepsilon^2} = \varepsilon$$

The case where some elements of f (k items) change at the same rate

$$Hx = f = \begin{bmatrix} \mathrm{f}_1 \\ \mathrm{f}_2 \\ \vdots \\ \mathrm{f}_n \end{bmatrix}, \quad H\hat{x} = \hat{f} = \begin{bmatrix} \mathrm{f}_1 + \varepsilon \\ \mathrm{f}_2 + \varepsilon \\ \vdots \\ \mathrm{f}_k + \varepsilon \\ \mathrm{f}_{k+1} \\ \vdots \\ \mathrm{f}_n \end{bmatrix},$$

$$\hat{f} - f = \begin{bmatrix} \varepsilon \\ \varepsilon \\ \vdots \\ \varepsilon \\ 0 \\ \vdots \\ 0 \end{bmatrix}$$

$$\|x - \hat{x}\|_2 = \frac{\left\|f - \hat{f}\right\|_2}{\sqrt{n}} = \frac{1}{\sqrt{n}}\sqrt{\varepsilon^2 + \varepsilon^2 + \cdots + \varepsilon^2}$$
$$= \frac{1}{\sqrt{n}}\sqrt{k\varepsilon^2} = \sqrt{\frac{k}{n}}\varepsilon$$

The case where all elements of f change at different rates

$$Hx = f = \begin{bmatrix} f_1 \\ f_2 \\ \vdots \\ f_n \end{bmatrix}, \quad H\hat{x} = \hat{f} = \begin{bmatrix} f_1 + \varepsilon_1 \\ f_2 + \varepsilon_2 \\ \vdots \\ f_n + \varepsilon_n \end{bmatrix},$$

$$\hat{f}-f=\begin{bmatrix}\varepsilon_1\\ \varepsilon_2\\ \vdots\\ \varepsilon_n\end{bmatrix}$$

$$\|x-\hat{x}\|_2=\frac{\|f-\hat{f}\|_2}{\sqrt{n}}=\frac{1}{\sqrt{n}}\sqrt{\varepsilon_1^2+\varepsilon_2^2+\cdots+\varepsilon_n^2}$$

$$=\frac{1}{\sqrt{n}}\sqrt{\sum_{i=1}^{n}\varepsilon_i^2}$$

The case where some elements of f (k items) change at different rates

$$Hx=f=\begin{bmatrix}f_1\\ f_2\\ \vdots\\ f_n\end{bmatrix},\quad H\hat{x}=\hat{f}=\begin{bmatrix}f_1+\varepsilon_1\\ f_2+\varepsilon_2\\ \vdots\\ f_k+\varepsilon_k\\ f_{k+1}\\ \vdots\\ f_n\end{bmatrix},$$

$$\hat{f}-f=\begin{bmatrix}\varepsilon_1\\ \varepsilon_2\\ \vdots\\ \varepsilon_k\\ 0\\ \vdots\\ 0\end{bmatrix}$$

$$\|x-\hat{x}\|_2=\frac{\|f-\hat{f}\|_2}{\sqrt{n}}=\frac{1}{\sqrt{n}}\sqrt{\varepsilon_1^2+\varepsilon_2^2+\cdots+\varepsilon_k^2}$$

$$=\frac{1}{\sqrt{n}}\sqrt{\sum_{i=1}^{k}\varepsilon_i^2}$$

So if we generalize the above four cases:
using (13);

$$\frac{\|x-\hat{x}\|_2}{\|x\|_2}=\frac{\|f-\hat{f}\|_2}{\|f\|_2}\xrightarrow{\|x\|_2=\frac{\|f\|_2}{\sqrt{n}}}\|x-\hat{x}\|_2$$

$$=\frac{\|f\|_2}{\sqrt{n}}\frac{\|f-\hat{f}\|_2}{\|f\|_2}=\frac{\|f-\hat{f}\|_2}{\sqrt{n}}$$

$$\|x-\hat{x}\|_2=\frac{\|f-\hat{f}\|_2}{\sqrt{n}} \quad (14)$$

is obtained. This results in

$$\|x-\hat{x}\|_2=\frac{1}{\sqrt{n}}\sqrt{\varepsilon_1^2+\varepsilon_2^2+\cdots+\varepsilon_k^2}$$

$$=\frac{1}{\sqrt{n}}\sqrt{\sum_{i=1}^{k}\varepsilon_i^2} \quad (15)$$

If necessary, subheadings can be added under the main heading [5].

4. Results and Discussion

While the relative error and absolute error in the solution of the $Ax=f$ problem for any matrix A are evaluated according to the lower and upper limits, it can be found exactly how much error was made in the solution of the SLEHC. This error is due to the change in the f vector. That is, if the error in the *f* vector is known exactly, the relative error in the solution of the system can be found with the following equation:

$$\frac{\|x-\hat{x}\|_2}{\|x\|_2}=\frac{\|f-\hat{f}\|_2}{\|f\|_2} \quad (16)$$

Absolute error as a result of changes in the *f* vector can be calculated using the (following) equation

$$\|x-\hat{x}\|_2=\frac{1}{\sqrt{n}}\sqrt{\sum_{i=1}^{k}\varepsilon_i^2} \quad (17)$$

As a result of this equation, the following equations can be written:

For $\varepsilon_i=\varepsilon$; $\quad k=n\Rightarrow\|x-\hat{x}\|_2=\varepsilon$

$$k<n\Rightarrow\|x-\hat{x}\|_2=\frac{\sqrt{k}}{\sqrt{n}}\varepsilon$$

For $\varepsilon_i\neq\varepsilon_j$; $\quad k=n\Rightarrow\|x-\hat{x}\|_2=\frac{1}{\sqrt{n}}\sqrt{\sum_{i=1}^{n}\varepsilon_i^2}$

$$k<n\Rightarrow\|x-\hat{x}\|_2=\frac{1}{\sqrt{n}}\sqrt{\sum_{i=1}^{k}\varepsilon_i^2}$$

Equation (17) shows that the absolute error in solving the problem $Hx=f$ is related to the size of the system (in other words, the size of the *H* matrix).

Theoretically, (15) and (17) are formulas that give the absolute error exactly, but if we consider that this calculation is in practice made in a computer environment, there will be a rounding error again due to the computer's ability to store numbers in a limited capacity. However, since the $Hx=f$ system is a "perfectly conditioned" problem, the error in question will be quite small. That is the important thing is how sensitive the error is intended to be.

Acknowledgment

This study was prepared by making use of a part of E.TuğbaAkyüz's PhD thesis.

Statement of Research and Publication Ethics

The study is complied with research and publication ethics

References

[1] R. K. R. Yarlagadda and J. E. Hershey, *Matrix Analysis and Synthesis*. USA: Kluwer Academic Publishers, 1997

[2] K. J. Horadam, *Hadamard Matrices and Their Applications*. Princeton University Press, 2007.

[3] A. Hedayat and W. D. Wallis, "Hadamard matrices and their applications," *The Annals of Statistics*, vol. 6, no. 6, pp. 1184–1238, 1978.

[4] J. Seberry, B. J. Wysocki, and T. A. Wysocki, "On some applications of Hadamard matrices," *Metrika*, vol. 62, pp. 221–239, 2005.

[5] G. H. Golub and C. F. Van Loan, *Matrix Computations (Third edition)*. Baltimore, MD: Johns Hopkins University Press, 1996.

[6] L. W. Johnson and R. D. Riess, *Numerical Analysis (Second eddition)*. Addison Wesley Publishing Company, 1982.

[7] E. T. Akyüz, "Hadamard Matrices and the Ax=f Problem," Selcuk University, Institute of Sciences, Konya, 2010.

[8] D. R. Kincaid and E. W. Cheney, *Numerical Analysis:Mathematics of Scientific Computing*. Brooks/Cole Publishing Company, 1996

Bitlis Eren Üniversitesi Fen Bilimleri Dergisi
BİTLİS EREN UNIVERSITY JOURNAL OF SCIENCE
ISSN: 2147-3129/e-ISSN: 2147-3188
VOLUME: 11 NO: 4 PAGE: 1117-1137 YEAR: 2022
DOI: 10.17798/bitlisfen.1191601

Examination of 3D Finite Difference Analyses of Zonguldak-Kozlu CCR Dam Subjected Strong Ground Motions Considering Dam-Foundation-Reservoir Interaction

Murat ÇAVUŞLU[1*]

[1]*Zonguldak Bulent Ecevit University, Department of Civil Engineering, 67100, Zonguldak, Turkey (ORCID:0000-0002-2285-8513)*

Keywords: Clay Core Rockfill Dam, Finite-Difference Method, Free-Field Boundary Condition, Interaction Problem, Seismic Analysis.

Abstract

Dams are one of the most important water structures built to meet people's vital needs such as irrigation and energy. It is important to examine the seismic safety of important water structures such as dams. In addition, it is vital to investigate the interaction behavior of dams due to the bodies of the dams, the reservoir water, and the foundation being in constant interaction. Therefore, this study investigates the seismic behavior of clay core rockfill (CCR) dams by considering the dam-foundation-reservoir interaction. The Kozlu CCR dam built in Turkey-Zonguldak is chosen for seismic analyses. Three-dimensional (3D) modeling and analysis of the dam are performed utilizing the FLAC3D program. The foundation section is extended down to the dam's height, and free-field and quiet non-reflecting boundary conditions are defined to the lateral boundaries of the foundation. Besides, the fix boundary condition is considered the foundation's base section. The Mohr-Coulomb material model is utilized for dam body material and foundation. Special interaction elements have been assigned between the discrete surfaces. These elements are affected by the 3D model of the dam in the x, y, and z directions. A total of 12 different earthquakes (magnitudes of earthquakes are between 5.9 and 7.6) are used for earthquake analyses. X, Y, and Z directions of ground motion accelerations are defined in the program, and accelerations are applied to the base of the dam. As a result of the earthquake analyses, it is concluded that significant displacement and principal stresses occurred in the dam body for each earthquake. Moreover, it is inferred that the seismic principal stress values occurring in the dam body with interaction elements are smaller than the values observed in the dam body without interaction elements.

1. Introduction

Dams are very important water structures built to meet the vital needs of people. Many types of dams have been built from the past to the present. One of the most important of these dam types is the clay core rockfill (CCR) dam. These dams are the most preferred type of dam in many countries of the world. CCR dams are exposed to many external loads (such as reservoir loads, and earthquake loads) and the structural behavior of these dams can change significantly under external loads. In addition, the bodies of CCR dams are in constant interaction with the reservoir water and the foundation. This interaction situation is vital for the structural behavior of CCR dams. For this reason, examining the interaction behavior of CCR dams is very important for the future and safety of these dams. Turkey is located in a region with high seismicity. There are many fault lines in Turkey and one of the most important of these fault lines is the Northern Anatolian Fault (NAF) line. The NAF is one of the most important strike-slip faults in the world, whose

*Corresponding author: murat.cavusli@beun.edu.tr
Received: 19.10.2022, Accepted: 22.12.2022

seismological-seismic tectonic features are well known, and constitutes one of the most important tectonic elements of Turkey. The Kozlu dam that is the subject of this study is located on the NAF and it is of great importance to examine the seismicity of this dam. Fig. 1 shows the earthquake zone map of Zonguldak, where the Kozlu dam was built. Kozlu Dam was built between 1979-1986 in Turkey-Zonguldak. This dam is located on Ulutan Stream, and it was built to meet the supply of drinking water and industrial water. The body volume of the dam, which is a rock body fill type, is 1,675,000 m³. The height of the dam from the river bed is 60.15 m [28]. Besides, the volume of the lake at a normal water level is 25 hm³. The lake area at normal water level is 1.07 km². The dam provides 19 hm³ of drinking water per year [28]. Moreover, the depth of the dam body changes along the crest of the dam. A general view of the Kozlu dam is presented in Fig. 2. Also, the most critical section of the dam is shown in detail in Fig. 2. Material properties of the Kozlu dam are shown in Table 1.

Figure 1. Earthquake zone map of Zonguldak [25].

a)

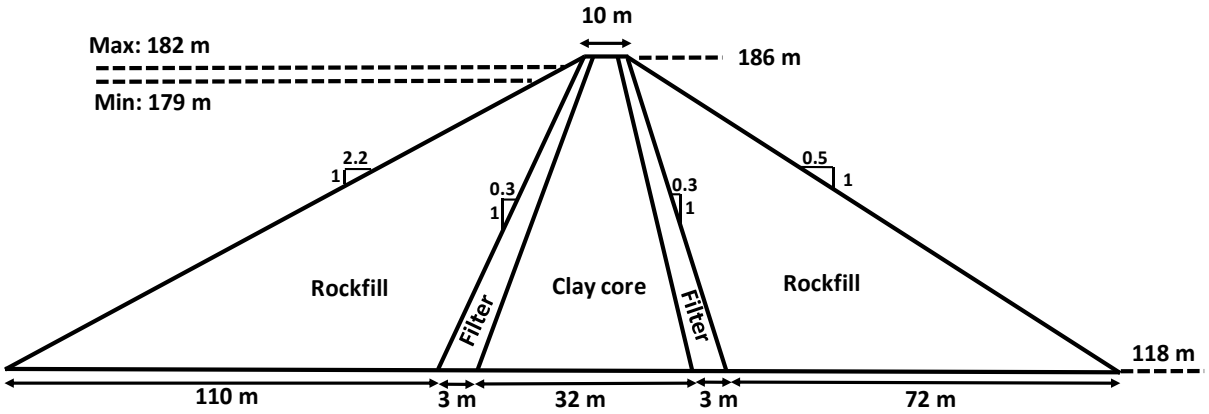

b)

Figure 2. a) General view of Kozlu dam b) the most critical section of the Kozlu dam [28].

Table 1. Material properties of the dam body [28].

Mat.	Den.	Por.	Wat. Cont.	Air cont.	Mat. Cont.	Shear Mod.
Unit	g/cm^3		%			GPa
Filter	2.74	18.61	4.05	14.56	81.39	25
Clay	2.68	25.75	7.78	17.97	74.25	-
Rockfill	3.01	25.25	1.50	23.75	74.75	32

In the literature, many studies have been carried out on the structural behavior of CCR dams. Cetin et al. (2000) examined the settlement behavior of clay core rockfill dams by considering measurement results. According to displacement results on the dam body, it was concluded that the largest settlement value observed on the dam body is 2.5 m [1]. Zhang and Chen (2006) investigated the seepage behavior of rockfill dams considering reservoir problems. It was seen that the seepage behavior of rockfill dams may change over time [2]. Sharp and Adalier (2006) assessed the seismic response of rockfill dams taking into account 3 various liquefiable foundation layers. As a result of this study, very important numerical results about the liquefaction behavior of the CCR dam were obtained [3]. Unal et al. (2007) examined the leakage behavior of rockfill dams. It was seen that after impoundment, total leakage in the dam had been directly affected by reservoir water [4]. Tosun et al. (2007) investigated the seismic hazard behavior of rockfill dams in Turkey. It was inferred that fifteen large rockfill dams in Turkey must be analyzed with high priority and redesigned to increase the safety of the embankments [5]. Oyanguren et al. (2008) evaluated the stability analyses of rockfill dams using in situ direct shear tests. It was seen that in situ testing permits the behavior of the dams to be predicted more accurately [6]. Sica et al. (2008) examined the seismic behavior of rockfill dams considering the effects of past loading history. Ground motion acceleration and displacement time histories on the rock materials of the rockfill dam were measured for the 14/3/1979, 19/9/1985, and 30/5/1990 earthquakes and

measurement results were compared with 2D finite element analysis results using the GEFDYN code [7]. The earthquake displacement ground motion behavior of rockfill dams was investigated taking into account special material models and numerical modeling [8-9]. Liu et al. (2012) evaluated the nonlinear principal stress (PS) and strain behavior of clay core rockfill dams. It was concluded that the proposed design for CCR dams is reasonable since no abnormal stresses and deformations occurred in the dam [10]. Yang and Chi (2014) examined the seismic stability behavior of rockfill dams considering the finite element method. A finite element limit analysis was developed and applied to two various types of rockfill dams using the algorithm software SDPT3 [11]. Mahinroosta et al. (2015) examined the collapse vertical displacement on high rockfill dams. A two-dimensional finite element model of the dam was created and it was seen that the highest collapse settlement during the first impounding is 0.8 cm. Moreover, it was concluded that the highest settlement in the dam body after phase II impounding is 2.25 m [12]. Albano et al. (2015) investigated the seismic behavior of bituminous-faced rockfill dams. The dam was modeled as three-dimensional and the numerical models were validated with centrifuge tests [13]. Liu et al. (2016) evaluated the stress-deformation analyses of the cut-off wall in clay-core rockfill dams. It was seen that the highest settlement and highest PS on the dam after impounding are 170 cm and 3 MPa, many intelligent methods. It was seen that intelligent methods are appropriate tools to solve problems with complex mechanisms and many factors, such as the prediction of the settlement of dams [15]. Han et al. (2016) examined the seismic response of rockfill dams using finite-element modeling. It was concluded that the acquired seismic deformations of the Yele rockfill dam are in agreement with field observations [16]. Park and Kim (2017) examined the earthquake behavior of cored rockfill dams' dynamic centrifuge modeling. The experimental tests for soil-cement mixture specimens were performed and the results helped to evaluate the seismic safety of core rockfill dams [17]. He et al. (2021) investigated the crack behavior of embankment dams using the scaled boundary finite element method. It was inferred that post-construction settlements are more critical than settlements during construction for the development of tensile cracking [18]. Wu et al. (2021) assessed the seismic performance of earth dams considering various pulse-like ground motions and non-pulse-like ground motions. The two-dimensional finite element model was created using free-field boundary conditions. According to numerical analysis results, it was seen that pulse-like and non-pulse-like earthquakes have different seismic effects on the earthquake behavior of rockfill dams [19]. As can be seen from studies in the literature [1-24], it is seen that the seismic behavior of CCR dams has not been examined considering the dam body-reservoir water-foundation interaction. In this study, to fill this gap in the literature, the seismic behavior of the Kozlu CCR dam, which was built in Turkey-Zonguldak and meets the irrigation needs of Zonguldak and surrounding provinces, was investigated in detail. First, the dam body model and the foundation were created with the help of the Fast Lagrangian Analysis of Continua 3D (FLAC3D) program based on the finite-difference method. While creating the body model of the dam, attention was paid to modeling the clay core and rockfill materials in the body following the project. After the dam body was modeled, the foundation section of the dam was created. The Mohr-Coulomb material model was used for the dam body and foundation section. Free-field and quiet boundary conditions were defined for the lateral boundaries of the dam model. Besides, the reflecting (fix) boundary condition was taken into account in the base section of the 3D model of the dam. Special interaction elements were defined between the dam body-reservoir water and the foundation in the x, y, and z directions. A total of 12 different earthquakes were utilized for the seismic analysis of the dam. As a result of the seismic analysis of the dam, important information was obtained about the interaction problems between the discrete surfaces of clay core rockfill dams. Moreover, it was observed how the interaction elements between the discrete surfaces changed the seismic behavior of clay core rockfill dams.

2. Three-Dimensional Modelling of Kozlu Dam

Examining the structural and seismic behavior of important water structures such as dams is of great importance for the safety and future of these structures. In this section, detailed information about the three-dimensional (3D) modeling of the Kozlu clay core rockfill (CCR) dam is presented in detail. Kozlu CCR dam has a large clay material in the middle of the body. While modeling, firstly, the clay material part was created. After the geometry of the clay material was generated, the rock fill material was modeled. Clay core and rockfill material were created following the dam project. After the dam body was formed, the meshing process was performed and the dam was subjected to creep analysis. According to the creep displacement results of the dam, the optimum mesh range was selected. The FLAC3D program provides special material models and fish functions to

model the creep behavior of geotechnical structures over time. In this study, the mesh range of the Kozlu dam model was obtained using time-dependent creep analyses, not random ones. Before the seismic analysis, 10 different creep analyzes of the dam were made. Different mesh ranges were used for 10 different creep analyses. Different creep displacements were obtained in the dam body for each mesh range. However, creep displacements in the dam body did not change after a certain mesh range. For this reason, the optimum mesh range of the dam was determined by considering the critical mesh ranges. According to the creep analyses, the optimum mesh range of the Kozlu dam is 11.5 m. The foundation section of the dam is extended downwards as far as the dam body. Moreover, towards the right and left sides of the dam, the foundation section was extended as far as the dam body. Finally, in the upstream and downstream parts of the dam, the foundation part was extended 3 times and 1 time of the height of the dam, respectively. The reservoir part was created considering the highest water level of the dam. In the dam model, special spring interaction elements are defined between the discrete surfaces (dam body-reservoir water-foundation). The mechanical properties of these elements are defined in the FLAC3D program with the help of special fish functions. A fish function is used by naming an input line according to the researchers' intended use. Fish functions are utilized to create geometry, material property, boundary conditions, and all the structures. Moreover, fish functions are created by users using codes suitable for the FLAC3D programming language. Users can model all structures and grounds thanks to the fish functions. Interaction elements are defined in the x, y, and z directions. Thanks to these interaction elements, important information about the interaction problems of clay core rockfill dams have been presented. The value of the interaction elements defined between the discrete surfaces is 10^8 Pa/m [27]. Then, the Mohr-Coulomb material model was defined for the clay core, rockfill, and foundation parts of the dam. The Mohr-Coulomb material model is generally used for many rockfill materials in the FLAC3D software [31]. In this material model, PS ($\sigma_1;\sigma_2;\sigma_3$) is used for the out-of-plane PS ($\sigma_{ZZ} and \sigma_{YY}$). Moreover, the failure criterion is defined in the plane $\sigma_1;\sigma_3$ as seen in Fig. 3 [26]. In this study, the density, shear modulus, and bulk modulus of the dam body and foundation materials are defined in the FLAC3D program.

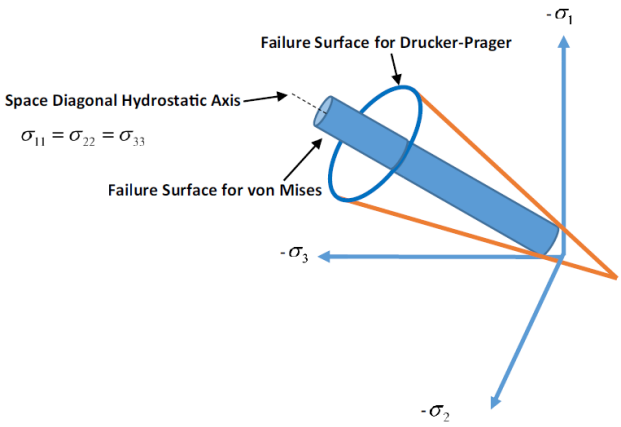

Figure 3. Mohr-Coulomb failure criterion [26, 31].

Considering the material parameters of the dam (G/Gmax), special hysteresis damping is calculated for each material and the calculated damping rates are defined in the FLAC3D. Free-field and quiet non-reflecting boundary conditions are taken into account on the lateral surfaces of the dam model. With the help of these non-reflecting boundary conditions, the back reflections of earthquake waves in the model are prevented. Furthermore, realistic seismic analysis results are obtained with the help of these boundary conditions. Free-field and quiet non-reflecting boundary conditions ensure that the earthquake waves do not reflect inside the structure and allow us to obtain more accurate earthquake results. The free-field boundary condition is placed on the side boundaries to minimize wave reflections. Moreover, in the quiet boundary condition, the earthquake dashpots are considered and the normal and shear earthquake dashpots are calculated. Fix boundary conditions are considered at the base of the dam model. The three-dimensional model of the dam and the modeling stages are shown in Fig. 4 in detail. Moreover, the general views of the interaction elements defined on the discrete surfaces between the dam body, reservoir water, and foundation are presented in Fig. 5. A total of 12 different strong ground motions (magnitudes are between 5.9 and 7.6) were utilized in seismic analysis (Table 1). Earthquake accelerations are defined to the FLAC3D program. Moreover, the flow chart for the modeling of the Kozlu dam is shown in Fig. 6.

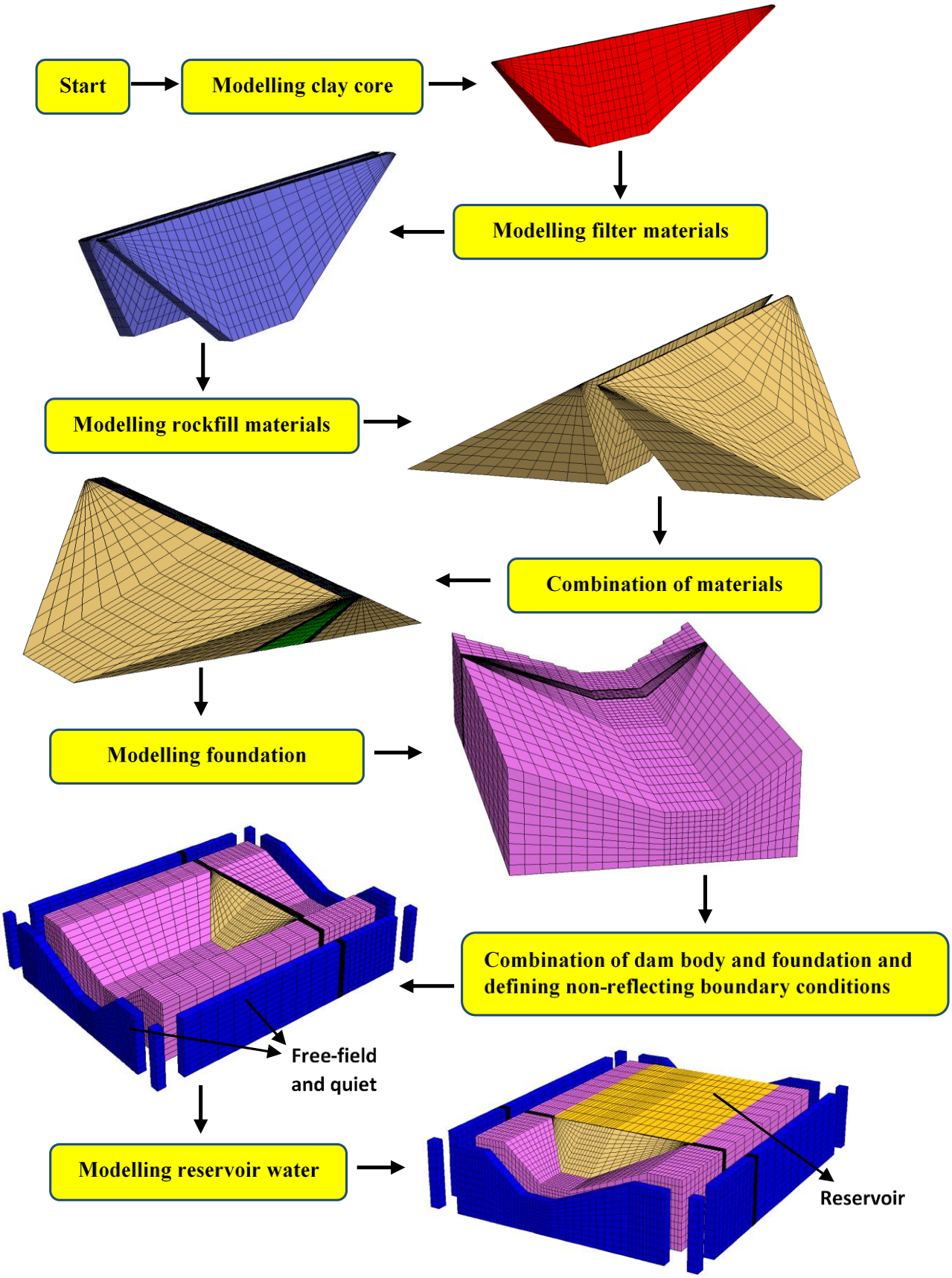

Figure 4. Modeling Kozlu clay core rockfill dam.

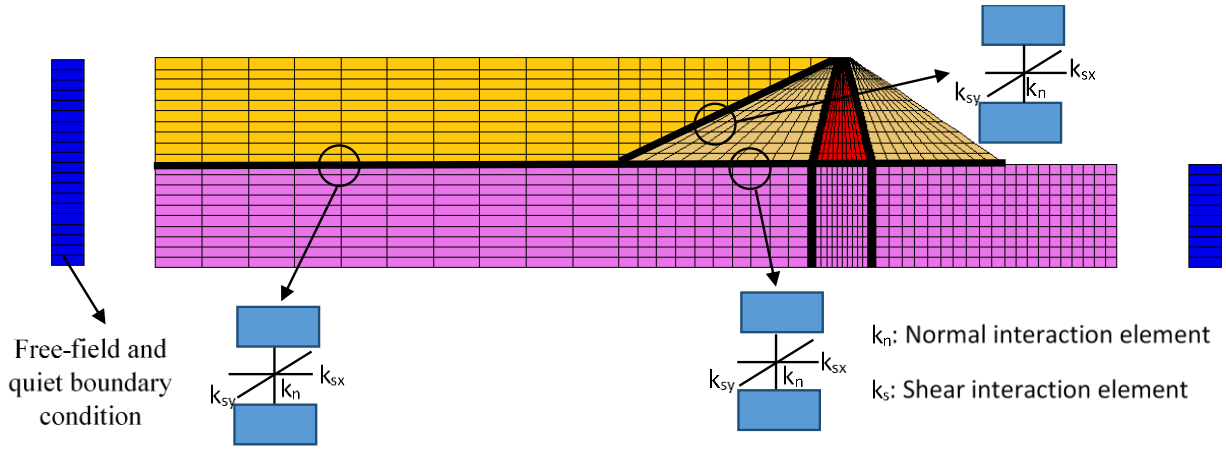

Figure 5. View of interaction elements between discrete surfaces.

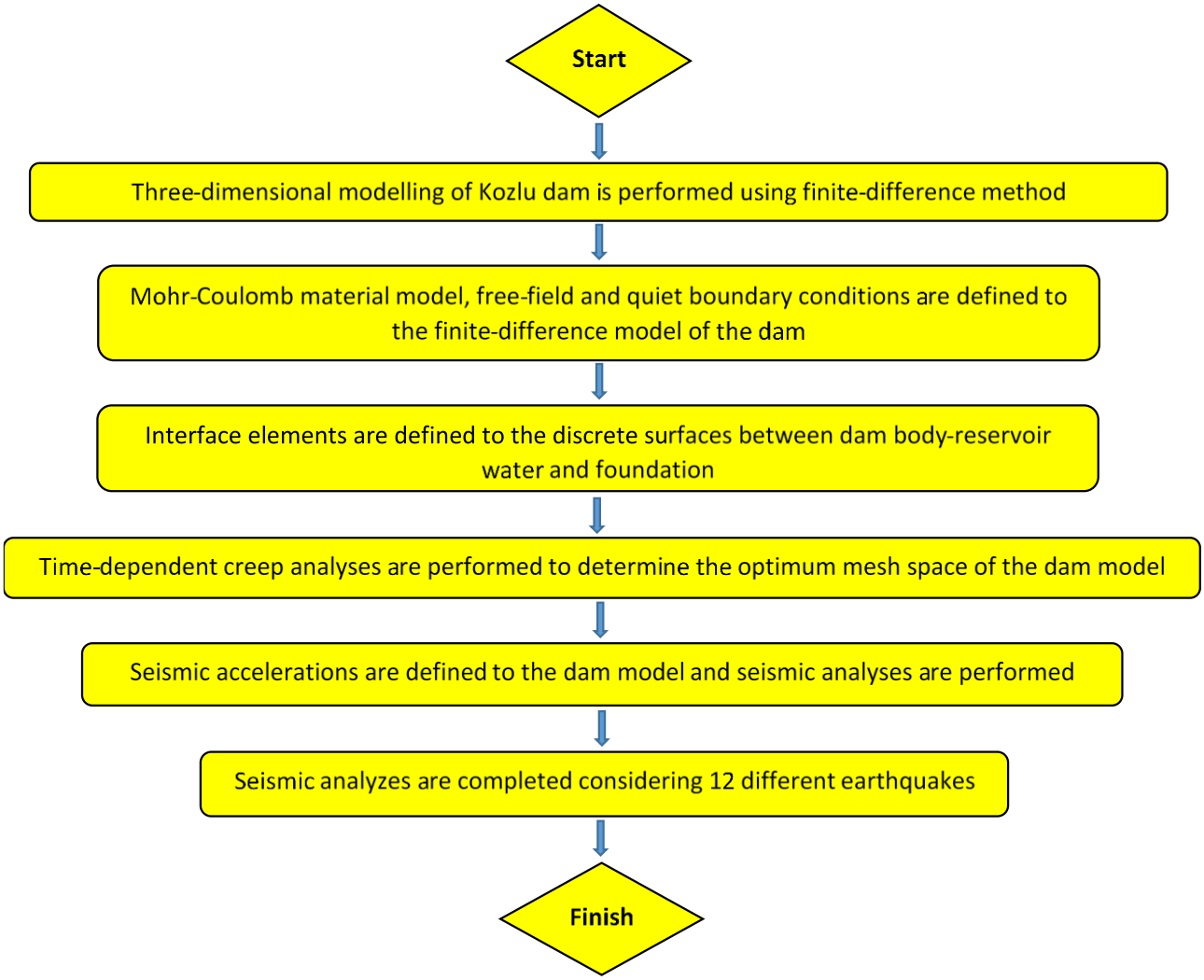

Figure 6. Flow chart for the modeling Kozlu dam.

3. Results and Discussion

In this section, the seismic behavior of the Kozlu clay core rockfill (CCR) dam is investigated under 12 different earthquakes. After the 3D model is created, earthquake accelerations in the x, y, and z directions are applied to the base of the dam model. These earthquake accelerations are defined in the FLAC3D program. The characteristic properties of 12 different earthquakes used in seismic analyzes are shown in Table 2 in detail. Earthquake data are obtained from PEER [29] and AFAD [30]. Furthermore, the earthquake data are acquired from important

earthquakes that have occurred both in Turkey and in many countries of the world. Kozlu dam was built on the Northern Anatolian fault line. For this reason, attention is paid to ensuring that earthquake magnitudes used in seismic analyses should not be below 6.0. Seismic analyzes are performed for a total of 2 different situations (Table 3).

The situation where interaction elements are not defined between discrete surfaces is called "Situation A". In addition, the “Situation B” definition was made for the case of defining the interaction elements between the discrete surfaces. In Fig. 8, the seismic principal stress (PS) results of the Kozlu dam are presented graphically. The PS results shown in the graphs are obtained from Point A at the base of the upstream section of the dam (Fig. 7).

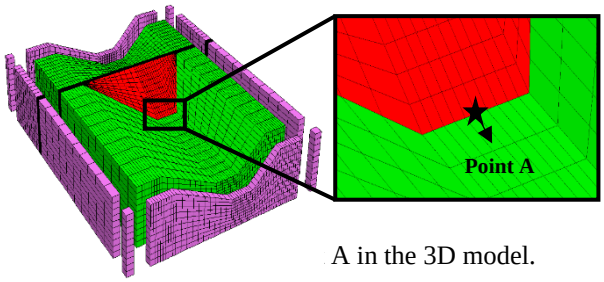

A in the 3D model.

Figure 7. View of Point A in the 3D model.

Table 2. Characteristic properties of earthquakes [29, 30].

Case	EQ	Year	M_w	d (km)	PGA	Ap/Vp	TP
1	Chi-Chi	1999	7.6	3.2	0.12	3.18	4.4
2		1999	7.6	1.1	0.46	1.72	10.9
3	Kobe	1995	6.9	0.6	0.82	9.93	0.9
4	Northridge.	1994	6.7	6.2	0.61	5.11	2.5
5	Cape Mend.	1992	7.1	18.5	0.39	8.7	1.2
6		1992	7.1	9.5	0.66	7.19	0.7
7	Loma Pr.	1989	6.9	13.0	0.32	7.30	3.1
8	Sup. Hills	1987	6.6	0.7	0.45	3.94	2.2
9	N. Palm Spr..	1986	6.0	8.2	0.59	7.93	1.4
10	Imp. Val.	1979	6.5	4.2	0.36	4.59	4.3
11	Kocaeli	1999	7.6	17	0.42	1.88	9.7
12	Düzce	2022	5.9	6.8	0.59	7.86	1.3

Table 3. Various situations for seismic analyses.

Situation	Describing
A	Without interaction elements
B	With interaction elements

According to Fig. 8, it is seen that the greatest PS values occurring in Point A are different from each other for Situation A and Situation B. For Case 1 earthquake, the largest PS values for Situation A and Situation B are 5.87 MPa and 1.83 MPa, respectively (Fig. 8a). This result clearly shows the effects of interaction elements on the seismic behavior of CCR dams. During the Case 2 earthquake, the greatest PS value for Situation A is 8.1 MPa. Moreover, for Situation B, the highest PS value observed in Point A is 3.2 MPa (Fig. 8b). For the Case 3 earthquake, the highest PS values for Situation A and Situation B are 4.3 MPa and 1.1 MPa, respectively (Fig. 8c). During the Case 4 earthquake, the maximum PS value for Situation A is 4.2 MPa. Besides, for Situation B, the highest PS value on Point A is 1.7 MPa (Fig. 8d). For the Case 5 earthquake, the maximum PS values on Point A for Situation A and Situation B are 7.1 MPa and 2.3 MPa, respectively (Fig. 8e). This result clearly shows that different earthquakes significantly change the interaction behavior of CCR dams. During the Case 6 earthquake, it is seen that the greatest PS value for Situation A is 8.9 MPa. When Cases 1-6 are compared with each other, it is seen that the highest PS value occurred on the dam is observed for Case 6 earthquake (Fig. 8f). During the Case 7 earthquake, the greatest PS value for Situation A is 5.6 MPa. Furthermore, the highest PS value in the dam body for Situation B is 1.4 MPa (Fig. 8g). For Situation A and Situation B, the greatest PS values obtained on the Kozlu dam body during the Case 8 earthquake are 4.4 MPa and 1.3 MPa, respectively (Fig. 8h). In addition, for the Case 9 earthquake, the highest PS value for Situation A is 8.1 MPa (Fig. 8i). Finally, the highest PS values obtained at the base of the Kozlu dam during the Case 10 earthquake are 7.4 MPa and 2.5 MPa for Situation A and Situation B, respectively (Fig. 8j). Then, the seismic ground motion behavior of the Kozlu dam is shown for 1999 Kocaeli earthquake in Fig. 8k. According to Fig. 8j, it is seen that the maximum PS value occurring on the dam body without interaction elements is 8.1 MPa. Besides, for dam with interaction elements, the greatest PS value observed on the dam body is 1.7 MPa (Fig. 8k). In Fig. 8l, numerical analysis results of the dam are presented for the 2022 Düzce earthquake. This earthquake occurred in Düzce, Turkey in 2022. For this reason, this earthquake analysis is very important for evaluating the structural behavior of the Kozlu dam. According to Fig. 8l, the maximum PS value on the dam body without interaction elements is 4.2 MPa. Furthermore, when both situations of the dam are compared, fewer PS values are observed on the dam body for the dam with interaction elements.

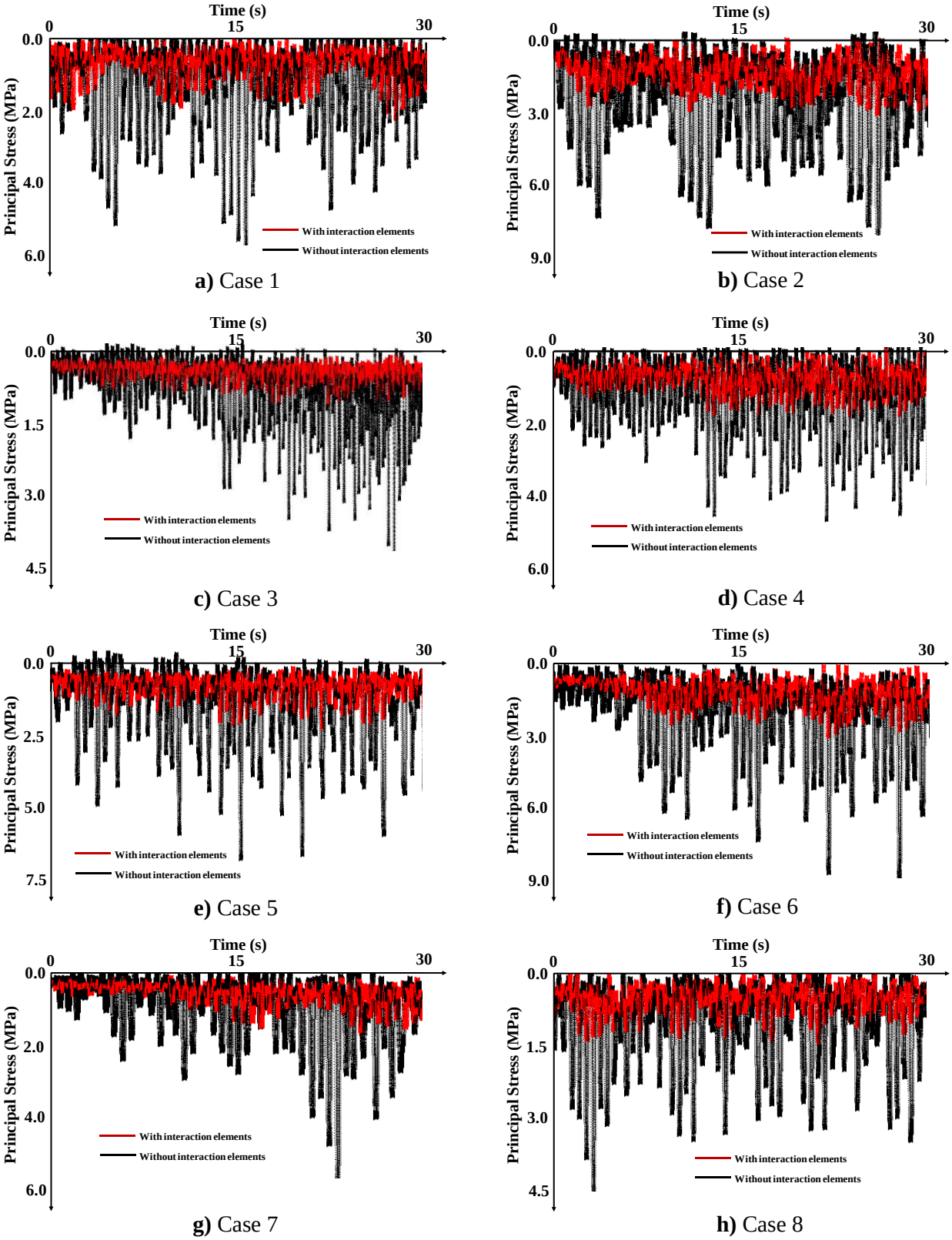

Figure 8. Seismic PS results on Point A for 12 various earthquakes.

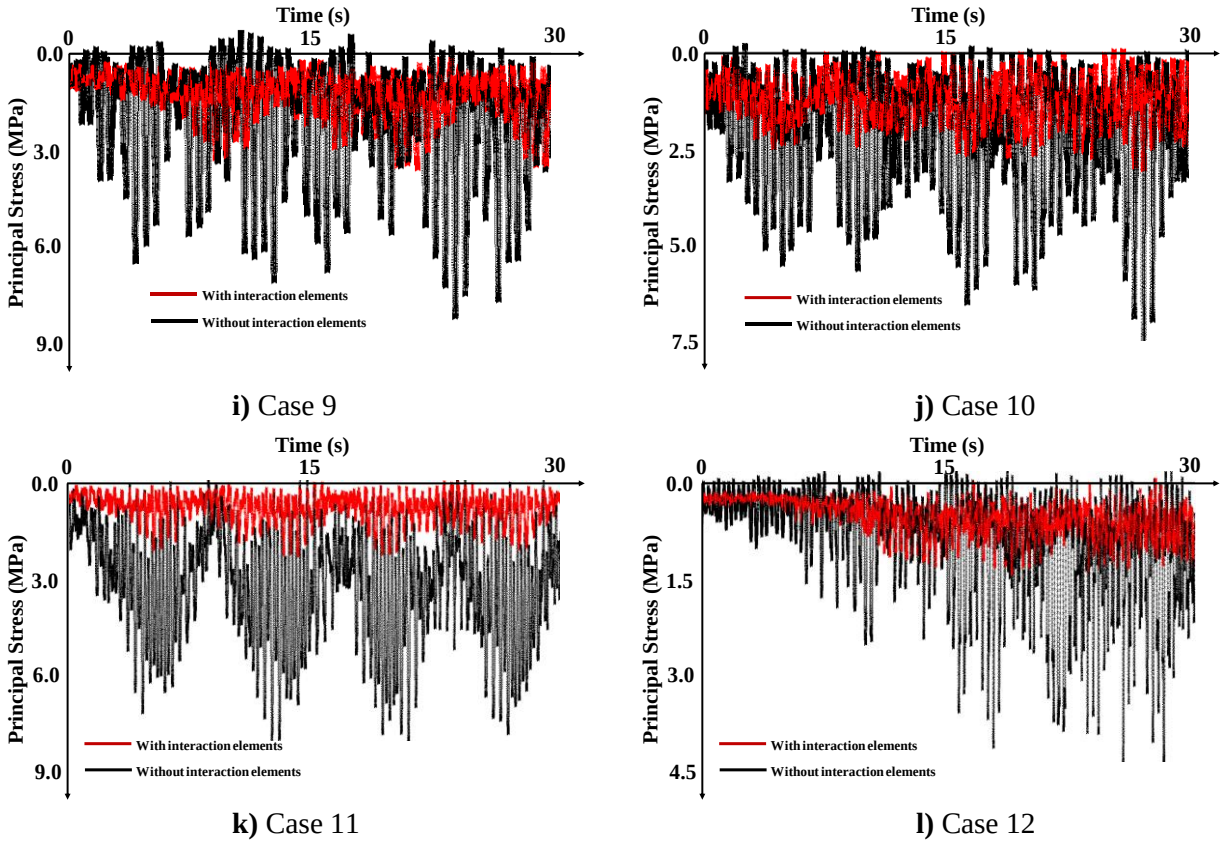

Figure 8. Continuing.

According to the seismic PS results, it is seen that the highest PS values that took place on the dam body for Situation A are approximately 2 times that of Situation B. This result shows the importance of interaction elements between discrete surfaces in CCR dams. In Fig. 9, the earthquake behavior of the Kozlu dam is examined with the help of contour diagrams. Contour diagrams are presented for 12 different earthquakes, and these diagrams are shown separately for Situation A and Situation B. According to Fig. 9a, the highest PS values for Case 1 are observed in the middle parts of the dam body. Besides, minimum PS values are acquired on the crest of the dam. When the two-dimensional contour of the dam is examined, it is seen that significant PS values occurred in the clay core of the dam (Fig. 9a). Moreover, for Situation B, the highest PS values are observed in the lateral sections of the Kozlu dam body and significant PS values are gained in the clay core of the dam (Fig. 9b). In Fig. 10, the seismic PS behavior of the dam is examined for Case 2. According to Fig. 10, the highest PS values for Situation A are obtained in the middle sections of the dam body. In addition, fewer PS values are observed in the side sections of the dam as compared to the middle sections of the dam. For Situation B, significant PS values took place in the clay core of the dam (Fig. 10b).

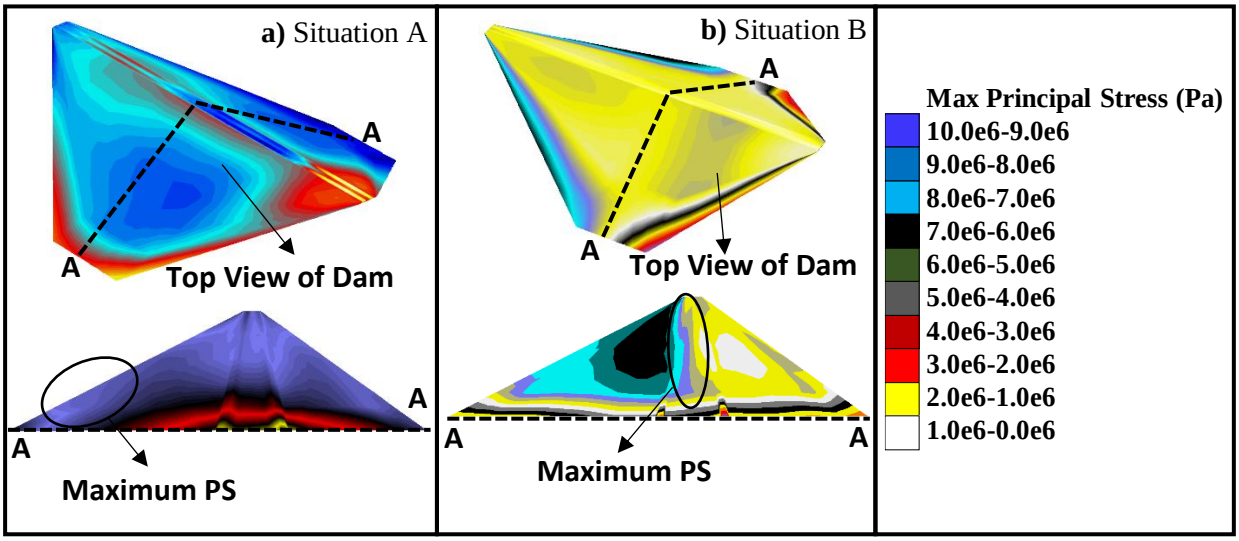

Figure 9. Seismic contours for Situation A and Situation B (Case 1).

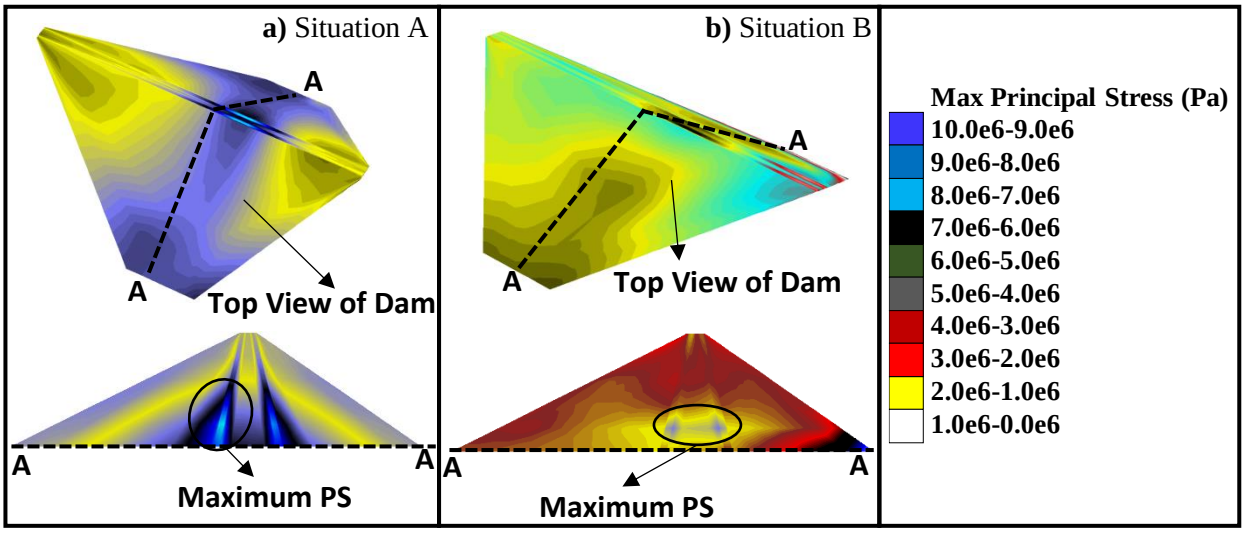

Figure 10. Seismic contours for Situation A and Situation B (Case 2).

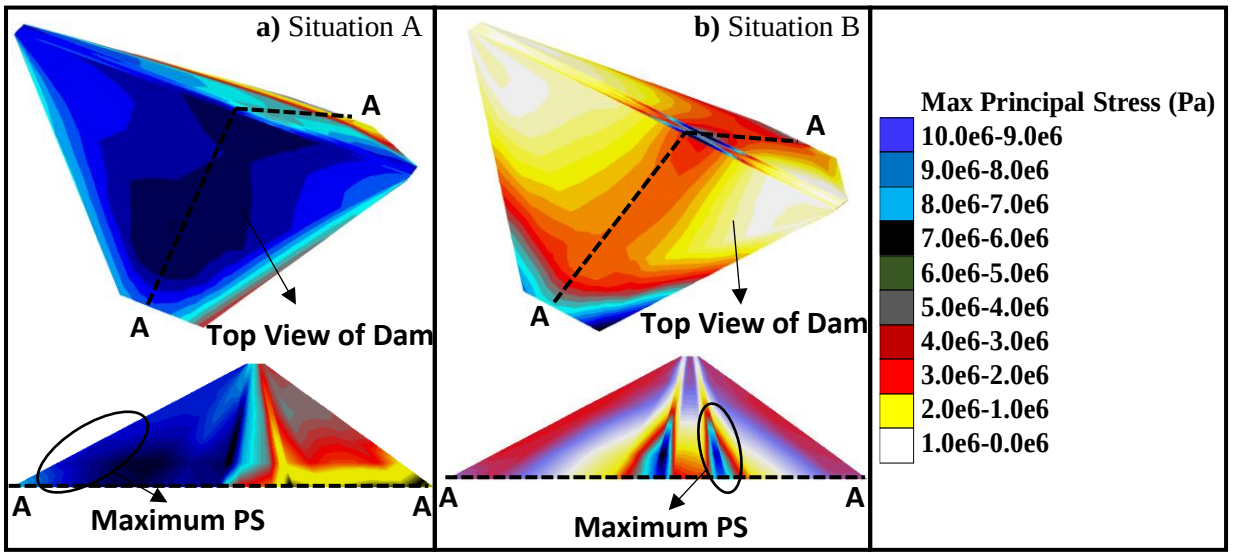

Figure 11. Seismic contours for Situation A and Situation B (Case 3).

In Fig. 11, the seismic behavior of the Kozlu dam is examined for Case 3. It is concluded that the PS values occurring in the dam body for Situation A and Situation B are very different from each other. For Situation A, it is observed that higher PS values occurred in the upstream parts of the dam than in the downstream parts. Moreover, for Situation B, higher PS values are acquired around the clay core material of the dam as compared to the other sections. This result shows the importance of the interaction situation between the discrete surfaces of CCR dams. During the Case 4 earthquake, the highest PS values for Situation A took place in the upstream parts of the dam. Approximately 10 MPa highest PS values are observed in the middle parts of the dam. For Situation B, 7.2 MPa PS values are acquired around the rockfill material of the dam. Besides, approximately 5 MPa PS values occurred around the clay core material (Fig. 12). In Fig. 13, the seismic PS behavior of the Kozlu CCR dam is investigated for the Case 5 earthquake. For Situation A, approximately 8 MPa PS value is obtained in the middle sections of the dam body. Moreover, significant PS values are observed at the base of the dam (Fig. 13a). For Situation B, serious PS values are obtained around the rockfill and clay core materials. During the Case 6 earthquake, the highest PS values for Situation A took place at the lower sides of the dam body. Furthermore, significant PS values are observed around the clay core material for Situation B. It is clear from this result that the clay core material is of great importance for the PS behavior of CCR dams. During the Case 6 earthquake, significant PS values are obtained at the base of the dam. Fewer PS values occurred in the downstream parts of the dam as compared to the upstream parts. For Situation B, approximately 9 MPa maximum PS value is observed around the clay core material of the Kozlu dam (Fig. 14b). In Fig. 15, the PS behavior of the dam is presented for the Case 7 earthquake in detail. For Situation A, higher PS values occurred at the bottom of the upstream part of the dam when compared to other parts of the dam. Besides, significant PS values are acquired at the base of the dam for Situation B (Fig. 15b). Furthermore, about 6 MPa PS value is observed around the clay core material of the dam. Fig. 16 shows the seismic behavior of the dam for Case 8. During the Case 8 earthquake, approximately 9 MPa PS value is acquired around the clay core material of the dam for Situation A. Besides, significant PS values are observed in the upstream parts of the dam. For Situation B, approximately 8 MPa PS values occurred on the underside of the clay core material of the dam (Fig. 16b). From these results, it is seen how the interaction elements defined between the discrete surfaces of the dam change the seismic behavior of CCR dams.

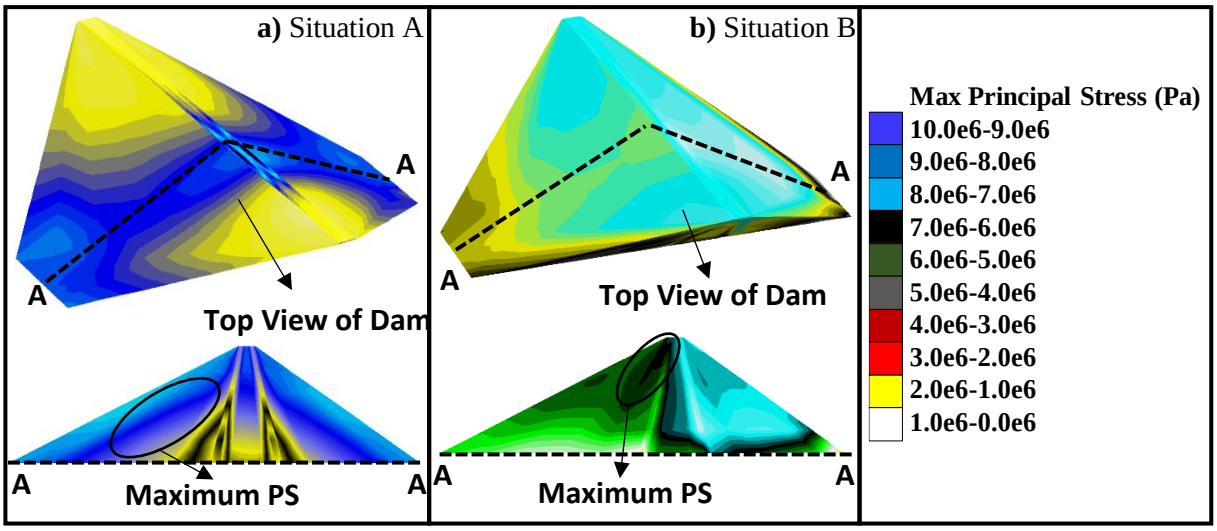

Figure 12. Seismic contours for Situation A and Situation B (Case 4).

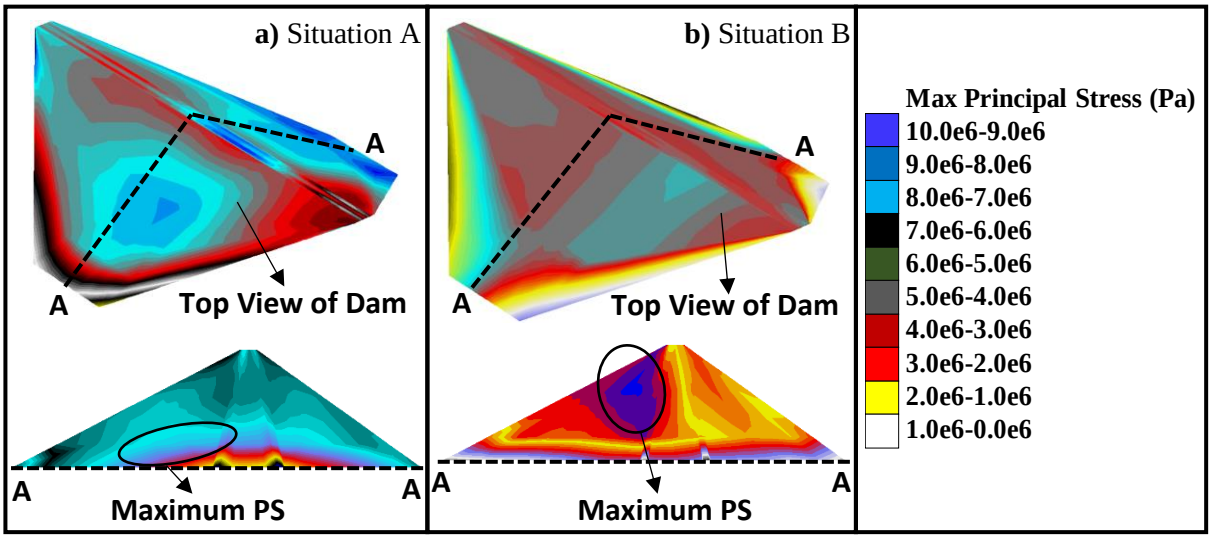

Figure 13. Seismic contours for Situation A and Situation B (Case 5).

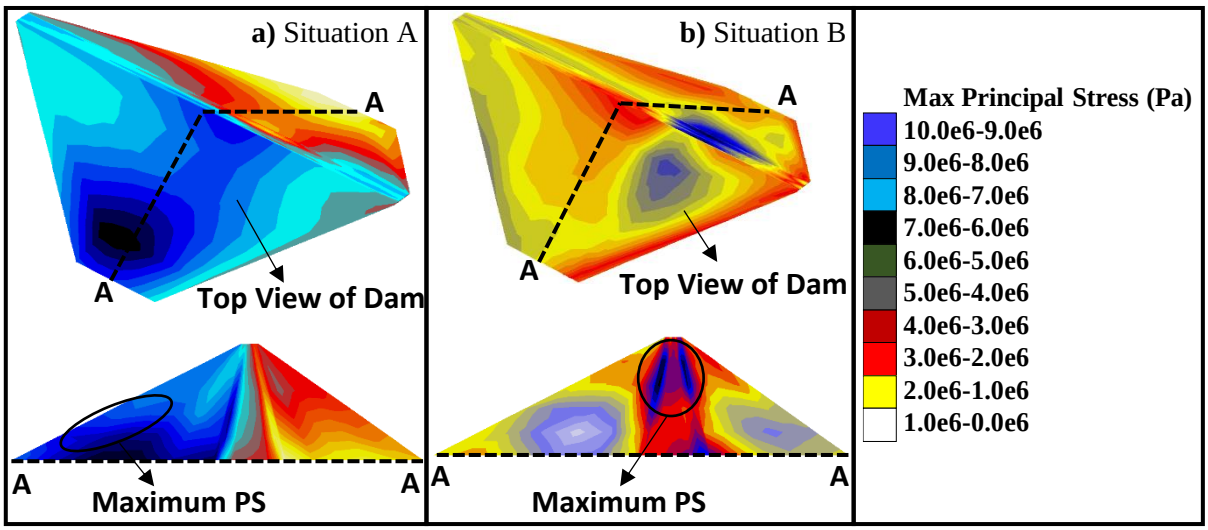

Figure 14. Seismic contours for Situation A and Situation B (Case 6).

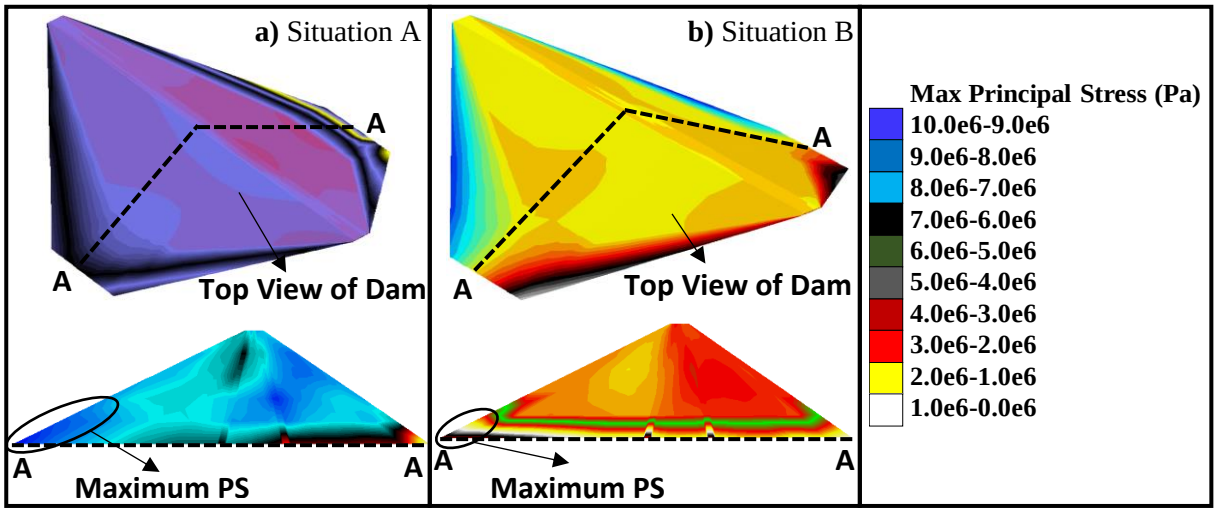

Figure 15. Seismic contours for Situation A and Situation B (Case 7).

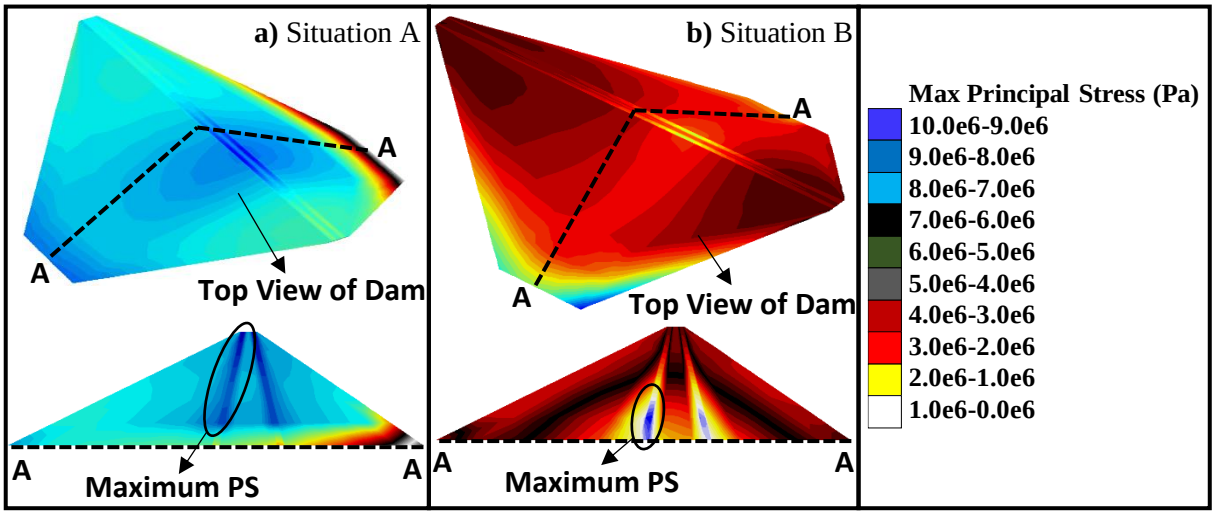

Figure 16. Seismic contours for Situation A and Situation B (Case 8).

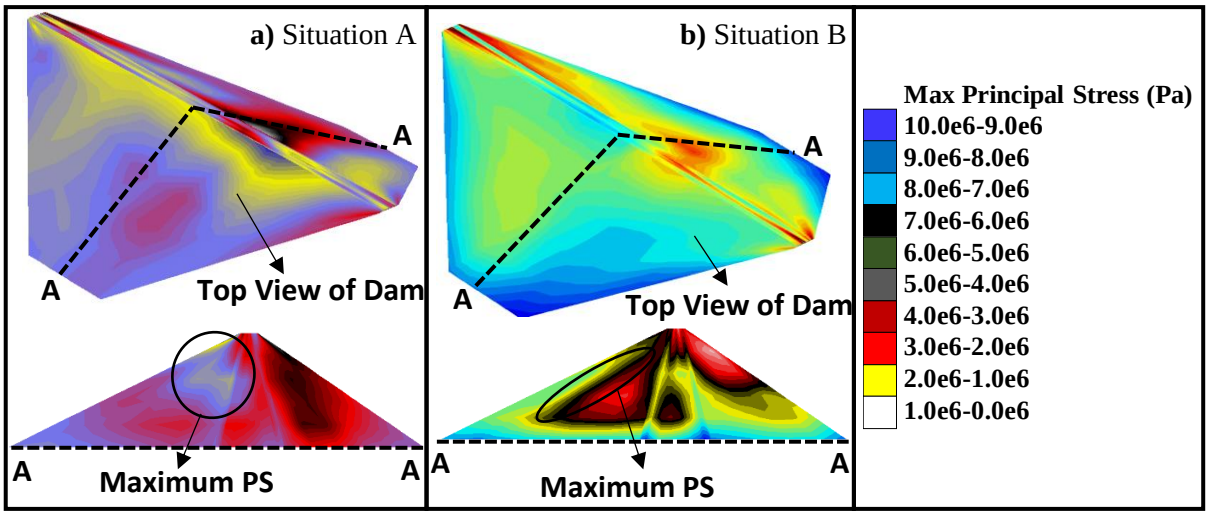

Figure 17. Seismic contours for Situation A and Situation B (Case 9).

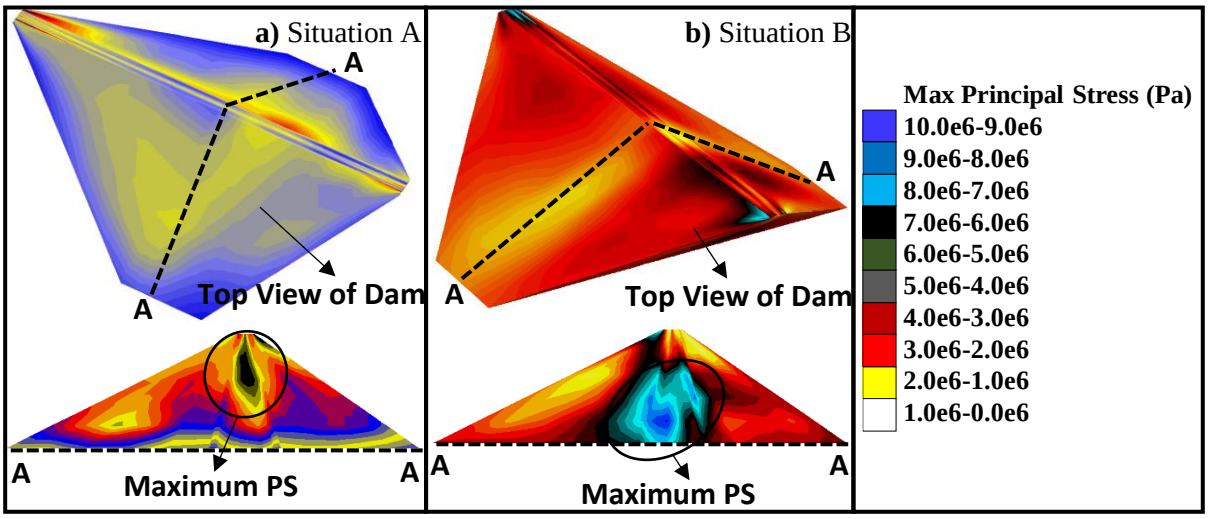

Figure 18. Seismic contours for Situation A and Situation B (Case 10).

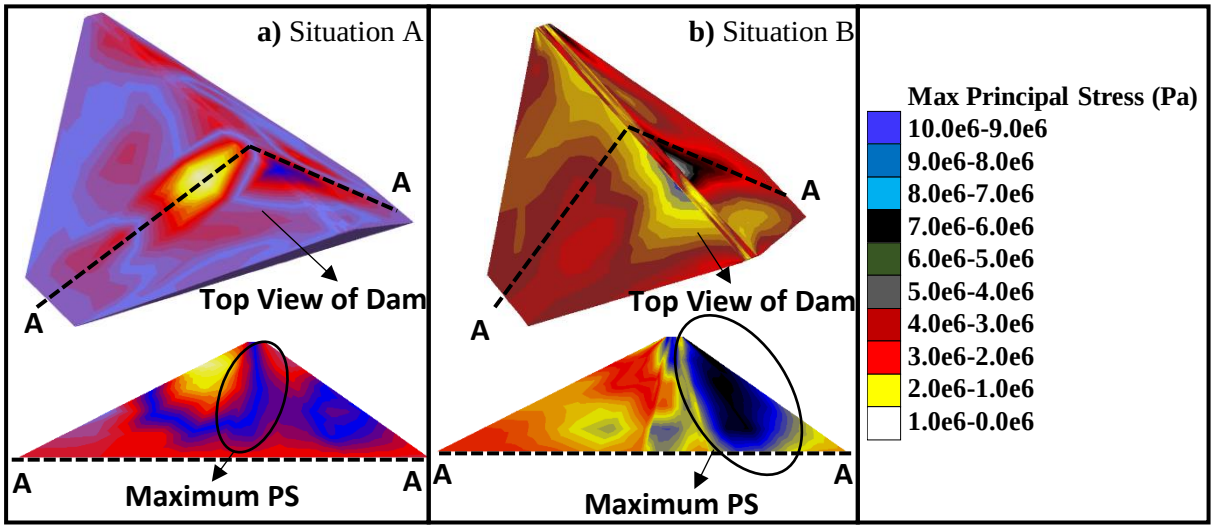

Figure 19. Seismic contours for Situation A and Situation B (Case 11).

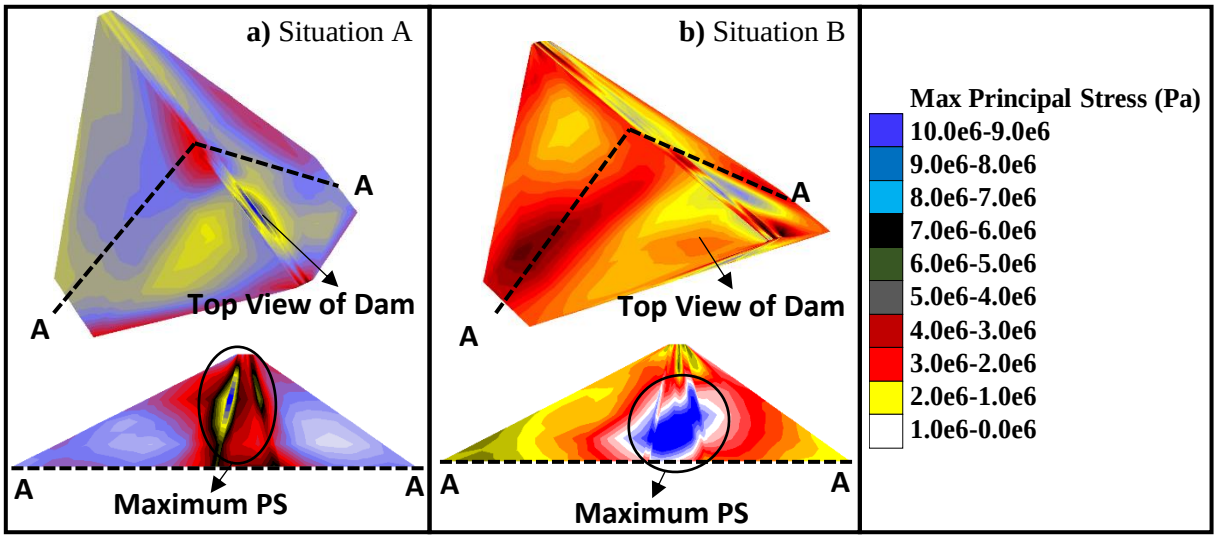

Figure 20. Seismic contours for Situation A and Situation B (Case 12).

In Fig. 17, the seismic PS behavior of the Kozlu dam is examined for Case 9. For Situation A, higher PS values occurred in the upstream parts of the dam body than in the downstream parts. It is concluded that the PS values obtained on the dam body for Situation B are lower than for Situation A (Fig. 17b). For Situation B, approximately 7 MPa PS values are acquired around the clay core and filter materials of the dam. This result shows the importance of clay core and filter materials for the seismic behavior of CCR dams. During the Case 10 earthquake, significant PS values are observed in the clay core material for Situation A (Fig. 18a). For Situation B, approximately 8 MPa PS values are observed at the base of the clay core material of the dam. It is clear from the contour diagrams that the interaction elements between the discrete surfaces of the dam have significantly changed the seismic behavior of the CCR dams. For this reason, as a result of this study, it is recommended that the interaction elements defined between discrete surfaces should not be neglected during the modeling and analysis of CCR dams. In Figs. 19 and 20, the seismic ground motion effects of interaction elements between discrete surfaces on the earthquake behavior of CCR dams are seen in detail. It is concluded that significant PS values occurred around the clay core for both dams, especially during the Düzce earthquake (Case 12) that occurred in 2022 (Fig. 20). Since Düzce province is very close to the Kozlu dam, it is understood that the dam was significantly affected by this earthquake. The seismic displacement results of the Kozlu dam are presented in Figs. 21-32 in detail. Fig. 21 shows the seismic displacement results of the dam for Case 1. For Situation A, the highest displacement values on the dam crest are 19 cm (x direction), 20 cm (y direction), and 32 cm (z-direction). In addition, the highest vertical displacement value observed at the dam crest for Situation B is 21 cm. From this result, the effects of interaction elements on the seismic displacement behavior of CCR dams are seen.

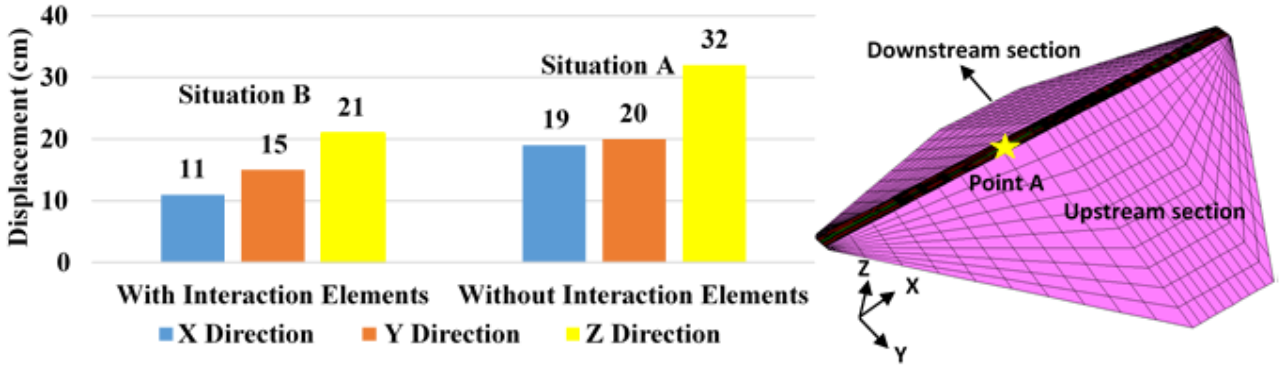

Figure 21. Highest seismic displacement results of Point A for Case 1.

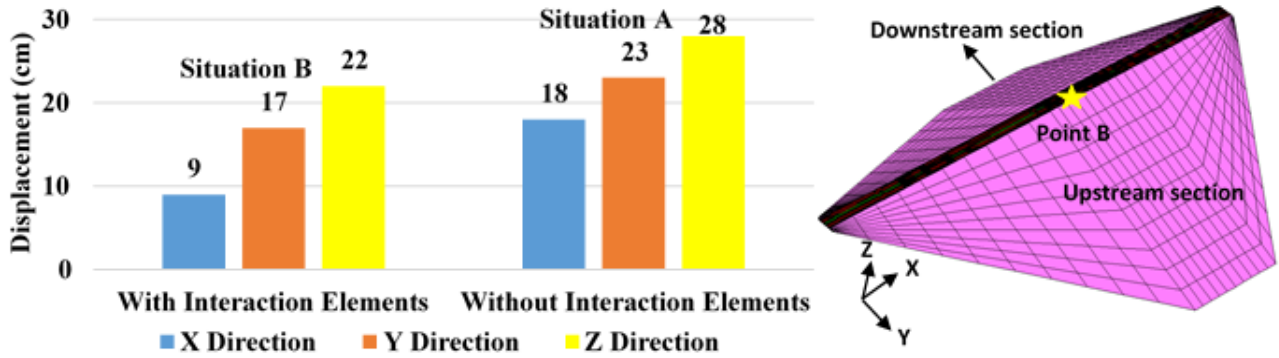

Figure 22. Highest seismic displacement results of Point B for Case 2.

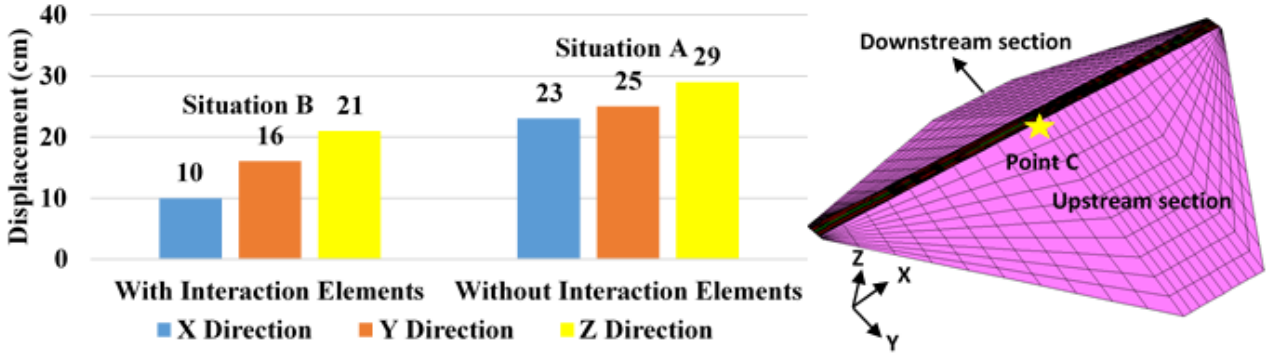

Figure 23. Highest seismic displacement results of Point C for Case 3.

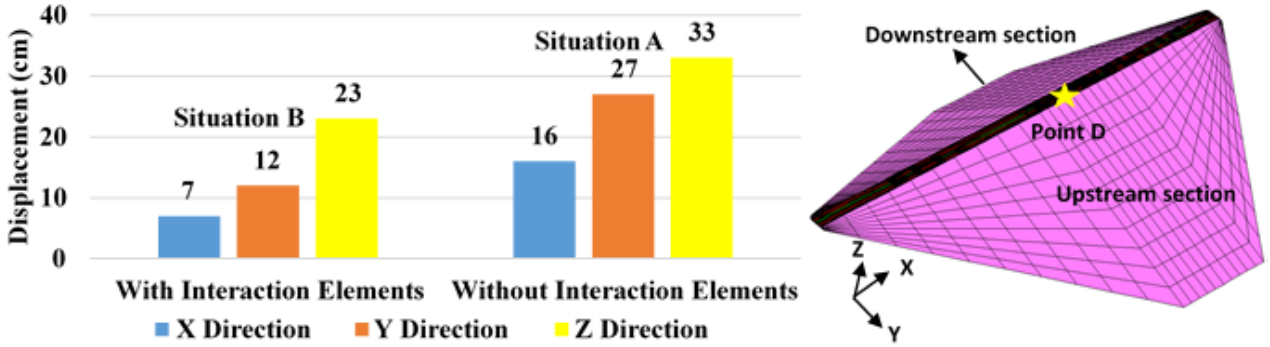

Figure 24. Highest seismic displacement results of Point D for Case 4.

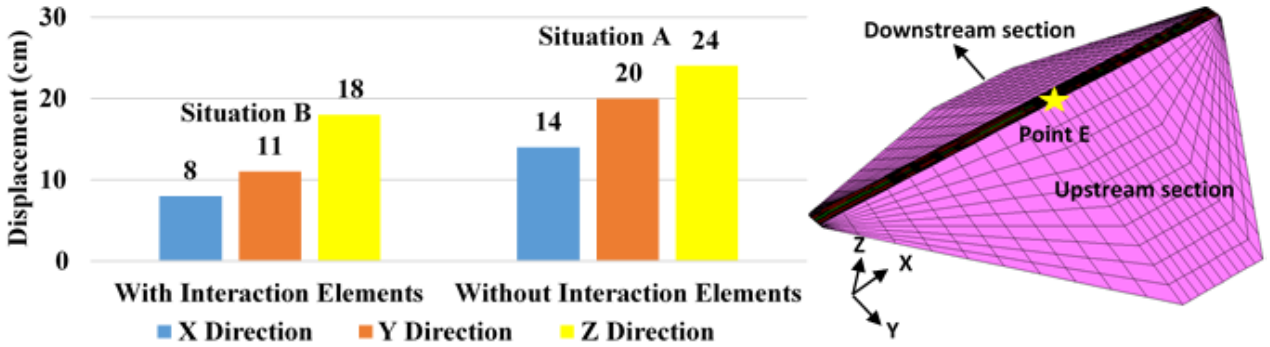

Figure 25. Highest seismic displacement results of Point E for Case 5.

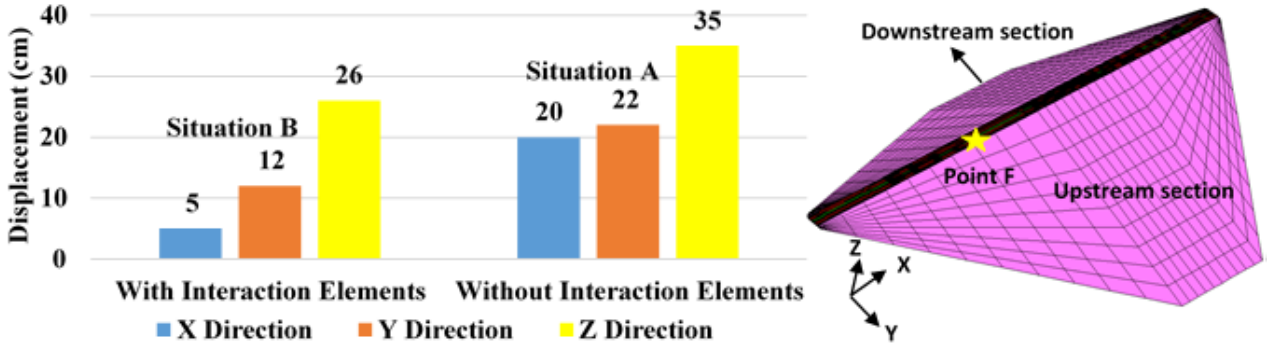

Figure 26. Highest seismic displacement results of Point F for Case 6.

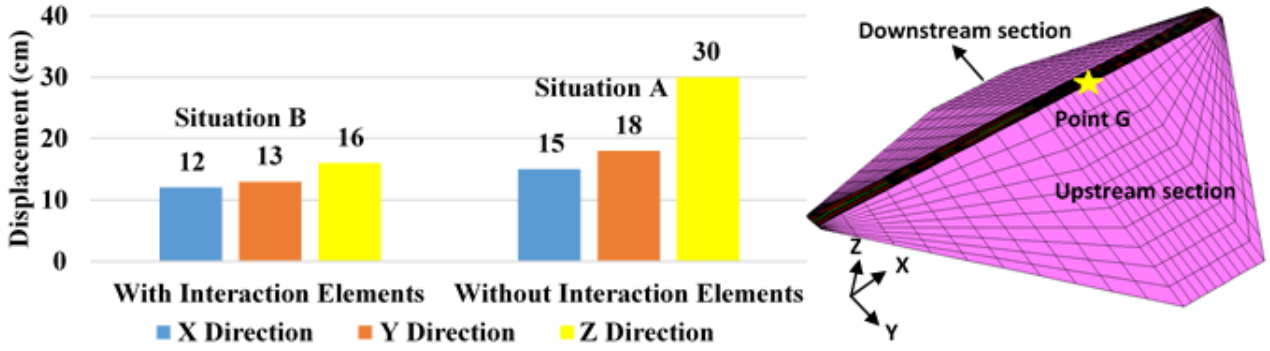

Figure 27. Highest seismic displacement results of Point G for Case 7.

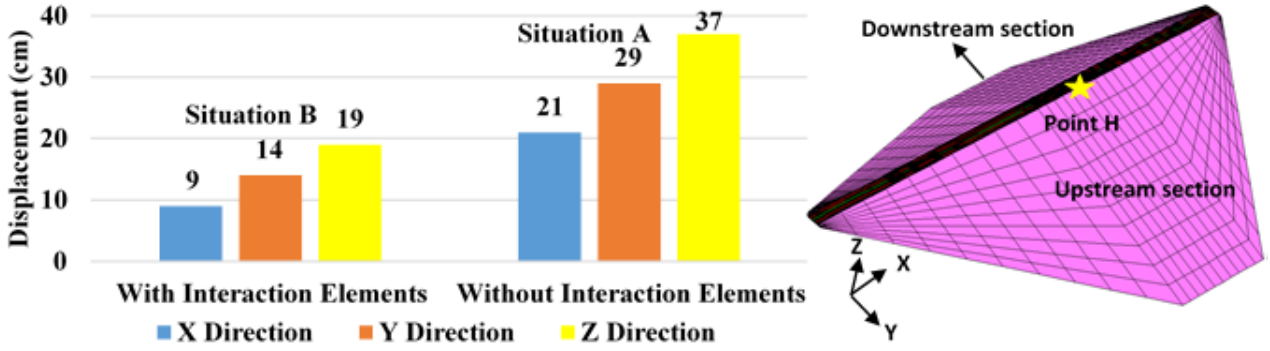

Figure 28. Highest seismic displacement results of Point H for Case 8.

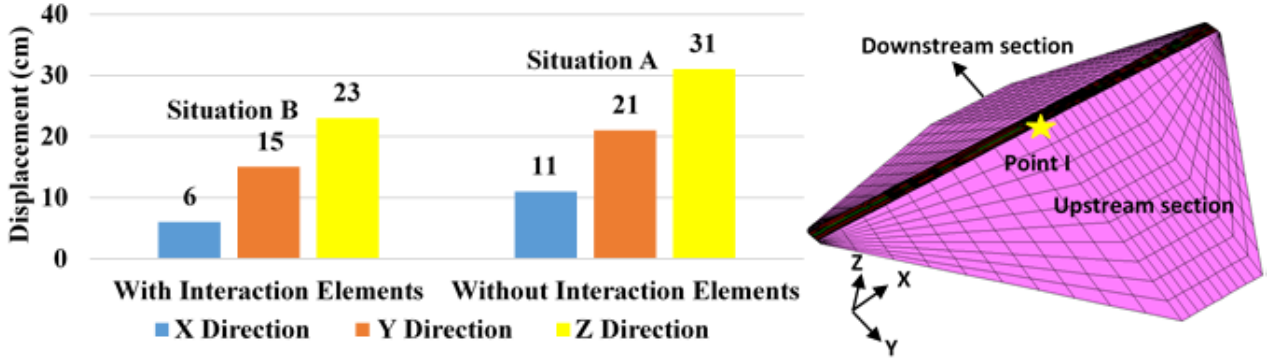

Figure 29. Highest seismic displacement results of Point I for Case 9.

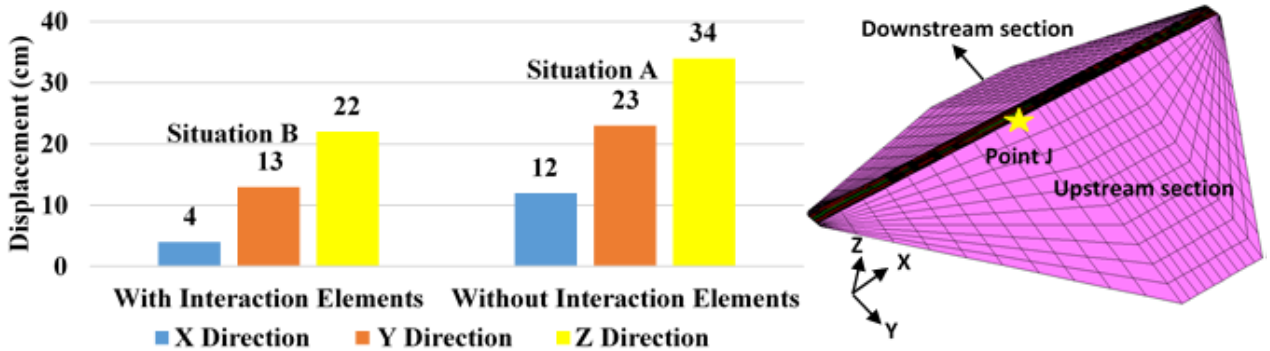

Figure 30. Highest seismic displacement results for Point J Case 10.

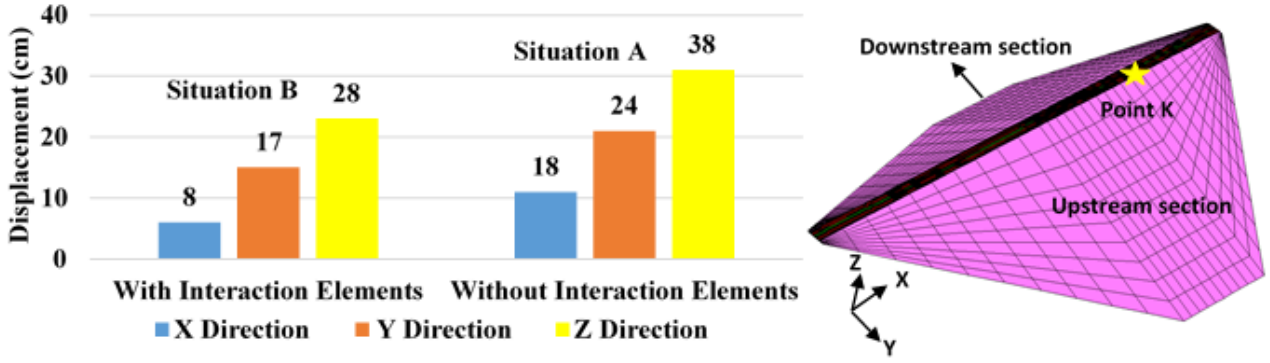

Figure 31. Highest seismic displacement results of Point K for Case 11.

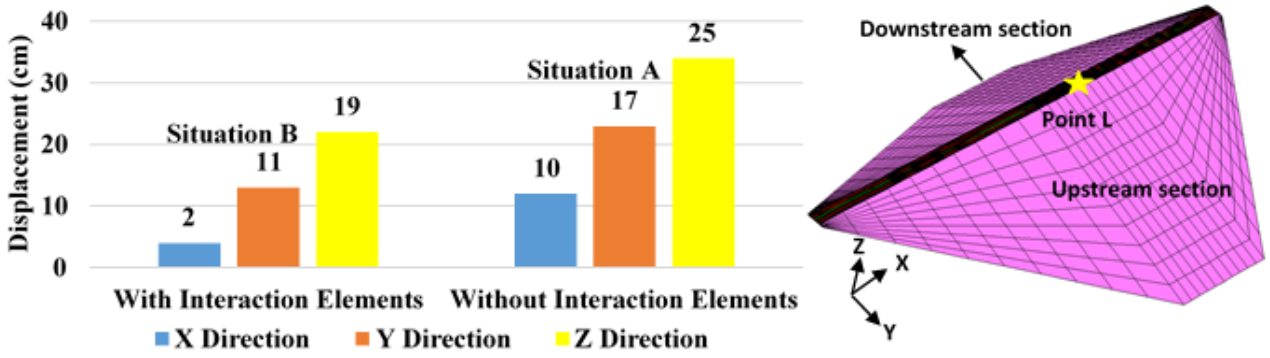

Figure 32. Highest seismic displacement results for Point L Case 12.

In Fig. 22, the seismic displacement behavior of the Kozlu dam is examined for Case 2. For Situation A, the largest displacement values occurring in the x, y, and z directions on the dam crest are 18 cm, 23 cm, and 28 cm, respectively. Moreover, the largest settlement value observed on the dam crest for Situation B is 22 cm. During the Case 3 earthquake, the highest horizontal displacement values acquired on the dam crest for Situation A and Situation B are 25 cm and 16 cm, respectively (Fig. 23). In Fig. 24, the seismic displacement behavior of Kozlu dam is assessed for the Case 4 earthquake. For Situation A, the greatest x, y, and z displacement values on the dam crest are 16 cm, 27 cm, and 33 cm, respectively. Moreover, the largest settlement value for Situation B is 23 cm. During the Case 5 earthquake, the maximum x and y displacements on the dam for Situation A are 14 cm and 20 cm, respectively (Fig. 25). In Fig. 26, the seismic displacement behavior of the Kozlu dam is evaluated for Case 6. The largest settlement values on the dam crest for Situation A and Situation B are 35 cm and 26 cm, respectively. During the Case 7 earthquake, the maximum x, y, and z displacements for Situation A are 15 cm, 18 cm, and 30 cm, respectively. Besides, the highest horizontal displacement value for Situation B is 13 cm (Fig. 27). In Fig. 28, the highest seismic displacement values at the crest of the dam are presented for the Case 8 earthquake. The largest settlement value for Situation A is 37 cm. Furthermore, the maximum x, y, and z displacement values for Situation B are 9 cm, 14 cm, and 19 cm, respectively. During the Case 9, Case 10, Case 11, and Case 12 earthquakes, it is observed that the largest seismic displacement values for Situation A are greater than for Situation B (Figs. 29-32). According to the seismic displacement results, it is concluded that the interaction elements defined between the discrete surfaces of the CCR dams significantly reduce the seismic displacement values occurring on the dam crest.

4. Conclusion and Suggestions

The finite-difference (FD) method-based FLAC3D program offers very important material models and boundary conditions for the investigation of the structural behavior of geotechnical structures. In this study, it is recommended to use the FD method utilized in this study to examine the structural behavior of CCR dams. Besides, the seismic behavior of the Kozlu clay core rockfill (CCR) dam is investigated by considering the body-foundation-

reservoir interaction. The 3D model of the dam was created by considering the finite-difference method. Non-reflecting boundary conditions are defined for the lateral boundaries of the dam model. The fix boundary condition is taken into account at the base of the dam model. Special interaction elements are defined between the dam body, foundation, and reservoir water. These interaction elements are assigned between discrete surfaces in the x, y, and z directions. A total of 12 different ground motions are utilized to examine the seismic analyzes of the dam. According to the numerical analysis results, the following important results are acquired.

- It is concluded that the seismic behavior of CCR dams significantly changes when interaction elements are assigned between the discrete surfaces. According to the earthquake analyses, it is observed that the PS and displacement values on the dam body significantly reduce as the interaction elements are defined between the dam body, foundation, and reservoir water. As a result of this study, it is strongly suggested that the definition of interaction elements between discrete surfaces should not be neglected while modeling and analyzing CCR dams.
- The 2022 Düzce-Gölyaka earthquake is of great importance to investigate the earthquake behavior of the Kozlu dam. As a result of the 2022 Düzce-Gölyaka earthquake (Case 12) that occurred in the region close to the Kozlu dam in 2022, the maximum principal stress value occurring on the dam body with interaction elements is 1.3 MPa. Moreover, for Case 12, the greatest principal stress value observed on the dam body without interaction elements is 4.28 MPa. As a result of the Düzce-Gölyaka earthquake analysis, the maximum displacement values on the dam body with interaction elements and the dam body without interaction elements are 19 cm and 25 cm, respectively.
- As a result of the earthquake analyses, it is observed that the seismic PS values on the dam body significantly diminish when the interaction elements are assigned between the discrete surfaces. Moreover, for Situation A (without interaction elements) and Situation B (with interaction elements), the largest PS values occurred around the clay core and filter materials. This result shows that the most critical materials for the PS behavior of CCR dams are the clay core and filter.
- According to the seismic displacement results, it is inferred that the highest displacement values on the dam crest for Situation A (without interaction elements) are greater than for Situation B (with interaction elements). This result shows that the definition of interaction elements in the x, y, and z directions between the discrete surfaces significantly decreases the seismic displacement values taking place in the dam body.

Statement of Research and Publication Ethics

The author declares that this study complies with Research and Publication Ethics.

References

[1] H. Cetin, M. Laman, A. Ertunc, "Settlement and slaking problems in the world's fourth largest rock-fill dam, the Ataturk Dam in Turkey," *Engineering Geology*, vol. 56, pp. 225–242, 2000.

[2] L.M. Zhang, Q. Chen, "Seepage failure mechanism of the Gouhou rockfill dam during reservoir water infiltration," *Soils and Foundations*, vol. 46, pp. 557-568, 2006.

[3] M.K. Sharp, K. Adalier, "Seismic response of earth dam with varying depth of liquefiable foundation layer," *Soil Dynamics and Earthquake Engineering*, vol. 26, pp. 1028–1037, 2006.

[4] B. Unal, M. Eren, M.G. Yalcin, "Investigation of leakage at Ataturk dam and hydroelectric power plant by means of hydrometric measurements," *Engineering Geology*, vol. 93, pp. 45-63, 2007.

[5] H. Tosun, İ. Zorluer, A. Orhan, E. Seyrek, H. Savaş, M. Türköz, "Seismic hazard and total risk analyses for large dams in Euphrates basin, Turkey," *Engineering Geology*, vol. 89, pp. 155-170, 2007.

[6] P.R. Oyanguren, C.G. Nicieza, M.I.Á. Fernández, C.G. Palacio, "Stability analysis of Llerin Rockfill Dam: An in situ direct shear test," *Engineering Geology*, vol. 100, pp. 120-130, 2008.

[7] S. Sica, L. Pagano, A. Modaressi, "Influence of past loading history on the seismic response of earth dams," *Computers and Geotechnics*, vol. 32, pp. 61-85, 2008.

[8] R. Noorzad, M. Omidvar, "Seismic displacement analysis of embankment dams with reinforced cohesive shell," *Soil Dynamics and Earthquake Engineering*, vol. 30, pp. 1149–1157, 2010.

[9] T. Ohmachi, T. Tahara, "Nonlinear earthquake response characteristics of a central clay core rockfill dam," *Soils and Foundations*, vol. 51, pp. 227-238, 2011.
[10] C. Liu, L. Zhang, B. Bai, J. Chen, J. Wang, "Nonlinear analysis of stress and strain for a clay core rock-fill dam with FEM," *Procedia Engineering*, vol. 31, pp. 497-501, 2012.
[11] X.g. Yang, S.c. Chi, "Seismic stability of earth-rock dams using finite element limit analysis," *Soil Dynamics and Earthquake Engineering*, vol. 64, pp. 1-10, 2014.
[12] R. Mahinroosta, A. Alizadeh, B. Gatmiri, "Simulation of collapse settlement of first filling in a high rockfill dam," *Engineering Geology*, vol. 187, pp. 32-44, 2015.
[13] M. Albano, G. Modoni, P. Croce, G. Russo, "Assessment of the seismic performance of a bituminous faced rockfill dam," *Soil Dynamics and Earthquake Engineering*, vol. 75, pp. 183-198, 2015.
[14] S.h. Liu, L.j. Wang, Z.j. Wang, E. Bauer, "Numerical stress-deformation analysis of cut-off wall in clay-core rockfill dam on thick overburden," *Water Science and Engineering*, vol. 9, pp. 219-226, 2016.
[15] D. Behnia, K. Ahangari, K. Goshtasbi, S.R. Moeinossadat, M. Behnia, " Settlement modeling in central core rockfill dams by new approaches," *International Journal of Mining Science and Technology*, vol. 26, pp. 703-710, 2016.
[16] B. Han, L. Zdravkovic, S. Kontoe, D.M.G. Taborda, " Numerical investigation of the response of the Yele rockfill dam during the 2008 Wenchuan earthquake," *Soil Dynamics and Earthquake Engineering*, vol. 88, pp. 124-144, 2016.
[17] D.S. Park, N.R. Kim, " Safety evaluation of cored rockfill dams under high seismicity using dynamic centrifuge modeling," *Soil Dynamics and Earthquake Engineering*, vol. 97, pp. 345-363, 2017.
[18] K. He, C. Song, R. Fell, " Numerical modelling of transverse cracking in embankment dams," *Computers and Geotechnics*, vol. 132, 104028, 2021.
[19] Q. Wu, D.Q. Li, Y. Liu, W. Du, " Seismic performance of earth dams founded on liquefiable soil layer subjected to near-fault pulse-like ground motions," *Soil Dynamics and Earthquake Engineering*, vol. 143, 106623, 2021.
[20] M. Dolezalova, I. Hladik, " Long-term behavior and safety assessment of Sance Rockfill Dam," *Front. Archit. Civ. Eng. China*, vol. 5, pp. 79-89, 2011.
[21] J. Zhang, L. Zhang, " 3-D Seismic Response Analysis Methods of High Core Rockfill Dams," *Arab J Sci Eng*, vol. 38, pp. 839–848, 2013.
[22] N. Javadi, T.F. Mahdi, " Experimental investigation into rockfill dam failure initiation by overtopping," *Natural Hazards*, vol. 74, pp. 623–637, 2014.
[23] S. Durmaz, D. Ülgen, " Prediction of earthquake-induced permanent deformations for concrete-faced rockfill dams," *Natural Hazards*, vol. 105, pp. 587–610, 2021.
[24] J. Yu, Z. Shen, Z. Huang, " Analysis on damage causes of built-in corridor in core rock-fill dam on thick overburden: A case study," Frontiers of Structural and Civil Engineering, 2022.
[25] AFAD, Disaster and Emergency Management Presidency, Turkey earthquake regions map. https://www.afad.gov.tr/, 2022.
[26] M.E. Kartal, M. Çavusli, M. Genis, " 3D Nonlinear Analysis of Atatürk Clay Core Rockfill Dam Considering Settlement Monitoring," Int. J. Geomech, vol. 19, 04019034, 2019.
[27] M. Karalar, M. Çavuşli, " Effect of Normal and Shear Interaction Stiffnesses on Three-Dimensional Viscoplastic Creep Behaviour of a CFR Dam," *Advances in Civil Engineering*, vol. 2018, pp. 0-17, 2018.
[28] DSI, General Directorate of State Hydraulic Works, Regional Directorate, Zonguldak, Turkey, 2022.
[29] PEER, Pacific Earthquake Engineering Research Center (PEER), 2022.
[30] AFAD, Disaster and Emergency Management Presidency, 2022.
[31] M. E. Kartal, M. Çavuşli, M. Geniş, " 3D Nonlinear Analysis of Atatürk Clay Core Rockfill Dam Considering Settlement Monitoring," *International Journal of Geomechanics*, vol. 19(5), 2019.

Bitlis Eren Üniversitesi Fen Bilimleri Dergisi
BİTLİS EREN UNIVERSITY JOURNAL OF SCIENCE
ISSN: 2147-3129/e-ISSN: 2147-3188
VOLUME: 11 NO: 4 PAGE: 1138-1145 YEAR: 2022
DOI:10.17798/bitlisfen.1192821

Evaluation of Structural Safety of a Steel School Building with Partially Modified Structural System

R. Kadir PEKGÖKGÖZ [1*], Fatih AVCİL[2], M. Arif GÜREL[1]

[1]*Department of Civil Engineering, Harran University, Sanliurfa, Turkey*
[2]*Department of Civil Engineering, Bitlis Eren University, Bitlis,, Turkey*
(ORCID: 0000-0002-3083-2241) (ORCID: 0000-0001-6550-550X) (ORCID: 0000-0002-1046-4410)

Keywords: Structural safety, Truss system, Steel construction.

Abstract

In order to meet the basic needs of foreign asylum seekers coming to our countries such as shelter, nutrition, and education, our government has established temporary shelters in different regions of our country. One of them is a completely disassembled steel school building with 23 classrooms, the carrier system of which is steel construction, in order to meet the educational needs of the temporary shelter located in the Ceylanpınar district of Şanlıurfa city. The roof of this school was designed as a plane truss system made of steel construction. The truss system, which was designed as a single part in the architectural and static application projects of the building, was separated from the symmetry axis and manufactured in two parts since it provides ease of transportation, manufacturing, and assembly by the contractor company. These parts were connected with bolts during manufacturing. In this study, as a result of the examinations carried out according to the regulations and standards in force at the time the building was designed, it was determined that constructing the system in two parts and connecting it with bolts does not pose a problem in terms of service safety of the building.

1. Introduction

Turkish people always offer a helping hand with compassion toward those in trouble. In recent years, as a result of the undesirable events in Syria, our country's south-eastern neighbor, many people had to leave their countries and seek refuge in neighboring countries. Turkey has been one of the countries that faced the greatest human migration among these neighboring countries. Our country has deemed it appropriate to keep the refugees in temporary accommodation centers in order to keep the first wave of immigration under control and to enable them to live in harmony with our people. For this purpose, 26 temporary accommodation centers established in 10 different cities have hosted Syrian refugees. In addition to the shelter needs of those staying in temporary accommodation centers, education services, health services, the opportunity to worship in houses of worship, and market services were provided to all school-age children, including pre-schoolers. In addition, non-professional asylum seekers were provided with the opportunity to acquire a profession through adult education centers.

One of the temporary accommodation centers established for Syrian refugees in our country is located in the Ceylanpınar district of our Şanlıurfa city. In this center, a school building with 23 classrooms and steel construction was built in order to provide educational services. In the following years, when the need for the temporary camp center disappears, it was preferred that the structural system is steel in order to ensure that the building can be dismantled and moved to another place where it is needed. The most important feature of the building is that it is completely dismantled and portable except for the reinforced concrete foundation.

Although steel material has a wide range of uses, the most used area is the construction sector. Steel carrier systems are used at a rate of 65% in

*Corresponding author: recepkadir@harran.edu.tr
Received: 21.10.2022, Accepted: 22.12.2022

industrial buildings, 15% in commercial buildings, 2% in residences, 3% in bridges, and 15% in other types of structures in Turkey [1]. As can be seen, the use of steel in residential buildings is very low. This may be because it is expensive compared to reinforced concrete structures and requires more qualified personnel. However, new steel multi-storey structures have started to take place in our cities. Due to reasons such as changing population balance, making new zoning regulations, and changing the existing design regulations, changes in the purpose of use or renovations are required in the existing building stocks. These effects cause the formation of mixed building groups, and even steel systems are preferred more because of their advantages [2].

The main objective of the projects planned to be built is to complete the work by meeting the planned time, cost, and adequate quality conditions. It is frequently encountered that the construction projects of which implementation projects have been prepared and the construction of which has been started by obtaining the license are continued by revising the projects according to the emerging needs. These revisions should be made in official ways, with the approval of the employer, contractor company, and control mechanisms. Otherwise, serious legal problems will inevitably arise between the above-mentioned authorities. In the thesis study conducted by S. Şavklı, the issue of regulating the legal rights on the contracts describing the rights and duties of the mentioned authorities was examined in order to prevent the conflicts that may arise between the employer, the contractor company and the control unit of the changes to be made in the implementation projects [3].

In general, these reasons can be sorted; earthquake and vibration effects, changes in the ground structure of the building, increase in the loads to which the structure is exposed, the possibility of deterioration of stability, changes in the purpose of use of the structure, project errors, application errors, inspection deficiencies, material errors, changing regulation conditions, etc. It can be said that the need for repair and reinforcement will arise in the structures affected by one or more of these facts. The repair and strengthening process varies depending on whether the structure is reinforced concrete, steel, wood, etc. It can be stated that the causes and solutions of the damage in wooden and steel structures are more obvious than the damage in reinforced concrete structures. In other words, the causes and solutions of damage in reinforced concrete structures are more complex than in wooden and steel structures. Damages in concrete and reinforced concrete structures can be seen mostly in the form of cracks, fragment ruptures, and segregation [4].

Although the buildings are under strict control during the project and construction phase, sometimes important productions can take place without the approval of the construction control mechanism. When this situation is noticed, dismantling the production and having it done again according to the project cause serious time and economic losses. When such a situation is encountered during the construction of buildings, two options can be made. The first is to dismantle the wrongly made production and have it rebuilt in accordance with the approved project, which is the most correct method. However, it is inevitable to encounter serious time and economic losses with this option. The second option is to evaluate whether manufacturing not suitable for the project endangers the safe use of the building by checking it and evaluating it in a report. If the experts state in their reports that manufacturers that are not made in accordance with the project do not endanger the safe use of the building, the building is allowed to be used in its current form. Thus, the economic and time losses that will be encountered by dismantling the productions that are not made in accordance with the project and having the productions made in accordance with the project are prevented. When it is determined that the usage safety of the building is in danger, manufacturing not suitable for the project should be dismantled and it should be ensured that they are made in accordance with the project.

2. Material and Method

2.1. General Features of the School Building

The general architectural geometry of the building is similar to the letter "U", its long dimension is approximately 61 m and its short dimension is 24 m. The building is planned as a total of two floors, the ground floor and, the first floor. The ground floor consists of 11 classrooms, an administrative section, a canteen, a ladies' prayer room, a boiler room, and convenience facilities. The first floor consists of 12 classrooms, an administrative section, a teachers' room, a men's prayer room, and convenience facilities. The usage area of the classrooms is 520 m^2 on the ground floor, 570 m^2 on the first floor, and a total of 1090 m^2. The passage of the school building between the ground floor and the first floor is provided by three stairs. The general view of the school building is shown in Figure 1.

Figure 1. General view of the school building considered in the study

The building is placed on a 0.5 m thick reinforced concrete raft foundation. The total height from the foundation level is 8.9 m, with a basement height of 0.60 m, a ground floor height of 3 m, a first-floor height of 3.3 m, and a roof height of 2 m. The design of the building started in 2016 and revision projects were prepared in 2017. The static design was made according to the Regulation on structures to be built in disaster zones 2007 (TEC 2007), which was in force at that time [5]. The steel construction and joint calculations of the building were made according to the Principles on the Design, Calculation, and Construction of Steel Structures 2016 [6]. The necessary information for the material, soil, and earthquake calculation of the building is presented in Table 1.

Table 1. Information for the material, ground, and earthquake calculation of the school

Concrete grade	C30	Soil Type	D
Rebar of the reinforced concrete	S420	Unit Volume Weight of Soil	21 kN/m^3
Steel	S235	Effective Ground Acceleration Coefficient (A_0)	0.4
Safe Bearing Capacity	100 kN/m^2	Building important factor (I)	1.4
Local Soil Classification	Z4	Structural behavior coefficient (R)	4.0
Bearing Coefficient of the Soil	10^4 kN/m^3		

3. Results and Discussion

3.1. Evaluation of the Existing Situation of the School

When the approved architectural project and static application projects of the building are examined, it is understood that SHS 120x120x5 tube section columns are used on the reinforced concrete raft foundation, the ground floor ceiling consists of composite flooring, and the roof section consists of a single part truss system with bars. It is planned that the roof trusses will be manufactured in one piece in the workshop and assembled on-site. The contractor company decided that the roof trusses, which are thought to be manufactured as one piece, would be difficult to assemble both in transportation and in the construction area, and decided to manufacture them in two parts by separating the large span trusses from the symmetry axis.

The roof trusses, manufactured by the contractor company as two parts, were connected with 5 M22 bolts at the construction site. During the manufacture of some roof trusses, the strut bars in the symmetry axis were manufactured incorrectly, as shown in Figure 2.

Figure 2. Roof trusses manufactured in two parts

Due to this faulty manufacturing, separation up to 30 mm has been detected from the squareness of the uprights in the part where the mentioned roof trusses meet on the symmetry axis. After this situation was determined by the control unit, it was concluded that the issue should be evaluated and reported by the expert team in order to eliminate the concerns about whether the manufacturers made in this way endanger the safety of the building. The report, which is the basis of the study, has been prepared by the authors for this purpose.

3.2. Evaluation of the Buildings Made Different from the Implementation Projects of the Building in Terms of Structural Safety of the Building

Using the static and architectural application projects of the school building, a three-dimensional model was created in the Idecad Static structure analysis program, taking into account the regulations and standards in force in the years it was designed [7]. The building model in which the roof trusses made of steel profiles are considered as one piece is shown in Figure 3.

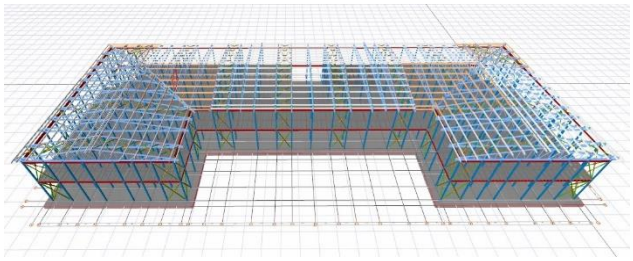

Figure 3. Building model in which the roof trusses are formed as one part

As a result of the examinations made by the control unit of the building, trusses made in two parts by separating from the symmetry axis in the building and trusses deviation from the squareness of the strut bars on the symmetry axis were determined. The model created by considering this situation of the building is shown in Figure 4.

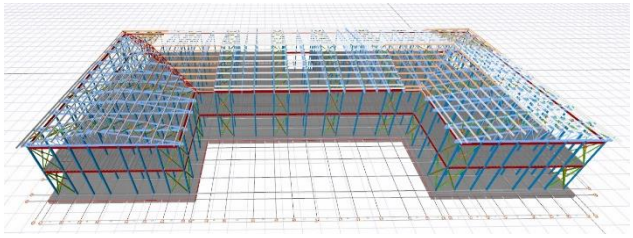

Figure 4. Building model in which the roof trusses are formed in two parts

Both building models were analyzed under the influence of constant loads (G, Q), vertical loads such as snow loads (S), and horizontal loads such as wind (W) and earthquake loads (E). The reports created as a result of the analyzes were examined and the results were evaluated.

3.3. Evaluation of the School Building with Roof Trusses Consisting of One part

As a result of the analyzes made in the building model, in which the roof trusses are considered as a single piece, it has been determined that the foundation, columns, beams, composite floors, and roof trusses that make up the structure safely carry the loads on them. Since it will take a lot of space to give the analysis results of all structural components of the building here, the stresses occurring in the elements of the roof truss which are the longest and have the highest loads, TRS031 have been examined. This roof truss is shown in Figure 5.

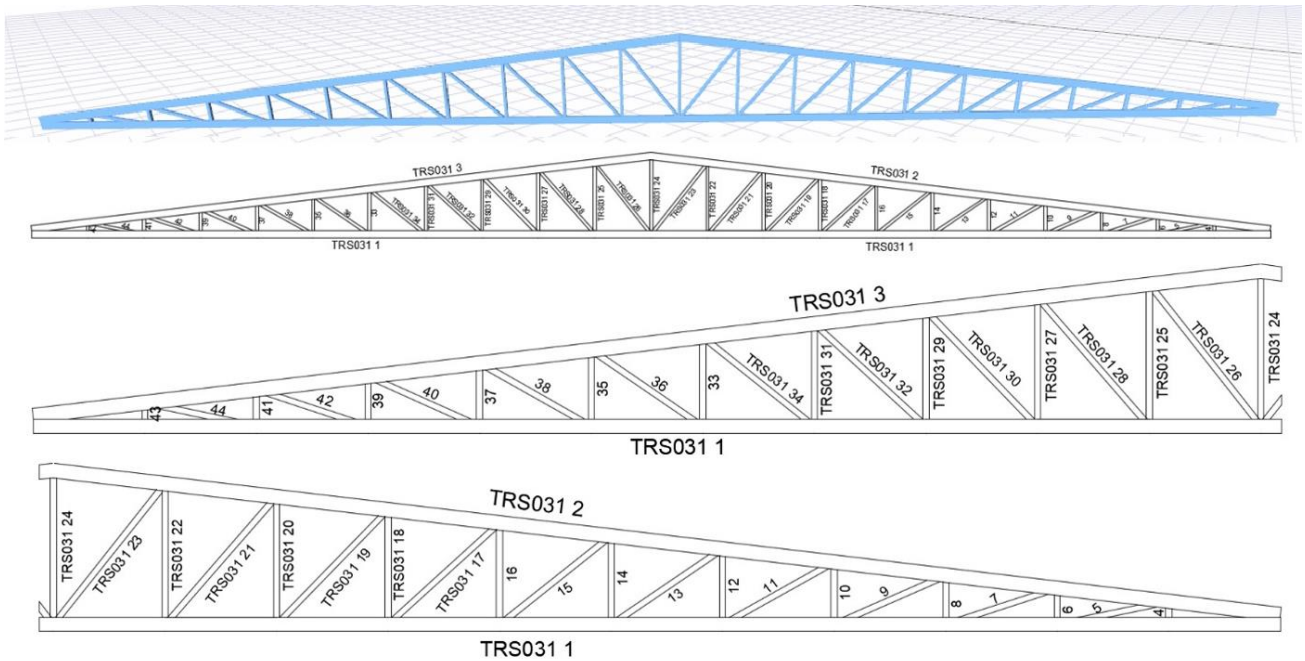

Figure 5. One-part roof truss (number TRS031)

If the internal forces consisting of external loads acting on the structural system of the building are accepted as demand, the ratio of the demand to the section capacity is expressed as the PMM ratio (demand/capacity ratio). The internal forces of the elements forming the truss under the influence of the most unfavorable load combinations and the resulting PMM ratios are shown in Table 2. After examining the table, it was understood that the PMM ratios were less than 1.0. This shows that the examined trusses can safely carry the loads acting on them.

Table 2. Axial force and PMM ratios in one-part roof truss no. TR031

Name	Member	Section	Load combination	Axial force (kN)	PMM ratio	Strength check
TR031-1	Bottom bar	RHS 80x140x6	G-0.7Ey	-176.57	0.55	√
TR031-2	Top bar	RHS 80x140x6	G-0.7Ex	-192.15	0.61	√
TR031-3	Top bar	RHS 80x140x6	G-0.7Ex	-196.05	0.61	√
TR031-4	Vertical	SHS 60x3	G+0.75Q-0.53Ex+0.75S	-7.11	0.081	√
TR031-5	Cross	SHS 60x3	G+0.75Q-0.53Ex+0.75S	10.73	0.12	√
TR031-6	Vertical	SHS 60x3	G+0.75Q-0.53Ex+0.75S	-4.78	0.055	√
TR031-7	Cross	SHS 60x3	G+0.75Q-0.53Ex+0.75S	10.56	0.12	√
TR031-8	Vertical	SHS 60x3	G+0.75Q-0.53Ex+0.75S	-2.59	0.03	√
TR031-9	Cross	SHS 60x3	G+0.75Q-0.53Ex+0.75S	-4.58	0.059	√
TR031-10	Vertical	SHS 60x3	G+0.75Q-0.53Ex+0.75S	2.57	0.029	√
TR031-11	Cross	SHS 60x3	G+0.75Q-0.53Ex+0.75S	-7.28	0.095	√
TR031-12	Vertical	SHS 60x3	G+0.75Q-0.53Ex+0.75S	3.75	0.043	√
TR031-13	Cross	SHS 60x3	G+0.75Q-0.53Ex+0.75S	-7.41	0.099	√
TR031-14	Vertical	SHS 60x3	G+0.75Q-0.53Ex+0.75S	4.56	0.052	√
TR031-15	Cross	SHS 60x3	G+0.75Q-0.53Ex+0.75S	-5.98	0.081	√
TR031-16	Vertical	SHS 60x3	G+0.75Q-0.53Ex+0.75S	4.42	0.05	√
TR031-17	Cross	SHS 60x3	G-0.7Ey	-4.57	0.064	√
TR031-18	Vertical	SHS 60x3	G+0.7Ey	3.45	0.039	√
TR031-19	Cross	SHS 60x3	G+0.75Q-0.53Ex+0.75S	-5.96	0.085	√
TR031-20	Vertical	SHS 60x3	G+S	-14.81	0.194	√
TR031-21	Cross	SHS 60x3	G+0.75Q-0.53Ex+0.75S	12.64	0.143	√
TR031-22	Vertical	SHS 60x3	G+0.75Q-0.53Ex+0.75S	-9.58	0.13	√
TR031-23	Cross	SHS 60x3	G+0.75Q-0.53Ex+0.75S	11.86	0.134	√
TR031-24	Vertical	SHS 60x3	G+0.75Q-0.53Ex+0.75S	-3.07	0.043	√
TR031-25	Vertical	SHS 60x3	G+S	-10.26	0.139	√
TR031-26	Cross	SHS 60x3	G+S	11.50	0.13	√
TR031-27	Vertical	SHS 60x3	G+S	-15.10	0.198	√
TR031-28	Cross	SHS 60x3	G+S	14.99	0.17	√
TR031-29	Vertical	SHS 60x3	G+0.75Q-0.53Ex+0.75S	-2.20	0.028	√
TR031-30	Cross	SHS 60x3	G+0.75Q-0.53Ex+0.75S	2.49	0.028	√
TR031-31	Vertical	SHS 60x3	G+0.75Q-0.53Ex+0.75S	-5.47	0.068	√
TR031-32	Cross	SHS 60x3	0.6G-0.7Ey	72.01	0.072	√
TR031-33	Vertical	SHS 60x3	G-0.7Ey	-3.38	0.041	√
TR031-34	Cross	SHS 60x3	G-0.7Ey	-5.27	0.072	√
TR031-35	Vertical	SHS 60x3	G+0.75Q-0.53Ex+0.75S	3.72	0.042	√
TR031-36	Cross	SHS 60x3	G+0.75Q-0.53Ex+0.75S	-6.27	0.084	√
TR031-37	Vertical	SHS 60x3	G+0.75Q-0.53Ex+0.75S	2.59	0.029	√
TR031-38	Cross	SHS 60x3	G+0.75Q-0.53Ex+0.75S	-6.34	0.083	√
TR031-39	Vertical	SHS 60x3	G+0.75Q-0.53Ex+0.75S	0.79	0.009	√
TR031-40	Cross	SHS 60x3	G+0.75Q-0.53Ex+0.75S	-3.68	0.048	√
TR031-41	Vertical	SHS 60x3	G+0.75Q-0.53Ex+0.75S	-1.22	0.014	√
TR031-42	Cross	SHS 60x3	G-0.7Ey	-1.79	0.023	√
TR031-43	Vertical	SHS 60x3	G+0.75Q-0.53Ex+0.75S	-3.50	0.04	√
TR031-44	Cross	SHS 60x3	G+0.75Q-0.53Ex+0.75S	6.52	0.074	√

3.4. Evaluation of the School Building with Roof Trusses Consisting of Two parts

Roof trusses produced by the contractor company in the workshop are made of two parts in order to be easily transported and easily lifted and assembled. During the construction of the building, it was determined that most of the roof trusses, which were produced from two parts, came back to back during assembly, but a small part of the strut bars on the symmetry axis was not made perfectly vertical, resulting in separations of 30 mm between them. Considering this situation of the building, a three-dimensional model was created and analyzed. In this section, truss no. TRS031, which is considered in the case where the roof truss is a single part, is examined in detail. The general view of this truss and the part where the two parts are joined with bolts are shown in Figure 6.

Figure 6. Modeling of the roof truss as two parts (number TRS031)

The axial forces and PMM ratios formed in the elements of the TRS031 truss are shown in Table 3. Although there is a slight increase in the normal force value of the strut rods deviation from the squareness of the truss made in two parts, compared to the case where the same truss is one piece, it is understood from the examination of Table 3 that the existing cross-sections are capable of carrying these forces safely. In addition, in the evaluation, it was determined that the PMM ratios in all truss elements were less than 1.0. This result showed that the members that make up the examined truss have sufficient security to carry the internal forces on them. It has been determined that the five bolts connecting the roof trusses made in two parts are sufficiently secure to carry the cross-sectional effects on them.

It has been determined that the construction of some roof trusses in two parts does not pose a problem in terms of user safety of the building. As a result of two-part manufacturing, in case of any deformation due to the loads on the roof trusses, the formation of deformations in the roof covering is an inevitable result. In the observations and examinations made on the roof of the building, it was determined that there was no deformation. This observation supports the accuracy of analyzes and investigations.

Table 3. Axial force and PMM ratios in two-part roof truss no. the TR031

Name	Member	Section	Load combination	Axial force (kN)	PMM ratio	Strength check
TR031-1	Bottom bar	RHS 80x140x6	G-0.7Ey	-29.17	0.517	√
TR031-2	Top bar	RHS 80x140x6	G-0.7Ex	-19.45	0.703	√
TR031-3	Top bar	RHS 80x140x6	G-0.7Ey	-13.83	0.175	√
TR031-4	Vertical	SHS 60x3	G-0.7Ex	-3.38	0.717	√
TR031-5	Cross	SHS 60x3	0.6G-0.7Ex	-3.81	0.31	√
TR031-6	Vertical	SHS 60x3	G+0.75Q-0.53Ex+0.75S	-3.02	0.23	√
TR031-7	Cross	SHS 60x3	0.6G-0.7Ex	-3.22	0.126	√
TR031-8	Vertical	SHS 60x3	G-0.7Ex	-2.56	0.157	√
TR031-9	Cross	SHS 60x3	G-0.7Ex	-11.88	0.347	√
TR031-10	Vertical	SHS 60x3	G-0.7Ex	18.4	0.202	√
TR031-11	Cross	SHS 60x3	G-0.7Ex	-60.76	0.563	√
TR031-12	Vertical	SHS 60x3	G-0.7Ex	3.9	0.106	√
TR031-13	Cross	SHS 60x3	G-0.7Ex	-60.57	0.846	√
TR031-14	Vertical	SHS 60x3	G-0.7Ex	5.36	0.223	√
TR031-15	Cross	SHS 60x3	G+0.75Q-0.53Ex+0.75S	-5.23	0.392	√
TR031-16	Vertical	SHS 60x3	G-0.7Ex	3.01	0.137	√
TR031-17	Cross	SHS 60x3	G-0.7Ex	-4.13	0.133	√

TR031-18	Vertical	SHS 60x3	0.6G-0.7Ex	-11.4	0.115	√
TR031-19	Cross	SHS 60x3	0.6G-0.7Ex	-14.4	0.632	√
TR031-20	Vertical	SHS 60x3	G-0.7Ey	-18.1	0.202	√
TR031-21	Cross	SHS 60x3	G+0.75Q-0.53Ex+0.75S	13.53	0.149	√
TR031-22	Vertical	SHS 60x3	G+0.75Q-0.53Ex+0.75S	-10.1	0.733	√
TR031-23	Cross	SHS 60x3	G+0.7Ey	7.16	0.283	√
TR031-24	Vertical	SHS 60x3	G-0.7Ex	14.64	0.748	√
TR031-25	Vertical	SHS 60x3	G+0.75Q-0.53Ex+0.75S	-9.72	0.719	√
TR031-26	Cross	SHS 60x3	G-0.7Ey	7.85	0.143	√
TR031-27	Vertical	SHS 60x3	G+S	-14.33	0.845	√
TR031-28	Cross	SHS 60x3	G-0.7Ey	35.51	0.909	√
TR031-29	Vertical	SHS 60x3	G-0.7Ey	-3.5	0.17	√
TR031-30	Cross	SHS 60x3	G-0.7Ey	35.51	0.909	√
TR031-31	Vertical	SHS 60x3	G+0.75Q-0.53Ex+0.75S	-4.94	0.377	√
TR031-32	Cross	SHS 60x3	G+0.75Q-0.53Ex+0.75S	4.61	0.064	√
TR031-33	Vertical	SHS 60x3	G+0.75Q-0.53Ex+0.75S	-8.39	0.915	√
TR031-34	Cross	SHS 60x3	G+0.75Q-0.53Ex+0.75S	7.12	0.08	√
TR031-35	Vertical	SHS 60x3	G-0.7Ey	2.26	0.095	√
TR031-36	Cross	SHS 60x3	G+0.75Q-0.53Ex+0.75S	-5.08	0.328	√
TR031-37	Vertical	SHS 60x3	G+0.75Q-0.53Ex+0.75S	3.14	0.144	√
TR031-38	Cross	SHS 60x3	G+0.75Q-0.53Ex+0.75S	-7.37	0.433	√
TR031-39	Vertical	SHS 60x3	G-0.7Ex	1.42	0.09	√
TR031-40	Cross	SHS 60x3	G+0.75Q-0.53Ex+0.75S	-7.37	0.433	√
TR031-41	Vertical	SHS 60x3	G-0.7Ex	-0.9	0.086	√
TR031-42	Cross	SHS 60x3	G-0.7Ey	-2.55	0.105	√
TR031-43	Vertical	SHS 60x3	G+0.75Q-0.53Ex+0.75S	-3.72	0.177	√
TR031-44	Cross	SHS 60x3	0.6G-0.7Ey	-3.81	0.127	√

4. Conclusion and Suggestions

In order to meet the educational needs of the refugees who came to our country, school buildings were made of steel construction in different regions of our country, as they are demountable. One of these buildings is a two-storey school building built in the Ceylanpınar district of Şanlıurfa city. As a result of the examinations and analyzes, it was determined that the roof trusses, which should be made in one part according to the static and architectural application projects, were manufactured in two parts and these two parts were connected with five bolts. In addition, it has been determined that the safe use of the structure is not endangered by the separations from the squares of up to 30 mm due to manufacturing faults at the joints in the symmetry axis of some roof trusses.

This finding is also supported by the fact that no deformation occurred in the roof covering system as a result of visual inspection. If any deformation had been detected due to the loads on the roof trusses, it would have been inevitable for this situation to manifest itself with the deformation that would occur in the roof covering.

As a result of the analysis and modeling, it has been determined that the roof trusses are made in two parts, so the safe use of the building does not endanger. Achieving this result has prevented financial and time losses. Due to the conclusion of this review as mentioned above, a gain has been made to our country's economy. The importance of engineering knowledge in solving different problems encountered has been understood once again.

It is hoped that the study, with its method and methodology, will be a guide for solving similar problems to be encountered in the future.

Contributions of the authors

Design/Concept and Modelling: RKP; Literature Search and Data Collection: FA; Drafting manuscript and critical revision of the manuscript: MAG.

Conflict of Interest Statement

There is no conflict of interest between the authors.

Statement of Research and Publication Ethics

The study complied with research and publication ethics.

References

[1] M. R. Aydın, A. Günaydın, "Steel Structures (in Turkish)," *Birsen Press*, İstanbul 2016.
[2] S. Bekiroğlu, B. Sevim, A. Şahin, Y. Ayvaz, "Betonarme Yapı Üzerine Çelik Taşıyıcı Sisteme Sahip Çok Amaçlı Salon Tasarımı" *5. Çelik Yapılar Sempozyumu. TUCSA* - Türk Yapısal Çelik Derneği, pp. 1-9, 2013.
[3] S. Şavklı, "Yapım Projelerinde Değişiklik Talimatları İle Kalite İlişkisi" *Master Thesis,* Yıldız Technical University, İstanbul, Türkiye, 2011.
[4] E. Özgan, M.M. Uzunoğlu, S. Subaşı, "Okul Binalarında Büyük Onarım Maliyetlerinin İncelenmesi ve Maliyet Tahmini," *International Earthquake Symposium,* pp. 1-5, 2007. (in Turkish)
[5] BİB "Afet Bölgelerinde Yapılacak Yapılar Hakkında Yönetmelik," *T.C. Ministry of Development and Housing*, 2007
[6] ÇŞB, "Çelik Yapıların Tasarım Hesap ve Yapımına Dair Esaslar," *T.C. The Ministry of Environment and Urbanization*, 2016.
[7] IdeCad. (V10.94). [Online]. Available: https://www.idecad.com.tr/index/

Bitlis Eren Üniversitesi Fen Bilimleri Dergisi
BİTLİS EREN UNIVERSITY JOURNAL OF SCIENCE
ISSN: 2147-3129/e-ISSN: 2147-3188
VOLUME: 11 NO: 4 PAGE: 1146-1151 YEAR: 2022
DOI:10.17798/bitlisfen.1195588

The Effect of Periodic Inspection and Safety Criteria on the Service Life of Steel Construction Conveyors

Ersin Asım GÜVEN[1*]

[1]*University of Kocaeli, Faculty of Engineering, Department of Mechanical Engineering 41040 Kocaeli / Türkiye*
(ORCID:0000-0003-0153-6774)

Keywords: Structural Steel, Service Life, Periodic Inspection

Abstract

Steel construction structures are seen in many different applications in our country and in the world. However, the periodic maintenance of these steel construction products is explained by national and international laws and regulations. According to the relevant regulation in our country, it is obligatory to carry out periodic inspections of these constructive structures, which are referred to as machinery and equipment, once a year. As in many facilities, it is obvious that these structures are the main elements of the facility and will be used throughout the life of the facility. It is not clear under which conditions these structures, which are generally produced using structural steels and which are connected by welding or bolts, will be examined in the periodic inspections. As a result of the research on the lifetime of general structural steels, it has been proved by many researchers that these structures have an infinite life if they reach the number of million repetitions. However, the life of welding or bolts, which are the connecting elements of the structure, remains uncertain. In this study, accident breaking studies were carried out by detailing the damage due to a tragic accident in a steel construction that has served for about 36 years. By keeping company and personal information confidential, the steel structure and bolt connections of the construction were examined in terms of strength, hardness and microstructure, and the results were detailed.

1. Introduction

Belt conveyors are used for the transportation of bulk materials, such as ore, coal e.g., along a horizontal or an inclined conveyor track and can be used in various operational environments [1]. The handling of bulk solids is generally associated with significant wear on equipment and components. This is caused by either permanent or temporary contact between bulk solids and a wear body, e.g., component walls, tools, etc., with simultaneous relative movement or impact [2]. The researchers are widely investigated the failure mechanism of conveyor components. V. V. Poovakaud et al. are studied the fretting fatigue in high strength steel bolted connections [3]. M. Sundar et al. are investigated the corrosion behavior of conveyor chain pin [4]. W. Bochnowski et al. are researched the damage characterization of 330Nb alloy wire conveyor belt under carburizing atmosphere [5]. M.A. Khattak et al. are studied the failure of 430 welded steel plates for conveyor belts [6]. D. R. H. Jones is investigated the fatigue failure of drums for conveyors [7]. As the researchers mentioned, there are many reasons for improving equipment reliability [8], [9]. Unfortunately, the more catastrophic failures, such as whole of structural collapse, have been experienced and resulted as tragedy. These kinds of tragedies could be sourced by improper design or inaccurate assembly, insufficient maintenances, and overloads. However, the monthly and annual maintenance procedure could be summarized as, belt slippage, roller seizure, gearbox checks, electrical component checks (such as, fuse, conductor, emergency stop), ball roller checks, and irregular vibration and noise checks [10]. As can be

*Corresponding author: asimguven@kocaeli.edu.tr
Received: 27.10.2022, Accepted: 21.12.2022

seen, even if detailed in the design criteria [11], the steel structure, welded areas and bolt connections are not taken into account in the periodic controls.

In this study, collapse of a coal conveyor has been investigated. The steel components, welded zones and bolt joints have been studied in terms of corrosion, strength, hardness, and microstructural analysis. Location and time information is hidden due to personal data protection law.

2. Material and Method

The conveyor, investigated in this study, has been established 36 years ago from the collapse time. Conveyor has been designed as 167 m long and 14° incline angle, the final peak level was 45 m, above the ground. The structure of conveyor has been constructed as 23 different galleries. And each gallery has been combined with 138 pieces of M20 bolt joints to the other. Each gallery was 12 m long and nearly 11.7 tons. The conveyor has been designed and built on two tubular central and two sliding end supports, and total weight is 423.708 kg. The calculated wind load is vertically 12.369 kg and laterally 131.676 kg, and the snow load is 75.150 kg. The full capacity coal load is 131.000 kg. Under these loadings, the maximum shear and tensile stresses per bolt are nearly150 and 200 MPa respectively. But unfortunately, the pre-tension and torque level of bolts couldn't be determined. For that reason, the design safety factor for the bolts could be calculated as 2.5 - 3.0.

It is detected form Technical Sheets of the conveyor that, St3Sx class structural steel was used for construction, the chemical composition is given in Table 1. This structural steel class is known as Poland Standard (PN-88 H-84020). And it is equivalent to DIN 17100 USt37-2 (S235JRG1) [12].

Table 1. Chemical composition of St 3Sx (wt.%).

C	Cr	Cu	Mn	Ni	Si	P	S	Fe
0.2 2	0.3 0	0.3 0	1.1 0	0.3 0	0.0 7	0.0 5	0.0 5	Bal .

The M20 bolts and nuts, surrounded on the edge of gallery, are detected as 8.8 and 10.9 class. On the lower segment of the gallery, which was loaded both tensile and shear stress, the bolts and nuts were selected as 10.9 class, other ones were 8.8.

To determine the corrosion and fatigue evidence of steel, the structural steel samples were taken from unstrained part of the wreckage. The samples were taken from the "U" and "I" type profiles, which are the carriers of the gallery. These profiles were chosen from the lower segment and the side wall, representing the entire gallery (Figure 1). Profile samples taken from the lower segment were selected from the region with both coal accumulation (Sample type A) and non-accumulation (Sample type TB), and it was tried to determine whether the coal affected the mechanical properties. In addition, one sample (Sample type U) was taken in the ceiling profile.

Figure 1. Structural steel samples.

Bolt and nut samples were also chosen in a variety to represent the whole gallery and larger numbers of samples were selected from the lower segment, where the coal dust accumulation located (Figure 2).

Steel tensile test samples were machined according to the TS 138 EN 10002, and the tensile tests were carried out according to the ISO 6892. Bolt and nut tensile tests were carried out according to the ISO 898-1. The tensile tests were carried out on 600 kN Dartec servo-hydrolic test machine.

Sections of steel and bolt samples were grinded by using the Metcon Forcipol 2V rotating polishing machine with various grades of SiC papers up to 2400 grid. Specimens were subjected to fine polishing by using 1 μm diamond paste and then final polishing by colloidal-silica suspension. Polished specimens were immersed into Nital solution for 5 s and washed with alcohol. Leica optical microscope and Clemex Image Analyzer were used for microstructural examinations.

The hardness tests were carried out on Zwick micro-hardness test device and results were reported in Vickers unit.

3. Results and Discussion

Due to the fact that the A2 profile was in the lower segment covered with coal dust, the corrosion effect on the sample was tried to be investigated. In the sample taken on this profile, it was observed that there was only corrosion on the outer surfaces, but no

corrosive effect penetrating into the base metal occurred, and it was determined that the material microstructure was in accordance with the standard "Beynitic" structure of St3Sx structural steel (Figure 3).

Figure 2. Bolt and nut samples.

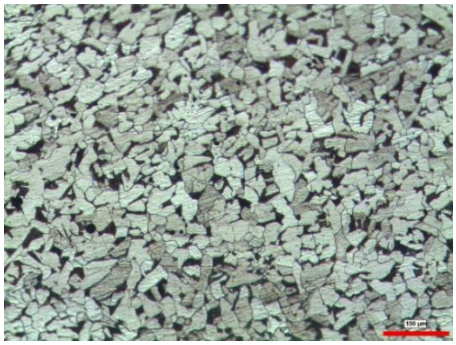

Figure 3. Microstructural image of A2 sample.

However, in the examination, made on the welded part, corrosion and crack formations were observed, and showed in Figure 4. But even if the cracks were critical size, the lack of load bearing functions of the welded seams was not considered as the main cause of collapse.

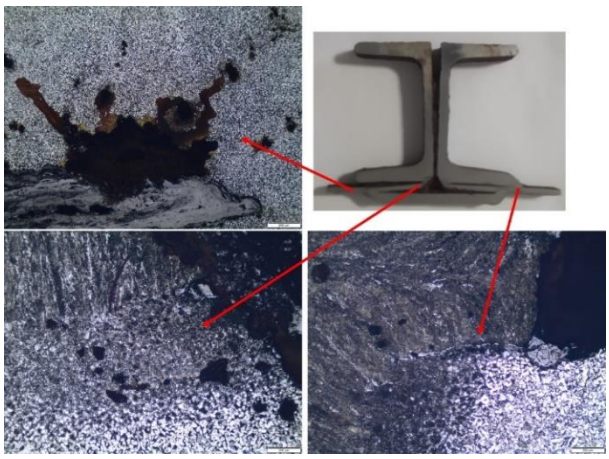

Figure 4. Welded zone of U type profile.

In the examination made on the bolt, it was determined that the corrosion layer (Figure 5) observed on the surfaces did not penetrate the material, therefore corrosion did not adversely affect the mechanical properties of the material. The hardness change of the bolt material from the outside to the inside was investigated by making micro-hardness measurements. As seen in Figure 5, it was observed that there was no microhardness difference between the outer surface and the inner part of the bolt, the hardness results preserved the trend and mean value is about 320 HV.

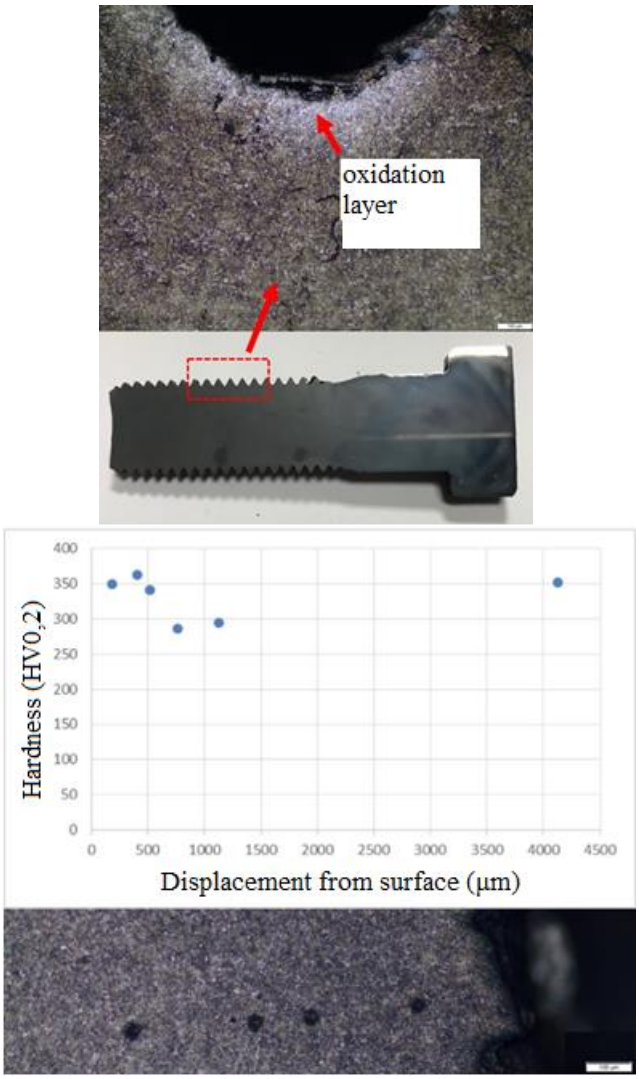

Figure 5. Oxidation layer on the bolt outer layer and hardness.

According to the tensile tests seen in Figure 6, it has been understood that the St3Sx structural steel, which forms the structure, meets the yield and tensile stresses and % elongation at break values determined in the standards. Accordingly, despite the 36-year service period, there was no decrease in

strength in the samples taken. For this reason, it has been understood that all profile drawing specimens comply with the design standards [13].

It was understood that coal dust accumulated in the lower segment had no effect on the steel, since no strength reduction was observed in the samples coded A1-A2 and A3 taken from the lower segment.

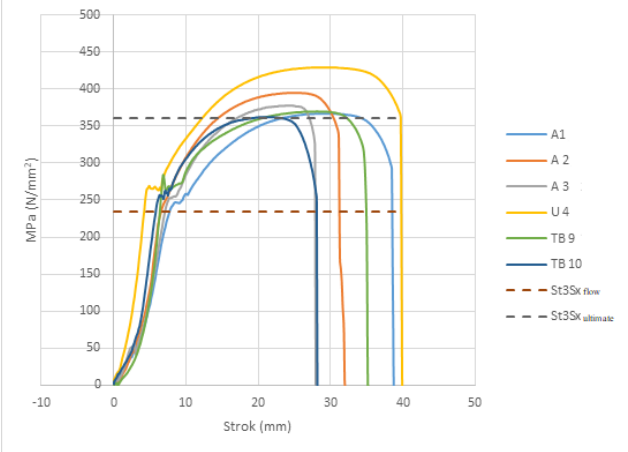

Figure 6. Tensile test results of steel samples

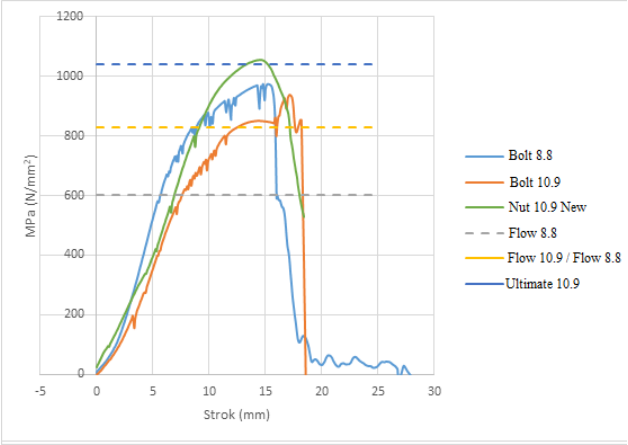

Figure 7. Tensile test results of bolt and nut.

In the tensile tests performed on the bolts, the tensile damage area in the 8.8 class bolt is in the bolt thread region as expected (Figure 7 and Figure 8). This bolt met the tensile strength with yielding [13]. In the tensile tests performed with two different bolts of 10.9 class, the damage is in the region of the nut threads (Figure 9). According to yield and tensile strength, 10.9 bolt-nut connection could not meet the standard values [14]. According to ISO 898-1 and 898-2 standards, the yield limit of the nut material is expected to be higher than the bolt material under all conditions, and it is known that the damage should be on the bolt instead of the nut.

Accordingly, a nut whose class is known with certainty was obtained and a 10.9 class bolt was subjected to a tensile test again (Figure 9). The 10.9 quality bolt taken on the gallery and the newly supplied 10.9 class nut were pulled together and this time no damage was observed on the nut. It has been observed that the connection (bolt - nut) has the strength values specified in the standard.

Figure 8. Bolt damage of 10.9 class.

Figure 9. Nut damage of 10.9 class.

Accordingly, a nut whose quality class is known with certainty was obtained and the 10.9 quality bolt was subjected to the pull test again (Figure 10). The 10.9 quality bolt taken on the gallery and the newly supplied 10.9 quality nut were pulled together and this time no damage was observed on the nut. It has been observed that the connection (bolt - nut) has the strength values specified in the standard.

Figure 10. 10.9 Bolt and Nut match.

According to the tensile test results, since both quality bolts are in M20 dimensions, it is thought that an 8.8 quality nut was attached to the 10.9 quality bolt that should be used in the lower segment. According to the video records, in the area that is thought to be the first broken gallery, parts of the damage type observed in the tensile tests were found in the 10.9 bolt-nut pair used as the fastener at the lower segment joint (Figure 11).

Figure 11. Nut stripped of its threads in damaged gallery lower segment.

In order to determine the cause of unexpected damage to the nut threads, the damaged nut, the undamaged 10.9 quality nut removed from the gallery, and the newly supplied unused 10.9 quality nut thread regions, the microstructure of the completely stripped nut was coarse-grained and 170 HV hardness, as can be seen in Figure 12 (a). It has been determined that (b) sample is finer grained and has a hardness of 220 HV, and sample (c) has a "Martensitic Needle-like" structure and has a hardness of 300 HV. According to both hardness and microstructure images, some nuts used in the gallery should be 10.9 quality, but it strengthens the thesis that they are manufactured from 8.8 quality nuts.

As detailed, structural steel strength level was detected that, these steel components are still in their service life. The corrosion effects are located only the outer surface and no evidence is detected in main core. However, the welding seams of steel joints contain heavy corrosion cracks and corrosion effect reach the interior side. But the good part of this situation is, the welded joints were not subjected to loading.

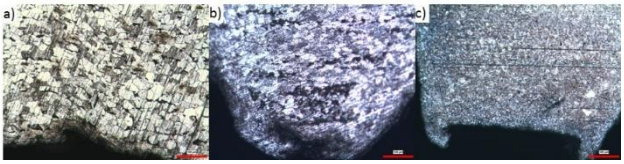

Figure 12. Microstructures of a damaged tensile tested nut (a), an undamaged grade 10.9 nut (b) remove from the gallery, and a newly supplied unused grade 10.9 nut (c).

Additionally, the corrosive effects of coal on the structural steel have been studied and detected that, the corrosion rate rises after %55 moisture [16]. The coal carried on related conveyor has a % 27 moisture. This is another reason why the corrosion effect remains on the steel surface. Similar surface corrosion effects were detected in bolts and nuts. The bolt strength was also detected in both the 8.8 and 10.9 class. But, due to disastrous mistake, the 8.8 nuts were attached to the 10.9 bolts.

Even if the designed safety factor for bolts is over 2.0, during the service life of thirty years, the vibration and dynamic loads could be responsible for the loosening. For that reason, the stress per bolt especially on the lover side has been increased and reach the critical level. During the inspections of collapsed construction, it is expected that the lover side of conveyor bridge was completely closed, and any manholes were not designed. This design insufficiency prevents the periodic control of bolt torques. Additionally, during the inspection of collapsed construction, the lover side of the conveyor bridge has a gap of 6 x 0.5 meter. Over the thirty years of service life, the coal dust takes place in this gap and keeps water in it (as seen in Figure 1). The coal dust accumulation reaches nearly half of the gallery and creates 116.000 kg additional load. This additional load is nearly one fourth of death weight of construction because bulk density of coal dust heavier than the coal grains that carried.

The structural steel and bolts can both provide fatigue-free service life. Unfortunately, the improper assembly and design insufficiency combination can cause as dramatic collapses and death of workers.

4. Conclusion and Suggestions

According to the design parameters, structural steels can provide fatigue-free service for many years.

If the coal moisture remains below 50%, the corrosion effect on structural steel is only superficial. Corrosion effect of 36 years old coal dust is only superficial in 8.8 and 10.9 class bolt-nut pairs.

The manholes are the design criteria that should not be forgotten and must be used for periodic control. The bolt pre-tension and torque level must be checked and prevented to loosen.

The gaps that will cause material accumulation must be checked. It should be noted that the material filled into the gaps will be in dust form and the bulk density will be heavier.

Incorrect assembly and unpredictable loads can cause catastrophe. For this, a risk assessment should be made.

Statement of Research and Publication Ethics

The study is complied with research and publication ethics

References

[1] T. Żur, Belt conveyors in mining, Śląsk Publishers, Katowice, 1979

[2] Miriam A., Anna G., Daniela M., "Measurement and simulation of impact wear damage to industrial conveyor belts", *Wear* 2016 368, 400 - 407.

[3] V.V. Poovakaud, C. J. Peña, R. Talemi, S. Coppieters, D. Debruyne, "Assessment of fretting fatigue in high strength steel bolted connections with simplified Fe modelling techniques", *Tribology International*, 143, 2020.

[4] M. Sundar, S. Thirumalai Kumaran, Rendi Kurniawan, Farooq Ahmed, "Investigating the corrosion behaviour of conveyor chain pin and link", *Materials Today: Proceedings*, 50, pp. 855-860 2022.

[5] W. Bochnowski, Ł. Szyller, M. Osetek, "Damage characterization of belt conveyor made of the 330Nb alloy after service in a carburizing atmosphere in a continuous heat treatment furnace", *Engineering Failure Analysis*, 103, pp.173-183, 2019.

[6] M.A. Khattak, S. Zaman, S. Kazi, H. Ahmed, H.M. Habib, H.M. Ali, M.N. Tamin, "Failure investigation of welded 430 stainless steel plates for conveyor belts", *Engineering Failure Analysis*, 116, 2020.

[7] D. R. H. Jones, "Fatigue failures of welded conveyor drums", *Engineering Failure Analysis*, 12, pp. 59-69, 1995.

[8] BS Dhillon mining equipment reliability Springer 2008 p57

[9] S. Dunn, "Optimizing production scheduling for maximum plant utilization and minimum downtime: the reliability revolution". Presented at the Dollar Driven Mining Conference, Perth, Australia, July 1997.

[10] The Basics of Conveyor Maintenance, [Online] Available: https://limblecmms.com/blog/conveyor-maintenance-plan/ [Accessed: Oct. 27, 2022]

[11] TS 3964 ISO 5048, Sürekli mekanik taşıma donanımları – taşıyıcı makaralı bant konveyörler - çalışma gücünün ve çekme kuvvetlerinin hesaplanması, TSE, 2004.

[12] C. Wegst, M. Wegst, Stahlschlussel, Verlag Stahlschlussel Wegst GmbH, 2004

[13] Mine Planning and Equipment Selection 2004: Proceedings of the Thirteenth International Symposium on Mine Planning and Equipment Selection, Wroclaw, Poland, 1-3 September 2004, 484

[14] ISO 898-1 / 898-2 Gr.8.8, Properties of Grade 8.8 Bolts and Nut, ISO, 2009.

[15] ISO 898-1 / 898-2 Gr.10.9, Properties of Grade 10.9 Bolts and Nut, ISO, 2009.

[16] C.P. Gardiner, R.E. Melchers, "Corrosion of mild steel by coal and iron ore", *Corrosion Science* 44 pp. 2665–2673, 2002.

Bitlis Eren Üniversitesi Fen Bilimleri Dergisi
BİTLİS EREN UNIVERSITY JOURNAL OF SCIENCE
ISSN: 2147-3129/e-ISSN: 2147-3188
VOLUME: 11 NO: 4 PAGE: 1152-1158 YEAR: 2022
DOI:10.17798/bitlisfen.1196754

On Certain Properties of Bipolar Fuzzy Supra Preopen Sets

Banu PAZAR VAROL[1*]

[1]*Department of Mathematics, Faculty of Arts and Science, Kocaeli University, Kocaeli-TURKIYE (ORCID: 0000-0002-8627-7910)*

Keywords: Bipolar valued fuzzy set, BF supra topology, BF supra preopen set, BF supra pre-continuous mapping.

Abstract
The goal of this paper is to investigate the certain properties of bipolar fuzzy supra preopen sets (BF supra preopen set). We introduce and study the concepts of bipolar fuzzy supra pre-interior (BF supra pre-interior) and bipolar fuzzy supra pre-closure (BF supra pre-closure) operators. Furthermore, we define new type of bipolar fuzzy supra continuous mapping based on the BF preopen sets.
.

1. Introduction

Fuzzy set theory was introduced by Zadeh [1] in 1965 and it has been developed by many researchers. This theory is one of the most efficient decision methods providing the ability to deal with uncertainty. Several papers are published with various fuzzy set applications in the fields of pure and applied mathematics and also several kinds of fuzzy set extensions were defined such as intuitionistic fuzzy sets [2], interval-valued fuzzy sets [3], vague sets [4], etc. Bipolar-valued fuzzy set [5] is another an extension of fuzzy set and its membership degree range is different from the above sets. Membership degree range is [-1, 1] for bipolar valued fuzzy set. Lee [6] initiated an extension of fuzzy set named bipolar fuzzy set in 2000. In recent years a series of works was published related to bipolar fuzzy sets. Anitha et. al. [7] investigated the notion of bipolar valued fuzzy subgroup. Pazar Varol [8] defined bipolar fuzzy submodule and studied some certain properties. Azhagappan and Kamaraj [9] introduced the concept of bipolar fuzzy topology. Kim et. al. [10] introduced bipolar fuzzy points and examined the topological structures of bipolar fuzzy set, such as neighborhood, continuity, base, subbase.

Supra topology was defined by dropping a finite intersection condition of topological spaces by Mashhour et al. [11] in 1983. Although supra topological space is the weaker type of classical topological space, supra topology can be more convenient to solve some practical problems. The fuzzy supra topology were introduced by El Monsef and Ramadan [12]. They also investigated fuzzy supra continuous mappings and obtained some basic characterizations. Using the notion of intuitionistic fuzzy sets, Turanlı [13] defined intuitionistic fuzzy supra topology in 2003. Malkoç and Pazar Varol [14] discussed BF supra topological spaces as a generalization of supra topologies to bipolar fuzzy topologies.

The concept of preopen sets in topological spaces was defined by Mashhour et. al. [15] in 1982. Then, the concept of fuzzy preopen sets in fuzzy topological spaces was given by Singal et.al. [16] in 1991. Sayed [17] defined supra preopen set in 2010 and fuzzy version of this concept was studied by Srikirutika et. al. [18] as “fuzzy supra preopen sets” in 2018.

In this work, we introduce and investigate bipolar fuzzy supra preopen sets using bipolar fuzzy supra open sets. Then, we define new type of bipolar continuous mapping based on the bipolar fuzzy preopen sets.

*Corresponding author: banupazar@kocaeli.edu.tr
Received: 31.10.2022, Accepted:19.12.2022

2. Preliminaries

We recall the following definitions and results which will be needed in this work.

Definition 2.1: [19] Let $U \neq \emptyset$ be universal set. $\mathcal{Q} = \{< v, \mu_{\mathcal{Q}}^{+}(v), \mu_{\mathcal{Q}}^{-}(v) >: v \in U\}$ denotes a bipolar fuzzy set (BF set) in U where $\mu_{\mathcal{Q}}^{+}: U \longrightarrow [0,1]$ and $\mu_{\mathcal{Q}}^{-}: U \longrightarrow [-1,0]$ are two mappings. Here, $\mu_{\mathcal{Q}}^{+}(v)$ denotes the positive memberships ranges over [0,1] and $\mu_{\mathcal{Q}}^{-}(v)$ denotes the negative memberships ranges over $[-1,0]$.

We will use the notation $BPF(U)$ for the family of all bipolar fuzzy set in U.
For each bipolar fuzzy set $\boldsymbol{\mathcal{Q}}$ and $\boldsymbol{v} \in \boldsymbol{U}$, if $\boldsymbol{0} \leq \boldsymbol{\mu_{\mathcal{Q}}^{+}(v)} - \boldsymbol{\mu_{\mathcal{Q}}^{-}(v)} \leq \boldsymbol{1}$ then $\boldsymbol{\mathcal{Q}}$ is an intuitionistic fuzzy set [2]. $\boldsymbol{\mu_{\mathcal{Q}}^{+}(v)}$ (resp. $\boldsymbol{\mu_{\mathcal{Q}}^{-}(v)}$) denotes the membership degree (resp. non-membership degree) of $\boldsymbol{v} \in \boldsymbol{U}$.

Example 2.2: $\boldsymbol{\mathcal{Q}} = \{< \boldsymbol{a}, \boldsymbol{0.5}, \boldsymbol{-0.3} >, < \boldsymbol{b}, \boldsymbol{0.7}, \boldsymbol{-0.2} >, < \boldsymbol{c}, \boldsymbol{0.4}, \boldsymbol{-0.4} >\}$ is a BF set in $\boldsymbol{U} = \{\boldsymbol{a}, \boldsymbol{b}, \boldsymbol{c}\}$.

Definition 2.3: [9] 1. $\mathcal{Q} \in BPF(U)$ is called universal BF set if $\mu_{\mathcal{Q}}^{+}(v) = 1_{BP}^{+}(v) = 1$ and $\mu_{\mathcal{Q}}^{-}(v) = 1_{BP}^{-}(v) = -1$, for each $v \in U$ and we write $1_{BP} = (1_{BP}^{+}, 1_{BP}^{-})$.
2. $\mathcal{Q} \in BPF(U)$ is called empty BF set if $\mu_{\mathcal{Q}}^{+}(v) = 0_{BP}^{+}(v) = 0_{BP} = 0_{BP}^{-}(v) = \mu_{\mathcal{Q}}^{-}(v)$, for each $v \in U$ and we write $0_{BP} = (0_{BP}^{+}, 0_{BP}^{-})$.

Definition 2.4: [19] Let $\mathcal{Q}, \mathcal{R} \in BPF(U)$. Then;
1. $\mathcal{Q} \subseteq \mathcal{R} \iff \mu_{\mathcal{Q}}^{+}(v) \leq \mu_{\mathcal{R}}^{+}(v)$ and $\mu_{\mathcal{Q}}^{-}(v) \geq \mu_{\mathcal{R}}^{-}(v)$, $\forall\, v \in U$.
2. $\mathcal{Q} = \mathcal{R} \iff \mu_{\mathcal{Q}}^{+}(v) = \mu_{\mathcal{R}}^{+}(v)$ and $\mu_{\mathcal{Q}}^{-}(v) = \mu_{\mathcal{R}}^{-}(v)$, $\forall\, v \in U$.
3. The complement of $\mathcal{Q}$ is defined by, $\mathcal{Q}^{c} = \{< v, 1 - \mu_{\mathcal{Q}}^{+}(v), -1 - \mu_{\mathcal{Q}}^{-}(v) >: v \in U\}$.
4. $\mathcal{Q} \cap \mathcal{R} = \{< v, \mu_{\mathcal{Q}\cap\mathcal{R}}^{+}(v), \mu_{\mathcal{Q}\cap\mathcal{R}}^{-}(v) >: v \in U\}$, where $\mu_{\mathcal{Q}\cap\mathcal{R}}^{+}(v) = \min\{\mu_{\mathcal{Q}}^{+}(v), \mu_{\mathcal{R}}^{+}(v)\}$ and $\mu_{\mathcal{Q}\cap Y}^{-}(v) = \max\{\mu_{\mathcal{Q}}^{-}(v), \mu_{\mathcal{R}}^{-}(v)\}$.
5. $\mathcal{Q} \cup Y = \{< v, \mu_{\mathcal{Q}\cup\mathcal{R}}^{+}(v), \mu_{\mathcal{Q}\cup\mathcal{R}}^{-}(v) >: v \in U\}$, where $\mu_{\mathcal{Q}\cup\mathcal{R}}^{+}(v) = \max\{\mu_{\mathcal{Q}}^{+}(v), \mu_{\mathcal{R}}^{+}(v)\}$ and $\mu_{\mathcal{Q}\cup Y}^{-}(v) = \min\{\mu_{\mathcal{Q}}^{-}(v), \mu_{\mathcal{R}}^{-}(v)\}$.

Proposition 2.5: [10] Let $\mathcal{Q}, \mathcal{R}, \mathcal{Z} \in BPF(U)$. Then the following statements are satisfied:
1. $\mathcal{Q} \cup \mathcal{Q} = \mathcal{Q}$ and $\mathcal{Q} \cap \mathcal{Q} = \mathcal{Q}$.
2. $\mathcal{Q} \cup \mathcal{R} = \mathcal{Q} \cup \mathcal{R}$ and $\mathcal{Q} \cap \mathcal{R} = \mathcal{R} \cap \mathcal{Q}$.
3. $\mathcal{Q} \cup (\mathcal{R} \cup \mathcal{Z}) = (\mathcal{Q} \cup \mathcal{R}) \cup \mathcal{Z}$ and $\mathcal{Q} \cap (\mathcal{R} \cap \mathcal{Z}) = (\mathcal{Q} \cap \mathcal{R}) \cap \mathcal{Z}$.
4. $\mathcal{Q} \cup (\mathcal{R} \cap \mathcal{Z}) = (\mathcal{Q} \cup \mathcal{R}) \cap (\mathcal{Q} \cup \mathcal{Z})$ and $\mathcal{Q} \cap (\mathcal{R} \cup \mathcal{Z}) = (\mathcal{Q} \cap \mathcal{R}) \cup (\mathcal{Q} \cap \mathcal{Z})$.
5. $\mathcal{Q} \cup (\mathcal{Q} \cap \mathcal{R}) = \mathcal{Q}$ and $\mathcal{Q} \cap (\mathcal{Q} \cup \mathcal{R}) = \mathcal{Q}$.
6. $\mathcal{Q} \cap \mathcal{R} \subset \mathcal{Q}$ and $\mathcal{Q} \cap \mathcal{R} \subset \mathcal{R}$.
7. $\mathcal{Q} \subset \mathcal{Q} \cup \mathcal{R}$ and $Y \subset \mathcal{Q} \cup \mathcal{R}$.
8. $(\mathcal{Q}^{c})^{c} = \mathcal{Q}$.
9. $(\mathcal{Q} \cup \mathcal{R})^{c} = \mathcal{Q}^{c} \cap \mathcal{R}^{c}$ and $(\mathcal{Q} \cap \mathcal{R})^{c} = \mathcal{Q}^{c} \cup \mathcal{R}^{c}$.
10. If $\mathcal{Q} \subset \mathcal{R}$ and $\mathcal{R} \subset \mathcal{Z}$, then $\mathcal{Q} \subset \mathcal{Z}$.
11. If $\mathcal{Q} \subset \mathcal{R}$, then $\mathcal{Q} \cap \mathcal{Z} \subset \mathcal{R} \cap \mathcal{Z}$ and $\mathcal{Q} \cup \mathcal{Z} \subset \mathcal{R} \cup \mathcal{Z}$.

Definition 2.6: [19] Let $U \neq \emptyset$ and $(\mathcal{Q}_j)_{j\in J} \subset BPF(U)$.
1. The intersection of $(\mathcal{Q}_j)_{j\in J}$, represented by $\bigcap_{j\in J} \mathcal{Q}_j$, and defined as $\left(\bigcap_{j\in J} \mathcal{Q}_j\right)(v) = \left(\bigwedge_{j\in J} \mu_{\mathcal{Q}_j}^{+}(v), \bigvee_{j\in J} \mu_{\mathcal{Q}_j}^{-}(v)\right)$, $\forall v \in U$.
2. The union of $(\mathcal{Q}_j)_{j\in J}$, represented by $\bigcup_{j\in J} \mathcal{Q}_j$ and defined as $\left(\bigcup_{j\in J} \mathcal{Q}_j\right)(v) = \left(\bigvee_{j\in J} \mu_{\mathcal{Q}_j}^{+}(v), \bigwedge_{j\in J} \mu_{\mathcal{Q}_j}^{-}(v)\right)$, $\forall v \in U$.

Definition 2.7: [10] Let $\varphi: U_1 \longrightarrow U_2$ be a mapping and $\mathcal{Q} \in BPF(U_1)$, $\mathcal{R} \in BPF(U_2)$.
1. The image of $\mathcal{Q}$ under φ is represented by $\varphi(\mathcal{Q})(w) = \left(\mu_{\varphi(\mathcal{Q})}^{+}(w), \mu_{\varphi(\mathcal{Q})}^{-}(w)\right) = \left(\varphi(\mu_{\mathcal{Q}}^{+})(w), \varphi(\mu_{\mathcal{Q}}^{-})(w)\right)$, and it is a bipolar fuzzy set in U_2 defined as

$$\varphi(\mu_{\mathcal{Q}}^{+})(w) = \begin{cases} \bigvee \mu_{\mathcal{Q}}^{+}(v), & v \in \varphi^{-1}(w), \\ 0, & other \end{cases}$$

$$\varphi(\mu_{\mathcal{Q}}^{-})(w) = \begin{cases} \bigwedge \mu_{\mathcal{Q}}^{-}(v), & v \in \varphi^{-1}(w), \\ 0, & other \end{cases}, \quad \forall\, w \in U_2.$$

2. The preimage of $\mathcal{R}$ under φ is represented by $\varphi^{-1}(\mathcal{R}) = (\varphi^{-1}(\mu_{\mathcal{R}}^{+}), \varphi^{-1}(\mu_{\mathcal{R}}^{-}))$, is a bipolar fuzzy set in U_1 defined by $[\varphi^{-1}(\mu_{\mathcal{R}}^{+})](v) = \mu_{\mathcal{R}}^{+} \circ \varphi(v)$ and $[\varphi^{-1}(\mu_{\mathcal{R}}^{-})](v) = \mu_{\mathcal{R}}^{-} \circ \varphi(v)$, $\forall\, v \in U_1$.

Corollary 2.8: [10] Let $\varphi: U_1 \longrightarrow U_2$ be a mapping and $\mathcal{Q}, \mathcal{Q}_1, \mathcal{Q}_2 \in BPF(U_1)$, $(\mathcal{Q}_j)_{j\in J} \subset BPF(U_1)$, $\mathcal{R}$, $\mathcal{R}_1, \mathcal{R}_2 \in BPF(U_2)$ and $(\mathcal{R}_j)_{j\in J} \subset BPF(U_2)$. Then the followings are satisfied;
1. If $\mathcal{Q}_1 \subset \mathcal{Q}_2$, then $\varphi(\mathcal{Q}_1) \subset \varphi(\mathcal{Q}_2)$,

2. $\varphi(\mathcal{Q}_1 \cup \mathcal{Q}_2) = \varphi(\mathcal{Q}_1) \cup \varphi(\mathcal{Q}_2)$, $\varphi\left(\bigcup_{j\in J} \mathcal{Q}_j\right) = \bigcup_{j\in J} \varphi\left(\mathcal{Q}_j\right)$,
3. $\varphi(\mathcal{Q}_1 \cap \mathcal{Q}_2) \subset \varphi(\mathcal{Q}_1) \cap \varphi(\mathcal{Q}_2)$, $\varphi\left(\bigcap_{j\in J} \mathcal{Q}_j\right) \subset \bigcap_{j\in J} \varphi\left(\mathcal{Q}_j\right)$,
4. If φ is 1-1, then $\varphi(\mathcal{Q}_1 \cap \mathcal{Q}_2) = \varphi(\mathcal{Q}_1) \cap \varphi(\mathcal{Q}_2)$, $\varphi\left(\bigcap_{j\in J} \mathcal{Q}_j\right) = \bigcap_{j\in J} \varphi\left(\mathcal{Q}_j\right)$,
5. If $\mathcal{R}_1 \subset \mathcal{R}_2$, then $\varphi^{-1}(\mathcal{R}_1) \subset \varphi^{-1}(\mathcal{R}_2)$,
6. $\varphi(\mathcal{Q}) = 0_{\mathrm{BP}} \Leftrightarrow \mathcal{Q} = 0_{\mathrm{BP}}$,
7. $\varphi^{-1}(\mathcal{R}_1 \cup \mathcal{R}_2) = \varphi^{-1}(\mathcal{R}_1) \cup \varphi^{-1}(\mathcal{R}_2)$, $\varphi^{-1}\left(\bigcup_{j\in J} \mathcal{R}_j\right) = \bigcup_{j\in J} \varphi^{-1}\left(\mathcal{R}_j\right)$,
8. $\varphi^{-1}(\mathcal{R}_1 \cap \mathcal{R}_2) = \varphi^{-1}(\mathcal{R}_1) \cap \varphi^{-1}(\mathcal{R}_2)$, $\varphi^{-1}\left(\bigcap_{j\in J} \mathcal{R}_j\right) = \bigcap_{j\in J} \varphi^{-1}\left(\mathcal{R}_j\right)$,
9. $\varphi^{-1}(\mathcal{R}) = 0_{BP} \Leftrightarrow \mathcal{R} \cap \varphi(1_{BP}) = 0_{BP}$,
10. $\mathcal{Q} \subset (\varphi^{-1} o \varphi)(\mathcal{Q})$, in particular $\mathcal{Q} = (\varphi^{-1} o \varphi)(\mathcal{Q})$ if φ is injective,
11. $(\varphi o \varphi^{-1})(\mathcal{R}) \subset \mathcal{R}$, in particular $\mathcal{R} = (\varphi o \varphi^{-1})(\mathcal{R})$ if φ is surjective,
12. $\varphi^{-1}(\mathcal{R}^c) = \left(\varphi^{-1}(\mathcal{R})\right)^c$.

Definition 2.9: [9] Let $U \neq \emptyset$ and $\tau \subset BPF(U)$. Then τ is called a BF topology on U if it satisfies the followings;
(BFT1) $0_{BP}, 1_{BP} \in \tau$.
(BFT2) $\mathcal{Q} \cap \mathcal{R} \in \tau$, for $\mathcal{Q}, \mathcal{R} \in \tau$.
(BFT3) $\left(\bigcup_{j\in J} \mathcal{Q}_j\right) \in \tau$ for every $\left(\mathcal{Q}_j\right)_{j\in J} \subset \tau$.

(U,τ) is named to be BF topological space and members of τ are called to be BF open sets. $\mathcal{Q} \in BPF(U)$ is called BF closed sets in (U,τ), if $\mathcal{Q}^c$ is BF open set.

Definition 2.10: [14] Let $U \neq \emptyset$ and $\tau \subset BPF(U)$. Then τ is called a BF supra topology on U if it satisfies the followings;
(BFST1) $0_{BP}, 1_{BP} \in \tau$.
(BFST2) $\left(\bigcup_{j\in J} \mathcal{Q}_j\right) \in \tau$ for every $\left(\mathcal{Q}_j\right)_{j\in J} \subset \tau$.

(U,τ) is named to be BF supra topological space and members of τ are called BF supra open sets. $\mathcal{Q} \in BPF(U)$ is called BF supra closed sets in (U,τ), if $\mathcal{Q}^c$ is BF supra open set. We denote the family of all bipolar fuzzy supra topologies on U as $BPFST(U)$.

Let τ^* be a BF topology and τ be a BF supra topology on U. Then, τ^* is named to be associated BF topology with the τ if and only if $\tau^* \subset \tau$.

Examples 2.11: [14]. Let $\tau \in BPFST(U)$. Then, the families $\tau^+ = \left\{\mu_{\mathcal{Q}}^+ \in I^U \mid \mathcal{Q} \in \tau\right\}$ and $\tau^- = \left\{-\mu_{\mathcal{Q}}^- \in I^U \mid \mathcal{Q} \in \tau\right\}$ are two fuzzy supra topologies in the sense of [12].

Theorem 2.12: [14] Let (U,τ) be a BF supra topological space and $\mathcal{K}$ be the family of all BF supra closed sets in U. Then the followings are true;
i. $0_{BP}, 1_{BP} \in \mathcal{K}$.
ii. $(\bigcap_{i\in J} \mathcal{Q}_i) \in \mathcal{K}$ for every $(\mathcal{Q}_i)_{j\in J} \subset \mathcal{K}$.

Definition 2.13: [14] Let $\tau \in BPFST(U)$ and $\mathcal{Q} \in BPF(U)$. Then;
i. Bipolar fuzzy supra interior of $\mathcal{Q}$, denoted by $int_\tau(\mathcal{Q})$, is defined as
$$int_\tau(\mathcal{Q}) = \bigcup\{O : O \subseteq \mathcal{Q} \text{ and } O \in \tau\}.$$
ii. Bipolar fuzzy supra closure of $\mathcal{Q}$, denoted by $cl_\tau(\mathcal{Q})$, is defined as
$$cl_\tau(\mathcal{Q}) = \bigcap\{K : \mathcal{Q} \subseteq K \text{ and } K^c \in \tau\}.$$
(1) The BF supra closure of $\mathcal{Q}$ is the smallest BF supra closed set containing $\mathcal{Q}$.
(2) The BF supra interior of $\mathcal{Q}$ is the largest BF supra open set contained in $\mathcal{Q}$.
(3) Let (U,τ) be an associated BF supra topological space with the BF topological space (U,τ^*) and $\mathcal{Q} \in BPF(U)$. Then $int_{\tau^*}(\mathcal{Q}) \subseteq int_\tau(\mathcal{Q}) \subseteq \mathcal{Q} \subseteq cl_\tau(\mathcal{Q}) \subseteq cl_{\tau^*}(\mathcal{Q})$.

Theorem 2.14: [14] Let $\mathcal{Q}, \mathcal{R} \in BPF(U)$ and $\tau \in BPFST(U)$. Following statements are true;
1. $\mathcal{Q}$ is a BF supra open (closed) set $\Leftrightarrow \mathcal{Q} = int_\tau(\mathcal{Q})$ $(\mathcal{Q} = cl_\tau(\mathcal{Q}))$
2. If $\mathcal{Q} \subseteq \mathcal{R}$, then $int_\tau(\mathcal{Q}) \subseteq int_\tau(\mathcal{R})$ and $cl_\tau(\mathcal{Q}) \subseteq cl_\tau(\mathcal{R})$.
3. $cl_\tau(\mathcal{Q}) \cup cl_\tau(\mathcal{R}) \subseteq cl_\tau(\mathcal{Q} \cup \mathcal{R})$.
4. $int_\tau(\mathcal{Q}) \cup int_\tau(\mathcal{R}) \subseteq int_\tau(\mathcal{Q} \cup \mathcal{R})$.
5. $int_\tau(\mathcal{Q} \cap \mathcal{R}) \subseteq int_\tau(\mathcal{Q}) \cap int_\tau(\mathcal{R})$.
6. $cl_\tau(\mathcal{Q} \cap \mathcal{R}) \subseteq cl_\tau(\mathcal{Q}) \cap cl_\tau(\mathcal{R})$.
7. $int_\tau(1_{BP} - \mathcal{Q}) = 1_{BP} - cl_\tau(\mathcal{Q})$.
8. $cl_\tau(1_{BP}) = 1_{BP} = int_\tau(1_{BP})$ and $cl_\tau(0_{BP}) = 0_{BP} = int_\tau(0_{BP})$.
9. $int_\tau\left(int_\tau(\mathcal{Q})\right) = int_\tau(\mathcal{Q})$, $cl_\tau\left(cl_\tau(\mathcal{Q})\right) = cl_\tau(\mathcal{Q})$.

Definition 2.15: [14] Let $\tau \in BPFST(U_1)$, $\sigma \in BPFST(U_2)$ and $\varphi: (U_1,\tau) \longrightarrow (U_2,\sigma)$ be a mapping. Then, φ is called a BF supra continuous mapping if $\varphi^{-1}(\mathcal{Q}) \in \tau$ for every $\mathcal{Q} \in \sigma$.

3. Bipolar Fuzzy Supra Preopen Sets

In this chapter, we initiate and study a new type of supra open sets named to be bipolar fuzzy supra preopen sets.

Definition 3.1: Let $\tau \in BPFST(U)$. A BF set $\mathcal{Q}$ is called
(i) a bipolar fuzzy supra preopen set (BF supra preopen set) if $\mathcal{Q} \subseteq int_\tau(cl_\tau(\mathcal{Q}))$.

(ii) a bipolar fuzzy supra preclosed set (BF supra preclosed set) if $cl_\tau(int_\tau(\mathcal{Q})) \subseteq \mathcal{Q}$.
It is obvious that the complement of a bipolar fuzzy supra preopen set is a bipolar fuzzy supra preclosed set.

Definition 3.2: Let $\tau \in BPFST(U)$. A BF set $\mathcal{Q}$ is called
(i) a bipolar fuzzy supra α−open set if $\mathcal{Q} \subseteq int_\tau(cl_\tau(int_\tau(\mathcal{Q})))$.
(ii) a bipolar fuzzy supra b−open set if $\mathcal{Q} \subseteq int_\tau(cl_\tau(\mathcal{Q})) \cup cl_\tau(int_\tau(\mathcal{Q}))$.
(iii) a bipolar fuzzy supra β−open set if $\mathcal{Q} \subseteq cl_\tau(int_\tau(cl_\tau(\mathcal{Q})))$.
(iv) a bipolar fuzzy supra semi-open set if $\mathcal{Q} \subseteq cl_\tau(int_\tau(\mathcal{Q}))$.
(v) a bipolar fuzzy supra R−open set if $int_\tau(cl_\tau(\mathcal{Q})) \neq 0_{BP}$ or $\mathcal{Q} = 0_{BP}$.

The following diagram gives the relations between the bipolar fuzzy open sets. In this work, we only focus on bipolar fuzzy supra pre-open set.

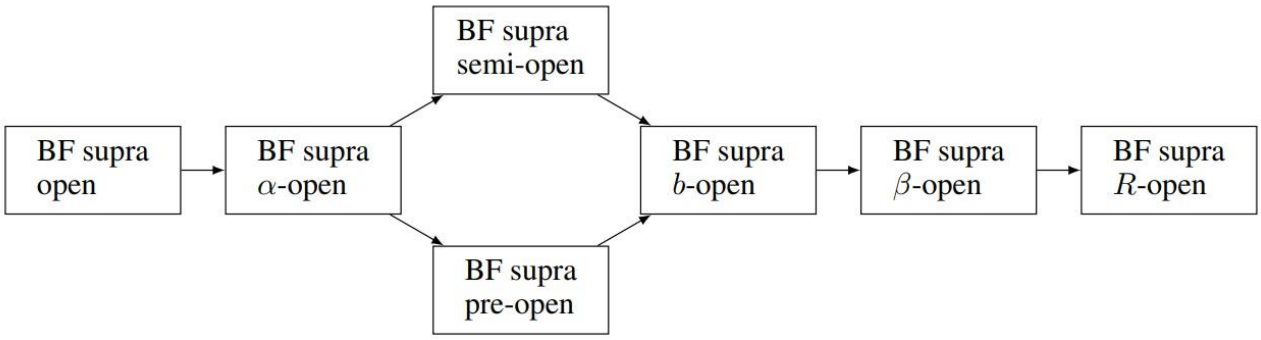

Theorem 3.3: Let $\tau \in BPFST(U)$. If $\mathcal{Q}$ is BF supra open set, then $\mathcal{Q}$ is BF supra preopen set.
Proof: Let $\mathcal{Q} \in \tau$. Then $int_\tau(\mathcal{Q}) = \mathcal{Q}$. Since $\mathcal{Q} \subseteq cl_\tau(\mathcal{Q})$ and properties of BF supra interior, $int_\tau(\mathcal{Q}) \subseteq int_\tau(cl_\tau(\mathcal{Q}))$.
Hence, $\mathcal{Q} \subseteq int_\tau(cl_\tau(\mathcal{Q}))$.

We show that the implication in above theorem is not reversible;

Example 3.4: Let $U = \{u_1, u_2\}$,
$\mathcal{Q} = \{< u_1, 0.5, -0.3 >, < u_2, 0.3, -0.4 >\}$
$\mathcal{R} = \{< u_1, 0.3, -0.6 >, < u_2, 0.6, -0.5 >\}$
$\mathcal{Z} = \{< u_1, 0.5, -0.8 >, < u_2, 0.4, -0.5 >\}$
and $\tau = \{0_{BP}, 1_{BP}, \mathcal{Q}, \mathcal{R}, \mathcal{Q} \cup \mathcal{R}\}$. Then τ is a BF supra topology on U and $\mathcal{Z}$ is a BF supra preopen set (we obtain $int_\tau(cl_\tau(\mathcal{Z})) = 1_{BP}$, so $\mathcal{Z} \subseteq int_\tau(cl_\tau(\mathcal{Z}))$) but not BF supra open set.

Theorem 3.4: Let $\tau \in BPFST(U)$. If $\mathcal{Q}$ is BF supra closed set, then $\mathcal{Q}$ is BF supra preclosed set.
Proof: Let $\mathcal{Q}$ be a BF supra closed set in (U, τ). Then $\mathcal{Q} = cl_\tau(\mathcal{Q})$. Since $int_\tau(\mathcal{Q}) \subseteq \mathcal{Q}$, we get $cl_\tau(int_\tau(\mathcal{Q})) \subseteq cl_\tau(\mathcal{Q}) = \mathcal{Q}$.

Theorem 3.5: Let $\mathcal{Q}$ be a BF set in BF supra topological space (U, τ), then $\mathcal{Q}$ is a BF supra preopen set if and only if $\mathcal{Q}^c$ is a BF supra preclosed set.

Proof: ($\Longrightarrow$) Let $\mathcal{Q}$ be a BF preopen set in U. Then we have $\mathcal{Q} \subseteq int_\tau(cl_\tau(\mathcal{Q}))$.
$\Rightarrow \quad \mathcal{Q}^c \supseteq \left(int_\tau(cl_\tau(X))\right)^c = cl_\tau(cl_\tau(\mathcal{Q})^c) = cl_\tau(int_\tau(\mathcal{Q}^c))$.
$\Rightarrow \mathcal{Q}^c$ is a BF supra preclosed set.
($\Longleftarrow$) Let $\mathcal{Q}^c$ be a BF supra preclosed set. Hence, we have $cl_\tau(int_\tau(\mathcal{Q}^c)) \subseteq \mathcal{Q}^c$.
$\Rightarrow (\mathcal{Q}^c)^c \subseteq \left(cl_\tau(int_\tau(\mathcal{Q}^c))\right)^c$
$\Rightarrow \mathcal{Q} \subseteq int_\tau(int_\tau(\mathcal{Q}^c))^c = int_\tau(cl_\tau(\mathcal{Q}^c)^c)$
$= int_\tau(cl_\tau(\mathcal{Q}))$.
Hence, $\mathcal{Q}$ is a BF preopen set.

Theorem 3.6: Let $\tau \in BPFST(U)$.
(i) If $\{\mathcal{Q}_i : i \in J\}$ is a collection of BF supra preopen sets, then $\cup_{i\in J} \mathcal{Q}_i$ is a BF supra preopen set.
(ii) If $\{\mathcal{R}_i : i \in J\}$ is a collection of BF supra preclosed sets, then $\cap_{i\in J} \mathcal{R}_i$ is a BF supra preclosed set.
Proof: (i) Let $\{\mathcal{Q}_i : i \in J\}$ be a collection of BF supra preopen sets.
Then for each $i \in J$, $\mathcal{Q}_i \subseteq int_\tau(cl_\tau(\mathcal{Q}_i))$.
$\Rightarrow \quad \cup_{i\in J} \mathcal{Q}_i \subseteq \cup_{i\in J} int_\tau(cl_\tau(\mathcal{Q}_i)) \subseteq int_\tau(\cup_{i\in J} cl_\tau(\mathcal{Q}_i)) \subseteq int_\tau(cl_\tau(\cup_{i\in J}\mathcal{Q}_i))$.
(ii) By (i), we get $\cup_{i\in J} \mathcal{Q}_i \subseteq int_\tau(cl_\tau(\cup_{i\in J}\mathcal{Q}_i))$.
$\Rightarrow \left(\cup_{i\in J} \mathcal{Q}_i\right)^c \supseteq \left(int_\tau\left(cl_\tau(\cup_{i\in J}\mathcal{Q}_i)\right)\right)^c$.

$\Rightarrow \quad \cap_{i\in J}(\mathcal{Q}_i)^c \quad \supseteq cl_\tau\left(\left(cl_\tau(\cup_{i\in J}\mathcal{Q}_i)\right)^c\right) = cl_\tau\left(int_\tau\left(\cap_{i\in J}\mathcal{Q}_i^c\right)\right)$.

Definition 3.7: Let $\tau \in BPFST(U)$ and $\mathcal{Q} \in BPF(U)$.
(i) The bipolar fuzzy supra preinterior of a bipolar fuzzy set $\mathcal{Q}$ is defined by
$pint_\tau(\mathcal{Q}) = \cup\{\ \mathcal{O} :\ \mathcal{O} \subseteq \mathcal{Q}$ and $\mathcal{O}$ is a bipolar fuzzy supra preopen set in $U\}$.
(ii) The bipolar fuzzy supra preclosure of a bipolar fuzzy set $\mathcal{Q}$ is defined by
$pcl_\tau(\mathcal{Q}) = \cap\{\ \mathcal{K}: \mathcal{Q} \subseteq \mathcal{K}$ and $\mathcal{K}$ is a bipolar fuzzy supra preclosed set in $U\}$.

Remark 3.8: We see that $pint_\tau(\mathcal{Q})$ is a BF supra preopen set and $pcl_\tau(\mathcal{Q})$ is a BF supra preclosed set.

Theorem 3.9: Let $\mathcal{Q}$ be a BF set in (U,τ).
(i) $pint_\tau(\mathcal{Q}) \subseteq \mathcal{Q}$ and $pint_\tau(\mathcal{Q}) = \mathcal{Q}$ if and only if $\mathcal{Q}$ is a BF supra preopen set.
(ii) $\mathcal{Q} \subseteq pcl_\tau(\mathcal{Q})$ and $\mathcal{Q} = pcl_\tau(\mathcal{Q})$ if and only if $\mathcal{Q}$ is a BF supra preclosed set.
(iii) $(pint_\tau(\mathcal{Q}))^c = pcl_\tau(\mathcal{Q}^c)$.
(iv) $(pcl_\tau(\mathcal{Q}))^c = pint_\tau(\mathcal{Q}^c)$.
Proof: Straightforward.

Theorem 3.10: Let $\mathcal{Q}$ and $\mathcal{R}$ be two BF sets in (U,τ). If $\mathcal{Q} \subseteq \mathcal{R}$, then $pint_\tau(\mathcal{Q}) \subseteq pint_\tau(\mathcal{R})$ and $pcl_\tau(\mathcal{Q}) \subseteq pcl_\tau(\mathcal{R})$.
Proof: Since $pint_\tau(\mathcal{Q})$ is the largest BF supra preopen set contained in $\mathcal{Q}$, $pint_\tau(\mathcal{Q}) \subseteq \mathcal{Q}$. Then, $pint_\tau(\mathcal{Q}) \subseteq \mathcal{Q} \subseteq \mathcal{R}$. $pint_\tau(\mathcal{Q})$ is the BF supra preopen set contained in $\mathcal{R}$, but $pint_\tau(\mathcal{R})$ is the largest BF supra preopen set contained in $\mathcal{Q}$. So, $pint_\tau(\mathcal{Q}) \subseteq pint_\tau(\mathcal{R})$. For the other part, $\mathcal{Q} \subseteq \mathcal{R} \Leftrightarrow \mathcal{R}^c \subseteq \mathcal{Q}^c$. Then $pint_\tau(\mathcal{R}^c) \subseteq pint_\tau(\mathcal{Q}^c)$ and we obtain $(pcl_\tau(\mathcal{R}))^c \subseteq (pcl_\tau(\mathcal{Q}))^c$ and hence $(pcl_\tau(\mathcal{Q}))^c = pint_\tau(\mathcal{Q}^c)$.

Theorem 3.11: Let $\mathcal{Q}$ and $\mathcal{R}$ be two BF sets in (U,τ). Then:
(i) $pint_\tau(\mathcal{Q}) \cup pint_\tau(\mathcal{R}) \subseteq pint_\tau(\mathcal{Q} \cup \mathcal{R})$.
(ii) $pint_\tau(\mathcal{Q} \cap \mathcal{R}) \subseteq pint_\tau(\mathcal{Q}) \cap pint_\tau(\mathcal{R})$.
(iii) $pcl_\tau(\mathcal{Q} \cap \mathcal{R}) \subseteq pcl_\tau(\mathcal{Q}) \cap pcl_\tau(\mathcal{R})$.
(iv) $pcl_\tau(\mathcal{Q}) \cup pcl_\tau(\mathcal{R}) \subseteq pcl_\tau(\mathcal{Q} \cup \mathcal{R})$.
Proof: (i) We have $\mathcal{Q} \subseteq \mathcal{Q} \cup \mathcal{R}$ and $\mathcal{R} \subseteq \mathcal{Q} \cup \mathcal{R}$, then $pint_\tau(\mathcal{Q}) \subseteq pint_\tau(\mathcal{Q} \cup \mathcal{R})$ and $pint_\tau(\mathcal{R}) \subseteq pint_\tau(\mathcal{Q} \cup \mathcal{R})$. Hence, $pint_\tau(\mathcal{Q}) \cup pint_\tau(\mathcal{R}) \subseteq pint_\tau(\mathcal{Q} \cup \mathcal{R})$.
The other statements are obtained by similar way.

4. Bipolar Fuzzy Supra Pre-continuous Mappings

Here, we define a new type of continuous mappings called a bipolar fuzzy supra pre-continuous mapping and also discussed their basic properties.

Definition 4.1: Let (U_1,τ) and (U_2,σ) be two BF supra topological spaces, τ^* and σ^* be two associated BF topologies with τ and σ, respectively. A mapping $\varphi: (U_1,\tau^*) \longrightarrow (U_2,\sigma^*)$ is called bipolar fuzzy supra pre-continuous mapping if $\varphi^{-1}(B) \subseteq U_1$ is BF supra preopen set for every $B \in \sigma^*$.

Theorem 4.2: Every BF supra continuous mapping is a BF supra pre-continuous mapping.
Proof: Let $\varphi: (U_1,\tau^*) \longrightarrow (U_2,\sigma^*)$ be a BF continuous mapping and $\mathcal{Q} \in \sigma^*$. Then $\varphi^{-1}(\mathcal{Q}) \in \tau^*$. Since τ is associated with τ^*, then $\tau^* \subseteq \tau$. Hence, $\varphi^{-1}(\mathcal{Q}) \in \tau$. By the Theorem 3.3, $\varphi^{-1}(\mathcal{Q})$ is a BF supra preopen set and φ is a BF supra pre-continuous mapping.

The implication in above theorem is not reversible;

Example 4.3: Let $U_1 = \{a,b\}$, $U_2 = \{u,v\}$ and
$\mathcal{Q} = \{< a, 0.5, -0.3 >, < b, 0.2, -0.4 >\}$
$\mathcal{R} = \{< a, 0.3, -0.6 >, < b, 0.4, -0.5 >\}$
$\mathcal{Z} = \{< u, 0.5, -0.3 >, < v, 0.4, -0.4 >\}$
$\mathcal{Y} = \{< u, 0.5, -0.6 >, < v, 0.4, -0.5 >\}$
Then $\tau = \{0_{BP}, 1_{BP}, \mathcal{Q}, \mathcal{R}, \mathcal{Q} \cup \mathcal{R}\}$ is a BF supra topology on U_1 and $\sigma = \{0_{BP}, 1_{BP}, \mathcal{Z}, \mathcal{Y}, \mathcal{Z} \cup \mathcal{Y}\}$ is a BF supra topology on U_2.
Define a mapping $\varphi: (U_1,\tau) \longrightarrow (U_2,\sigma)$ by $\varphi(a) = u$ and $\varphi(b) = v$. For $\mathcal{Z} \in \sigma$, we obtain $\varphi^{-1}(\mathcal{Z}) = \{< a, 0.5, -0.3 >, < b, 0.4, -0.4 >\} \notin \tau$ and $\varphi^{-1}(\mathcal{Z}) \subseteq int_\tau(cl_\tau(\varphi^{-1}(\mathcal{Z})))$, so $\varphi^{-1}(\mathcal{Z})$ is a BF supra preopen set. Therefore, φ is a BF supra pre-continuous mapping but not be a BF supra continuous mapping.

Theorem 4.4: Let $\tau \in BPFST(U_1)$ and $\sigma \in BPFST(U_2)$, τ^* and σ^* be two associated with BF topologies with τ and σ, respectively. Let $\varphi: (U_1,\tau^*) \longrightarrow (U_2,\sigma^*)$ be a function. Then the following statements are equivalent:
(1) φ is BF supra pre-continuous mapping.
(2) The inverse image of a closed set in U_2, is a BF supra pre-closed set in U_1.
(3) $pcl\left(\varphi^{-1}(\mathcal{R})\right) \subseteq \varphi^{-1}\left(cl(\mathcal{R})\right), \forall\, \mathcal{R} \in BPF(U_2)$.

(4) $\varphi\left(pcl(\mathcal{Q})\right) \subseteq cl\left(\varphi(\mathcal{Q})\right), \forall\, \mathcal{Q} \in BPF(U_1)$.
(5) $\varphi^{-1}\left(int(\mathcal{R})\right) \subseteq pint\left(\varphi^{-1}(\mathcal{R})\right), \forall\, \mathcal{R} \in BPF(U_2)$.
Proof: (1 ⟹2) Let $\mathcal{R}$ be a BF supra closed in U_2. Then $\mathcal{R}^c$ is BF supra open set. By hypothesis $\varphi^{-1}(\mathcal{R}^c) = (\varphi^{-1}(\mathcal{R}))^c$ is BF supra preopen set in U_1. So, $\varphi^{-1}(\mathcal{R})$ is BF supra pre-closed set in U_1.
(2 ⟹3) Let $\mathcal{R} \in BPF(U_2)$. Since $cl(\mathcal{R})$ is BF supra closed set in U_2, $\varphi^{-1}(cl(\mathcal{R}))$ is BF supra pre-closed set in U_1. Then, $pcl\left(\varphi^{-1}(\mathcal{R})\right) \subseteq \varphi^{-1}\left(cl(\mathcal{R})\right)$.
(3 ⟹4) Let $\mathcal{Q} \in BPF(U_1)$. By hypothesis $\varphi^{-1}\left(cl(\varphi(\mathcal{Q}))\right) \supseteq pcl(\varphi^{-1}(\varphi(\mathcal{Q}))) \supseteq pcl(\mathcal{Q})$ and then $\varphi\left(pcl(\mathcal{Q})\right) \subseteq cl\left(\varphi(\mathcal{R})\right)$.
(4 ⟹5) Let $\mathcal{R} \in BPF(U_2)$. By hypothesis we get $\varphi\left(pcl((\varphi^{-1}(\mathcal{R}))^c)\right) \subseteq cl(\varphi((\varphi^{-1}(\mathcal{R}))^c))$ and $\varphi((pint(\varphi^{-1}(\mathcal{R}))^c) \subseteq cl(\mathcal{R}^c) = \left(int(\mathcal{R})\right)^c$.
Hence, we obtain $\left(pint\varphi^{-1}(\mathcal{R})\right)^c \subseteq \varphi^{-1}(\left(int(\mathcal{R})\right)^c)$ and then $\varphi^{-1}\left(int(\mathcal{R})\right) \subseteq pint\left(\varphi^{-1}(\mathcal{R})\right)$.
(5⟹1) Let $\mathcal{R}$ be a BF supra open set in U_2 and $\varphi^{-1}\left(int(\mathcal{R})\right) \subseteq pint\left(\varphi^{-1}(\mathcal{R})\right)$. Then, $\varphi^{-1}(\mathcal{R}) \subseteq pint(\varphi^{-1}(\mathcal{R})$. Hence, $\varphi^{-1}(\mathcal{R}) \subseteq pint(\varphi^{-1}(\mathcal{R}))$, but $pint(\varphi^{-1}(\mathcal{R})) \subseteq \varphi^{-1}(\mathcal{R})$. Then, $\varphi^{-1}(\mathcal{R}) = pint(\varphi^{-1}(\mathcal{R}))$. Therefore, $\varphi^{-1}(\mathcal{R})$ is a BF supra preopen set in U_1.

Theorem 4.5: Let $\varphi: (U_1, \tau) \longrightarrow (U_2, \sigma)$ be a BF supra pre-continuous and $g: (U_2, \sigma) \longrightarrow (U_3, \delta)$ be a BF supra continuous. Then $g \circ \varphi: (U_1, \tau) \longrightarrow (U_3, \delta)$ is a BF supra pre-continuous mapping.
Proof: Straightforward.

Theorem 4.6: $\varphi: (U_1, \tau) \longrightarrow (U_2, \sigma)$ is a BF supra pre-continuous mapping if one of the followings holds:

(1) $\varphi^{-1}\left(pint(\mathcal{R})\right) \subseteq pint\left(\varphi^{-1}(\mathcal{R})\right), \forall\, \mathcal{R} \in BPF(U_2)$.
(2) $cl(\varphi^{-1}(\mathcal{R})) \subseteq \varphi^{-1}(pcl\mathcal{R}), \forall\, \mathcal{R} \in BPF(U_2)$.
(3) $\varphi\left(cl(\mathcal{Q})\right) \subseteq pcl\left(\varphi(\mathcal{Q})\right), \forall\, \mathcal{Q} \in BPF(U_1)$.
Proof: Let (1) be satisfied and $\mathcal{R}$ be a BF supra open set in U_2. Then, $\varphi^{-1}\left(pint(\mathcal{R})\right) \subseteq pint\left(\varphi^{-1}(\mathcal{R})\right)$. We have $\varphi^{-1}(\mathcal{R}) \subseteq int(\varphi^{-1}(\mathcal{R}))$. Hence $\varphi^{-1}(\mathcal{R})$ is a BF supra open set. We know that every BF supra open set is BF supra preopen set.
The others can be proven similarly.

4. Conclusion and Suggestions

We have established a new extension of bipolar fuzzy open sets named bipolar fuzzy supra preopen set. We hope that the finding in this manuscript will be helpful for the researchers concerned with kind of supra open sets.

Acknowledgment

The author expresses thanks to the reviewers and editors for their valuable suggestions which helped to improve the paper.

Contributions of the Authors

The authors contributed equally to the study.

Conflict of Interest Statement

There is no conflict of interest between the authors.

Statement of Research and Publication Ethics

The study is complied with research and publication ethics

References

[1] L. Zadeh, Fuzzy sets, *Information and control*, vol.8, pp.338–353, 1965.
[2] K. T. Atanassov, Intuitionistic fuzzy sets, *Fuzzy sets and Systems*, vol.20, pp.87-96, 1986.
[3] L. Zadeh, "The concept of a linguistic variable and its application to approximate reasoning-I", *Inform. Sci*., vol.8, pp.199–249, 1975.
[4] W. L. Gau and D. J. Buehrer, Vague sets, *IEEE Transactions on Systems, Man and Cybernetics*, vol. 23, no.2, pp. 610-614, 1993.
[5] W-R. Zhang, "Bipolar fuzzy sets and relations: a computational framework for cognitive modeling and multiagent decision analysis", *NAFIPS/IFIS/NASA'94*, pp.305-309, 1994.
[6] K. M. Lee, "Bipolar-valued fuzzy sets and their operations", *Proc. Int. Conf. on Intelligent Technologies Bangkok Thailand*, pp. 307-312, 2000.
[7] M. S. Anitha, K. L. Muruganantha and K. Arjunan, "Notes on bipolar valued fuzzy subgroups of a

Group", *The Bulletin of Society for Mathematical Services and Standards*, vol.7, pp. 40-45, 2013.
[8] B. Pazar Varol, "An approach to bipolar fuzzy submodules", *TWMS J. App. and Eng. Math*., vol.11, no.1, pp. 168-175, 2021.
[9] M. Azhagappan and M. Kamaraj, "Notes on bipolar valued fuzzy RW-closaed and bipolar valued fuzzy RW-open sets in bipolar valued fuzzy topological spaces", *International Journal of Mathematical Archive*, vol.7, no. 3, pp. 30-36, 2016.
[10] J. Kim, S. K. Samanta, P. K. Lim, J. G. Lee, K. Hur, "Bipolar fuzzy topological spaces", *Annals of Fuzzy Mathematics and Informatics*, vol.17, no. 3, pp. 205-229, 2019.
[11] A. S. Mashhour, A. A. Allam, F. S. Mahmoud and F.H. Khedr, "On Supra Topological spaces", *Indian J.Pure Appl. Math.*, vol. 14, no. 4, pp. 502-510, 1983.
[12] M. E. Abd El-Monsef and A. E. Ramadan A. E, "On Fuzzy Supra Topological Spaces", *Indian J. Pure Appl. Math.*, vol.18, no.4, pp.322-329, 1987.
[13] N. Turanlı, "An overview of intuitionistic fuzzy supra topological spaces", *Hacettepe Journal of Mathematics and Statistics*, vol.32, pp. 17-26, 2003.
[14] H. Malkoç and B. Pazar Varol, Bipolar Fuzzy Supra "Topological Spaces", *Sakarya University Journal of Science*, vol.26, no.1, pp. 156-168, 2022.
[15] A. S. Mashhour et al., "On precontinuous and weak precontinuous mappings", *Proc. Math. Phys. Soc. Egypt*., vol. 53, pp.47– 53, 1982.
[16] M. K. Signal and Niti Rajvanshi, "Fuzzy preopen sets and preseparation axioms", *Fuzzy Sets and Systems*, vol.44, pp. 273-281, 1991.
[17] O. R. Sayed, "Supra preopen sets and Supra precontinuity on topological spaces," *Scientific Studies and Research, Series Mathematics and Informatics*, vol.20, no.2, pp.79-88, 2010.
[18] J. Srikiruthika and A. Kalichelvi, "Fuzzy Supra Preopen Sets", *Global Journal of Pure and Applied Mathematics*, vol. 14, no.1, pp. 57-66, 2018.
[19] K. M. Lee, "Comparison of interval-valued fuzzy sets, intuitionistic fuzzy sets and bipolar- valued fuzzy Sets", J. *Fuzzy Logic Intelligent Systems* vol.14, pp.125-129, 2004.

Bitlis Eren Üniversitesi Fen Bilimleri Dergisi
BİTLİS EREN UNIVERSITY JOURNAL OF SCIENCE
ISSN: 2147-3129/e-ISSN: 2147-3188
VOLUME: 11 NO: 4 PAGE: 1159-1174 YEAR: 2022
DOI:10.17798/bitlisfen.1205860

Archaeometric Investigation of Gold Coins (Byzantine Period, Romanus Iii) By Means of Portable Xrf: Characterization and Comparison

Murat BAYAZİT[1], Nesrin ŞEKER[2]*
[1]*Department of Ceramics, Faculty of Fine Arts, Batman University, Batı Raman Campus, Batman, Turkey*
[2]*Directorate of Diyarbakır Archeology Museum, Diyarbakır, Turkey*
(ORCID: 0000-0003-1453-249X) (ORCID: 0000-0002-8914-3133)

Keywords: Materials Characterization, Gold Coin, p-XRF, Archaeometry, Coin Analysis

Abstract
Some of the ancient materials in museums can only be examined on-site, which requires in-situ analysis techniques. Coins made of precious metals are one of such materials and portable X-ray fluorescence (p-XRF) spectrometry is one of the most preferred technique for gold and silver-based coins that need to be characterized in situ and non-destructively. In this study, a detailed archaeometric investigation was carried out for the gold coins which were unearthed after the excavations in Melik Ahmet Street (Diyarbakır, 1992) and brought to Directorate of Diyarbakır Museum through confiscation. The chemical compositions of the samples were specified by means of portable XRF which was applied on 45 gold coins of the Romanus III period. The main element in the composition was found as gold detected as 93.89% in average. Silver was the most abundant element after gold, however the highest silver rate did not exceed 9% (5.25% in average). Copper and iron were identified respectively in 12 coins (Cu: 1.05-2.46%) and 18 coins (Fe: 0.87-6.5%). Manganese, nickel, titanium, lead, iridium and osmium were seen in one sample each. The hierarchical clustering analysis applied with gold-silver-copper-iron and gold-silver suggested three different groups. The hierarchical clustering analysis was also applied considering the p-XRF data achieved in this study (belonging to the Romanus III period), solidus samples belonging to six Byzantine period emperors, and for the hollow coins belonging to four Byzantine period emperors. Taking into account the distribution, classification and the variations, the coins of different emperor periods were compared.

1. Introduction

In the most general sense, archaeometry covers the characterization process applied to identify the raw materials and production technologies of the materials found in archaeological research. Spectroscopic and microscopic analysis are the most preferred techniques in terms of elucidating the production stages of the ancient materials. In this context, X-ray fluorescence (XRF), X-ray diffraction (XRD), optical microscopy and scanning electron microscopy/energy dispersive X-ray spectroscopy (SEM/EDX) come forward in archaeometric investigations. On the other hand, the artifacts exhibited in the museums can only be analyzed by means of non-destructive and/or portable analysis devices, which may limit the number of analyses to be used. In such cases, the samples must be analyzed in-situ, and should not be deformed. Coins are one of the best examples for this situation. The coins made of precious metals such as gold and silver can be analyzed on-site by means of portable XRF in order to identify the amounts of Au, Ag and other possible elements like cupper, iron, titanium etc. By determining the chemical composition with the archaeometric studies on the coins, the socio-economic status of the periods, when the coin was struck, can be evaluated [1]-[3].

*Corresponding author: murat.bayazit@batman.edu.tr
Received: 16.11.2022, Accepted:26.12.2022

Determining the value of goods has revealed the idea of "value" and accordingly the idea of "equivalent", and consequently, money was needed as a means of exchange, and at first, cereal products, animals and manufactured tools were used instead of money [4]. As a result of the increase in people's relations with each other, shopping increased and the way of paying with animals began to seem useless, which resulted in using metal tools (e.g. shovel, hoe, ax) and ornaments (e.g. ring, earring, bracelet) [5]. Since these goods, which are used as money, were difficult to protect, produce and transport, only precious metals such as silver and gold have been used as money over time [4]. The tradition of using precious metals (especially silver) as money goes back to the 2400s BC in Mesopotamia [6].

Constantine VIII, who was on the throne in the Byzantine Empire between 1025 and 1028 AD, had three daughters. Since Constantine III had no successor, he married his middle daughter, Zoe, to Romanus Argyros, who came from an aristocratic family from Constantinople and was the ruler (economos) of Hagia Sophia, in order to take the throne after his death. Three days after marriage Constantine VIII has died and Romanus Argyros (Romanus III) became the Byzantine Emperor in 1028 AD. The coins struck during the reign of Romanus III, who is considered to be the founder of the Peribleotos Church and Monastery, have intense depictions of Mary as an indication of his devotion to her. On the solidus, which are the gold coins of the Romanus III period, there is Mary depicted standing, crowning the emperor [7], [8].

In the present study, the Romanus III period coins, which were confiscated to the Diyarbakır Museum Directorate in 1992, were analyzed by the portable X-ray fluorescent (p-XRF) method and their elemental contents were determined. Before the analyzes, the necessary permits were obtained for the study, and the analyzes were carried out in the museum with the p-XRF device under the supervision of the museum authorities. After the study, the samples were put back to their places in the inventory by the authorities.

2. Material and Method

2.1. Samples

Within the scope of the thesis study, 45 Romanus III period gold coins in Diyarbakır Museum were on-site characterized under the supervision of the museum officials. Although the information on the front and back of the coins, such as the descriptions, inscriptions, period, also the way it came to the museum and the date of arrival are the same, the code, inventory number, diameter, thickness and weight of the coins occasionally vary. A representative coin from the sample set is given in Figure 1 [9], [10].

Description of the front side of the coins: The bearded Jesus is depicted with a halo on his head, sitting on a throne with a double row of dotted borders. Depicted from the front, Jesus is holding a dot-decorated book on his knee with his left hand while his right hand is on his chest in a consecrated position. There is an inscription in the form of “IhSXISRЄX RЄϚNANTıhm” around the depictions within the double-dotted border.

Description of the back side of the coins: On the left, the emperor is depicted frontally holding the loros, his right hand on his chest, and his left hand holding the crusader globus, which symbolizes the world domination. On the right, there is Mary, whose head is in a halo, crowning the emperor with her long tunic and long cloak called maphorion. There is a double line dotted border around the depictions and there is the inscription “ΘCЄbOHΘ RωmAnω” inside the border.

Figure 1. A representative sample of Romanus III coins analyzed in the present work [9], [10].

2.2. Portable X-ray Fluorescence (p-XRF)

Innov-X Omega portable X-ray Fluorescence (p-XRF) spectrometer was used and analyzes were carried out in the "precious metals" mode of the device. During the study, the coins were taken out of the inventory one by one by the museum authorities. After the completion of analysis for each sample, the analyzed coin was put back into the inventory, and then the other coin was removed from the inventory. The fact that the coins were gold eliminated the risk of skidding that would affect the X-rays during the analysis. There were no obvious impurities on the surfaces of the coins, in general, which could affect

the analysis results. Therefore, no additional processing was done for the coins before or after the p-XRF application, and the analyzes were carried out entirely on the original states of the coins. Analyzes were applied separately for the front and back surfaces of each coin

3. Results and Discussion

3.1. Portable XRF results of the Coins

The p-XRF results of the samples are given in Table 1 in which the data obtained for both the front and back sides of the coins are presented

Table 1. Portable XRF results of the Romanus III coins.

Code (RM)	Analysis Surface*	Au	Ag	Cu	Fe	Ti	Mn	Os	Ir	Ni	Pb
1	F	95,64	4,35	-	-	-	-	-	-	-	-
	B	95,62	4,37	-	-	-	-	-	-	-	-
2	F	92,16	5,74	2,10	-	-	-	-	-	-	-
	B	92,21	5,74	2,05	-	-	-	-	-	-	-
3	F	94,46	4,41	1,12	-	-	-	-	-	-	-
	B	95,48	4,51	-	-	-	-	-	-	-	-
4	F	95,70	4,29	-	-	-	-	-	-	-	-
	B	95,73	4,26	-	-	-	-	-	-	-	-
5	F	95,89	4,10	-	-	-	-	-	-	-	-
	B	95,88	4,11	-	-	-	-	-	-	-	-
6	F	94,48	4,38	1,13	-	-	-	-	-	-	-
	B	94,49	4,32	1,18	-	-	-	-	-	-	-
7	F	92,45	5,72	1,82	-	-	-	-	-	-	-
	B	92,49	5,74	1,77	-	-	-	-	-	-	-
8	F	95,80	4,19	-	-	-	-	-	-	-	-
	B	94,78	4,17	-	1,04	-	-	-	-	-	-

**F: Front Surface, B: Back Surface*

Table 1. Portable XRF results of the Romanus III coins (continued).

Code (RM)	Analysis Surface*	Au	Ag	Cu	Fe	Ti	Mn	Os	Ir	Ni	Pb
9	F	92,83	5,74	1,42	-	-	-	-	-	-	-
	B	93,51	5,16	1,32	-	-	-	-	-	-	-
10	F	94,16	4,61	-	1,22	-	-	-	-	-	-
	B	94,52	4,49	-	0,984	-	-	-	-	-	-
11	F	94	6	-	-	-	-	-	-	-	-
	B	93,15	5,98	-	0,874	-	-	-	-	-	-
12	F	94,32	5,68	-	-	-	-	-	-	-	-
	B	94,36	5,64	-	-	-	-	-	-	-	-
13	F	95,48	4,51	-	-	-	-	-	-	-	-
	B	95,55	4,44	-	-	-	-	-	-	-	-

14	F	94,24	4,89	-	0,871	-	-	-	-	-	-
	B	91,23	4,76	-	4,01	-	-	-	-	-	-
15	F	95,83	4,16	-	-	-	-	-	-	-	-
	B	95,76	4,23	-	-	-	-	-	-	-	-
16	F	94,51	3,96	-	1,52	-	-	-	-	-	-
	B	94,48	4,15	-	1,35	-	-	-	-	-	-
17	F	93,77	5,07	1,15	-	-	-	-	-	-	-
	B	94,98	5,02	-	-	-	-	-	-	-	-
18	F	92,88	5,97	-	1,14	-	-	-	-	-	-
	B	94,03	5,97	-	-	-	-	-	-	-	-
19	F	94,02	4,29	-	1,69	-	-	-	-	-	-
	B	95,89	4,10	-	-	-	-	-	-	-	-
20	F	86,39	6,86	-	6,5	-	-	-	-	0,255	-
	B	91,65	6,33	-	2,01	-	-	-	-	-	-
21	F	90,26	5,82	1,88	0,89	-	-	0,9	0,28	-	-
	B	90,55	5,71	1,63	2,10	-	-	-	-	-	-
22	F	94,41	5,59	-	-	-	-	-	-	-	-
	B	94,42	5,58	-	-	-	-	-	-	-	-
23	F	91,77	8,23	-	-	-	-	-	-	-	-
	B	91,68	8,32	-	-	-	-	-	-	-	-
24	F	95,86	4,13	-	-	-	-	-	-	-	-
	B	94,62	4,22	-	1,15	-	-	-	-	-	-
25	F	95,90	4,09	-	-	-	-	-	-	-	-
	B	95,36	4,63	-	-	-	-	-	-	-	-
26	F	92,75	5,12	1,22	0,89	-	-	-	-	-	-
	B	93,56	5,22	1,22	-	-	-	-	-	-	-
27	F	94,61	5,39	-	-	-	-	-	-	-	-
	B	95,05	4,95	-	-	-	-	-	-	-	-

**F: Front Surface, B: Back Surface*

Table 1. Portable XRF results of the Romanus III coins (continued).

Code (RM)	Analysis Surface*	Au	Ag	Cu	Fe	Ti	Mn	Os	Ir	Ni	Pb
28	F	89,35	6,38	1,96	1,28	-	0,73	-	-	-	0,29
	B	93,17	6,83	-	-	-	-	-	-	-	-
29	F	93,88	5,07	-	1,05	-	-	-	-	-	-
	B	95,09	4,91	-	-	-	-	-	-	-	-
30	F	95,37	4,62	-	-	-	-	-	-	-	-
	B	95,43	4,56	-	-	-	-	-	-	-	-
31	F	91,7	8,3	-	-	-	-	-	-	-	-
	B	91,7	8,3	-	-	-	-	-	-	-	-
32	F	95,13	4,87	-	-	-	-	-	-	-	-
	B	94,99	5,00	-	-	-	-	-	-	-	-
33	F	93,21	5,74	-	1,05	-	-	-	-	-	-
	B	94,34	5,66	-	-	-	-	-	-	-	-

34	F	91,93	6,71	1,36	-	-	-	-	-	-	-
	B	90,97	6,57	2,46	-	-	-	-	-	-	-
35	F	96,20	3,79	-	-	-	-	-	-	-	-
	B	95,80	4,19	-	-	-	-	-	-	-	-
36	F	93,53	6,47	-	-	-	-	-	-	-	-
	B	87,14	6,27	1,05	4,91	0,6	-	-	-	-	-
37	F	95,12	4,87	-	-	-	-	-	-	-	-
	B	95,46	4,54	-	-	-	-	-	-	-	-
38	F	94,55	5,45	-	-	-	-	-	-	-	-
	B	94,6	5,4	-	-	-	-	-	-	-	-
39	F	93,4	5,08	1,51	-	-	-	-	-	-	-
	B	93,58	5,06	1,34	-	-	-	-	-	-	-
40	F	92,56	6,53	-	0,905	-	-	-	-	-	-
	B	93,62	6,38	-	-	-	-	-	-	-	-
41	F	92,68	6,39	-	0,932	-	-	-	-	-	-
	B	92,78	6,29	-	0,925	-	-	-	-	-	-
42	F	95,08	4,92	-	-	-	-	-	-	-	-
	B	94,99	5,00	-	-	-	-	-	-	-	-
43	F	95,01	4,99	-	-	-	-	-	-	-	-
	B	95,03	4,96	-	-	-	-	-	-	-	-
44	F	94,94	5,05	-	-	-	-	-	-	-	-
	B	94,04	4,9	-	1,05	-	-	-	-	-	-
45	F	94,18	4,57	1,24	-	-	-	-	-	-	-
	B	94,51	4,32	1,16	-	-	-	-	-	-	-
Maximum	***F,B***	***96,20***	***8,32***	***2,46***	***6,5***	***0,6***	***0,73***	***0,9***	***0,28***	***0,255***	***0,29***
Minimum	***F,B***	***86,39***	***3,79***	***1,05***	***0,871***	***0,6***	***0,73***	***0,9***	***0,28***	***0,255***	***0,29***
Mean	***F,B***	***93,89***	***5,24***	***1,50***	***1,68***	***0,6***	***0,73***	***0,9***	***0,28***	***0,255***	***0,29***

**F: Front Surface, B: Back Surface*

According to the p-XRF analysis data, the amount of gold in coins varies in the range of 86.39-96.20% (93,89% in average). After gold, the highest element observed in coins was silver. The silver ratio in the samples varies between 3.79% and 8.32% (5.24% in average). Copper was found in 13 coins (1.05-2.46%), and iron in 18 coins (0.87-6.5%). Manganese (RM 28 Front; %0,73), nickel (RM 20 Front; %0,255), titanium (RM 36 Back; %0,6), lead (RM 28 Front; %0,29), iridium (RM 21 Front; %0,73) and osmium (RM 21 Front; %0,9) were seen in one sample each. Since these six elements are thought as the possible contaminations on the coins' surfaces (considering the coin production at Byzantine period), they are not included for the evaluation and comparison of the results.

The distribution of elements with an average of more than 1% in coins is given in Figure 2. Considering the variations in chemical composition, it has been observed that the amount of gold is quite dominant and only the coin RM 20 contains significantly less gold. Only three samples were identified in the sample set containing gold less than 90% (RM 20, RM 28 and RM 36).

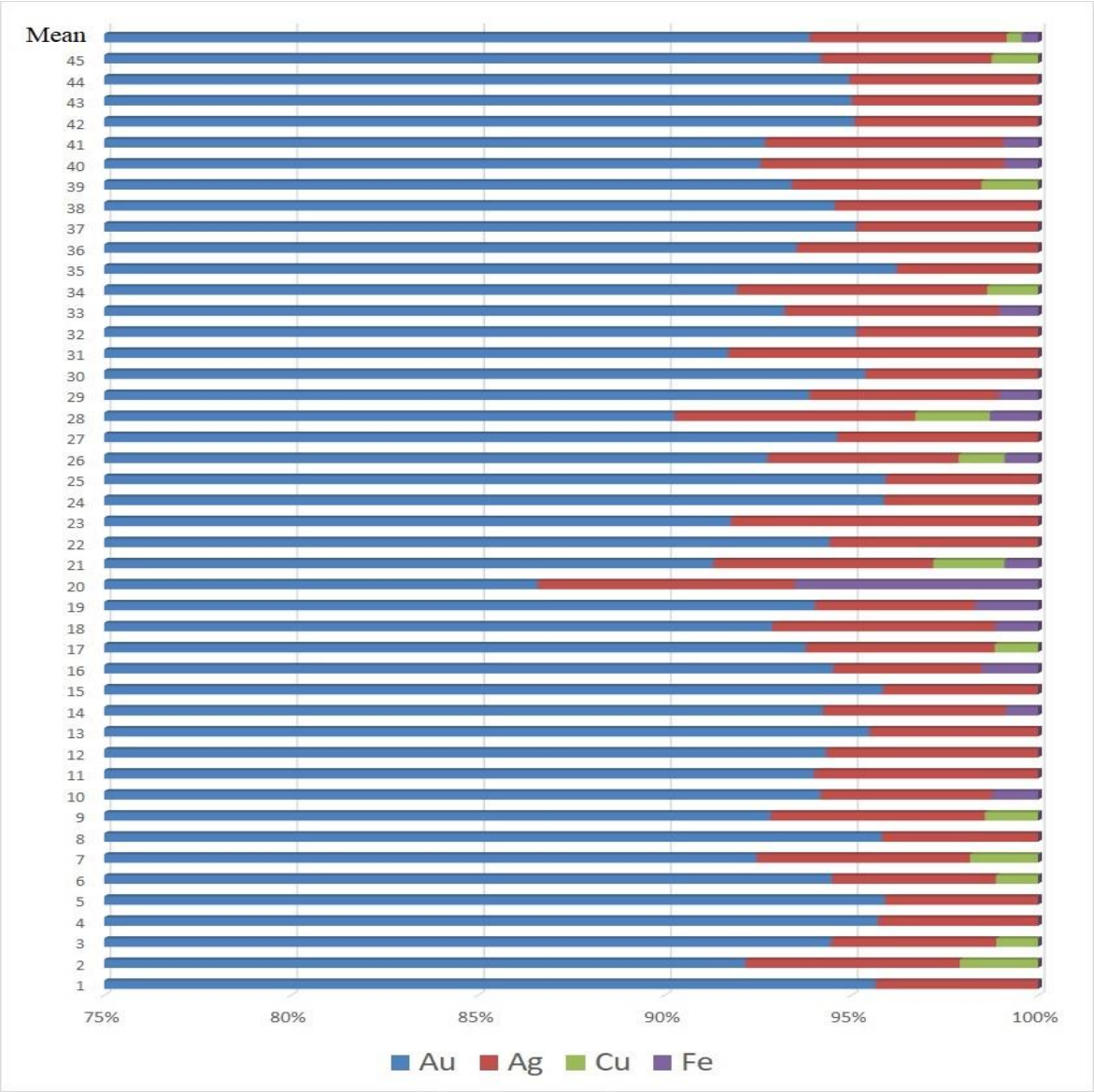

Figure 2. The distribution of elements with an average of more than 1%.

The samples can be initially separated as four main groups given as the followings;

i. The samples possessing only gold and silver: RM 1, RM4, RM 5, RM 12, RM 13, RM 15, RM 22, RM 23, RM 25, RM 27, RM 30, RM 31, RM 32, RM 35, RM 37, RM 38, RM 42, RM 43.

ii. The samples possessing gold, silver and copper: RM 2, RM 3, RM 6, RM 7, RM 9, RM 17, RM 34, RM 39, RM 45.

iii. The samples possessing gold, silver and iron: RM 8, RM 10, RM 11, RM 14, RM 16, RM 18, RM 19, RM 20, RM 24, RM 26, RM 29, RM 33, RM 40, RM 41, RM 44.

iv. The samples possessing gold, silver, copper and iron: RM 21, RM 28, RM 36.

In order to see the correlation between the coins more clearly, hierarchical clustering analysis was carried out with gold, silver, copper and iron contents (Figure 3). Since the predominance of gold amount suggested a sample set with a single type chemical composition, the majority of the samples were accordingly gathered in one group in the hierarchical clustering analysis carried out considering the data achieved for the front surfaces of the coins. Three groups were determined in the classification made with gold-silver-copper-iron, and the majority of the coins (42 samples) were in a single group and three subgroups were identified in this group. The second group included only RM 21 and RM 28. The third group alone constituted RM 20. The lowest gold amounts were thought to be the decisive factor in the formation of the second and

third groups. The samples forming separate groups also showed themselves in the scatter plot of gold and silver (Figure 4)

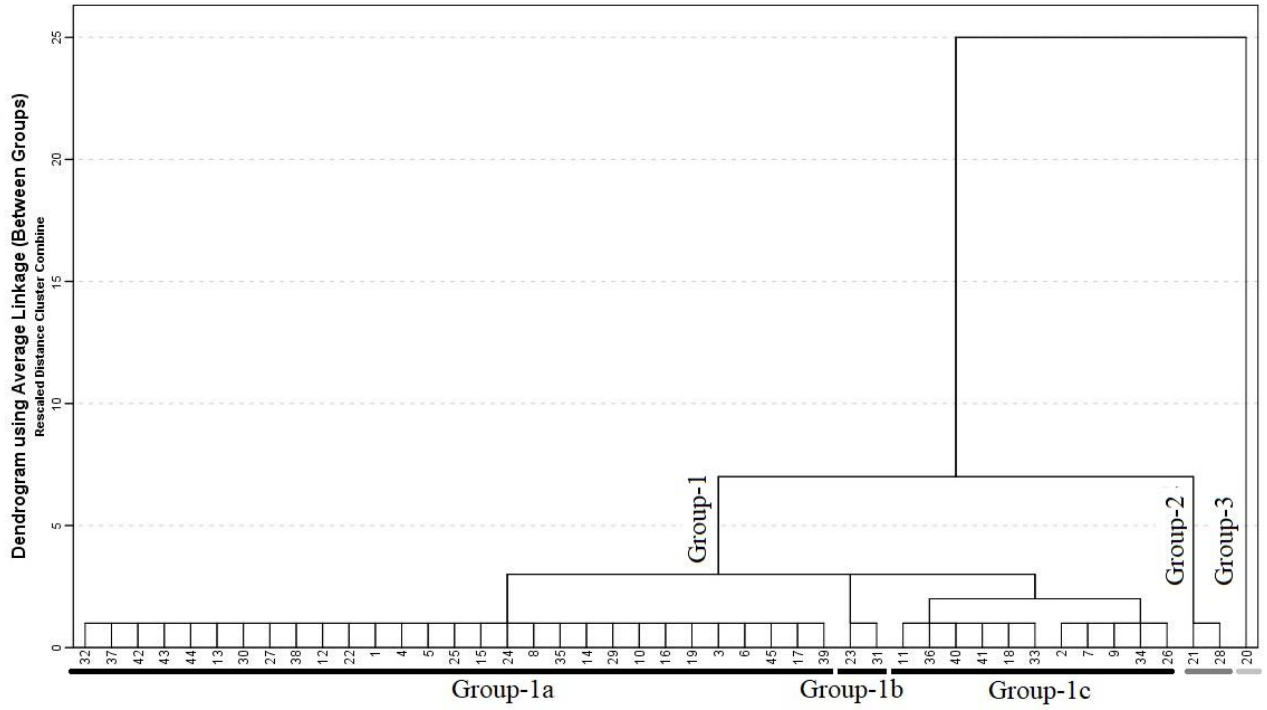

Figure 3. Dendrogram showing the groups (considering gold, silver, copper and iron).

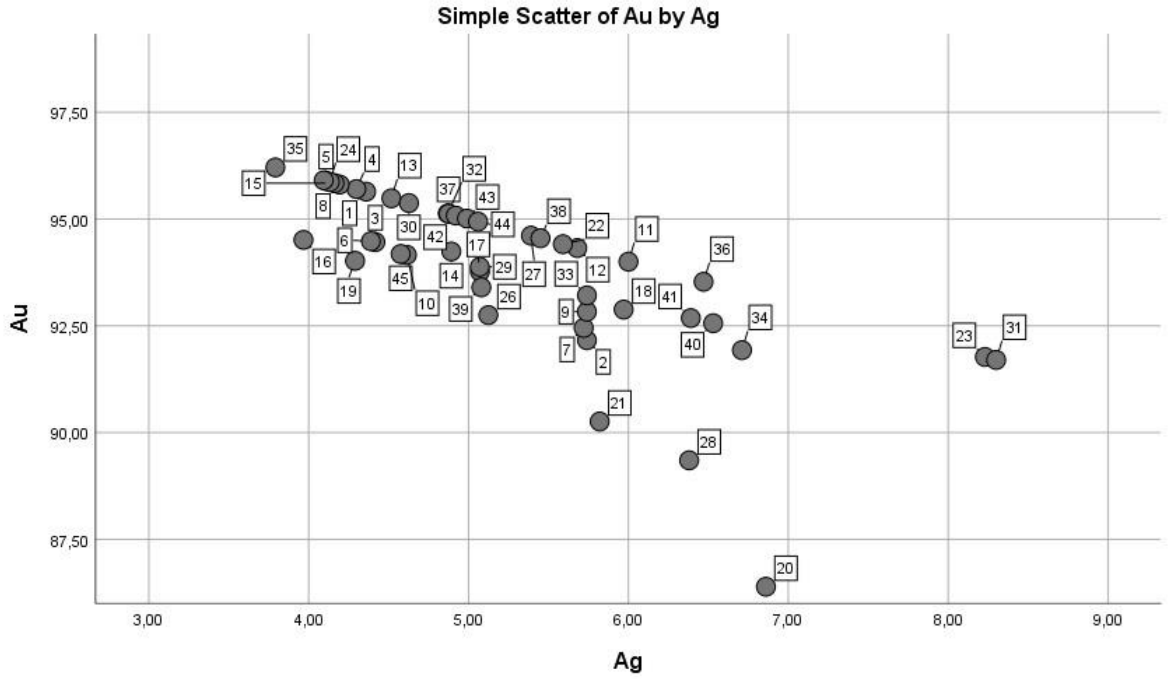

Figure 4. Scatter plot of gold and silver.

For the Figures 2-4, please see the codes (RM) given in Table 1 to follow the samples.

3.2. Comparison with the Solidus Coins of Six Byzantine Emperors

The coins of the Romanus III period (1028-1034) analyzed within the scope of this work are in the solidus group. Based on this, the examples in the present research were compared with the solidus coins belonging to the periods of Leo I (457-474 AD), Anastasius I (491-518 AD), Mauricius Tiberius (539-602 AD), Constans II (641-668 AD), Constantinus IV (668-685 AD) and Iustinianus II (685-695 AD) [11], [12]. The distribution of gold and silver in the solidus samples from different periods mentioned and from the Romanus III period is given in Figure 5 (sample order: 1-3 Leo I; 4,5 Anastasius I; 6,7 Mauricius Tiberius; 8-13 Constans II; 14-20 Constantinus IV; 21-28 Iustinianus II; 29-73 Romanus III). According to the variation in terms of gold and silver contents, it was observed that the gold ratio in the solidus coins of six emperors, who have been on the throne between 457-695 AD, was close to the solidus samples of the Romanus III period, yet was relatively higher. It was seen that the solidus samples of the Romanus III period were mostly close to each other and likewise the solidus samples of other emperors, who have been on the throne in different periods, in general. The silver ratio was seen to increase during the Romanus III period, which indicated that silver was used instead of gold in parallel with the decrease in the gold rate with the Romanus III period. In a way, this may suggest that the cost of gold, the precious element in coins, would have been reduced

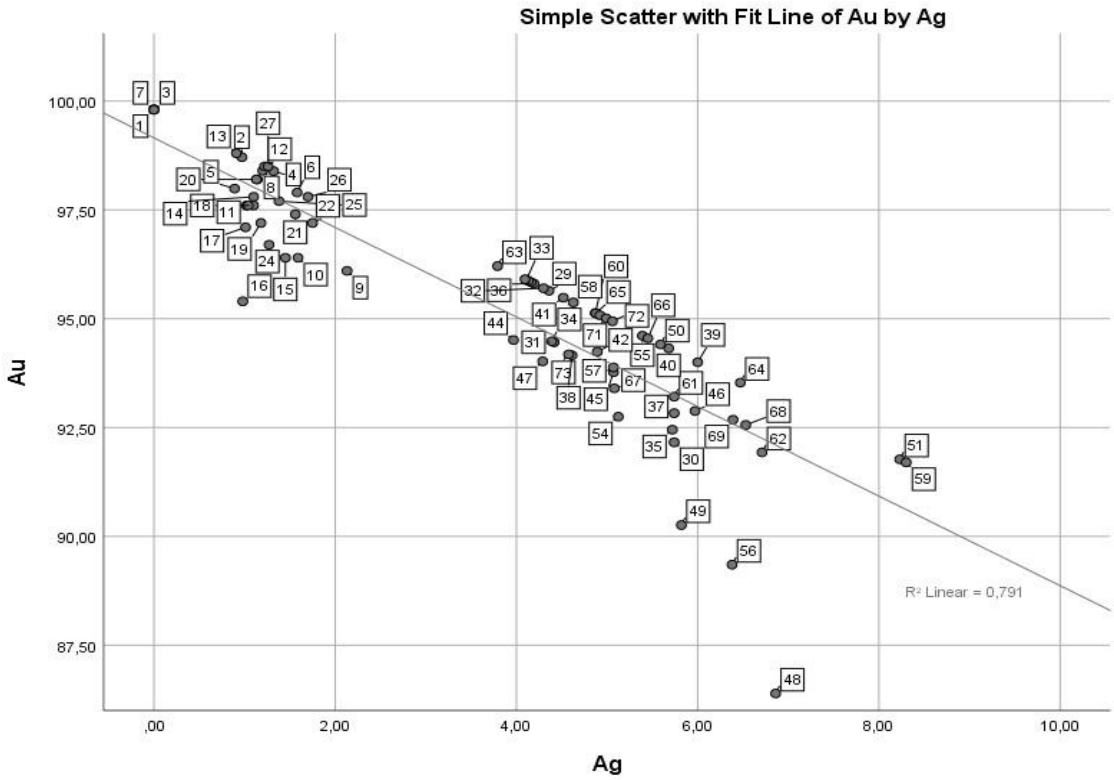

Figure 5. Scatter plot of Au and Ag (comparison of Romanus III coins with solidus samples of six emperors).

3.3. Comparison with the Hollow Coins of Four Byzantine Emperors

The Romanus III period coins examined within the scope of the study were also compared with the data of the Byzantine hollow coins (electrum) from Diyarbakır Museum, which were analyzed with the same p-XRF device by Ayhan (2021) [3]. In Ayhan's work, the hollow coins respectively belong to Constantine Ducas X (1059-1067), Romanus Diogenes IV (1068-1071), Michael Ducas VII (1071-1078) and John II (1118-1143) periods [3]. The distribution of gold, silver, copper and iron in the solidus samples of Romanus III together with the hollow coins of four Byzantine emperors is given in Figure 6. Considering the gold and silver contents, it can be deduced that the dominant gold amounts decreased significantly after Romanus III, which may indicate that the cost of precious metals in coins would have been reduced. It has been observed that the amount of silver and copper started to increase with the period of Constantine Ducas X (1059-1067), and the silver ratio increased significantly, especially in the period of Michael Ducas VII (1071-1078). In the samples of John II (1118-1143) period, it was seen that copper almost approached the level of silver

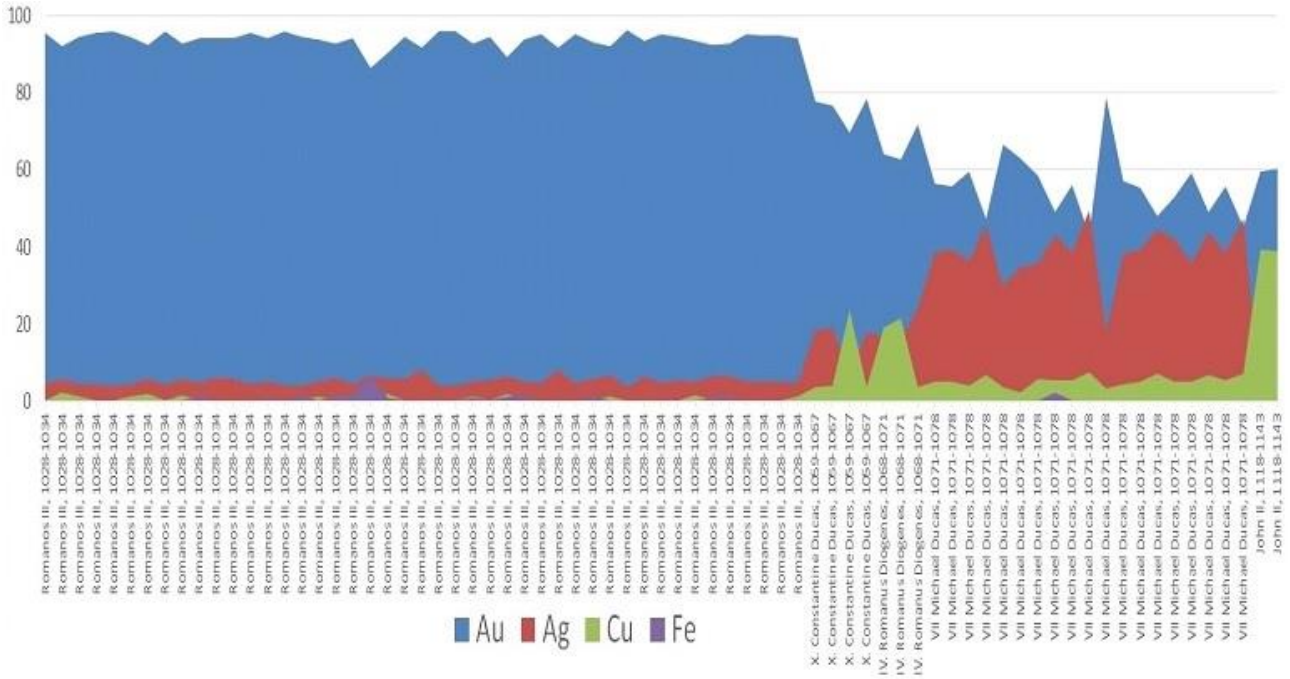

Figure 6. The distribution of gold, silver, copper and iron in the solidus samples of Romanus III, and the hollow coins of four Byzantine emperors.

In the comparison of the gold, silver and copper ratios in the Romanus III period coins with the hollow coins (Figure 7), it was observed that the coins of the same period mostly came together among themselves. This indicated that there were no significant changes in the coin production (in general) during the period of each emperor, but there were fluctuations in the use of precious metals as the emperor changed. The decrease in the amount of gold and the corresponding increase in the silver content in the coins caused a negative correlation (Figure 8) between these two precious metals. This may suggest a gold-silver alloy (electrum) in some examples.

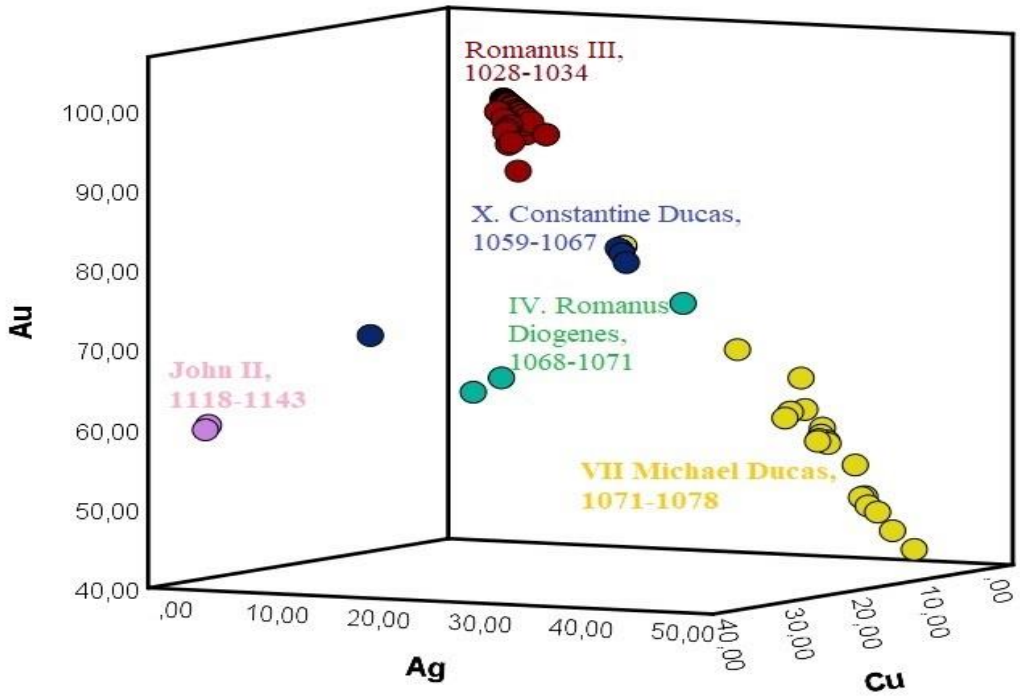

Figure 7. Distribution of Au, Ag and Cu in solidus coins of Romanus III, and the hollow coins.

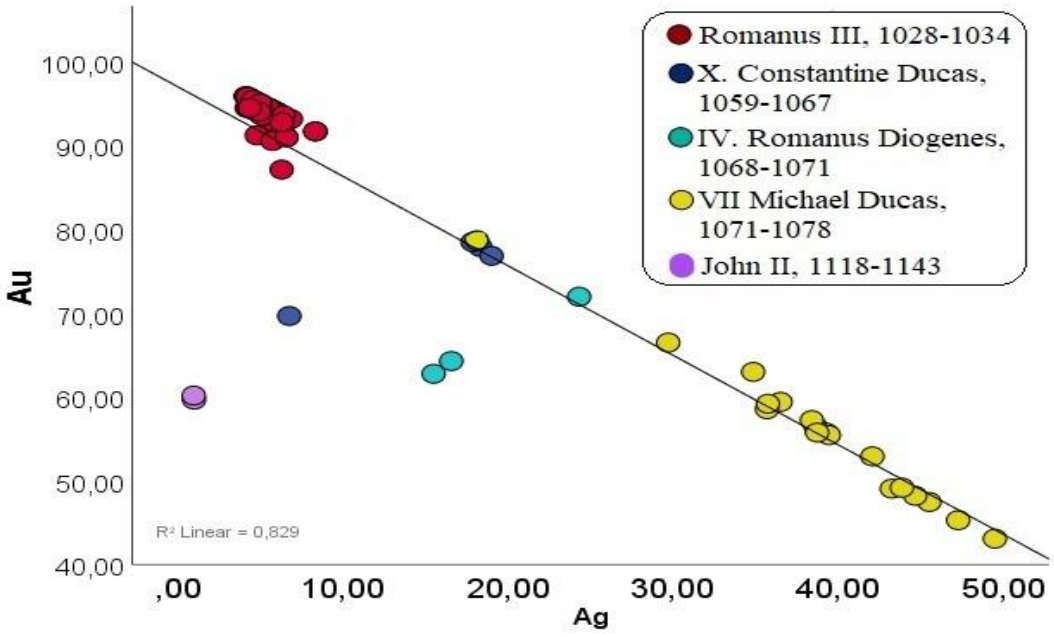

Figure 8. The correlation between gold and silver (Romanus III, and the hollow coins).

3.4. Comparison of All Solidus and Hollow Coins

When the gold-silver-copper distribution of solidus and hollow coins from different periods is examined, it could be seen that the solidus samples with high gold ratios are close together, and hollow coins with lower gold ratios and higher silver ratios come together within themselves (Figure 9; sample order: 1-3 Leo I; 4,5 Anastasius I; 6,7 Mauricius Tiberius; 8-13 Constans II; 14-20 Constantinus IV; 21-28 Iustinianus II; 29-73 Romanus III; 74-77 Constantine Ducas X; 78-80 Romanus Diogenes IV; 81-99

Michael Ducas VII; 100,101 John II). While the coins of the John II period (100-101 in Fig 9), which are the coins with the highest copper content, form a separate group, two hollow coins of Romanus Diogenes IV (78-79 in Figure 9), which also contain high copper, formed a different group due to its high silver content (please see the references [3], [10], [11], [12] for the details).

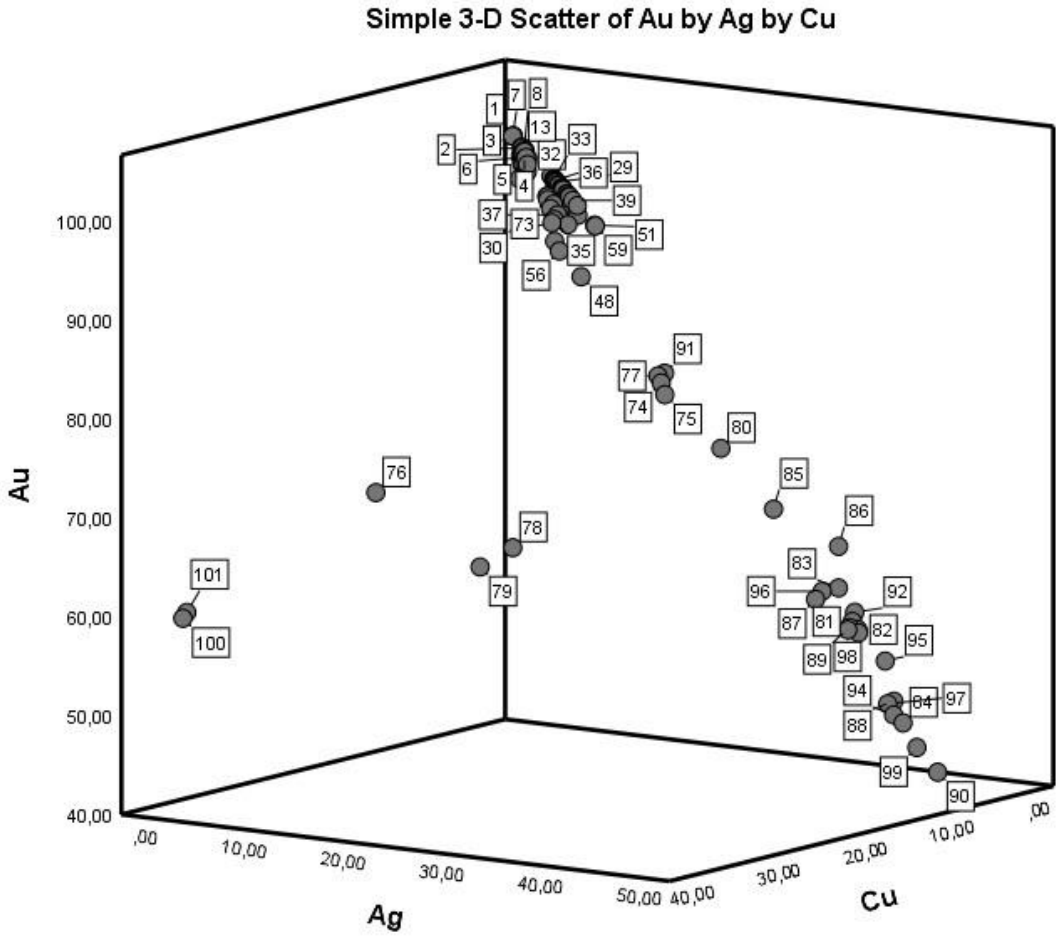

Figure 9. Au-Ag-Cu distribution in all solidus and hollow coins from different periods.

The data of all coins (Au, Ag, Cu, Fe) were subjected to hierarchical clustering analysis in order to make a classification. According to the results of the clustering analysis (Figure 10), the samples were generally divided into two groups and each group has two subgroups. All solidus coins and only four hollow coins (with a high gold rate) took place in Group-1. In Group-1a, there are solidus coins with a gold percentage over 95.36%, in Group-1b there are three Romanus Diogenes IV and one Michael Ducas VII hollow coins with a gold percentage above 70%. These data showed that the high gold ratio was effective in the formation of Group-1. The second group consists of hollow coins, which are outside of Group-1b. There are 18 hollow coins in total in the first subgroup (Group-2a) of the second group. The element averages of these coins are as follows; Au 54.35%, Ag 40.10%, Cu 5.38%. Only one of the hollow coins in Group-2a contains iron with a percentage of 2.34%. The second subgroup (Group-2b) of the second group consisted of 5 hollow coins, 1 of Constantine Ducas X, 2 of Romanus Diogenes IV and 2 of John II. The fact that the coins in Group-2b are the ones with the highest copper content showed that the most important factor in the formation of this group was the high copper ratio in the coins.

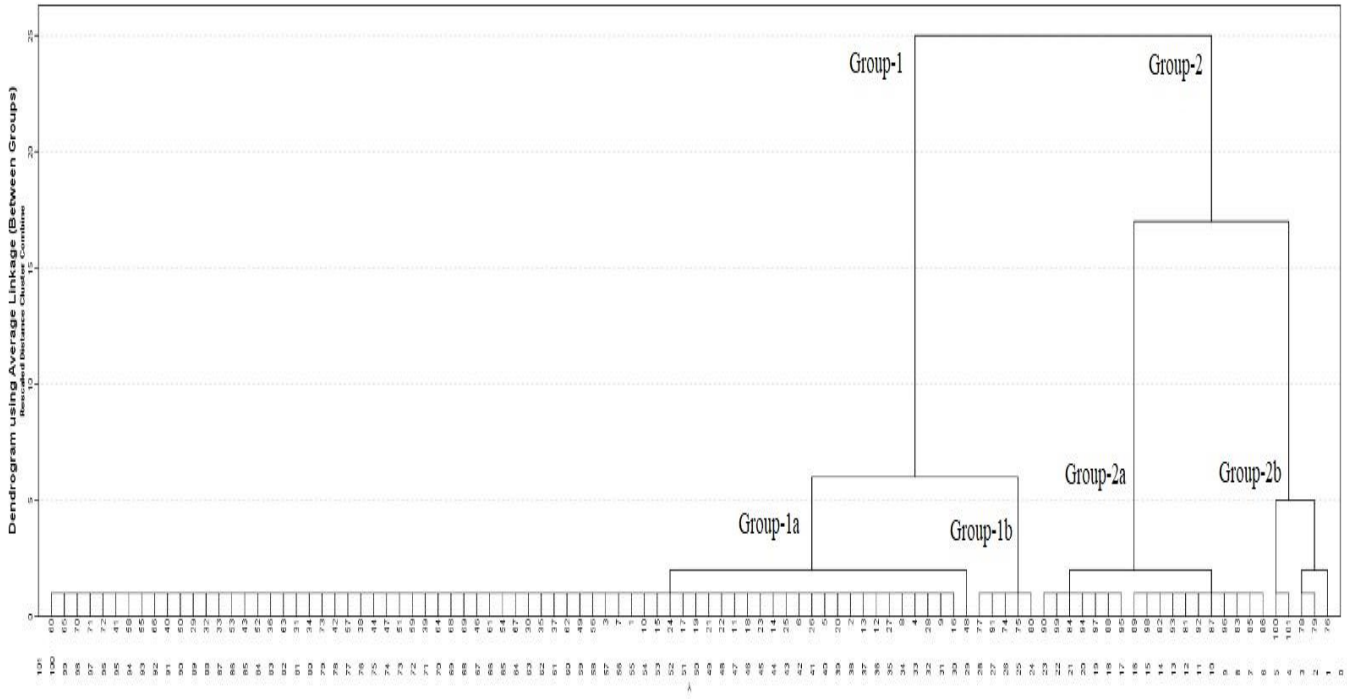

Figure 10. Dendrogram showing the groups identified by clustering analysis applied for all coins.

Finally, Table 2 shows the presence of gold-silver, gold-silver-copper, gold-silver-iron, gold-silver-copper-iron, gold-iron and gold-iron-copper for an overview in order to see the main elemental distribution comparatively in all of the samples. It can be seen that gold, silver, copper and iron are simultaneously present in most of the early samples (from Leo I to Iustinianus II). At the period of Romanus III, the solely existence of gold and silver is obvious, while the coexistence of iron and/or copper in such coins is limited. At the periods of Michael Ducas VII and John II, excluding only one sample, it can be observed that iron does not exist in the coins which are consisted of gold, silver and copper.

Table 2. Presence of Au, Ag, Cu, Fe in the solidus and hollow coins.

SPSS No	Emperor*	Au, Ag, Cu, Fe
1	Leo I (M.S. 457-474)	Au-Fe
2	Leo I (M.S. 457-474)	Au-Ag-Cu-Fe
3	Leo I (M.S. 457-474)	Au-Fe-Cu
4	Anastasius I (M.S. 491-518)	Au-Ag-Cu-Fe
5	Anastasius I (M.S. 491-518)	Au-Ag-Cu-Fe
6	Mauricius Tiberius (539-602)	Au-Ag-Cu-Fe
7	Mauricius Tiberius (539-602)	Au-Fe-Cu
8	Constans II (MS 641-668)	Au-Ag-Cu-Fe
9	Constans II (MS 641-668)	Au-Ag-Cu
10	Constans II (MS 641-668)	Au-Ag-Cu-Fe
11	Constans II (MS 641-668)	Au-Ag-Cu-Fe
12	Constans II (MS 641-668)	Au-Ag-Cu-Fe
13	Constans II (MS 641-668)	Au-Ag-Cu-Fe
14	Constantinus IV (MS 668-685)	Au-Ag-Cu-Fe

15	Constantinus IV (MS 668-685)	Au-Ag-Cu-Fe
16	Constantinus IV (MS 668-685)	Au-Ag-Fe
17	Constantinus IV (MS 668-685)	Au-Ag-Cu-Fe
18	Constantinus IV (MS 668-685)	Au-Ag-Cu-Fe
19	Constantinus IV (MS 668-685)	Au-Ag-Cu-Fe
20	Constantinus IV (MS 668-685)	Au-Ag-Cu-Fe
21	Iustinianus II (MS 685-695)	Au-Ag-Cu-Fe
22	Iustinianus II (MS 685-695)	Au-Ag-Cu-Fe
23	Iustinianus II (MS 685-695)	Au-Ag-Cu-Fe
24	Iustinianus II (MS 685-695)	Au-Ag-Cu-Fe
25	Iustinianus II (MS 685-695)	Au-Ag-Cu-Fe
26	Iustinianus II (MS 685-695)	Au-Ag-Cu-Fe
27	Iustinianus II (MS 685-695)	Au-Ag-Cu-Fe
28	Iustinianus II (MS 685-695)	Au-Ag-Cu-Fe
29	Romanus III (1028-1034)	Au-Ag
30	Romanus III (1028-1034)	Au-Ag-Cu
31	Romanus III (1028-1034)	Au-Ag-Cu
32	Romanus III (1028-1034)	Au-Ag
33	Romanus III (1028-1034)	Au-Ag
34	Romanus III (1028-1034)	Au-Ag-Cu
35	Romanus III (1028-1034)	Au-Ag-Cu
36	Romanus III (1028-1034)	Au-Ag
37	Romanus III (1028-1034)	Au-Ag-Cu
38	Romanus III (1028-1034)	Au-Ag-Fe
39	Romanus III (1028-1034)	Au-Ag
40	Romanus III (1028-1034)	Au-Ag

**Please see the references [3], [10], [11], [12] for the details.*

Table 2. Presence of Au, Ag, Cu, Fe in the solidus and hollow coins (continued).

SPSS No	**Emperor***	**Au, Ag, Cu, Fe**
41	Romanus III (1028-1034)	Au-Ag
42	Romanus III (1028-1034)	Au-Ag-Fe
43	Romanus III (1028-1034)	Au-Ag
44	Romanus III (1028-1034)	Au-Ag-Fe
45	Romanus III (1028-1034)	Au-Ag-Cu
46	Romanus III (1028-1034)	Au-Ag-Fe
47	Romanus III (1028-1034)	Au-Ag-Fe
48	Romanus III (1028-1034)	Au-Ag-Fe
49	Romanus III (1028-1034)	Au-Ag-Cu-Fe
50	Romanus III (1028-1034)	Au-Ag
51	Romanus III (1028-1034)	Au-Ag
52	Romanus III (1028-1034)	Au-Ag
53	Romanus III (1028-1034)	Au-Ag
54	Romanus III (1028-1034)	Au-Ag-Cu-Fe

55	Romanus III (1028-1034)	Au-Ag
56	Romanus III (1028-1034)	Au-Ag-Cu-Fe
57	Romanus III (1028-1034)	Au-Ag-Fe
58	Romanus III (1028-1034)	Au-Ag
59	Romanus III (1028-1034)	Au-Ag
60	Romanus III (1028-1034)	Au-Ag
61	Romanus III (1028-1034)	Au-Ag-Fe
62	Romanus III (1028-1034)	Au-Ag-Cu
63	Romanus III (1028-1034)	Au-Ag
64	Romanus III (1028-1034)	Au-Ag
65	Romanus III (1028-1034)	Au-Ag
66	Romanus III (1028-1034)	Au-Ag
67	Romanus III (1028-1034)	Au-Ag-Cu
68	Romanus III (1028-1034)	Au-Ag-Fe
69	Romanus III (1028-1034)	Au-Ag-Fe
70	Romanus III (1028-1034)	Au-Ag
71	Romanus III (1028-1034)	Au-Ag
72	Romanus III (1028-1034)	Au-Ag
73	Romanus III (1028-1034)	Au-Ag-Cu
74	Constantine Ducas X (1059-1067)	Au-Ag-Cu
75	Constantine Ducas X (1059-1067)	Au-Ag-Cu
76	Constantine Ducas X (1059-1067)	Au-Ag-Cu
77	Constantine Ducas X (1059-1067)	Au-Ag-Cu
78	Romanus Diogenes IV (1068-1071)	Au-Ag-Cu
79	Romanus Diogenes IV (1068-1071)	Au-Ag-Cu
80	Romanus Diogenes IV (1068-1071)	Au-Ag-Cu
81	Michael Ducas VII (1071-1078)	Au-Ag-Cu

**Please see the references [3], [10], [11], [12] for the details.*

Table 2. Presence of Au, Ag, Cu, Fe in the solidus and hollow coins (continued).

SPSS No	**Emperor***	**Au, Ag, Cu, Fe**
82	Michael Ducas VII (1071-1078)	Au-Ag-Cu
83	Michael Ducas VII (1071-1078)	Au-Ag-Cu
84	Michael Ducas VII (1071-1078)	Au-Ag-Cu
85	Michael Ducas VII (1071-1078)	Au-Ag-Cu
86	Michael Ducas VII (1071-1078)	Au-Ag-Cu
87	Michael Ducas VII (1071-1078)	Au-Ag-Cu
88	Michael Ducas VII (1071-1078)	Au-Ag-Cu-Fe
89	Michael Ducas VII (1071-1078)	Au-Ag-Cu
90	Michael Ducas VII (1071-1078)	Au-Ag-Cu
91	Michael Ducas VII (1071-1078)	Au-Ag-Cu
92	Michael Ducas VII (1071-1078)	Au-Ag-Cu
93	Michael Ducas VII (1071-1078)	Au-Ag-Cu
94	Michael Ducas VII (1071-1078)	Au-Ag-Cu
95	Michael Ducas VII (1071-1078)	Au-Ag-Cu
96	Michael Ducas VII (1071-1078)	Au-Ag-Cu

97	Michael Ducas VII (1071-1078)	Au-Ag-Cu
98	Michael Ducas VII (1071-1078)	Au-Ag-Cu
99	Michael Ducas VII (1071-1078)	Au-Ag-Cu
100	John II (1118-1143)	Au-Ag-Cu
101	John II (1118-1143)	Au-Ag-Cu

**Please see the references [3], [10], [11], [12] for the details.*

4. Conclusions

When all the coins in the study are evaluated from a numismatic point of view, it could be seen that the samples show the characteristics of the period they belong. As an example, it is possible to talk about the depiction of Jesus sitting on a throne with a backrest, which was first seen on Byzantine coins during the Romanus III period. In addition, the present research has provided a detailed archaeometric data basis for the coins. The results were initially evaluated for the Romanus III coins and then discussed with the other solidus and hollow coins in order to make a comparison in terms of chemical composition. The main element was gold detected as 93.89% in average, and silver was the most abundant element after gold, but the highest silver rate did not exceed 9% (5.25% in average). Copper and iron were identified respectively in 12 coins (Cu: 1.05-2.46%) and 18 coins (Fe: 0.87-6.5%). Manganese, nickel, titanium, lead, iridium and osmium were seen in one sample each. The ignorable amounts of these elements were attributed to possible contaminations on the coins' surfaces which may occur during the delivery of the coins to the museum.

Considering all the coins of the emperors who ruled in different periods, the highest gold content was seen in the Leo I period solidus with 99.81%, and the lowest in the Michael Ducas VII period hollow coin with 43.08%. While the gold average is 93.89% in the samples of Romanus III period, this rate is 97.82% in the solidus samples belonging to the pre-Romanus III period. The average value of gold is 59.95% for the hollow coins. While the highest silver rate with 47.28% is seen in the Michael Ducas VII period hollow coin, it is possible to show a total of three solidus samples, two of which belong to the Leo I period and one belonging to Mauricius Tiberius, as the lowest rate, in which no silver was found in the analysis. The negative correlation between gold and silver (in general) indicated that there were no significant changes in coin material in each emperor's own period, but there were fluctuations in the use of precious metals in coins, especially in hollow coins, as the emperor changed. In the comparison made between the coins of the Romanus III period (studied in the present research) and the coins of the other imperial periods, it should be noted that the samples belonging to the period of six emperors, who were on the throne between 457-695 AD, were composed of solidus, while the others were made of hollow coins.

In this archaeometric research, the portable XRF has been successfully applied on the gold coins as a non-destructive method which is also an in-situ analysis technique allowing the users to analyze the samples on-site. This kind of portable devices are frequently preferred for the artifacts in the museums and the immovable building materials such as stone, plaster, mortar and tile. It is predicted that the analytical data of the coins and use of p-XRF in this work would be a good reference for the further archaeometric investigations.

Acknowledgements

We gratefully thank the officials and staff of the Directorate of Diyarbakır Museum (Diyarbakır Governorship, Directorate of Provincial Culture and Tourism) for providing the required permissions and allowing us to work on the artifacts (Romanus III gold coins) registered in Diyarbakır Museum inventory, and also for their contributions during the analyses. We also thank Assoc. Prof. Dr. Mahmut Aydın (Batman University) for his support and assistance during the analyses and interpretation. This manuscript includes the data of the master thesis [10] submitted to the Department of Archaeometry at the Institute of Graduate Studies, Batman University (2022) by Nesrin Şeker.

Contributions of the Authors

Murat Bayazit; application of p-XRF analysis, statistical analyses, interpreting the results, editing. Nesrin Şeker; application of p-XRF analysis, interpreting the results.

Conflict of Interest Statement

There is no conflict of interest between the authors.

Statement of Research and Publication Ethics
The study is complied with research and publication ethics

References

[1] M. Bayazit, "Arkeometride seramik petrografi," *Batman Üniversitesi, Yaşam Bilimleri Dergisi,* Cilt: 7-Sayı: 2/2, pp. 36-44, 2017.

[2] M. Bayazit, "Archaeometric study of possible Ninevite-5 pottery from upper Tigris region using SEM-EDS, PEDXRF, and OM," *X-Ray Spectrometry*, vol. 47, no. 1, pp. 92-104, 2018.

[3] M.K. Ayhan, "Diyarbakır Müzesi'nde bulunan Bizans Dönemi altın çukur sikkelerin arkeometrik ve nümizmatik incelenmeleri," Yüksek Lisans Tezi, *Batman Üniversitesi Fen Bilimleri Enstitüsü*, Batman, pp. 69-84, 2021.

[4] O. Tekin, *Eskiçağda Para-Antik Nümismatiğe Giriş*, Eskiçağ Bilimleri Enstitüsü Yayınları, İstanbul, 1998.

[5] S. Atlan, *Grek Sikkeleri (Arkaik, Klasik, Hellenistik)*, Arkeoloji ve Sanat Yayınları, 1. Baskı, İstanbul, 1993.

[6] C. Eagleton, J. Williams, *Paranın Tarihi*, Türkiye İş Bankası Kültür Yayınları, İstanbul, 2011.

[7] I. Zonaras, *Tarihlerin Özeti*, çev. Bilge Umar, Arkeoloji ve Sanat Yayınları, İstanbul, 2008.

[8] Z. Gökalp Demirel, "Bolu Arkeoloji Müzesinde'ki Bizans Altın Sikkeleri," *Anadolu Üniversitesi Sosyal Bilimler Dergisi*, cilt: 11, sayı: 2, pp. 147-156, 2011.

[9] Diyarbakır Museum Directorate Archive, (Accessed in 2022).

[10] N. Şeker, "Diyarbakır Sur ilçesi kazılarında ele geçen Bizans Dönemi (III. Romanus) altın sikkelerin arkeometrik incelemesi," Yüksek Lisans Tezi, *Batman Üniversitesi, Lisansüstü Eğitim Enstitüsü, Arkeometri Anabilim Dalı*, 2022

[11] M. Aydın, S. Mutlu, "Bizans Dönemi'ne ait altın sikke orijinalliğinin tespitinde tahribatsız arkeometrik ve görsel analiz yöntemlerinin kullanılması," in *Türkiye'de Arkeometrinin Ulu Çınarları*, A.A. Akyol, K. Özdemir, Eds. Homer Kitapevi, İstanbul, 2012, pp. 97-106,

[12] M. Aydın, L. Zoroğlu, "Altın sikke orijinalliğinin P-XRF ile tespit çalışmaları," in *Kaunos/Kbid Toplantıları 3 Anadolu Nümismatik Araştırmaları Çalıştayı*, Z. Çizmeli Öğün, Ed. Anatolia/Anadolu Ek Dizi I.3 Supplement Series I.3, 2016, pp. 75-88.